Physics of the Solid State, Vol. 45, No. 8, 2003, pp. 1409–1414. Translated from Fizika Tverdogo Tela, Vol. 45, No. 8, 2003, pp. 1345–1350.

METALS AND SUPERCONDUCTORS

Palladium Isotope Separation under High Mechanical Stresses Induced in Pd Foils upon Loading with Deuterium

A. G. Lipson[1, 2], G. H. Miley[2], V. A. Kuznetsov[1], E. I. Saunin[1], and N. Asami[3]

[1] *Institute of Physical Chemistry, Russian Academy of Sciences, Leninskiĭ pr. 31, Moscow, 119915 Russia*
e-mail: tsiv@phyche.ac.ru

[2] *University of Illinois at Urbana-Champaign, Department of Nuclear, Plasma and Radiological Engineering, Urbana IL, 61801 USA*

[3] *Institute of Applied Energy, New Hydrogen Energy Laboratory, Sapporo 004, Japan*

Received December 16, 2002

Abstract—The effects of a significant decrease in the sputtering rate and of the symmetrical separation of the isotope pairs ^{108}Pd–^{105}Pd and ^{110}Pd–^{104}Pd at depths up to 500 Å are experimentally detected in Pd specimens saturated with deuterium during electrolysis (i.e., having a high concentration of internal stresses). These effects are shown to be qualitatively explained using the concepts of isotope separation by centrifugation and diffusion with allowance for defects and mechanical stresses that appear in the near-surface Pd layer during deuterium penetration. © *2003 MAIK "Nauka/Interperiodica".*

1. INTRODUCTION

The interaction of hydrogen (deuterium) with metallic Pd is known to cause the formation of PdH_x hydrides ($x \sim 0.7$), which is accompanied by the generation of numerous structural defects [1–3] and changes in the shape and linear sizes of specimens [4] and their electrophysical properties [5]. The hydrogenation of Pd leads to extremely high vacancy concentrations in specimens (more than 20% of their volume) [6]. The formation of $PdH_{0.7}$ hydrides in cold-rolled Pd foils is accompanied by the generation of dislocations with a density of 2×10^{11} cm^{-2} [4]. These structural changes during hydride formation in metallic Pd (internal loading) indicate the generation of giant mechanical micro- and macrostresses in the metallic crystal lattice, which are likely unachievable by the traditional methods of external mechanical loading of metals [7].

The generation of such high mechanical stresses in Pd during its hydrogenation should cause not only the activation of diffusion of defects and impurities but also the self-diffusion of Pd isotopes belonging to the metallic matrix. If the mobility of Pd atoms is sufficiently high, the mechanical stresses affecting them could result in the local separation of the matrix isotopes in the zones of stress concentration (dislocation loops, Frank–Read dislocation sources, vacancy aggregates, and so on). The authors of [8–11] detected significant deviations of isotope compositions from the stoichiometric values in the surface layers of semiconductors and metals with a high hydrogen affinity during ion bombardment. However, they did not relate the changes in the isotope compositions to the effect of surface mechanical stresses.

Lipson *et al.* [12] found that irradiation with an ultraweak flux of thermalized neutrons (UFTN) at a neutron concentration of ~10^{-3} cm^{-3} (flux $\Phi_n \sim 10^2$ neutrons/(s cm^2), energy $E_n \sim 60$ meV) noticeably increased the level of mechanical stresses in loaded crystals [13], in particular, in electrochemically saturated crystals with hydrogen [12]. Therefore, the application of an UFTN during electrochemical loading of Pd can increase the mechanical stresses and favor isotope separation in it.

The purpose of this work is to experimentally observe the effect of Pd isotope separation under high mechanical stresses generated during saturation of Pd with hydrogen. In some cases, the stresses are enhanced by the irradiation of specimens with an UFTN.

2. EXPERIMENTAL

To analyze the isotope composition of Pd specimens, we used secondary-ion mass spectrometry (SIMS). A CAMECA IMS 5f device in the high-resolution mode (1 : 20 000) allowed us to reliably select all Pd isotopes (102–110) and separate them from the hydrides (deuterides) that correspond to these isotopes, have similar masses, and enter into the composition of the secondary-ion beam. Using SIMS, we could also obtain Pd isotope depth profiles (to a depth of 0–0.16 μm) and determine the sputtering-rate depth profiles. The typical etching rate was 4.1 Å/s at a primary-ion beam current of 10 nA (O^{2+} ions with an energy of $E = 8.0$ keV). The error in SIMS measurement of the Pd isotope concentration at a depth $h > 100$ Å was less than 1 at. %. The error for surface layers of thicknesses comparable to the roughness of specimens (<100 Å) is

1063-7834/03/4508-1409$24.00

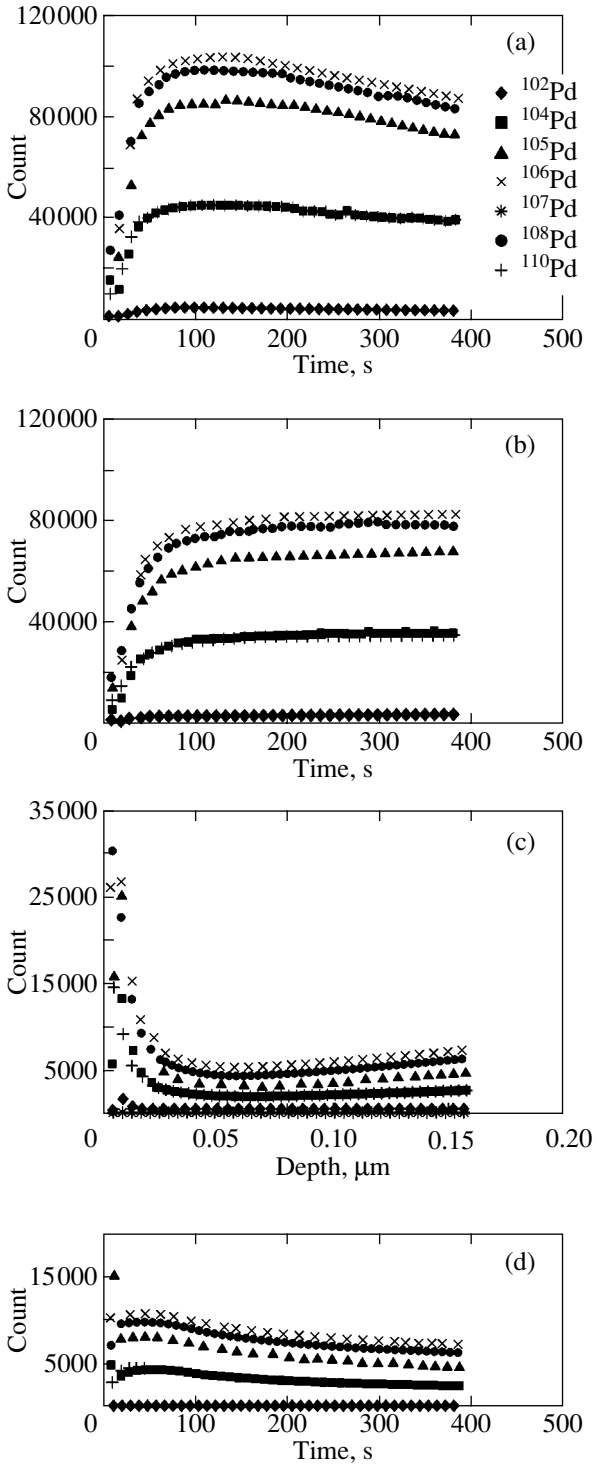

Fig. 1. Depth profiles (in the range 0–0.16 μm) of the intensities of Pd specimen sputtering according to the SIMS data: (a) initial specimens; (b) specimens subjected to electrolysis for three days under the conditions of a natural neutron background; (c) specimens subjected to electrolysis and, simultaneously, to UFTN irradiation at Φ_n = 200 neutrons/(s cm^2) for three days; and (d) the same specimens as in (c) but after additional vacuum annealing (p = 10^{-10} Torr) at T = 800°C.

slightly higher (~3.0%) because of the deterioration of the SIMS spatial resolution.

For investigation, we used cold-rolled Pd (99.99% purity) foils 100 μm thick. Specimens 5 × 2 cm in size cut from one Pd sheet were subjected to electrolysis in a 1 M NaOD solution in a cell with separated anode and cathode spaces at an electrolysis current density of I_e = 30 mA/cm^2 for 1–3 days at room temperature. The composition of the final deuteride PdD_x obtained after the completion of electrolysis was determined using thermal desorption [5] and varied in the range $0.72 < x < 0.80$. In special experiments, we irradiated the specimens with an UFTN at a flux energy of E_n = 60 meV and a flux density of Φ_n = 200 neutrons/(s cm^2) during electrolysis. We used a ^{252}Cf neutron source with an intensity of $I_n = 2.0 \times 10^4$ neutrons/s in 4π steradians surrounded by a large mass of moderator (PE(Co)); the technique used is described in detail in [12, 13].

After the completion of electrolysis, we measured the macroscopic buckling l of a specimen and the residual plastic strain ε_p [12]. For electrolysis under the conditions of a natural neutron background, the average values of these parameters were found to be $\langle l \rangle$ = 1.5 cm and $\langle \varepsilon_p \rangle = 3.0 \times 10^{-3}$. For electrolysis in the presence of the UFTN, these deformation characteristics were much higher: $\langle l_n \rangle$ = 5.0 cm and $\langle \varepsilon_{pn} \rangle = 1.3 \times 10^{-2}$.

Samples 10 × 10 mm in size were cut from the samples after deuteration and were analyzed using SIMS. The spot area of the primary SIMS beam was 100 × 100 μm^2. Five spots per sample were analyzed. To reveal the effect of mechanical stresses on the isotope distribution, the samples saturated with deuterium and analyzed by SIMS were annealed in high vacuum (p = 10^{-10} Torr) at T = 800°C for 5 h and them slowly cooled at a rate of ~0.2 K/min.

3. EXPERIMENTAL RESULTS AND DISCUSSION

Figures 1a–1d show the data on the rate of Pd specimen sputtering. It is seen that the character of Pd sputtering at depths 0–0.16 μm from the surfaces of the initial specimens (not subjected to deuteration and annealing) differs only insignificantly from that for the specimens saturated with deuterium under the conditions of a natural neutron background (Figs. 1a, 1b). The sputtering rate of the specimens with deuterium is 20% lower than that of the initial ones (on the average over all isotopes, ^{102}Pd–^{110}Pd). However, the rate and character of sputtering of the specimen subjected to electrolysis during the UFTN irradiation, i.e., more severely strained (Fig. 1c), sharply differ from those of the initial specimen (Fig. 1a). For example, at a depth of ~500 Å, the sputtering rate of Pd isotopes in the specimen represented in Fig. 1c is, on the average, 20 times lower than that in the initial one. At depths h < 100 Å, the sputtering rates of these specimens become equal.

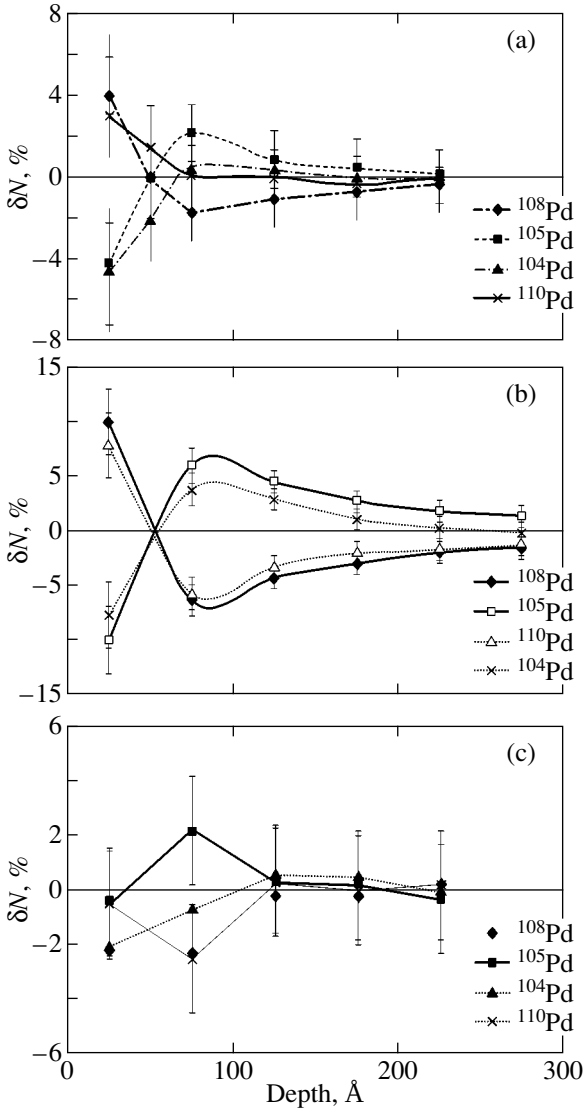

Fig. 2. Depth profiles of the concentration δN of the matrix isotopes ^{104}Pd, ^{105}Pd, ^{108}Pd, and ^{110}Pd from which the similar data for the initial specimen (not subjected to electrolysis) are subtracted: (a) specimen subjected to electrolysis for three days under the conditions of a natural neutron background; (b) specimen subjected to electrolysis and, simultaneously, to UFTN irradiation for three days; and (c) the same specimen as in (b) but after additional annealing at T = 800°C.

After annealing of the specimen represented in Fig. 1c, its sputtering rate increases (Fig. 1d) and becomes close to that of the initial sample (Fig. 1a). Thus, the deuteration of the Pd specimens through electrolysis results in a sharp change in their sputtering rate, which is likely due to the different mechanical properties of the near-surface layers of the initial (annealed) specimens and the specimens with deuteration-induced structural defects.

Measurements of the Pd isotope depth profiles showed that the concentrations of ^{104}Pd, ^{105}Pd, ^{108}Pd, and ^{110}Pd isotopes considerably deviate from stoichiometry (natural isotopic composition) in the specimens subjected to deuteration (Figs. 1b, 1c) and, hence, having residual deformation in a thin surface layer up to 500 Å thick. However, the changes in the concentrations of ^{102}Pd, ^{106}Pd, and ^{107}Pd isotopes are insignificant.

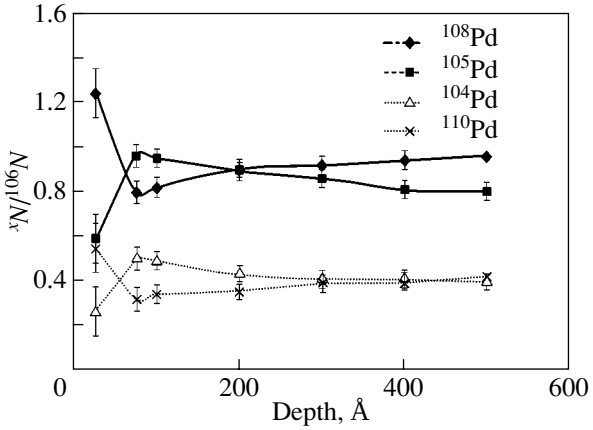

Fig. 3. Concentrations ^{x}N of Pd isotopes at x = 104, 105, 108, and 110 for the specimen of Fig. 2b normalized to the corresponding concentration of the ^{106}Pd isotope ^{106}N. The natural concentrations of the ^{104}Pd, ^{105}Pd, ^{108}Pd, and ^{110}Pd isotopes normalized to the natural concentration of the ^{106}Pd isotope are indicated in the ordinate on the right.

Figures 2a–2c show the concentration depth profiles of the ^{104}Pd, ^{105}Pd, ^{108}Pd, and ^{110}Pd isotopes from which the depth profiles for the initial specimen (not subjected to electrolysis and/or annealing) are subtracted. As is seen from Fig. 2a, the separation of the ^{108}Pd–^{105}Pd and ^{110}Pd–^{104}Pd isotope pairs in the 200-Å-thick surface layer in the specimen subjected to electrolysis under the conditions of a natural neutron background is statistically insufficient. A layer with h < 50 Å is enriched in the heavy (108, 110) isotopes and depleted of the light (104, 105) isotopes. At h > 50 Å, the isotope composition is inverted, so that the layer is enriched in the light isotopes and depleted of the heavy ones. At h > 200 Å, no isotope separation is observed. The isotope separation in the specimen subjected to electrolysis during the UFTN irradiation is more pronounced and statistically significant (Figs. 2b, 3). The degree of enrichment in the heavy isotopes (and of depletion of the light ones) in a near-surface layer at h < 50 Å reaches 10–12%. The depth profiles of the heavy (108, 110) and light (105, 104) isotopes are completely symmetrical. Figure 3 shows the isotope separation in more detail: the data for the ^{104}Pd, ^{105}Pd, ^{108}Pd, and ^{110}Pd isotopes are normalized to the ^{106}Pd isotope concentration, which virtually does not vary with depth. As is seen from Fig. 3, the symmetry of separation is pronounced for the ^{108}Pd–^{105}Pd and ^{110}Pd–^{104}Pd pairs. The depth at which the separation of the ^{108}Pd–^{105}Pd pair is noticeable is greater

(400–500 Å) than that for the ^{110}Pd–^{104}Pd pair (200–250 Å).

The separation of the Pd isotopes in near-surface layers (Figs. 2a, 2b) fully disappears after vacuum annealing (Fig. 2c), i.e., after the internal stresses are relieved. As follows from Fig. 2c, the specimen represented in Fig. 2b exhibits no statistically important differences δN and no separation into heavy and light isotopes over the whole depth range after annealing.

Thus, we have found that cold-rolled Pd foils subjected to electrochemical loading with deuterium (which causes significant mechanical deformation) exhibit a decrease in the rate of surface atom sputtering (Figs. 1b, 1c) and symmetrical separation of the ^{108}Pd–^{105}Pd and ^{110}Pd–^{104}Pd isotope pairs at depths of up to 500 Å. These specific features disappear after vacuum annealing, which relieves internal stresses.

Let us consider possible causes of these effects.

As noted above, the hydrogenation of the Pd specimens leads to high internal stresses generating numerous structural defects: vacancies, dislocations, low-angle tilt boundaries, grain boundaries, etc. Therefore, the internal mechanical stresses are most likely responsible for the effects under study in the specimens subjected to electrochemical saturation with deuterium.

Indeed, the decrease in the rate of Pd specimen sputtering as the level of deformation increases (Figs. 1a–1d) could be related to an increase in the vacancy concentration in near-surface layers. However, it is unlikely that the vacancy concentration in the deformed specimens can rise by 20 times. To find the cause of the sharp decrease in the sputtering rate of deformed PdD_x specimens, we consider the basic SIMS equation as applied to the yield of secondary Pd ions $Y_t(E_p)$ [14]:

$$Y_t(E_p) = \frac{3}{4\pi^2 C_0}\frac{\alpha S_n(E_p)}{U_s}(\cos\psi)^{-f}, \qquad (1)$$

where $E_p = 8$ keV is the energy of the incident (primary) O^{2+} ions, C_0 is the scattering constant for primary ions, $U_s = 3.9$ eV is the surface binding energy of Pd ions, α is a dimensionless constant depending on the ratio of the masses of a target atom (M_{2q}) and a primary-beam particle (M_1), $S_n(E_p)$ is the nuclear stopping cross section of the target (Pd) (depending on the concentration of the target nuclei), ψ is the angle of incidence of the primary beam measured from the normal to the surface, and $f = 5/3$ for $M_2/M_1 \approx 3$ [15].

As follows from Eq. (1), the yield Y_t of secondary ions from Pd targets in different states under the same conditions of the primary beam depends only on U_s, $S_n(E)$, and $\cos\psi$. The value of U_s can vary only insignificantly (within 20% in the presence of deformation). At the same time, at low energies of the primary beam and under severe deformation, the quantity $S_n(E)$ can vary such that most of the energy loss of the primary beam is redistributed toward the electron $S_e(E)$ and/or phonon $S_{ph}(E)$ components of $S(E)$ because of an increase in the cross section of inelastic beam scattering in a layer with severe plastic deformation [14, 15]. In this case, the total stopping cross section $S(E) = S_n(E) + S_e(E) + S_{ph}(E)$ remains virtually constant, whereas the energy loss of the primary beam shifts toward inelastic processes described by the quantities $S_e(E)$ and $S_{ph}(E)$. Whence it follows that the nuclear stopping cross section in a plastically deformed layer with a high defect concentration can significantly decrease during strongly inelastic scattering. Therefore, a decrease in $S_n(E)$ should be taken into account in severely deformed specimens.

However, in the presence of internal stresses and significant surface roughness, the yield of secondary ions can be most strongly affected by variations in the angle of incidence ψ of the primary beam with respect to the crystallographic planes at the surface of the specimen. In the presence of a large number of point defects and dislocations in the surface layer of a specimen subjected to deuteration (deformation) and having high roughness as compared to the initial specimen, the orientation of the crystallographic planes in the surface layer and, hence, the angle ψ can vary, which would cause a strong decrease in the yield Y_t compared to the yield in the initial (undeformed) specimen.

Thus, the decrease in the yield of the secondary ions of the palladium matrix in a deformed specimen (subjected to electrolysis) can be due both to a decrease in the elastic scattering cross section of the primary beam and to the surface roughness caused by supersaturation of the surface layer with defects and resulting in a change in the effective angle between the beam and the specimen surface. It should be noted, however, that none of the factors affecting Eq. (1) can even qualitatively explain the experimentally observed separation of the palladium isotopes in a thin surface layer (Figs. 2, 3).

We consider possible models for isotope separation in deformed (deuterated) Pd foils on the example of a specimen irradiated with an UFTN during electrolysis (Fig. 1c). Assuming that, on average, the ^{108}Pd concentration decreases by 5% and the ^{105}Pd concentration increases by 5% (for the ^{110}Pd–^{104}Pd pair, on average, the corresponding change is 4%) at a depth of $h >$ 100 Å, we calculate the total enrichment factors for them [16]:

$$A = \frac{N_F/(1-N_F)}{N_I/(1-N_I)}, \qquad (2)$$

where $\langle N_F\rangle = 0.265$ is the average ^{105}Pd concentration and $\langle N_I\rangle = 0.225$ is the average ^{108}Pd concentration. Thus, we have $A_1 = 1.24$. Similarly, for the ^{110}Pd–^{104}Pd pair, we have $A_2 = 2.55$. We apply the diffusion model of Pd isotope separation; that is, we assume that the Pd isotopes diffuse through vacancy layers during self-diffusion (by analogy with gaseous-diffusion separation,

where isotopes go through a porous material in their gaseous state). Here, we assume that the mobility of the palladium isotopes in a defect surface layer with a high vacancy concentration is very high in comparison with their mobility in the bulk of the specimen. In this case, the self-diffusion activation energy of palladium atoms significantly decreases [1, 17] and, their mean free path increases to a length exceeding the lattice parameter. The heavy isotopes (108, 110) will be entrapped by vacancies in the Pd crystal lattice in a near-surface layer of the specimen, whereas the light isotopes (104, 105) will retain their high mobility and diffuse to the surface. As a result, near-surface layers at $h > 50$ Å become enriched in the light isotopes and depleted of the heavy ones. In this case, according to Eq. (1), the sputtering rate of the light isotopes is higher than that of the heavy ones, since the binding energy U_s of the light (mobile) isotopes is lower than that of the heavy (entrapped by vacancies) isotopes, all other things being equal. Therefore, the SIMS yield of the light Pd isotopes is also higher.

Based on the model considered, we calculate the minimum thickness of the surface layer required for isotope diffusion separation. Taking into account that the isotope separation factor for diffusion is $\alpha = (M_2/M_1)^{1/2}$, where M_2 and M_1 are the masses of the heavy and light isotopes, respectively, we obtain $\alpha_1 = 1.0142$ and $\alpha_2 = 1.0284$ for the ^{108}Pd–^{105}Pd and ^{110}Pd–^{104}Pd pairs, respectively. Since the total enrichment factor and the separation factor for a single event are interrelated as $A = \alpha^s$ (where s is the number of separation stages) [16], the numbers of stages needed are $s_1 = 16$ and $s_2 = 33$, respectively. Assuming that the minimum spacing between vacancies is equal to the Pd lattice parameter ($a_0 = 3.89$ Å), it can be shown that the thickness of the layer required for diffusion separation is $R \sim 2a_0 s$. Therefore, $R_1 = 117$ Å and $R_2 = 257$ Å. It follows that, in order to provide the experimentally observed isotope separation during self-diffusion of Pd atoms, the atoms have to move a minimum distance $120 < R < 260$ Å from the bulk toward the surface.

A different situation arises in a layer at $h < 50$ Å, in the immediate vicinity of the specimen–vacuum interface. As follows from Fig. 2b, the isotope separation changes sign, so that the heavy isotopes enrich the surface. The degree of separation immediately at the surface is much higher than in a layer at $h > 100$ Å, and the total enrichment factors for the ^{108}Pd–^{105}Pd and ^{110}Pd–^{104}Pd pairs are $A_1 = 3.05$ and $A_2 = 4.55$, respectively. Within the framework of the diffusion model, such high values of A require the numbers of separation stages to be $s_1 = 80$ and $s_2 = 54$, respectively, or the minimum depths of diffusion layers, $R_1 = 620$ Å and $R_2 = 420$ Å. In our case, however, the maximum depth of the surface layer enriched in the heavy Pd isotopes and depleted of the light isotopes does not exceed 50 Å (Fig. 2b), which means that the diffusion model is inapplicable here. Therefore, we have to assume that other, more efficient mechanisms of isotope separation operate in the surface layer. Such mechanisms can be associated with screw dislocations, dislocation loops (Frank–Read dislocation sources), or spiral steps forming at the intersection points of screw dislocations with the surface [7]. If the linear defects, in which mass transfer (motion of Pd atoms) occurs, rotate at a velocity close to the sound velocity in Pd, then these sources can serve as efficient "nanocentrifuges," in which isotope separation proceeds. Indeed, the separation factor for a single event α in this case is defined as [16]

$$\alpha = \exp\left[\frac{(M_2 - M_1)v_s^2}{2RT}\right], \quad (3)$$

where v_s is the rotational velocity of the source, which is taken to be half the sound velocity v_0; R is the gas constant; and T is the source temperature. According to Eq. (3), we have $\alpha = 2.60$ for the ^{108}Pd–^{105}Pd pair and $\alpha = 6.50$ for the ^{110}Pd–^{104}Pd pair. As follows from the relation $A = \alpha^s$, isotope separation during centrifugation is rather efficient and can be accomplished in one stage ($s \le 1$) in a layer at $h < 50$ Å. Note that, during isotope centrifugal separation, the heavy isotopes move toward the periphery of a source (unlike the diffusion separation), whereas the light isotopes remain left in place (i.e., entrapped by dislocations). Therefore, the result will be opposite to that for the method of diffusion separation: the surface will be enriched in the heavy (movable) Pd isotopes and depleted of the light Pd isotopes (bound to dislocation cores).

For deeper insight into the mechanisms of Pd isotope separation under the effect of high internal stresses, further experimental and theoretical investigations are needed.

It should be noted that the effects of isotope separation detected in this study can be much more pronounced and occur at a larger depth for a low amount of impurities in Pd [15]. Since impurities tend to segregate only in the regions of concentrated internal stresses, the isotope separation models described above are most applicable to impurity atoms diffusing in the Pd matrix.

Moreover, the results obtained (in particular, the decrease in the sputtering rate of the Pd matrix in specimens with a high defect concentration) indicate that the application of SIMS can give substantial errors in determining the concentration and isotopic shifts of impurity atoms. This circumstance can shed light on the problem of the so-called "transmutations" in electrochemical experiments upon saturation of palladium with heavy hydrogen isotopes [18, 19]. The results obtained in this study allow one to conclude that the isotopic shifts and changes in the concentrations of most elements can be satisfactorily interpreted using the concepts of isotope separation in palladium under the action of high internal stresses stimulated by the interaction of palladium with hydrogen (deuterium).

It should also be noted that errors in determining the impurity concentrations and isotopic shifts can appear not only when using SIMS but neutron activation analysis as well. Within the model considered, the cross section of the interaction between thermal neutrons and nuclei localized in regions of concentrated internal stresses can be several orders of magnitude larger, as was shown in [20]. This effect may cause overestimation of the concentration of a particular isotope localized in these regions.

REFERENCES

1. *Hydrogen in Metals*, Ed. by G. Alefeld and J. Voekl (Springer, New York, 1978; Mir, Moscow, 1981), Vol. 2, Top. Appl. Phys. **29**.
2. L. Schlapbach, I. Anderson, and J. P. Burger, in *Materials Science and Technology*, Ed. by K. H. Jurgen Buschow (Weinheim, New York, 1994), Vol. 3B, Part 2, p. 287.
3. B. J. Heuser and J. S. King, J. Alloys Compd. **261**, 225 (1997).
4. J. N. Han, J. W. Lee, M. Seo, and S. I. Pyun, J. Electroanal. Chem. **506**, 1 (2001).
5. A. G. Lipson, B. F. Lyakhov, D. M. Sakov, and V. A. Kuznetsov, Fiz. Tverd. Tela (St. Petersburg) **39** (12), 2113 (1997) [Phys. Solid State **39**, 1891 (1997)].
6. Y. Fukai and N. Okuma, Phys. Rev. Lett. **73**, 1640 (1994).
7. P. I. Polukhin, S. S. Gorelik, and V. K. Vorontsov, *Physical Fundamentals of Plastic Deformation* (Metallurgiya, Moscow, 1982).
8. H. Yamazaki, Nucl. Instrum. Methods Phys. Res. B **134**, 121 (1998).
9. P. C. Zalm, Rep. Prog. Phys. **58**, 1321 (1995).
10. I. P. Chernov, N. N. Nikitenkov, M. Krening, *et al.*, Izv. Ross. Akad. Nauk, Ser. Fiz. **64** (11), 2181 (2000).
11. L. N. Puchkareva, I. P. Chernov, and N. N. Nikitenkov, Izv. Ross. Akad. Nauk, Ser. Fiz. **66** (8), 1219 (2002).
12. A. G. Lipson, I. I. Bardyshev, V. A. Kuznetsov, and B. F. Lyakhov, Fiz. Tverd. Tela (St. Petersburg) **40** (2), 254 (1998) [Phys. Solid State **40**, 229 (1998)].
13. A. G. Lipson, D. M. Sakov, V. I. Savenko, and E. I. Saunin, Pis'ma Zh. Éksp. Teor. Fiz. **70** (2), 118 (1999) [JETP Lett. **70**, 123 (1999)].
14. A. Benninghover, F. G. Rudenauer, and H. W. Werner, *Secondary Ion Mass Spectrometry. Basic Consepts, Instrumental Aspects, Application and Trends* (Wiley, New York, 1987).
15. R. G. Wilson, F. A. Stevie, and L. W. Magee, *Secondary Ion Mass Spectrometry. A Practical Handbook for Depth Profiling and Bulk Impurity Analysis* (Wiley, New York, 1989).
16. J. Kaplan, *Nuclear Physics* (Addison-Wesley, Cambridge, Mass., 1955).
17. Y. Fukai and H. Sugimoto, Adv. Phys. **34**, 263 (1985).
18. Y. Iwamura, N. Gotoh, T. Itoh, and I. Toyoda, Fusion Technol. **33** (4), 476 (1998).
19. T. Mizuno *et al.*, Electrochemistry **64** (11), 1160 (1996).
20. A. G. Lipson, D. M. Sakov, and E. I. Saunin, Pis'ma Zh. Éksp. Teor. Fiz. **62** (10), 805 (1995) [JETP Lett. **62**, 828 (1995)].

Translated by K. Shakhlevich

Physics of the Solid State, Vol. 45, No. 8, 2003, pp. 1415–1422. Translated from Fizika Tverdogo Tela, Vol. 45, No. 8, 2003, pp. 1351–1357.

METALS AND SUPERCONDUCTORS

Generalization of Luttinger's Theorem for Strongly Correlated Electron Systems

M. M. Korshunov and S. G. Ovchinnikov

Kirensky Institute of Physics, Siberian Division, Russian Academy of Sciences, Akademgorodok, Krasnoyarsk, 660036 Russia

e-mail: mkor@iph.krasn.ru; sgo@iph.krasn.ru

Received October 4, 2002; in final form, January 16, 2003

Abstract—By on the analyzing the general structure of the Green function of a strongly correlated electron system, it is shown that, for the regime of strong correlations, Luttinger's theorem should be generalized in the following way: the volume of the Fermi surface of the system of noninteracting particles is equal to that of the quasiparticles in the strongly correlated system with due regard for the spectral weight of the quasiparticles. An investigation of the *t–J* model and of the Hubbard model, as applied to the paramagnetic nonsuperconducting phase, shows that the generalized Luttinger theorem is valid for these models. © *2003 MAIK "Nauka/Interperiodica".*

1. INTRODUCTION

At present, it is widely believed that Luttinger's theorem [1] is violated for strongly correlated systems, among which is, in particular, the broad class of superconducting cuprates. This theorem states that the volume of the Fermi surface of interacting particles is equal to that of the noninteracting particles. The proof of Luttinger's theorem [1] is valid for the normal Fermi liquid only. A topological proof of the theorem for strongly correlated electron systems (without resort to perturbation theory) was given in [2] on the assumption that these systems are normal Fermi liquids. Since the proof given in [2] is based on general considerations, it is valid for the *t–J* model and the Hubbard model as applied to the Fermi-liquid phase. In the strongly correlated electron system, however, other phases can also exist, whose properties differ from those of the Fermi liquid. Deviations from the Fermi-liquid behavior reveal themselves in the redistribution of the spectral weight of a quasiparticle between different Hubbard subbands and in the fact that the imaginary part of the self-energy $\mathrm{Im}\Sigma_k(E)$ is nonzero on the Fermi surface. Indeed, the relationship $\mathrm{Im}\Sigma_k(E) \sim (E - \varepsilon_F)^2$ is valid in the vicinity of the Fermi level ε_F of the Fermi liquid.

Calculations carried out for the Hubbard model in the dynamical mean-field theory, which is exact in the limit of infinite dimensionality ($d = \infty$) [3–5], demonstrated that the distribution function of the quasiparticles has a jump in the vicinity of the Fermi level. This jump continuously decreases down to zero with increasing the parameter of the on-site Coulomb repulsion U. Nevertheless, the Fermi-liquid pattern persist up to a certain critical value U_c in this case, after which the system transfers to the insulating state. Edwards and Hertz [6], however, demonstrated (using an interpolation scheme for the Hubbard model not based on the limit $d = \infty$) that the imaginary part of the self-energy is nonzero on the Fermi surface at $U \sim U_c$ and near the half-filling ($x \ll 1$, where $n = 1 - x$ is the electron concentration). But with a deviation from the half-filling, the Fermi-liquid properties of the system are restored fairly rapidly. That the Fermi liquid properties in the Hubbard model with $U = 8t$ (t is the hopping integral) begin to be restored already at $x > 0.1$ was shown in [7] in the framework of the dynamical cluster approximation without resorting to perturbation theory. At present, the problem of the transition from the Fermi liquid phase to a metallic non-Fermi-liquid state with strong electron correlations (and of the behavior of the system in the transition range) has only been stated and is far from being solved (see, for example, [8]).

The most interesting range is $x \ll 1$, because in real materials the transition to the metal state is observed in this range. At extremely small values of x, it would be expected that the additional carriers will be localized in the vicinity of the bottom of the band and the condition $\mathrm{Im}\Sigma_k(\varepsilon_F) \neq 0$ will be valid for them. As x increases further, however, the Fermi level falls within the range of delocalized states, for which the imaginary part of the self-energy is equal to zero, but the non-Fermi-liquid effects are still present due to redistribution of the spectral weight between the Hubbard subbands. Deviations from Luttinger's theorem for the Hubbard model in the region where $\mathrm{Im}\Sigma_k(\varepsilon_F) \neq 0$ were discussed in [9] in the framework of the FLEX approximation. In this paper, we restrict ourselves to the concentration range over which $\mathrm{Im}\Sigma_k(\varepsilon_F) = 0$.

As for the case when the spectral weight of a quasiparticle in a strongly correlated electron system is not equal to unity, the properties of the system are different

1063-7834/03/4508-1415$24.00

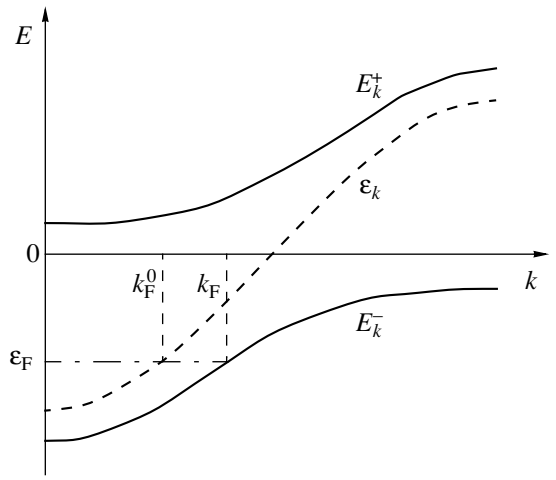

Fig. 1. Dispersion law of the Hubbard bands $E_k^{\pm}$ and of the one-particle spectrum ε_k. ε_F is the Fermi level, and k_F and k_F^0 are the Fermi momenta for the Hubbard bands and free electrons, respectively.

from those of the normal Fermi liquid and the original Luttinger theorem is violated. Indeed, the Fermi momentum k_F of the Hubbard bands is larger than the Fermi momentum k_F^0 for free electrons at the same Fermi energy ε_F (Fig. 1); therefore, the geometric volume of the Fermi surface is larger for the Hubbard bands [10]. However, the system is in the metallic state in this case and, since the distribution function of quasiparticles undergoes a jump in the vicinity of the Fermi level, Luttinger's theorem can be generalized to quasiparticles in the following way: the volume of the Fermi surface of noninteracting particles is equal to that of the interacting quasiparticles with allowance for the spectral weight of the quasiparticles. In this paper, by analyzing the general structure of the Green function and thoroughly investigating the Hubbard-I solution for the *t*–*J* model and for the Hubbard model [11], we shown that this generalized formulation of Luttinger's theorem is valid for metallic, strongly correlated electron systems. Actually, such a metallic system is not rather a normal but a "compressible" Fermi liquid, which is due to the spectral weight of the quasiparticles being different from unity and to the Fermi surface being "loose". Such an idea of the system makes it possible to eliminate the inconsistency between the concentration of the excess carriers in the superconducting cuprates and the unduly large volume of the Fermi surface calculated in the framework of the model of the normal Fermi liquid.

2. GENERAL STRUCTURE OF THE GREEN FUNCTION

Luttinger has shown [1] that the equality between the volumes of the Fermi surface in the momentum space for interacting particles, V_{FS}, and for noninteracting particles, V_{FS}^0,

$$V_{FS} = V_{FS}^0 \tag{1}$$

follows from the fact that the average number of particles $\langle N\rangle$ for interacting and noninteracting fermions is the same. Indeed, for a system without interaction, we have

$$\begin{aligned}\langle N\rangle &= \sum_k \theta(\mu_0 - \varepsilon_k)\\ &= \frac{V}{(2\pi)^3}\int dk\,\theta(\mu_0 - \varepsilon_k) = \frac{V}{(2\pi)^3}V_{FS}^0\end{aligned} \tag{2}$$

and, for the Fermi liquid system with interaction [1], we have

$$\begin{aligned}\langle N\rangle &= \sum_k \theta(\mu - \varepsilon_k - \mathrm{Re}\,\Sigma_k)\\ &= \frac{V}{(2\pi)^3}\int dk\,\theta(\mu - \varepsilon_k - \mathrm{Re}\,\Sigma_k) = \frac{V}{(2\pi)^3}V_{FS}.\end{aligned} \tag{3}$$

Here, V is the volume of the system of fermions; μ and μ_0 are the chemical potentials of the system with and without interaction, respectively; ε_k are one-particle energies; $\mathrm{Re}\,\Sigma_k$ is the self-energy part of the Green function; and $\theta(x)$is the Heaviside unit-step function.

For strongly correlated electron systems, however, the definition of the average number of particles as the sum of the Heaviside unit-step functions is invalid, because the spectral weight of each quasiparticle in the system is taken to be the unit in this definition. One of the essential peculiarities of strongly correlated electron systems is a variation of the spectral weight from unity in each band due to its redistribution between the Hubbard subbands at $U \gg W$ (W is the half-width of the band). For this reason, analogs of Eqs. (2) and (3) should be derived for this case.

In what follows, we use the Hubbard X operators [12] defined in the following way: $X_f^{pq} \equiv |p\rangle\langle q|$, where $|p\rangle$ and $\langle q|$ are states at site f. Since the number of root vectors $\alpha(p, q)$ is finite, they can be enumerated; thus, we have

$$X_f^{pq} \rightleftarrows X_f^{\alpha(p,q)} \rightleftarrows X_f^{\alpha_m} \rightleftarrows X_f^m. \tag{4}$$

Here, index $m \rightleftarrows (p, q)$ enumerates quasiparticles with the energies

$$\omega_m = \omega_{pq} = \varepsilon_p(N+1) - \varepsilon_q(N), \tag{5}$$

where ε_p is the energy level with index p for the N-electron system.

The Hubbard operators are related to one-electron creation and annihilation operators in the following way:

$$a^{+}_{f\lambda\sigma} = \sum_m \gamma^*_{\lambda\sigma}(m) X^{+m}_{f\sigma}, \quad a_{f\lambda\sigma} = \sum_m \gamma_{\lambda\sigma}(m) X^m_{f\sigma}, \quad (6)$$

where $\gamma_{\lambda\sigma}(m)$ is the partial weight of a quasiparticle m with spin σ and orbital index λ.

The average occupation numbers $\langle n_{k\lambda\sigma}\rangle$ for the particles with momentum k and spin σ are expressed in terms of the electron Green function written in the energy representation, $G_{k\lambda\sigma} = \langle\langle a_{k\lambda\sigma} | a^{+}_{k\lambda\sigma}\rangle\rangle_{E+i\eta}$, in the following way:

$$\langle n_{k\lambda\sigma}\rangle = \int dE\, f_F(E)\left(-\frac{1}{\pi}\mathrm{Im}\, G_{k\lambda\sigma}\right), \quad (7)$$

where $f_F(E)$ is the Fermi function, $\eta \longrightarrow 0$, and $\eta > 0$. In the X representation, the Green function has the form

$$\langle\langle a_{k\lambda\sigma} | a^{+}_{k\lambda\sigma}\rangle\rangle_{E+i\eta} = \sum_{m,p} \gamma_{\lambda\sigma}(m)\gamma^*_{\lambda\sigma}(p)\langle\langle X^m_{k\sigma} | X^{+p}_{k\sigma}\rangle\rangle_{E+i\eta}. \quad (8)$$

For the matrix Green function $D^{m,p}_{k\sigma}(E) = \langle\langle X^m_{k\sigma} | X^{+p}_{k\sigma}\rangle\rangle_{E+i\eta}$, the generalized Dyson equation [13] can be written as

$$\hat{D}_{k\sigma}(E) = \{[\hat{G}^{(0)}_{k\sigma}(E)]^{-1} + \hat{\Sigma}_{k\sigma}(E)\}^{-1}\hat{P}_{k\sigma}(E). \quad (9)$$

Here, $\hat{\Sigma}_{k\sigma}(E)$ and $\hat{P}_{k\sigma}(E)$ are the self-energy and the force operator, respectively. The presence of the force operator is due to the redistribution of the spectral weight and is an intrinsic feature of strongly correlated electron systems. The concept of the force operator was introduced earlier in a diagram technique for spin systems [14]. The Green function $\hat{G}^{(0)}_{k\sigma}(E)$ in Eq. (9) is defined by the formula

$$[\hat{G}^{(0)}_{k\sigma}(E)]^{-1} = \hat{G}^{-1}_0(E) - \hat{P}_{k\sigma}(E)\hat{T}_{k\sigma}, \quad (10)$$

where $\hat{T}_{k\sigma}$ is the interaction matrix element (for the Hubbard model, $T^{m,p}_{k\sigma} = \gamma_\sigma(m)\gamma^*_\sigma(p)t_k$).

In the Hubbard-I approximation at $U \gg W$, the structure of the exact Green function (9) remains unchanged but the self-energy is supposed to be zero and the force operator $P^{m,p}_{k\sigma}(E)$ is replaced by $P^{m,p}_{k\sigma}(E) \longrightarrow P^{m,p}_{0\sigma} = \delta_{m,p}F^m_\sigma$, where $F^m_\sigma \equiv F(p, q) = \langle X^{pp}_f\rangle + \langle X^{qq}_f\rangle$ is the occupation factor, which is referred to as the end factor in the diagram technique for the X operators developed in [15]. In terms of the Hubbard-I approximation, the following formula is derived from Eq. (9):

$$\hat{D}^{(0)}_{k\sigma} = \{\hat{G}^{-1}_0(E) - \hat{P}_{0\sigma}\hat{T}_{k\sigma}\}^{-1}\hat{P}_{0\sigma}. \quad (11)$$

In order to estimate the contributions to Eq. (11) in higher order approximations (with respect to the Hubbard-I approximation), let us compare the exact equation (9) for the Green function with Eq. (11), written in the Hubbard-I approximation. First, there is a difference due to the renormalization of the occupation factors F^m_σ which arises when the exact equation for the force operator $\hat{P}_{k\sigma}(E)$ is used. However, taking into account the corrections due to the force operator keeps the structure of the Hubbard bands unchanged and, therefore, does not lead to a qualitative difference of the exact Green function from that in the Hubbard-I approximation. A second essential difference is the renormalization of the real part of the self-energy $\hat{\Sigma}_{k\sigma}(E)$ and the appearance of quasiparticle damping. The latter implies non-Fermi-liquid behavior of the system and, as mentioned above, the consideration of the region where $\mathrm{Im}\Sigma_k(\varepsilon_F) = 0$. In this region, the exact Green function given by Eq. (9) can be rewritten as the sum of one-pole contributions over the quasiparticle bands labeled by index ξ (for the t–J model, ξ has one value, $\xi = 1$; for the Hubbard model, $\xi = 1, 2$). In the general multiband case, the exact Green function is

$$G_{k\lambda\sigma}(E) = \sum_\xi \frac{F_{k\lambda\sigma}(\xi)}{E - \Omega_{k\sigma}(\xi) + \mu + i\eta}. \quad (12)$$

Here, the real part of the self-energy contributes not only to the renormalization of the dispersion law but also to the renormalization of the spectral weight. Such a representation for the electron Green function has been obtained earlier in the Hubbard model in terms of the spectral density approach (SDA) [16]. This approach is nonperturbative and assumes the absence of the quasiparticle damping only. The spectral weights $F_{k\lambda\sigma}(\xi)$ and the band energies $\Omega_{k\sigma}(\xi)$ are calculated in the SDA by using the method of moments (see the review and comparison with other methods in [17]).

As for the renormalization of the real part of the self-energy, this effect introduces corrections to the energy spectrum $\Omega_{k\sigma}(\xi)$ and qualitatively does not change the further reasoning. The fact that the structure of the Green function is correct even in the Hubbard-I approximation (it is the structure of the Green function that is essential for further derivation of Luttinger's theorem) follows from a comparison of the Hubbard-I solution and the exact solution in the infinite-dimensionality limit obtained by using the method of the dynamical mean-field theory [4, 5], as well as from a comparison of the Hubbard-I solution and a numerical solution obtained using the exact quantum Monte Carlo method for the Hubbard model [18]. A comparison of

the spectral densities obtained in the Hubbard-I approximation at $U \gg W$ and those derived by the quantum Monte Carlo method shows [18] numerical coincidence between them in the region of the phase diagram, where the long-range magnetic order is absent. In terms of the diagram technique for the X operators, it has also been demonstrated that this approximation gives simple and pictorial relationships which correctly describe the physics of the phenomena at $U \gg t$ [13, 19].

Substituting Eq. (12) into Eq. (7) and using the spectral theorem, we obtain

$$\begin{aligned}\langle n_{k\lambda\sigma}\rangle &= \int dE\, f_F(E)\sum_{\xi} F_{k\lambda\sigma}(\xi)\delta(E-\Omega_{k\sigma}(\xi)+\mu)\\ &= \sum_{\xi} F_{k\lambda\sigma}(\xi)\, f_F(\Omega_{k\sigma}(\xi)-\mu).\end{aligned} \tag{13}$$

Taking into account that the quantities in Eq. (13) do not depend on spin in the paramagnetic phase, the average number of particles $\langle N\rangle$ at zero temperature can be written in the compact form

$$\langle N\rangle = \sum_{k,\lambda}\langle n_{k\lambda\sigma}\rangle = \sum_{k,\xi} F_k(\xi)\theta(\mu-\Omega_k(\xi)), \tag{14}$$

$$F_k(\xi) = 2\sum_{\lambda} F_{k\lambda\sigma}(\xi). \tag{15}$$

For noninteracting particles, we have $F_k(\xi) = 1$; the equation for $\langle N\rangle$ completely coincides with Eq. (2) in this case. For the system of interacting quasiparticles, Eq. (14) can be written as

$$\begin{aligned}\langle N\rangle &= \frac{V}{(2\pi)^3}\sum_{\xi}\int dk F_k(\xi)\theta(\mu-\Omega_k(\xi))\\ &= \frac{V}{(2\pi)^3}\sum_{\xi} V_{FS}^{\xi}.\end{aligned} \tag{16}$$

By comparing Eq. (2) with Eq. (16), we obtain

$$V_{FS}^0 = \sum_{\xi} V_{FS}^{\xi}, \tag{17}$$

where V_{FS}^{ξ} is the volume of the energy subband ξ taking into account the spectral weight $F_k(\xi)$ of this subband,

$$V_{FS}^{\xi} = \int dk F_k(\xi)\theta(\mu-\Omega_k(\xi)). \tag{18}$$

Equation (17) is the generalized Luttinger theorem: the right-hand side of the equality is a superposition of the volumes V_{FS}^{ξ} for the different energy subbands ξ rather than the volume V_{FS} and each state $|k, \sigma\rangle$ for band ξ enters with a decreased spectral weight.

Therefore, the region bounded by the Fermi surface in the k space becomes "less dense." Indeed, let us use the relationship $m_{FS} = \rho_{FS}V_{FS}$, where m_{FS} is the "mass" of the Fermi surface, ρ_{FS} is its "density," and V_{FS} is its volume. It is obvious that the mass m_{FS} is proportional to the average number of particles $\langle N\rangle$ and ρ_{FS} is the spectral weight of the quasiparticles in the region bounded by the Fermi surface. For the system of noninteracting particles, we have $m_{FS}^0 = \rho_{FS}^0 V_{FS}^0$. Further, from the equality $m_{FS} = m_{FS}^0$, it follows that $\rho_{FS}V_{FS} = \rho_{FS}^0 V_{FS}^0$ and

$$V_{FS} = \frac{1}{\rho_{FS}}V_{FS}^0, \tag{19}$$

because, for the system without interaction, we have $\rho_{FS}^0 = 1$. It is seen that, if the spectral weight of the quasiparticles differs from unity, we have the inequality $V_{FS} \neq V_{FS}^0$. It is precisely this case ($\rho_{FS} \leq 1$) that is realized in strongly correlated electron systems. On the other hand, the quantity given by Eq. (19) is invariant under the interaction in the system; therefore, the generalization of Luttinger's theorem for quasiparticles is as follows: the volume of the Fermi surface of a system of noninteracting particles is equal to that of interacting quasiparticles with allowance for the spectral weight of these quasiparticles. This formulation of the theorem is valid for both the band electrons and the quasiparticles in metallic, strongly correlated electron systems in the limit $U \gg W$.

The deviation of the spectral weight from unity can be considered to be a transition to a space with a different metric. This is demonstrated in Section 5, in which it is shown that the quantity given by Eq. (19) rather than by Eq. (1) is invariant under this transition.

3. t–J MODEL

The Hamiltonian of the Hubbard model in the X-operator representation [11] has the form

$$\begin{aligned}H &= \sum_{f,\sigma}\left((\varepsilon-\mu)(X_f^{\sigma\sigma}+X_f^{SS})+\frac{U}{2}X_f^{SS}\right)\\ &+ \sum_{f\neq g,\sigma} t_{fg}(X_f^{\sigma 0}+2\sigma X_f^{S\bar{\sigma}})(X_g^{0\sigma}+2\sigma X_g^{\bar{\sigma}S}).\end{aligned} \tag{20}$$

The Hamiltonian of the t–J model can be derived form Eq. (20) in the limit of the strong Coulomb interaction, $U \gg t$:

$$H_{t-J} = \sum_{f,\sigma}(\varepsilon-\mu)X_f^{\sigma\sigma} + \sum_{f\neq g,\sigma} t_{fg}X_f^{\sigma 0}X_g^{0\sigma} + J\sum_{f\neq g}\left(\mathbf{S}_f\mathbf{S}_g - \frac{1}{4}n_f n_g\right), \quad (21)$$

where t_{fg} is the hopping integral, J is the exchange integral, $\mathbf{S}_f$ is the spin operator, and n_f is the operator of the number of particles. Here, there is only one fermionic root vector, $\{X_f^{0\sigma}\} \rightleftarrows \{X_f^1\}$; therefore, the Green function in the region $\mathrm{Im}\Sigma_k(E) = 0$ has the form

$$D_{k\sigma}(E) = \frac{F(1)}{E - E_k + \mu}, \quad (22)$$

where $F(1)/2 = (1 - x)/2$ is the spectral weight of the only band $\xi = 1$ and E_k is the spectrum of the system in the Hubbard-I approximation,

$$E_k = \varepsilon + t_k\left(\frac{1-x}{2}\right) - \frac{J}{2}\left(\frac{1+x}{2}\right). \quad (23)$$

Here, $t_k = 2t(\cos k_x + \cos k_y)$ is the Fourier transform of the hopping integral in the case of a square lattice. The number of particles is

$$\langle N\rangle = \sum_{k,\sigma}\langle X_k^{\sigma 0}X_k^{0\sigma}\rangle = \sum_k (1-x) f_F(E_k - \mu). \quad (24)$$

At zero temperature, we have

$$\langle N\rangle = \sum_k (1-x)\theta(\mu - E_k). \quad (25)$$

This equation coincides with Eq. (14); thus, the volume of the Fermi surface is $V_{FS}^0 = F(1)V^- = (1-x)V^-$, where $V^- = \int dk\,\theta(\mu - E_k)$. In multiband models, such as the Hubbard model, the spectral weight of the quasiparticles is redistributed between the bands due to strong correlations. In our case, there is only one band, but its spectral weight is smaller than unity [see Eq. (25)] because part of the spectral weight goes to the upper Hubbard band. In deriving the equations for the t–J model from the Hubbard model, this band is taken into account only in terms of the perturbation theory with respect to the parameter $t/U \ll 1$ and does not appear in the Hamiltonian (21) because of the constraint of two-particle excitations being absent, $\langle X_f^{SS}\rangle \longrightarrow 0$.

4. HUBBARD MODEL

The basis fermion operators for the Hubbard model (20) are $\{X_f^{0\sigma}, X_f^{\bar{\sigma}S}\} \rightleftarrows \{X_f^1, X_f^2\}$, where $|S\rangle = |\uparrow, \downarrow\rangle$ is a two-particle singlet, $|0\rangle$ is the vacuum state, and $|\sigma\rangle$ and $|\bar{\sigma}\rangle$ are one-particle singlets. The Green function has the form

$$\hat{D}_{k\sigma}(E) = \frac{1}{\det}\begin{pmatrix} \frac{F(1)}{2}\left(E - \varepsilon + \mu - U - t_k\frac{1+x}{2}\right) & 2\sigma t_k\frac{F(2)}{2}\frac{F(1)}{2} \\ 2\sigma t_k\frac{F(1)}{2}\frac{F(2)}{2} & \frac{F(2)}{2}\left(E - \varepsilon + \mu - t_k\frac{1-x}{2}\right)\end{pmatrix}, \quad (26)$$

where $\det = (E - E_k^+ + \mu)(E - E_k^- + \mu)$ and $F(1)/2 = (1 - x)/2$, and $F(2)/2 = (1 + x)/2$ are the occupation factors of the lower and upper Hubbard bands, respectively. The energy spectrum of the system is

$$E_k^\pm = \left(t_k + U \pm \sqrt{t_k^2 + U^2 + 2t_k U x}\right)/2. \quad (27)$$

The number of particles can be easily found using the Green function (26):

$$\langle N\rangle = \sum_k\left\{\left[1 + \frac{x(U + t_k x)}{E_k^+ - E_k^-}\right] f_F(E_k^+ - \mu) + \left[1 - \frac{x(U + t_k x)}{E_k^+ - E_k^-}\right] f_F(E_k^- - \mu)\right\}. \quad (28)$$

This equation coincides with Eq. (14). The expressions in square brackets in Eq. (28) are the spectral weights of the upper and lower Hubbard bands, respectively. Their sum (taking into account the spin) is equal to the spectral weight of noninteracting electrons, as it must be. Now, let us analyze Eq. (28) in the regime of strong Coulomb repulsion $U \gg t$. In this case, the denominator $E_k^+ - E_k^-$ can be expanded in powers of the small parameter $t/U \ll 1$. Neglecting second-order terms, we have

$$\langle N\rangle = \sum_k((1+x) f_F(E_k^+ - \mu) + (1-x) f_F(E_k^- - \mu)). \quad (29)$$

At zero temperature, this equation becomes

$$\langle N\rangle = \sum_k((1+x)\theta(\mu - E_k^+) + (1-x)\theta(\mu - E_k^-)). \quad (30)$$

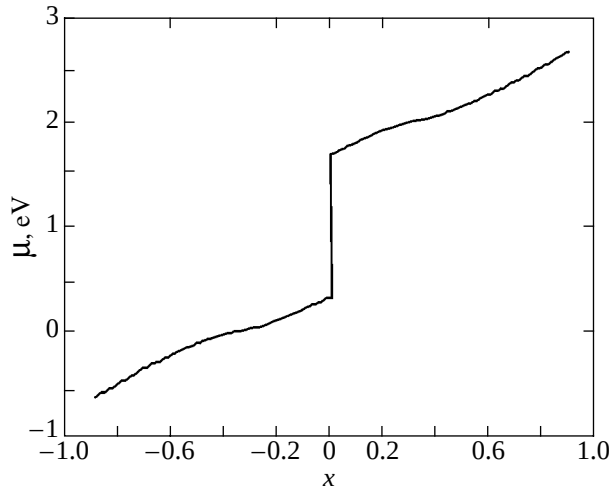

Fig. 2. Dependence of the chemical potential μ on x.

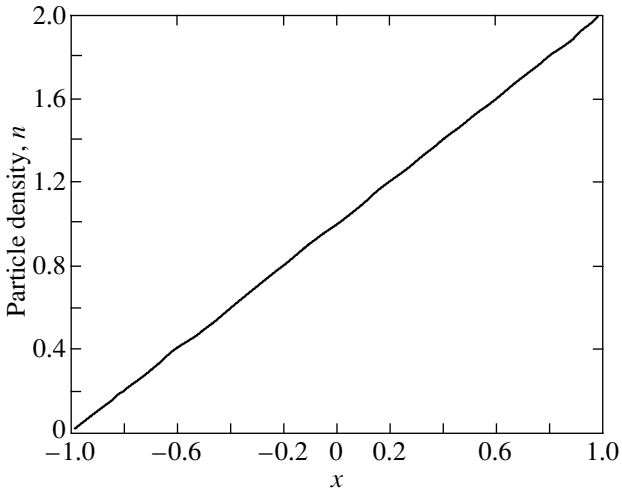

Fig. 3. Dependence of the density of particles $n = \langle N \rangle / N$ on x (N is the number of vectors in the momentum space).

The relation between the volumes of the Fermi surfaces is

$$V_{FS}^0 = F(2)V^+ + F(1)V^- = (1+x)V^+ + (1-x)V^-, \quad (31)$$

where $V^\pm = \int dk\theta(\mu - E_k^\pm)$. It is clearly seen that the strong Coulomb interaction redistributes the spectral weight between the lower and upper subbands. It is this effect that necessitates generalization of Luttinger's theorem for strongly correlated electron systems.

The splitting into two Hubbard bands is clearly seen in Eqs. (29)–(31); therefore, it is easy to transform the Hubbard model to the t–J model simply by neglecting the influence of the upper (or lower) band, because the bands are separated by a gap U (the interband hopping was already eliminated by the expansion in powers of t/U). The occupation numbers are immediately found to be

$$\lim_{U\to\infty} \langle N \rangle = \sum_k (1-x) f_F(E_k^- - \mu). \quad (32)$$

This expression coincides with Eq. (24), obtained for the number of particles in the t–J model. Thus, the decrease in the spectral weight in the t–J model is a result of the approximations used ($t/U \ll 1$) rather than of its spontaneous disappearance.

Figures 2 and 3 show the results of calculations for zero temperature at $U = 10|t|$ and $t = -0.2$ eV. Calculations for finite temperatures were also carried out, but they did not reveal any qualitative difference from the case of zero temperature. The chemical potential μ calculated self-consistently by using Eq. (28) is shown in Fig. 2. Figure 3 shows the dependence of the density of particles $n = \langle N \rangle / N$ on x calculated by using Eq. (29). It is clearly seen that this dependence is linear and, moreover, $n = 1 + x$. Actually, the last equality means that the generalized Luttinger theorem is valid. Indeed, the left-hand side of Eq. (29) is the number of particles calculated with due regard for the interaction in the system, while the right-hand side of the equation is the number of noninteracting particles. The equality of these two quantities is a prerequisite for the equality of the Fermi surface volumes multiplied by the corresponding spectral weights, as given by Eq. (31).

5. QUASIPARTICLE DESCRIPTION AS A TRANSFORMATION OF THE METRIC SPACE

Let $\mathbf{e}_\mu$ be natural reference vectors associated with the system of curvilinear (in general) coordinates x^μ. In what follows, upper indices indicate contravariant quantities and lower indices, covariant ones. The metric tensor is defined as

$$g_{\mu\nu} = (\mathbf{e}_\mu \cdot \mathbf{e}_\nu). \quad (33)$$

In going to new coordinates y^μ, we have

$$\mathbf{e}_\mu = a_\mu^\nu \mathbf{e}'_\nu,$$

$$g_{\mu\nu} = (\mathbf{e}_\mu \cdot \mathbf{e}_\nu) = a_\mu^\rho a_\nu^\eta (\mathbf{e}_\rho \cdot \mathbf{e}_\eta) = a_\mu^\rho a_\nu^\eta g'_{\rho\eta},$$

where $a_\mu^\nu = \dfrac{\partial y^\nu}{\partial x^\mu}$ are the coefficients of the axis transformation.

By definition, an elementary volume of the n-dimensional space is

$$d\tau = dx^1 dx^2 \ldots dx^n. \quad (34)$$

In this case, the value $\sqrt{-g}\,d\tau$ rather than the volume element $d\tau$ is invariant under transition to another sys-

tem of coordinates. Here, $g = \det g_{\mu\nu}$ is the determinant of the components of the metric tensor; i.e.,

$$\sqrt{-g'}d\tau' = \sqrt{-g}d\tau. \quad (35)$$

Now, let us consider two n-dimensional spaces: one for quasiparticles with the spectral weight ρ' (quantities referred to this space are labelled by prime) and one for quasiparticles with the spectral weight ρ. Obviously, a transition between these coordinate systems can be made by simply changing the axis scales, $a_\mu^\nu = \sqrt[n]{\rho/\rho'}$. The corresponding transformation of the metric tensor is

$$g_{\mu\nu} = \left(\frac{\rho}{\rho'}\right)^{2/n} g'_{\mu\nu}. \quad (36)$$

The relation between the elementary volumes can be derived from Eqs. (35) and (36) to be

$$d\tau = \frac{\rho'}{\rho}d\tau', \quad (37)$$

this equation coincides with Eq. (19) at $\rho' = 1$. A similar relationship takes place in the hydrodynamic theory for a compressible liquid. Thus, in the case of quasiparticles with a spectral weight smaller than unity, we deal with modification of the normal Fermi liquid instead of the normal Fermi liquid; by analogy with hydrodynamics, this modification can be called the compressible Fermi liquid. The original Luttinger theorem is valid only for quasiparticles with a spectral weight equal to unity and, therefore, is of limited use. In systems with different spectral weights of quasiparticles, the quantity given by Eq. (35) rather than the volume of the Fermi surface is conserved; thus, the scalar density of noninteracting particles $\sqrt{-g'}d\tau'$ is equal to the scalar density of quasiparticles with interaction, $\sqrt{-g}d\tau$. It is clearly seen that Luttinger's theorem [1] is a special case of this statement.

6. CONCLUSION

One of the problems of the theory of strongly correlated electron systems is whether Luttinger's theorem is valid for them. This question is of great importance in describing high-temperature superconductors, because they belong to the category of strongly correlated electron systems. It has been shown that, in the Hubbard model, Luttinger's theorem [1] is violated for underdoped samples ($x < x_{opt}$) because of the presence of short-range magnetic order and the occurrence of spin fluctuations associated with it [9, 10, 18]. However, Luttinger's theorem is valid in the overdoped regime ($x > x_{opt}$), where the paramagnetic metal state takes place. Actually, the original Luttinger theorem in the form of Eq. (1) is not valid for strongly correlated electron systems; the proof of theorem (1) is inapplicable to such systems, because it does not take into account the difference of the spectral weight of quasiparticles from unity, which is one of the most remarkable peculiarities of strongly correlated systems [13]. In this paper, we have formulated Luttinger's theorem (17) generalized to the case of quasiparticle description within the Hubbard-I approximation. Qualitative analysis of this generalization given by Eq. (19), as well as analytically exact derivation of Eq. (37) for the scalar densities, showed that the region of k space bounded by the Fermi surface becomes less compact (or, in other words, less dense) in quasiparticle systems: the contribution of each state is renormalized because of a decrease in the spectral weight of the corresponding quasiparticle.

The momentum space is divided into quantum cells, each of which can contain one electron or, taking into account the Pauli principle, two electrons with opposite spins. Some states from the whole set of quantum states in a cell move away to infinite energies due to strong electron correlations. Therefore, the spectral weight F of the remaining states is smaller than unity; quasiparticle excitations in such a system become renormalized, and their spectral weight $F < 1$. It is this effect that causes the k space to be less compact.

From Eq. (37) for the scalar densities, it is seen that we deal with a compressible Fermi liquid. A normal Fermi liquid belongs to a subclass of the class of compressible Fermi liquids; in this subclass, the spectral weights of the quasiparticles are equal to unity. The generalized Luttinger theorem is formulated for the case of a compressible Fermi liquid in which the effects of strong electron correlations necessitate deviation from the description of the system as a normal Fermi liquid.

In this paper, we have considered basic models of strongly correlated systems, such as the t–J model and the Hubbard model. It has been shown that, in the nonsuperconducting paramagnetic phase, these models satisfy a generalized Luttinger theorem. In the Hubbard model, the spectral weight is redistributed between the Hubbard subbands; in the t–J model, a decrease in the spectral weight occurs, because part of the states moves away to infinite energies due to the strong correlation between the electrons (the upper Hubbard subband is separated form the lower band by a gap $U \gg t$).

ACKNOWLEDGMENTS

The authors are grateful to V.V. Val'kov for helpful remarks.

This work was supported by the INTAS (grant no. INTAS-01-0654), the Russian Foundation for Basic Research and the Krasnoyarsk Kraĭ Science Foundation (program "Eniseĭ," project no. 02-02-97705), the program of the Russian Academy of Sciences "Quantum Macrophysics," and the Russian Academy of Sciences, Siberian Division (Lavrent'yev Contest for Youth Projects).

REFERENCES

1. J. M. Luttinger, Phys. Rev. **119** (4), 1153 (1960).
2. M. Oshikawa, Phys. Rev. Lett. **84** (15), 3370 (2000).
3. W. Metzner and D. Vollhardt, Phys. Rev. Lett. **62** (3), 324 (1989).
4. X. Y. Zhang, M. J. Rozenberg, and G. Kotliar, Phys. Rev. Lett. **70**, 1666 (1993).
5. A. Georges, G. Kotliar, W. Krauth, and M. J. Rozenberg, Rev. Mod. Phys. **68** (1), 13 (1996).
6. D. M. Edwards and J. A. Hertz, Physica B (Amsterdam) **163**, 527 (1990).
7. Th. A. Maier, Th. Pruschke, and M. Jarrell, Phys. Rev. B **66** (7), 075102 (2002).
8. Yu. A. Izyumov, Usp. Fiz. Nauk **165** (4), 403 (1995) [Phys. Usp. **38**, 385 (1995)].
9. J. Schmalian, M. Langer, S. Grabowski, and K. N. Bennemann, Phys. Rev. B **54** (6), 4336 (1996).
10. J. Beenen and D. M. Edwards, Phys. Rev. B **52** (18), 13636 (1995).
11. J. C. Hubbard, Proc. R. Soc. London, Ser. A **276**, 238 (1963).
12. J. C. Hubbard, Proc. R. Soc. London, Ser. A **277**, 237 (1964).
13. V. V. Val'kov and S. G. Ovchinnikov, *Quasiparticles in Strongly Correlated Systems* (Sib. Otd. Ross. Akad. Nauk, Novosibirsk, 2001).
14. V. G. Bar'yakhtar, V. N. Krivoruchko, and D. A. Yablonskiĭ, *Green's Functions in the Theory of Magnetism* (Naukova Dumka, Kiev, 1984).
15. R. O. Zaĭtsev, Zh. Éksp. Teor. Fiz. **70** (3), 1100 (1976) [Sov. Phys. JETP **43**, 574 (1976)].
16. W. Nolting, Z. Phys. B: Condens. Matter **255**, 25 (1972).
17. T. Herrmann and W. Nolting, J. Magn. Magn. Mater. **170**, 253 (1997).
18. C. Grober, R. Eder, and W. Hanke, Phys. Rev. B **62** (7), 4336 (2000).
19. Yu. A. Izyumov and Yu. N. Skryabin, *Basic Models in the Quantum Theory of Magnetism* (Ural. Otd. Ross. Akad. Nauk, Yekaterinburg, 2002).

Translated by A. Pushnov

Physics of the Solid State, Vol. 45, No. 8, 2003, pp. 1423–1428. Translated from Fizika Tverdogo Tela, Vol. 45, No. 8, 2003, pp. 1358–1363.

METALS AND SUPERCONDUCTORS

Modulation Instability of Electromagnetic Excitations in Nonlocal Josephson Electrodynamics of Thin Films of Nonmagnetic and Magnetic (Two- and Three-Dimensional) Superconductors

A. I. Lomtev

Donetsk Physicotechnical Institute, National Academy of Sciences of Ukraine, 83114 Ukraine
e-mail: lomtev@kinetic.ac.donetsk.ua

Received December 17, 2002

Abstract—Modulation instability of nonlinear electromagnetic excitations (oscillating with the Josephson frequency) of finite amplitude is investigated in a Josephson junction in a film of a nonmagnetic, as well as of a magnetic (two- or three-dimensional), superconductor. The instability is accompanied by a nonlinear shift in frequency. Dispersion relations are derived for the time increment of small perturbations of the amplitude. It is shown that, for this type of excitations in a Josephson junction in a thin film of nonmagnetic superconductor, modulation instability develops only in a certain finite range of wave vectors, whereas in a thin film of a two- or three-dimensional magnetic superconductor it develops for any wave vector. *© 2003 MAIK "Nauka/Interperiodica".*

1. INTRODUCTION

A great number of magnetic superconductors exhibiting new unique properties [1–3] are presently known and attract considerable interest. Coexistence of magnetism and superconductivity has been observed not only in ternary compounds [4] but also in high-temperature superconductors, such as *RE*BaCuO and *RE*CuO, where *RE* is a rare-earth ion. One of the important features of high-T_c superconductors is the fairly strong antiferromagnetic correlation of the spins of copper atoms in the CuO_2 planes [5].

Continued attention also focuses on a wide range of instabilities of waves in various nonlinear systems and media [6, 7]. It is known that compression of a nonlinear wave can occur both in the cross section and in the direction of propagation of the wave beam. Examples are the self-focusing of light predicted by Askar'yan [8] and the instability of waves to breaking up into wave packets and the self-compression of wave packets (modulation instability) first studied by Lighthill [9]. Modulation instability of electromagnetic waves observed in optical fibers corresponds to the instability of solutions to a nonlinear Schrödinger equation [10], and that observed in distributed Josephson junctions, to the instability of solutions to the sine-Gordon equation [11, 12]. Modulation instability is of interest from the fundamental point of view and for practical applications. For example, this phenomenon is used for generating series of ultrashort optical pulses with a high repetition frequency [10] and for developing novel logic units [13].

In many cases, spatially nonlocal modifications of the nonlinear Schrödinger equation [14] and of the sine-Gordon equation [15–26] should be used in studying modulation instability. For example, it was shown in [15, 16] that spatial nonlocality can be significant even in junctions of bulk superconductors of large thickness $d \gg \lambda$ (λ is the London penetration depth) along the magnetic field (vortex lines), i.e., in the cases where the local approximation was used earlier. For junctions in thin films of $d \ll \lambda$, there is no local limit and the spatial nonlocality is significant and becomes a determining factor. The corresponding equations were derived and investigated in [17–20]. It has been shown [21–23] that, in the Josephson electrodynamics of thin films of magnetic (two- and three-dimensional) superconductors, not only spatial effects but also time nonlocality (which is ultimately due to retardation effects) must be taken into account. The Josephson junction at the interface between two superconducting layers of finite thickness along a direction perpendicular to the magnetic vortex field was studied in [24]. In [25, 26], a butt junction and a tilted (tapered) junction (having, therefore, a finite thickness along the magnetic field of vortices) were considered for arbitrary values of the ratio d/λ.

Due to the difference in geometry of the problems considered in the papers mentioned above, the equations for the Josephson electrodynamics in them differ in the form of the kernel of the integral operator describing the spatial nonlocality. However, in all those papers, the spatial nonlocality of the equations for the phase difference is due to the nonlocal relation between

1063-7834/03/4508-1423$24.00

the fields at the interface and in the superconductor. This origin of spatial nonlocality is universal for the electrodynamics of Josephson junctions; therefore, the nonlocality itself is the rule rather than the exception.

In the framework of the spatially nonlocal Josephson electrodynamics of the junction at the interface between bulk superconductors, the modulation instability was first considered in [15]. It was shown that increasing small perturbations of the amplitude and phase correspond to the development of modulation instability in the electromagnetic wave with a finite constant amplitude; the instability is characterized by a nonlinear shift in frequency and by the dispersion law of the linear approximation. It was also found that spatial nonlocality suppresses the modulation instability. Abdullaev [27] also considered the Josephson junction at the interface of bulk superconductors and investigated the modulation instability of a plane nonlinear electromagnetic wave with a finite amplitude and with a frequency equal to the Josephson frequency. It was shown that the instability causes small perturbations of the amplitude to increase and brings about the breaking up of the wave into wave packets.

It is of interest to investigate the modulation instability of electromagnetic excitations (in the framework of the nonlocal Josephson electrodynamics) in thin two-dimensional superconducting films, as this has not been done to date. This type of instability may arise in the Josephson junction in an ultrathin film of a nonmagnetic or (two- or three-dimensional) magnetic superconductor of thickness $d \ll \lambda$.

A thin film of a magnetic superconductor can be two- or three-dimensional, in terms of its magnetic properties, depending on whether the (time-dependent) magnetic permeability μ of the film is a function of two coordinates (in the plane of the film) or three coordinates. The point is that, in a film which is two-dimensional in terms of superconducting properties, the magnetic subsystem may exhibit two-dimensional (in the film plane) or three-dimensional magnetic ordering (in the film plane and across the film thickness) because of the short-range interaction between the spins of impurity atoms.

The geometry of the problem under study is as follows: the film plane is taken to be the *xy* plane, the current flows along the *y* axis, and weak links are oriented along the *x* axis.

2. FILM OF A TWO-DIMENSIONAL MAGNETIC SUPERCONDUCTOR

We assume that the film is two-dimensional in terms of its superconducting and magnetic properties; therefore, its magnetic permeability can be written as

$$\mu(\mathbf{r} - \mathbf{r}', t - t') = \mu(\boldsymbol{\rho} - \boldsymbol{\rho}', t - t')\delta(z - z'), \quad (1)$$

where $\mathbf{r} = (x, y, z)$ and $\boldsymbol{\rho} = (x, y)$.

The dynamics of the phase change $\varphi(x, t)$ across the Josephson junction, for any type of magnetic ordering in the thin two-dimensional magnetic superconducting film, is described by the nonlinear integrodifferential sine-Gordon equation with spatial and time nonlocality [21, 22]

$$\sin\varphi(x, t) + \frac{\beta}{\omega_J^2}\frac{\partial\varphi(x, t)}{\partial t} + \frac{1}{\omega_J^2}\frac{\partial^2\varphi(x, t)}{\partial t^2} = l_J\int_{-\infty}^{\infty}dx'\int_{-\infty}^{\infty}dt' K\left(\frac{x - x'}{2\lambda_{\text{eff}}}, t - t'\right)\frac{\partial^2\varphi(x', t')}{\partial x'^2}. \quad (2)$$

Here, ω_J is the Josephson frequency, β is a dissipation parameter, $l_J = \lambda_J^2/\lambda$, λ_J is the Josephson length, $\lambda_{\text{eff}} = \lambda^2/d$ is the Pearl penetration depth, and the kernel $K\left(\frac{x - x'}{2\lambda_{\text{eff}}}, t - t'\right)$, nonlocal in the spatial and time variables, has the form

$$K\left(\frac{x - x'}{2\lambda_{\text{eff}}}, t - t'\right) = \int_0^{\infty}\frac{dq}{\pi}\int_{-\infty}^{\infty}\frac{d\omega}{2\pi}\frac{2\lambda_{\text{eff}}J_0[q(x - x')]\exp[-i\omega(t - t')]}{\mu(\mathbf{q}, \omega) + 2q\lambda_{\text{eff}}}, \quad (3)$$

where $J_0(qx)$ is the zero-order Bessel function. The time nonlocality in Eq. (2) is due to the frequency dispersion of the magnetic permeability $\mu(\mathbf{q}, \omega)$.

Since $\lambda \gg a$ (a is the crystal lattice parameter), we can use the hydrodynamic approximation for the magnetic subsystem. In the paramagnetic temperature range, the magnetic permeability has the form [28]

$$\mu(\mathbf{q}, \omega) = 1 + 4\pi\chi_0\frac{iD_2q^2}{\omega + iD_2q^2}, \quad (4)$$

where χ_0 is the static magnetic susceptibility and $D_2 = (1/3)(2\pi)^{1/2}Ja^2[s(s + 1)]^{1/2}$ is the spin diffusion coefficient for two-dimensional Heisenberg magnets [29] (J is the intralayer exchange constant, s is the spin).

Let us consider the evolution of nonlinear waves (of the breather type) with a frequency equal to the Josephson frequency ω_J and with a small, but finite, amplitude produced in the junction. The phase change $\varphi(x, t)$ can be written as

$$\varphi(x, t) = u(x, t)\exp(-i\omega_J t) + u^*(x, t)\exp(i\omega_J t), \quad |u(x, t)| \ll 1. \quad (5)$$

In Eq. (2), in the dissipationless limit $\beta = 0$, we retain the lowest order nonlinear terms at the fundamental frequency ω_J and restrict ourselves to the approximation in which the amplitude $u(x, t)$ varies slowly in time and, therefore, the condition $|\partial^2u(x, t)/\partial t^2| \ll 2\omega_J|\partial u(x, t)/\partial t|$ is satisfied. Substituting

Eq. (5) into Eq. (2), we obtain the following equation for $u(x, t)$ in this case:

$$i\frac{2}{\omega_J}\frac{\partial u(x,t)}{\partial t} + \frac{1}{2}|u(x,t)|^2 u(x,t) + l_J\int_{-\infty}^{\infty}dx'\int_{-\infty}^{\infty}dt' K\left(\frac{x-x'}{2\lambda_{\text{eff}}}, t-t'\right) \times \exp[i\omega_J(t-t')]\frac{\partial^2 u(x',t')}{\partial x'^2} = 0. \quad (6)$$

This nonlinear nonlocal "Schrödinger equation" has an exact solution in the form of a plane nonlinear wave with a uniform amplitude A and with a shift in frequency,

$$u_0(t) = A\exp(iA^2\omega_J t/4), \quad A \ll 1. \quad (7)$$

In order to investigate the stability of this solution, we introduce a small perturbation of the amplitude:

$$u(x,t) = [A + \psi(x,t)]\exp(iA^2\omega_J t/4), \quad |\psi(x,t)| \ll A. \quad (8)$$

It follows from Eq. (6) that the small perturbation $\psi(x, t)$ satisfies the linear equation

$$i\frac{2}{\omega_J}\frac{\partial \psi(x,t)}{\partial t} + \frac{1}{2}A^2[\psi(x,t) + \psi^*(x,t)] + l_J\int_{-\infty}^{\infty}dx'\int_{-\infty}^{\infty}dt' K\left(\frac{x-x'}{2\lambda_{\text{eff}}}, t-t'\right) \times \exp[i\omega_J(1-A^2/4)(t-t')]\frac{\partial^2 \psi(x',t')}{\partial x'^2} = 0. \quad (9)$$

Substituting $\psi(x, t) = v(x, t) + iw(x, t)$ into Eq. (9), we obtain the following equations for the real and imaginary parts of the perturbation:

$$\frac{2}{\omega_J}\frac{\partial v(x,t)}{\partial t} + l_J\int_{-\infty}^{\infty}dx'\int_{-\infty}^{\infty}dt' K\left(\frac{x-x'}{2\lambda_{\text{eff}}}, t-t'\right) \times \exp[i\omega_J(1-A^2/4)(t-t')]\frac{\partial^2 w(x',t')}{\partial x'^2} = 0,$$

$$-\frac{2}{\omega_J}\frac{\partial w(x,t)}{\partial t} + A^2 v(x,t) + l_J\int_{-\infty}^{\infty}dx'\int_{-\infty}^{\infty}dt' K\left(\frac{x-x'}{2\lambda_{\text{eff}}}, t-t'\right) \times \exp[i\omega_J(1-A^2/4)(t-t')]\frac{\partial^2 v(x',t')}{\partial x'^2} = 0. \quad (10)$$

An arbitrary perturbation can be represented as a superposition of the waves

$$v(x,t) = V(Q,\Omega)\exp[i(Qx-\Omega t)], \quad w(x,t) = W(Q,\Omega)\exp[i(Qx-\Omega t)], \quad (11)$$

propagating along the Josephson junction with a wave vector $\mathbf{Q}$ and a frequency Ω. From Eqs. (10), we obtain the dispersion relation $\tilde{\Omega} = \tilde{\Omega}(\tilde{Q})$ for these waves:

$$\tilde{\Omega}^2 = \frac{L}{2\pi}\tilde{Q}^2 J_{(2)}(\tilde{Q},\tilde{\Omega})\left[\frac{2L}{\pi}\tilde{Q}^2 J_{(2)}(\tilde{Q},\tilde{\Omega}) - A^2\right], \quad (12)$$

where

$$J_{(2)}(\tilde{Q},\tilde{\Omega}) = \int_0^{\infty}dx\left[1 + \tilde{Q}\cosh x + \frac{4\pi\chi_0\tilde{Q}^2\cosh^2 x}{-i\eta_2(\tilde{\Omega}+1-A^2/4)+\tilde{Q}^2\cosh^2 x}\right]^{-1}; \quad (13)$$

we also introduced the dimensionless quantities $\tilde{Q} = 2Q\lambda_{\text{eff}}$ and $\tilde{\Omega} = \Omega/\omega_J$ and the parameters $L = l_J/2\lambda_{\text{eff}}$ and $\eta_2 = (2\lambda_{\text{eff}})^2\omega_J/D_2$.

The implicit dispersion relation (12) for $\tilde{\Omega}(\tilde{Q})$, in combination with Eq. (13), has a complex solution $\tilde{\Omega}(\tilde{Q}) = \text{Re}\tilde{\Omega}(\tilde{Q}) + i\text{Im}\tilde{\Omega}(\tilde{Q})$. In the case of $\text{Im}\tilde{\Omega}(\tilde{Q}) > 0$, small perturbations of the amplitude in the form of Eqs. (11) will increase with time; therefore, modulation instability of the plane nonlinear electromagnetic wave (7) will develop in the Josephson junction in a thin film of a two-dimensional magnetic superconductor.

3. FILM OF A THREE-DIMENSIONAL MAGNETIC SUPERCONDUCTOR

Now, we consider a film which is two-dimensional in terms of its superconducting properties but is three-dimensional in terms of its magnetic properties; therefore, the magnetic permeability μ of the film is a function of three spatial coordinates and time: $\mu = \mu(\mathbf{r} - \mathbf{r}', t - t')$.

In this case, for any type of magnetic ordering in the thin film of a three-dimensional magnetic superconductor, the dynamics of the phase change $\varphi(x, t)$ across the Josephson junction is described by the nonlinear inte-

grodifferential sine-Gordon equation with spatial and time nonlocality [22, 23]

$$\sin\varphi(x,t) + \frac{\beta}{\omega_J^2}\frac{\partial\varphi(x,t)}{\partial t} + \frac{1}{\omega_J^2}\frac{\partial^2\varphi(x,t)}{\partial t^2} = l_J\int_{-\infty}^{\infty}dx'\int_{-\infty}^{\infty}dt'K\left(\frac{x-x'}{2\lambda_{\text{eff}}}, t-t'\right)\frac{\partial^2\varphi(x',t')}{dx'^2}. \quad (14)$$

The kernel $K\left(\frac{x-x'}{2\lambda_{\text{eff}}}, t-t'\right)$ is nonlocal in the spatial and time variables and has the form

$$K\left(\frac{x-x'}{2\lambda_{\text{eff}}}, t-t'\right) = \int_0^{\infty}\frac{dq}{\pi}\int_{-\infty}^{\infty}\frac{d\omega}{2\pi}\frac{\lambda_{\text{eff}}J_0[q(x-x')]\exp[-i\omega(t-t')]}{q[R(\mathbf{q},\omega)+\lambda_{\text{eff}}]}, \quad (15)$$

where $R(\mathbf{q}, \omega)$ is given by

$$R(\mathbf{q},\omega) = \int_{-\infty}^{\infty}\frac{dp}{2\pi}\frac{\mu(\mathbf{q},p,\omega)}{p^2+q^2}. \quad (16)$$

The nonlocality of Eq. (14) in time is due to the frequency dispersion of the magnetic permeability $\mu(\mathbf{q}, p, \omega)$ involved in the function $R(\mathbf{q}, \omega)$.

In the case of $\lambda \gg a$, as in the previous section, we use the hydrodynamic approximation in describing the magnetic subsystem. In the paramagnetic temperature range, the magnetic permeability has the form

$$\mu(\mathbf{q},p,\omega) = 1 + 4\pi\chi_0\frac{iD_3(q^2+p^2)}{\omega + iD_3(q^2+p^2)}, \quad (17)$$

where D_3 is the spin diffusion coefficient for a three-dimensional Heisenberg magnet.

Substituting Eq. (17) into Eq. (16), we represent $R(\mathbf{q}, \omega)$ in the form

$$R(\mathbf{q},\omega) = \frac{f_0(q,\omega) + i4\pi\chi_0 q}{2q f_0(q,\omega)}, \quad (18)$$

where $f_0(q, \omega)$ is given by

$$f_0(q,\omega) = [(q^4+\omega^2/D_3^2)^{1/2}/2 - q^2/2]^{1/2} + i[(q^4+\omega^2/D_3^2)^{1/2}/2 + q^2/2]^{1/2}. \quad (19)$$

Equations (2) and (14) for the phase change differ only in the form of the kernel $K\left(\frac{x-x'}{2\lambda_{\text{eff}}}, t-t'\right)$ given by Eqs. (3) and (15), respectively. Therefore, following the same line of reasoning and mathematical manipulation as in the previous section in deriving the dispersion relation (12) from Eq. (2), we, starting with Eq. (14), find the following dispersion relation $\tilde{\Omega} = \tilde{\Omega}(\tilde{Q})$ giving the time increment of small perturbations of the amplitude:

$$\tilde{\Omega}^2 = \frac{L}{2\pi}\tilde{Q}^2 J_{(3)}(\tilde{Q},\tilde{\Omega})\left[\frac{2L}{\pi}\tilde{Q}^2 J_{(3)}(\tilde{Q},\tilde{\Omega}) - A^2\right], \quad (20)$$

where

$$J_{(3)}(\tilde{Q},\tilde{\Omega}) = \int_0^{\infty}\frac{dx F_0(\tilde{Q}\cosh x,\tilde{\Omega})}{F_0(\tilde{Q}\cosh x,\tilde{\Omega})(1+\tilde{Q}\cosh x) + i4\pi\chi_0\tilde{Q}\cosh x}, \quad (21)$$

$$F_0(x,y) = \{[x^4+\eta_3^2(y+1-A^2/4)^2]^{1/2}/2 - x^2/2\}^{1/2} + i\{[x^4+\eta_3^2(y+1-A^2/4)^2]^{1/2}/2 + x^2/2\}^{1/2}, \quad (22)$$

and, as before, we use the notation $\tilde{Q} = 2Q\lambda_{\text{eff}}$, $\tilde{\Omega} = \Omega/\omega_J$, $L = l_J/2\lambda_{\text{eff}}$, and $\eta_3 = (2\lambda_{\text{eff}})^2\omega_J/D_3$.

The implicit dispersion relation (20) for $\tilde{\Omega}(\tilde{Q})$, in combination with Eqs. (21) and (22), has a complex solution $\tilde{\Omega}(\tilde{Q}) = \text{Re}\tilde{\Omega}(\tilde{Q}) + i\,\text{Im}\tilde{\Omega}(\tilde{Q})$ In the case of $\text{Im}\tilde{\Omega}(\tilde{Q}) > 0$, small perturbations of the amplitude in the form of Eqs. (11) will increase with time; therefore, modulation instability of the plane nonlinear electromagnetic wave (7) will develop in the Josephson junction in a thin film of a three-dimensional magnetic superconductor.

4. FILM OF A NONMAGNETIC SUPERCONDUCTOR

In the case of a nonmagnetic superconducting film, we have $\chi_0 = 0$ and the integrals in Eqs. (13) and (21) become identical and depend only on the wave vector $\tilde{Q}$ (see also [20]):

$$J(\tilde{Q}) = \frac{1}{2\sqrt{1-\tilde{Q}^2}}\ln\frac{1+\sqrt{1-\tilde{Q}^2}}{1-\sqrt{1-\tilde{Q}^2}} \quad \text{for} \quad \tilde{Q}\le 1,$$
$$J(\tilde{Q}) = \frac{2}{\sqrt{\tilde{Q}^2-1}}\arctan\frac{\sqrt{\tilde{Q}^2-1}}{1+\tilde{Q}} \quad \text{for} \quad \tilde{Q}\ge 1. \quad (23)$$

The dispersion relations (12) and (20) also become identical and reduce to an explicit equation for $\tilde{\Omega}(\tilde{Q})$:

$$\tilde{\Omega}^2(\tilde{Q}) = \frac{L}{2\pi}\tilde{Q}^2 J(\tilde{Q})\left[\frac{2L}{\pi}\tilde{Q}^2 J(\tilde{Q}) - A^2\right]. \quad (24)$$

This equation has a solution with a positive time increment of perturbations $\text{Im}\tilde{\Omega}(\tilde{Q}) > 0$ in a finite range of wave vectors $0 < \tilde{Q} < \tilde{Q}_B$, where, therefore, modula-

tion instability develops. In the wave-vector range $\tilde{Q} \geq \tilde{Q}_B$, we have $\mathrm{Im}\tilde{\Omega}(\tilde{Q}) = 0$ and the wave is stable. The wave-vector limit $\tilde{Q}_B$ of the stability region can be found from the equation

$$\tilde{Q}_B^2 J(\tilde{Q}_B) = \frac{\pi A^2}{2L}. \quad (25)$$

It follows from dispersion relations (12), (20), and (24) that the maximum time increment of perturbations for a nonmagnetic superconducting film, as well as for films of two- and three-dimensional magnetic superconductors, is equal to

$$\mathrm{Im}\tilde{\Omega}(\tilde{Q}) = A^2/4 \quad (26)$$

and is reached at a wave vector $\tilde{Q}_m$, which is a root of the equation

$$\tilde{Q}_m^2 J(\tilde{Q}_m) = \frac{\pi A^2}{4L}. \quad (27)$$

5. NUMERICAL CALCULATIONS

Thus, from Eqs. (24) and (23), it follows that, in the Josephson junction in a thin film of a nonmagnetic superconductor ($\chi_0 = 0$), the modulation instability is suppressed with increasing wave vector $\tilde{Q}$. The results of numerical calculations are presented in Fig. 1, where the wave-vector range of modulation instability of the plane nonlinear electromagnetic wave (7) is shown for a fixed value of the amplitude A and three values of the parameter L.

For a thin film of a two-dimensional magnetic superconductor with $\chi_0 = 10^{-2}$ [1] and $\eta_2 = 1$, according to numerical calculations, the dispersion relation (12) together with Eq. (13) has a solution with a positive time increment of amplitude perturbations $\mathrm{Im}\tilde{\Omega}(\tilde{Q})$ for any value of the wave vector $\tilde{Q}$. Figure 2 shows the wave-vector dependence of the time increment, affected by the magnetic subsystem, for a fixed value of the amplitude A and three values of the parameter L.

In the case of a thin film of a three-dimensional magnetic superconductor with the same value of the parameter χ_0 and $\eta_3 = 1$, numerical calculations show that the dispersion relation (20) together with Eqs. (21) and (22) has a solution with a positive time increment of amplitude perturbations $\mathrm{Im}\tilde{\Omega}(\tilde{Q})$ also for any value of the wave vector $\tilde{Q}$. Figure 3 shows the wave-vector dependence of the time increment, affected by the magnetic subsystem, for a fixed value of the amplitude A and three values of the parameter L.

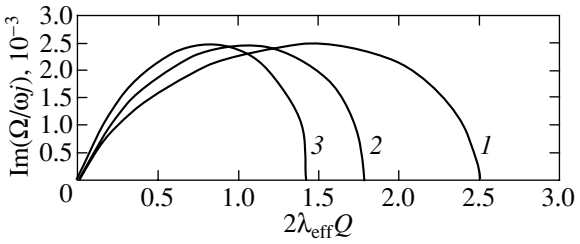

Fig. 1. Modulation instability of the plane nonlinear electromagnetic wave (7) in a thin film of a nonmagnetic superconductor for amplitude $A = 0.1$ and different values of the parameter L: (*1*) 0.5×10^{-2}, (*2*) 0.75×10^{-2}, and (*3*) 10^{-2}.

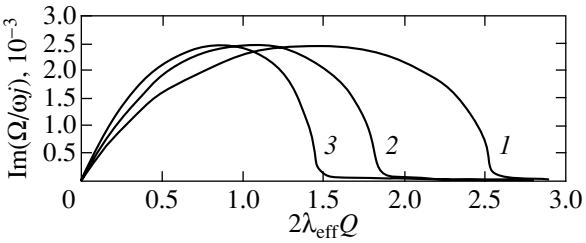

Fig. 2. Wave-vector dependence of the time increment of small perturbations of the amplitude of the plane nonlinear electromagnetic wave (7) in a thin film of a two-dimensional magnetic superconductor for amplitude $A = 0.1$ and different values of the parameter L: (*1*) 0.5×10^{-2}, (*2*) 0.75×10^{-2}, and (*3*) 10^{-2}.

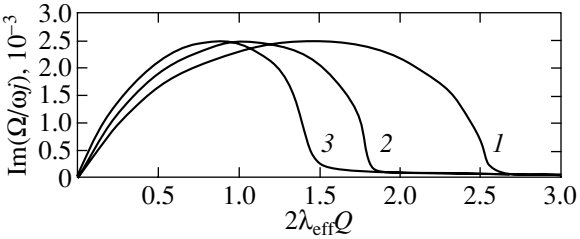

Fig. 3. Wave-vector dependence of the time increment of small perturbations of the amplitude of the plane nonlinear electromagnetic wave (7) in a thin film of a three-dimensional magnetic superconductor for amplitude $A = 0.1$ and various values of the parameter L: (*1*) 0.5×10^{-2}, (*2*) 0.75×10^{-2}, and (*3*) 10^{-2}.

Figures 2 and 3 are similar on the scale used, because the value of χ_0 is small; the respective curves in these figures differ only in the eighth decimal place, except for the maximum time increments, which are identical for the respective curves.

By comparing Figs. 1–3, we see that the dependence of the time increment $\mathrm{Im}\tilde{\Omega}(\tilde{Q})$ on wave vector $\tilde{Q}$ exhibits a crossover in a narrow range near the limiting

[1] Such values of the static magnetic susceptibility are typical of ternary compounds and high-temperature superconductors containing rare-earth ions near the magnetic-ordering temperature $T_N \propto 1$ K.

value $\tilde{Q} = \tilde{Q}_B$ in the thin films of two- and three-dimensional magnetic superconductors. Therefore, there are two adjacent wave-vector ranges of modulation instability: the range $0 < \tilde{Q} < \tilde{Q}_B$, where the instability is strong, $\mathrm{Im}\tilde{\Omega}(\tilde{Q}) \propto 10^{-3}$ for $A = 0.1$, and the range $\tilde{Q} > \tilde{Q}_B$, where the instability is weak, $\mathrm{Im}\tilde{\Omega}(\tilde{Q}) \propto 10^{-6}$–$10^{-7}$. Since $\tilde{Q} \longrightarrow \infty$, we have $\mathrm{Im}\tilde{\Omega}(\tilde{Q}) \longrightarrow 0$.

As the modulation instability develops, the plane nonlinear wave oscillating with the Josephson frequency transforms gradually into a series of pulses (small-amplitude breathers) whose repetition frequency is determined by the modulation period of the initial wave $L_0 = 2\pi/Q$.

6. CONCLUSIONS

Thus, we have considered the time-nonlocal equation of the dynamics of the phase change across the Josephson junction in a thin film of a two- or three-dimensional magnetic superconductor in the dissipationless limit. It has been shown that the inclusion of the time nonlocality that is associated with the frequency dispersion of the magnetic permeability caused by two- or three-dimensional diffusion of spin waves in the magnetic subsystem brings about additional modulation instability of plane nonlinear electromagnetic waves in the wave-vector range $\tilde{Q} \geq \tilde{Q}_B$, where such waves were stable in a film of a nonmagnetic superconductor.

ACKNOWLEDGMENTS

The author is grateful to Yu.V. Medvedev and I.B. Krasnyuk for their encouragement and helpful discussions and to A.N. Artemov and S.M. Orel for helpful advice on numerical calculations.

REFERENCES

1. A. I. Buzdin, L. N. Bulaevskiĭ, M. L. Kulich, and S. V. Panyukov, Usp. Fiz. Nauk **144** (4), 597 (1984) [Sov. Phys. Usp. **27**, 927 (1984)].
2. A. I. Buzdin and L. N. Bulaevskiĭ, Usp. Fiz. Nauk **149** (1), 45 (1986) [Sov. Phys. Usp. **29**, 412 (1986)].
3. Yu. A. Izyumov, N. M. Plakida, and Yu. N. Skryabin, Usp. Fiz. Nauk **159** (4), 621 (1989) [Sov. Phys. Usp. **32**, 1060 (1989)].
4. *Superconductivity in Ternary Compounds*, Ed. by E. Fisher and M. Maple (Springer, Heidelberg, 1982; Mir, Moscow, 1985).
5. *Physical Properties of High Temperature Superconductors*, Ed. by D. M. Ginsberg (World Sci., Singapore, 1989; Mir, Moscow, 1990), Chaps. 4, 6.
6. V. I. Karpman, *Non-Linear Waves in Dispersive Media* (Nauka, Moscow, 1973; Pergamon, Oxford, 1975).
7. B. B. Kadomtsev, *Collective Phenomena in a Plasma* (Nauka, Moscow, 1976).
8. G. A. Askar'yan, Zh. Éksp. Teor. Fiz. **42** (6), 1567 (1962) [Sov. Phys. JETP **15**, 1088 (1962)]; V. I. Bespalov and V. I. Talanov, Pis'ma Zh. Éksp. Teor. Fiz. **3** (12), 471 (1966) [JETP Lett. **3**, 307 (1966)].
9. M. J. Lighthill, J. Inst. Math. Appl. **1** (2), 269 (1965); Proc. R. Soc. London, Ser. A **229**, 1, 28 (1967).
10. A. Hasegawa, Opt. Lett. **9** (3), 288 (1984).
11. N. N. Akhmediev, V. M. Eleonskiĭ, and N. E. Kulagin, Izv. Vyssh. Uchebn. Zaved. Radiofiz. **31** (2), 244 (1988).
12. N. M. Frcolani, M. G. Forest, and D. W. McLaughlin, Lett. Appl. Math. **23** (1), 149 (1986).
13. M. Islam, *Ultra Fast Optical Devices* (Oxford Univ. Press, Oxford, 1993).
14. M. Alfimov, V. M. Eleonsky, and N. E. Kulagin, Chaos **2** (4), 454 (1992).
15. Yu. M. Aliev, V. P. Silin, and S. A. Uryupin, Sverkhprovodimost: Fiz. Khim. Tekh. **5** (2), 228 (1992).
16. A. Gurevich, Phys. Rev. B **46** (5), 3187 (1992).
17. Yu. M. Ivanchenko and T. K. Soboleva, Pis'ma Zh. Éksp. Teor. Fiz. **51** (2), 100 (1990) [JETP Lett. **51**, 114 (1990)].
18. Yu. M. Ivanchenko and T. K. Soboleva, Phys. Lett. A **147** (1), 65 (1990).
19. Yu. M. Ivanchenko and T. K. Soboleva, Fiz. Tverd. Tela (Leningrad) **32** (7), 2029 (1990) [Sov. Phys. Solid State **32**, 1181 (1990)].
20. R. G. Mints and I. B. Snapiro, Phys. Rev. B **51** (5), 3054 (1995).
21. A. I. Lomtev, Pis'ma Zh. Éksp. Teor. Fiz. **69** (2), 132 (1999) [JETP Lett. **69**, 148 (1999)].
22. A. I. Lomtev, Fiz. Tverd. Tela (St. Petersburg) **42** (1), 16 (2000) [Phys. Solid State **42**, 15 (2000)].
23. A. I. Lomtev, Zh. Tekh. Fiz. **70** (9), 63 (2000) [Tech. Phys. **45**, 1159 (2000)].
24. I. O. Kulik and I. K. Yanson, in *Josephson Effect in Superconducting Tunnel Structures* (Nauka, Moscow, 1970).
25. Yu. E. Kuzovlev and A. I. Lomtev, Zh. Éksp. Teor. Fiz. **111** (5), 1803 (1997) [JETP **84**, 986 (1997)].
26. A. I. Lomtev, Zh. Éksp. Teor. Fiz. **113** (6), 2256 (1998) [JETP **86**, 1234 (1998)].
27. F. Kh. Abdullaev, Pis'ma Zh. Tekh. Fiz. **23** (2), 8 (1997) [Tech. Phys. Lett. **23**, 52 (1997)].
28. B. I. Halperin and P. C. Hohenberg, Phys. Rev. **188** (2), 898 (1969).
29. P. M. Richards and M. B. Salamon, Phys. Rev. B **9** (1), 32 (1974).

Translated by Yu. Epifanov

Physics of the Solid State, Vol. 45, No. 8, 2003, pp. 1429–1434. Translated from Fizika Tverdogo Tela, Vol. 45, No. 8, 2003, pp. 1363–1368.

METALS AND SUPERCONDUCTORS

Band Structure of Superconducting Dodecaborides YB_{12} and ZrB_{12}

I. R. Shein and A. L. Ivanovskiĭ

Institute of Solid-State Chemistry, Ural Division, Russian Academy of Sciences, Pervomaĭskaya ul. 91, Yekaterinburg, 620219 Russia

e-mail: shein@ihim.uran.ru

Received January 28, 2003

Abstract—The band structure of superconducting UB_{12}-like cubic dodecaborides, namely, YB_{12} and ZrB_{12}, is calculated in the framework of the self-consistent full-potential linearized muffin-tin orbital (FLMTO) method. The calculated parameters of the electronic subsystems of YB_{12} and ZrB_{12} dodecaborides are analyzed and compared with the relevant parameters of the hypothetical dodecaborides $\square B_{12}$ ($\square$ is a metal vacancy) and BB_{12}; nonsuperconducting AlB_2-like layered diborides, namely, YB_2 and ZrB_2; and a new superconductor, MgB_2. © *2003 MAIK "Nauka/Interperiodica".*

1. INTRODUCTION

The recent discovery of the critical transition ($T_C \approx$ 40 K) in magnesium diboride MgB_2 [1] and the preparation of superconducting MgB_2-based materials (films, ceramics, long wires, tapes) [2, 3] have stimulated an active search for new superconductors and detailed investigations into the superconductivity of other metal borides.

A comparative analysis of different classes of binary (semiborides Me_2B, monoborides MeB, diborides MeB_2, tetraborides MeB_4, and a number of higher borides, such as hexaborides MeB_6, dodecaborides MeB_{12}, and MeB_{66}-like borides), ternary, and quaternary borides [3] has demonstrated that the majority of the known superconductors are characterized by a relatively low boron content ($B/Me \le 2.0$–2.5). These crystals contain boron in the form of isolated atoms or linear and planar structures (chains or networks of boron atoms).

The superconducting properties are less pronounced in higher borides ($B/Me \ge 6$), whose structure is formed by stable polyhedral groupings of boron atoms, namely, octahedra B_6 (MeB_6), icosahedra B_{12} (MeB_{12}), or their combinations (MeB_{66}). For example, among the large number of metal borides containing B_{12} polyhedra, low-temperature superconductivity is found only for four MeB_{12} phases (Me = Sc, Y, Zr, Lu) [3].

It should be noted that the most stable crystalline modifications of elemental boron (α-B_{12}, β-B_{105}), in which the main structural units are boron polyhedra (icosahedra or giant icosahedra B_{84}), exhibit semiconductor properties under equilibrium conditions [4–7]. Recent experiments on compression under ultrahigh pressures have revealed that polycrystalline rhombohedral β-B_{105} transforms into a superconducting state ($T_C \approx 11.2$ K) at pressures above 250 GP [8].

The aim of the present work was to investigate the band structure of two of the aforementioned higher borides, namely, the low-temperature superconductors YB_{12} and ZrB_{12}, and to analyze the electronic factors responsible for their superconducting properties. For this purpose, the energy bands, the densities of states, and the partial compositions of the near-Fermi bands of yttrium and zirconium dodecaborides were calculated and compared with the relevant parameters for boride phases of these metals with a low boron content ($B/Me = 2$), such as AlB_2-like layered diborides, YB_2 and ZrB_2, in which no superconductivity is observed [3], and superconducting MgB_2.

2. OBJECTS OF INVESTIGATION AND CALCULATION TECHNIQUE

As was already noted, the basic polyhedra of isostructural YB_{12} and ZrB_{12} cubic phases (UB_{12} type, space group O_h^5-$Fm3m$) are polyatomic clusters with icosahedral symmetry B_{12}. The structure of these dodecaborides can be formally represented as a simple structure of the rock-salt type in which metal atoms (Me = Y, Zr) occupy sodium sites, whereas the B_{12} icosahedra are centered at chlorine sites [9]. The unit cell contains 52 atoms ($Z = 4$) with the following coordinates: 4*Me* (*a*) 0, 0, 0; 48B (*i*) 1/2, *x*, *x* ($x = 0.166$).

In order to elucidate the role played by the metal atoms and B_{12} polyhedra in the formation of the band structure of MeB_{12} compounds, we also calculated the band structure for two hypothetical crystals. These crystals were simulated by the following methods: (i) removal of an *Me* atom from the MeB_{12} lattice

Table 1. Critical transition temperatures (T_C, K) [3] and lattice parameters (Å) for YB_{12}, ZrB_{12}, YB_2, and ZrB_2

Boride	T_C	[9]		Our data	
		a	*c*	*a*	*c*
YB_{12}	4.7	7.506	–	7.469	–
ZrB_{12}	5.8	7.408	–	7.419	–
YB_2	–	3.303	3.842	3.212	4.008
ZrB_2	–	3.165	3.547	3.170	3.532

($\square B_{12}$, where $\square$ is a metal vacancy) and (ii) substitution of boron atoms for *Me* atoms (BB_{12}). For these model dodecaborides, we used the structural parameters of YB_{12}.

The band structures of the above systems were calculated using the scalar relativistic self-consistent full-potential linearized muffin-tin orbital (FLMTO) method [10, 11] with allowance made for the exchange–correlation effects in the framework of the generalized gradient approximation [12, 13]. The densities of states were calculated by the tetrahedron method. The structural parameters of the studied borides were optimized. The results obtained are given in Table 1.

3. RESULTS AND DISCUSSION

The results of calculations of the band structures of yttrium and zirconium dodecaborides are presented in Figs. 1 and 2. Let us consider the specific features of the formation of their energy bands in comparison with the hypothetical dodecaboride $\square B_{12}$ (Fig. 1). For this compound, the energy dispersion of the bands is determined by a rather complex system of intraicosahedral and intericosahedral B–B bonds. The total width of the valence band of the $\square B_{12}$ compound (without regard for the low-energy quasi-core B 2*s* bands located ~14 eV below the Fermi level E_F) is determined to be ~10.3 eV. The valence band contains two groups of hybrid B 2*s* and B 2*p* bands in the ranges from –11.0 to –8.80 and from –8.45 to 0 eV, which are separated by an energy gap of ~0.4 eV. The lower bands are composed mainly of B 2*s* states, and the upper bands are formed by B 2*s* and B 2*p* states. Depending on their participation in the effects of interatomic bonding in the crystal, the B 2*s* and B 2*p* states of the upper bands can be divided into three types.

Electron states of the first type are the B 2*s* and B 2*p* bonding states, which are responsible for the formation of intracluster covalent bonds, specifically of three-center B–B bonds in planes of the icosahedron faces. In turn, these bonds are responsible for the stabilization of individual B_{12} polyhedra and depend only slightly on the type of packing in the crystal (symmetry of the B_{12} sublattice) and in the icosahedra (B_{12}–B_{12}). Similar bands reside in polymorphic modifications of elemental boron, whose lattices are formed by B_{12} clusters [4–7], and virtually retain their form in YB_{12} and ZrB_{12} (Fig. 1).

The second type of electron states involves B 2*s* and B 2*p* bonding states responsible for the formation of intericosahedral bonds. Electron states of the third type are the B 2*s* and B 2*p* nonbonding states localized in the vicinity of empty sites of the $\square B_{12}$ dodecaboride. These states form partially occupied quasi-flat bands near the Fermi level E_F and correspond to narrow resonance peaks B' and B" in the density of states (Fig. 3). As a result, the energy spectrum of the $\square B_{12}$ dodecaboride exhibits a metal-like nature. This is in contrast with the spectrum of the stable semiconductor α-B_{12} [4–7], in which the bands are occupied completely.

The metallization of hypothetical $\square B_{12}$ is associated with a deficit of electrons due to a partial transfer of the electron density into the region of empty spheres at the yttrium sites in the YB_{12} structure. According to our estimates, each of these spheres accumulates up to ~0.95*e*. As a consequence, the upper valence bands are partially free and the system, as a whole, has a high density of states at the Fermi level [$N(E_F)$ = 6.1771 1/eV cell]. It should be noted that these states are approximately 96 percent composed of B 2*p* orbitals.

The energy spectrum of $\square B_{12}$ is characterized by a band gap (~1.36 eV, the direct transition at the *X* point), which is comparable to the band gap of α-B_{12} (~1.43–1.70 eV, the indirect transition $Z \longrightarrow \Gamma$ [4–7]).

We also calculated the band structure of a BB_{12} hypothetical dodecaboride isoelectronic to YB_{12} in which the superstoichiometric boron atoms are substituted for yttrium atoms. It was found that the valence *s* and *p* states of these atoms are localized in the vicinity of the Fermi level E_F and are occupied only partially. These states are responsible for the metal-like nature of the energy spectrum of BB_{12} with the density of states at the Fermi level $N(E_F)$ = 3.0341 1/eV cell. The main contribution to $N(E_F)$ is also made by the B 2*p* states (~72%).

Thus, the near-Fermi regions of $\square B_{12}$ and BB_{12} hypothetical crystals have a similar structure. The former crystal can be treated as a structural model of elemental boron with a disordered lattice formed by B_{12} icosahedra. The structure of the latter crystal simulates the presence of intericosahedral boron atoms in the crystal. Both systems have a metal-like energy spectrum with a high density of B 2*p* states at the Fermi level.

Papaconstantopoulos and Mehl [14] believed that a similar structure of the near-Fermi states is responsible for pressure-induced superconductivity of boron. However, the inferences made by the authors in [14] were

based on calculations of the band spectrum of a hypothetical face-centered cubic phase of boron.

The results obtained suggest that the superconducting transition observed in [8] for β-B can be induced not only by lattice distortions but also by a partial destruction of initial B_{12} icosahedra during which part of the boron atoms occupy intericosahedral sites under high external pressures. Owing to the high cohesiveness of elemental boron [4–7], these effects can become more probable than the phase transition β-B ⟶ face-centered cubic boron [14]. The final conclusion regarding the most probable mechanisms of structural transformations of the boron lattice and the stabilization of its possible crystal structures under high pressures calls for evaluation of the energy effects.

The main differences between the band structures of YB_{12} and $\square B_{12}$ are associated with the valence *s*, *p*, and *d* states of yttrium. These states are hybridized with outer B 2*p* states, which form both intericosahedral bonds in the $\square B_{12}$ system and nonbonding quasi-flat bands near the Fermi level E_F. The width of the valence band in YB_{12} is approximately equal to 12.98 eV. The valence band involves two groups of completely occupied hybrid B 2*s* and B 2*p* bands 2.82 and 8.89 eV wide which are separated by a pseudogap (bands *A*, *B* in Fig. 2). Near-Fermi bands of the hybrid Y–B type possess a considerable energy dispersion.

Upon the transition YB_2 ⟶ ZrB_2, the band structure, as a whole, changes insignificantly. The main effect is associated with the band occupation due to an increase in the electron concentration in the system (Fig. 1).

It should be noted that the Fermi level E_F for YB_{12} and ZrB_{12} is located in the region of an extended plateau in the density of states between the bonding and antibonding bands formed by the B 2*s* and B 2*p* states (Fig. 2). The change in the metal sublattice type (YB_2, ZrB_2) affects both the profile of the density of states for these phases and the magnitude and composition of $N(E_F)$ only slightly. It can be seen from Table 2 that, in the given sequence of borides, the density of states at the Fermi level $N(E_F)$ increases by no more than ~16% and the dominant contribution to the density of states $N(E_F)$ is made by the *Me* 4*d* states.

Therefore, reasoning from the shape of the electronic spectra, we can conclude that attempts to dope binary dodecaborides (for example, when preparing $Y_xZr_{1-x}B_{12}$ solid solutions) with the purpose of optimizing their superconducting properties, which are very efficient for controlling the critical temperatures T_C of other superconducting borides (such as MgB_2 [2, 3] or YNi_2B_2C [7, 15]), will be inefficient for MeB_{12} phases.

However, the specific features of the electronic spectrum of the MeB_{12} phases indicate that their superconducting properties are stable to changes in the chemical composition of the system. In other words, the synthesis conditions of MeB_{12} low-temperature superconductors should not impose rigid requirements on the stoichiometry of the prepared samples, unlike the synthesis of MgB_2 or YNi_2B_2C superconductors.

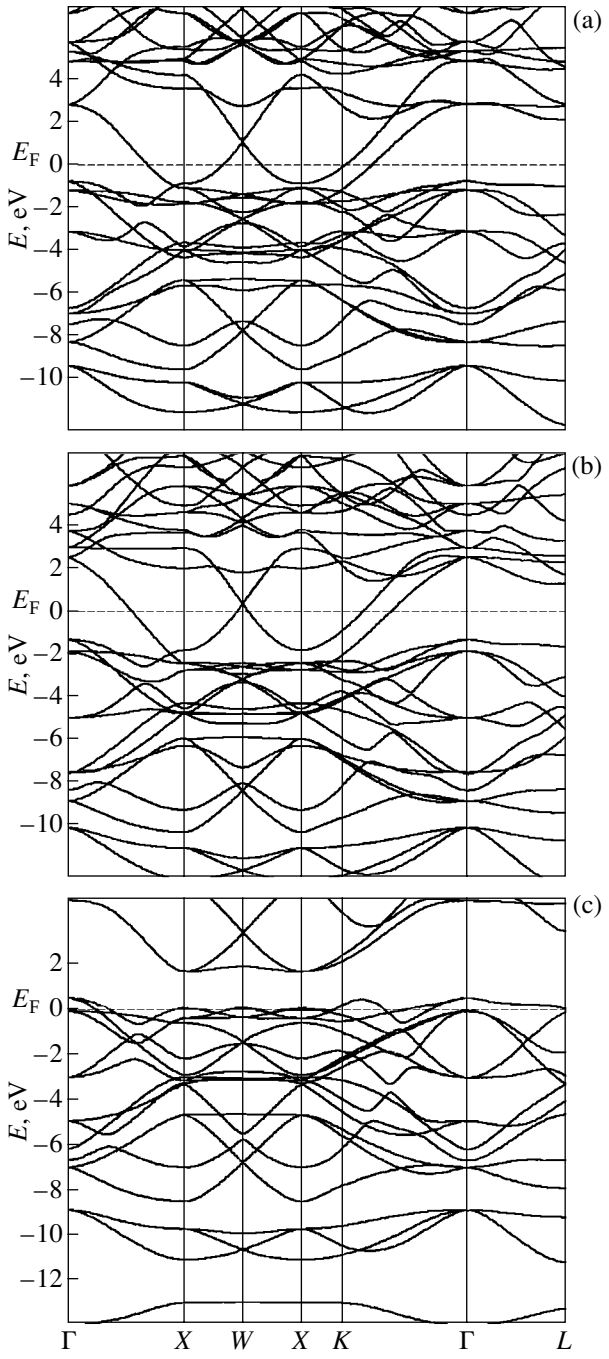

Fig. 1. Energy bands of (a) YB_{12}, (b) ZrB_{12}, and (c) a model structure of the $\square B_{12}$ dodecaboride.

It is known that YB_{12} and ZrB_{12} are classical Bardeen–Cooper–Schrieffer systems with the electron–phonon mechanism of superconductivity [3]. For these

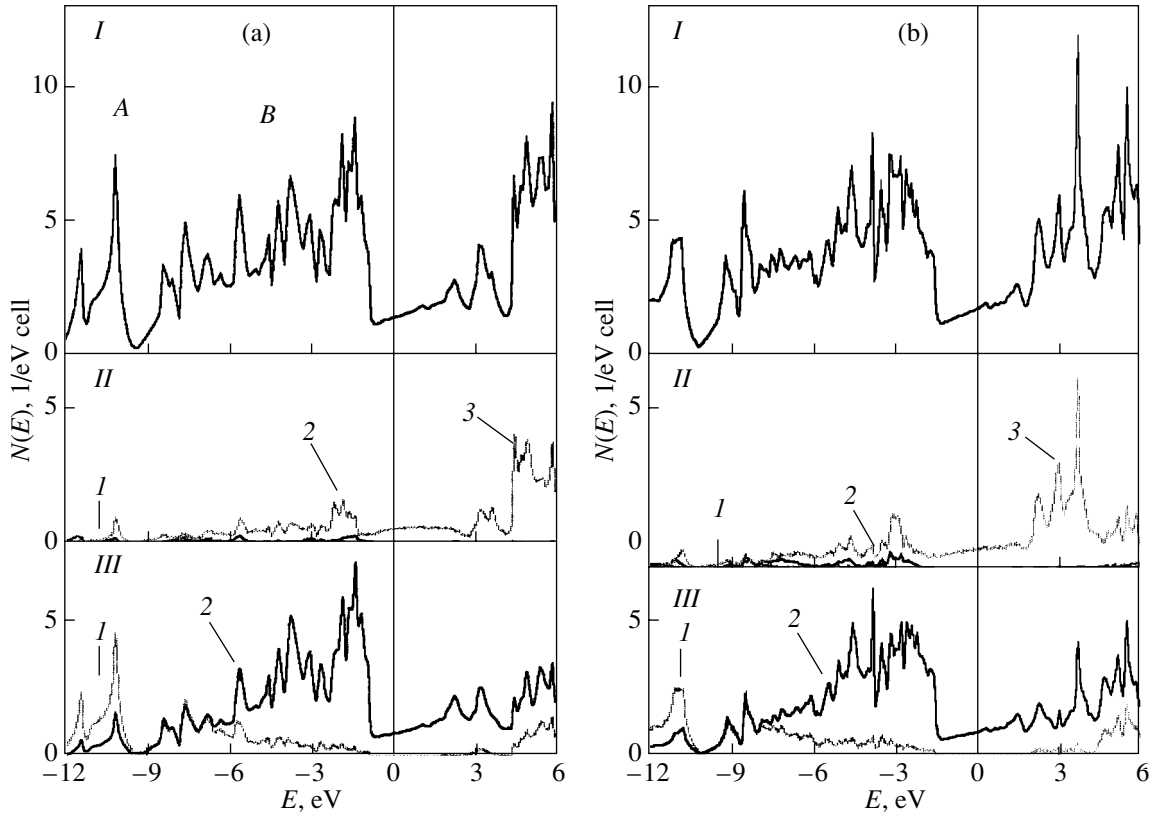

Fig. 2. (*I*) Total and (*II*, *III*) local densities of valence (*1*) *s* states, (*2*) *p* states, and (*3*) *d* states in (*II*) yttrium and zirconium and (*III*) boron sublattices of (a) YB_{12} and (b) ZrB_{12}.

systems, the important parameter responsible for the formation of their superconducting properties is the orbital composition of the density of states $N(E_F)$ [16]. According to our data, an increase in the critical temperature T_c from 4.7 (YB_{12}) to 5.8 K (ZrB_{12}) [3] can be caused by an increase in the contribution of the *Me* 4*d* states to the density of states $N(E_F)$ from 0.532 (YB_{12}) to 0.743 1/eV cell (ZrB_{12}). Note that the contributions of all the other valence states remain virtually unchanged (Table 2).

Let us now compare the specific features of the band structure of MeB_{12} with those of AlB_2-like layered diborides of these metals and of the isostructural superconductor MgB_2, which we calculated in the framework of the method used in the present work. The band structure of the above diborides was described in our recent paper [17]. As was shown in [2, 3, 17–20], the specific features of the band structure of superconducting MgB_2 are governed by the $\sigma(2p_{x,y})$ and $\pi(p_z)$ states of boron. Quasi-two-dimensional bands of the B $2p_{x,y}$ type intersect the Fermi level E_F and are responsible for the metal-like properties of MgB_2 (Table 2). One of the most important features of MgB_2 is the existence of B $2p_{x,y}$ hole states. In the Γ–*A* direction, these states reside above the Fermi level E_F and form hole-type cylindrical elements of the Fermi surface [17–20]. By comparing the band structures of diborides in the series $MgB_2 \longrightarrow YB_2 \longrightarrow ZrB_2$ (Fig. 4), we revealed the fol-

Table 2. Total density of states and orbital contributions at the Fermi level (1/eV cell)

Boride	Total density of states	*Me s*	*Me p*	*Me d*	B *s*	B *p*
YB_{12}	1.458	0.005	0.003	0.532	0.033	0.885
ZrB_{12}	1.687	0.008	0.006	0.743	0.042	0.888
YB_2	1.665	0.042	0.106	0.983	0.001	0.294
ZrB_2	0.163	0.001	0.002	0.130	0.001	0.030
MgB_2	0.719	0.040	0.083	0.138	0.007	0.448

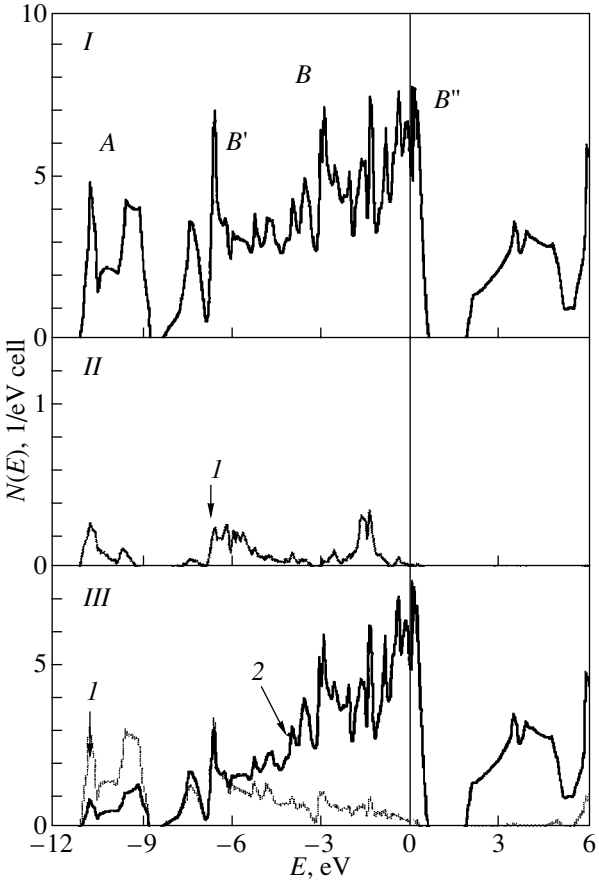

Fig. 3. (*I*) Total and (*II*, *III*) local densities of (*1*) *s* states and (*2*) *p* states of (*II*) an empty sphere □ and (*III*) boron in a model structure of the $\square B_{12}$ dodecaboride.

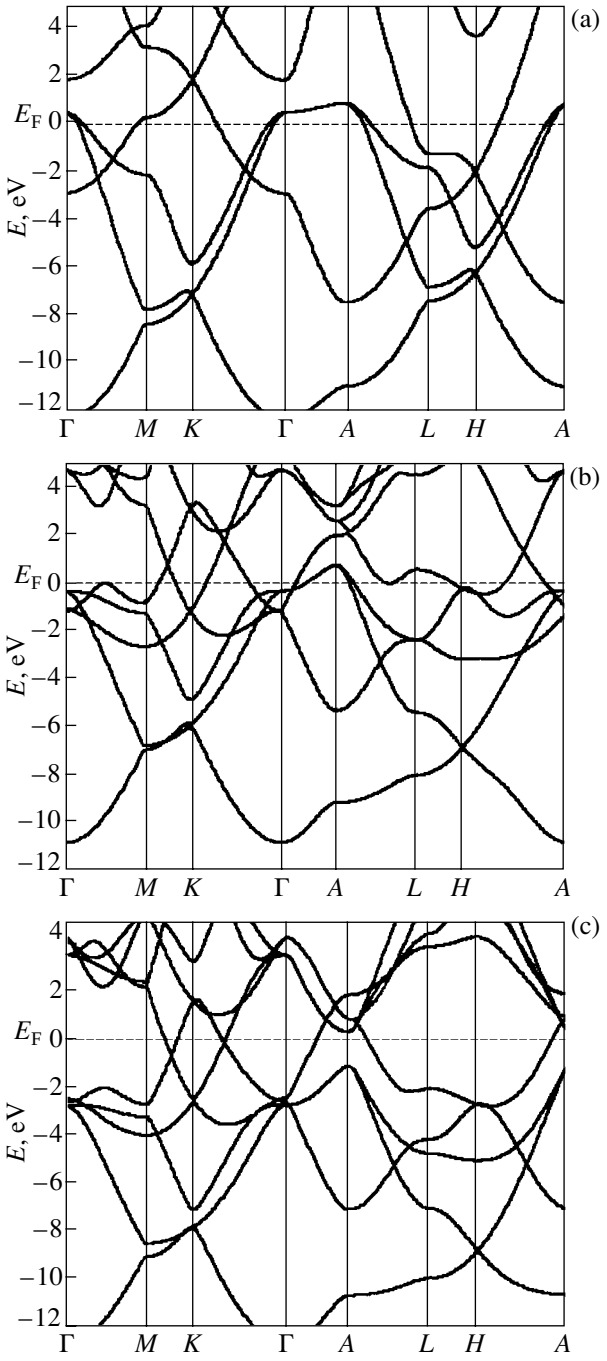

Fig. 4. Energy bands of (a) MgB_2, (b) YB_2, and (c) ZrB_2.

lowing fundamental differences between the superconductivity of YB_2 and ZrB_2 and the superconductivity of MgB_2: (i) the occupation of B $2p_{x,y}$ bonding bands and the absence of hole-type σ states in YB_2 and ZrB_2, (ii) an enhancement of the interaction between the boron and metal layers in YB_2 and ZrB_2 due to the hybridization of B 2*p* and M *d* states (an increase in the dispersion of boron σ bands in the Γ–*A* direction of the Brillouin zone), and (iii) changes in the magnitude and orbital composition of the density of states $N(E_F)$, among which the valence 4*d* states of metals play the dominant role for YB_2 and ZrB_2 (Table 2).

In the series $MgB_2 \longrightarrow YB_2 \longrightarrow ZrB_2$, the contributions of the B 2*p* states to $N(E_F)$ decrease monotonically. By contrast, the contributions of the *Me* 4*d* states vary nonmonotonically and reach a maximum for YB_2. The lowest density of states at the Fermi level $N(E_F)$ is observed for ZrB_2, in which the Fermi level is located in the pseudogap between the bonding and antibonding states. This circumstance suggests that the superconducting properties are less probable for ZrB_2. This is in agreement with the results obtained by Leyarovska and Leyarovski [21], according to which no critical transition in ZrB_2 occurs down to $T < 0.7$ K.

4. CONCLUSIONS

Thus, in this work, we analyzed the parameters of the band structure of UB_{12}-like dodecaborides of yttrium and zirconium. It was demonstrated that an increase in the critical temperature T_C (by ~1.1 K) upon

the transition $YB_2 \longrightarrow ZrB_2$ correlates with an increase in the contribution of the *Me* 4*d* states to the near-Fermi region. The characteristic feature of the band structure of these borides is the location of the Fermi level E_F in the region of an extended plateau in the density of states between the bonding and antibonding bands. This implies that the superconducting properties of these phases are sufficiently stable to variations in their chemical composition.

The absence of superconductivity in yttrium and zirconium borides with a low boron content, especially in yttrium and zirconium layered diborides, was explained in terms of the fundamental differences between their band spectra and the band spectrum of the isostructural superconductor MgB_2.

Based on the results of the band calculations performed for $\square B_{12}$ and BB_{12} hypothetical dodecaborides, we assumed that the transformation of β-boron into the superconducting state under high pressures [8] can be caused by the metallization of the system due to distortions of the crystal lattice and a partial destruction of B_{12} polyhedra, during which part of the boron atoms occupy intericosahedral sites.

REFERENCES

1. J. Nagamatsu, N. Nakagawa, T. Muranaka, *et al.*, Nature **410**, 6824 (2001).
2. A. L. Ivanovskiĭ, Usp. Khim. **70** (9), 711 (2001).
3. C. Buzea and T. Yamashita, Supercond. Sci. Technol. **14** (11), R115 (2001).
4. S. Lee, D. M. Bylander, and L. Kleinman, Phys. Rev. B **42** (2), 1316 (1990).
5. C. Maihiot, J. B. Grant, and A. K. McMahan, Phys. Rev. B **42** (14), 9033 (1990).
6. D. Li, Y.-N. Xu, and W. Y. Ching, Phys. Rev. B **45** (11), 5895 (1992).
7. A. L. Ivanovskiĭ and G. P. Shveĭkin, *Quantum Chemistry in Materials Science: Boron, Its Alloys and Compounds* (Yekaterinburg, 1997).
8. M. L. Eremets, V. V. Struzhkin, H.-K. Mao, and R. J. Hemley, Science **203**, 272 (2001).
9. Yu. B. Kuz'ma, *Crystal Chemistry of Borides* (Vysshaya Shkola, L'vov, 1983).
10. M. Methfessel, C. Rodriquez, and O. K. Andersen, Phys. Rev. B **40** (3), 2009 (1989).
11. S. Y. Savrasov, Phys. Rev. B **54** (23), 16470 (1996).
12. J. P. Perdew and Y. Wang, Phys. Rev. B **45** (23), 13244 (1992).
13. J. P. Perdew, S. Burke, and M. Ernzerhof, Phys. Rev. Lett. **77** (18), 3865 (1996).
14. D. A. Papaconstantopoulos and M. J. Mehl, cond-mat/0111385 (2001).
15. A. L. Ivanovskiĭ, Usp. Khim. **67** (5), 403 (1998).
16. S. V. Vonsovskiĭ, Yu. A. Izyumov, and É. Z. Kurmaev, *Superconductivity of Transition Metals, Their Alloys, and Compounds* (Nauka, Moscow, 1977).
17. I. R. Shein and A. L. Ivanovskiĭ, Fiz. Tverd. Tela (St. Petersburg) **44** (10), 1752 (2002) [Phys. Solid State **44**, 1833 (2002)].
18. J. Kortus, I. I. Mazin, K. D. Belaschenko, *et al.*, Phys. Rev. Lett. **86** (20), 4656 (2001).
19. J. M. An and W. E. Pickett, Phys. Rev. Lett. **86** (19), 4366 (2001).
20. N. I. Medvedeva, A. L. Ivanovskii, J. E. Medvedeva, and A. J. Freeman, Phys. Rev. B **64** (2), R020502 (2001).
21. L. Leyarovska and E. Leyarovski, J. Less-Common Met. **67** (2), 249 (1979).

Translated by N. Korovin

Physics of the Solid State, Vol. 45, No. 8, 2003, pp. 1435–1439. Translated from Fizika Tverdogo Tela, Vol. 45, No. 8, 2003, pp. 1369–1372.

SEMICONDUCTORS AND DIELECTRICS

Mn^{2+} 3*d* Luminescence Kinetics in $Zn_{1-x}Mn_xSe$

V. F. Agekyan*, N. N. Vasil'ev*, V. I. Konstantinov, A. Yu. Serov*, N. G. Filosofov*, and V. N. Yakimovich****

**Fok Institute of Physics, St. Petersburg State University, ul. Pervogo Maya 100, Petrodvorets, St. Petersburg, 198504 Russia*

***Institute of Solid-State and Semiconductor Physics, Academy of Sciences of Belarus, ul. Brovki 17, Minsk, 220072 Belarus*

Received January 14, 2003

Abstract—Intracenter luminescence (IL) of Mn^{2+} in $Zn_{1-x}Mn_xSe$ (x = 0.07, 0.02) was studied under pulsed excitation by the neodymium laser second harmonic. At 4 K, the IL saturation originates from the nonlinearity of the system only at the instant of excitation, the IL decay kinetics after the exciting pulse termination depending only weakly on the pumping level. At 77 K, the decay kinetics in $Zn_{0.93}Mn_{0.07}Se$ depends substantially on the pumping level, because the migration of intracenter excitation over the manganese ions initiates up-conversion, which is a slow nonlinear process. As shown by IL decay measurements in $Zn_{0.98}Mn_{0.02}Se$ (x = 0.02), excitation migration over the Mn^{2+} ions is insignificant even at a high temperature and under strong optical pumping. © *2003 MAIK "Nauka/Interperiodica".*

1. INTRODUCTION

The best known family of dilute magnetic semiconductors (DMSs) is the II–VI compounds, with part of the cations substituted for by iron-group ions (manganese is most frequently used at high magnetic ion concentrations). The specific properties of DMSs originate from the strong exchange coupling of the manganese ions with one another and with electrons (antiferromagnetism, the giant magnetooptic Zeeman and Faraday effects, magnetic polarons). Another feature of the DMSs is the optical transitions between the levels of the unfinished 3*d* shells of iron-group ions, which produce intracenter absorption (IA) and intracenter luminescence (IL). To date, intracenter transitions have been sufficiently studied for high concentrations of magnetic ions in $Cd_{1-x}Mn_xTe$ ($x > 0.4$) [1–8] and for their low concentrations in the wide-band-gap crystals $Zn_{1-x}Mn_xSe$ ($x = 10^{-2}$–10^{-3}) [9, 10]. Intracenter transitions in crystals with an Mn^{2+} concentration on the order of a few percent have been studied to a much lesser degree. This concentration region is of interest because it contains the threshold for intracenter excitation migration over manganese ions.

Many publications have appeared recently on studies of manganese IL in two-dimensional layers and nanocrystals of the II–VI compounds [11–19]. The interest in these crystals stems from the changes in the *sp*–*d* interaction and in the conditions of migration of intracenter excitations observed as one goes over from bulk crystals to two- and zero-dimensional quantum systems. A decrease in the dimensionality of a system should considerably affect the kinetics, quantum yield, and temperature dependence of the IL. Extending experimental and theoretical studies to nanostructures requires detailed information on the relaxation of intracenter excitation in bulk matrices of the II–VI compounds for as broad a range of magnetic component concentrations as possible.

This communication reports on a study of intracenter transitions occurring in a bulk $Zn_{1-x}Mn_xSe$ crystal with x = 0.02 and 0.07. Attention is focused on the IL saturation and the dependence of the IL kinetics on temperature and the optical excitation level.

2. SAMPLES AND EXPERIMENTAL TECHNIQUE

The ZnSe crystals were grown using the Bridgman method. A manganese layer was evaporated on the crystal surface in vacuum, and Mn^{2+} ions were subsequently thermally diffused into the lattice and occupied cation positions. This method of manganese incorporation naturally results in a nonuniform manganese distribution over the bulk crystal. The elemental composition was determined at different points of the sample by using x-ray microprobe analysis; two regions with the above manganese concentrations were selected for optical studies.

The IL was excited by 0.18-μs-long neodymium laser pulses emitted at a repetition frequency of 2 kHz; when the focusing was sharp enough, an excitation level I_e in excess of 10^6 W cm^{-2} was attained. The photon energy was 2.34 eV (the second harmonic), which is less than the width of the $Zn_{1-x}Mn_xSe$ band gap. Thus, the excitation was made directly into the first absorption band of Mn^{2+} 3*d* transitions ($^6A_1$–$^4T_1$ transition), with the band electronic states of the crystal not being involved in the single-photon process. Dia-

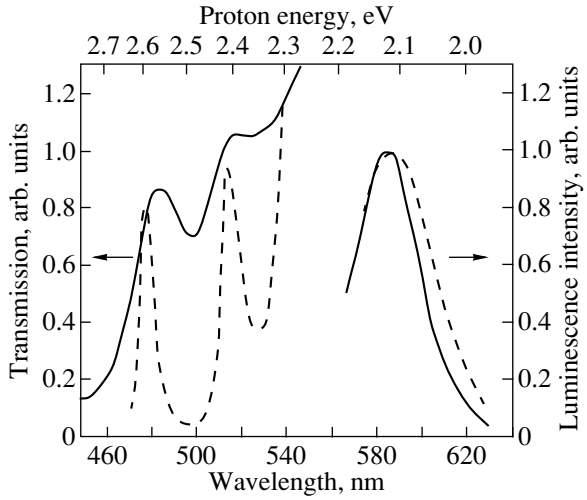

Fig. 1. Transmission and luminescence spectra of $Zn_{0.98}Mn_{0.02}Se$ (solid lines) and $Zn_{0.93}Mn_{0.07}Se$ (dashed lines) obtained in the region of Mn^{2+} intracenter transitions. $T = 77$ K.

phragms were employed to cut off the peripheral part of the laser spot on the sample, so that the IL was detected only from the region of uniform excitation. In our experiments, the uniformity is important, because strong pumping saturates the IL, which can make the contribution due to weakly excited regions noticeable. The IL kinetics was measured at a number of points in its band profile at temperatures of 4 and 77 K.

3. EXPERIMENTAL RESULTS AND DISCUSSION

The Stokes shift in the intracenter absorption spectra increases with increasing manganese concentration, with the maximum of IA shifting toward higher energies and the maximum of IL, toward lower energies (Fig. 1), thus indicating enhancement of the electron–phonon coupling. Another reason for the energy shifts of the intracenter transitions could be a change in the crystal field acting on the Mn^{2+} ion as the zinc is replaced by manganese; in this case, however, the IA and IL bands shift in the same direction in accordance with the change in the zero-phonon transition energy.

At 4 K, the kinetic curves measured at different values of I_e differ from one another only slightly (Fig. 2a), but the IL intensity saturates with increasing I_e. One may conclude that the saturation is due to a fast nonlinear process, which is not detected directly in our experimental conditions. This process is most likely two-step excitation of the Mn^{2+} ion, which is favored by the long ion lifetime in the lowest excited state $^4T_1$–$^6A_1$. The efficiency of two-step excitation of the Mn^{2+} 3*d* shell in II–VI-compound matrices is substantiated by the fact that excitation of $Cd_{0.5}Mn_{0.5}Te$ crystals with a continuous He–Ne laser (photon energy 1.96 eV) reveals the whole IL band peaking at 2.0 eV [20]. The two-step excitation of manganese can occur via the Mn^{2+} levels or with the involvement of impurity levels of a different origin that lie considerably lower than the intracenter absorption threshold. Two-photon excitation of the 3*d* shell is also possible; when estimating its contribution, one should take into account that the single-photon transition $^4T_1$–$^6A_1$ in the Mn^{2+} ion is an intercombination transition and, hence, is forbidden in the dipole approximation. This transition becomes partially allowed due to the odd component of the crystal field and to the interaction of the 3*d* electrons with phonons. Processes involving two photons depend on I_e^2 and bring about saturation of I_l, because the energy of at least one photon transferring an electron from the lowest excited state $^4T_1$–$^6A_1$ to a higher lying state of the Mn^{2+} ion or to the $Zn_{1-x}Mn_xSe$ conduction band dissipates in a nonradiative way. Such processes take place only during the action of a laser pulse on the Mn^{2+} ions. As a result of the IL kinetic curves measured at 4 K being identical for different I_e, the shape of the IL saturation curve does not depend on the time interval t_0 between the pump pulse and the instant of the IL intensity measurement (Fig. 3b).

At 77 K, the IL decay kinetics depends strongly on the excitation level for times $t_0 < 15$ μs (Fig. 2b). For this reason, the shape of the IL saturation curve varies with the delay time t_0 (Fig. 3a). As already mentioned, processes involving two photons play a certain role during the pump pulse at low temperatures. These processes do not affect the shape of the kinetic curve, which was measured with a resolution not better than the laser pulse length. If the dopant concentration is high enough, an increase in temperature initiates the migration of intracenter excitations. In this case, up-conversion becomes significant, because it is a slow nonlinear process directly connected to migration [21]; the part this process plays increases with increasing I_e and is proportional to the squared number of excited manganese ions. Experimentally, the up-conversion manifests itself in the dependence of the IL kinetic curves, $I_l(t)$, on the pumping level I_e. Up-conversion grows in strength with increasing I_e, and the IL decay time in the initial part of the kinetic curve decreases.

As seen from a comparison of the kinetic curves obtained at the center of the IL band for large and small values of I_e at 77 K, the pump level I_e plays a noticeable part for $Zn_{1-x}Mn_xSe$ with $x = 0.07$, whereas for $x = 0.02$, its effect is negligible (Fig. 2c). This suggests that a manganese concentration of about 2% is close to the concentration threshold for intracenter excitation migration at 77 K for the ZnSe matrix. The clearly pronounced variation of the kinetics within the IL band profile at $T = 77$ K (Fig. 2d) likewise indicates that a substantial role is played by intracenter excitation migration for $x = 0.07$.

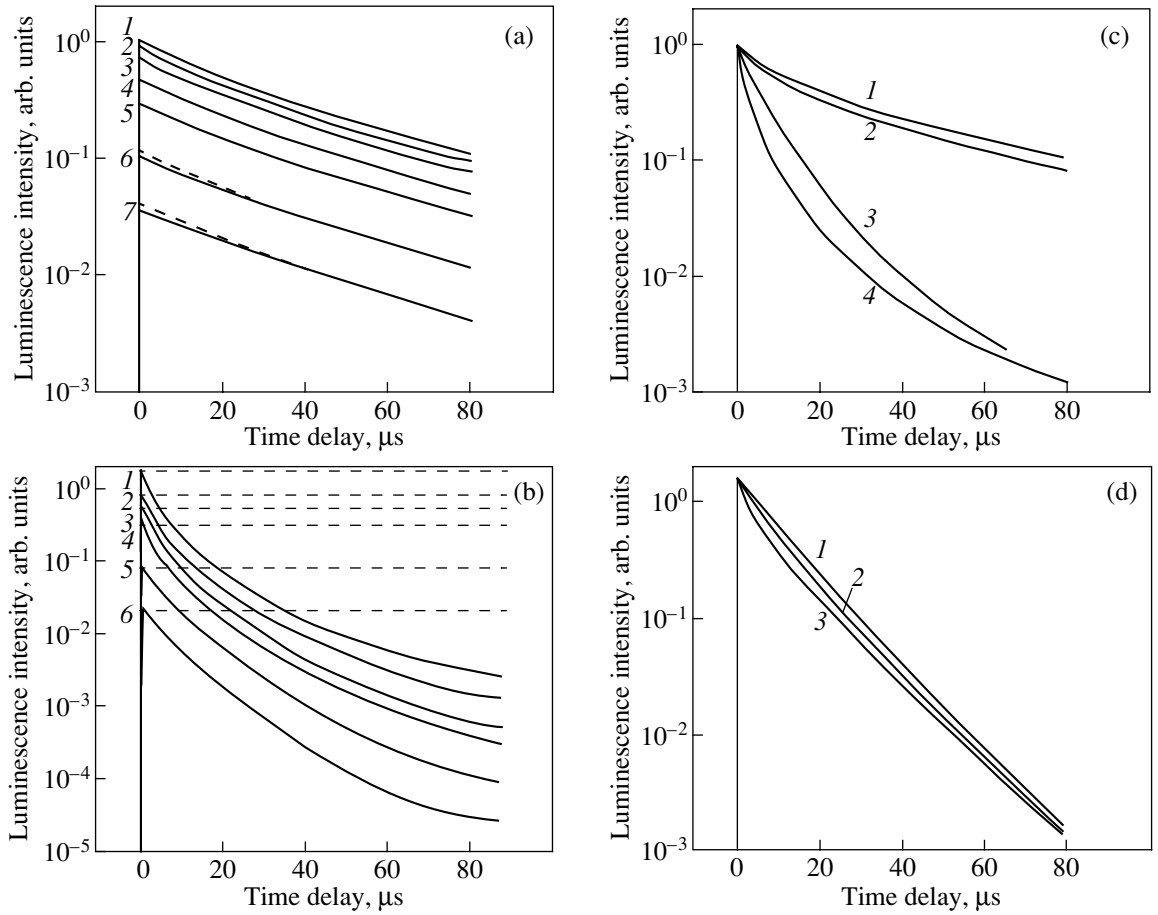

Fig. 2. Decay kinetics of Mn^{2+} intracenter luminescence in $Zn_{1-x}Mn_xSe$ (in panels (c) and (d), the luminescence intensity is normalized to zero delay). (a) $x = 0.07$, $T = 4$ K; the values of the pump level I_e are (*1*) 1, (*2*) 0.65, (*3*) 0.43, (*4*) 0.15, (*5*) 0.06, (*6*) 0.02, and (*7*) 0.002 MW cm^{-2}; dashed lines are plots of the rate equation (2). (b) $x = 0.07$, $T = 77$ K; I_e is equal to (*1*) 1, (*2*) 0.28, (*3*) 0.15, (*4*) 0.06, (*5*) 0.02, and (*6*) 0.002 MW cm^{-2}; dashed lines represent calculated values of I_l upon termination of the pump pulse. (c) Decay curves at the luminescence band maximum for (*1*, *2*) $x = 0.02$ and (*3*, *4*) 0.07 obtained for I_e equal to (*1*, *3*) 0.01 and (*2*, *4*) 2 MW cm^{-2}; $T = 77$ K. (d) Decay curves for $x = 0.07$ obtained at points of the luminescence band profile corresponding to energies of (*1*) 2.01, (*2*) 2.10, and (*3*) 2.18 eV for $I_e = 0.02$ MW cm^{-2}; $T = 4$ K.

At some points in the $x = 0.07$ crystal, the IL decay time in the tails of the kinetic curves at 77 K was observed to increase with increasing I_e. This effect can be assigned to the recharging of a substantial part of the centers responsible for the nonradiative recombination of intracenter excitation of the Mn^{2+} ions (such centers can be native defects and iron-group ions other than manganese). If these centers in a new charge state can no longer quench the IL and remain in this state long enough, the IL decay time increases in the region of large t_0 where up-conversion is already insignificant.

Knowing the intracenter absorption coefficient at the pump frequency, the laser pulse parameters, and the Mn^{2+} lifetime in the excited state $^4T_1$, one can estimate the relative concentration of ions residing in the excited state upon termination of the laser pulse. Our estimation was based on the assumptions that (i) the manganese ion lifetime in the $^4T_1$ state against the radiative transition to the ground state and excitation transfer to another excited ion is long compared to the laser pulse duration and (ii) each absorbed photon excites the Mn^{2+} ion to the $^4T_1$ state. In this case, the concentration of excited ions under strong pumping is a few percent, so the effect of saturation on the dependence of the IL kinetics on I_e should be small. Note that taking two-photon and two-stage processes into account reduces the calculated excited-ion concentration.

The IL properties can be described in the following way. Because of inhomogeneous broadening, the manganese ions residing in different cation environments (a single ion, ion in a small manganese cluster, ion at the center and in the periphery of a large cluster, and so on) have different excited-state energies and different radiative recombination rates *w*. There are *k* types of Mn^{2+}

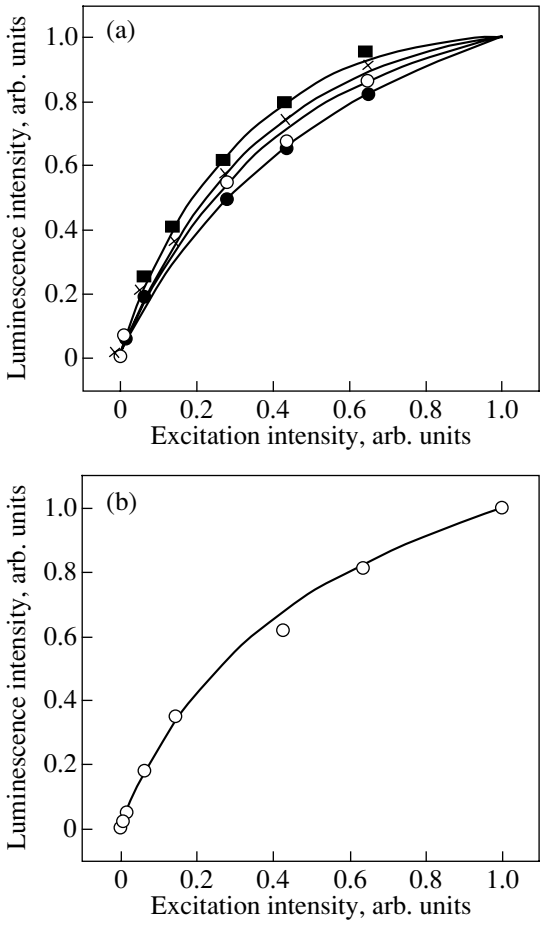

Fig. 3. Intensity I_l at the maximum of the Mn^{2+} intracenter luminescence band in $Zn_{0.93}Mn_{0.07}Se$ plotted vs. the pulsed excitation level I_e for a photon energy of 2.35 eV. The values of I_l are normalized to the excitation level I_e = 1 MW cm^{-2}. (a) T = 77 K; measurement time delays t_0 are 0 (circles), 10 (crosses), and 35 μs (squares); the curve labeled by open circles corresponds to a time-integrated value of I_l. (b) T = 4 K; the relations are the same for all values of t_0.

ions. At 4 K, the IL intensity decay after termination of the laser pulse is described by a sum of exponentials, which are solutions to coupled linear differential equations of the type

$$\{\dot{n}_k = -w_k n_k\}_k,$$

where n_k and w_k are the population and radiative recombination rate for the lowest excited state $^4T_1$ of Mn^{2+} ions of the species k. To take into account the processes occurring during the pump pulse, we introduce the generation rate G into the rate equation. The nonlinear term accounting for the luminescence saturation is nonzero at 4 K only during the laser pulse and can be included in the generation rate G. Now, the coupled equations take on the form

$$\{\dot{n}_k = -w_k n_k + G(t, I_{las})\}_k. \quad (1)$$

We write the generation term in the form $G(t, I_{las}) = F(I_e)I_{las}(t)$, where $I_e = \int_0^\tau I_{las}(t)dt$ (τ is the laser pulse duration) and I_{las} is the instantaneous value of the laser pump intensity. The experimental curves of the IL saturation are well fitted if we assume the existence of two mutually interacting radiative recombination channels for intracenter excitation whose relative contribution depends on the value of I_e. These channels can be identified with the single-photon and two-stage (double-photon) IL excitation. This situation can be quantified by the relation $aI + bI^2 = I_e$, where I is a quantity proportional to the IL intensity. In this case, we have

$$F(I_e) = (a/2b)[-1 + (1 + I_e 4b/a^2)^{1/2}], \quad (2)$$

i.e., the generation rate depends on the excitation level in a complex manner, and this dependence governs the IL saturation. As follows from numerical processing of the experimental data, at 4 K, it is sufficient to take into account in Eq. (1) two species of Mn^{2+} ions (k = 1, 2) with the radiative recombination ratio $w_1/w_2 = 3$.

To describe the IL kinetics at high temperatures (T = 77 K), one should add a nonlinear term responsible for up-conversion to the rate equation (1). In this case, Eq. (1) can be recast as

$$\{\dot{n}_k = -w_k n_k - q_k n_k^2 + G(t, I_{las})\}_k \quad (k = 1, 2),$$

where the generation rate has the same form as in Eq. (1). Because up-conversion is efficient only under intracenter excitation migration, the coefficient q_k will have a noticeable value only for the Mn^{2+} ions that are contained in large clusters.

REFERENCES

1. H.-E. Gumlich, J. Lumin. **23**, 73 (1981).
2. D. Boulanger, R. Parrot, U. W. Pohl, *et al.*, Phys. Status Solidi B **213**, 79 (1999).
3. E. Muller, W. Gebhardt, and V. Gerhardt, Phys. Status Solidi B **113**, 209 (1982).
4. V. F. Agekyan, Yu. V. Rud', and R. Shvabe, Fiz. Tverd. Tela (Leningrad) **29**, 1685 (1987) [Sov. Phys. Solid State **29**, 970 (1987)].
5. J. Gregus, J. Watanabe, and J. Nakahara, J. Phys. Soc. Jpn. **66**, 1810 (1997).
6. L. D. Park, S. Yamamoto, J. Watanabe, *et al.*, J. Phys. Soc. Jpn. **66**, 3289 (1997).
7. V. F. Agekyan, N. N. Vasil'ev, and A. Yu. Serov, Fiz. Tverd. Tela (St. Petersburg) **41**, 49 (1999) [Phys. Solid State **41**, 41 (1999)].
8. S. Yamamoto, K. Takamura, and J. Nakahara, Phys. Status Solidi B **211**, 111 (1999).
9. V. F. Aguekian, N. N. Vasil'ev, A. Yu. Serov, and N. G. Filosofov, J. Cryst. Growth **214/215**, 391 (2000).
10. V. F. Agekyan, N. N. Vasil'ev, A. Yu. Serov, and N. G. Filosofov, Fiz. Tverd. Tela (St. Petersburg) **43**, 1562 (2001) [Phys. Solid State **43**, 1626 (2001)].

11. J. Zhou, Y. Zhou, S. Buddhudu, *et al.*, Appl. Phys. Lett. **76**, 3513 (2000).
12. R. N. Bhargava, J. Cryst. Growth **214/215**, 926 (2000).
13. R. N. Bhargava, V. Chhabra, T. Som, *et al.*, Phys. Status Solidi B **229**, 897 (2002).
14. A. A. Bol and A. Meijerink, J. Lumin. **87/89**, 315 (2000).
15. S.-M. Liu, F.-Q. Liu, H.-Q. Guo, *et al.*, Solid State Commun. **115**, 615 (2000).
16. W. Park, T. C. Jones, S. Schon, *et al.*, J. Cryst. Growth **184/185**, 1123 (1998).
17. J. Nakahara, K. Takamura, and S. Yamamoto, Phys. Status Solidi B **211**, 223 (1999).
18. Wei Chen, R. Sammynaiken, and Yining Huang, J. Appl. Phys. **88**, 5188 (2000).
19. A. D. Dinsmore, D. S. Hsu, S. B. Qadri, *et al.*, J. Appl. Phys. **88**, 4985 (2000).
20. V. F. Agekyan and Fan Zung, Fiz. Tverd. Tela (Leningrad) **27**, 1216 (1985) [Sov. Phys. Solid State **27**, 732 (1985)].
21. V. V. Ovsyankin and P. P. Feofilov, Opt. Spektrosk. **37**, 262 (1973).

Translated by G. Skrebtsov

Physics of the Solid State, Vol. 45, No. 8, 2003, pp. 1440–1450. From Fizika Tverdogo Tela, Vol. 45, No. 8, 2003, pp. 1373–1381.

SEMICONDUCTORS AND DIELECTRICS

A Point Group Approach to Selection Rules in Crystals*

V. P. Smirnov[1], R. A. Evarestov[2], and P. Tronc[3]

[1] *Institute of Fine Mechanics and Optics, St. Petersburg, 197101 Russia*

[2] *St. Petersburg State University (Petrodvorets Branch), Universitetskiĭ pr. 2, Petrodvorets, 198904 Russia*

[3] *Ecole Supérieure de Physique et Chimie Industrielles, F-75005 Paris, France*

Received January 23, 2003

Abstract—The problem of generation of the selection rules for a transition between Bloch states at any point of the Brillouin zone in crystals is equivalent to the problem of the decomposition of Kronecker products of two representations (reps) of a space group into irreducible components (the full group method). This problem can be solved also by the subgroup method where small reps of little groups are used. In this article, we propose a third method of generation of the selection rules, which is formulated in terms of projective reps of crystal point groups. It is based on a well-known relation between small irreducible reps (irreps) of little space groups and projective irreps of the corresponding little cogroups. The proposed procedure is illustrated by calculations of the Kronecker products for different irreps at the *W* point of the Brillouin zone for the nonsymmorphic space group O_h^7, which is one of the most complicated space groups for the generation of selection rules. As an example, the general procedure suggested is applied to obtain the selection rules for direct and phonon-assisted electrical dipole transitions between certain states in crystals with the space group O_h^7. © *2003 MAIK "Nauka/Interperiodica".*

1. INTRODUCTION

Knowledge of the selection rules is well known to be of great importance in the study of the optical properties of crystals, electron–phonon interaction, and phase transitions in solids. It is evident that the generation of selection rules for transitions between states related to the center $\mathbf{k} = 0$ of the Brillouin zone (BZ) can be expressed in terms of representations (reps) of the crystal point group. For direct transitions between the states with $\mathbf{k} \neq 0$ and for indirect transitions, the generation of selection rules is more complex because of the complicated structure of the space group reps (subgroup method [1–4], full group method [5]).

The optical properties at the Γ point in the BZ of materials used for optoelectronic devices are of crucial importance since the materials are direct gap semiconductors. Among them, one can find stoichiometric crystals (such as GaAs, InP, or CaN) and alloys (for example, ternary compounds, such as AlGaAs, or quaternary compounds, such as GaInAsS and GaInAsSb). In any of these materials, the fundamental optical transition takes place at the Γ point, insuring strong absorption and recombination. By varying the ratios of various elements in the alloys, it is possible to tailor the band gap value at point Γ to fit the required operating wavelength. Many nanostructures, such as quantum wells (QWs), superlattices (SLs), quantum wires (QWIs), and quantum dots (QDs), are made of the materials mentioned above. Nanostructures are usually studied in the envelope function approximation based on the properties of the Bloch functions at the Γ point in the BZ of the bulk materials they are built from.

On the other hand, germanium Ge and silicon Si (the most widely used semiconductors) have indirect gaps. Silicon is used to build integrated circuits and other devices based on charge transport phenomena (GaAs and related compounds can also be used for such devices when a high carrier mobility is needed). Some nanostructures, such as type II GaAs/AlAs SLs, also have indirect gaps.

In any bulk semiconductor or semiconductor structure, it is necessary to study direct transitions also at points in the BZ other than Γ and indirect transitions when one or both states correspond to $\mathbf{k} \neq 0$ (participation of a particle with a finite wave vector). The more frequent case is that of phonon assisted transitions. Note that the high symmetry points in the BZ are particularly important since they generally correspond to a high density of phonon states. Deduction of the selection rules in the general case is much more complicated since the symmetry of the Bloch states and hence the selection rules depend on the location of the BZ points involved in the process.

In [3, Chapter 4], the procedure for generating selection rules in the crystals is based on a sufficiently refined mathematical groundwork (double and triple coset decompositions of space groups, use of the Mackey theorem for induced reps). This procedure was realized using a computer program, and the results were collected in the three-volume tables [4].

* This article was submitted by the authors in English.

A simpler approach to the selection rule problem can be developed based on the well-known relation between small irreducible reps (irreps) of little space groups and projective irreps of the corresponding little cogroups [6, 7]. We demonstrate in this paper that the procedure of generation of the selection rules for a transition between any states in a crystal can be formulated in terms of projective irreps of point groups. In Section 2, all the necessary notations are introduced and the connection between irreps of space groups and projective irreps of point groups is considered in detail. The general procedure of generation of the selection rules is formulated in Section 3. Each step of its realization is illustrated by calculations of the Kronecker products for different irreps at the W point of the BZ for nonsymmorphic space group O_h^7, which is one of the most complicated space groups for the generation of selection rules. In Section 4, as an example, the general procedure is applied to obtain the selection rules for direct and phonon-assisted electrical dipole transitions between some states in crystals with space group O_h^7.

2. CONNECTION BETWEEN SMALL REPRESENTATIONS OF SPACE GROUPS AND PROJECTIVE REPRESENTATIONS OF POINT GROUPS

Let the space group G of a crystal consist of the elements $g = (R|\mathbf{v}_R + \mathbf{a_n}) \in G$, where the orthogonal operation R is followed by the improper translation $\mathbf{v}_R$ and lattice translation $\mathbf{a_n}$. The vectors $\mathbf{a_n}$ form the invariant subgroup T of the space group G ($T \lhd G$). The point group F of the n_F orthogonal operations R describes the symmetry of directions in the crystal and is called the crystalline class or point symmetry group of the crystal. The set of left cosets $(R_i|\mathbf{v}_i)T$ in the decomposition of G with respect to the translation subgroup T,

$$G = \sum_{i=1}^{n_F} (R_i|\mathbf{v}_i)T \tag{1}$$

forms a factor group G/T isomorphic to the point group F ($F \rightleftarrows G/T$) of order n_F. The translation group T is Abelian. All its irreps are one-dimensional and are classified by wave vectors $\mathbf{k}$ in the BZ:

$$d^{(\mathbf{k})}(\mathbf{a_n}) = \exp(-i\mathbf{k}\mathbf{a_n}). \tag{2}$$

The elements $g \in G$ leaving the wave vector $\mathbf{k}$ invariant up to reciprocal lattice vector $\mathbf{B_m}$,

$$g^{(\mathbf{k})}\mathbf{k} = R^{(\mathbf{k})}\mathbf{k} = \mathbf{k} + \mathbf{B_m} \tag{3}$$

form the little group $G_\mathbf{k}$ of the wave vector $\mathbf{k}$. The group $G_{-\mathbf{k}}$ consists of the same elements as the group $G_\mathbf{k}$. The little cogroup $F_\mathbf{k} = F_{-\mathbf{k}}$ includes the elements $R^{(\mathbf{k})}$ ($(R^{(\mathbf{k})}|\mathbf{v}_{R^{(\mathbf{k})}}) \in G_\mathbf{k}$). The representatives $g_i = (R_j|\mathbf{v}_j)$ of left cosets $g_jG_\mathbf{k}$ in the decomposition of G with respect to $G_\mathbf{k} \subset G$,

$$G = \sum_{j=1}^{t} g_jG_\mathbf{k}, \quad g_1 = (E|0) \tag{4}$$

determine the so-called irreducible star $^*\mathbf{k}$ of the wave vector $\mathbf{k}$ consisting of wave vectors t:

$$^*\mathbf{k}: \mathbf{k}_j = g_j\mathbf{k} = R_j\mathbf{k}, \quad j = 1, 2, \ldots, t. \tag{5}$$

The little groups $G_{\mathbf{k}_j}$ for different points of the star $^*\mathbf{k}$ are isomorphous to the little group $G_\mathbf{k}$:

$$G_{\mathbf{k}_j} = g_jG_\mathbf{k}g_j^{-1}. \tag{6}$$

The irreps of G (full irreps) are labeled by the irreducible star $^*\mathbf{k}$ of the wave vector $\mathbf{k}$ and by the index γ numbering the inequivalent irreps within the same star $^*\mathbf{k}$: $[G]_\gamma^{(^*\mathbf{k})}$. The full irrep $[G]_\gamma^{(^*\mathbf{k})}$ of G is in a one-to-one correspondence with the small irrep $[G_\mathbf{k}]_\gamma$ of $G_\mathbf{k} \subset G$ and is obtained from the latter by the induction procedure [7, 8]:

$$[G]_\gamma^{(^*\mathbf{k})} = [G_\mathbf{k}]_\gamma \uparrow G. \tag{7}$$

The set of all small irreps of all little groups $G_\mathbf{k}$, with $\mathbf{k}$ being in a representation domain of the BZ, determines unambiguously all the irreps of the space group G. That is why the tables of space group irreps, as a rule, contain the small irreps of little groups $G_\mathbf{k}$ [3, 9–12].

The matrices $D^{([G_\mathbf{k}]_\gamma)}(g_{i,\mathbf{n}})$ ($g_{i,\mathbf{n}} \in G_\mathbf{k}$) of the small irreps $[G_\mathbf{k}]_\gamma$ of $G_\mathbf{k}$ are in one-to-one correspondence with the matrices $d^{([F_\mathbf{k}]_\gamma)}(R_i)$ of the so-called projective irreps $[F_\mathbf{k}]_\gamma$ of $F_\mathbf{k}$ as follows:

$$\begin{aligned} D^{([G_\mathbf{k}]_\gamma)}(g_{i,\mathbf{n}}) &= e^{-i\mathbf{k}\mathbf{a}_\mathbf{n}}d^{([F_\mathbf{k}]_\gamma)}(R_i), \\ g_{i,\mathbf{n}} &= (R_i|\mathbf{v}_i + \mathbf{a_n}) \in G_\mathbf{k}, \quad R_i \in F_\mathbf{k}. \end{aligned} \tag{8}$$

In particular, the matrices $D^{([G_\mathbf{k}]_\gamma)}(g_{i,0})$ and $d^{([F_\mathbf{k}]_\gamma)}(R_i)$ coincide

$$\begin{aligned} D^{([G_\mathbf{k}]_\gamma)}(g_{i,0}) &= d^{([F_\mathbf{k}]_\gamma)}(R_i), \\ g_{i,0} &= (R_i|\mathbf{v}_i) \in G_\mathbf{k}, \quad R_i \in F_\mathbf{k}. \end{aligned} \tag{9}$$

The multiplication law for the matrices $d^{([F_\mathbf{k}]_\gamma)}(R_i)$ of projective irreps $[F_\mathbf{k}]_\gamma$ of a cogroup $F_\mathbf{k}$ follows from the multiplication law for space group elements:

$$\begin{aligned} &d^{([F_\mathbf{k}]_\gamma)}(R_i)d^{([F_\mathbf{k}]_\gamma)}(R_{i'}) \\ &= d^{([F_\mathbf{k}]_\gamma)}(R_iR_{i'})\omega^{(\mathbf{k})}(R_i, R_{i'}), \end{aligned} \tag{10}$$

where the set of

$$\omega^{(\mathbf{k})}(R_i, R_{i'}) = e^{-i\mathbf{k}(\mathbf{v}_i + R_i\mathbf{v}_{i'} - \mathbf{v}_{i,i'})},$$
$$|\omega(R_i, R_{i'})|^2 = 1, \quad R_i, R_{i'} \in F_{\mathbf{k}} \tag{11}$$

is a factor system for the projective irreps $[F_{\mathbf{k}}]_\gamma$ ($g_{i',0} = (R_i, R_{i'}|\mathbf{v}_{ii'}) \in G_{\mathbf{k}}$). The characters of these projective irreps can be taken directly from tables [3, 9, 10, 12]. If all the factors in (11) are equal to unity, then the projective irrep becomes an ordinary one. In particular, this is the case of all the little cogroups $F_{\mathbf{k}}$ of all the symmorphic space groups (since all $\mathbf{v}_{j'} = 0$).

There exist projective irreps $\overline{[F_{\mathbf{k}}]_\gamma}$ with another choice of the factor system (*p*-equivalent to $[F_{\mathbf{k}}]_\gamma$):

$$D^{([F_{\mathbf{k}}]_\gamma)}(g_{i,\mathbf{n}}) = e^{-i\mathbf{k}(\mathbf{v}_i + \mathbf{a}_\mathbf{n})} d^{(\overline{[F_{\mathbf{k}}]_\gamma})}(R_i),$$
$$g_{i,\mathbf{n}} = (R_i|\mathbf{v}_i + \mathbf{a}_\mathbf{n}) \in G_{\mathbf{k}}, \quad R_i \in F_{\mathbf{k}},$$
$$\overline{\omega}^{(\mathbf{k})}(R_i, R_{i'}) = e^{i(\mathbf{k} - R_i^{-1}\mathbf{k})\mathbf{v}_{i'}},$$
$$|\overline{\omega}(R_i, R_{i'})|^2 = 1, \quad R_i, R_{i'} \in F_{\mathbf{k}}. \tag{12}$$

They are used in [11]. The matrices $D^{([G_{\mathbf{k}}]_\gamma)}(g_{i,0})$ and $d^{(\overline{[F_{\mathbf{k}}]_\gamma})}(R_i)$ differ only by the factor $e^{-i\mathbf{k}\mathbf{v}_i}$:

$$D^{([F_{\mathbf{k}}]_\gamma)}(g_{i,0}) = e^{-i\mathbf{k}\mathbf{v}_i} d^{(\overline{[F_{\mathbf{k}}]_\gamma})}(R_i),$$
$$g_{i,0} = (R_i|\mathbf{v}_i) \in G_{\mathbf{k}}, \quad R_i \in F_{\mathbf{k}}. \tag{13}$$

Let relation (8) between the reps $[G_{\mathbf{k}}]_\gamma$ of $G_{\mathbf{k}}$ and $[F_{\mathbf{k}}]_\gamma$ of $F_{\mathbf{k}}$ be denoted by the symbols

$$[G_{\mathbf{k}}]_\gamma = [F_{\mathbf{k}}]_\gamma \Uparrow G_{\mathbf{k}}, \quad [F_{\mathbf{k}}]_\gamma = [G_{\mathbf{k}}]_\gamma \Downarrow F_{\mathbf{k}}. \tag{14}$$

Then, the relation between the irreps $[G]_\gamma^{(*\mathbf{k})}$ of space group G and the projective irreps $[F_{\mathbf{k}}]_\gamma$ or $\overline{[F_{\mathbf{k}}]_\gamma}$ of little cogroups has the form

$$[G]_\gamma^{(*\mathbf{k})} = ([F_{\mathbf{k}}]_\gamma \Uparrow G_{\mathbf{k}}) \uparrow G,$$
$$\text{or} \quad [G]_\gamma^{(*\mathbf{k})} = (\overline{[F_{\mathbf{k}}]_\gamma} \Uparrow G_{\mathbf{k}}) \uparrow G. \tag{15}$$

The basis functions of irreps $[G]_\gamma^{(*\mathbf{k})}$ of space group G can always be chosen to be the basis functions of small irreps $[G_{\mathbf{k}}]_\gamma$ of little groups $G_{\mathbf{k}}$ and projective irreps $[F_{\mathbf{k}}]_\gamma$ (or $\overline{[F_{\mathbf{k}}]_\gamma}$) of little cogroups $F_{\mathbf{k}}$.

For generation of the selection rules, it is necessary to consider the direct product of small reps of two of the little groups. The latter is possible only for the common elements of little groups, i.e., for their intersection. Let $[G_{\mathbf{k}_1}]_\alpha$ and $[G_{\mathbf{k}_2}]_\beta$ be small reps of the two little groups $G_{\mathbf{k}_1}$ and $G_{\mathbf{k}_2}$. The direct product of their subductions on their intersection $([G_{\mathbf{k}_1}]_\alpha \downarrow (G_{\mathbf{k}_1} \cap G_{\mathbf{k}_2}) \times [G_{\mathbf{k}_2}]_\beta \downarrow (G_{\mathbf{k}_1} \cap G_{\mathbf{k}_2}))$ is a small rep of the group $(G_{\mathbf{k}_1} \cap G_{\mathbf{k}_2})$. Every element $g_{i,0} \in (G_{\mathbf{k}_1} \cap G_{\mathbf{k}_2})$ leaves invariant the wave vectors $\mathbf{k}_1$ and $\mathbf{k}_2$ and, therefore, their sum $\mathbf{k}_3 = \mathbf{k}_1 + \mathbf{k}_2$: $(G_{\mathbf{k}_1} \cap G_{\mathbf{k}_2}) \subseteq G_{\mathbf{k}_3}$. The little group $G_{\mathbf{k}_3}$ has no other common elements either with $G_{\mathbf{k}_1}$ or with $G_{\mathbf{k}_2}$. Indeed, let us assume the contrary, that

$$\tilde{g} \in G_{\mathbf{k}_3}, \quad \tilde{g} \in G_{\mathbf{k}_1}, \quad \tilde{g} \notin (G_{\mathbf{k}_1} \cap G_{\mathbf{k}_2}). \tag{16}$$

Such an element $\tilde{g}$ would leave invariant $\mathbf{k}_3$ and $\mathbf{k}_1$ and, therefore, $\mathbf{k}_2 = \mathbf{k}_3 - \mathbf{k}_1$; i.e., it would be contained in $G_{\mathbf{k}_1} \cap G_{\mathbf{k}_2}$ in contradiction to the initial assumption. Let $d^{([F_{\mathbf{k}_1}]_\alpha)}$ and $d^{([F_{\mathbf{k}_2}]_\beta)}$ be the matrices of subductions of the projective reps $[F_{\mathbf{k}_1}]_\alpha \downarrow (F_{\mathbf{k}_1} \cap F_{\mathbf{k}_2})$ and $[F_{\mathbf{k}_2}]_\beta \downarrow (F_{\mathbf{k}_1} \cap F_{\mathbf{k}_2})$ of two little cogroups $F_{\mathbf{k}_1}$ and $F_{\mathbf{k}_2}$ with factor systems $\omega^{(\mathbf{k}_1)}(R_i, R_j)$ and $\omega^{(\mathbf{k}_2)}(R_i, R_j)$ ($R_i, R_j \in F_{\mathbf{k}_1} \cap F_{\mathbf{k}_2}$), respectively. The direct product $d^{([F_{\mathbf{k}_1}]_\alpha)} \times d^{([F_{\mathbf{k}_2}]_\beta)}$ is a projective rep $d^{([F_{\mathbf{k}_3}]_{\alpha\beta})}$ ($\mathbf{k}_3 = \mathbf{k}_1 + \mathbf{k}_2$) of the group $(F_{\mathbf{k}_1} \cap F_{\mathbf{k}_2}) \subset F_{\mathbf{k}_3}$ with the factor system $\omega^{(\mathbf{k}_3)}(R_i, R_j) = \omega^{(\mathbf{k}_1)}(R_i, R_j)\omega^{(\mathbf{k}_2)}(R_i, R_j)$. Indeed, let

$$d^{([F_{\mathbf{k}_3}]_{\alpha\beta})}(R) \equiv d^{([F_{\mathbf{k}_1}]_\alpha)}(R) \times d^{([F_{\mathbf{k}_2}]_\beta)}(R), \quad R \in (F_{\mathbf{k}_1} \cap F_{\mathbf{k}_2}) \tag{17}$$

be matrices of the direct product of two projective reps. Then,

$$\begin{aligned}
&d^{([F_{\mathbf{k}_3}]_{\alpha\beta})}(R_1) d^{([F_{\mathbf{k}_3}]_{\alpha\beta})}(R_2) \\
&= \left\{ d^{([F_{\mathbf{k}_1}]_\alpha)}(R_1) \times d^{([F_{\mathbf{k}_2}]_\beta)}(R_1) \right\} \\
&\times \left\{ d^{([F_{\mathbf{k}_1}]_\alpha)}(R_2) \times d^{([F_{\mathbf{k}_2}]_\beta)}(R_2) \right\} \\
&= \left\{ d^{([F_{\mathbf{k}_1}]_\alpha)}(R_1) d^{([F_{\mathbf{k}_2}]_\alpha)}(R_2) \right\} \\
&\times \left\{ d^{([F_{\mathbf{k}_1}]_\beta)}(R_1) d^{([F_{\mathbf{k}_2}]_\beta)}(R_2) \right\} \\
&= \left\{ d^{([F_{\mathbf{k}_1}]_\alpha)}(R_1 R_2) \omega^{(\mathbf{k}_1)}(R_1, R_2) \right\} \\
&\times \left\{ d^{([F_{\mathbf{k}_2}]_\beta)}(R_1, R_2) \omega^{(\mathbf{k}_2)}(R_1, R_2) \right\} \\
&= (d^{([F_{\mathbf{k}_3}]_{\alpha\beta})}(R_1 R_2) \omega^{(\mathbf{k}_1)}(R_1, R_2) \omega^{(\mathbf{k}_2)}(R_1, R_2))
\end{aligned} \tag{18}$$

$$= (d^{([F_{\mathbf{k}_3}]_{\alpha\beta})}(R_1R_2)\omega^{\mathbf{k}_3}(R_1, R_2))$$

for both (11) and (12) factor systems.

Let the coset representatives $g_s^{(j)} \in G_{\mathbf{k}_j}$ in the decomposition of $G_{\mathbf{k}_j}$ with respect to the translation group T,

$$G_{\mathbf{k}_j} = \sum_s g_s^{(j)} T, \quad g_s^{(1)} \in G_{\mathbf{k}} \tag{19}$$

be chosen in the form $g_s^{(j)} \equiv (R_s^{(j)}|\mathbf{v}_s^{(j)})$; i.e., they are among the representatives $(R_i|\mathbf{v}_i)$ in the decomposition (1). The element $g_j g_s^{(1)} g_j^{-1} \in G_{\mathbf{k}_j}$, with g_j taken from decomposition (4) (see also (6)), may differ from $g_s^{(j)}$ by some lattice translation. This is why the notations of the small irreps of the little groups $G_{\mathbf{k}}$ and $G_{\mathbf{k}_j}$ (and the projective irreps of the corresponding little cogroups) may differ.

In particular, let $g_{j_0}\mathbf{k} = -\mathbf{k}$. The groups $G_{\mathbf{k}}$ and $G_{-\mathbf{k}}$ are composed of the same elements. The whole set of small irreps of the little group $G_{-\mathbf{k}}$ is complex conjugated with respect to the whole set of small irreps of the little group $G_{\mathbf{k}}$, but the notations of the irreps of $G_{\mathbf{k}}$ and of $G_{-\mathbf{k}}$ may differ (see example in Section 3).

Let Q be a group and H be its subgroup ($H \subset Q$). Let $d^{(\alpha)}$ and $D^{(\beta)}$ be irreps of H and Q, respectively. Then, the frequency of the irrep $D^{(\beta)}$ of Q in the rep $(d^{(\alpha)} \uparrow Q)$ induced by the irrep $d^{(\alpha)}$ of H is equal to the frequency of the irrep $d^{(\alpha)}$ of H in the rep $(D^{(\beta)} \downarrow H)$ subducted by $D^{(\beta)}$ on H (Frobenius reciprocity theorem). This theorem can be applied also to the projective irreps of a group and its subgroup with the same factor system [6].

3. PROCEDURE OF GENERATION OF THE SELECTION RULES USING PROJECTIVE REPRESENTATIONS OF POINT GROUPS

The stationary states of a system with space group symmetry G are classified according to the irreps of G, and their full group-theoretical notation is as follows: $|\mathbf{k}, \gamma, m, \mu\rangle$, where $\mathbf{k} = \mathbf{k}_1, \mathbf{k}_2, \ldots, \mathbf{k}_t$ (star $^*\mathbf{k}$), m numbers the basis vectors of the small irrep γ of the little group $G_{\mathbf{k}}$, and μ numbers the independent bases of equivalent reps of $G_{\mathbf{k}}$.

Let us consider the selection rules for the transitions between the stationary states $|\mathbf{k}^{(f)}, \gamma^{(f)}, m^{(f)}, \mu^{(f)}\rangle$ and $|\mathbf{k}^{(i)}, \gamma^{(i)}, m^{(i)}, \mu^{(i)}\rangle$ caused by an operator $P(\mathbf{k}^{(p)}, \gamma^{(p)}, m^{(p)})$ transforming according to the irrep $(\mathbf{k}^{(p)}, \gamma^{(p)})$ of G. If the operator P transforms according to a reducible rep of G, one can obtain the selection rules for each of its irreducible components separately. The transition probability is governed by the value of the matrix element:

$$\langle \mathbf{k}^{(f)}, \gamma^{(f)}, m^{(f)}, \mu^{(f)}|P(\mathbf{k}^{(p)}, \gamma^{(p)}, m^{(p)}) \times |\mathbf{k}^{(i)}, \gamma^{(i)}, m^{(i)}, \mu^{(i)}\rangle. \tag{20}$$

The transition is said to be allowed by symmetry if the triple direct (Kronecker) product

$$(\mathbf{k}^{(f)}, \gamma^{(f)})^* \times (\mathbf{k}^{(p)}, \gamma^{(p)}) \times (\mathbf{k}^{(i)}, \gamma^{(i)}) \tag{21}$$

contains the identity irrep of G. This condition can be rewritten in one of three forms:

$$[(\mathbf{k}^{(p)}, \gamma^{(p)}) \times (\mathbf{k}^{(i)}, \gamma^{(i)})] \cap (\mathbf{k}^{(f)}, \gamma^{(f)}) \neq 0, \tag{22}$$

$$[(\mathbf{k}^{(f)}, \gamma^{(f)}) \times (\mathbf{k}^{(i)}, \gamma^{(i)})^*] \cap (\mathbf{k}^{(p)}, \gamma^{(p)}) \neq 0, \tag{23}$$

$$[(\mathbf{k}^{(f)}, \gamma^{(f)}) \times (\mathbf{k}^{(p)}, \gamma^{(p)})^*] \cap (\mathbf{k}^{(i)}, \gamma^{(i)}) \neq 0. \tag{24}$$

Whatever the form of the selection rules, it is necessary to find the direct product of two (or three (21)) irreps of the space group G (complex conjugate irreps are also irreps of G).

We discuss now the procedure of generating the selection rules using projective irreps of point groups. To illustrate each step of this procedure, we have chosen the small irreps of the little group G_W in the space group O_h^7 given in the tables in [9]. Note that translations $\mathbf{a_n}$ are mapped in [9] by the factor $\exp(i\mathbf{k}\mathbf{a_n})$. According to the general definition

$$\hat{t}_{\mathbf{a_n}}\psi(\mathbf{r}) \equiv \psi(\mathbf{r} - \mathbf{a_n}) = \exp(-i\mathbf{k}\mathbf{a_n})\psi(\mathbf{r}), \tag{25}$$

we choose the translations $\mathbf{a_n}$ to be mapped by the factor $\exp(-i\mathbf{k}\mathbf{a_n})$. This choice does not affect the notations used in [9] for small irreps in the case when $\mathbf{k}$ is equivalent to $-\mathbf{k}$ or the small irreps $[G_{\mathbf{k}}]_\gamma$ from [9] refer to the wave vector $-\mathbf{k}$ in other cases (when $\mathbf{k}$ and $-\mathbf{k}$ are different vectors of the same star or belong to different stars).

The star $^*W$ consists of six vectors: $W^{(1)} = (1, 0, 2)$, $W^{(2)} = (1, 2, 0)$, $W^{(3)} = (2, 1, 0)$, $W^{(4)} = (0, 1, 2)$, $W^{(5)} = (0, 2, 1)$, and $W^{(6)} = (2, 0, 1)$ (in units of π/a along Cartesian axes, with a being the lattice constant). The little group $G_{W^{(j)}}$ has two single-valued ($[G_{W^{(j)}}]_\gamma$, $\gamma = 1, 2$) and five double-valued ($[G_{W^{(j)}}]_\gamma$, $\gamma = 3, 4, 5, 6, 7$) small irreps [9, 12], which are unambiguously related (see Section 2) to the corresponding projective irreps $[F_{W^{(j)}}]_j$ of little cogroups $F_{W^{(j)}} = D_{2d}^{(j)}$ (see Table 1). As the characters (and matrices) of the elements $(R|\mathbf{v}_R) \in G_{W^{(j)}}$ and $R \in F_{W^{(j)}}$ are the same, we use the notations $W_\gamma \equiv [G_{W^{(j)}}]_\gamma$ ($\gamma = 1$–7) of small irreps of the little groups $G_{W^{(j)}}$ also for the corresponding projective

Table 1. Characters of single- and double-valued projective irreps of the small cogroups $F_{W^{(i)}} \equiv D_{2d}^{(i)}$ (i = 1–6) and single- and double-valued small irreps of the little groups $G_{W^{(i)}}$ (i = 1–6) (for six vectors in the star $*W$: (102), (120), (210), (012), (021), and (201) in units of π/a along Cartesian axes, with a being the lattice constant) in the BZ in crystals with space group O_h^7 and $\varepsilon = \exp(i\pi/4)$

$D_{2d}^{(1)}$	$D_{2d}^{(2)}$	E	S_{4x}	S_{4x}^{-1}	C_{2x}	U_{yz}	$U_{y\bar{z}}$	σ_y	σ_z
$D_{2d}^{(3)}$	$D_{2d}^{(4)}$	E	S_{4y}	S_{4y}^{-1}	C_{2y}	U_{xz}	$\bar{U}_{x\bar{z}}$	σ_z	σ_x
$D_{2d}^{(5)}$	$D_{2d}^{(6)}$	E	S_{4z}	S_{4z}^{-1}	C_{2z}	U_{xy}	$\bar{U}_{x\bar{y}}$	σ_x	σ_y
W_1	W_1^*	2	$\sqrt{2}\,\varepsilon^*$	$\sqrt{2}\,\varepsilon$	0	0	0	0	0
W_2	W_2^*	2	$-\sqrt{2}\,\varepsilon^*$	$-\sqrt{2}\,\varepsilon$	0	0	0	0	0
W_3	W_5^*	1	ε^*	$-\varepsilon$	i	1	$-i$	$-\varepsilon^*$	$-\varepsilon$
W_4	W_6^*	1	$-\varepsilon^*$	ε	i	–1	i	$-\varepsilon^*$	$-\varepsilon$
W_5	W_3^*	1	ε^*	$-\varepsilon$	i	–1	i	ε^*	ε
W_6	W_4^*	1	$-\varepsilon^*$	ε	i	1	$-i$	ε^*	ε
W_7	W_7^*	2	0	0	$-2i$	0	0	0	0

irreps of little cogroups $G_{W^{(j)}} = D_{2d}^{(j)}$. Since $\mathbf{k}_{W^{(j)}} \neq -\mathbf{k}_{W^{(j)}}$ and $\mathbf{k}_{W^{(2)}} \sim -\mathbf{k}_{W^{(1)}}$, we take the irreps of the little group $G_{W^{(2)}}$ from [9] as the irreps of the little group $G_{W^{(1)}}$ (see (25) and the remark thereunder). Moreover, as $\mathbf{k}_{W^{(2)}} \sim -\mathbf{k}_{W^{(1)}}$, the total sets of single- and double-valued irreps of little groups $G_{W^{(1)}}$ and $G_{W^{(2)}}$ are complex conjugate, but the elements of $G_{W^{(2)}} = IG_{W^{(1)}}I^{-1}$, which are isomorphic to the elements of $G_{W^{(1)}}$ according to (6), may differ from the coset representatives in decomposition (4) in some of their lattice translations. This may change the numbering of the irreps of the little group $G_{W^{(2)}}$ (and projective irreps of the corresponding little cogroup $F_{W^{(2)}}$) with respect to those of $G_{W^{(1)}}$ (of $F_{W^{(1)}}$, see Table 1; for example, $W_3(D_{2d}^{(2)}) = W_5^*(D_{2d}^{(1)})$).

Taking form (22) for the selection rules, we consider the Kronecker product of the irreps of the space group G,

$$[G]_{\gamma^{(p)}\gamma^{(i)}} \equiv [G]_{\gamma^{(p)}}^{(*\mathbf{k}^{(p)})} \times [G]_{\gamma^{(i)}}^{(*\mathbf{k}^{(i)})} \tag{26}$$

whose basis vectors are the products

$$\begin{aligned} &|\mathbf{k}_n^{(p)}, \gamma^{(p)}, m^{(p)}\rangle |\mathbf{k}_l^{(i)}, \gamma^{(i)}, m^{(i)}\rangle \\ &(n = 1, \ldots, s^{(p)};\ l = 1, \ldots, s^{(i)}; \\ &m^{(p)} = 1, \ldots, t^{(p)};\ m^{(i)} = 1, \ldots, t^{(i)}), \end{aligned} \tag{27}$$

where $s^{(p)}$, $s^{(i)}$ are the numbers of rays in the stars $*\mathbf{k}^{(p)}$, $*\mathbf{k}^{(i)}$ and $t^{(p)}$, $t^{(i)}$ are the dimensions of small irreps $[G_{\mathbf{k}_n^{(p)}}]_{\gamma^{(p)}}$ and $[G_{\mathbf{k}_l^{(i)}}]_{\gamma^{(i)}}$ of little groups $G_{\mathbf{k}_n^{(p)}}$ and $G_{\mathbf{k}_l^{(i)}}$, respectively.

In the case of the W point in the BZ for the space group O_h^7, the basis (27) of the Kronecker product (26) for $\gamma^{(p)} = \gamma^{(i)} = 1$ ($*\mathbf{k}^{(p)} = *\mathbf{k}^{(i)} = *W$; $s^{(p)} = s^{(i)} = 6$, $[G]_{11} \equiv [G]_1^{(*W^{(p)})} \times [G]_1^{(*W^{(i)})}$) consists of $(2 \times 6) \times (2 \times 6) = 144$ vectors.

By decomposing the reducible rep $[G]_{11}$ of G, one finds all the irreducible stars $*\mathbf{k}^{(f)}$ contained in the reducible star of $[G]_{11}$ and the small irreps $[G_{\mathbf{k}^{(f)}}]_j$ of little groups $G_{\mathbf{k}^{(f)}}$ contained in the rep $[G]_{11}$. A star of $s^{(p)}s^{(i)}$ wave vectors

$$\begin{aligned} &\mathbf{k}_{n,l}^{(f)} = \mathbf{k}_n^{(p)} + \mathbf{k}_l^{(i)} + \mathbf{B}_{n,l} \\ &(n = 1, \ldots, s^{(p)},\ l = 1, \ldots, s^{(i)}) \end{aligned} \tag{28}$$

of basis functions (27) splits into irreducible stars and gives wave vector selection rules (the vector $\mathbf{B}_{n,l}$ is a reciprocal lattice vector which may be zero).

For Kronecker products $[G]_1^{(*W^{(p)})} \times [G]_1^{(*W^{(i)})}$ of two irreps of O_h^7 at the W point of BZ, the wave vector selection rules (28) give three irreducible stars (Γ, X, Σ; see Table 2). This is easily shown by rewriting the vectors of the W star in components of the primitive translations of the reciprocal lattice. For example, as $W^{(1)}$ = (1/2, 3/4, 1/4) and $W^{(2)}$ = (1/2, 1/4, 3/4), one obtains $W^{(1)} + W^{(2)}$ = (1, 1, 1) ($\sim\Gamma$) and $W^{(1)} + W^{(1)}$ = (1, 3/2, 1/2) ($\sim X^{(x)}$). Thus, 144 products (27) are partitioned in such a way that $4 \times 6 = 24$ of them corresponds to Γ, $4 \times 6 = 24$ to X, and $4 \times 4 \times 6 = 96$ to Σ points of the BZ.

The set of wave vectors $\mathbf{k}_{n,l}^{(f)}$ (28) contains all the rays of all the irreducible stars appearing in the Kronecker product (26) and may be arranged in a table like that shown in Table 2. Rows and columns of this table are numbered by the rays of the irreducible stars $*\mathbf{k}^{(p)}$ and $*\mathbf{k}^{(i)}$ (by n and l), respectively. Representatives of all the irreducible stars in (26) appear in any row of this table. Indeed, all the rows of the table ($n = 2, \ldots, s^{(p)}$ in (28)) may be obtained from the first one ($n = 1$) by applying the operations $R_n^{(p)}$, which transform the wave vector $\mathbf{k}_1^{(p)}$ into $\mathbf{k}_n^{(p)}$ ($n = 2, \ldots, s^{(p)}$). Under symmetry operations $R_n^{(p)}$, the set of wave vectors $\mathbf{k}_l^{(i)}$ of the star $*\mathbf{k}^{(i)}$ remains unchanged and the irreducible stars formed by wave vectors $\mathbf{k}_{1,l}^{(f)}$ may change their representatives but can neither disappear, give rise to new irreducible stars, nor change the number of each star representatives. The same consideration is valid for the columns. Finally, all the rows (columns) of the entire table contain as many representatives of each irreducible star as the first row (column). Therefore, all necessary information about the wave vector selection rules for the Kronecker product (26) is contained in any row (column) of the corresponding table. The wave vector selection rules for all the symmetry points of the BZ of space group O_h^7 are represented in Table 3. The latter is composed of the first rows of tables similar to Table 2 and corresponding to Kronecker products $*\Gamma \times *\Gamma$, $*X \times *X$, $*L \times *L$, $*W \times *W$, $*\Gamma \times *X$, $*\Gamma \times *L$, $*\Gamma \times *W$, $*X \times *L$, $*X \times *W$, and $*L \times *W$.

At the next step of generating the selection rules, one needs to find the irreducible components of the reducible reps for each star satisfying the wave vector selection rules.

Let $\mathbf{k}_m^{(f)} \equiv \mathbf{k}_{n,l}^{(f)}$ be a wave vector of some irreducible star (m is fixed). The set of $t^{(p)}t^{(i)}$ basis functions (27) with this wave vector forms the space Ω_1 of some projective rep $[\tilde{F}_{\mathbf{k}_m^{(f)}}]_{\mathrm{Kr}} \equiv [F_{\mathbf{k}_n^{(p)}} \cap F_{\mathbf{k}_l^{(i)}}]_{\mathrm{Kr}}$ of the little cogroup $\tilde{F}_{\mathbf{k}_m^{(f)}} \equiv F_{\mathbf{k}_n^{(p)}} \cap F_{\mathbf{k}_l^{(i)}}$ or small rep $[\tilde{G}_{\mathbf{k}_m^{(f)}}]_{\mathrm{Kr}} \equiv [G_{\mathbf{k}_n^{(p)}} \cap G_{\mathbf{k}_l^{(i)}}]_{\mathrm{Kr}}$ of the little group $\tilde{G}_{\mathbf{k}_m^{(f)}} \equiv G_{\mathbf{k}_n^{(p)}} \cap G_{\mathbf{k}_l^{(i)}}$ and

$$[\tilde{F}_{\mathbf{k}_m^{(f)}}]_{\mathrm{Kr}} = [\tilde{G}_{\mathbf{k}_m^{(f)}}]_{\mathrm{Kr}} \Downarrow \tilde{F}_{\mathbf{k}_m^{(f)}}. \tag{29}$$

The characters of the projective rep $[\tilde{F}_{\mathbf{k}_m^{(f)}}]_{\mathrm{Kr}}$ of the cogroup $\tilde{F}_{\mathbf{k}_m^{(f)}}$ in space Ω_1 are the products of the characters of the cogroup $F_{\mathbf{k}_n^{(p)}}$ and $F_{\mathbf{k}_l^{(i)}}$ irreps subducted on the cogroup $\tilde{F}_{\mathbf{k}_m^{(f)}}$:

$$\chi^{\left(\left[\tilde{F}_{\mathbf{k}_m^{(f)}}\right]_{\mathrm{Kr}}\right)}(R) = \chi^{\left(\left[\tilde{F}_{\mathbf{k}_n^{(p)}}\right]_{\gamma^{(p)}}\right)}(R)\chi^{\left(\left[\tilde{F}_{\mathbf{k}_l^{(i)}}\right]_{\gamma^{(i)}}\right)}(R), \quad R \in \tilde{F}_{\mathbf{k}_m}(f). \tag{30}$$

Table 2. Types of wave vectors in Kronecker products of $[G]_i^{(*W)} \times [G]_j^{(*W)}$

	$W^{(1i)}$	$W^{(2i)}$	$W^{(3i)}$	$W^{(4i)}$	$W^{(5i)}$	$W^{(6i)}$
$W^{(1p)}$	$X^{(xf)}$	$\Gamma^{(f)}$	$\Sigma^{(2f)}$	$\Sigma^{(1f)}$	$\Sigma^{(6f)}$	$\Sigma^{(7f)}$
$W^{(2p)}$	$\Gamma^{(f)}$	$X^{(xf)}$	$\Sigma^{(3f)}$	$\Sigma^{(4f)}$	$\Sigma^{(5f)}$	$\Sigma^{(8f)}$
$W^{(3p)}$	$\Sigma^{(2f)}$	$\Sigma^{(3f)}$	$X^{(yf)}$	$\Gamma^{(f)}$	$\Sigma^{(10f)}$	$\Sigma^{(9f)}$
$W^{(4p)}$	$\Sigma^{(1f)}$	$\Sigma^{(4f)}$	$\Gamma^{(f)}$	$X^{(yf)}$	$\Sigma^{(11f)}$	$\Sigma^{(12f)}$
$W^{(5p)}$	$\Sigma^{(6f)}$	$\Sigma^{(5f)}$	$\Sigma^{(10f)}$	$\Sigma^{(11f)}$	$X^{(zf)}$	$\Gamma^{(f)}$
$W^{(6p)}$	$\Sigma^{(7f)}$	$\Sigma^{(8f)}$	$\Sigma^{(9f)}$	$\Sigma^{(12f)}$	$\Gamma^{(f)}$	$X^{(zf)}$

Note: The wave vector stars $X*X$ and $*\Sigma$ consist of vectors: $X^{(jf)}$ ($i = x, y, z$; (2, 0, 0), (0, 2, 0), (0, 0, 2)) and $\Sigma^{(jf)}$ (j = 1–12; (110), (1 $\bar{1}$ 0), ($\bar{1}$ $\bar{1}$ 0), ($\bar{1}$ $\bar{1}$ 0), (101), ($\bar{1}$ 10), ($\bar{1}$ 0 $\bar{1}$), (10 $\bar{1}$), (011), (01 $\bar{1}$), (0 $\bar{1}$ $\bar{1}$), (0 $\bar{1}$ 1)), respectively (in units of π/a along Cartesian axes, with a being the lattice constant).

Table 3. Types of wave vectors in Kronecker products of $(*\mathbf{k}_1) \times (*\mathbf{k}_2)$ ($\mathbf{k}_1, \mathbf{k}_2 = \Gamma, X, L, W$)

Γ	$X^{(xi)}$	$X^{(yi)}$	$X^{(zi)}$	$L^{(1i)}$	$L^{(2i)}$	$L^{(3i)}$	$L^{(4i)}$
$X^{(xp)}$	$\Gamma^{(f)}$	$X^{(zf)}$	$X^{(yf)}$	$L^{(3f)}$	$L^{(4f)}$	$L^{(1f)}$	$L^{(2f)}$
$L^{(1p)}$	$L^{(3f)}$	$L^{(4f)}$	$L^{(2f)}$	$\Gamma^{(f)}$	$X^{(zf)}$	$X^{(xf)}$	$X^{(yf)}$
$W^{(1p)}$	$W^{(2f)}$	$\Delta^{(2f)}$	$\Delta^{(1f)}$	$\Sigma^{(12f)}$	$\Sigma^{(11f)}$	$\Sigma^{(10f)}$	$\Sigma^{(9f)}$
Γ	$W^{(1i)}$	$W^{(2i)}$	$W^{(3i)}$	$W^{(4i)}$	$W^{(5i)}$	$W^{(6i)}$	
$X^{(xp)}$	$W^{(2f)}$	$W^{(1f)}$	$\Delta^{(3f)}$	$\Delta^{(4f)}$	$\Delta^{(6f)}$	$\Delta^{(5f)}$	
$L^{(1p)}$	$\Sigma^{(12f)}$	$\Sigma^{(10f)}$	$\Sigma^{(8f)}$	$\Sigma^{(6f)}$	$\Sigma^{(4f)}$	$\Sigma^{(2f)}$	
$W^{(1p)}$	$X^{(xf)}$	$\Gamma^{(f)}$	$\Sigma^{(2f)}$	$\Sigma^{(1f)}$	$\Sigma^{(6f)}$	$\Sigma^{(7f)}$	

Note: The wave vector stars $*L$ and $\Delta*$ consist of vectors: $L^{(jf)}$ (j = 1–4; (1, 1, 1), ($\bar{1}$, $\bar{1}$, 1), (1, $\bar{1}$, $\bar{1}$), ($\bar{1}$, 1, $\bar{1}$)) and $\Delta^{(jf)}$ (j = 1–6; (1, 0, 0), ($\bar{1}$, 0, 0), (0, 1, 0), (0, $\bar{1}$, 0), (0, 0, 1), (0, 0, $\bar{1}$)) (in units of π/a along Cartesian axes, with a being the lattice constant).

The multiplication of two projective irreps of the group $\tilde{F}_{\mathbf{k}_m^{(f)}}$ with factor systems $\omega^{(\mathbf{k}_n^{(p)})}$ and $\omega^{(\mathbf{k}_l^{(i)})}$ gives a projective rep of the same group with the factor system $\omega^{(\mathbf{k}_m^{(f)})}$ (as $\mathbf{k}_m^{(f)} \equiv \mathbf{k}_{nl}^{(f)} = \mathbf{k}_n^{(p)} + \mathbf{k}_l^{(i)} + \mathbf{B}_{nl}$ see also Section 2). The group $\tilde{F}_{\mathbf{k}_m^{(f)}}$ ($\tilde{G}_{\mathbf{k}_m^{(f)}}$) either coincides with the little cogroup $F_{\mathbf{k}_m^{(f)}}$ (little group $G_{\mathbf{k}_m^{(f)}}$ or is a subgroup of it:

$$\tilde{F}_{\mathbf{k}_m^{(f)}} \subseteq F_{\mathbf{k}_m^{(f)}} \quad (\tilde{G}_{\mathbf{k}_m^{(f)}} \subseteq G_{\mathbf{k}_m^{(f)}}). \tag{31}$$

When $\tilde{F}_{\mathbf{k}_m^{(f)}} = F_{\mathbf{k}_m^{(f)}}$, the projective rep (30) can be decomposed into irreps in the usual way, the characters of irreps being taken from tables of small irreps of little groups (for example, [9]). This possibility appears, for instance, when $\mathbf{k}_{n1}^{(p)} = 0$ or $\mathbf{k}_{l2}^{(i)} = 0$.

If $\tilde{F}_{\mathbf{k}_m^{(f)}} \subset F_{\mathbf{k}_m^{(f)}}$, the cogroup $F_{\mathbf{k}_m^{(f)}}$ is decomposed into left cosets of $\tilde{F}_{\mathbf{k}_m^{(f)}}$:

$$F_{\mathbf{k}_m^{(f)}} = \sum_{i=1}^{w} R_i \tilde{F}_{\mathbf{k}_m^{(f)}}, \quad R_1 = E,$$
$$R_i \in F_{\mathbf{k}_m^{(f)}}, \quad R_i \notin \tilde{F}_{\mathbf{k}_m^{(f)}} \quad \text{for} \quad i = 2, \ldots, w. \tag{32}$$

The operators R_i change both wave vectors $\mathbf{k}_n^{(p)}$ and $\mathbf{k}_l^{(i)}$ but leave their sum unchanged modulo the reciprocal lattice vector. This means that the space Ω_1 transforms under the operations R_i into linearly independent spaces $\Omega_i = \hat{R}_i \Omega_1$ and

$$\Omega = \sum_{i=1}^{w} \Omega_i \tag{33}$$

which is the space of the rep of the group $F_{\mathbf{k}_m^{(f)}}$ induced by the rep $[\tilde{F}_{\mathbf{k}_m^{(f)}}]_{\mathrm{Kr}}$ of its subgroup $\tilde{F}_{\mathbf{k}_m^{(f)}} \subset F_{\mathbf{k}_m^{(f)}}$

$$[F_{\mathbf{k}_m^{(f)}}]_{\mathrm{Kr}} = [\tilde{F}_{\mathbf{k}_m^{(f)}}]_{\mathrm{Kr}} \uparrow F_{\mathbf{k}_m^{(f)}}. \tag{34}$$

Further, the small rep $[G_{\mathbf{k}_m^{(f)}}]_{\mathrm{Kr}} = [F_{\mathbf{k}_m^{(f)}}]_{\mathrm{Kr}} \Uparrow G_{\mathbf{k}_m^{(f)}}$ is contained in the Kronecker product (26), which is the subject under consideration. The characters $\chi^{\left(\left[F_{\mathbf{k}_m^{(f)}}\right]_{\mathrm{Kr}}\right)}(g)$ ($g \in F_{\mathbf{k}_m^{(f)}}$) of this projective induced rep of $F_{\mathbf{k}_m^{(f)}}$ (or induced small rep of $G_{\mathbf{k}_m^{(f)}}$) can be calculated in the usual way:

$$\chi^{\left(\left[F_{\mathbf{k}_m^{(f)}}\right]_{\mathrm{Kr}}\right)}(g) = \sum_i \chi_i^{(\mathrm{Kr})}(g) \tag{35}$$

where

$$\chi_i^{(\mathrm{Kr})}(g) = \begin{cases} 0, & \text{if} \quad g_i^{-1} g g_i \notin \tilde{F}_{\mathbf{k}_m^{(f)}} \\ \chi^{\left(\left[\tilde{F}_{\mathbf{k}_m^{(f)}}\right]_{\mathrm{Kr}}\right)}(g_i^{-1} g g_i), & \text{if} \quad g_i^{-1} g g_i \in \tilde{F}_{\mathbf{k}_m^{(f)}}. \end{cases} \tag{36}$$

As the characters of projective irreps of $F_{\mathbf{k}_m^{(f)}}$ (of small irreps of $G_{\mathbf{k}_m^{(f)}}$) are known (taken from [9], for example), the projective rep of $[F_{\mathbf{k}_m^{(f)}}]_{\mathrm{Kr}}$ can be decomposed into irreducible components in the same way as for ordinary reps of point groups.

If the projective irreps $[\tilde{F}_{\mathbf{k}_m^{(f)}}]_j$ with the same factor system as the projective irreps of the cogroup $F_{\mathbf{k}_m^{(f)}}$ are known, there is a more simple procedure of rep decomposition based on the Frobenius reciprocity theorem (see Section 2). This possibility arises in the two following cases:

(a) when the rep $[\tilde{F}_{\mathbf{k}_m^{(f)}}]_{\mathrm{Kr}}$ is irreducible itself: i.e., its characters satisfy the condition

$$\sum_{g \in \tilde{F}} \left|\chi^{([\tilde{F}])}(g)\right|^2 = n_{\tilde{F}} \tag{37}$$

where $n_{\tilde{F}}$ is the order of $\tilde{F}$ (see Subsection 3.2);

(b) when the subduction of the irreps of the cogroup $F_{\mathbf{k}_m^{(f)}}$ onto the group $\tilde{F}_{\mathbf{k}_m^{(f)}}$ directly gives the irreps of $\tilde{F}_{\mathbf{k}_m^{(f)}}$.

What is more, the irreps of $\tilde{F}_{\mathbf{k}_m^{(f)}}$ can be taken from [6], where the characters of the standard form for all projective irreps with all possible factor systems for all crystallographic point groups are given. In our example of the $[G]_1^{(*W^{(p)})} \times [G]_1^{(*W^{(i)})}$ Kronecker product, the following intersections of point groups are considered: $\tilde{F}_\Gamma \equiv F_{W^{(1)}} \cap F_{W^{(2)}}$ ($D_{2d}^{(1)} \cap D_{2d}^{(2)} = D_{2d}^{(1)}$) for the Γ component, $\tilde{F}_{X^{(x)}} \equiv F_{W^{(1)}} \cap F_{W^{(1)}}$ ($D_{2d}^{(1)} \cap D_{2d}^{(1)} = D_{2d}^{(x)}$) for the X component, and $\tilde{F}_X \equiv F_{W^{(1)}} \cap F_{W^{(4)}}$ ($D_{2d}^{(1)} \cap D_{2d}^{(4)} = C_s$) for the Σ component (see Tables 2, 3).

Table 4. Characters of the Kronecker product $[D^{(1)}_{2d}]_1 \times [D^{(2)}_{2d}]_1 \equiv \chi$ and the characters of some ordinary irreps of the point group $D^{(1)}_{2d}$

$D^{(1)}_{2d}$	E	S_{4x}	S^{-1}_{4x}	C_{2x}	U_{yz}	$U_{y\bar{z}}$	σ_y	σ_z
χ	4	2	2	0	0	0	0	0
a_1	1	1	1	1	1	1	1	1
a_2	1	1	1	1	–1	–1	–1	–1
e	2	0	0	–2	0	0	0	0

3.1. Γ *States in the Kronecker Products* $[G]^{(*W)}_i \times [G]^{(*W)}_j$

In this case, the irreps of $\tilde{F}_{\mathbf{k}^{(f)}_m} = \tilde{F}_\Gamma$ are ordinary irreps of the point group $D^{(1)}_{2d}$. The characters of the Kronecker product of the projective irreps $[F_{W^{(1)}}]_1 \times [F_{W^{(2)}}]_1 \equiv [D^{(1)}_{2d}]_1 \times [D^{(2)}_{2d}]_1$ obtained from Table 1 are given in Table 4 with the characters of those ordinary irreps of the little cogroup $D^{(1)}_{2d}$ which appear in the decomposition

$$[D^{(1)}_{2d}]_1 \times [D^{(2)}_{2d}]_1 = a_1 + a_2 + e. \qquad (38)$$

This rep of $D^{(1)}_{2d}$ induces into $F_\Gamma = O_h$ the rep $\Gamma^+_1\Gamma^-_2\Gamma^\pm_3\Gamma^\pm_4\Gamma^\pm_5\Gamma^+_4\Gamma^-_5$. This decomposition of the induced rep is obtained using the Frobenius reciprocity theorem (see Table 5).

The same procedure may be used for all possible Kronecker products $[D^{(1)}_{2d}]_i \times [D^{(2)}_{2d}]_j$ $(i, j = 1\text{–}7)$ both for single- and double-valued irreps. As a result, one obtains Table 5, where the subduction of single- and double-valued ordinary irreps of O_h on $D^{(1)}_{2d}$ are also given. For example, the direct product $[G]^{(*W)}_3 \times [G]^{(*W)}_4$ has the Γ component $\Gamma^-_1\Gamma^-_3\Gamma^+_5$ (rep $[O_h]_{\mathrm{Kr}}$ is induced from the ordinary irrep b_1 of $D^{(1)}_{2d}$). After induction (15), one obtains Table 6, which gives directly the Γ components of the Kronecker products involved.

3.2. X States in the Kronecker Products $[G]^{(*W)}_i \times [G]^{(*W)}_j$

The irreps of $\tilde{F}_{X^{(x)}} \subset D^{(x)}_{4h}$ may be obtained directly from Table 1 by multiplying $[D^{(1)}_{2d}]_3$ by $[D^{(1)}_{2d}]_{3\text{–}7}$ (for the single-valued projective irreps $[D^{(x)}_{2d}]_{1\text{–}5}$ or

Table 5. Kronecker products $[D^{(1)}_{2d}]_i \times [D^{(2)}_{2d}]_j$ of projective single- and double-valued irreps of the little cogroup D_{2d} in terms of ordinary irreps of the point group D_{2d} and subduction of ordinary irreps of the point group O_h onto the point group $D^{(1)}_{2d}$

	W_1	W_2	W_3	W_4	W_5	W_6	W_7
W_1	a_1, a_2, e	b_1, b_2, e	$\bar{e}_1$	$\bar{e}_2$	$\bar{e}_1$	$\bar{e}_2$	$\bar{e}_1, \bar{e}_2$
W_2	b_1, b_2, e	a_1, a_2, e	$\bar{e}_2$	$\bar{e}_1$	$\bar{e}_2$	$\bar{e}_1$	$\bar{e}_1, \bar{e}_2$
W_3	$\bar{e}_1$	$\bar{e}_2$	a_2	b_1	a_1	b_2	e
W_4	$\bar{e}_2$	$\bar{e}_1$	b_1	a_2	b_2	a_1	e
W_5	$\bar{e}_1$	$\bar{e}_2$	a_1	b_2	a_2	b_1	e
W_6	$\bar{e}_2$	$\bar{e}_1$	b_2	a_1	b_1	a_2	e
W_7	$\bar{e}_1, \bar{e}_2$	$\bar{e}_1, \bar{e}_2$	e	e	e	e	a_1, a_2, b_1, b_2

$[O_h]_i$ $(\Uparrow O^7_h)$	Γ^+_1	Γ^+_2	Γ^+_3	Γ^+_4	Γ^+_5	Γ^+_6	Γ^+_7	Γ^+_8
$[O_h]_i$ $\downarrow D_{2d}$	a_1	b_2	a_1, b_2	a_2, e	b_1, e	$\bar{e}_2$	$\bar{e}_1$	$\bar{e}_1, \bar{e}_2$
$[O_h]_i$ $(\Uparrow O^7_h)$	Γ^-_1	Γ^-_2	Γ^-_3	Γ^-_4	Γ^-_5	Γ^-_6	Γ^-_7	Γ^-_8
$[O_h]_i$ $\downarrow D_{2d}$	b_1	a_2	a_2, b_1	b_2, e	a_1, e	$\bar{e}_1$	$\bar{e}_2$	$\bar{e}_1, \bar{e}_2$

Table 6. Γ states in the Kronecker products $[G]_i^{(*W)} \times [G]_j^{(*W)}$

	W_1	W_2	W_3	W_4	W_5	W_6	W_7
W_1	$1^+, 2^-, 3^\pm, 4^+(2), 4^-, 5^+, 5^-(2)$	$1^-, 2^+, 3^\pm, 4^+, 4^-(2), 5^+(2), 5^-$	$6^-, 7^+, 8^\pm$	$6^+, 7^-, 8^\pm$	$6^-, 7^+, 8^\pm$	$6^+, 7^-, 8^\pm$	$6^\pm, 7^\pm, 8^\pm(2)$
W_2	$1^-, 2^+, 3^\pm, 4^+, 4^-(2), 5^+(2), 5^-$	$1^+, 2^-, 3^\pm, 4^+(2), 4^-, 5^+, 5^-(2)$	$6^+, 7^-, 8^\pm$	$6^-, 7^+, 8^\pm$	$6^+, 7^-, 8^\pm$	$6^-, 7^+, 8^\pm$	$6^\pm, 7^\pm, 8^\pm(2)$
W_3	$6^-, 7^+, 8^\pm$	$6^+, 7^-, 8^\pm$	$2^-, 3^-, 4^+$	$1^-, 3^-, 5^+$	$1^+, 3^+, 5^-$	$2^+, 3^+, 4^-$	$4^\pm, 5^\pm$
W_4	$6^+, 7^-, 8^\pm$	$6^-, 7^+, 8^\pm$	$1^-, 3^-, 5^+$	$2^-, 3^-, 4^+$	$2^+, 3^+, 4^-$	$1^+, 3^+, 5^-$	$4^\pm, 5^\pm$
W_5	$6^-, 7^+, 8^\pm$	$6^+, 7^-, 8^\pm$	$1^+, 3^+, 5^-$	$2^+, 3^+, 4^-$	$2^-, 3^-, 4^+$	$1^-, 3^-, 5^+$	$4^\pm, 5^\pm$
W_6	$6^+, 7^-, 8^\pm$	$6^-, 7^+, 8^\pm$	$2^+, 3^+, 4^-$	$1^+, 3^+, 5^-$	$1^-, 3^-, 5^+$	$2^-, 3^-, 4^+$	$4^\pm, 5^\pm$
W_7	$6^\pm, 7^\pm, 8^\pm(2)$	$6^\pm, 7^\pm, 8^\pm(2)$	$4^\pm, 5^\pm$	$4^\pm, 5^\pm$	$4^\pm, 5^\pm$	$4^\pm, 5^\pm$	$1^\pm, 2^\pm, 3^\pm(2), 4^\pm, 5^\pm$

Note: Numbers (m) in parentheses mean that the preceding irrep enters m times in the product.

$[D_{2d}^{(1)}]_{1-2}$ (for the double-valued projective irreps $[D_{2d}^{(x)}]_{6-7}$ (see Table 7).

As seen from Table 2 for $*\mathbf{k}^{(p)} = *\mathbf{k}^{(i)} = *W$, $\gamma^{(p)} = \gamma^{(i)} = 1$, the space of eight functions (27) with $n = l = 1, 2$; $t^{(p)} = t^{(i)} = 2$ transforms according to some small rep of the little cogroup $D_{4h}^{(x)}$. For function (27) with $n = l = 1$; $t^{(p)} = t^{(i)} = 2$ transforms according to the projective rep

$$\alpha \equiv (D_{2d}^{(1)})_1 \times (D_{2d}^{(1)})_1 = (D_{2d}^{(x)})_1 + (D_{2d}^{(x)})_3 + (D_{2d}^{(x)})_5 \quad (39)$$

of the point group $D_{2d}^{(x)} = D_{2d}^{(1)}$ with the factor system corresponding to the little cogroup $D_{4h}^{(x)}$. Functions (27) with $n = l = 1$ and $n = l = 2$ can be considered basis functions of the projective rep of the little cogroup $D_{4h}^{(x)}$ induced by the rep α (39) of $D_{2d}^{(x)}$ with the factor system corresponding to the little group $D_{4h}^{(x)}$. This induction can be made using the Frobenius theorem.

At the same time, they are the basis functions of the small rep of the little group $G_{X^{(x)}}$ contained in the basis of the Kronecker product (26) and which, due to the relation

$$[G]_{WW}^{(*X)} = ((\alpha \uparrow F_{X^{(x)}}) \Uparrow G_{X^{(x)}}) \uparrow G, \quad (40)$$

determines all the $*X$ components in the Kronecker product (26). For example, the single-valued irreps $[G_X]_i$, $i = 1, 2, 3, 4$, are contained in (26) (see Table 8, where all the Kronecker products $[D_{2d}^{(1)}]_i \times [D_{2d}^{(1)}]_j$ and the subduction of single- and double-valued projective irreps of $D_{4h}^{(x)}$ on $D_{2d}^{(x)}$ are given). After induction (15), one obtains Table 9, which gives directly the X components of the Kronecker products involved.

Table 7. Characters of single- and double-valued projective irreps of the little cogroup $D_{2d}^{(x)}$ with the factor system corresponding to the little cogroup $D_{4h}^{(x)}$

D_{2d}	E	S_{4x}	S_{4x}^{-1}	C_{2x}	U_{yz}	$U_{y\bar{z}}$	σ_y	σ_z
$[D_{2d}^{(x)}]_1 \equiv 1$	1	$-i$	i	-1	1	-1	$-i$	i
$[D_{2d}^{(x)}]_2 \equiv 2$	1	i	$-i$	-1	-1	1	$-i$	i
$[D_{3d}^{(x)}]_3 \equiv 3$	1	$-i$	i	-1	-1	1	i	$-i$
$[D_{2d}^{(x)}]_4 \equiv 4$	1	i	$-i$	-1	1	-1	i	$-i$
$[D_{2d}^{(x)}]_5 \equiv 5$	2	0	0	2	0	0	0	0
$[D_{2d}^{(x)}]_6 \equiv 6$	2	$\sqrt{2}i$	$\sqrt{2}i$	0	0	0	0	0
$[D_{2d}^{(x)}]_7 \equiv 7$	2	$-\sqrt{2}i$	$-\sqrt{2}i$	0	0	0	0	0

4. SELECTION RULES FOR ELECTRICAL DIPOLE TRANSITIONS

The symmetry of the dipole operator is the vector rep of O_h^7: $\Gamma_v = [G_\Gamma]_{4-} = \Gamma_4^-$. Since the vector $\mathbf{k}^{(p)} = 0$, $\mathbf{k}_m^{(f)} = \mathbf{k}_l^{(i)}$ (the so-called direct transitions $\Gamma \rightleftarrows \Gamma$, $X \rightleftarrows X$, $L \rightleftarrows L$, $W \rightleftarrows W$, etc., are only allowed). The symmetry of allowed final states for $W \rightleftarrows W$ transitions is pointed out in Table 5 by the entries of the columns containing b_2 and e ($\Gamma_4^- \downarrow D_{2d} = b_2 + e$) in the row corresponding to the symmetry of the initial state. For example, direct transition is allowed from the initial state of symmetry W_3 to the final states of symmetry W_6 and W_7.

Table 8. Kronecker products $[D_{2d}^{(1)}]_i \times [D_{2d}^{(1)}]_j$ in terms of the projective irreps of $D_{2d}^{(x)}$ (with the factor system of the little cogroup $D_{4h}^{(x)}$; Table 7) and subduction of the projective irreps of the little cogroup $D_{4h}^{(x)}$ onto the point group $D_{2d}^{(x)}$

	W_1	W_2	W_3	W_4	W_5	W_6	W_7
W_1	1, 3, 5	2, 4, 5	6	7	6	7	6, 7
W_2	2, 4, 5	1, 3, 5	7	6	7	6	6, 7
W_3	6	7	1	2	3	4	5
W_4	7	6	2	1	4	3	5
W_5	6	7	3	4	1	2	5
W_6	7	6	4	3	2	1	5
W_7	6, 7	6, 7	5	5	5	5	1, 2, 3, 4
$[D_{4h}^{(x)}]_i$ ($\Uparrow G_{X^{(x)}}$)			X_1	X_2	X_3	X_4	X_5
$[D_{4h}^{(x)}]_i \downarrow D_{2d}^{(x)}$			5	5	2, 3	1, 4	6, 7

Table 9. X states in the Kronecker products $[G]_i^{(*W)} \times [G]_j^{(*W)}$

	W_1	W_2	W_3	W_4	W_5	W_6	W_7
W_1	1, 2, 3, 4	1, 2, 3, 4	5	5	5	5	5(2)
W_2	1, 2, 3, 4	1, 2, 3, 4	5	5	5	5	5(2)
W_3	5	5	4	3	3	4	1, 2
W_4	5	5	3	4	4	3	1, 2
W_5	5	5	3	4	4	3	1, 2
W_6	5	5	4	3	3	4	1, 2
W_7	5(2)	5(2)	1, 2	1, 2	1, 2	1, 2	3(2), 4(2)

Note: Numbers (m) in parentheses mean that the preceding irrep enters m times in the product.

In the case of phonon-assisted electric dipole transitions, these selection rules have to be supplemented with the selection rules where the operator has the symmetry of the phonon participating in the transition. In silicon crystal, Si atoms occupy the site a of symmetry T_d. The symmetries of phonons in this crystal are given by the rep of the space group $G = O_h^7$ induced (indrep) by the vector rep t_2 of the site symmetry group T_d [8, 11]. The short symbol of this indrep is

$$\Gamma(4^-, 5^+), X(1, 3, 4), L(1^+, 2^-, 3^+, 3^-), W(1, 2, 2).$$

It gives the symmetry of phonons at the symmetry points of the BZ. For example, the electric dipole transitions are allowed from the initial electronic W_3 state to the intermediate W_6 and W_7 states (when spin–orbit interaction is taken into account; see Table 5). From these states, with assistance from the phonons of symmetry W_1, the transitions are allowed in the final Γ and X states of symmetry Γ_6^+, Γ_7^-, $\Gamma_8^\pm$, X_5 and $\Gamma_6^\pm$, $\Gamma_7^\pm$, $2\Gamma_8^\pm$, $2X_5$ (see Tables 5, 8).

5. CONCLUSIONS

Our approach to the selection rules in crystals is based on the projective irreps of point groups and consists of three steps.

(1) First, one finds the wave vector selection rules. The results may be given in the form of tables with the rows and columns numbered by the wave vectors of the direct product factors. Any row (column) of this table contains the representatives of all irreducible stars of the Kronecker product.

(2) Next, it is sufficient to fix one row (the first wave vector) of this table and then consider only columns (the second wave vector) that give, at the intersection with the chosen row, wave vectors of different irreducible stars. Each wave vector is related to some small cogroup. Two cogroups correspond to the two factors in the Kronecker product, and the third, to the resulting one. The intersection of the two former cogroups is also a subgroup of the resulting cogroup (the corresponding wave vectors satisfy the wave vector selection rule). The Kronecker product of the projective irreps of these cogroups taken on elements of their intersection is a small projective rep with the needed factor system of the resulting cogroup and can be decomposed into irreducible components if the projective irreps of the latter are known.

(3) Finally, the induction procedure from the projective rep of intersection of the two initial cogroups to the resulting small cogroups is realized in order to find the definitive selection rules for allowed transitions (subduction coefficients of Kronecker products). The Frobenius reciprocity theorem may be used at this stage if the projective rep of the intersection of the cogroups is decomposed into irreducible ones.

The suggested approach seems to be the most easy to use, as compared to the traditional subgroup [1–4] and full group [5] methods. It does not depend either on the choice of the coordinate system origin and of the **k**-star vectors in the description of space groups and their small irreps or on the form of presentation of the irreps of space groups (small irreps of little groups [9, 10] or p-equivalent projective irreps of small cogroups [11]). Our approach may be easily supplemented for the computer program generating irreps of space groups given at the Bilbao Crystallographic Server [12, 13].

ACKNOWLEDGMENTS

One of the authors (V.P.S.) acknowledges the support of the Ministére de la Recherche (France).

REFERENCES

1. R. J. Elliott and R. J. Loudon, J. Phys. Chem. Solids **15**, 146 (1960).
2. M. Lax and J. Hopfield, Phys. Rev. **124**, 115 (1961).
3. C. J. Bradley and A. P. Cracknell, *The Mathematical Theory of Symmetry in Solids* (Clarendon, Oxford, 1972).
4. A. P. Cracknell, B. L. Davis, S. C. Miller, and W. F. Love, *Kronecker Products Tables* (Plenum, New York, 1979), Vols. 1–4.
5. J. L. Birman, *Theory of Crystal Space Groups and Infra-Red and Raman Lattice Processes of Insulating Crystals* (Springer, Berlin, 1974), Handbuch der Physik, Vol. 25/2b.
6. G. L. Bir and G. E. Pikus, *Symmetry and Strain-Induced Effects in Semiconductors* (Nauka, Moscow, 1972; Wiley, New York, 1974).
7. S. L. Altmann, *Induced Representations in Crystals and Molecules* (Academic, London, 1977).
8. R. A. Evarestov and V. P. Smirnov, *Site Symmetry in Crystals: Theory and Applications*, 2nd ed. (Springer, Berlin, 1997), Springer Series in Solid State Sciences, Vol. 108.
9. S. C. Miller and W. F. Love, *Tables of Irreducible Representations of Space Groups and Corepresentations of Magnetic Space Groups* (Pruett, Boulder, 1967).
10. *The Irreducible Representations of Space Groups*, Ed. by J. Zak (Benjamin, Elmsford, N.Y., 1969).
11. O. V. Kovalev, *Representations of the Crystallographic Space Groups: Irreducible Representations, Induced Representations and Corepresentations*, 2nd ed. (Gordon and Breach, Philadelphia, PA, 1993).
12. E. Kroumova, C. Capillas, A. Kirov, *et al.*, Bilbao Crystallographic Server, www.cryst.ehu.es.
13. S. Ivantchev, E. Kroumova, J. M. Madariaga, *et al.*, J. Appl. Crystallogr. **33**, 1190 (2000).

Physics of the Solid State, Vol. 45, No. 8, 2003, pp. 1451–1454. Translated from Fizika Tverdogo Tela, Vol. 45, No. 8, 2003, pp. 1382–1385.

SEMICONDUCTORS AND DIELECTRICS

High-Frequency EPR of Cr^{2+} Ions in $CdGa_2S_4$

A. G. Avanesov*, V. V. Badikov*, and G. S. Shakurov**

**Kuban State University, ul. Karla Libknekhta 9, Krasnodar, 350640 Russia*

***Zavoiskiĭ Physicotechnical Institute, Kazan Scientific Center, Russian Academy of Sciences, Sibirskiĭ trakt 10/7, Kazan 29, 420029 Tatarstan, Russia*

e-mail: shakurov@kfti.knc.ru

Received December 15, 2002

Abstract—High-frequency broad-band (65–240 GHz) EPR is used to study impurity centers of bivalent chromium in a $CdGa_2S_4$ crystal. It is found that the EPR spectra correspond to tetragonal symmetry. The spin Hamiltonian $H = \beta \mathbf{B} \cdot \mathbf{g} \cdot \mathbf{S} + B_2^0 O_2^0 + B_4^0 O_4^0 + B_4^4 O_4^4$ with the parameters $B_2^0 = 23659 \pm 2$ MHz, $B_4^0 = 1.9 \pm 1$ MHz, $|B_4^4| = 54.2 \pm 2$ MHz, $g_\parallel = 1.93 \pm 0.02$, and $g_\perp = 1.99 \pm 0.02$ is used to describe the observed spectra. It is concluded that chromium ions occupy one of the tetrahedrally coordinated cation positions.© *2003 MAIK "Nauka/Interperiodica".*

1. INTRODUCTION

Compounds of the composition $A^{II}B_2^{III}C_4^{VI}$ (A = Zn, Cd; B = Ga, In; C = S, Se) are characterized by high values of the nonlinear susceptibility and are transparent up to 15–18 μm. These properties find use in various devices of nonlinear optics, such as optical filters, optical switching devices, parametric light oscillators, and other devices working in the medium IR region. A wide transparent region and the tetrahedral coordination of the cation positions make these compounds attractive as matrices for activation by transition-metal ions of the iron group. It is known that the introduction of ions of the transition-metal group, particularly Cr^{2+}, into $A^{II}B^{VI}$ compounds has made it possible to extend their capabilities and to create active media for highly efficient room-temperature tunable lasers [1–4]. No studies devoted to the possible fabrication of laser luminophors based on activated $A^{II}B_2^{III}C_4^{VI}$ crystals are known at present. Virtually no spectroscopic studies of transition-metal impurities in these compounds have been made. It should be noted, however, that, even in undoped samples uncontrolled impurities and intrinsic defects can create deep levels in the band gap and fundamentally restrict practical use of these crystals. Therefore, the problem of identifying impurities and determining their position in the lattice, the valence, local symmetry, and so on, is quite important.

This work is devoted to the study of Cr-activated cadmium thiogallate ($CdGa_2S_4$) single crystals by using high-frequency EPR.

Crystals of $CdGa_2S_4$ have a tetragonal structure, with the cations being in a tetrahedral environment (space group S_4^2, number of formula units per unit cell $Z = 2$, lattice constants $a = 5.536$, $c = 10.16$ Å [5]). Distinct from chalkopyrite, whose structure can be considered a basis for constructing thiogallate structure, some of the cation positions in the thiogallate structure remain unoccupied and have an ordered arrangement.

EPR of bivalent chromium in the tetrahedral coordination has been observed previously in $A^{II}B^{VI}$ and $A^{III}B^{V}$ compounds with chromium substituting for both cadmium and gallium ions [6, 7]. Despite the fact that these crystals are cubic, the observed spectra showed tetragonal symmetry. The occurrence of distortion was explained by the static Jahn–Teller effect. We also observed Jahn–Teller tetragonal Cr^{2+} centers but in crystals of BaF_2 with eightfold coordination of Cr [8]. EPR of bivalent chromium ions in tetragonal crystals has not been studied to date.

The ground-state term of the bivalent chromium ion (^5D) in a cubic field is split into an orbital triplet and a doublet; for tetrahedral coordination, the triplet corresponds to the ground state. In a tetragonal crystal field, the ground level is an orbital singlet split by the second-order spin–orbit interaction into five ($S = 2$) spin sublevels (one singlet and two doublets). The observation of EPR in such systems is hampered, because the energy states between which resonance transitions are allowed are separated by an energy gap that is usually larger than the quanta of the rf field of *X*- and *Q*-band spectrometers. Intradoublet transitions due to mixed wave functions can be observed for tetragonal centers only in parallel (static and alternating) magnetic fields and do not allow certain identification of the Cr^{2+} ions. This is why most EPR studies of Cr^{2+} ions have been performed using a high-frequency EPR technique.

1063-7834/03/4508-1451$24.00

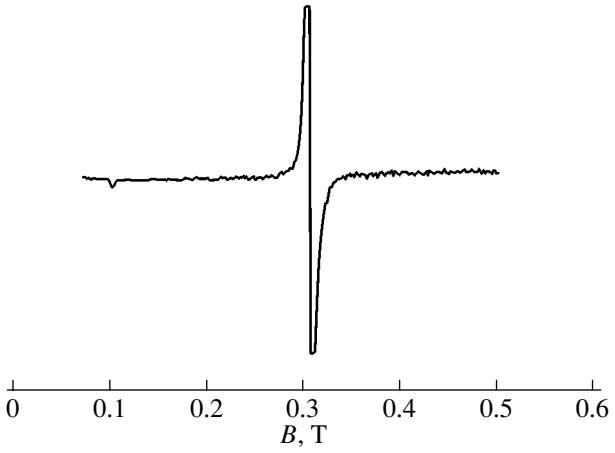

Fig. 1. EPR spectrum of $CdGa_2S_4 : Cr^{2+}$ for the orientation **B** || **c** at a frequency of 205 GHz.

2. EXPERIMENT

Crystals of $GdGa_2S_4$ of high optical quality were grown using the Bridgman–Stockbarger method from a melt of stoichiometric composition in quartz cells at a rate of 6 mm/day. The content of chromium ions in the starting material was 0.13 mol %. A 10-mm-high prism-shaped sample with the base in form of a rhombus with an 11-mm side was chosen for the studies. The crystallographic *c* axis was directed along the major diagonal of the rhombus. The sample was an optically transparent yellow crystal with ground faces. The EPR spectra were observed with the aid of a broad-band (65–500 GHz) quasioptical spectrometer with a backward-wave tube used as an oscillator for high-frequency emission. The experiments were performed, for the most part, at liquid-helium temperature in magnetic fields of up to 0.9 T. The details of the experiment are described in [9].

Let us denote the spin levels as $|0\rangle$, $|\pm1\rangle$, and $|\pm2\rangle$. The EPR spectra of bivalent chromium were recorded in the frequency ranges 64–100 GHz (transitions $|0\rangle \rightleftharpoons |\pm1\rangle$) and 190–240 GHz (transitions $|\pm1\rangle \rightleftharpoons |\pm2\rangle$). No other EPR lines were observed in these frequency ranges. The spectra for the orientation **B** || **c** are shown in Fig. 1. The intense line corresponds to the allowed transition with the spin projection changing by unity, and the weak line, to the transition with the projection changing by three, although in reality the states $|\pm2\rangle$ are mixed in weak magnetic fields and the "forbidden" transition occurs due to the presence of both spin projections in the wave function. With increasing magnetic field, the wave function becomes "purer" and the weak line becomes progressively less intense and disappears. Figure 2 shows the variations of the frequencies of all observed resonance lines with the magnetic-field intensity for the crystal orientation **B** || **c** and **B** || **a**. It can be seen from Fig. 2a that, for the $|\pm1\rangle \rightleftharpoons |\pm2\rangle$ transitions, there is an energy gap of 1.3 GHz between the levels $|\pm2\rangle$; therefore, these levels may be called a doublet only conventionally. All the splittings in a zero field were measured using the direct method and are equal to 70.75, 212.4, and 213.7 GHz. The absolute precision of frequency measurement was ±0.5 GHz; however, the relative change in frequency was determined with an accuracy of 0.05 GHz. The angular variation of the resonance field with rotation of the crystal in the (100) plane is shown in Fig. 3 for several resonance transitions. For the space group S_4^2, the existence of a defect showing a singlefold angular periodicity is possible only for the local position with symmetry S_4; therefore, the angular variations indicate that the spectra should be assigned to a tetragonal center. The line width for the orientation **B** || **c** was about 8 mT with somewhat spread wings. This made it impossible to resolve the hyperfine structure of the EPR spectra.

In order to determine the sequence order of the energy positions of the spin states (the sign of B_2^0), the transition $|\pm1\rangle \rightleftharpoons |\pm2\rangle$ was measured at various temperatures in the range 4.2–12 K. However, the above objective was not attained, because the line shape changed and became asymmetrical with an increase in temperature. The origin of this effect is inclear.

3. THEORY AND DISCUSSION

To describe the observed spectra theoretically, we use the spin Hamiltonian

$$H = \beta \mathbf{B} \cdot \mathbf{g} \cdot \mathbf{S} + B_2^0 O_2^0 + B_4^0 O_4^0 + B_4^4 O_4^4$$

and the wave functions $(|+1\rangle + |-1\rangle)/\sqrt{2}$, $(|+1\rangle - |-1\rangle)/\sqrt{2}$, $(|+2\rangle + |-2\rangle)/\sqrt{2}$, $(|+2\rangle - |-2\rangle)/\sqrt{2}$, and $|0\rangle$, with the *z* axis directed along the $\langle 001\rangle$ axis of the crystal.

In a zero magnetic field, the Hamiltonian matrix is diagonal. By using the measured zero-field splittings, the values of B_n^m are determined to be $|B_2^0| = 23659 \pm 20$, $B_4^0 = 1.9 \pm 1$, and $B_4^4 = 54.2 \pm 2$ MHz. For the orientation **B** || **c**, the dependence of the energy levels on magnetic field can be written in an analytical form, which allows the $g_\parallel$ factor to be determined, using the least-square procedure, from the field dependence of the EPR spectra. For the perpendicular orientation of a sample, the parameters of the Hamiltonian were calculated numerically to first-order corrections in the perturbation theory. The *g* factor was also determined from the field dependence of the EPR spectra for the orientation **B** || **a** by minimizing the deviations of the theoretical curve from the experimental values. The *g* values were found to be $g_\parallel = 1.93 \pm 0.02$ and $g_\perp = 1.99 \pm 0.02$. The values obtained were used to find the angular variations of the resonance fields, shown in Fig. 3. It is seen that there is good agreement between the theory and

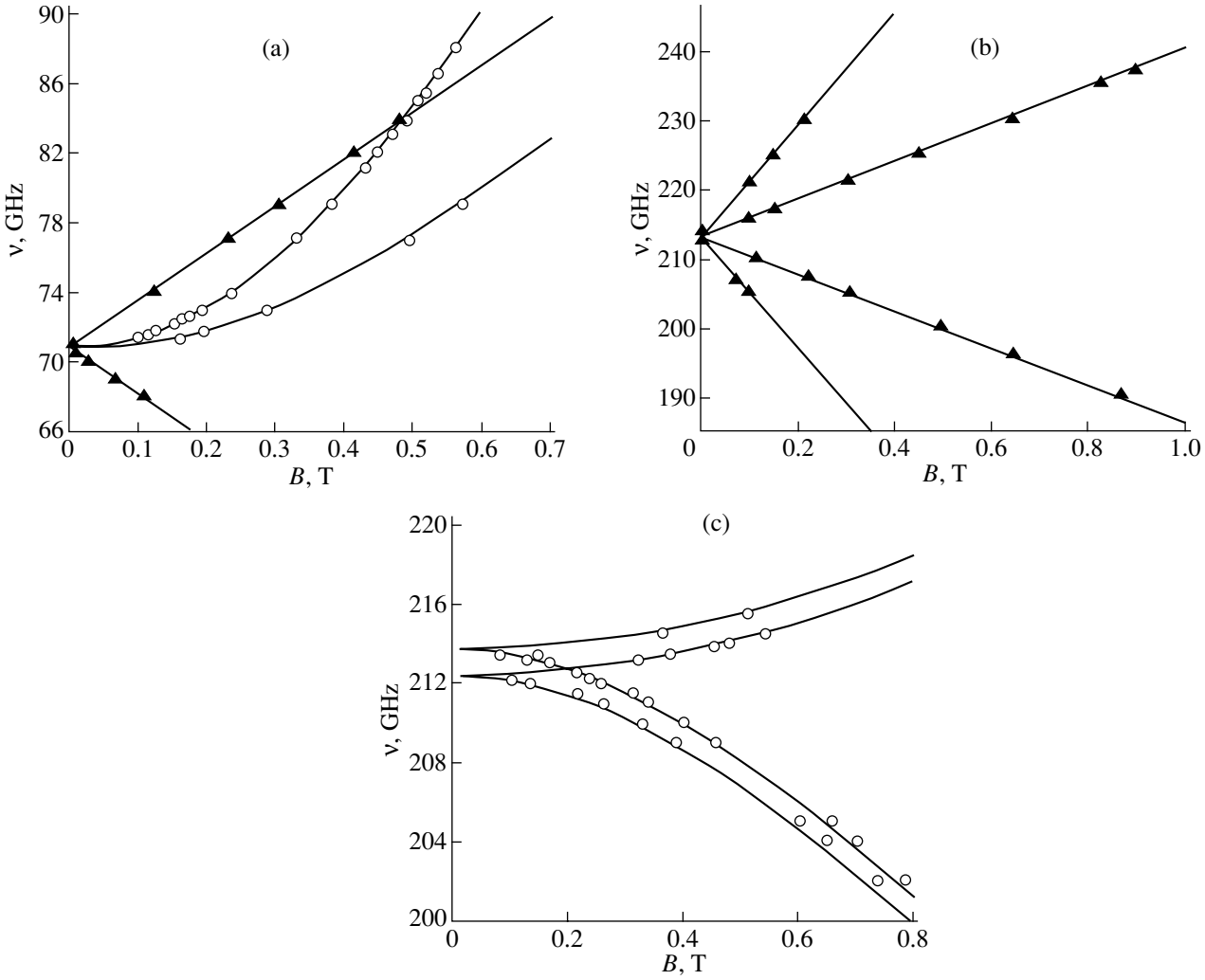

Fig. 2. Resonance transition frequencies as a function of external magnetic field **B**. Triangles correspond to **B** || **c**, and circles, to **B** || **a**; theoretical calculations are represented by solid lines. (a) Transition $|0\rangle \rightleftharpoons |\pm1\rangle$ and (b, c) transition $|\pm1\rangle \rightleftharpoons |\pm2\rangle$.

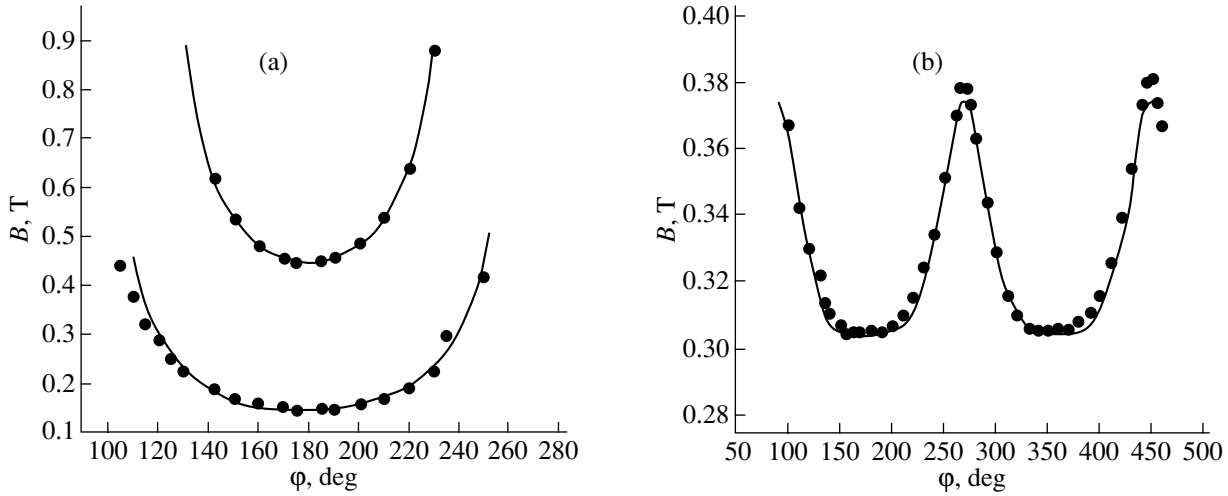

Fig. 3. Angular variation of the resonance magnetic field with rotation of the crystal in the (100) plane. Theoretical calculations are shown by solid lines, and experimental values, by points; φ = 180° corresponds to **B** || **c**. (a) Transition $|\pm1\rangle \rightleftharpoons |\pm2\rangle$, frequency 225 GHz; and (b) transition $|0\rangle \rightleftharpoons |\pm1\rangle$, frequency 79 GHz.

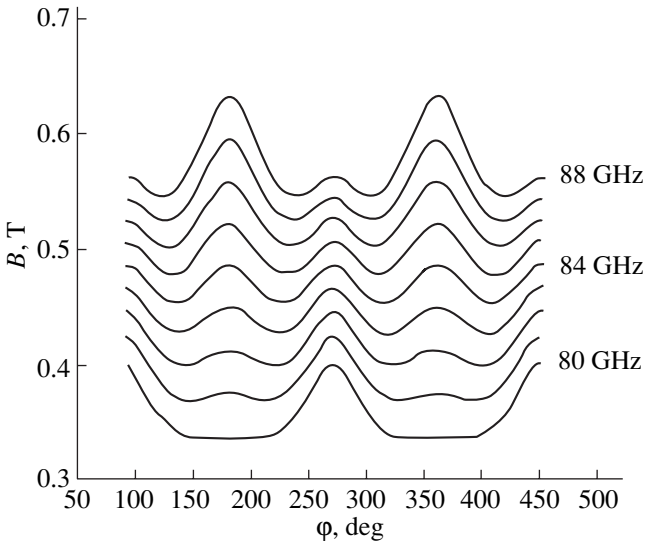

Fig. 4. Family of calculated angular dependences of the resonance magnetic field corresponding to rotation of the crystal in the (100) plane. The bottom curve corresponds to the frequency 80 GHz, and the top curve, to 88 GHz; the spacing between the curves is 1 GHz.

experiment. While the curves obtained are typical of non-Kramers ions and resemble the $1/\cos\alpha$ dependence, we came up against an untypical case which may be of some interest from the methodical standpoint. We deal here with the transition $|0\rangle \rightleftharpoons |+1\rangle$ near the frequency 84 GHz. As can be seen from Fig. 2a, two frequency-versus-field curves corresponding to parallel and perpendicular orientations of the sample intersect near this frequency. The angular variation of the EPR line is such that at frequencies lower than 84 GHz, the orientation **B** || **c** corresponds to the low field extreme point, while at frequencies higher than 84 GHz, to the high field extreme point. Figure 4 shows a family of calculated angular dependences of the resonance field for this range of frequencies. It is seen that, in the vicinity of 84 GHz, the angular variation most likely belongs to a cubic rather than to a tetragonal center. For a spectrometer working at a fixed frequency, this situation could lead to misinterpretation of the symmetry of the center.

At the same time, we failed to determine the type of substitution. It is most probable that Cr^{2+} substitutes for bivalent cadmium, although there are some reasons to support the possibility that the substitution $Cr^{2+} \longrightarrow Ga^{3+}$ takes place. First, the substitution $Cr^{2+} \longrightarrow Ga^{3+}$ without involvement of a local charge compensator is known to exist in GaAs. If a similar substitution takes place in our case, the EPR spectra should also have a tetragonal symmetry. Second, we observed EPR spectra of Cr^{2+} ions in related Ga-containing $A^{I}B^{III}C_2^{VI}$ compound semiconductors, whose structure is also built on the basis of a chalcopyrite structure but without cation vacancies. These compounds do not contain a bivalent cation at all. Some help in determining the type of substitution may provide data on the optical spectra of Cr^{2+}, but we did not find such data in the literature.

4. CONCLUSION

The main results can be summarized as follows. A new bivalent chromium center with tetragonal coordination has been found and identified in a $CdGa_2S_4$ crystal. It was is concluded that this center has tetragonal symmetry. The fine-structure constants and the values of the *g* factors were determined.

4. ACKNOWLEDGMENTS

The authors are grateful to V.A. Shustov for the x-ray analysis and V.A. Ulanov for helpful discussions.

REFERENCES

1. L. Deloach, R. H. Page, G. D. Wilke, *et al.*, IEEE J. Quantum Electron. **32** (5), 885 (1996).
2. R. H. Page, K. I. Schaffers, L. D. Deloach, *et al.*, IEEE J. Quantum Electron. **33** (4), 609 (1997).
3. M. Birnbaum, M. B. Camargo, S. Lee, *et al.*, OSA TOPS Adv. Solid-State Lasers **10**, 148 (1997).
4. G. J. Wagner, T. J. Carrig, R. H. Page, *et al.*, Opt. Lett. **24** (1), 19 (1999).
5. A. A. Lavrentyev, B. V. Gabrelian, V. A. Dubeiko, *et al.*, J. Phys. Chem. Solids **63** (2), 227 (2002).
6. J. T. Vallin and G. D. Watkins, Phys. Rev. B **9** (5), 2051 (1974).
7. R. J. Wagner and A. M. White, Solid State Commun. **32** (5), 399 (1979).
8. M. M. Zaripov, V. F. Tarasov, V. A. Ulanov, and G. S. Shakurov, Fiz. Tverd. Tela (St. Petersburg) **38** (2), 452 (1996) [Phys. Solid State **38**, 249 (1996)].
9. V. F. Tarasov and G. S. Shakurov, Appl. Magn. Reson. **2** (3), 571 (1991).

Translated by A. Zalesskiĭ

Physics of the Solid State, Vol. 45, No. 8, 2003, pp. 1455–1458. Translated from Fizika Tverdogo Tela, Vol. 45, No. 8, 2003, pp. 1386–1389.

SEMICONDUCTORS AND DIELECTRICS

Hindered Rotation of the CH_3 Group in *L*-Alanine Single Crystals: Temperature-Induced Transformation of the ESR Spectrum

V. V. Lemanov and L. S. Sochava

Ioffe Physicotechnical Institute, Russian Academy of Sciences, Politekhnicheskaya ul. 26, St. Petersburg, 194021 Russia

e-mail: Lev.Sochava@pop.ioffe.rssi.ru

Received December 25, 2002

Abstract—Temperature-induced transformation of the ESR spectrum in γ-irradiated single crystals of the protein aminoacid *L* alanine, caused by hindered rotation of the CH_3 group was studied. The rotation parameters as derived from the transformation of the ESR spectrum (activation energy $U = 0.18$ eV, prefactor $\omega_0 = 1 \times 10^{13}$ s^{-1}) are in satisfactory agreement with the values obtained earlier from measurements of the proton spin–lattice relaxation in polycrystalline alanine samples. *© 2003 MAIK "Nauka/Interperiodica".*

1. INTRODUCTION

Intramolecular rotations of atomic groups considerably affect the physical properties of a molecule itself and of the corresponding molecular crystal. Because the rotating group interacts with the surrounding atoms, such rotations are hindered [1] and are characterized by the height U of the barrier separating equivalent configurations and by the prefactor in the temperature dependence of the hopping frequency $\omega = \omega_0 e^{-U/kT}$.

Hindered rotation of the CH_3 and NH_3 groups in protein aminoacid crystals has been the subject of a series of studies carried out primarily by measuring the temperature dependence of the proton spin–lattice relaxation time T_1 in NMR spectra [2–4]. An analysis of the data obtained in a time-consuming experiment using modified Bloch equations [5, 6] yielded both the barrier height U and the factor ω_0. The modified Bloch equations were also used in [7] to process ESR data bearing on the methyl group rotation in alanine. To reduce the resonance line width and, thus, make quantitative analysis of the spectra possible, deuterated alanine samples had to be used [7].

In the present experiment, we inferred the rotation of the CH_3 group in an L-alanine single crystal from the temperature-induced transformation of the ESR spectrum of irradiated alanine crystals. It was established as far back as in the 1960s that crystals of aminoacids subjected to ionizing radiation (γ- and x-rays) produce an ESR spectrum originating from the interaction of the irradiation-produced unpaired electron with four protons. The anisotropic character of the hyperfine interaction accounts for the complex pattern of the spectrum, which depends on the crystal orientation with respect to the external magnetic field. The fairly fast rotation of the CH_3 group should bring about a temperature-induced transformation of the ESP spectrum when the temperature is such that the reorientation frequency of the CH_3 group becomes comparable to or higher than the corresponding splittings in the ESR spectrum (the well-known averaging of the magnetic resonance spectrum caused by atomic motion, which was considered for the case of NMR in [5, 6]).

For quantitative analysis of the temperature-induced transformation of spectra, we employed a substantially simpler method of experimental data processing than that described in [7]. In this method, which is based on a theoretical study of Anderson [8], the experiment is essentially reduced to obtaining the temperature dependence of the width of the resonance lines in the temperature regions where the lines undergo broadening and narrowing; no use is mode of the Bloch equations.

2. EXPERIMENTAL TECHNIQUE

The alanine molecule has one of the simplest structures of the 20 protein aminoacids (Fig. 1). The L ala-

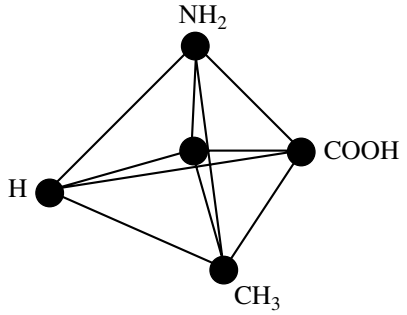

Fig. 1. Structure of the alanine molecule.

1063-7834/03/4508-1455$24.00 © 2003 MAIK "Nauka/Interperiodica"

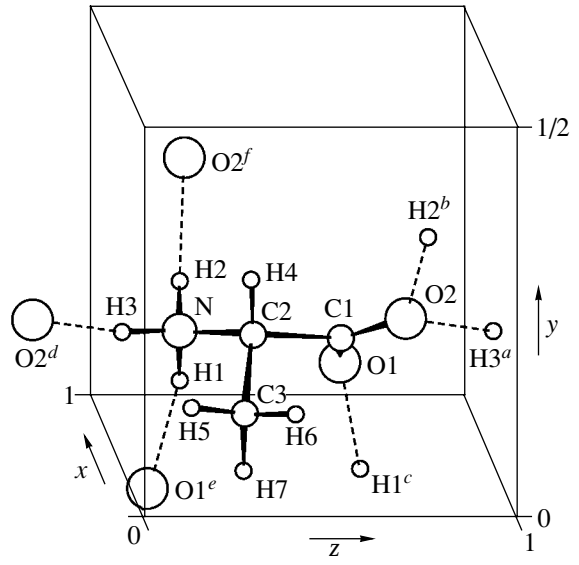

Fig. 2. L-alanine molecule in the L-alanine crystal [10]. Dashed lines show hydrogen bonds, and indices *a*–*f* refer to atom positions (see [10]).

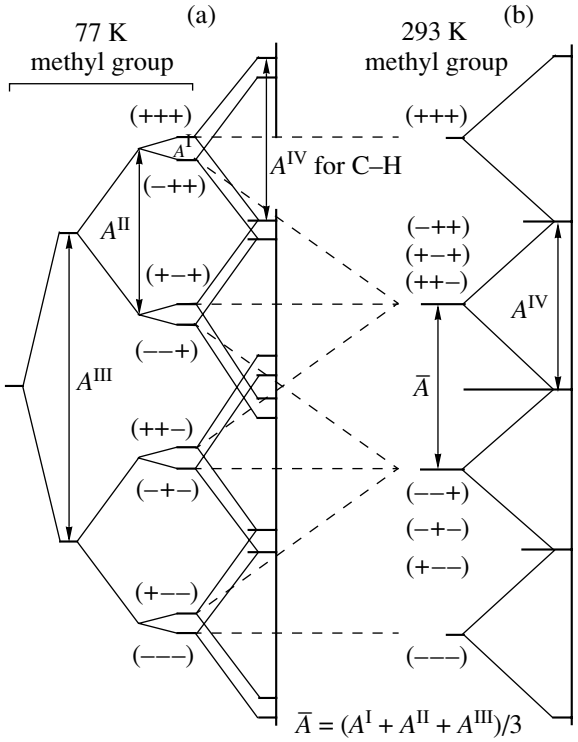

Fig. 3. Energy levels originating from hyperfine interaction of the unpaired electron with the four protons in a γ-irradiated alanine crystal at *T* equal to (a) 77 and (b) 293 K [7]. **H** ‖ [001]. The plus and minus signs identify the proton spin states in the methyl group.

nine crystal has D_2^4 ($P2_12_12_1$) symmetry [9, 10]. The molecules of the crystal interact via a hydrogen bond that connects the oxygen in the COO^- carboxyl group to the hydrogen in the aminogroup of the neighboring molecule (O2 and H2, H3 in Fig. 2). Irradiation ruptures the C–N bond to form the $CH_3\dot{C}HCOO$ radical, where the dot denotes, as usual, an unpaired electron.

Large (about 1 cm^3 in volume) transparent crystals of L alanine were grown by slowly cooling the corresponding solution. The γ radiation was provided by ^{60}Co (irradiation at $T = 300$ K to a dose of 2×10^4 Gy).

The ESR spectra were measured on a modified SE/X-2544 Radiopan spectrometer (*X* range, 9.3 GHz). The temperature could be stabilized within the range 100–300 K to within ±0.2 K by blowing through nitrogen vapor.

3. RESULTS AND DISCUSSION

3.1. ESR Spectrum

The ESR spectrum observed in an irradiated crystal originates from the hyperfine interaction of the unpaired electron with four protons, three of which are contained in the methyl group (H5–H7 in Fig. 2) and the fourth (H4) is coupled to the carbon C2. Because of the strong anisotropy of this interaction, the spectrum obtained on a crystal arbitrarily oriented in an external magnetic field **H** is fairly complex. If the field **H** is directed along one of the C_2 crystal axes (the C_2 ‖ [001] axis in the notation used in [7]), the spectrum measured at $T = 77$ K consists of 12 lines (Fig. 3). In this orientation, the hyperfine interaction constants *A* differ strongly among the four protons [7] ($A_{H5} = 5.1$ G, $A_{H6} = 27.6$ G, $A_{H7} = 46.1$ G, $A_{H4} = 27.6$ Oe), with the result that, for example, four rather than one line at the center of the spectrum correspond to the zero value of the projection of the total nuclear spin of the four protons. The energy level diagram and the spectrum obtained in this orientation are shown schematically in Fig. 3, taken from [7].

As the temperature increases, the gradual increase in the methyl group rotation rate brings about an averaging of the hyperfine interaction constants A_{H5}–A_{H7}; at room temperature and for **H** ‖ [001], the constants *A* for the three protons of the methyl group assume the same value of 26.3 G, which happens to coincide in these conditions with the value of *A* for the fourth proton. Thus, at room temperature and for **H** ‖ [001], the unpaired electron interacts with four equivalent protons. Indeed, the experimental spectrum obtained in these conditions (Fig. 4) represents a symmetric quintet because of the five possible values of the total spin projection (2, 1, …, –2). The intensity ratios of the five components turned out to be very close to the values calculated for the case of four equivalent protons (1 : 4 : 6 : 4 : 1).

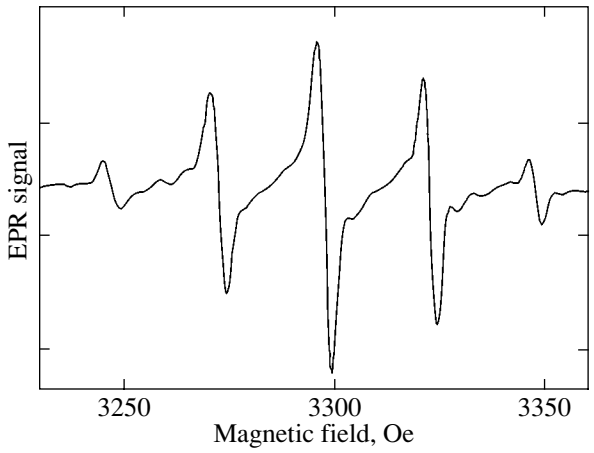

Fig. 4. ESR spectrum of an irradiated L-alanine crystal measured at $T = 300$ K. **H** || [001], $f = 9.24$ GHz. The weak lines are due to slight misorientation of the sample.

3.2. Temperature-Induced Transformation of the ESR Spectrum

As the temperature is increased from liquid nitrogen to room temperature, the strongest change in the spectrum obtained in the **H** || [001] orientation occurs with the central group of lines, which consists, as already mentioned, of a quartet at 77 K and of a single line at 300 K (Fig. 3). It is these lines that were chosen by us for quantitative study of the rotation of the CH_3 groups.

The increase in the rate of rotation of the CH_3 groups with increasing temperature gives rise to a classical pattern [8] of transformation of the central quartet; namely, first some of its components broaden to eventually merge into one line, which narrows with a further increase in temperature. Figure 5a illustrates the measured widths $\delta H(T)$ of these lines. This change in the linewidth is seen to be strong enough to allow quantitative measurements; indeed, δH changes by three and six times in the regions of the line narrowing and broadening, respectively (experimental points *1*, *2* in Fig. 5a).

According to theory [8], in the temperature region where the lines broaden with increasing temperature such that δH becomes considerably larger than the initial width, the linewidth (expressed in units of frequency) $\delta f = (g\beta/\hbar)\delta H$ (f is the ESR frequency used, g is the g factor, β is the Bohr magneton) coincides with the frequency ω_e of the process responsible for the spectral transformation:

$$\delta f = \omega_e.$$

In the temperature region of line narrowing, we have, according to [8],

$$\delta f \sim 1/\omega_e.$$

Therefore, the data from Fig. 5a can be used to derive the temperature dependence of the frequency of the averaging process, more specifically, of the CH_3 rate of rotation. This dependence is plotted on the log–linear scale in Fig. 5b. In both regions, the $\omega_e(T)$ relation is seen to be well fitted by a single exponential with an activation energy $U = 0.18 \pm 0.01$ eV and a prefactor $\omega_0 = (1 \pm 0.4) \times 10^{13}$ s^{-1}.

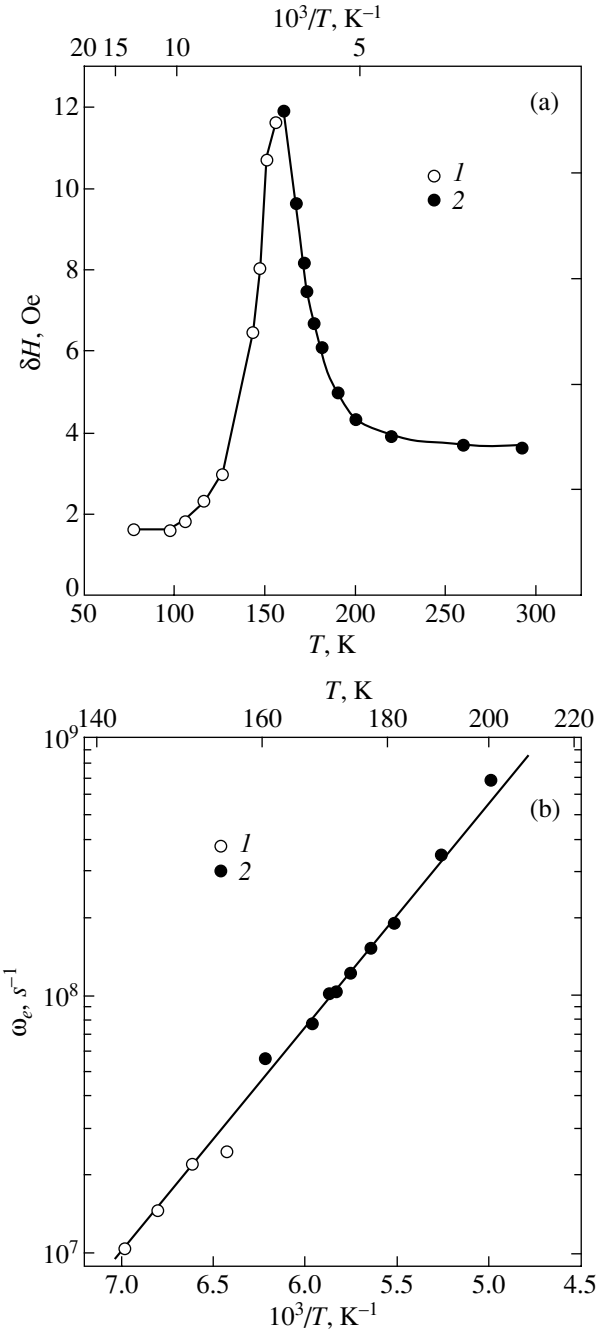

Fig. 5. (a) Temperature dependence of the width of the central ESR line of alanine and (b) temperature dependence of the CH_3 group rotation rate derived from the former. Points *1* specify the width of one of the central quartet lines, and *2*, the width of the averaged central line.

The above values of U and ω_0 agree satisfactorily with the results obtained earlier [2, 4] using the tradi-

Rotation parameters U and ω_0 of the CH_3 group in L alanine

U, eV	ω_0, s^{-1}	Reference
0.15	–	[2]
0.23	7×10^{12}	[4]
0.16	1×10^{13}	[7]
0.18 (line broadening region)	1×10^{13}	This work
0.18 (line narrowing region)	1×10^{13}	"

tional method, namely, by studying the temperature dependence of proton spin–lattice relaxation (see table). It should be stressed that the method used in the present investigation is substantially simpler from the experimental standpoint.

It appears of interest to compare the results obtained by us with the study performed in [11] on the temperature dependence of piezoelectric response in crystals of certain protein aminoacids. The minima observed in those relations were assigned to relaxation decay of ultrasonic vibrations (frequency 10 MHz) caused by their connection with the hindered rotation of the CH_3 and NH_3 groups. Unfortunately, no distinct minimum in the piezoelectric response was observed in L-alanine crystals; this is apparently due to the superposition of the temperature dependences of other parameters governing the magnitude of the piezoelectric response. It can only be maintained that the minimum lies in the interval from 170 to 200 K (see [11, Fig. 3]). Using the values derived here for U and ω_0, we obtain 170 K for the temperature of the decay minimum, which is in accord with the values quoted in [11].

On the other hand, DL alanine exhibited clearly pronounced minima in the temperature dependence of the piezoelectric response [11, Fig. 3], which yielded for the hindered rotation of the CH_3 group $U = 0.2$ eV and $\omega_0 = 10^{13}$ s^{-1}; these values are very close to the data obtained in this study for L alanine. Although crystals of DL alanine, in contrast to L alanine, belong to a *polar* symmetry group C_{2v}^9 ($Pna2_1$), the closeness of these crystals in structure is a relevant, interesting feature [9]. The coincidence of the parameters characterizing the hindered rotation of the CH_3 group in L and DL alanines may be considered a manifestation of this similarity [7].

Thus, the values of the parameters U and ω_0 obtained in [11] and in this study are in remarkably good agreement.

ACKNOWLEDGMENTS

The authors are indebted to A.G. Razdobarin for assistance in the experiment.

This study was supported in part by the Russian Foundation for Basic Research, project no. 02-02-17666.

REFERENCES

1. M. V. Vol'kenshteĭn, *Structure and Physical Properties of Molecules* (Akad. Nauk SSSR, Moscow, 1955).
2. M. R. Zaripov, in *Radiospectroscopy*, Ed. by B. K. Kozyrev (Nauka, Moscow, 1973), p. 193.
3. E. R. Andrew, W. S. Hinshow, M. G. Hutchins, and R. O. I. Sjoblom, Mol. Phys. **31**, 1479 (1976).
4. E. R. Andrew, W. S. Hinshow, M. G. Hutchins, and R. O. I. Sjoblom, Mol. Phys. **32**, 795 (1976).
5. H. C. Gutowsky, D. W. McCall, and C. P. Slichter, J. Chem. Phys. **21**, 279 (1953).
6. J. A. Pople, W. G. Schneider, and H. J. Bernstein, *High-Resolution Nuclear Magnetic Resonance* (McGraw-Hill, New York, 1959; Inostrannaya Literatura, Moscow, 1962).
7. I. Miyagawa and K. Itoh, J. Chem. Phys. **36**, 2157 (1962).
8. P. W. Anderson, J. Phys. Soc. Jpn. **9**, 316 (1954).
9. H. I. Simpson and R. E. Marsh, Acta Crystallogr. **20**, 550 (1966).
10. R. Destro, R. Bianchi, and G. Morosi, J. Phys. Chem. **93**, 4447 (1989).
11. V. V. Lemanov, S. N. Popov, and G. A. Pankova, Fiz. Tverd. Tela (St. Petersburg) **44**, 1840 (2002) [Phys. Solid State **44**, 1929 (2002)].

Translated by G. Skrebtsov

Physics of the Solid State, Vol. 45, No. 8, 2003, pp. 1459–1464. Translated from Fizika Tverdogo Tela, Vol. 45, No. 8, 2003, pp. 1390–1395.

SEMICONDUCTORS AND DIELECTRICS

EPR of Ce^{3+} Ions in Mixed Yttrium–Lutecium Orthoaluminates

H. R. Asatryan*, J. Rosa, and J. A. Mares****

**Ioffe Physicotechnical Institute, Russian Academy of Sciences, Politekhnicheskaya ul. 26, St. Petersburg, 194021 Russia*
e-mail: hike.asatryan@mail.ioffe.ru

***Institute of Physics, Czech Academy of Sciences, Division of Solid State Physics, Prague 6, 16200 Czech Republic*

Received September 3, 2002; in final form, December 29, 2002

Abstract—The results of EPR studies of Ce^{3+} ions incorporated into single crystals of mixed yttrium–lutecium orthoaluminates $Y_{1-x}Lu_xAlO_3$ (YLuAP, $x = 0.1, 0.3$) are reported. In compositionally disordered YLuAP compounds, in comparison to $YAlO_3$, new paramagnetic Ce^{3+} centers are found. These centers are caused by the changes in symmetry and in the crystal field magnitude due to the isomorphic substitution of Y^{3+} ions by Lu^{3+} in the yttrium sublattice of orthoaluminates. It is shown that the formation of 27 different types of centers is possible in YLuAP with variation of the Lu content. The probabilities of formation of new paramagnetic centers are calculated. © *2003 MAIK "Nauka/Interperiodica".*

1. INTRODUCTION

Single crystals of $YAlO_3$ (YAP) activated by rare-earth impurities are widely used in quantum electronics [1, 2]. The interest aroused in these compounds in recent years stems from the possibility of using Ce-activated YAP as effective fast-response scintillators [3–7]. Crystals of Ce-activated lutecium orthoaluminate are the most efficient scintillators for positron-emitting tomography (PET-imaging) in medicine [8]. However, the growth of sufficiently large high-quality single crystals of Ce^{3+}-activated $LuAlO_3$ is a relatively complicated technological problem. Success has been achieved in the growth of mixed yttrium–lutecium orthoaluminates with Ce^{3+} impurities, which are also very promising scintillators for the fabrication of high-sensitive positron-emitting tomographs. Progress in this field depends, in many respects, on our knowledge of the spectroscopic properties of these scintillators. One straightforward and informative method of studying such properties is through electron paramagnetic resonance (EPR) [9, 10], which makes it possible to identify an impurity and determine the charge and local symmetry of the impurity center and the composition of the nearest neighbor environment.

A sufficiently large number of studies have been made on light absorption and luminescence of rare-earth and of transition-metal ions incorporated into yttrium orthoaluminate crystals. However, up to now, only a few of them have been devoted to studies of $YAlO_3$ crystals using the EPR method. This method has so far been used for studying some transition elements (Cr^{3+}, Fe^{3+}, Ti^{3+}), Gd^{3+} [11–18], and rare-earth ions, such as Er^{3+}, Nd^{3+}, and Ce^{3+} [19, 20]. It is of interest to study crystals of mixed yttrium–lutecium orthoaluminates $Y_{1-x}Lu_xAlO_3$ (YLuAP) with $0 \le x \le 1$. Part of the Y^{3+} ions in these crystals is isostructurally substituted by Lu^{3+} ions with the formation of solid solutions. In this publication, the results of a detailed study of EPR spectra of mixed yttrium–lutecium orthoaluminate $Y_{1-x}Lu_xAlO_3$ single crystals with $x = 0.1$ and 0.3 are first reported.

2. EXPERIMENTAL

Single crystals of YLuAP activated by cerium ions up to ±0.05 at. % were used in this study. The crystal growth was performed by Preciosa Crytur Co., Ltd. (Turnov, Czech Republic) using the Czochralski method. EPR spectra of Ce^{3+}-doped $Y_{1-x}Lu_xAlO_3$ single crystals were recorded with the aid of conventional JEOL-JES-PE-3X and ERS-230 3-cm-band radiospectrometers in the temperature range 4–50 K. Prior to measurements, the samples were oriented using the x-ray diffraction method with an accuracy of ±0.5° and cut in the form of rectangular parallelepipeds $1.5 \times 2 \times 5$ mm in size with their faces parallel to the *ab*, *ac*, and *bc* crystal planes. More precise orientation of the principal magnetic axes with respect to an external magnetic field was performed directly inside the rf cavity of a radiospectrometer by calibrating against the known EPR signals.

3. CRYSTAL STRUCTURE

The crystal structure of yttrium orthoaluminate belongs to the orthorhombic space group D_{2h}^{16}–P_{bnm} and is described in detail in the literature (see e.g., [21–23]). The orthorhombic unit cell of $YAlO_3$ contains four distorted perovskite pseudocells. Therefore, Y^{3+} and Al^{3+} ions form four structurally nonequivalent positions. Aluminum ions are surrounded by six oxygen ions forming a slightly distorted octahedron (local symme-

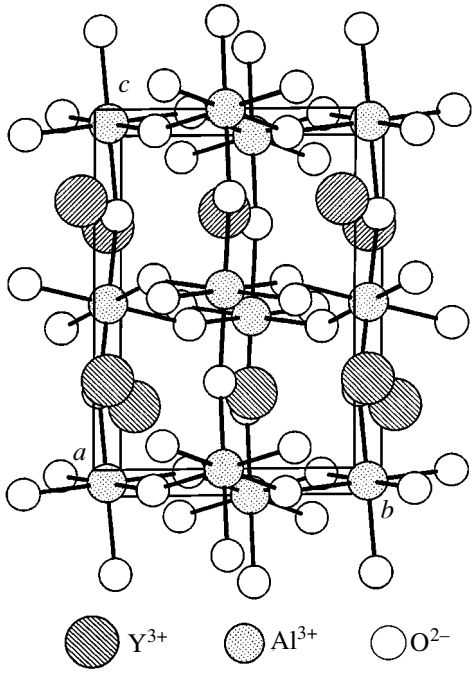

Fig. 1. Structure of yttrium orthoaluminate.

try C_i). The nearest neighbor environment of Y^{3+} ions is more complicated and more strongly distorted (local symmetry C_s). Figure 1 shows the positions of Y^{3+} ions, which are substituted by rare-earth and Ce^{3+} ions, in the structure of yttrium orthoaluminate. The distances from the central yttrium ion to the nearest neighbor oxygen ions vary from 2.28 to 3.0148 Å. The second coordination shell of the yttrium site contains six other yttrium ions forming a distorted octahedron, which is considered in detail below in Section 5. In distinction from the aluminum ion positions, all oxygen and yttrium ions are shifted by several tenths of an angstrom with respect to ideal perovskite positions. Aluminum sites possess only inversion symmetry, and yttrium sites have a mirror symmetry plane normal to the *c* axis of the crystal.

Yttrium ions in yttrium orthoaluminate crystals are located in a mirror symmetry plane perpendicular to the *c* axis, i.e., in the *ab* plane. Therefore, for the paramagnetic ions localized at these lattice sites, one of the principal axes of the *g* tensor always coincides with the *c* axis of the crystal, while the other two axes lie in the *ab* plane. Furthermore, the Y^{3+} positions make up pairs so that the operation of inversion through an aluminum site takes the members of the corresponding pair into each other; therefore, there are only two magnetically nonequivalent positions in the EPR spectra for an arbitrarily directed external magnetic field **B**, as well as for **B** rotating in the *ab* plane.

4. EXPERIMENTAL RESULTS

EPR of Ce^{3+} ions in yttrium orthoaluminate (without Lu^{3+} ions) was thoroughly studied in [19, 20]. The Ce^{3+} ion has the electron configuration $4f^1$ (one unpaired electron) and the ground state $^2F_{5/2}$. Because of large splitting of the Stark components, only the ground state is observed in the EPR spectra. The cerium ions in yttrium orthoaluminate crystals substitute for Y^{3+} ions, as do the majority of rare-earth elements. Natural cerium has only two even isotopes, ^{140}Ce and ^{142}Ce, with zero nuclear spin. Because of the absence of odd isotopes with nonzero nuclear spin, no magnetic hyperfine structure is observed in the EPR spectra for Ce^{3+} ion. Highly anisotropic angular variations of the EPR spectra for Ce^{3+} in $YAlO_3$ single crystals are described by the spin Hamiltonian of orthorhombic symmetry in the form

$$H = \beta \mathbf{B} \mathbf{g} S + \mathbf{S} \mathbf{A} \mathbf{I}, \quad (1)$$

where $S = 1/2$ is the effective spin, β is the Bohr magneton, and **g** and **A** are the *g*-factor and hyperfine-interaction tensors, respectively. The following values of the components of the **g** tensor were obtained: $g_x = 0.395 \pm 0.005$, $g_y = 0.402 \pm 0.001$, and $g_z = 3.614 \pm 0.005$. The local principal magnetic axes of a Ce^{3+} ion in yttrium orthoaluminate are oriented so that the *x* axis is directed along the *c* axis of the crystal and the *y* and *z* axes lie in the *ab* plane. The local magnetic *y* axis makes an angle of 31.8° with the crystallographic *a* axis in the *ab* plane. The mean *g* factor is $\langle g \rangle = 1.47$, which is consistent with the *g* factor for the Kramers doublet Γ_6 of Ce^{3+} ions in a crystal field of cubic symmetry, $g = 1.43$ [9].

For single crystals of $YAlO_3$: Ce^{3+} containing lutecium ions as an additional dopant, i.e., for mixed orthoaluminates $Y_{1-x}Lu_xAlO_3$ ($0 \le x \le 1$), the EPR spectra exhibit several new lines in addition to the two principal intense lines from magnetically nonequivalent paramagnetic centers Ce^{3+}. These new lines are grouped near the principal cerium lines and are strongly anisotropic, and their widths are equal to those of the principal lines. The integrated intensities and the number of new EPR lines depend on the content of the additional lutecium dopant and increase with *x*. The angular and temperature variations of these lines, as well as the mean *g* values, provide unambiguous evidence that the observed new EPR lines in Ce-activated mixed orthoaluminates also belong to the Ce^{3+} ions, which substitute for Y^{3+}. An increase in the content of lutecium ions causes the spectra in the 3-cm band to broaden, some new lines to appear, and the angular variations of the spectra to become so complicated and cumbersome that detailed analysis in a wide range of angles θ becomes impossible. Such analysis is possible only at a small content of the additional dopant ($x < 0.15$).

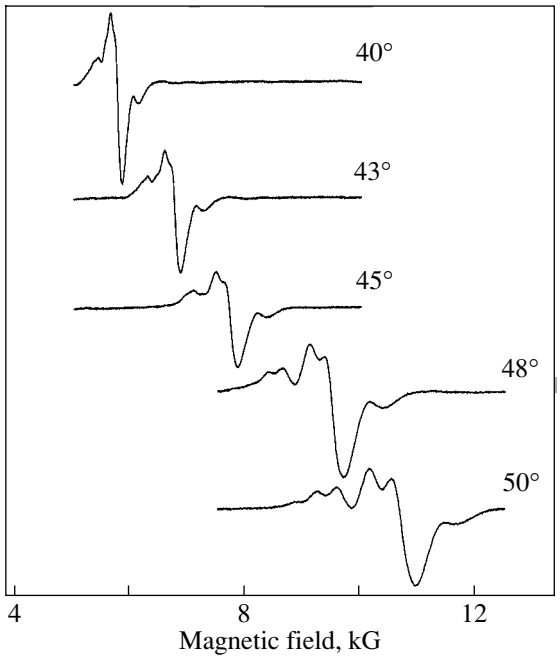

Fig. 2. EPR spectra of Ce^{3+} ions in mixed orthoaluminate $Y_{0.9}Lu_{0.1}AlO_3$ at ν = 9.24 GHz and T = 9 K in the range of angle θ from 40° to 50°.

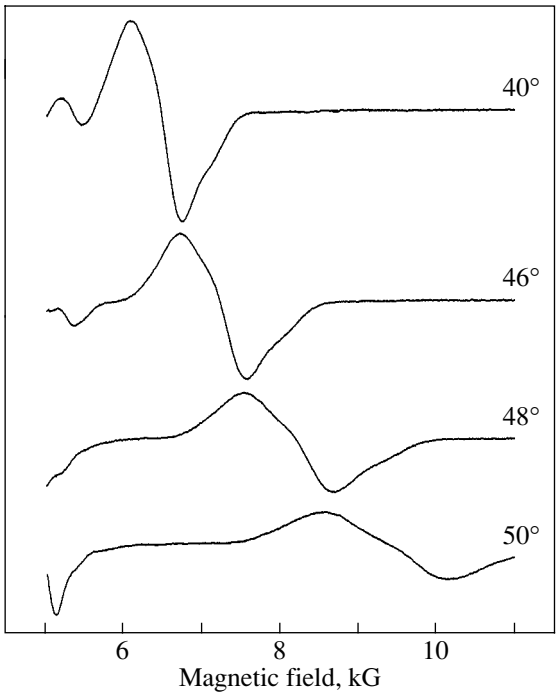

Fig. 3. EPR spectra of Ce^{3+} ions in mixed orthoaluminate $Y_{0.7}Lu_{0.3}AlO_3$ at ν = 9.24 GHz and T = 9 K in the range of angle θ from 40° to 50°.

EPR spectra of Ce^{3+} ions in a $Y_{0.9}Lu_{0.1}AlO_3$ single crystal at a frequency of 9.24 GHz and a temperature of 9 K are shown in Fig. 2 for the angle θ varying in the *ab* plane from 40° to 50°. In this range of angles, when the magnetic field **B** rotates in the *ab* plane, the best resolution of additional EPR lines from cerium in the YLuAP crystal is observed. At small angles θ, the additional lines are not resolved and superimposed on the principal line and the EPR spectrum becomes identical to the usual spectrum from a Ce^{3+} ion in $YAlO_3$. For comparison, Fig. 3 shows similar spectra for the single crystal of $Y_{0.7}Lu_{0.3}AlO_3$, where the resolution of lines is not as high as in the case of x = 0.1. Decomposition into components of the most resolved EPR spectra from Ce^{3+} ions for $Y_{0.9}Lu_{0.1}AlO_3$ shows that the spectrum consists of at least six additional lines superimposed on the principal EPR line of a Ce^{3+} ion. Figure 4 shows, on an enlarged scale of the magnetic field, the angular dependences of all EPR lines observed experimentally from Ce^{3+} ions. Dashed lines *1–6* in Fig. 4 correspond to new cerium centers Ce1–Ce6 in YLuAP, and the solid line, to the Ce^{3+} center in YAP. It can be seen that, along with the intense central line, there exist six lines located in the immediate vicinity of the central component. The values of the effective g factors are listed in the table for the case where the angle between the external magnetic field and the *a* axis in the *ab* plane is equal to 50°, which corresponds to the best resolution of the spectrum.

It should be noted that the additional EPR lines from cerium paramagnetic centers observed in the mixed orthoaluminates differ in intensity but are qualitatively similar (in the number of lines and angular variations) to the satellite lines in $YAlO_3$ [19, 20]. This similarity is evidence that low-intensity lines from Ce^{3+} ions in orthoaluminates with and without lutecium can be caused by paramagnetic centers of the same nature.

5. DISCUSSION

As noted above, the results of EPR studies indicate that Ce^{3+} impurity ions isostructurally substitute for Y^{3+} ions in the crystal lattice. Our studies showed that the Ce^{3+} EPR spectra for solid solutions $Y_{1-x}Lu_xAlO_3$ also belong (irrespective of x) to Ce^{3+} ions at yttrium sites. However, in distinction to "pure" YAP (YLuAP with x = 0), EPR spectra of cerium ions in single crystals of mixed orthoaluminates consist of several lines. This effect is caused by the formation of paramagnetic centers of different types in the crystal. The Ce^{3+} ions are

Effective g factors of the Ce^{3+} ion in $YAlO_3$ and of additional Ce^{3+} centers in $Y_{0.9}Lu_{0.1}AlO_3$ at ν = 9.24 GHz, T = 9 K, and θ = 50°

Ce1	Ce2	YAP : Ce	Ce3	Ce4	Ce5	Ce6
0.581	0.594	0.626	0.646	0.685	0.715	0.746

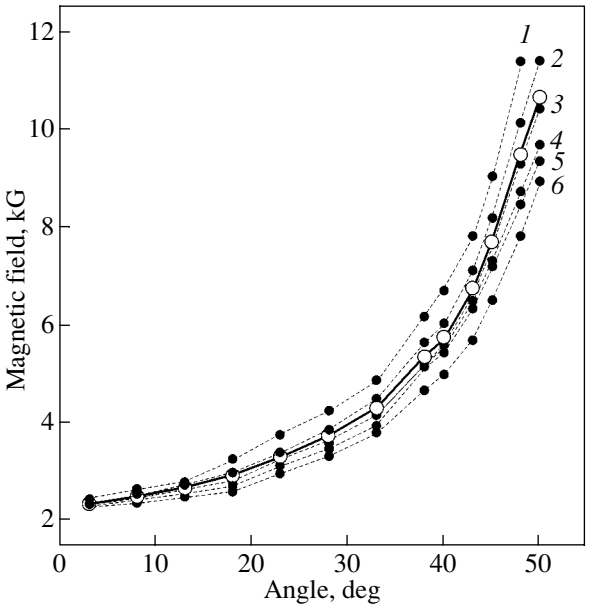

Fig. 4. Experimental angular variations of resonance magnetic fields of Ce^{3+} centers in $Y_{0.9}Lu_{0.1}AlO_3$ at ν = 9.24 GHz and T = 9 K. The results for new centers Ce1–Ce6 are shown by dashed lines *1–6*; the solid line shows the results for Ce^{3+} in $YAlO_3$.

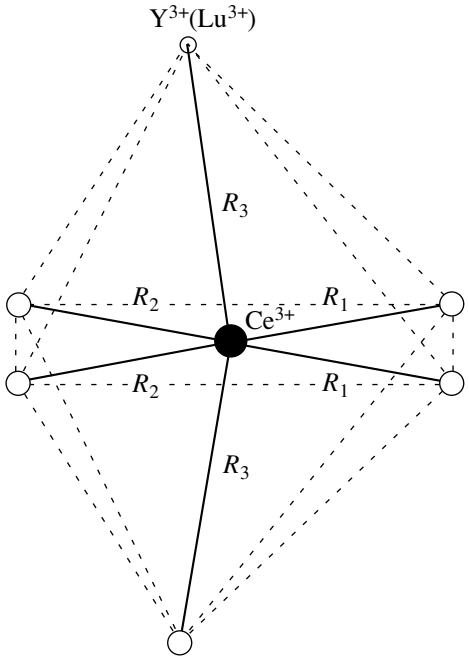

Fig. 5. Structure of the yttrium nearest neighbor environment of the Ce^{3+} ion in orthoaluminate. R_1, R_2, and R_3 are the distances from the paramagnetic center to the Y^{3+} or Lu^{3+} sites.

localized only at yttrium sites, but the crystal fields at these sites differ in magnitude and symmetry due to the local lattice deformation caused by the substitution of Y^{3+} ions by Lu^{3+} ions in the nearest neighbor environment of a paramagnetic center. The variety of types of Ce^{3+} centers in mixed YLuAP aluminates depends on the lutecium content and is caused only by statistical fluctuations in the distribution of Lu^{3+} ions over the sites of the yttrium sublattice. The isovalent substitution $Y^{3+} \longrightarrow Lu^{3+}$ in YLuAP crystals does not affect the electrostatic interaction of the cations at yttrium and aluminum sites with their environment. Therefore, the introduction of rare-earth impurity ions into $YAlO_3$ will not be accompanied by the formation of defects compensating for the difference between the charges of the substitutional impurity and the substituted ions. However, the mixed crystals (solid solutions) possess a statistically disordered structure [24]. Lutecium ions substituting for yttrium ions in the orthoaluminate lattice become nearest neighbors of Ce^{3+} activation centers and distort the symmetry of their nearest neighbor environment (inherent in YAP). Thus, the variety of types of Ce^{3+} centers in mixed orthoaluminates is the consequence of statistical fluctuations.

In order to understand the nature of the observed new Ce^{3+} EPR lines, let us consider the structure of the nearest neighbor environment of the paramagnetic center in the crystal lattice of orthoaluminate. Each Ce^{3+} ion in $YAlO_3$ has eight oxygen ions in its nearest neighbor environment, which form a distorted dodecahedron. The next coordination shell contains six Y^{3+} ions and octahedrally coordinated Al^{3+} ions. Since Lu^{3+} ions substitute for Y^{3+} ions, we should examine more closely the configuration of these sites around the paramagnetic Ce^{3+} center. This center is surrounded by six Y^{3+} or Lu^{3+} ions located at three different distances, R_1 = 3.641 Å, R_2 = 3.730 Å, and R_3 = 3.792 Å. These sites form a distorted octahedron. Figure 5 illustrates the model of this center. For simplicity, the Al^{3+} and O^{2-} ions are not depicted and only Y^{3+} ions are shown.

The presence of an Lu^{3+} ion with a smaller ionic radius (0.97 Å) at the Y^{3+} (1.02 Å) site alters the interionic distances and shifts the O^{2-} ions surrounding both Ce^{3+} and Lu^{3+} ions, thereby forming different crystal fields at those cerium ions that have an yttrium environment with partial substitution by one of several lutecium ions. The magnitude of the oxygenion shift is determined by the ratio of the Y^{3+} and Lu^{3+} ionic radii. Therefore, the Lu^{3+} ion located in the second coordination shell of Ce^{3+} affects the symmetry and magnitude of the crystal field by deforming the oxygen dodecahedron that surrounds the paramagnetic center.

In mixed $Y_{1-x}Lu_xAlO_3$ orthoaluminates of the same composition x, the Ce^{3+} ion can have a different rare-earth environment. The symmetry and magnitude of the crystal field will be different for those Ce^{3+} centers which have a different number of Y^{3+} ions substituted

by Lu^{3+} ions (from one to six) in their nearest neighbor environment.

In yttrium orthoaluminate crystals, in the case of isomorphic substitution and equiprobable distribution of substitutional ions, one may assume that the probability of finding an Lu^{3+} ion at a site of the yttrium cation sublattice is the same for all positions, as is the case in other similar crystals, e.g., in fluorite, corundum, garnet, and spinel [25]. In this case, we can calculate the probabilities that 1, 2, …, or n identical or different ions will be in the nearest neighbor cation coordination shell of the paramagnetic center. The concentration of single and complex centers can be determined by the formula for repeated trials from the probability theory (binomial distribution) [26]. In our case, the coordination number is equal to six; therefore, the probability of n (n = 0, 1, 2, …., 6) Lu^{3+} ions being in the rare-earth octahedron is [27, 28]

$$P_{6n} = \frac{6!}{n!(6-n)!}x^n(1-x)^{6-n}, \qquad (2)$$

where P_{6n} is the concentration of Ce^{3+} ions that have n Lu^{3+} ions in their nearest neighbor yttrium coordination shell and x is the concentration of Lu^{3+} ions in $Y_{1-x}Lu_xAlO_3$. The solid lines in Fig. 6 show the variations of these probabilities as a function of Lu^{3+} content in single crystals of $YAlO_3$. From these dependences, it follows that at x = 0.1 the fraction of cerium centers with n = 0 is 53.1%; 35.1% of cerium centers have one lutecium ion in their nearest neighbor environment, 9.8% have two Lu^{3+} ions, and the concentration of the Ce^{3+} centers with three Lu^{3+} ions is 1.5%. The ratio of the integrated intensities (experimental points in Fig. 6) of the principal and additional EPR lines of Ce^{3+} ions in the $Y_{0.9}Lu_{0.1}AlO_3$ crystal agrees with the calculated dependences of the probabilities of formation of additional centers in $Y_{1-x}Lu_xAlO_3$, which also testifies to the equiprobable distribution of lutecium ions in the yttrium sublattice of this crystal. For x = 0.3, there is only qualitative agreement between the calculated and experimental intensity ratios. For this concentration of the additional impurity in the crystal, the following concentrations of single and complex centers will be observed: 11.8% of paramagnetic centers will have no Lu^{3+} ions in there environment (n = 0), 30.3% of Ce^{3+} ions will have one Lu^{3+} ion in there nearest neighbor environment, 32.4% will have two Lu^{3+} ions, 18.5% of Ce^{3+} ions will have three Lu^{3+} ions (n = 3), and 6% of cerium centers will have four Lu^{3+} ions (n = 4). The variety of different type of centers is not limited by the six types associated with the various number of Lu^{3+} neighbors in the Y^{3+} positions. Even for the same value of n but for different arrangements of Lu^{3+} ions at the vertices of the distorted octahedron formed by yttrium sites, the crystal fields created by the additional lutecium impurity and acting on the paramagnetic Ce^{3+}

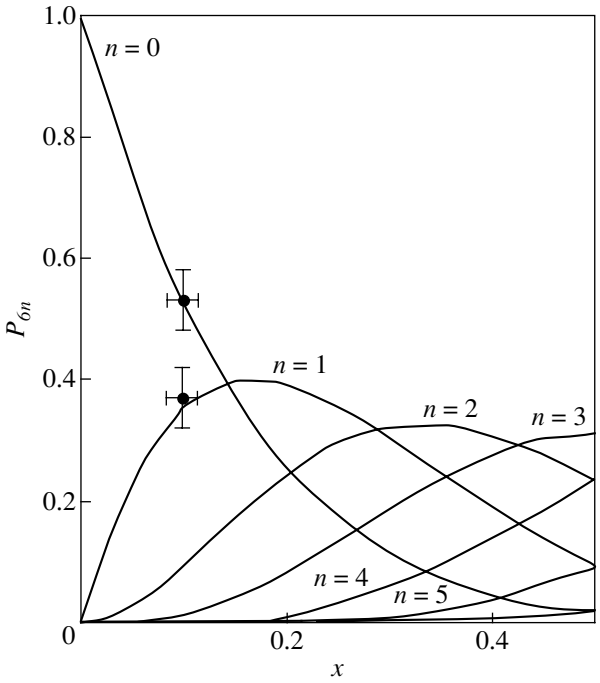

Fig. 6. Probabilities of n Lu^{3+} ions being in the yttrium nearest neighbor environment of the Ce^{3+} center in orthoaluminate as a function of Lu^{3+} content.

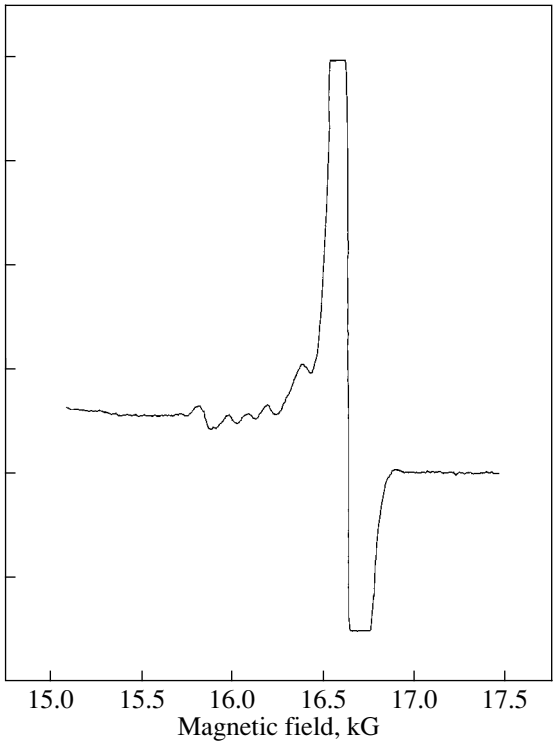

Fig. 7. EPR spectrum of Ce^{3+} ions in a $YAlO_3$ single crystal at ν = 9.24 GHz, T = 9 K, and θ = 56°.

ions will be different. For example, when there is one substitutional ion, three different centers are created; the substitution of two yttrium ions may result in the formation of seven different centers. Thus, at $x = 0.1$, eleven different paramagnetic centers can be created in YLuAP, of which only seven centers could be observed in detail (see Fig. 4, table). In the case of three substitutional ions, three centers with a different arrangement of Lu^{3+} are formed. All possible combinations in the arrangement of Y^{3+} and Lu^{3+} ions around Ce^{3+} correspond to 27 different paramagnetic centers.

The additional EPR lines of Ce^{3+} observed in mixed yttrium–lutecium orthoaluminates have different intensities; however, qualitatively (in the number of lines and in the angular dependences), they are similar to the satellite lines in $YAlO_3$ [19, 20]. This similarity means that in both cases additional EPR lines are caused by paramagnetic centers of the same origin. For comparison, Fig. 7 shows the EPR spectrum of Ce^{3+} ions in $YAlO_3$ observed at high amplification. Thus, the results support the assumption that the satellite EPR lines of Ce^{3+} ions in yttrium orthoaluminate are due to deviations from the stoichiometric crystal composition. These deviations manifest themselves in the occurrence of yttrium ions in aluminum positions and vise versa, which, according to [29], is possible within the range of 1 to 1.5% in high-temperature crystals.

ACKNOWLEDGMENTS

The authors are grateful to I. Kvapil for providing the single crystals of mixed yttrium–lutecium orthoaluminates doped with cerium, to P.G. Baranov and M. Nikl for a detailed discussion of the results, and to M.P. Pimenova for help in the experiments.

REFERENCES

1. A. A. Kaminskiĭ, *Laser Crystals* (Nauka, Moscow, 1975).
2. A. A. Kaminskiĭ and B. M. Antipenko, *Multilevel Functional Schemes of Crystalline Lasers* (Nauka, Moscow, 1989).
3. G. Blasse, Chem. Mater. **6**, 1465 (1994).
4. M. Ishii and M. Kobayashi, Prog. Cryst. Growth Charact. Mater. **23**, 245 (1992).
5. J. A. Mares, M. Nikl, C. Pedrini, *et al.*, Mater. Chem. Phys. **32**, 342 (1992).
6. J. A. Mares and J. Kvapil, Ches. Chas. Fyz. A **38**, 248 (1988).
7. W. Rossner and B. C. Grabmaier, J. Lumin. **48**, 29 (1991).
8. J. A. Mares, M. Nikl, J. Chval, *et al.*, Chem. Phys. Lett. **241**, 311 (1995).
9. A. Abragam and B. Bleaney, *Electron Paramagnetic Resonance of Transition Ions* (Clarendon, Oxford, 1970; Mir, Moscow, 1972), Vol. 1.
10. S. A. Al'tshuler and B. M. Kozyrev, *Electron Paramagnetic Resonance in Compounds of Transition Elements* (Nauka, Moscow, 1972; Halsted, New York, 1975).
11. J. P. van der Ziel, F. R. Merrit, and L. G. van Uitert, J. Chem. Phys. **50**, 4317 (1969).
12. A. Pinto, N. Z. Sherman, and M. J. Weber, J. Magn. Reson. **6**, 422 (1972).
13. R. L. White, G. F. Herrmann, J. W. Carson, and M. Mandel, Phys. Rev. A **136**, 231 (1964).
14. O. F. Shirmer, K. W. Blazey, W. Berlinger, and R. Diehl, Phys. Rev. B **11**, 4201 (1975).
15. N. M. Nizamutdinov, N. M. Khasanova, G. R. Bulka, *et al.*, Kristallografiya **32**, 695 (1987) [Sov. Phys. Crystallogr. **32**, 408 (1987)].
16. N. M. Khasanova, N. M. Nizamutdinov, G. R. Bulka, V. M. Vinokurov, V. A. Akkerman, G. A. Ermakov, and A. A. Markelov, *Physics of Minerals and Their Synthetic Analogs* (Kazan. Gos. Univ., Kazan, 1988), p. 73.
17. M. Yamaga, H. Takeuchi, T. P. J. Han, and B. Henderson, J. Phys.: Condens. Matter **5**, 8097 (1993).
18. M. Yamaga, T. Yosida, B. Henderson, *et al.*, J. Phys.: Condens. Matter **4**, 7285 (1992).
19. H. R. Asatryan, J. Rosa, and J. A. Mares, Solid State Commun. **104**, 5 (1997).
20. G. R. Asatryan and J. Rosa, Fiz. Tverd. Tela (St. Petersburg) **44**, 830 (2002) [Phys. Solid State **44**, 864 (2002)].
21. S. Geller and V. Bala, Acta Crystallogr. **9**, 1019 (1956).
22. P. Coppens and M. Eibschutz, Acta Crystallogr. **19**, 524 (1965).
23. R. Diehl and G. Brandt, Mater. Res. Bull. **10**, 85 (1975).
24. A. A. Kaminskiĭ and V. V. Osiko, Izv. Akad. Nauk SSSR, Neorg. Mater. **3**, 417 (1967).
25. V. V. Osiko, Izv. Akad. Nauk SSSR, Neorg. Mater. **5**, 433 (1969).
26. A. A. Borovkov, *Course of the Theory of Probability* (Nauka, Moscow, 1972).
27. H. R. Asatryan, A. G. Petrosyan, E. G. Sharoyan, *et al.*, Phys. Status Solidi B **102**, 249 (1980).
28. H. R. Asatryan, Phys. Status Solidi B **150**, 253 (1988).
29. S. Geller, G. P. Espinoza, L. D. Fullmer, and P. B. Grandall, Mater. Res. Bull. **7**, 1219 (1972).

Translated by A. Zalesskiĭ

Physics of the Solid State, Vol. 45, No. 8, 2003, pp. 1465–1470. Translated from Fizika Tverdogo Tela, Vol. 45, No. 8, 2003, pp. 1396–1401.

DEFECTS, DISLOCATIONS, AND PHYSICS OF STRENGTH

Structural Defects in Molecular Crystals Based on Heterospin Copper Complexes

Yu. A. Osip'yan*, R. B. Morgunov*, A. A. Baskakov*, V. I. Ovcharenko, and S. V. Fokin****

** Institute of Solid State Physics, Russian Academy of Sciences, Chernogolovka, Moscow oblast, 142432 Russia*
e-mail: morgunov@ifft.as.ru

*** International Tomography Center, Siberian Division, Russian Academy of Sciences, Novosibirsk, 630090 Russia*

Received December 25, 2002

Abstract—Jumplike changes in the microhardness, sample dimensions, and parameters of the EPR spectrum were observed in molecular $Cu(hfac)_2L^{Et}$ crystals undergoing a phase transition. Defects that appear upon plastic deformation (e.g., dislocations) and paramagnetic defects were revealed. The latter defects are likely breaks in polymer chains and can serve as spin marks for investigating the magnetic state of the crystal lattice. © *2003 MAIK "Nauka/Interperiodica".*

1. INTRODUCTION

To successfully develop the methods of synthesizing and controlling the properties of new organic and molecular crystals, it is necessary to investigate the role of structural defects in the formation of their magnetic and electrical properties. Defects in molecular magnets have been revealed to date in only a few works; they were studied predominantly, by using only x-ray diffraction or by measuring the temperature dependence of the magnetic moment [1–6]. The absence of information on the effect of defects on physical properties hampers both adequate interpretation of the results of molecular and spin design and understanding of the crystal growth mechanisms. Moreover, it hinders the development of the concepts of their mechanical properties, which are necessary for practical applications.

The purpose of this work is to reveal structural defects and to establish their contribution to the magnetic and mechanical properties of novel polymer single crystals $Cu(hfac)_2L^{Et}$, where $Cu(hfac)_2$ is copper (II) hexafluoroacetylacetonate [hfac = CF_3–C(O)–CH–C(O)–CF_3], Et is ethyl C_2H_5, and L^{Et} is the stable nitronyl nitroxide radical based on 2-imidazolyne cycle with a pyrazole substituent in a side chain (Fig. 1a) [5]. The possibility of controlling the atomic structure of high-spin molecules and structural phase transitions in the crystals allows us to consider the series of compounds $Cu(hfac)_2L^R$ (where R = Me, Et, Pr, Bu) as one of the most promising candidates for actualizing molecular magnetism at high temperatures [6].

2. EXPERIMENTAL

Dark opaque $Cu(hfac)_2L^{Et}$ crystals ~5 mm in size were grown from a solution of $Cu(hfac)_2$ and L^{Et} in hexane upon cooling from +50°C to room temperature and subsequent evaporation for two days. We repeated this procedure 15–20 times by using single crystals from the previous solidification as single-crystalline seeds for the subsequent solidification. The Vickers hardness (H) was measured on the well-developed face in the *ab* plane (Fig. 1b) at a load of 0.1 N for a loading time of 10 s. For indentation at low temperatures, we designed an attachment to a microhardness tester to measure hardness in a controlled flow of cold nitrogen gas and to maintain the sample, indenter, and thermocouple at the same temperature (to check this, we carried out special experiments). An indication that the apparatus operated correctly was the fact that we could observe the microhardness jump detected in [7] during the sc–fcc phase transition in C_{60} fullerite single crystals (inset to Fig. 2b). Some regions of the crystals grown contained internal stresses, which appeared upon growing and thermal cycling; in some cases, the stresses caused microexplosions in the zone of contact between the indenter and the crystal. Therefore, to measure H, we used only indentations without microexplosions and cracks.

The magnetic properties of the crystals, powders, and their solutions were studied with an X-band EPR spectrometer at a modulation frequency of 100 kHz, modulation amplitude of 0.6–1.0 Oe, and power of ~1 mW. EPR signals recorded were proportional to the derivative $d\chi/dB$ of the real part of the magnetic susceptibility with respect to the magnetic field strength B.

3. EXPERIMENTAL RESULTS

The microhardness of the crystals at room temperature was measured to be about 150 MPa, which is typical of most molecular solids (Fig. 2b). As the tempera-

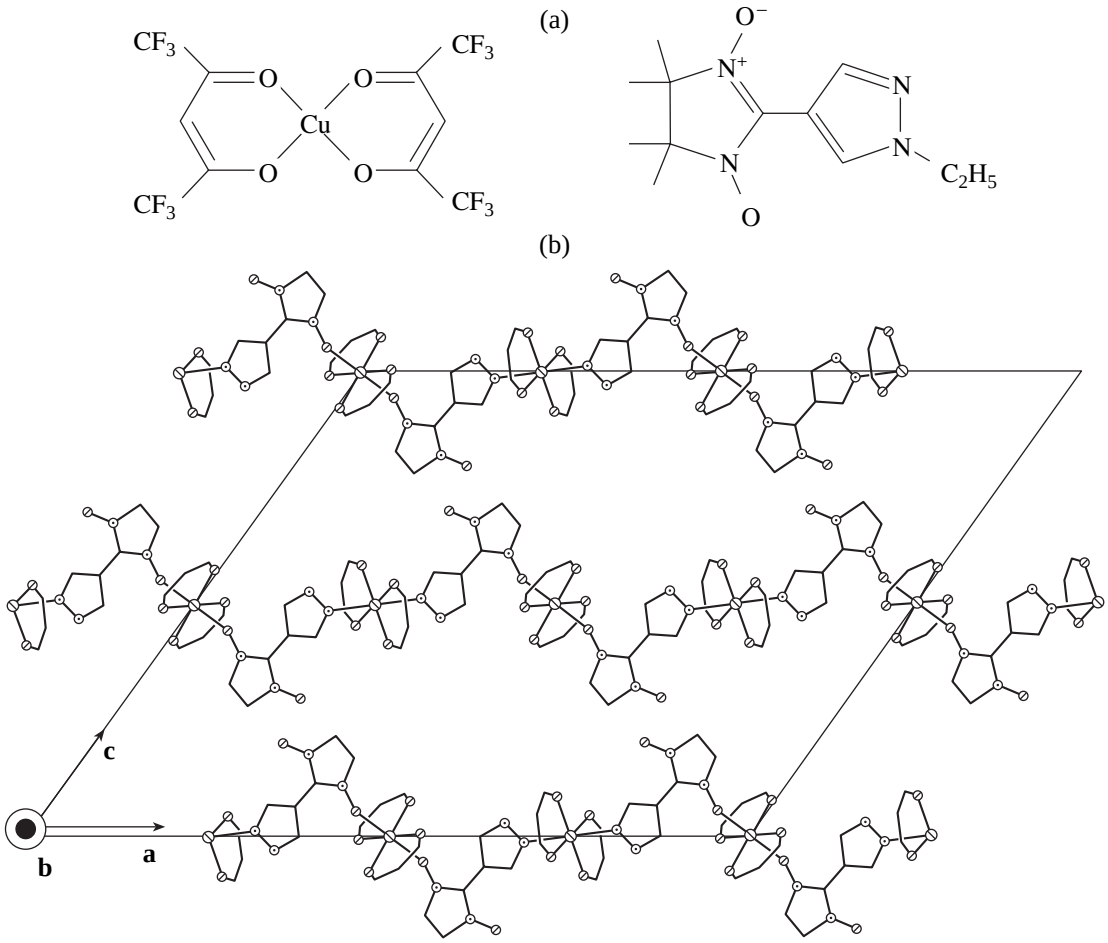

Fig. 1. (a) Structural formulas of copper hexafluoroacetylacetonate (on the left) and nitronyl nitroxide radical (on the right) and (b) the atomic structure of the molecule $Cu(hfac)_2L^{Et}$ and the relative positions of polymer chains with respect to the faces of a crystal (according to x-ray diffraction data from [5]).

ture decreases, the microhardness doubles near the phase transition at $T^* = 220$ K against the background of a slight, smooth increase in H (Fig. 2b). The temperature range of this sharp rise ($\Delta T \sim 20$ K) is comparable to the ΔT value obtained in [7] upon studying the effect of phase transitions on the mechanical properties of C_{60} fullerite and is somewhat wider than the width of this transition region determined from the change in the magnetic moment studied in [5] (Fig. 2a).

The development of plastic deformation during indentation is generally accompanied by the generation of defects. To reveal them, we designed a technique of chemical etching. The high solubility of the crystals allowed us to achieve selective etching only in a cold ($T = 273$ K) etching agent (pentane) under the conditions of its rapid evaporation from the surface of a crystal in an airflow. Figures 3a–3c present micrographs of the sample surface before and after etching. Etching of a crystal subjected to indenting induces the appearance of these defects near an indentation. It was found that one of the angles between the rays of an indentation rosette is ~70° (Fig. 3c) [6]. An increase in the etching duration or the dissolution of the ~50-μm-thick surface layer did not change the initial arrangement of etch pits in the vicinity of the indentation. Double etching also allows us to reveal regions with flat-bottomed and sharp pits (Fig. 3d). Macroplastic deformation of the crystals in an Instron testing machine at room temperature led to their cracking. The surfaces of chopped-off crystal fragments contain series of bands which are oriented at an angle of 70° to each other and resemble dislocation slip bands (Fig. 4).

X-ray diffraction examination that can be used to detect jumplike changes in the interatomic distances when passing $T^* = 220$ K has not been carried out. Therefore, to be sure that a structural phase transition exists, we studied the temperature dependence of the relative change in the crystal size $\Delta L(T)/L(293)$ along the a direction (i.e., along polymer chains). A sample was fixed under the of objective a microscope, and the decrease in L during cooling was measured over the temperature range 180–293 K. In a narrow range near

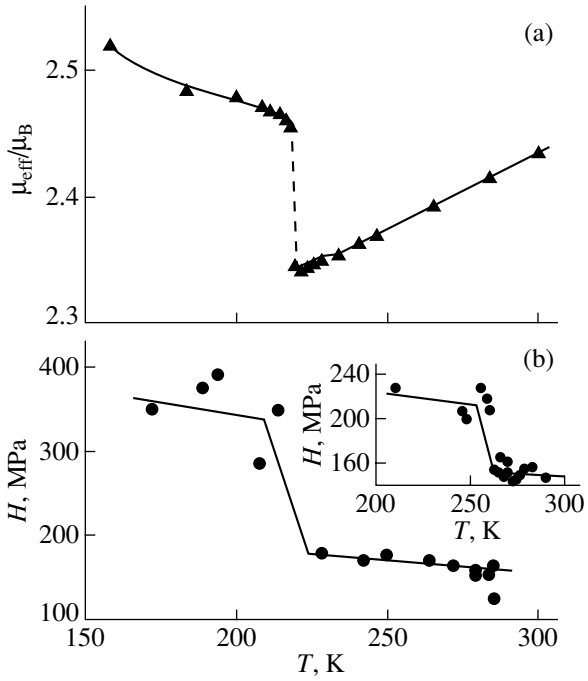

Fig. 2. Temperature dependences (a) of the magnetic moment μ_{eff} of a sample (in units of the Bohr magneton μ_B) [5] and (b) of the microhardness of the $Cu(hfac)_2L^{Et}$ single crystals. For comparison, the inset shows the $H(T)$ dependence for C_{60} crystals [7].

T^* = 220 K, nonmonotonic changes in the crystal size were observed (Fig. 5). Below the temperature of the phase transition, the temperature dependences of the lattice parameter a and of the crystal length L differ from each other (Fig. 5). We detected no hysteresis of the crystal size during thermal cycling. Long-term (~5 min) holding of the crystal at T^* is accompanied by considerable self-excited oscillations of the sample surface with an amplitude of $\Delta L/L \sim 0.1\%$. Thus, at 220 K, a first-order structural phase transition occurs that is accompanied by jumplike changes in the magnetic moment, microhardness, and crystal size.

We also recorded EPR spectra of the new compound in solution and in the solid state. When crystals were dissolved in a weakly polar toluene (concentration ~10^{-5}%), the observed EPR spectrum consisted of five lines corresponding to the g factor $g_L = 2.00$. Freezing of the solution results in the broadening and confluence of these lines (Fig. 6, curves *1*, *2*). The EPR spectrum of the single crystal (curves *3*–*7*) consists of a broad singlet of Lorentzian shape. Against the background of this signal, a weaker spectrum is observed at $g = 2.00$; this spectrum coincides in position and shape with that of the nitronyl nitroxide radical in the frozen solution (Fig. 6). A decrease in the temperature down to T = 220 K leads to strong restructuring of the EPR spectrum of defects: the lines become split, their shape is distorted, and their total area increases by a factor of

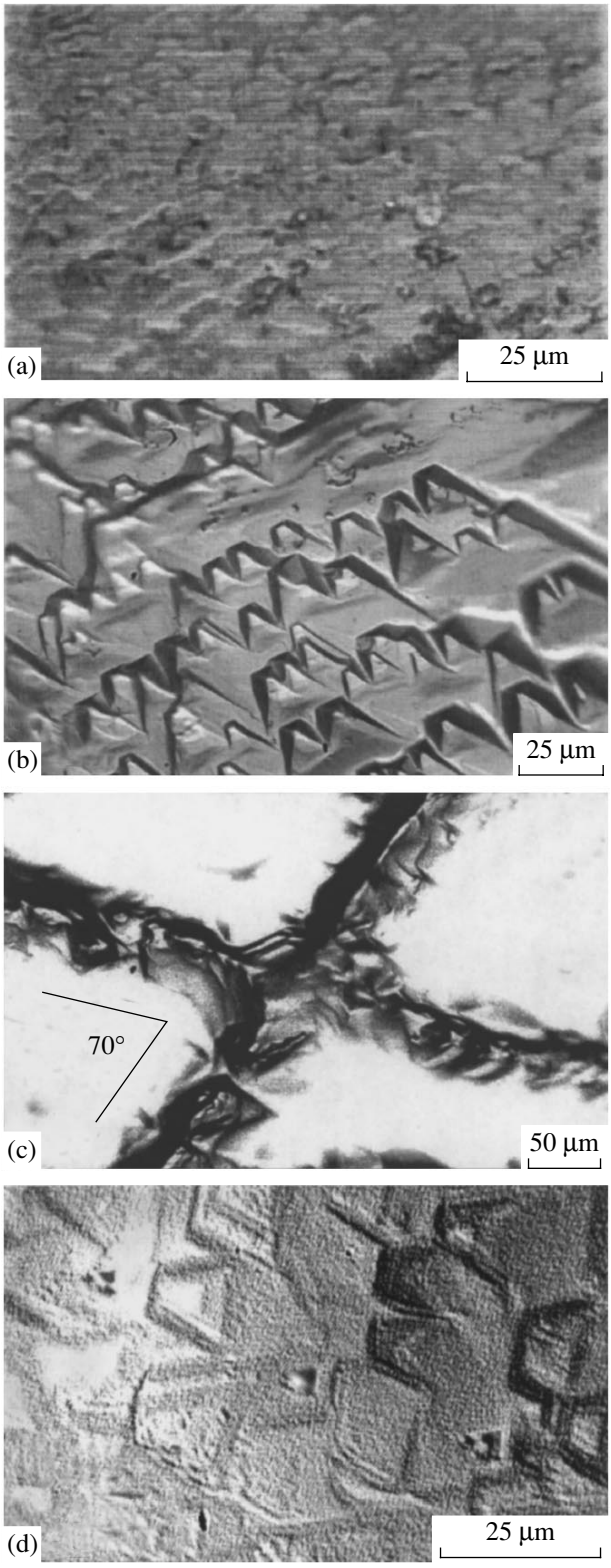

Fig. 3. The surface of an undeformed sample (a) before and (b) after chemical etching and the surfaces (c) of a sample after indentation (the indentation is at the center) and chemical etching and (d) of a sample subjected to double etching after deformation.

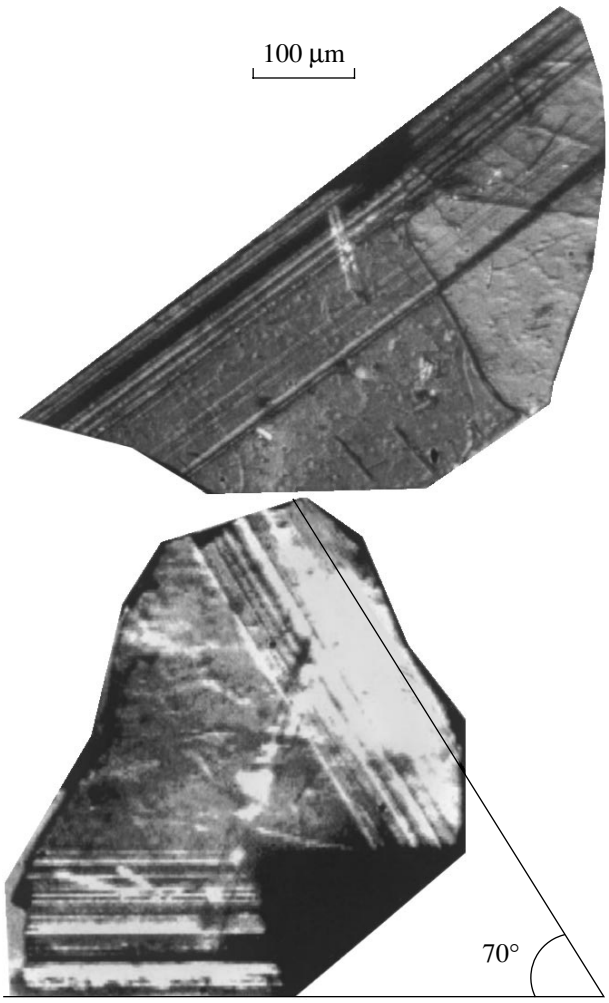

Fig. 4. Fragments of the $Cu(hfac)_2L^{Et}$ crystal deformed to failure.

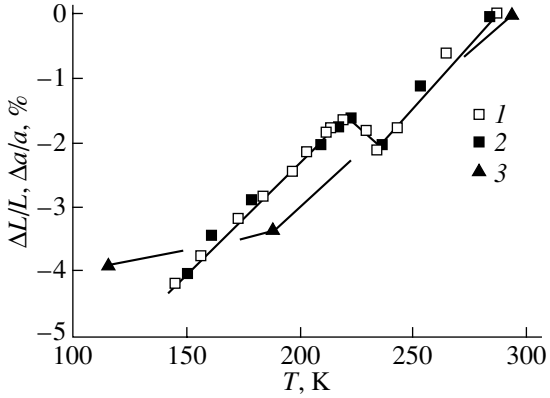

Fig. 5. Temperature dependence of the relative variation of the sample length $\Delta L/L(293)$ upon (*1*) cooling and (*2*) heating. (*3*) The temperature dependence of the relative variation of the lattice parameter $\Delta a/a$ (according to x-ray diffraction data from [5]).

10–50 (Fig. 6). Plastic deformation of the crystals by 1–3%, which increases the number of dislocations by two or three orders of magnitude, and milling of the samples into powders with a mean particle size of 1–10 μm, which increases the surface area by two or three orders of magnitude, do not change the portion of the spectrum at $g = 2.00$ corresponding to the paramagnetic defects found.

4. DISCUSSION OF THE RESULTS

Prior to discussing the causes of the changes in the microhardness during the phase transition (Fig. 2b), we will briefly dwell on the possible mechanisms of plastic deformation in the $Cu(hfac)_2L^{Et}$ crystals and the properties of the defects generated upon mechanical loading. The regular equal facets of the etch pits appearing after indentation (Fig. 3) indicate that they correspond to structural defects with certain crystallographic orientations. Since the pit arrangement in the vicinity of an indentation remains the same after a 50-μm-thick surface layer has been etched, selective etching can be used to reveal linear defects generated by plastic deformation. The fact that flat-bottomed and sharp pits are observed after double etching (Fig. 3d) indicates that the linear defects move in the field of internal mechanical stresses. These defects are most likely dislocations. In this case, the etch pits disclosed without loading (Fig. 3a) can correspond to growth dislocations. Note that growth dislocations have been observed earlier only in thin films from among the whole set of compounds based on the nitronyl nitroxide radical and metal complexes [8].

According to x-ray diffraction data [5, 6], polymer chains are bound by the van der Waals interaction and are placed in layers parallel to the *ab* plane (Fig. 1b). In these alternating layers, polymer chains make an angle of 70° with the chains of the next layer. Hence, the angles of ~70° between the rays of the indentation rosette (Fig. 3) and between the slip bands on the crystal surface (Fig. 4) can be accounted for by the preferred directions of the arrangement of polymer molecules in the adjacent layers.

The structural defects found can move during plastic deformation (Fig. 3d), thereby contributing to the microhardness. Therefore, we can assume that the jump in *H* during the phase transition (Fig. 2b) is similar to the *H* jump in fullerenes [7], where it is explained by a change in the dislocation mobility depending on the character of energy dissipation near dislocation cores [9]. In the crystals under study, the freezing of the rotation of the side groups *F*, which was detected in [5] from changes in the infrared transmission spectra caused by the phase transition, can decrease the dislocation mobility and induce an increase in *H* as the temperature is reduced below 220 K. Another cause of the sharp change in *H* can be a change in the strength and

length of intermolecular bonds. For example, according to the x-ray diffraction data, one of the O–Cu–O axes in the CuO_4N_2 bipyramid is strongly elongated along the direction of the applied load (Fig. 1a).

As for the magnetic properties of the crystals, we note that the temperature dependence of the effective magnetic moment μ_{eff} measured in [5, 6] showed the absence of long-range order at 4–300 K and a jumpwise change in μ_{eff} at $T = 220$ K (Fig. 2a) [5]. Ovcharenko *et al.* [5] assumed that the cause of the sharp μ_{eff} jump could be a change in the environment of the Cu^{2+} ions inside the coordination polyhedra CuO_4N_2 and CuO_6 (i.e., a change in the lengths of the $Cu–O_L$ and Cu–N axial bonds in the CuO_6 and CuO_4N_2 polyhedra, respectively) during the structural phase transition. To establish the role of the defects in the formation of the magnetic properties of the crystals during the phase transition, we will discuss the EPR spectra recorded in this work.

The broad line in the EPR spectrum of the single crystal corresponds to a g factor equal to 2.08, which agrees well with the value of $g = (g_{Cu} + g_L)/2$ of the copper–nitroxyl system with exchange coupling, where $g_{Cu} = 2.16$ is the g factor of Cu^{2+} in hexafluoroacetylacetonate [10]. The calculation of the number of spins forming this EPR signal showed that almost all spins of the crystal lattice contribute to this broad singlet. An estimation of the number of spins forming the additional signal at $g = 2.00$ gives 10^{-3} of their total number in the crystal at $T = 293$ K. Hence, the corresponding EPR spectrum characterizes paramagnetic defects. Note that the spectrum of these defects virtually coincides with the EPR spectrum of the frozen solution of $Cu(hfac)_2L^{Et}$ in toluene (Fig. 6, spectrum *2*). The EPR spectrum of $Cu(hfac)_2L^{Et}$ in liquid toluene consists of several lines, which appear to correspond to transitions between the levels of the radical L^{Et} (spin 1/2) split by the hyperfine interaction with the N^7 nuclei (nuclear spin 1) (Fig. 6, spectrum *1*). The broadening and confluence of these lines upon freezing the toluene are likely due to a decrease in the radical rotational mobility (Fig. 6). We assume that the same effect can also be caused by the low rotational mobility of the L^{Et} radicals in the single crystals and that the paramagnetic defects forming the spectrum at $g = 2.00$ contain L^{Et}.

What is the nature of these paramagnetic centers? Since the EPR spectra at $g = 2.00$ remain unchanged after plastic deformation of the crystals, we assume that the nucleation and motion of the defects that appear during the plastic deformation are not accompanied by breaks in the polymer chains and are reduced to displacements of molecules with respect to one another. This mechanism of defect formation requires a significantly lower energy in comparison with the case of breaking the intermolecular chemical bonds. Thus, the defects that nucleate during deformation do not contribute to the EPR signal at $g = 2.00$.

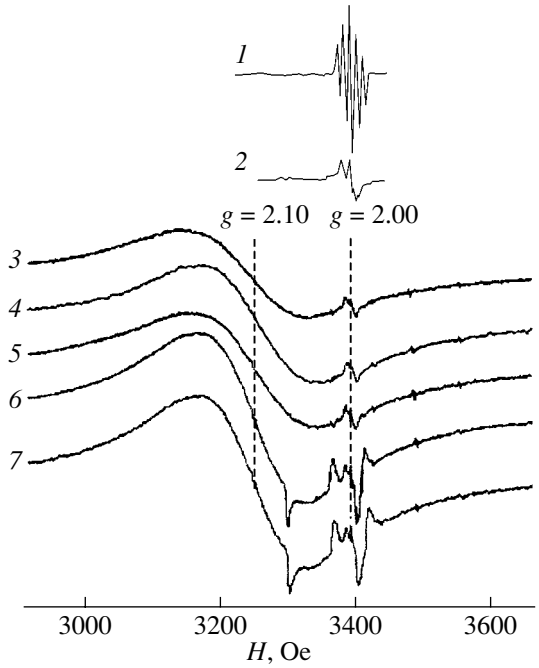

Fig. 6. EPR spectra of $Cu(hfac)_2L^{Et}$ (*1*) dissolved in toluene and (*2*) in the frozen toluene solution and (*3–7*) EPR spectra of the $Cu(hfac)_2L^{Et}$ single crystal with its *ab* plane normal to the static magnetic field at a temperature of (*3*) 293, (*4*) 285, (*5*) 228, (*6*) 209, and (*7*) 182 K.

We could also assume that the paramagnetic centers found are L^{Et} radicals, for example, "squeezed" between molecules making up the lattice. In this case, however, the number of spins should be independent of temperature. Actually, at $T \sim 220$ K, the number of spins of the paramagnetic defects with $g = 2.00$ strongly increases; this increase is equivalent to a 3–5% increase in the effective magnetic moment (i.e., it is comparable to the jump in μ_{eff} detected in [5, 6]) (Fig. 6). Therefore, these defects are most likely breaks in polymer chains caused by changes in the molecule sizes and by thermal expansion of the crystals. In this case, the length of a polymer chain should consist of $\sim 10^3$ fragments at $T > 220$ K and $\sim 10^2$ fragments at $T < 220$ K. This assumption is also supported by the fact that the "weakest chain link" is the bond with the L^{Et} radical; therefore, it is the L^{Et} radical that will additionally contribute to the EPR spectrum during mechanical tension of the chain to its break.

The recovery of the EPR spectrum upon heating the crystal above the temperature of the phase transition (i.e., the disappearance of the paramagnetic defects that appeared upon cooling) may imply that an increase in the mobility of radicals allows them to recover the initial chemical bonds with a broken polymer molecule. The similar reversible nucleation is also inherent in those defects that cause a difference in the temperature dependences of the relative variations in the lattice

parameter $\Delta a/a$ and the crystal length $\Delta L/L$ below the phase transition temperature (Fig. 5). Since no hysteresis of the crystal length is observed during a cooling–heating cycle (Fig. 5), a certain equilibrium concentration of these defects can be assumed to exist at temperatures below $T = 220$ K.

5. CONCLUSIONS

Thus, molecular heterospin $Cu(hfac)_2L^{Et}$ crystals have been established to undergo a structural phase transition at 220 K, which is accompanied by a jumplike change in the microhardness, sample dimensions, and parameters of the EPR spectrum.

Two types of structural defects have been revealed: linear defects nucleating during plastic deformation (dislocations, microtwins, etc.) and paramagnetic centers containing the nitronyl nitroxide radical L^{Et}. Plastic deformation of the crystals was found to be accompanied by the nucleation and motion of linear defects, which do not change the shape of the EPR spectrum. Note that, although mobile dislocations in polymers have not yet been detected experimentally, the possibility of their appearance is supported by the results of molecular-dynamics simulations [11, 12].

The paramagnetic defects, which are likely breaks in polymer chains, significantly contribute to the change in the effective magnetic moment during the phase transition. These defects should be taken into account in order to adequately interpret the magnetic properties of the defect-free part of a crystal. The paramagnetic centers detected can serve as spin marks for investigating the magnetic state of the crystal lattice, since their EPR spectrum is highly sensitive to changes in the structure and interatomic distances.

ACKNOWLEDGMENTS

This work was supported by the Russian Foundation for Basic Research, project nos. 02-15-99302, 00-15-96703, and 00-03-32987.

REFERENCES

1. A. L. Buchachenko, Usp. Khim. **59**, 529 (1990).
2. V. I. Ovcharenko and R. Z. Sagdeev, Usp. Khim. **68**, 381 (1999).
3. *Molecular Magnetism*, Ed. by Koichi Itoh and Minoru Kinoshita (Gordon and Breach, Tokyo, 2000).
4. V. I. Ovcharenko, S. V. Fokin, G. V. Romanenko, *et al.*, Mol. Phys. **100**, 1300 (2002).
5. V. I. Ovcharenko, S. V. Fokin, G. V. Romanenko, *et al.*, Zh. Strukt. Khim. **43**, 163 (2002).
6. A. L. Buchachenko, in *Proceedings of I All-Russian Conference on High-Spin Molecules and Molecular Ferromagnetics* (2002), p. 1.
7. M. Tachibana, M. Michyama, and K. Kojima, Phys. Rev. B **49**, 14945 (1994).
8. J. Fraxedas, J. Caro, A. Figueras, *et al.*, Surf. Sci. **415**, 241 (1998).
9. V. D. Natsik, S. V. Lubenets, and L. S. Fomenko, Fiz. Nizk. Temp. **22**, 337 (1996) [Low Temp. Phys. **22**, 264 (1996)].
10. A. A. Shklyaev and V. F. Anufrienko, Zh. Strukt. Khim. **16**, 1082 (1975).
11. G. L. Liang, D. W. Noid, B. G. Sumpter, and B. Wunderlich, J. Phys. Chem. **98**, 11739 (1994).
12. B. Wunderlich and S. N. Kreitmeier, MRS Bull. **20**, 17 (1995).

Translated by K. Shakhlevich

Physics of the Solid State, Vol. 45, No. 8, 2003, pp. 1471–1474. Translated from Fizika Tverdogo Tela, Vol. 45, No. 8, 2003, pp. 1402–1405.

DEFECTS, DISLOCATIONS, AND PHYSICS OF STRENGTH

Study of the Motion of Individual Triple Junctions in Aluminum

S. G. Protasova, V. G. Sursaeva, and L. S. Shvindlerman

Institute of Solid State Physics, Russian Academy of Sciences, Chernogolovka, Moscow oblast, 142432 Russia

e-mail: sveta@issp.su.ac.ru

Received July 25, 2002; in final form, December 29, 2002

Abstract—The mobility of individual triple junctions in aluminum is studied. Triple junctions with ⟨111⟩, ⟨100⟩, and ⟨110⟩ tilt boundaries are studied. The data obtained show that, at low temperatures, the mobility of the system of grain boundaries with a triple junction is controlled by the mobility of the triple junction (the junction kinetics). At high temperatures, the system mobility is determined by the mobility of the grain boundaries (the boundary kinetics). There is a temperature at which the transition from the junction kinetics to the boundary kinetics occurs; this temperature is determined by the crystallographic parameters of the sample. *© 2003 MAIK "Nauka/Interperiodica".*

1. INTRODUCTION

Although triple junctions, along with grain boundaries, are main defects in polycrystals, they have attracted considerable interest only recently. The available data indicate that triple junctions and the grain boundaries they are made up of differ from each other. For example, it was shown in [1] that the diffusion coefficient of Zn along a triple junction in Al exceeds that along the grain boundaries it is made up of by three orders of magnitude. Triple junctions are the predominant sites of corrosion in Ni [2]. The presence of triple junctions specifies the mechanical properties of a material. For example, Rabukhin [3] found experimentally that the mechanical strength of thin filaments without triple junctions (the so-called "bamboo" structure) was twice as high as that of filaments with triple junctions. It was also shown in [4] that in the former case the plasticity is lower (by a factor of three to ten, depending on the grain size) and the internal friction is smaller almost by a factor of three.

The effect of triple junctions on grain-boundary migration was first considered theoretically in [5]. The velocity of the system of grain boundaries with a triple junction (Fig. 1) is determined by

$$V = \frac{2\theta m_{GB}\sigma}{a}, \quad (1)$$

where θ is the apex angle in the triple junction, m_{GB} is the grain-boundary mobility, σ is the surface tension of a grain boundary, and a is the grain width. On the other hand, the velocity of the triple junction experiencing the driving force $\sigma_{GB}(2\cos\theta - 1)$ is

$$V = m_{TJ}\sigma_{GB}(2\cos\theta - 1), \quad (2)$$

where m_{TJ} is the triple-junction mobility. Therefore, the equilibrium value of the angle θ for the case of steady-state motion of the system can be found from the condition

$$\frac{2\theta}{2\cos\theta - 1} = \frac{m_{TJ}a}{m_{GB}} = \Lambda. \quad (3)$$

Galina *et al.* [5] showed that, for a system of grain boundaries with a triple junction as presented in Fig. 1, two kinetic motion modes exist; in one of them, the system mobility is dictated by the triple-junction mobility, and in the other, it is dictated by the mobility of the grain boundaries. The value of the dimensionless parameter Λ is the criterion for the transition from one kinetics to the other. At $\Lambda \ll 1$, the angle $\theta \longrightarrow 0$ and the velocity of the system is controlled by the triple-junction mobility in accordance with Eq. (1) (the junc-

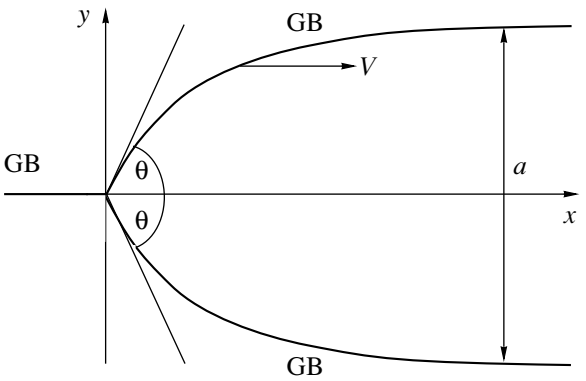

Fig. 1. Configuration of grain boundaries in a triple junction during steady-state motion.

1063-7834/03/4508-1471$24.00

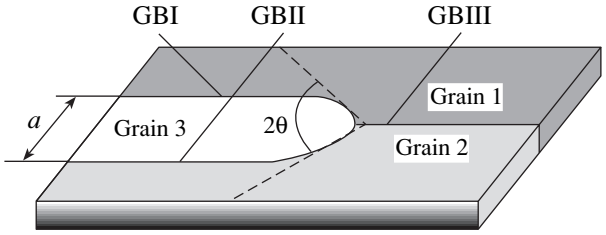

Fig. 2. Sample with a triple junction (schematic).

tion kinetics mode). At $\Lambda \gg 1$, the angle θ tends to its equilibrium value θ_{eq}. In this case, the velocity of the system of grain boundaries with a triple junction does not depend on the triple-junction mobility and is only determined by the boundary properties [Eq. (2), the boundary kinetics mode].

Czubayko *et al.* [6] were the first to experimentally confirm this prediction by studying the mobility of individual triple junctions in Zn. In this work, we study the migration of triple junctions in aluminum.

2. EXPERIMENTAL

For investigation, we used high-purity (99.999%) Al grown by directional solidification in an argon atmosphere. The schematic of a sample is shown in Fig. 2. The grain boundaries are normal to the sample surface and are tilt boundaries. We studied the motion of triple junctions in three crystallographic planes: (100), (110), and (111). The grain-boundary angle was determined using the Laue method. The crystallographic parameters of samples are given in the table.

To study the migration characteristics of individual triple junctions, we performed sequential high-temperature annealings of samples and determined the displacements of the triple junctions as a function of time using an x-ray device for continuous tracking of moving interfaces in crystalline solids [7].

The angle θ was determined by optical microscopy using thermal and chemical etch grooves (Fig. 3).

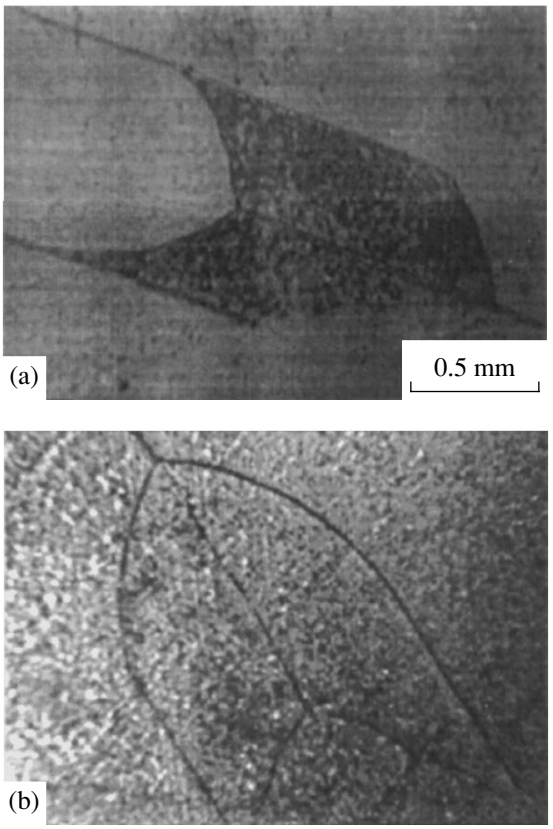

Fig. 3. Shape of a triple junction revealed by (a) chemical and (b) thermal etching.

To measure the migration velocity, a groove on a sample was removed by polishing prior to subsequent annealing.

To calculate Λ for a system of grain boundaries moving in a sample, we determined the ratio σ_3/σ (σ is the surface tension of boundaries GBI and GBII and σ_3 is that of boundary GBIII) assuming that θ reached its equilibrium value at temperatures close to the melting point. The value of θ near the melting temperature was

Crystallographic, kinetic, and thermodynamic parameters of triple junctions

Sample no.	1	2	3	4	5	6	7	8	9
GBI	21° ⟨111⟩	20° ⟨111⟩	20° ⟨111⟩	22° ⟨100⟩	12° ⟨100⟩	37° ⟨100⟩	12° ⟨100⟩	27° ⟨110⟩	44° ⟨110⟩
GBII	18° ⟨111⟩	25° ⟨111⟩	10° ⟨111⟩	28° ⟨100⟩	25° ⟨100⟩	25° ⟨100⟩	37° ⟨100⟩	22° ⟨110⟩	29° ⟨110⟩
GBIII	3° ⟨111⟩	5° ⟨111⟩	30° ⟨111⟩	6° ⟨100⟩	37° ⟨100⟩	12° ⟨100⟩	25° ⟨100⟩	5° ⟨110⟩	15° ⟨110⟩
ΔT, °C	398–479	380–420	470–510	460–495	590–610	500–550	520–570	469–591	530–591
H_{GB}, eV	1.0		0.4		1.3		0.9	1.4	1.3
A_{0GB}, m^2/s	0.03		3.9×10^{-6}		0.5		4.7×10^{-4}	2.3	0.4
H_{TJ}, eV	1.8	2.0		3.3		3.6	4.4	2.7	
A_{0TJ}, m^2/s	4.5×10^4	1.8×10^6		1.8×10^{13}		9.8×10^{14}	1.8×10^{19}	1.3×10^9	

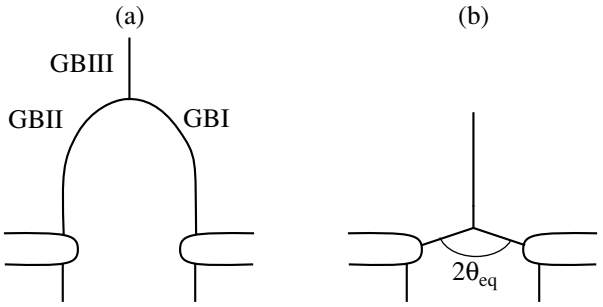

Fig. 4. Scheme of the experiment for determining θ_{eq}: (a) the system of grain boundaries with a triple junction (the lateral boundaries are notched) and (b) the same system after annealing.

obtained from the following experiment. Samples with triple junctions were annealed at $T = 655$°C (close to the melting temperature) for 5 min. To avoid complete disappearance of the grain between boundaries GBI and GBII, we made a notch (groove) as shown in Fig. 4. After annealing, the sample was rapidly cooled and the boundary position and the angle $2\theta \approx 2\theta_{eq}$ were determined with a microscope [8]. The value of σ_3/σ can also be calculated from the reported data [9].

The mobility of the system of grain boundaries with a triple junction was calculated, using the experimentally found velocity from the formulas [10]

$$A_{GB} \equiv \frac{Va}{2\theta} = m_{GB}\sigma_{GB} = A_{0GB}\exp\left(-\frac{H_{GB}}{kT}\right), \quad (4)$$

$$A_{TJ} \equiv \frac{Va}{2\cos\theta - \sigma_3/\sigma} = m_{TJ}\sigma_{GB}a = A_{0TJ}\exp\left(-\frac{H_{TJ}}{kT}\right), \quad (5)$$

where A_{GB} and A_{TJ} are the mobilities of the grain boundaries and triple junctions, respectively, and H_{GB} and H_{TJ} are their respective activation energies.

3. RESULTS AND DISCUSSION

Figure 5 shows the temperature dependences of the dimensionless parameter Λ for samples 1, 7, and 8. According to the approach proposed in [5], two motion modes of the system of grain boundaries with a triple junction can be distinguished in the temperature dependence of the parameter Λ. At low temperatures (up to 430°C for sample 1, 530°C for sample 7, and 510°C for sample 8), the parameter Λ is rather small and remains virtually unchanged. The system mobility is controlled by the triple-junction mobility (the junction kinetics). Then, the parameter Λ increases and the triple junction exerts a weaker effect on the system mobility. In this temperature range, the system mobility is specified by the grain-boundary mobility (the boundary kinetics).

For the temperature ranges differing in the Λ behavior, we calculated the mobility of the system of grain boundaries with a triple junction (Fig. 6). The lines with solid symbols show the mobilities of triple junctions demonstrating both motion modes, with the junction and boundary kinetics. As is seen from the curves, the three crystallographic systems exhibit common features; namely, at low temperatures (the junction kinetics), the motion of the system of grain boundaries with a triple junction is characterized by a high activation energy, whereas at high temperatures (the boundary kinetics), this system moves with a low activation

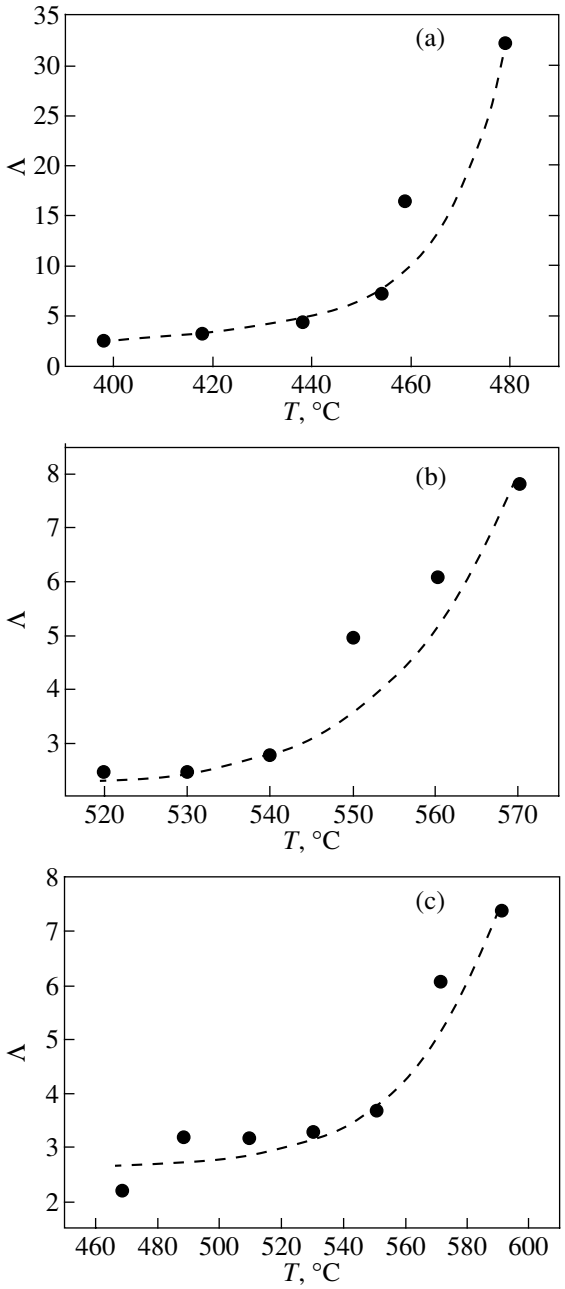

Fig. 5. Temperature dependences of the dimensionless parameter Λ for a triple junction: (a–c) samples 1, 7, and 8, respectively (see table).

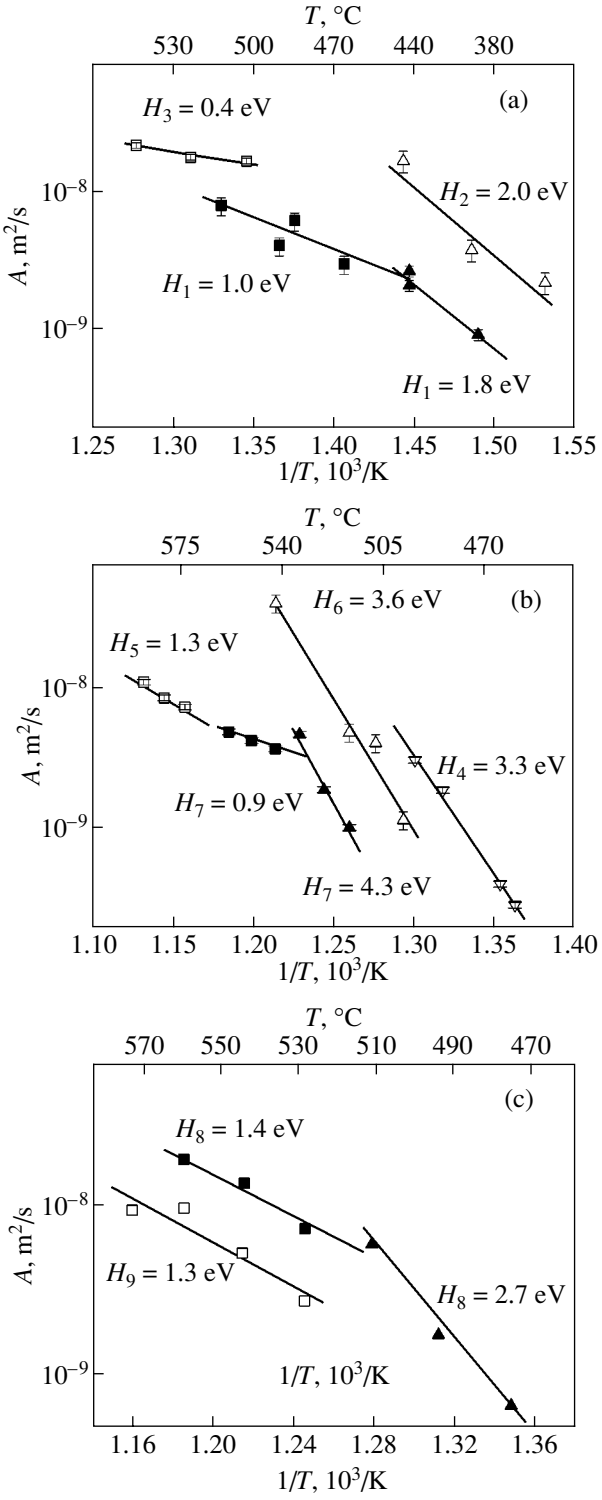

Fig. 6. Temperature dependences of the triple-junction mobility in the planes (a) (111), (b) (100), and (c) (110). H_1–H_9 are the activation energies in samples 1–9, respectively (see table). For samples 1, 7, and 8, two activation energies, corresponding to the low- and high-temperature ranges of the $H(T)$ dependences, are given.

energy. Additionally, Fig. 6 shows the mobilities of triple junctions with other values of the misorientation parameters of the neighboring grains; their motion was studied in narrow temperature ranges (lines with open symbols). However, it is seen that such systems demonstrate similar behavior in the high- and low-temperature ranges: motion with a high activation energy in the low-temperature ranges and a low activation energy in the high-temperature range. The calculated values of the grain-boundary (A_{0GB}) and triple-junction (A_{0TJ}) mobilities, as well as the corresponding activation energies (H_{0GB} and H_{0TJ}, respectively), are given in the table (ΔT is the temperature range of sample annealing).

4. CONCLUSIONS

The results obtained show that there are two modes of motion for the system of grain boundaries with a triple junction in aluminum: at low temperatures, the junction decreases the system mobility (the junction kinetics), whereas at high temperatures, the system mobility is controlled by the grain-boundary mobility (the boundary kinetics). There is a temperature at which the transition from the junction to boundary kinetics occurs; this temperature is determined by the crystallographic parameters of the sample.

REFERENCES

1. A. Peterline, S. Peterline, and O. Oreshina, Defect Diffus. Forum **194–199**, 1265 (2001).
2. G. Palumbo and K. T. Aust, Scr. Metall. Mater. **24**, 1771 (1990).
3. V. B. Rabukhin, Poverkhnost, No. 10, 5 (1983).
4. V. B. Rabukhin, Fiz. Met. Metalloved. **55** (1), 178 (1983).
5. A. V. Galina, V. E. Fradkov, and L. S. Shvindlerman, Fiz. Met. Metalloved. **63** (6), 1220 (1987).
6. U. Czubayko, V. G. Sursaeva, G. Gottstein, and L. S. Shvindlerman, Acta Mater. **46**, 5863 (1998).
7. U. Gubayko, D. Molodov, B.-C. Petersen, *et al.*, Meas. Sci. Technol. **6**, 947 (1995).
8. S. G. Protasova, G. Gottstein, D. A. Molodov, *et al.*, Acta Mater. **49**, 2519 (2001).
9. G. Hasson and C. Guox, Scr. Metall. **5**, 889 (1971).
10. G. Gottstein and L. S. Shvindlerman, *Grain Boundary Migration in Metals: Thermodynamics, Kinetics, Applications* (CRC, Boca Raton, 1999).

Translated by K. Shakhlevich

Physics of the Solid State, Vol. 45, No. 8, 2003, pp. 1475–1478. Translated from Fizika Tverdogo Tela, Vol. 45, No. 8, 2003, pp. 1406–1408.

MAGNETISM AND FERROELECTRICITY

Absorption of Light by Exchange-Coupled Ions in a 2D Antiferromagnet

E. A. Popov* and B. V. Beznosikov**

** Siberian State Aerospace University, Krasnoyarsk, 660014 Russia*

*** Kirensky Institute of Physics, Siberian Division, Russian Academy of Sciences, Akademgorodok, Krasnoyarsk, 660036 Russia*

e-mail: ise@iph.krasn.ru

Received October 28, 2002

Abstract—The optical absorption spectra of $Rb_2Mn_xCd_{1-x}Cl_4$ crystals are experimentally studied in the vicinity of a magnon sideband of the exciton band at a manganese content x ranging from 1.0 to 0.4. Additional absorption bands are observed with an increase in the magnetic structural disorder upon replacement of manganese ions by cadmium ions. An analysis of the evolution of the additional absorption bands in a magnetic field during the spin-flop phase transition and the change in the intensity with variations in the manganese content x demonstrates that these bands are associated with the excitation of the exchange-coupled pairs of manganese ions located in different environments in a plane square lattice. The phase boundary between the antiferromagnetic and spin-flop phases is constructed using the results of optical measurements. The manganese content corresponding to the magnetic percolation point is evaluated. *© 2003 MAIK "Nauka/Interperiodica".*

1. INTRODUCTION

As is known, a fine structure observed in the optical absorption spectra of antiferromagnets containing 3*d* ions is caused by interactions of different natures in the crystals. In addition to the bands attributed to the single-ion electron optical transitions, the spectra of magnetic crystals at optical frequencies exhibit bands associated with excitations of different origins (magnons, phonons, etc.). Since the main features of spectral bands of different natures are well known [1, 2], it is possible to identify the absorption bands and then to use available data on the optical spectra in analyzing the specific features of the excitation energy spectra and the magnetic structure of the crystal. Disordering of the crystal, for example, due to an appreciable impurity concentration, violates translational symmetry. In this case, the quasiparticle approach underlying the description of the optical spectra does not hold. If the order in a crystal is disturbed, one can expect qualitative changes in the absorption optical spectra. For example, the introduction of a magnetic impurity into a antiferromagnet can give rise to additional bands in the spectrum due to the occurrence of either the localized states or the resonance states [2, 3]. We succeeded in observing new bands in the spectrum of a two-dimensional (2D) antiferromagnet upon replacement of magnetic ions by nonmagnetic ions in an Rb_2MnCl_4 crystal diluted with Cd^{2+} ions.

Crystals of Rb_2MnCl_4 at room temperature have a tetragonal structure with D_{4h}^{17} symmetry. At the Néel temperature $T_N = 57$ K, the Rb_2MnCl_4 crystal is characterized by an antiferromagnetic order with easy-axis anisotropy parallel to the C_4 symmetry axis of the crystal [4]. The spin-flop transition occurs in the field $H_{SF} = 56$ kOe. The Mn^{2+} ions are located in layers perpendicular to the C_4 symmetry axis at sites of a plane square lattice of the crystal. The interlayer distance considerably exceeds the distance between the Mn^{2+} nearest neighbor ions located in the same layer. As a result, the intralayer exchange interaction between the manganese ions is two orders of magnitude stronger than their interlayer exchange interaction, which is responsible for the two-dimensional behavior of the magnetic system of the crystal.

2. SAMPLES AND EXPERIMENTAL TECHNIQUE

Crystals for study were grown using the Bridgman method in a vertical tube furnace. The optical absorption spectra were measured on a spectrometer with a resolution of 3 Å/mm at a temperature of 4.3 K. Magnetic fields with a strength up to 250 kOe were generated in a pulsed solenoid with a pulse duration of 20 ms. The spectra were recorded on photographic film.

3. RESULTS AND DISCUSSION

Figure 1 shows the absorption spectra of $Rb_2Mn_xCd_{1-x}Cl_4$ for the α polarization at frequencies close to ~26500 cm^{-1} and different manganese contents x. The absorption observed in this range is due to the transition $^6A_{1g}(^6S) \longrightarrow {}^4T_{2g}(^4D)$ inside the 3*d* shell of

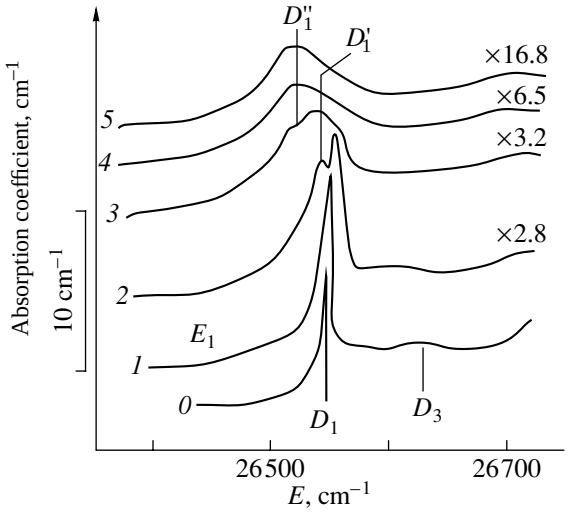

Fig. 1. Absorption spectra of $Rb_2Mn_xCd_{1-x}Cl_4$ crystals in the vicinity of the exciton–magnon absorption band D_1 for the α polarization with the wave vector $\mathbf{k} \parallel C_4$, the electric-field vector $\mathbf{E} \perp C_4$, T = 4.3 K, and different magnesium contents x: (*0*) 1.0 (calculated shape of the exciton–magnon band), (*1*) 1.0, (*2*) 0.9, (*3*) 0.8, (*4*) 0.7, and (*5*) 0.4.

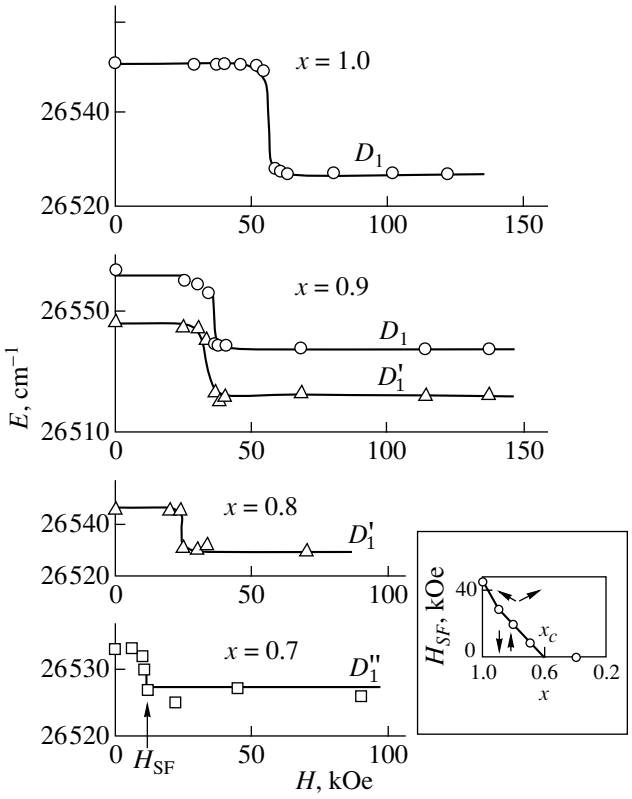

Fig. 2. Dependences of the energies of the bands D_1, D_1', and D_1'' on the magnetic field $\mathbf{H} \parallel C_4$ at different magnesium contents x. T = 4.3 K. The inset shows a fragment of the phase diagram plotted in the x–**H** coordinates at T = 4.3 K according to the results of spectral measurements.

Mn^{2+} ions. This figure represents a group of bands attributed to this transition in the long-wavelength range. It can be seen that the absorption spectra of the crystal at x = 1.0 contain a narrow electrodipole band D_1. The polarization of the D_1 band corresponds to selection rules for a single-magnon sideband of the exciton band. The intralayer exchange interaction between Mn^{2+} ions was estimated as J/k = –5.6 K from the results of magnetic [5] and magneto-optical [6] measurements. The energy of magnons with wave vectors at the boundary of the Brillouin zone, which, as a rule, make the main contribution to the exciton–magnon absorption in a collinear antiferromagnet, was estimated at 80 cm^{-1}. The magnetodipole exciton band at an energy of ~80 cm^{-1} below the energy corresponding to the D_1 band was revealed in the spectrum of magnetic circular dichroism [7]. Although this band was not observed in the absorption spectrum due to the low intensity, its energy location is indicated in Fig. 1 and the band itself is designated as E_1. Kojima *et al.* [8] calculated the line shape for exciton–magnon absorption of a 2D antiferromagnet with a square lattice. The line shape depends on many parameters and can be different. However, in the case when the interaction between the exciton and the magnon can be disregarded and the parameters of the resonance transmission of optical excitation from ion to ion are small (and, as a consequence, the dispersion of the exciton band is small), the band under consideration becomes narrow and strongly asymmetric. The line shape calculated for a square antiferromagnetic lattice under the above assumptions with the relationships described in [8] is presented in Fig. 1 (curve *0*). In these calculations, the exchange integral and the anisotropy field were taken from [6] and [5], respectively. The anisotropy field virtually does not affect the exciton–magnon band but eliminates the divergence in the expression for the line shape at the center of the Brillouin zone.

As the content of Mn^{2+} ions decreases, additional bands (D_1' and D_1'') appear in the range of the D_1 exciton–magnon band, whereas the D_1 band itself becomes less intense and almost disappears at x = 0.7 (curve *4* in Fig. 1).

Figure 2 depicts the dependences of the energy location of the bands D_1, D_1', and D_1'' on the magnetic field aligned parallel to the C_4 axis of the crystals. In the antiferromagnetic phase, the spin-flop transition leads to a jumplike shift of all the bands revealed in the α-polarized absorption spectrum (including the bands observed upon dilution of the magnetic crystal) by the same value. This suggests that all these bands are associated with the same exciton.

The magnitude of the jump in the energy of the absorption bands upon the spin-flop transition decreases almost linearly as the manganese content x

decreases, which reflects the decrease in the mean exchange field due to the dilution of the Rb_2MnCl_4 crystal, and vanishes at $x \approx 0.6$. The inset in Fig. 2 shows the dependence of the field of the spin-flop transition on the manganese content at $T = 4.3$ K, which was obtained from observations of the D_1, D_1', and D_1'' bands in a magnetic field. The estimate of the critical manganese content ($x_c = 0.6$) corresponding to a transition from the antiferromagnetic state to a disordered state of the crystal agrees well with the theoretical value (0.59) for the point of magnetic percolation in a plane square lattice.

For the Rb_2MnCl_4 crystal, the D_1 exciton–magnon band is unique with respect to its parameters owing to the small dispersion of the exciton band. The replacement of manganese ions by cadmium ions in the magnetic lattice disturbs both translational symmetry and the initial magnetic order. In this case, the contribution of the short-wavelength magnons (short-range magnetic order) to the exciton–magnon absorption increases and the band should become more symmetric and less intense with a decrease in the manganese content x. This behavior is observed for the D_1 band.

The energy location of the D_1' and D_1'' bands in the spectra of diluted crystals indicates that these bands are associated with the same process of excitation as in the case of the D_1 band. The energies at their maxima are $\sim E_m/4$ and $\sim E_m/2$ less than the energy at the maximum of the D_1 band. Here, E_m is the magnon energy at the boundary of the Brillouin zone. The energy separation between the states split along the projection of the spin in a local magnetic field decreases by the same value, provided the nearest environment of the Mn^{2+}–Mn^{2+} pair is considered a field source and, in the nearest environment itself, one or two Mn^{2+} ions are replaced by Cd^{2+} ions. The total absorption by an exchange-coupled pair of magnetic ions is proportional to the number of pairs. The probabilities of finding no Cd^{2+} ions, one Cd^{2+} ion, or two Cd^{2+} ions in the nearest environment of the Mn^{2+}–Mn^{2+} pair depend on the manganese content x. Figure 3 presents the statistical estimates of these probabilities obtained by statistical modeling. The analytical dependences of the probabilities on the manganese content x for these three cases obey the laws x^8, $6x^7(1-x)$, and $15x^6(1-x)^2$, respectively, and coincide with the curves depicted in Fig. 3. In the case when the D_1 exciton–magnon band shape remains unchanged upon dilution of the crystal and the D_1' and D_1'' bands have a Gaussian shape, the concentration dependences of the integrated intensities of these three bands after their separation approximately coincide with the curves shown in Fig. 3. The vertical lines in Fig. 3 indicate the ratios of the numbers of ion pairs for manganese contents at which the measurements were carried out. These ratios correlate well with the intensity ratios of the D_1, D_1', and D_1'' bands. Therefore, the D_1' and D_1'' bands appear in the absorption spectra of $Rb_2Mn_xCd_{1-x}Cl_4$ crystals as a result of the excitation of exchange-coupled pairs of Mn^{2+} ions in a spatially disordered magnetic structure, provided the nearest environment of the Mn^{2+} ions contains Cd^{2+} ions.

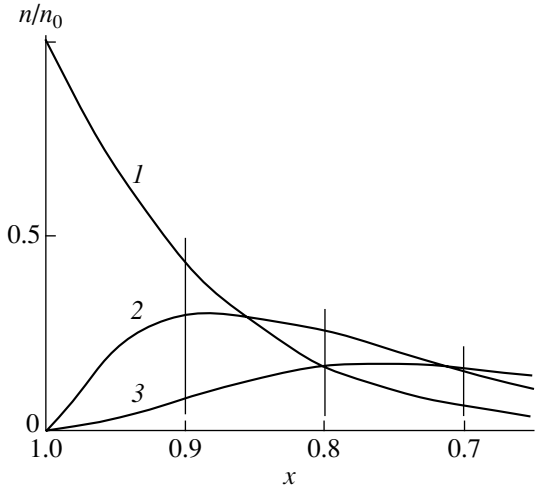

Fig. 3. Dependences of the relative number of nearest neighbor manganese ion pairs in a square lattice on the manganese content x when the nearest environment of manganese ions contains (*1*) no cadmium ions, (*2*) one cadmium ion, and (*3*) two cadmium ions.

In addition to the D_1 band, the spectra of the Rb_2MnCl_4 crystal exhibit magnon sidebands in the vicinity of the transitions ${}^6A_{1g}({}^6S) \longrightarrow {}^4T_{2g}({}^4D)$ [9] and ${}^6A_{1g}({}^6S) \longrightarrow {}^4A_{1g}^4E_g({}^4G)$. However, the line shape of these satellites does not allow one to observe additional bands similar to the bands D_1' and D_1''.

4. CONCLUSIONS

Thus, we studied the dependences of the optical absorption of a 2D magnet on the content of magnetic ions and on the magnetic field in the range of the exciton–magnon absorption. Owing to the unique parameters of the D_1 exciton–magnon band, the additional absorption bands associated with the optical excitation of exchange-coupled pairs of Mn^{2+} ions were observed for the first time in the spectrum of an antiferromagnetic crystal upon its dilution with a nonmagnetic impurity. The phase boundary between the antiferromagnetic and spin-flop phases was constructed using the results of optical measurements.

ACKNOWLEDGMENTS

We would like to thank I.S. Édel'man for his participation in discussions of the results.

This work was supported in part by the Russian Federal Program "Integration," project no. 0017.

REFERENCES

1. É. G. Petrov, *Theory of Magnetic Excitons* (Naukova Dumka, Kiev, 1976).
2. V. V. Eremenko, N. F. Kharchenko, Yu. G. Litvinenko, and V. M. Naumenko, *Magneto-Optics and Spectroscopy of Antiferromagnets* (Naukova Dumka, Kiev, 1989).
3. O. Cador, C. Mathoniere, and O. Kahn, Inorg. Chem. **39** (17), 3799 (2000).
4. H. T. Witteveen, J. Solid. State Chem. **11** (3), 245 (1974).
5. N. V. Fedoseeva, I. P. Spevakova, A. N. Bazhan, and B. V. Beznosikov, Fiz. Tverd. Tela (Leningrad) **20** (9), 2776 (1978) [Sov. Phys. Solid State **20**, 1600 (1978)].
6. E. A. Popov and M. M. Kotlyarskiĭ, Fiz. Tverd. Tela (Leningrad) **22** (10), 3019 (1980) [Sov. Phys. Solid State **22**, 1763 (1980)].
7. A. Vervoitte, J. C. Canit, B. Briat, and U. Cambli, Phys. Status Solidi B **124** (1), 87 (1984).
8. N. Kojima, T. Ban, and I. Tsujikawa, J. Phys. Soc. Jpn. **44** (3), 923 (1978).
9. E. A. Popov and M. M. Kotlyrskii, Phys. Status Solidi **96** (1), 163 (1979).

Translated by O. Moskalev

Physics of the Solid State, Vol. 45, No. 8, 2003, pp. 1479–1483. Translated from Fizika Tverdogo Tela, Vol. 45, No. 8, 2003, pp. 1409–1413.

MAGNETISM AND FERROELECTRICITY

The Exact Spectrum of Fermi Quasiparticles in Kondo–Anderson Ferromagnetic Lattice

S. G. Ovchinnikov and L. Ye. Yakimov

Kirensky Institute of Physics, Siberian Division, Russian Academy of Sciences, Akademgorodok, Krasnoyarsk, 660036 Russia

Received May 15, 2002; in final form, October 30, 2002

Abstract—The spectrum of Fermi excitations of a nondegenerate ferromagnetic semiconductor at $T = 0$ with one electron present is investigated in order to describe the electronic structure of manganites with inclusion of strong electron correlations within the Anderson periodic model with *s–d* exchange interaction. Exact dispersion relations and the Green functions for different spin projections are found. The density-of-states function is calculated for different positions of the *d* level relative to the band bottom. © *2003 MAIK "Nauka/Interperiodica".*

1. INTRODUCTION

To investigate Kondo systems or systems with variable valence, such as $La_{1-x}Ca_xMnO_3$ and $La_{1-x}Sr_xMnO_3$, a periodical Anderson model with *s–d* exchange is used in this work.

The interest in manganites stems from the fact that in these compounds the effect of colossal magnetic resistance is observed, whose maximum is reached at $x = 0.33$. In this case, the system can be considered a ferromagnetic [1] lattice of localized spins of Mn^{4+} ions with the electron configuration $3d^3$ (spin $S = 3/2$), into which some extra electrons of the corresponding concentration are added. These electrons can remain delocalized and interact with the lattice spins via exchange interaction of the Heisenberg type. As a result of possible hybridization, the electrons can become localized, forming a Mn^{3+} ion of $3d^4$ configuration at a lattice site. These two types of the electron state and two interactions are included in the Hamiltonian of the model, which is the periodical Anderson model with *s–d* exchange interactions.

This work is devoted to the specific case of a system containing one itinerant electron at $T = 0$. It is very important that, under these conditions, the problem turned out to have an exact solution. Formally speaking, this case corresponds to the lower limit of concentration, for which $x \longrightarrow 0$ and the ground state of the localized spin subsystem of manganites is antiferromagnetic. Not aiming to describe this antiferromagnetic case, we only note that this exact solution is important for manganites in the range of parameters where the ground state of the localized spin subsystem is ferromagnetic ($x = 0.15$–0.40). If we take an approximate solution in this range and consider the concentration of carriers as a parameter, then tending this parameter to zero (with the localized spin subsystem frozen in the ferromagnetic ground state) will lead to our exact solution. Thus, this solution may be useful for constructing and checking approximate solutions for the values of parameters corresponding to ferromagnetism in the localized spin subsystem.

This case is also a generalization of the problem of a magnetic polaron [2–4] with inclusion of hybridization interaction. Let us write the wave function of the $d^n s^m$ configuration as $|n, S, M; m, \sigma\rangle$, where S and M are the spin and its projection for a d^n ion, respectively; $m = 0$ or 1 is the number of *s* electrons per unit cell; and σ is the spin projection of an *l* electron. Then, in addition to the processes caused by the *s–d* exchange,

$$|n, S, S; 1, \downarrow\rangle \rightleftharpoons |n, S, S-1; 1, \uparrow\rangle \tag{1}$$

we will have the processes due to hybridization

$$\begin{aligned} &|n, S, S; 1, \downarrow\rangle \\ &\rightleftharpoons |n+1, S \pm 1/2, S-1/2; 0\rangle \\ &\rightleftharpoons |n, S, S-1; 1, \uparrow\rangle, \end{aligned} \tag{2}$$

$$|n, S, S; 1, \uparrow\rangle \rightleftharpoons |n+1, S+1/2, S+1/2; 0\rangle, \tag{3}$$

which are included in this work. The plus and minus signs in Eq. (2) correspond to two possible values of the total spin on a site. In general, when the electron is localized, the spin of the site can take on the values $S' = S + 1/2$ and $S' = S - 1/2$. The corresponding cases are called the high-spin and low-spin cases. A solution for the low-spin case was obtained in [5]. In manganites, when the itinerant electron is localized, we have the high-spin case; the $3d^4$ configuration possesses spin $S' = 2$, which is used in this work. The excitations of quasiparticles with a definite spin projection, which are forbidden in the low-spin case, become allowed in the high-spin case. As a result, the one-particle density of states in the high-spin case radically differs from that in the low-spin case.

In Section 2, the model Hamiltonian is written out, necessary transformations are described, and the exact

results (dispersion relations and Green functions) are presented. In Section 3, we discuss the density of states calculated using the exact solution.

2. EXACT ONE-PARTICLE GREEN FUNCTIONS

Taking interactions into account, we write down the Hamiltonian of the model in the form

$$H = H_{0a} + H_{0d} - J\sum_f S_f\sigma_f + V\sum_{f\sigma}(d^\dagger_{f\sigma}a_{f\sigma} + \text{H.c.}). \quad (4)$$

Here, $H_{0a} = \sum_{k\sigma}\varepsilon_k a^\dagger_{k\sigma}a_{k\sigma}$ describes delocalized states. The Hamiltonian H_{0d} describes localized states and generally can be written as

$$H_{0d} = \sum_{f,\lambda,\sigma}\varepsilon_\lambda d^\dagger_{f\lambda\sigma}d_{f\lambda\sigma} + \sum_{\substack{\Gamma_1,\Gamma_2,\Gamma_3,\Gamma_4\\ \sigma,\sigma'}}\langle\Gamma_1,\Gamma_2|v|\Gamma_3,\Gamma_4\rangle d^\dagger_{\Gamma_1\sigma}d^\dagger_{\Gamma_2\sigma'}d^\dagger_{\Gamma_4\sigma'}d^\dagger_{\Gamma_3\sigma}. \quad (5)$$

In the second term, the index Γ includes the site index f and the orbital index λ; v is the Coulomb interaction.

Let us pass to the space of eigenstates of the Hamiltonian H_{0d}. Each of them is defined by three quantum numbers, namely, the number of electrons, the total spin, and its projection ($|n, S, M\rangle$), and has energy $E_{n,S,M}$. In this representation, H_{0d} can be written as

$$H_{0d} = \sum_{f,n,S,M}E_{n,S,M}X_f^{n,S,M;\,n,S,M} \quad (6)$$

where we used the Hubbard operators

$$X_f^{n_1,S_1,M_1;\,n_2,S_2,M_2} = |n_1,S_1,M_1\rangle\langle n_2,S_2,M_2|. \quad (7)$$

In the case of manganites, for half-integer projections of the total spin, the values of the other two quantum numbers are $n = 3$ and $S = 3/2$, while for integer projections we have $n = 4$ and $S' = 2$. Therefore, we will indicate only the projection of the total spin for the Hubbard operators:

$$X_f^{M_1,M_2} = |n_1,S_1,M_1\rangle\langle n_2,S_2,M_2|. \quad (8)$$

Since we have only two configurations of localized electrons on a site that differ in energy, the energy of the state $|n = 3, S = 3/2, M\rangle$ can be taken to be zero; the energy of the other state, $|n = 4, S' = 2, M'\rangle$, will be designated as Ω.

As a result, H_{0d} can be written as [6]

$$H_{0d} = \Omega\sum_f\sum_{M'=-S'}^{S'}X_f^{M',M'}. \quad (9)$$

For further calculations, we express all operators acting on the localized states in terms of the Hubbard operators. In this case, the components of the operators S_f have the form

$$S_f^Z = \sum_{M=-S}^{S}MX_f^{M,M} + \sum_{M'=-S'}^{S'}M'X_f^{M',M'}, \quad (10)$$

$$S_f^+ = (S_f^-)^\dagger = \sum_{M=-S}^{S}\gamma_S(M)X_f^{M+1,M} + \sum_{M'=-S'}^{S'}\gamma_{S'}(M')X_f^{M'+1,M'}, \quad (11)$$

$$\gamma_S(M) = \sqrt{(S-M)(S+M+1)}. \quad (12)$$

The creation and annihilation operators for an electron on the localized d level can be written as

$$d^\dagger_{f\uparrow} = (d_{f\uparrow})^\dagger = \sum_M\sqrt{\frac{S+1+M}{2S+1}}X_f^{M+\frac{1}{2},M}, \quad (13)$$

$$d^\dagger_{f\downarrow} = (d_{f\downarrow})^\dagger = \sum_M\sqrt{\frac{S+1-M}{2S+1}}X_f^{M-\frac{1}{2},M}. \quad (14)$$

In calculating the densities of states of quasiparticles, we used the two-time retarded Green functions, while involve the creation and annihilation operators of the corresponding quasiparticles and the ferromagnetic ground state of the localized spin subsystem (thus, the ferromagnetic ordering in the localized spin subsystem, appearing due to spin exchange between manganese ions, is taken into account):

$$\langle\langle a_{p\sigma}(t)|a^\dagger_{p\sigma}(t')\rangle\rangle = -i\theta(t-t')\langle FM|[a_{p\sigma}(t), a^\dagger_{p\sigma}(t')]_+|FM\rangle. \quad (15)$$

Here,

$$\theta(t) = \begin{cases}1, & t>0\\ 0, & t<0.\end{cases} \quad (16)$$

The matrix element is taken for the ferromagnetic ground state $|FM\rangle$ of the system in the absence of carriers. In this state, the energy band is empty: $a_{f\sigma}|FM\rangle = 0$ and each lattice site has spin S and the maximum spin projection, $S_f^Z|FM\rangle = S|FM\rangle$.

The equations of motion can be reduced to the set of equations:

$$\begin{bmatrix} E-\varepsilon_p+\frac{JS}{2} & -V \\ -V & E-\Omega \end{bmatrix}\begin{bmatrix} \langle\langle a_{p\uparrow}|a_{p\uparrow}^{\dagger}\rangle\rangle \\ \langle\langle X_p^{S,S+\frac{1}{2}}|a_{p\uparrow}^{\dagger}\rangle\rangle \end{bmatrix} = \begin{bmatrix} 1 \\ 0 \end{bmatrix}, \quad (17)$$

from which we obtain a dispersion equation and an exact expression for the Green function (with spin up),

$$D_1(E) = E-\varepsilon_p-\frac{JS}{2}-\frac{V^2}{E-\Omega} = 0, \quad (18)$$

$$\langle\langle a_{p\uparrow}|a_{p\uparrow}^{\dagger}\rangle\rangle = D_1(E)^{-1}. \quad (19)$$

From Eqs. (17), it follows that the Green function $\langle\langle X_p^{S,S+\frac{1}{2}}|X_p^{S+\frac{1}{2},S}\rangle\rangle$ corresponds to a localized quasiparticle with spin up. Analogous calculations for this function give

$$D_2(E) = E-\Omega-\frac{V^2}{E-\varepsilon_p+\frac{JS}{2}} = 0, \quad (20)$$

$$\langle\langle X_p^{S,S+\frac{1}{2}}|X_p^{S+\frac{1}{2},S}\rangle\rangle = D_2(E)^{-1}. \quad (21)$$

For an itinerant and a localized quasiparticle with spin down, the corresponding set of equations is more complicated due to a larger variety of multiparticle processes [see Eqs. (1)–(3)], but at $T = 0$ and for one carrier, this set is also closed and allows an exact solution. It is significant that the ground state is assumed to be ferromagnetic in this case. The dispersion relation and the Green function (for an itinerant quasiparticle with spin down) are calculated exactly to be

$$D_3(E) = E-\varepsilon_p-\frac{JS}{2} + \frac{2V_1^2JS-\frac{1}{2}J^2S(E-\Omega)-V_1^2(\Delta^{-1}(E)-J/2),}{(E-\Omega)(\Delta^{-1}(E)-J/2)-2V_1^2S} = 0, \quad (22)$$

$$\langle\langle a_{p\downarrow}|a_{p\downarrow}^{\dagger}\rangle\rangle = D_3(E)^{-1}. \quad (23)$$

For a localized quasiparticle with spin down, we have

$$D_4(E) = E-\Omega + \frac{2V_1^2JS-2V_1^2S\left(E-\varepsilon_p-\frac{JS}{2}\right)-V_1^2(\Delta^{-1}(E)-J/2)}{\left(E-\varepsilon_p-\frac{JS}{2}\right)(\Delta^{-1}(E)-J/2)-\frac{J^2S}{2}} = 0, \quad (24)$$

$$\langle\langle X_p^{S,S-\frac{1}{2}}|X_p^{S-\frac{1}{2},S}\rangle\rangle = D_4(E)^{-1}. \quad (25)$$

Here, the following notation is introduced:

$$\Delta(E) = \frac{1}{N}\sum_k \frac{1}{E-\varepsilon_k+\frac{JS}{2}}, \quad V_1 = \frac{V}{\sqrt{2S+1}}. \quad (26)$$

It should be noted that if we neglect the hybridization effects in Eqs. (19) and (23), by setting $V = 0$, then these equations will coincide exactly with the corresponding equations for a magnetic polaron [2–4] obtained for the case of a ferromagnetic saturated semiconductor, in particular, for EuO at $T = 0$ [7].

3. ONE-PARTICLE DENSITIES OF STATES

In order to illustrate the exact solution obtained, the density of states was calculated for each quasiparticle. Making the change of variables $\varepsilon_p = E'$, we write

$$n(E) = -\frac{1}{\pi}\frac{1}{N}\sum_p \operatorname{Im} G(p, E+i0) = -\frac{1}{\pi}\int dE' n_0(E')\operatorname{Im} G(E', E+i0). \quad (27)$$

In order to calculate the density of states for localized electrons, the relation between the Green functions $\langle\langle d_{p\sigma}|d_{p\sigma}^{\dagger}\rangle\rangle$ and the functions $\langle\langle X_p^{S,S\pm\frac{1}{2}}|X_p^{S\pm\frac{1}{2},S}\rangle\rangle$ needs to be established. Making use of the definition of the Green functions, Eqs. (13) and (14), and the fact that the projection of any localized spin in the ground state equals S, we obtain

$$\langle\langle d_{p\downarrow}|d_{p\downarrow}^{\dagger}\rangle\rangle = \sum_{M,M'}\sqrt{\frac{S+1-M}{2S+1}}\sqrt{\frac{S+1-M'}{2S+1}} \times \langle\langle X_p^{M,M-\frac{1}{2}}|X_p^{M'-\frac{1}{2},M'}\rangle\rangle = \frac{1}{2S+1}\langle\langle X_p^{S,S-\frac{1}{2}}|X_p^{S-\frac{1}{2},S}\rangle\rangle. \quad (28)$$

The corresponding Green functions for a quasiparticle with spin up are

$$\langle\langle d_{p\uparrow}|d_{p\uparrow}^{\dagger}\rangle\rangle = \langle\langle X_p^{S,S+\frac{1}{2}}|X_p^{S+\frac{1}{2},S}\rangle\rangle. \quad (29)$$

Numerical calculations were performed using the parameters characteristic of manganites: $J = 0.5$ eV, $V = 0.1$ eV, $W = 4$ eV, and $S = 3/2$.

We note that the parameters obtained from the adjustment to the experiment are dependent on the model. For example, in our case, W is the width of the bare band. The resulting band of quasiparticles, as will be seen further on, contains two bands; the lower one is narrow, with the narrow-band limit taking place for it [8], while the upper one is wide, with its width exceeding the exchange parameter J.

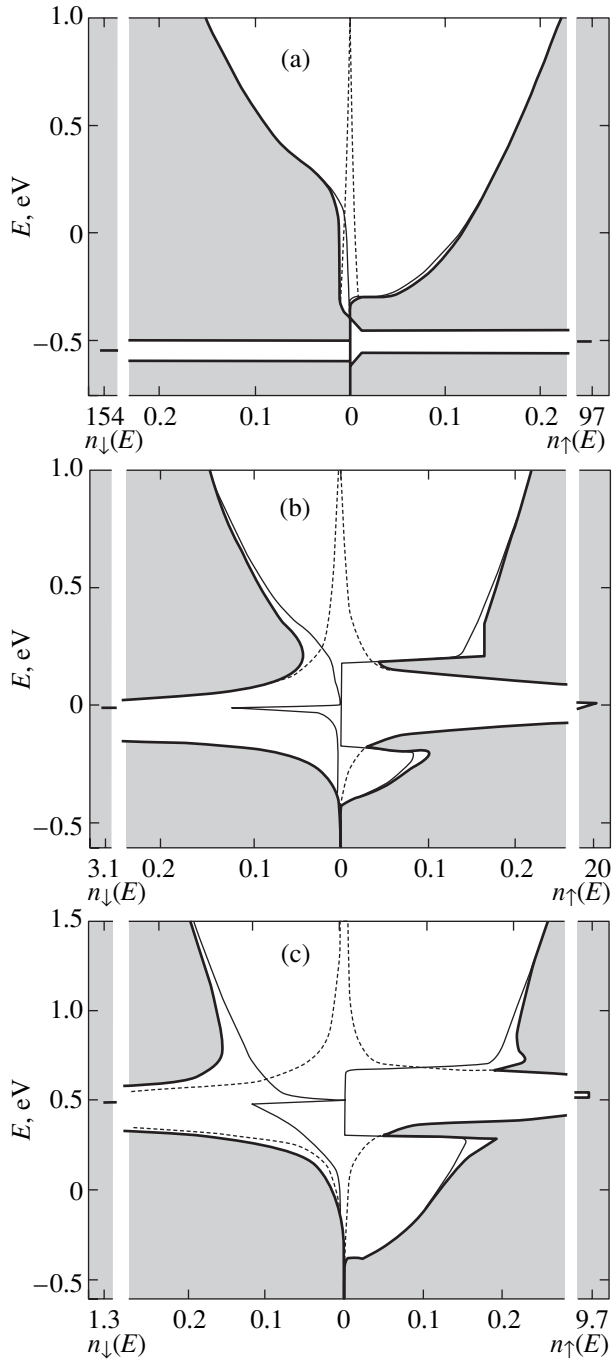

Fig. 1. Densities of states for Ω equal to (a) –0.5, (b) 0, and (c) 0.5 eV. The density of states with spin down is offset horizontally to the left and the one with spin up, to the right. Thin solid lines correspond to an itinerant quasiparticle, dashed lines to a localized quasiparticle, and thick solid lines to the total density for $J = 0.5$ eV, $V = 0.1$ eV, $W = 4$ eV, and $S = 3/2$.

For calculations, we used a quadratic dispersion law and the corresponding density of states

$$\varepsilon_x = \begin{cases} Wx^2, & x \in [-1, 1] \\ 0, & x \notin [-1, 1], \end{cases} \qquad (30)$$

where $x = p/p_B$,

$$n_0(E) = \begin{cases} \dfrac{3}{2W}\sqrt{\dfrac{E}{W}}, & E \in [0, W] \\ 0, & E \notin [0, W]. \end{cases} \qquad (31)$$

The localization energy Ω was chosen such that it fell in one of the three energy ranges into which the energy axis is divided by points $\pm JS/2 = \pm 0.375$ eV. For each value of Ω, the densities of states were calculated for itinerant and localized quasiparticles for both spin projections. The results are shown in Fig. 1.

Figure 1a shows the densities of states for Ω = –0.5 eV. In this case, the localized level lies below the band. The band densities of states for both spin projections have the same form as in the *s*–*d* model. The electrons with spin down exhibit a non-quasiparticle behavior in the region (–*JS*/2, *JS*/2), which is a known effect characteristic of the *s*–*d* model. The density of states of a localized quasiparticle for both spin projections has a narrow peak near the energy –0.5 eV. For both spin projections, there is a nonzero contribution near the conduction band bottom caused by hybridization.

This case (with the localized level lying below the band) resembles the situation in the *s*–*d* model with a negative *s*–*d* exchange parameter, where a deep discrete level appears corresponding to the band of spin-polaron states [3]. However, in this case, the localized level under the band has only an insignificant addition of polaron and band states, appearing due to hybridization, and consists mainly of the localized *d*-electron states.

Figure 1b presents the densities of states for Ω = 0. Here, the situation is more complicated because the localized level crosses the band in the region of the Stoner gap (–*JS*/2, *JS*/2). Hybridization effects are expressed in the blurring of the peaks of the densities of localized states.

For the spin up, in the region of the *d* level, there is a hybridization gap for an itinerant quasiparticle and a peak for a localized one. It should be noted that this does not happen in the low-spin case [5], because hybridization is impossible for this initial spin-up band state in this case. It is interesting to note that in the total density of states both effects are present; the peak of localized states dominates, but there are also dips (pseudogap) due to the hybridization gap.

Superposition of the localized level on the region of non-quasiparticle behavior (an itinerant quasiparticle with spin down) leads to the appearance of a narrow peak, above which a narrow pseudogap is observed. Nevertheless, localized *d* states dominate in the total density of states.

A qualitatively similar picture appears at Ω = +0.5 eV (Fig. 1c). However, in this case, the localized level lies above the Stoner gap. The band density of states (with spin down) changes in the same way as at

$\Omega = 0$. A narrow gap and a less expressed peak under it are observed.

4. CONCLUSION

Thus, the exact dispersion relations and the Green functions at $T = 0$ obtained in this work describe one carrier moving on the background of the ferromagnetic ground state of a lattice. Two types of interaction, *s–d* exchange and hybridization, have been taken into account in the strong-correlation regime. This case corresponds to the lower limit of the concentration x. Although manganites are no longer ferromagnets at low x, the results obtained in this work should be reproduced by all solutions found for the ferromagnetism region ($x = 0.15$–0.40) in the limit of small concentrations and low temperatures.

ACKNOWLEDGMENTS

This work was supported by the federal program "Integration" (project no. B 0017) and the Russian Foundation for Basic Research (project no. 02-02-97705).

REFERENCES

1. É. L. Nagaev, Usp. Fiz. Nauk **166** (8), 833 (1996) [Phys. Usp. **39**, 781 (1996)].
2. É. L. Nagaev, Zh. Éksp. Teor. Fiz. **56** (3), 1013 (1969) [Sov. Phys. JETP **29**, 545 (1969)].
3. Yu. A. Izyumov and M. V. Medvedev, Zh. Éksp. Teor. Fiz. **59** (2), 553 (1970) [Sov. Phys. JETP **32**, 302 (1971)].
4. B. S. Shastry and D. C. Mattis, Phys. Rev. B **24** (9), 5340 (1981).
5. M. Sh. Erukhimov, S. G. Ovchinnikov, and S. I. Yakhimovich, Fiz. Tverd. Tela (Leningrad) **31** (5), 52 (1989) [Sov. Phys. Solid State **31**, 749 (1989)].
6. V. V. Val'kov and S. G. Ovchinnikov, *Quasiparticles in Strongly Correlated Systems* (Ross. Akad. Nauk, Novosibirsk, 2001), p. 31.
7. W. Nolting, G. G. Reddy, A. Ramakanth, and D. Meyer, Phys. Rev. B **64** (15), 155109 (2001).
8. E. L. Nagaev, Phys. Rep. **346** (6), 387 (2001).

Translated by A. Titov

Physics of the Solid State, Vol. 45, No. 8, 2003, pp. 1484–1486. Translated from Fizika Tverdogo Tela, Vol. 45, No. 8, 2003, pp. 1414–1416.

MAGNETISM AND FERROELECTRICITY

The $2^{1/3}$ Rule and Other Properties of Ferromagnets near the Temperature of the Maximum of Magnetic Susceptibility

A. V. Korolev, M. I. Kurkin, and E. V. Rosenfel'd

Institute of Metal Physics, Ural Division, Russian Academy of Sciences, ul. S. Kovalevskoĭ 18, Yekaterinburg, 620219 Russia

e-mail: kurkin@imp.uran.ru

Received December 3, 2002

Abstract—The behavior of the magnetization M and the magnetic susceptibility χ is theoretically analyzed for ferromagnets at the temperature $T = T_m$ corresponding to the maximum of the function $\chi(T)$. Four new methods of determining the Curie temperature T_C with the use of the derived relationships are proposed. One of these methods is based on the relationship $\chi(T_m) = 2^{1/3}\chi(T_C)$ (the $2^{1/3}$ rule). The results are applied for processing experimental data obtained for lanthanum manganite of composition $La_{0.85}Sr_{0.15}MnO_3$. © *2003 MAIK "Nauka/Interperiodica".*

Since the Curie temperature T_C for ferromagnets is considered the most characteristic point on the temperature scale, all expressions for the magnetic characteristics of ferromagnets are usually related to T_C [1]. However, the experimental determination of T_C involves some difficulties due to a specific inhomogeneous distribution of the magnetization M, which is known as a domain structure [2]. In order to transform a ferromagnetic sample into a single-domain state with a homogeneous distribution of the magnetization M, it is necessary to apply a magnetic field $H > H_s$, where H_s is the field of magnetic saturation [2]. The magnetic fields H_s reach several kiloörsteds. In this case, all the thermodynamic peculiarities become smeared to an extent that the Curie temperature T_C can be represented by an ordinary point on the curve $M(T, H)$.

On the other hand, it has long been known that one more temperature is specific to ferromagnets, namely, $T = T_m$ [1], which corresponds to the maximum in the temperature dependence of the magnetic susceptibility:

$$\chi(T, H) = \partial M(T, H)/\partial H. \quad (1)$$

Figure 1 shows the experimental temperature dependences of the magnetic susceptibility $\chi(T)$ measured in several magnetic fields H for a lanthanum manganite single crystal of composition $La_{0.85}Sr_{0.15}MnO_3$. The magnetic measurements were performed on an MPMS-5XL Quantum Design SQUID magnetometer. It is evident from Fig. 1 that, first, the temperature T_m is well determined experimentally, and, second, since the condition $T_m > T_C$ is satisfied, the domain structure in the vicinity of T_m is absent. From these considerations, we came up with a proposal for using the temperature T_m at the maximum of the magnetic susceptibility for experimental determination of the magnetic characteristics of ferromagnets, including the Curie temperature T_C. To the best of our knowledge, similar studies have not been conducted before; hence, we had to obtain expressions relating the magnetization M and the magnetic susceptibility χ with the temperature T_m. We proceeded from the Landau expansion [3] for the thermodynamic potential Φ in terms of M, which is usually used for processing the results of magnetic measurements [1]:

$$\Phi = \Phi_0 - MH + (1/2)A(T - T_C)M^2 + (1/4)BM^4 + \ldots. \quad (2)$$

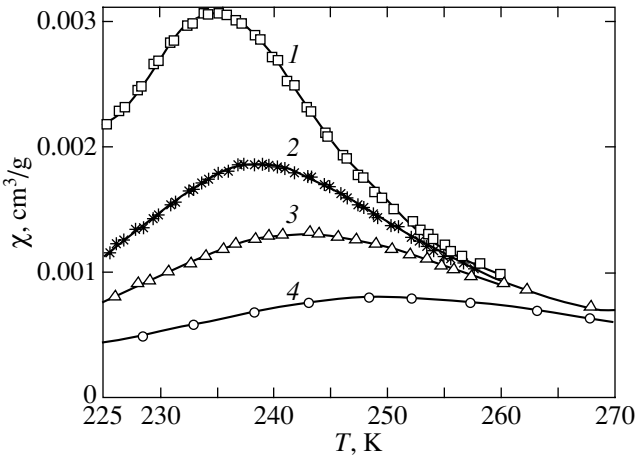

Fig. 1. Temperature dependences of the magnetic susceptibility of the lanthanum manganite single crystal doped with 15 at. % Sr in different magnetic fields. H, kOe: (*1*) 3, (*2*) 6, (*3*) 10, and (*4*) 20.

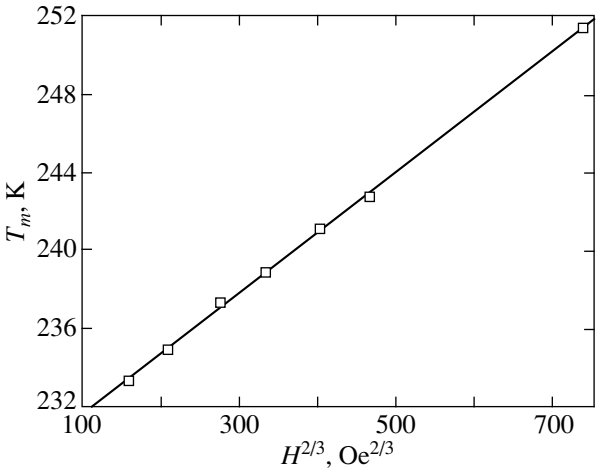

Fig. 2. Dependence of the temperature at the maximum of the magnetic susceptibility $\chi(T)$ on $H^{2/3}$.

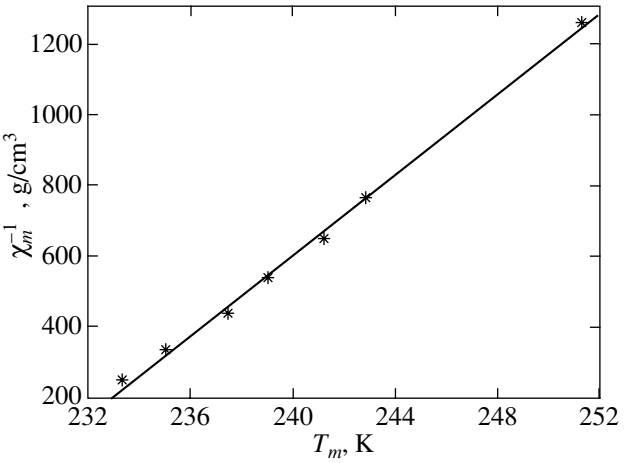

Fig. 3. Dependence of χ_m^{-1} on the temperature T_m at the maximum of the magnetic susceptibility.

The magnetization M corresponding to the minimum of the thermodynamic potential Φ can be determined by solving the cubic equation

$$DM^3 + A(T - T_c)M - H = 0. \quad (3)$$

As was noted above, we are interested here in solving the cubic equation (3) for a single value of the temperature $T = T_m$, which corresponds to the maximum of the function $\chi(T, H)$ [see expression (1)], under the condition

$$\partial\chi(T_m, H)/\partial T = \partial^2 M(T_m, H)/\partial T\partial H = 0. \quad (4)$$

For this point, we obtain the following exact relationships, which are valid for any magnetic field H:

$$M^2(T_m, H) = \frac{A}{3B}(T_m - T_c) = \frac{1}{6B}\chi^{-1}(T_m, H), \quad (5)$$

$$\chi^{-1}(T_m, H) = 2A(T_m - T_c), \quad (6)$$

$$T_m - T_c = \frac{3B}{A}\sqrt[3]{\left(\frac{H}{4B}\right)^2}, \quad (7)$$

$$\chi(T_m, H) = 2^{1/3}\chi(T_c, H). \quad (8)$$

The above relationships appeared to be relatively unexpected. First, these relationships are much simpler than those predicted from the Cardano formulas for the roots of the cubic equation. Second, formulas (5) and (6) almost coincide with the standard expressions for the temperature dependences of the magnetization $M(T)$ and the magnetic susceptibility $\chi(T)$ [1], which can be obtained from the cubic equation (3) in the limit of weak magnetic fields H,

$$M^2(T) = \frac{A}{B}(T_c - T), \quad \chi^{-1}(T) = 2A(T_c - T), \quad (9)$$

even though formulas (5) and (6) are valid in the paramagnetic region (since we have $T_m > T_C$) and the first formula (9) is applicable only under the condition $T < T_C$. Third, we failed to puzzle out the meaning of equality (8). Our attempts to use the symmetry or similarity considerations for this purpose were not successful, and we could not invent a better name than the "$2^{1/3}$ rule" for this equality.

The absence of a domain structure at $T = T_m$ allows one to use formulas (5)–(8) for experimental determination of the magnetic parameters A, B, and T_C. Note that, in this case, the Curie temperature T_C can be obtained from any one of these four formulas. Figures 2–4 present the results of the processing [using formulas (5)–(7)] of the experimental temperature dependences of the magnetization $M(T)$ and the magnetic susceptibility $\chi(T)$ for an $La_{0.85}Sr_{0.15}MnO_3$ single crystal at seven

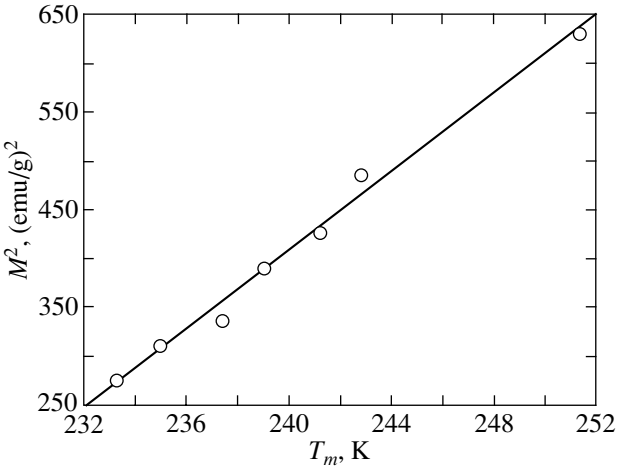

Fig. 4. Dependence of the square of the magnetization M^2 on the temperature T_m.

Curie temperatures T_C determined according to the $2^{1/3}$ rule from the curves $\chi(T)$ shown in Fig. 1

H, kOe	T_C, K
3	227.8
6	230.0
10	231.5
20	235.5

strengths of the magnetic field H (2.0, 3.0, 4.5, 6.0, 8.0, 10.0, and 20.0 kOe). The smallest dispersion of the experimental points is observed for the relationship $(T_m - T_C) \sim H^{2/3}$ (Fig. 2). This relationship offers the highest accuracy in determining the Curie temperature T_C; that is,

$$T_C = 228.7 \pm 0.2 \text{ K}. \quad (10)$$

The error in determining the Curie temperature T_C from the relationship $\chi(T_m) \sim (T_m - T_C)$ (Fig. 3) was found to be $\Delta T_C \approx \pm 10$ K. The largest error $\Delta T_C \approx \pm 20$ K was obtained from data on the temperature dependence of the magnetization $M(T)$ (Fig. 4).

The $2^{1/3}$ rule [formula (8)], as applied to the processing of the curves $\chi(T)$ (Fig. 1), also allows one to determine the Curie temperature T_C. The table presents the Curie temperatures T_C obtained from formula (8) for each of these curves.

The accuracy in determining the Curie temperature T_C by this method is no less than the accuracy in determining T_m: $\Delta T_C = \Delta T_m \approx \pm 0.2$ K. Thus, the drift of the Curie temperature T_C with an increase in the magnetic field H (see table) is an experimentally significant quantity. According to formula (10), this drift exceeds the error in determining the Curie temperature T_C from formula (7), even though it is less than the value of ΔT_C obtained from relationships (5) and (6).

The drift observed in the Curie temperature T_C with an increase in the magnetic field H means that the lanthanum manganite sample under investigation exhibits properties that defy description in terms of expression (2) even after the elimination of the domain structure. It would be tempting to attribute this drift to the critical phenomena [4]. However, other possible causes should not be discarded, for example, the differences in the Curie temperatures T_C due to the occurrence of inhomogeneities typical of lanthanum manganites [5]. The results of analyzing these causes will be presented in our future papers.

ACKNOWLEDGMENTS

We would like to thank A.A. Mukhin and A.E. Ermakov for their interest in this work and for a number of valuable remarks.

This work was supported in part by the Russian Foundation for Basic Research (project no. 02-02-16440) and the Russian Federal Program "Integration."

REFERENCES

1. K. P. Belov, *Magnetic Transitions* (Fizmatgiz, Moscow, 1959; Consultants Bureau, New York, 1961).
2. S. V. Vonsovskiĭ and Ya. S. Shur, *Ferromagnetism* (GITTL, Moscow, 1948).
3. L. D. Landau and E. M. Lifshitz, *Statistical Physics*, 2nd ed. (Nauka, Moscow, 1964; Pergamon, Oxford, 1980).
4. V. L. Pokrovskiĭ and A. Z. Patashinskiĭ, *Fluctuation Theory of Phase Transitions*, 2nd ed. (Pergamon, Oxford, 1979; Nauka, Moscow, 1982).
5. É. L. Nagaev, Usp. Fiz. Nauk **166**, 833 (1996) [Phys. Usp. **39**, 781 (1996)].

Translated by O. Moskalev

Physics of the Solid State, Vol. 45, No. 8, 2003, pp. 1487–1492. Translated from Fizika Tverdogo Tela, Vol. 45, No. 8, 2003, pp. 1417–1422.

MAGNETISM AND FERROELECTRICITY

Contribution of "Unusual" Domain Walls to the Magnetoresistance of Multilayer Magnetic Structures

A. I. Morozov

Moscow State Institute of Radioengineering, Electronics, and Automation (Technical University), pr. Vernadskogo 78, Moscow, 119454 Russia

e-mail: mor-alexandr@yandex.ru

Received December 16, 2002

Abstract—The contribution to electrical resistance due to scattering of charge carriers by domain walls is analyzed. It is revealed that "unusual" domain walls are created by frustrations in ferromagnet–antiferromagnet multilayer magnetic structures. The thickness of an unusual domain wall is substantially less than that of a usual domain wall. It is shown that scattering of charge carriers by unusual domain walls can contribute significantly to the magnetoresistance of ferromagnet–antiferromagnet multilayer magnetic structures. An analysis of the contribution made by the Levy–Zhang mechanism to the magnetoresistance demonstrates that the initial estimate obtained for this contribution is considerably exaggerated. *© 2003 MAIK "Nauka/Interperiodica".*

1. INTRODUCTION

The effect of domain walls in a ferromagnet on its electrical resistance has been investigated experimentally and theoretically [1–9]. Theoretical studies have dealt with different mechanisms of the influence exerted by domain walls on the electrical resistance. These mechanisms can be divided into two groups. The first group involves mechanisms that are responsible for contributions of domain walls to the electrical resistance but are not related to alternative mechanisms of charge carrier scattering (intrinsic scattering). The second groups includes the other mechanisms, i.e., mechanisms based on a modification of the wave functions of charge carriers by domain walls that does not lead directly to their scattering but affects both the densities of states of the charge carriers and the matrix elements of their interaction with other scatterers (phonons, impurities, etc.).

In this paper, we will restrict our consideration to the specific case of the paramagnetic contribution made by domain walls to intrinsic scattering of charge carriers due to the effect of an exchange field on the spin of a charge carrier. The diamagnetic contribution associated with the Lorentz force acting on the charge carriers was examined earlier by Cabrera and Falicov [1]. This contribution is of no importance at room temperature in the case when the mean free path of charge carriers is substantially shorter than the radius of the quasi-classical trajectory of the charge carriers in a magnetic field. Moreover, we will analyze the Levy–Zhang mechanism, which falls into the second group.

2. THE ADIABATIC APPROXIMATION

The adiabatic approximation is based on the assumption that the magnetization in a ferromagnet with domain walls varies in space in such a smooth manner that the spin projection of a charge carrier (an electron or a hole) during its motion manages to keep pace with a local direction of the magnetization. Therefore, the wave functions of charge carriers in the adiabatic approximation characterize states in which the spin projection of a charge carrier onto a local direction of the magnetization is equal to $\pm 1/2$.

We consider a ferromagnet with planar domain walls that are aligned parallel to each other but are perpendicular to the x axis in the Cartesian coordinate system. The magnetization vector $\mathbf{M}(\mathbf{r})$ in these walls rotates either about the x axis (Bloch domain walls) or about the y axis (Néel domain walls), which is perpendicular to the magnetization vector in the domains. The location of the magnetization vector can be specified by an angle θ between this vector and the z axis of the Cartesian coordinate system. The magnitude of the magnetization vector is assumed to be constant: $|\mathbf{M}(\mathbf{r})| = M_0$. In this case, the wave functions in the adiabatic approximation can be obtained from the standard Bloch functions $\psi_{\mathbf{k},\uparrow}(\mathbf{r})$ and $\psi_{\mathbf{k},\downarrow}(\mathbf{r})$ with a fixed spin projection of the charge carrier onto the z axis ($S_z = \pm 1/2$) through the gauge transformation [3]:

$$\Psi_{\mathbf{k}}(\mathbf{r}) = \hat{R}_\theta \begin{bmatrix} \psi_{\mathbf{k},\uparrow}(\mathbf{r}) \\ \psi_{\mathbf{k},\downarrow}(\mathbf{r}) \end{bmatrix}, \quad (1)$$

$$\hat{R}_\theta = \exp\left(-i\frac{\theta}{2}\sigma_x\right), \quad (2)$$

1063-7834/03/4508-1487$24.00

where σ_x is the Pauli matrix. Relationship (2) corresponds to the case of Bloch domain walls. For Néel domain walls, the matrix σ_x in formula (2) must be replaced by the matrix σ_y.

After the gauge transformation, the operator for the potential energy of the charge carrier takes the same form as for a single-domain ferromagnet. However, the operator for the kinetic energy does not commute with $\hat{R}_\theta$. As a result, the Hamiltonian can be written in the form [3, 6]

$$\hat{H} = \hat{H}_0 + \hat{W}, \tag{3}$$

$$\hat{H}_0 = -\frac{\hbar^2}{2m}\Delta + V(\mathbf{r}) - J\sigma_z, \tag{4}$$

$$\hat{W} = -\frac{\hbar}{2m}\sigma_x\theta_x'\hat{p}_x + \frac{i\hbar^2}{4m}\sigma_x\theta_{xx}'' + \frac{\hbar^2}{8m}(\theta_x')^2, \tag{5}$$

where $V(\mathbf{r})$ is the potential of the ionic lattice, $2J$ is the exchange splitting of the subbands with opposite spin projections, σ_z is the Pauli matrix, $\hat{p}_x$ is the operator of the momentum component, and m is the electron mass.

The wave functions defined by expression (1) are eigenfunctions of the operator $\hat{H}_0$. The operator $\hat{W}$ is treated as a perturbation and differs from zero in the region of the domain walls. The first two terms in relationship (5) account for the mixing of adiabatic wave functions with opposite spin projections. The perturbation is weak under the condition $k_F L \gg 1$, where k_F is the Fermi wave vector of conduction electrons and L is the thickness of the domain wall.

3. THE LEVY–ZHANG COHERENT CONTRIBUTION

Let us now consider the matrix element $W_0 = \langle \mathbf{k}|\hat{W}|\mathbf{k}\rangle$, which is diagonal with respect to the wave vector. The last term in relationship (5) provides only a constant correction (independent of S_z) to the energy of states, whereas the contribution of the second term to the diagonal matrix element is equal to zero. Therefore, the coherent contribution of domain walls to the resistance is determined by the first term in relationship (5); i.e. it is proportional to the Pauli matrix σ_x.

The fulfillment of the condition $W_0 \neq 0$ does not lead directly to the appearance of resistance in the system but causes a mixing of adiabatic wave functions corresponding to the same magnitude of the wave vector and antiparallel orientations of the spin. In turn, this brings about a change in the matrix elements accounting for scattering of charge carriers by impurities and phonons and, hence, is responsible for the contribution to the magnetoresistance. In [3], this contribution for a domain wall 150 Å thick was estimated at ~1%.

According to Levy and Zhang [3], the value of W_0 (which they designated as ξ) does not depend on the domain-wall concentration. This statement is invalid, because the normalization of the ψ functions leads to the relationship $\psi \propto 1/\sqrt{V}$, where V is the volume of the crystal. Upon integrating over the area of the domain wall, we found that a single domain wall makes a contribution proportional to D_x^{-1} where D_x is the crystal size in a direction perpendicular to the domain wall.

As would be expected, the coherent contribution $(\Delta\rho/\rho)_{coh}$ of identical domain walls to the magnetoresistance is proportional to the domain-wall concentration squared. However, the domain walls can differ from one another in the sense of magnetic rotation, specifically in the sign of the parameter θ_x'. If the concentrations of domain walls of both types are equal to each other, we have $W_0 = 0$; i.e., the Levy–Zhang effect is absent. Otherwise, we obtain $W_0 \propto n_+ - n_-$, where n_+ and n_- are the concentrations of domain walls with opposite senses of magnetic rotation. In this case, the quantity W_0 is virtually independent of the domain-wall thickness, because, after calculating the integral $\int \theta_x' dx$, the magnetic rotation angle in a domain wall proved to be equal to $\pm\pi$.

Finally, we obtain the following expression:

$$\left(\frac{\Delta\rho}{\rho}\right)_{coh} = \left(\frac{n_+ - n_-}{n_+ + n_-}\right)^2\left(\frac{L}{b}\right)^2\left(\frac{\Delta\rho}{\rho}\right)_{L-Zh}, \tag{6}$$

where b is the width of the domain and $(\Delta\rho/\rho)_{L-Zh}$ is the result of the calculation performed by Levy and Zhang [3]. For $b \sim 0.1$ μm, we obtain $(\Delta\rho/\rho)_{coh} \sim 0.01\%$ even at $n_+ \gg n_-$. This value is two orders of magnitude less than the result reported in [3]. Therefore, it can be concluded that the Levy–Zhang contribution to the magnetoresistance is insignificant and can reach 1% only in the case when the characteristic width of domains (rather than the thickness of their walls) is of the order of 100 Å.

4. THE INCOHERENT CONTRIBUTION TO THE MAGNETORESISTANCE

The incoherent contribution to the magnetoresistance is determined by the off-diagonal matrix elements of the operator $\hat{W}$ and is proportional to the first power of the domain-wall concentration.

It is assumed that the ψ functions of charge carriers can be considered de Broglie waves and $\theta(x) = \arcsin(\tanh x/L)$. Under these assumptions, by analogy with the calculation performed in [4, 9], we obtain

$$\langle k_x'|\hat{W}|k_x\rangle = A_{k_x', k_x}\sigma_x + B_{k_x', k_x}. \tag{7}$$

Here,

$$A_{k_x', k_x} = -\frac{\pi\hbar^2(k_x' + k_x)}{4mD_x \cosh\dfrac{\pi(k_x' - k_x)L}{2}} \times \sum_j \alpha_j \exp[-i(k_x' - k_x)x_j], \quad (8)$$

where x_j is the coordinate of the center of the jth domain wall and $\alpha_j = \pm 1$ depending on the sense of rotation of the magnetization vector. The two other components of the wave vector **k** in the initial and final states coincide with each other. The quantity B_{k_x', k_x} can be represented in the form

$$B_{k_x', k_x} = \frac{\pi\hbar^2(k_x' - k_x)}{8mD_x \sinh\dfrac{\pi(k_x' - k_x)L}{2}} \times \sum_j \exp[-i(k_x' - k_x)x_j]. \quad (9)$$

As a rule, this quantity is ignored in analyzing the contribution made by domain walls to the resistance, except when the subband splitting caused by an exchange field is sufficiently large, i.e., when

$$\frac{JL}{\hbar v_F} \gg 1, \quad (10)$$

where v_F is the Fermi velocity of charge carriers. Under this condition, the transitions of electrons between subbands with opposite local spin projections, which are governed by the matrix element A_{k_x', k_x}, are exponentially rare in occurrence and the dominant role is played by the charge carrier scattering without a change in the spin orientation, which is determined by the quantity B_{k_x', k_x}.

4.1. Scattering without a Spin Flip

According to the law of conservation of energy, only the transitions between states differing in the sign of the wave vector k_x are possible; i.e., there occurs an elastic reflection from the domain wall. As follows from expression (9), charge carriers with a wave vector magnitude $|k_x| \le (\pi L)^{-1}$ (Fig. 1a) undergo considerable scattering by domain walls. The scattering probability can be written in the form

$$w_1 = \frac{2\pi D_x}{\hbar}\int dk_x |B_{k_x', k_x}|^2 \delta\left[\frac{\hbar^2(k_x')^2}{2m} - \frac{\hbar^2 k_x^2}{2m}\right] \approx \frac{\pi^3\hbar|k_x|}{8mb\sinh^2(\pi k_x L)}. \quad (11)$$

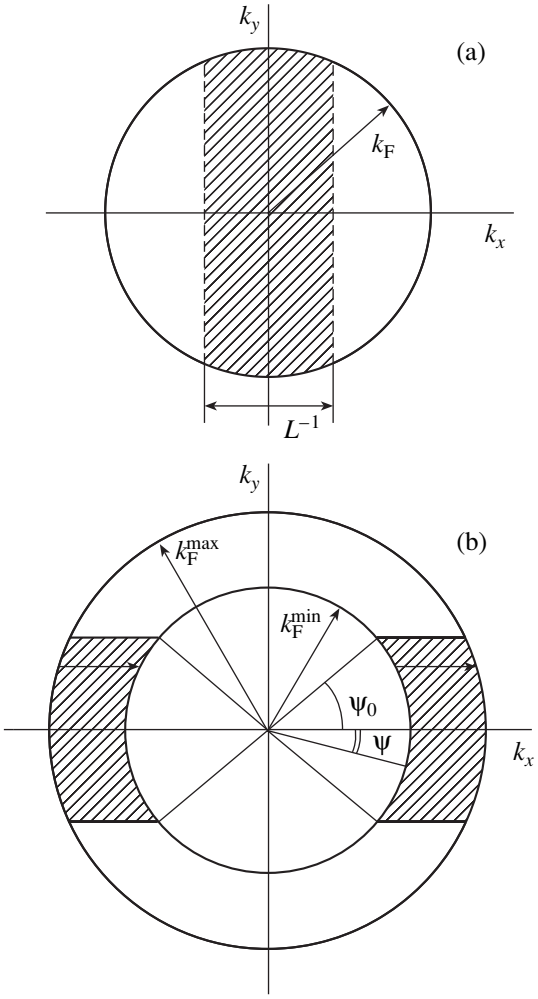

Fig. 1. Fermi surfaces (hatched regions) filled with charge carriers most strongly scattered by domain walls (a) without a spin flip and (b) with a spin flip.

It should be noted that scattering of charge carriers by domain walls affects only the σ_{xx} component of the electrical conductivity tensor of the ferromagnet and leaves the two other diagonal components unchanged: $\sigma_{yy} = \sigma_{zz} = \sigma_0$.

The above charge carriers with $|k_x| \le (\pi L)^{-1}$ constitute a fraction of the order of $|k_x|/k_F$ and have a low velocity v_x ($v_x = \hbar k_x/m \ll v_F$). Hence, the small correction to the electrical conductivity $\Delta\sigma_{xx}/\sigma_0$ for scattering of charge carriers by domain walls without a spin flip can be estimated as

$$\left(\frac{\Delta\sigma_{xx}}{\sigma_0}\right)_B \sim -\frac{\tau\hbar}{8\pi mbL^4 k_F^3} \sim -\frac{\tau\varepsilon_F}{4\pi\hbar(k_F b)(k_F L)^4}, \quad (12)$$

where τ is the characteristic mean free time in the absence of domain walls.

4.2. Scattering with a Spin Flip

For $J \ll \varepsilon_F$, the main contribution to charge carrier scattering with a spin flip is made not by the processes of reflection from a domain wall ($k_x' \approx -k_x$) but by the processes illustrated in Fig. 1b.

The dependence of the magnitude of the transferred wave vector on the initial value k_x can be represented by the following relationship:

$$|k_x' - k_x| = \sqrt{(k_x)^2 + (k_F^{max})^2 - (k_F^{min})^2} - k_x, \quad (13)$$

where k_F^{max} and k_F^{min} are the Fermi wave vectors of two subbands. Note that, in this case, the wave vectors satisfy the equation

$$\frac{\hbar^2}{2m}[(k_F^{max})^2 - (k_F^{min})^2] = 2J.$$

The minimum value of $|k_x' - k_x|$ is equal to $q_0 = k_F^{max} - k_F^{min}$ and corresponds to $\sin\psi = 0$ (see Fig. 1b). As the parameter ψ increases, the magnitude $|k_x' - k_x|$ increases and reaches $\sqrt{(k_F^{max})^2 - (k_F^{min})^2}$ at $\psi = \pi/2$.

Since the matrix element A_{k_x', k_x} decreases exponentially with an increase in $|k_x' - k_x|$, strong scattering is observed for charge carriers obeying the condition

$$|\sin\psi| \le \sin\psi_0 = (q_0 L)^{-1/2}. \quad (14)$$

For these carriers, the scattering probability has the form

$$w_2 = \frac{2\pi D_x}{\hbar}\int dk_x' |A_{k_x', k_x}|^2 \delta\left[\frac{\hbar^2 (k_x')^2}{2m} - \frac{\hbar^2 k_x^2}{2m} + 2J\right] \approx \frac{4\pi^3 \varepsilon_F}{\hbar (k_F b)} \exp(-\pi q_0 L). \quad (15)$$

In our case, unlike the case of scattering without a spin flip, the efficiently scattered carriers are characterized by the highest possible velocity v_x. It should also be noted that, in the process under consideration, the wave vector k_x changes by a relatively small value (q_0/k_F).

Finally, the expression for the correction $(\Delta\sigma_{xx}/\sigma_0)_A$ to the electrical conductivity takes the form

$$\left(\frac{\Delta\sigma_{xx}}{\sigma_0}\right)_A \sim -\frac{4\pi^2 \varepsilon_F \tau}{\hbar (k_F b)(k_F L)} \exp(-\pi q_0 L). \quad (16)$$

In addition to the above corrections to the electrical conductivity for charge carrier scattering or, in other words, the corrections determined by the contribution of the operator $\hat{W}$ to the imaginary component of the self-energy part of the Green's function for charge carriers, there exist both corrections associated with the contribution of the operator $\hat{W}$ to the real component of the self-energy part of the Green's function and corrections for a change in the current-density operator due to the gauge transformation [4, 6].

These corrections differ from those described by relationships (12) and (16) in that they do not contain the characteristic mean free time τ. Integration over the region far from the Fermi surface, to the second order in the perturbation theory for the operator $\hat{W}$, leads to a correction to the charge-carrier dispersion law. For an isotropic nonmagnetic metal, the contribution associated with the scattering of charge carriers by point defects introduces a correction to the dispersion law, which does not depend on the wave vector and spin and represents the renormalization of the chemical potential [10]. For a ferromagnetic metal with two subbands, analogous corrections prove to be different for these subbands owing to the difference in the densities of states and bring about their relative displacement, i.e., a change in the subband splitting J. A similar effect is observed in the presence of domain walls. Moreover, the above correction to the energy depends on the wave vector k_x due to anisotropy of the interaction between charge carriers and domain walls, which, in turn, results not only in the relative displacement of the subbands but also in a violation of the dispersion law. Since all these effects do not give rise to scattering, their contribution to the resistance is associated with changes both in the density of states and in the matrix elements describing the interaction of charge carriers with impurities and phonons. As a consequence, the relative correction to the electrical resistance does not depend on the mean free time τ.

The corrections described above were analyzed by Tatara and Fukuyama [4] and Brataas *et al.* [6]. For actual ratios between the relaxation times of the charge carriers involved in different subbands, the correction to the electrical conductivity $\Delta\sigma/\sigma$ was determined as

$$\left(\frac{\Delta\sigma}{\sigma}\right)_C = -\frac{\Delta\rho}{\rho} \sim -\gamma \frac{\pi}{2(bk_F)(Lk_F)}, \quad (17)$$

where ρ is the electrical resistivity and $\gamma \sim 2$–3.

In our calculations, we used the following parameters characteristic of metals: $k_F \sim 1$ Å^{-1}, $L \sim 300$ Å, $b \sim 3000$ Å, $\tau \sim 10^{-13}$ s, $\varepsilon_F \sim 3$ eV, and $q_0 \sim 0.1$ Å^{-1}. As a result, we found that $(\Delta\sigma_{xx}/\sigma_0)_B \sim 10^{-12}$, $(\Delta\sigma_{xx}/\sigma_0)_C \sim 3 \times 10^{-6}$, and $(\Delta\sigma_{xx}/\sigma_0)_A$ is negligible. Therefore, conventional wide domain walls do not appreciably contribute to the resistance and, consequently, to the magnetoresistance associated with the disappearance of domain walls in a magnetic saturation field.

5. FERROMAGNET–ANTIFERROMAGNET MULTILAYER MAGNETIC STRUCTURES

Since the discovery of the phenomenon of giant magnetoresistance in multilayer magnetic structures [11], these structures have been attracting close research attention. In recent years, the particular interest expressed by scientists engaged in this field has shifted to multilayer structures of the ferromagnet–layered antiferromagnet type. According to neutron diffraction investigations [12, 13], a few examples of such structures are provided by Fe/Cr multilayer structures in which a chromium layer of thickness $d < 45$ Å is considered as a set of ferromagnetic planes with antiparallel spin orientations in adjacent planes. Spins of chromium atoms lie in these planes, which, in turn, are aligned on average parallel to interlayer boundaries. A similar structure was observed in manganese layers in Fe/Mn multilayer structures [14, 15].

The presence of atomic steps (changing the thickness of the antiferromagnet by one monoatomic layer) at interlayer boundaries brings about frustrations in the ferromagnet–antiferromagnet system (Fig. 2a). The uniform distribution of order parameters in the layers ceases to correspond to an energy minimum.

Using a ferromagnet–antiferromagnet–ferromagnet three-layer system as an example, Levchenko *et al.* [16] examined "thickness–roughness" phase diagrams of multilayer magnetic structures. If the distance between the atomic steps on the surface of a layer (step width R) exceeds a critical value (domain-wall thickness), separation of ferromagnetic layers into domains with parallel and antiparallel orientations of ferromagnetic layer magnetizations becomes energetically favorable. Domain walls penetrate through all three layers, and their coordinates in the plane of layers coincide with those of atomic step edges on either of the two interfaces. The magnetizations of the ferromagnetic layers in a domain wall experience rotations in opposite directions. The antiferromagnetic order parameter rotates together with the magnetization vector of the ferromagnetic layer whose boundary with the antiferromagnetic layer does not contain a step at the given place (Fig. 2b).

An examination of the structure of domain walls created by frustrations [16] demonstrated that the characteristic domain-wall thickness amounts to several dozens of angstrom units; i.e., these unusual domain walls are considerably narrower than usual domain walls whose thicknesses are determined by competition between the exchange energy and the energy of anisotropy in a ferromagnet. The thickness δ_f of a domain wall created by a frustration in a ferromagnetic layer was estimated as

$$\delta_f \approx a\sqrt{\eta}, \tag{18}$$

where a is the layer thickness and η is the ratio between the exchange interaction energies of the nearest spins in the ferromagnetic and antiferromagnetic layers. For a = 10 Å and $\eta = 3$, we obtain the domain-wall thickness

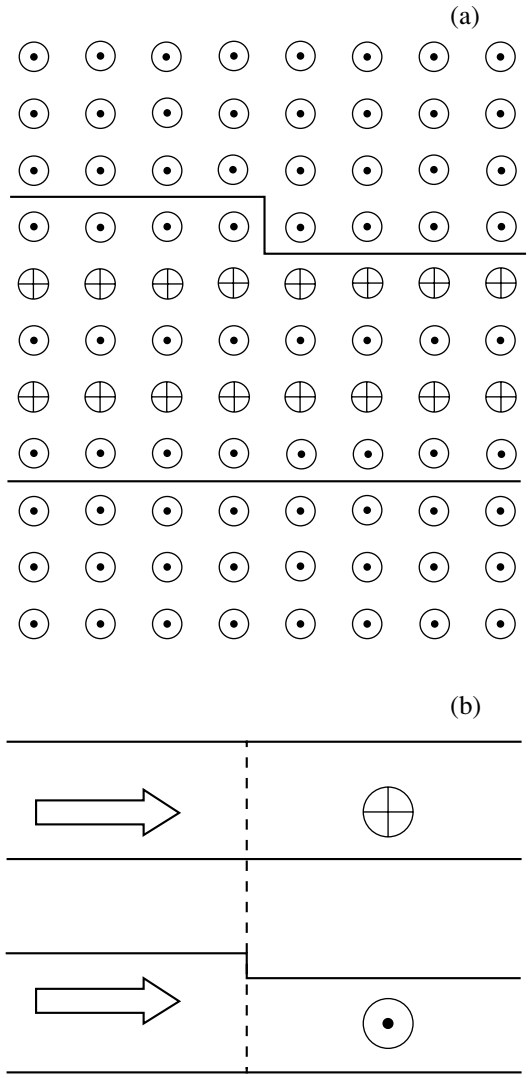

Fig. 2. (a) A frustration induced in a ferromagnet–antiferromagnet–ferromagnet system due to the presence of a step at the interlayer boundary and (b) the domain wall created by the frustration.

$\delta_f \approx 20$ Å. The size R of domains created by frustrations can be of the order of 100 Å. Upon substituting these values for L and b into formulas (12), (16), and (17), we obtain

$$(\Delta\sigma_{xx}/\sigma_0)_B \sim 10^{-6}, \quad (\Delta\sigma_{xx}/\sigma_0)_C \sim 2 \times 10^{-3},$$
$$(\Delta\sigma_{xx}/\sigma_0)_A \sim 0.02.$$

Therefore, in the case of unusual domain walls, it is this scattering of charge carriers by domain walls that makes a dominant contribution to the resistance, namely, the contribution A. It should be noted that the contribution A can be substantially greater in the case of thinner layers due to its exponential dependence on L. Moreover, this contribution increases at low temperatures as the result of an increase in the mean free time of charge carriers.

Domain walls are also created in antiferromagnetic layers. The theoretical treatment of charge carrier scattering by domain walls in these layers is identical to the analysis performed above. For a collinear antiferromagnet, degeneracy of the dispersion law of charge carriers with respect to the spin persists; hence, upon reflection from a domain wall, we have $A_{-k_x, k_x} = 0$ and the corresponding contribution to the resistance vanishes. The contribution from charge carrier scattering without a spin flip and the contribution $(\Delta\sigma_{xx}/\sigma_0)_C$ to the resistance for a collinear antiferromagnet are of the same order of magnitude as those for a ferromagnet. Therefore, the contribution from scattering of charge carriers by domain walls to the resistance of antiferromagnetic layers is less than that of ferromagnetic layers.

In the case when the domain walls break down in an external magnetic field, their contribution to the resistance vanishes and, as a consequence, the magnetoresistance becomes negative. Since the contribution under consideration is proportional to the concentration of domain walls, it reaches a maximum at $R \sim \delta_f$. At smaller R values, overlap of domain walls results in the transition to a state in which ferromagnetic layers are virtually homogeneous [16].

6. CONCLUSIONS

Thus, the main inferences drawn in the present work can be summarized as follows.

(1) For usual domain walls, the contribution made by domain walls to charge carrier scattering is insignificant and the key role is played by the renormalization of the dispersion law and the wave functions of charge carriers.

(2) For unusual domain walls created by frustrations, the dominant contribution made by domain walls to the magnetoresistance of ferromagnet–antiferromagnet multilayer magnetic structures is associated with the scattering of charge carriers by these walls.

(3) The magnetoresistance induced by this effect can be as high as 1–10%.

ACKNOWLEDGMENTS

This work was supported in part by the Russian–American Program of the Ministry of Education of the Russian Federation and the American Foundation for Civilian Research and Development for the promotion of cooperation with scientists from the New Independent States of the former Soviet Union (CRDF) (project no. VZ-010-0) and by the Russian Foundation for Basic Research (project no. 00-02-17162).

REFERENCES

1. G. G. Cabrera and L. M. Falicov, Phys. Status Solidi B **61** (2), 539 (1974); Phys. Status Solidi B **62** (1), 217 (1974).
2. J. F. Gregg, W. Allen, K. Ounadjela, *et al.*, Phys. Rev. Lett. **77** (8), 1580 (1996).
3. P. M. Levy and S. Zhang, Phys. Rev. Lett. **79** (25), 5110 (1997).
4. G. Tatara and H. Fukuyama, Phys. Rev. Lett. **78** (19), 3773 (1997).
5. R. P. van Gorkom, A. Brataas, and G. E. W. Bauer, Phys. Rev. Lett. **83** (21), 4401 (1999).
6. A. Brataas, G. Tatara, and G. E. W. Bauer, Phys. Rev. B **60** (5), 3406 (1999).
7. E. Simanek, Phys. Rev. B **63**, 224412 (2001).
8. R. Danneau, P. Warin, J. P. Attane, *et al.*, Phys. Rev. Lett. **88**, 157201 (2002).
9. V. K. Dudaev, J. Barnas, A. Lusakowski, and L. A. Turski, Phys. Rev. B **65**, 224419 (2002).
10. A. A. Abrikosov, L. P. Gor'kov, and I. E. Dzyaloshinskiĭ, *Methods of Quantum Field Theory in Statistical Physics* (Fizmatgiz, Moscow, 1962; Prentice Hall, Englewood Cliffs, N.J., 1963), Sect. 39.
11. M. N. Baibich, J. M. Broto, A. Fert, *et al.*, Phys. Rev. Lett. **61** (21), 2472 (1988).
12. A. Schreyer, C. F. Majkrzak, Th. Zeidler, *et al.*, Phys. Rev. Lett. **79** (24), 4914 (1997).
13. P. Bodeker, A. Schreyer, and H. Zabel, Phys. Rev. B **59** (14), 9408 (1999).
14. M. Chirita, G. Robins, R. L. Stamp, *et al.*, Phys. Rev. B **58** (2), 869 (1998).
15. S. Yan, R. Schreiber, F. Voges, *et al.*, Phys. Rev. B **59** (18), R11641 (1999).
16. V. D. Levchenko, A. I. Morozov, and A. S. Sigov, Zh. Éksp. Teor. Fiz. **121** (5), 1149 (2002) [JETP **94**, 985 (2002)].

Translated by O. Borovik-Romanova

Physics of the Solid State, Vol. 45, No. 8, 2003, pp. 1493–1499. Translated from Fizika Tverdogo Tela, Vol. 45, No. 8, 2003, pp. 1423–1428.

MAGNETISM AND FERROELECTRICITY

Effect of Nickel on the Magnetic State of Dysprosium in $Dy_{1-x}Ni_x$–Ni Bilayer Films

I. S. Édelman*, V. V. Markov*, S. G. Ovchinnikov*, A. E. Khudyakov*, V. N. Zabluda*, V. G. Kesler, and G. V. Bondarenko***

** Kirensky Institute of Physics, Siberian Division, Russian Academy of Sciences, Akademgorodok, Krasnoyarsk, 660036 Russia*

*** Institute of Semiconductor Physics, Siberian Division, Russian Academy of Sciences, pr. Akademika Lavrent'eva 13, Novosibirsk, 630090 Russia*

e-mail: ise@iph.krasn.ru

Received December 25, 2002

Abstract—This paper reports on the results of investigations into the temperature and spectral dependences of the magnetic circular dichroism in $Dy_{1-x}Ni_x$–Ni bilayer films prepared through thermal sputter deposition of components under ultrahigh vacuum. The distribution of the components over the layer thickness is examined by Auger spectroscopy. The nickel content x in $Dy_{1-x}Ni_x$ layers varies from 0.005 to 0.06. It is shown that, in the temperature range 80–300 K, the contribution made to the magnetic circular dichroism by a $Dy_{1-x}Ni_x$ layer in a bilayer film with a nickel content higher than the threshold value is approximately equal to the magnetic circular dichroism observed in an isolated $Dy_{1-x}Ni_x$ film at temperatures below the temperature of the phase transition to a ferromagnetic state (~100 K). This phenomenon is explained by magnetic ordering in the $Dy_{1-x}Ni_x$ layer of the bilayer film due to the combined effect of two factors, namely, the incorporation of nickel into a dysprosium layer and the presence of a continuous nickel sublayer in the film. © *2003 MAIK "Nauka/Interperiodica".*

1. INTRODUCTION

The mutual influence of 3*d* transition metals and 4*f* rare-earth elements in layered structures has been attracting considerable research attention due to the extensive use of these structures in data recording and storage devices. In recent years, particular interest has been expressed in complex magnetic structures of rare-earth metals and their high structural sensitivity to both external and internal actions. One of the factors affecting the magnetic state of rare-earth metal layers in layered structures and superlattices is the interaction of a rare-earth metal either with adjacent layers consisting of 3*d* transition metals or with 3*d* metal impurities in a layer of the rare-earth metal. Dysprosium is a convenient object for use in the study of these effects owing to its ability to undergo two magnetic phase transitions separated by a wide temperature interval: (i) the transition from the paramagnetic phase to the spiral antiferromagnetic phase at the Néel temperature $T_N = 175$ K and (ii) the transition from the spiral antiferromagnetic phase to the ferromagnetic phase at the Curie temperature $T_c = 85$ K [1–3]. It should be noted that, in this case, the temperature and character of the phase transitions occurring in dysprosium substantially depend on the applied magnetic field [1–4]. The magnetic structure of dysprosium is also strongly affected by the size and structure of the dysprosium sample. In particular, Mulyukov *et al.* [5] analyzed the influence of the crystallite size on the phase transitions in dysprosium fine-grained samples. Shevchenko *et al.* [6] showed that no spiral magnetic structure is formed in dysprosium nanoparticles distributed in an aluminum film.

There are many works concerned with the investigation of dysprosium layered structures containing 3*d* metals (see, for example, [7–9]). In our previous studies [10, 11], we revealed that 3*d* impurities at a low content (~5%) in a dysprosium layer substantially affect the temperature and spectral dependences of magneto-optical effects (linear with respect to magnetization), namely, the magnetic circular dichroism and the meridional magneto-optical Kerr effect, in $Dy_{1-x}(NiFe)_x$–NiFe and $Dy_{1-x}Fe_x$–Fe bilayer films. (Hereafter, x stands for the weight content.) It was demonstrated that, in the temperature range 80–300 K, the contribution made to the magneto-optical effect by a dysprosium layer in bilayer films containing no more than several weight percent of nickel and iron impurities is constant, temperature independent, and approximately equal to the magneto-optical effect observed in a dysprosium film only at temperatures below the temperature T_c of the phase transition to a ferromagnetic state. Moreover, we established that the magneto-optical effect does not depend on nickel and iron impurities contained in these amounts in dysprosium layers in the case when the adjacent layer of the 3*d* metal is absent. Consequently, the unusual behavior of the dysprosium magnetic system in the studied samples was explained by two factors: (1) the incorporation of transition metal

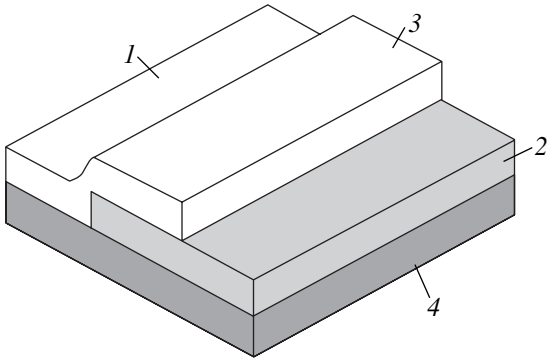

Fig. 1. Schematic drawing of a step-shaped film sample: (*1*) Dy_{1-x}–Ni_x layer, (*2*) Ni layer, (*3*) Ni–$Dy_{1-x}Ni_x$ bilayer film, and (*4*) glass substrate. The sample is separated into three parts along the visual boundaries between them.

atoms at low concentrations into the dysprosium layer throughout its depth and (2) the influence of the spin system of the adjacent transition-metal layer on the magnetic state of dysprosium through the incorporated 3*d* metal atoms. In order to gain better insight into the nature of the observed effect, it is expedient to examine the magnetic behavior of dysprosium in a bilayer film with an increase in the temperature of the 3*d* metal layer. However, since dysprosium exhibits a high reactivity, the heating of dysprosium samples leads to contradictory results. One way out is to decrease the Curie temperature of thin nickel films [12]. For a nickel bulk single crystal, the Curie temperature T_c is equal to 631 K [13]. The second important problem is to elucidate how the concentration of 3*d* metal atoms distributed in the layer of dysprosium affects its magnetic state. Moreover, the changeover from the NiFe alloy films studied in [9, 10] to one-component (nickel) layers should facilitate interpretation of the results. In the present work, the magnetic circular dichroism in $Dy_{1-x}Ni_x$ and Ni single-layer films and $Dy_{1-x}Ni_x$–Ni bilayer films was investigated as a function of the nickel content x and the thickness of the nickel layer.

2. SAMPLE PREPARATION AND EXPERIMENTAL TECHNIQUE

Samples were prepared by sputtering components from isolated sources under ultrahigh vacuum on an Angara molecular-beam epitaxy setup specially adapted for sputter deposition [14]. Films were deposited on glass substrates (thickness, 0.8 mm; optical quality; surface finish class, 13) at a temperature of 250°C. The sputtered materials were Ni (vacuum melting) and Dy (class DiM 1). The deposition rates for nickel and dysprosium were approximately equal to 0.05 and 2.00 Å s^{-1}, respectively. First, a nickel layer was deposited on the substrate. Then, nickel and dysprosium were sputtered simultaneously. A step-shaped film sample prepared with the use of flaps is represented schematically in Fig. 1. Three samples were obtained by this method under identical conditions: a Ni single-layer film, a $Dy_{1-x}Ni_x$ single-layer film, and a Ni–$Dy_{1-x}Ni_x$ bilayer film. The thickness of each layer in the bilayer film was equal to the thickness of the corresponding single-layer film. The nickel content in the dysprosium layer and the thickness of nickel layers were specified by the conditions of nickel sputtering. We prepared several series of film samples with 50- to 120-Å-thick Ni layers. The thickness of dysprosium layers was varied from 400 to 900 Å. For all samples, the content of each component was determined by x-ray fluorescence analysis.

The magnetic circular dichroism in the spectral range 350–650 nm was measured as the difference between the optical densities $\Delta D = (D_+ - D_-)$ obtained for the right-hand and left-hand circular polarizations of the light wave with respect to the direction of an external magnetic field. The magnetic field was directed perpendicularly to the sample plane and reached 5.0 kOe. The measurements of the magnetic circular dichroism were performed with the use of modulation of a light wave (from the right-hand to left-hand circular polarization) which was described for the first time by Jasperson and Schnatterly [15]. The accuracy in measuring the magnetic circular dichroism was equal to $\pm 10^{-4}$. The temperature investigations were carried out with samples placed in a nitrogen-flow cryostat in the range 80–300 K. The temperature was controlled accurate to within ±1 K. It is known that, by definition, the magnetic circular dichroism can only be observed in absorbing media. For this reason, neither a glass substrate nor quartz windows of the cryostat contribute to the measured value of magnetic circular dichroism. The magnetic circular dichroism was measured immediately after the samples were prepared.

The distribution of the components over the area and thickness of the samples was determined by Auger electron spectroscopy [16] (sensitivity, 0.3 at. %) after the magneto-optical measurements. The Auger electron spectra of the sample surfaces were recorded on a Riber OPC-2 Auger cylindrical-mirror analyzer with a relative resolution of 0.2%. The secondary electron spectrum was excited by an electron beam with an energy of 3 keV. The electron beam diameter was equal to 5 μm, and the electron beam current amounted to 100 nA. The high-voltage modulation of the analyzer used was 6.88 eV. For a layer-by-layer analysis, ion sputtering was accomplished using an argon ion beam with an energy of 3 keV at an ion beam current of 600 nA and a rate of approximately 10 Å/min. Since the substrate was prepared from a nonconducting material (glass), it was impossible to obtain spectral data for the film–glass interface due to strong charging of the glass surface. During the layer-by-layer analysis, the Auger signals of elements (Dy, 155 eV; Ni, 848 eV; O, 512 eV; and C, 272 eV) were measured as functions of the time

of sputter deposition of the sample with an argon ion beam.

In order to control the degree of oxidation of the dysprosium layers, the electrical conductivity of some samples was measured after the magneto-optical measurements.

3. RESULTS AND DISCUSSION

Figure 2 displays the Auger signals of the main elements in a Ni–Dy bilayer film ($x = 0$). As can be seen from this figure, nickel impurities are virtually absent throughout the entire thickness of the dysprosium layer, in contrast with the situation discussed in our earlier work [11]. It is worth noting that the oxygen content in the Ni–Dy bilayer film is relatively high, especially at the interfaces with the substrate and the atmosphere. A similar oxygen distribution is observed in a dysprosium single-layer film. In [11], we considered the problem of dysprosium oxidation in sufficient detail. It was demonstrated that, at least during magneto-optical experiments, dysprosium remains in the metallic state and its oxidation to Dy_2O_3 occurs only upon heating to a temperature of ~400°C. This inference is confirmed by the measurements of the electrical conductivity. For example, after the magneto-optical measurements, the electrical resistivity of the 600-Å-thick dysprosium film was equal to 5×10^{-5} Ω cm. In the case when nickel and dysprosium were sputtered simultaneously, nickel impurities were observed throughout the dysprosium layer at a content x ranging from 0.005 to 0.06 depending on the rate of nickel deposition.

The temperature dependences of the reduced magnetic circular dichroism ($MCD_T/MCD_{T = 90\,K}$) for nickel single-layer films of different thicknesses are depicted in Fig. 3. The magnetic circular dichroism of nickel has negative sign, as is the case with the magnetic circular dichroism of permalloy and iron [11]. The dependence of the magnetic circular dichroism on the wavelength is similar to the spectral dependence of the meridional magneto-optical Kerr effect for a nickel single crystal measured by Buschow *et al.* [17]: the magnetic circular dichroism is nearly constant in the wavelength range 400–700 nm and decreases rapidly with a decrease in the wavelength to 320 nm. Since the magnetic circular dichroism is a linear function of the magnetization, there is a one-to-one correspondence between the temperature dependences of the magnetization and magnetic circular dichroism of the studied samples. These dependences differ from the curves observed for nickel bulk crystals (see [13, Fig. 18.1]). As can be seen from Fig. 3, the smaller the film thickness, the larger the difference. For a nickel film with a minimum used thickness (~50 Å), the magnetic circular dichroism decreases by a factor of approximately two as the temperature increases from 80 to 300 K. For a nickel bulk crystal, the magnetization in this temperature range changes by ~5%. The above temperature behavior of

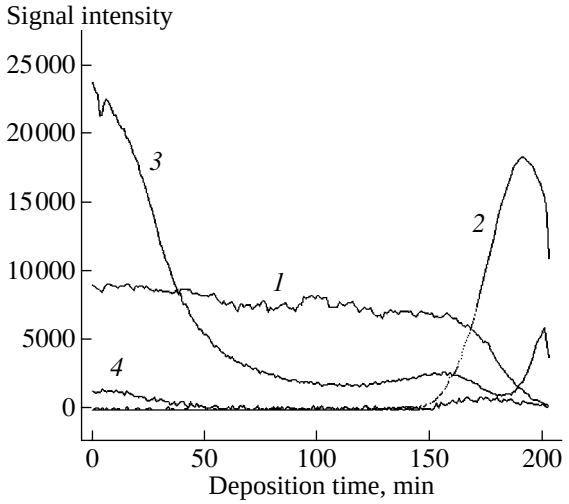

Fig. 2. Auger signals of the main elements in an Ni–Dy bilayer film: (*1*) dysprosium, (*2*) nickel, (*3*) oxygen, and (*4*) carbon. $d_{Ni} = 10$ nm, $d_{Dy} = 60$ nm.

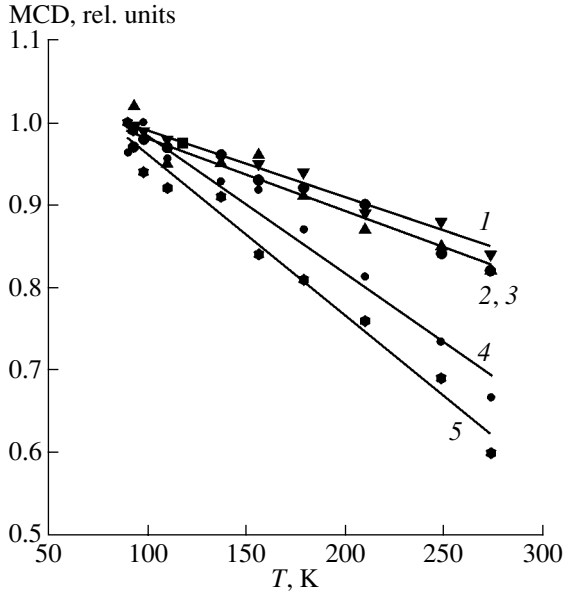

Fig. 3. Reduced temperature dependences of the magnetic circular dichroism ($MCD_T/MCD_{T = 90\,K}$) for nickel films of different thicknesses in the magnetic field $H = 4.5$ kOe at the wavelength $\lambda = 520$ nm. Film thickness: (*1*) 10 (*2*, *3*) 12, (*4*) 8, and (*5*) 6 nm.

the magnetic circular dichroism is similar to the temperature behavior observed for magnetization of very thin layers of nickel in [12] and, hence, can be used to compare the temperature dependences of the magnetic circular dichroism of $Dy_{1-x}Ni_x$ and Ni layers.

For dysprosium films, the temperature and spectral dependences of the magnetic circular dichroism are in good agreement with the data reported in our recent

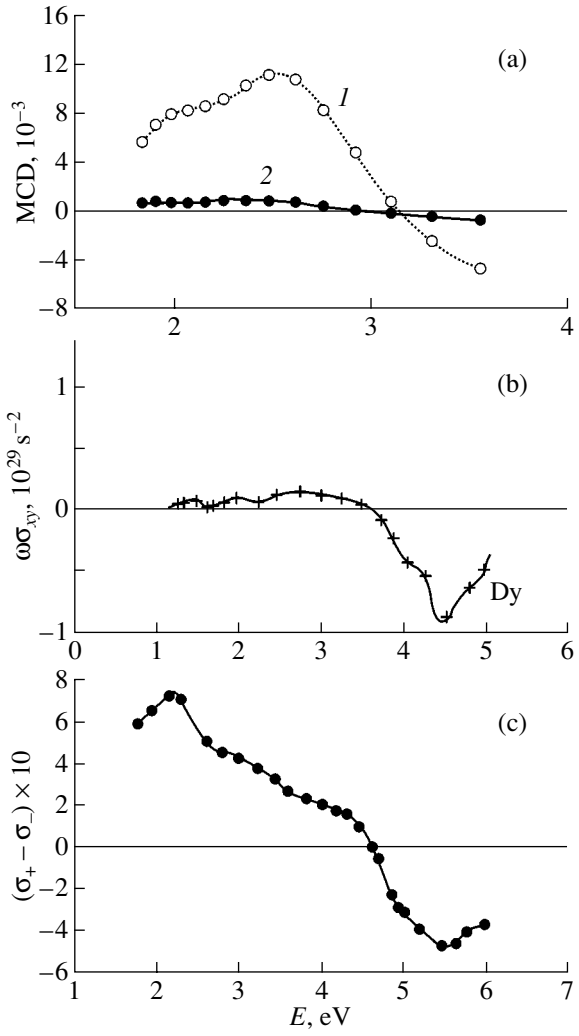

Fig. 4. (a) Magnetic circular dichroism spectra for a dysprosium film measured in a magnetic field of 5 kOe at temperatures of (*1*) 93 and (*2*) 300 K. (b) Spectrum of the off-diagonal component of the optical conductivity tensor for dysprosium [19]. (c) Difference in the optical conductivities for "+" and "–" electrons [20].

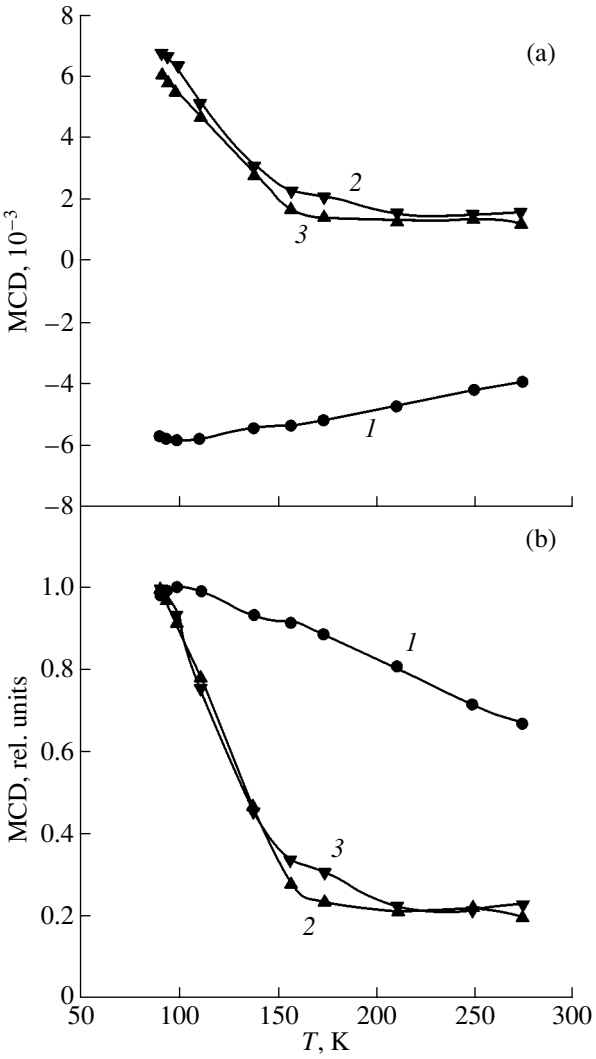

Fig. 5. Temperature dependences of the magnetic circular dichroism for (*1*) the Ni film (d = 6 nm), (*2*) the $Dy_{0.995}Ni_{0.005}$ film (d = 75 nm), and (*3*) the $Dy_{0.995}Ni_{0.005}$ layer in the Ni–$Dy_{0.995}Ni_{0.005}$ bilayer film according to (a) experimental data and (b) reduced magnitudes $MCD_T/MCD_{T = 90\ K}$. H = 4.5 kOe, λ = 520 nm.

paper [11]. Figure 4a shows the magnetic circular dichroism spectra for a dysprosium film measured in a magnetic field of 5 kOe at temperatures of 93 and 300 K. These spectra exhibit the following specific features. First, the magnetic circular dichroism at room temperature has a finite value and is approximately one order of magnitude less than that at a temperature of 93 K. The same ratio was observed for the magnetizations of fine-grained dysprosium samples measured at room and liquid-nitrogen temperatures by Mulyukov *et al.* [5]. For both temperatures, the magnetic circular dichroism reverses sign at an energy of about 3 eV. It should be noted that the point of sign reversal is somewhat displaced to higher energies with a decrease in the temperature. In the energy range 2–3 eV, there arises a pronounced maximum. In the same spectral range, Knyazev and Noskov [18] observed a maximum in the optical conductivity $\sigma = nk\nu$ for dysprosium. The magnetic circular dichroism spectra for different samples of dysprosium are similar to one another. Small differences observed in the vicinity of the maximum can be associated with imperfection of the films. However, the point at which the magnetic circular dichroism reverses sign remains the same for all the studied samples. The curve of the magnetic circular dichroism is closely similar to that of both the off-diagonal component of the optical conductivity tensor σ_{xy} given in [19] (Fig. 4b) and the difference in the optical conductivities determined in [20] for "+" and "–" electrons from the calculated densities of states of these electrons (Fig. 4c). As can be seen, the point of sign reversal for the above effects is displaced toward an increase in the light wave

energy upon changing over from the magnetic circular dichroism (Fig. 4a) to the off-diagonal component of the optical conductivity tensor (Fig. 4b) and then to the difference in the optical conductivities (Fig. 4c). Note that the curves depicted in Figs. 4a and 4b differ only slightly.

The magnetic circular dichroism of the Dy–Ni bilayer film, for which the Auger spectrum is displayed in Fig. 2, is equal to the sum of the magnetic circular dichroisms of its constituent layers of dysprosium and nickel at all the temperatures and wavelengths used in the measurements. A similar situation is observed at a low nickel content in a dysprosium layer. Figure 5 shows the temperature dependences of the magnetic circular dichroism for an Ni film (curve *1*), a $Dy_{0.995}Ni_{0.005}$ film (curve *2*), and a $Dy_{0.995}Ni_{0.005}$ layer in the Ni–$Dy_{0.995}Ni_{0.005}$ bilayer film (curve *3*). Curve *3* was obtained as the difference between the values of the magnetic circular dichroism measured in the bilayer film and the nickel single-layer film prepared in the same cycle of deposition. It can be seen from Fig. 5 that curves *2* and *3* almost coincide with each other. This suggests that nickel impurities at a content of 0.5% have no effect on the magnetic properties of dysprosium either in the form of a single-layer film or in the case when this film is applied on the nickel layer. However, at a nickel content $x \approx 0.01$ (i.e., 1.0%), the magnetic circular dichroism of the bilayer film differs from the sum of the magnetic circular dichroisms of the $Dy_{0.99}Ni_{0.01}$ and Ni layers (Fig. 6). For the $Dy_{0.99}Ni_{0.01}$ layer in the bilayer film at room temperature, the magnetic circular dichroism has a relatively large value. The sign of the observed effect corresponds to the sign of the magnetic circular dichroism in a single-layer film of the same composition. In the temperature range 120–300 K, the magnetic circular dichroism in both cases does not depend on the temperature. As the temperature decreases below 120 K, the magnetic circular dichroism in the $Dy_{0.99}Ni_{0.01}$ layer of the bilayer film increases in the same manner as in the $Dy_{0.99}Ni_{0.01}$ single-layer film. It is clearly seen that the temperature dependences of the magnetic circular dichroism in nickel (curve *1*) and $Dy_{0.99}Ni_{0.01}$ (curves *2*, *3*) films differ significantly. With a further increase in the nickel content *x*, the similarity of the temperature dependences of the magnetic circular dichroism for $Dy_{1-x}Ni_x$ single-layer films to those for single-layer films of the same composition but applied on the nickel layer gradually becomes less pronounced. In the entire temperature range covered, the magnetic circular dichroism of a $Dy_{1-x}Ni_x$ layer (x = 0.02) applied on the nickel layer is close to that measured for an isolated $Dy_{1-x}Ni_x$ layer at a temperature of 90 K. It is worth noting that the temperature dependence of the magnetic circular dichroism of the former $Dy_{1-x}Ni_x$ layer is very similar to that of the nickel film (Fig. 6, curve *4*). An increase in the nickel content *x* also leads to some variations in the spectral dependences of the magnetic circular dichroism of the $Dy_{1-x}Ni_x$ layer applied on the nickel layer. For example, the point at which the magnetic circular dichroism reverses sign is displaced to higher energies.

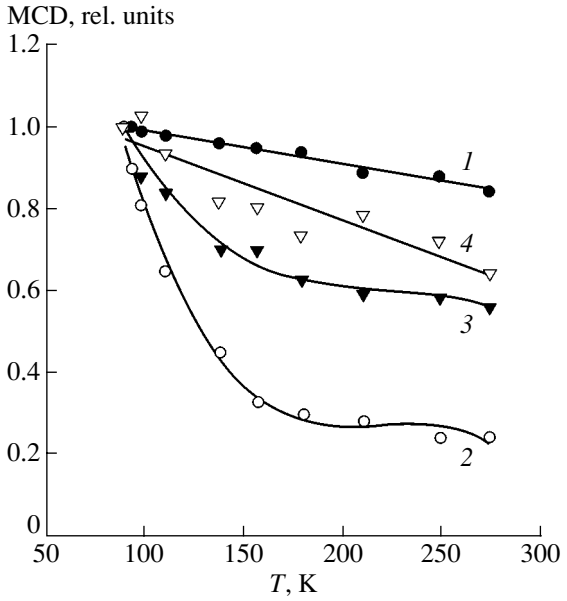

Fig. 6. Reduced temperature dependences of the magnitude of the magnetic circular dichroism ($MCD_T/MCD_{T=90\ K}$) for (*1*) the Ni film (d = 10 nm), (*2*) the $Dy_{0.95}Ni_{0.05}$ film (d = 60 nm), (*3*) the $Dy_{0.98}Ni_{0.02}$ layer in an Ni–$Dy_{1-x}Ni_x$ bilayer film, and (*4*) the $Dy_{0.95}Ni_{0.05}$ layer in an Ni–$Dy_{1-x}Ni_x$ bilayer film. H = 4.5 kOe, λ = 520 nm.

Summing up the above results of the magnetic circular dichroism measurements, we can draw the following conclusions: (i) nickel impurities in a dysprosium layer substantially affect the temperature and spectral dependences of the magnetic circular dichroism only in the case when the $Dy_{1-x}Ni_x$ layer is in contact with a nickel continuous layer; (ii) the threshold content of nickel in the dysprosium layer at which the temperature dependence of the magnetic circular dichroism of the $Dy_{1-x}Ni_x$ single-layer film ceases to be similar to that of a single-layer film of the same composition but applied on the nickel layer amounts to ~2%; and (iii) at a nickel content of approximately 2%, the temperature dependence of the magnetic circular dichroism of the $Dy_{1-x}Ni_x$ layer in a bilayer film is very similar to that of the nickel film. The last result is in agreement with the data obtained in our previous works [10, 11] concerned with the study of $Dy_{1-x}(Ni_{80}Fe_{20})_x$–NiFe and $Dy_{1-x}Fe_x$–Fe bilayer films with a content of $Ni_{80}Fe_{20}$ or Fe in the dysprosium layer approximately equal to 3%. As was shown in [10, 11], in the temperature range 80–300 K, the magnetic circular dichroism in $Ni_{80}Fe_{20}$ and Fe layers does not depend on temperature and the contribution made to the magnetic circular dichroism by a dysprosium layer containing nickel and iron impurities and involved in a bilayer film is also

temperature independent. The magnetic circular dichroism observed at temperatures considerably above the temperature of ferromagnetic ordering of a dysprosium bulk crystal (T_C = 85 K) can be associated with magnetic ordering in the $Dy_{1-x}Ni_x$ layer. The sign of the magnetic circular dichroism indicates that the magnetic moment of the $Dy_{1-x}Ni_x$ layer in the situation under investigation is aligned parallel to the magnetic moment of the nickel layer.

The magnetic polarization of 4*f* electrons of rare-earth metals on the surface of 3*d* metals was analyzed earlier theoretically and observed experimentally in very thin layers. In particular, Carbone *et al.* [21] observed the polarization of 4*f* electron spins in dysprosium monoatomic layers applied on the surface of a single crystal or a 3*d* metal film. The spin moments of dysprosium were antiparallel to those of the crystal surface or the 3*d* metal layer. Judging from the strong dependence of the temperature behavior of the magnetic circular dichroism in the $Dy_{1-x}Ni_x$ layer on the nickel content *x*, it can be assumed that, in the case under consideration, impurity nickel atoms and their bonds with a nickel continuous magnetically ordered layer are responsible for the effect of the 3*d* metal on the magnetic state of dysprosium at a large depth of the dysprosium layer.

Matveeva and Egorov [20] noted that, in the spectrum of dysprosium (Fig. 4c), excitations at low energies dominate in the system of "–" electrons, whereas excitations at high energies dominate in the system of "+" electrons. A drastic increase in the conductivity at the expense of "+" electrons near 4 eV corresponds to the threshold of 4*f* excitations. The magnetic circular dichroism and the off-diagonal component of the optical conductivity tensor σ_{xy} should also reverse sign at about the same energy, which is observed in the experiment. Therefore, the displacement of the point at which the magnetic circular dichroism passes through zero for the $Dy_{1-x}Ni_x$ single-layer film applied on the nickel layer is most likely associated with the transformation in the electronic structure of either the $Dy_{1-x}Ni_x$ layer or the film as a whole.

As is known [3], the magnetic structure of heavy rare-earth metals, including dysprosium, is determined primarily by the exchange interaction of conduction electrons with 4*f* electrons. The introduction of nickel atoms into a dysprosium layer leads to changes in the system of conduction electrons. The magnetic moments of nickel atoms can be polarized because of the presence of a continuous, magnetically ordered nickel layer. The threshold weight content of nickel at which dysprosium at room temperature undergoes magnetic ordering is approximately equal to 2%. With due regard for the atomic weights of the components, this value corresponds to ~5 vol %. It can easily be shown that, in the case of a uniform distribution of nickel over the dysprosium layer, the second coordination shell of each dysprosium ion contains a nickel ion with a spin aligned parallel to the magnetic moment of the nickel layer. The hybridization of Ni *d* states with Dy *f* states can stimulate magnetic ordering in the $Dy_{1-x}Ni_x$ layer. On the other hand, it can be assumed that the sample as a whole is characterized by a single system of conduction electrons. Consequently, all conduction electrons are polarized, including those provided by the Ni *s*, Dy *p*, and Dy *d* states. In this situation, spins of Dy 4*f* electrons undergo ordering due to the interaction with polarized band electrons. In both cases, the temperature dependences of the magnetization and, hence, the magnetic circular dichroism in the $Dy_{1-x}Ni_x$ layer should correlate with those of the nickel layer and with the nickel content in the dysprosium layer.

Moreover, nickel impurities bring about insignificant distortions in the dysprosium lattice because of the differences between the atomic and ionic radii (r_{Dy} = 1.773 Å, $r_{Dy^{3+}}$ = 1.07 Å, r_{Ni} = 1.25 Å, and $r_{Ni^{2+}}$ = 0.72 Å). These distortions can affect the magnetic structure of the layer due to strong spin–orbit coupling in dysprosium and competition between exchange interactions in different coordination shells. However, in this case, the magnetic ordering in the $Dy_{1-x}Ni_x$ layer should also be observed in the absence of the nickel layer, which is inconsistent with the available experimental data.

ACKNOWLEDGMENTS

This work was supported by the Russian Foundation for Basic Research, project nos. 00-02-16098 and 02-02-06734.

REFERENCES

1. D. R. Behrendt, S. Legvold, and F. H. Spedding, Phys. Rev. **109** (5), 1544 (1958).
2. K. P. Belov, *Rare-Earth Magnetic Materials and Their Application* (Nauka, Moscow, 1980).
3. S. A. Nikitin, *Magnetic Properties of Rare-Earth Metals and Alloys* (Mosk. Gos. Univ., Moscow, 1989).
4. Y. Shinoda and K. Taima, Phys. Soc. Jpn. **64**, 1334 (1995).
5. Ch. Ya. Mulyukov, G. F. Korznikova, and S. A. Nikitin, Fiz. Tverd. Tela (St. Petersburg) **37** (8), 2481 (1995) [Phys. Solid State **37**, 1359 (1995)].
6. N. B. Shevchenko, J. A. Christodoulides, and G. C. Hadjipanayis, Appl. Phys. Lett. **74**, 1478 (1999).
7. J. Tappert, J. Jungermann, B. Scholz, *et al.*, J. Appl. Phys. **76** (10), 6293 (1994).
8. K. Yoden, N. Hosoito, K. R. Kawaguchi, *et al.*, Jpn. J. Appl. Phys. **27** (9), 1680 (1988).
9. J. Tappert, W. Keune, R. A. Brand, *et al.*, J. Appl. Phys. **80** (8), 4503 (1996).
10. I. S. Édelman, A. E. Khudyakov, V. N. Zabluda, *et al.*, Pis'ma Zh. Éksp. Teor. Fiz. **67** (5), 322 (1998) [JETP Lett. **67**, 339 (1998)].

11. I. S. Édelman, V. V. Markov, V. G. Kesler, *et al.*, Fiz. Met. Metalloved. **91** (3), 60 (2001).
12. P. Poulopoulos and K. Baberschke, J. Phys.: Condens. Matter **11**, 495 (1999).
13. S. V. Vonsovskiĭ, *Magnetism: Magnetic Properties of Dia-, Para-, Ferro-, Antiferro-, and Ferrimagnets* (Nauka, Moscow, 1971).
14. E. G. Eliseeva, V. P. Kononov, V. M. Popel, *et al.*, Prib. Tekh. Éksp., No. 2, 141 (1997).
15. S. N. Jasperson and S. E. Schnatterly, Rev. Sci. Instrum. **40** (6), 6761 (1969).
16. *Practical Surface Analysis by Auger and X-ray Photoelectron Spectroscopy*, Ed. by D. Briggs and M. P. Seah (Wiley, New York, 1983; Mir, Moscow, 1987).
17. K. Y. J. Buschow, P. G. van Engen, and R. Jongebreur, J. Magn. Magn. Mater. **38**, 1 (1983).
18. Yu. V. Knyazev and M. M. Noskov, Fiz. Met. Metalloved. **30** (1), 214 (1970).
19. J. L. Erskine, G. A. Blake, and C. J. Flaten, J. Opt. Soc. Am. **64** (10), 1332 (1974).
20. T. A. Matveeva and R. F. Egorov, Fiz. Met. Metalloved. **51** (5), 950 (1981).
21. C. Carbone, R. Rochov, L. Braicovich, *et al.*, Phys. Rev. B **41** (6), 3866 (1990).

Translated by O. Borovik-Romanova

Physics of the Solid State, Vol. 45, No. 8, 2003, pp. 1500–1503. Translated from Fizika Tverdogo Tela, Vol. 45, No. 8, 2003, pp. 1429–1431.

MAGNETISM AND FERROELECTRICITY

Magnon Satellite Bands in the Optical Spectrum of Antiferromagnetic Rb_2MnCl_4

E. A. Popov* and S. G. Ovchinnikov**

** Siberian State Aerospace University, Krasnoyarsk, 660014 Russia*

*** Kirensky Institute of Physics, Siberian Division, Russian Academy of Sciences, Akademgorodok, Krasnoyarsk, 660036 Russia*

Received January 8, 2003

Abstract—The evolution of optical absorption in a two-dimensional antiferromagnet is investigated in the range of the transition ${}^6A_{1g} \longrightarrow {}^4A_{1g}, {}^4E_g({}^4G)$ observed in manganese ions in an external magnetic field inducing noncollinearity of the magnetic structure. It is revealed that hot and cold satellites of the exciton–magnon bands appear in the optical absorption spectrum and then increase in intensity. The shapes of the magnon satellite bands corresponding to a two-dimensional magnetic structure are calculated. It is demonstrated that magnons at the inner points of the Brillouin zone appreciably contribute to the absorption. The zero-point magnetic oscillations play a decisive role in the absorption associated with the magnon decay at low temperatures.

1. INTRODUCTION

As a rule, optical spectra of antiferromagnets containing ions with an open 3*d* shell are related to transitions forbidden with respect to the spin projection in the single-ion approximation. Consequently, in the optical spectra of these crystals, the intensive electrodipole absorption bands are caused by the excitation of groups of interacting ions, specifically by pairs of exchange-coupled ions belonging to different magnetic sublattices. The existence of single-magnon satellites of the exciton bands is characteristic of the absorption spectra of collinear antiferromagnets. In the case when the noncollinearity of the magnetic sublattices is induced by an external magnetic field, the optical transitions involving an even number of magnons become allowed [1]. The mechanism responsible for the formation of the light absorption bands can be elucidated by analyzing the dependences of the intensity and energy location of the absorption peak of the multimagnon satellites on the angle of canting of the magnetic sublattices. For example, the optical spectra of $RbMnCl_3$ and $CoCO_3$ compounds exhibit narrow isolated magnon satellite bands that correspond to the maxima observed in the density of exciton–magnon states at singular points of the Brillouin zone due to the participation of several magnons in light absorption [2] with the specific behavior in the magnetic field. In the present paper, we report results on the measurement of the optical absorption spectrum of an Rb_2MnCl_4 antiferromagnet in the frequency range of the transition ${}^6A_{1g} \longrightarrow {}^4A_{1g}, {}^4E_g({}^4G)$. The evolution of the absorption spectrum in the magnetic field was explained in terms of the two-dimensional magnetic structure responsible for the specific features in the density of states of quasiparticle combinations involved in optical excitations.

Crystals of Rb_2MnCl_4 at room temperature have a tetragonal structure with D_{4h}^{17} symmetry. At temperatures below the Néel point $T_N = 57$ K, the Rb_2MnCl_4 crystal is characterized by an antiferromagnetic order with easy-axis anisotropy. The magnetic moments are directed parallel to the C_4 symmetry axis of the crystal [3]. The exchange field is determined to be $H_E \approx 800$ kOe. The spin-flop transition occurs in the field $H_{SF} = 56$ kOe. The Mn^{2+} ions are located in layers perpendicular to the C_4 symmetry axis at sites of a plane square lattice of the crystal. The interlayer distance considerably exceeds the distance between the nearest neighbor Mn^{2+} ions located in the same layer. As a result, the intralayer exchange interaction between the Mn^{2+} ions is two orders of magnitude stronger than the interlayer exchange interaction, which causes the two-dimensional (2D) behavior of the magnetic system of the crystal.

2. EXPERIMENTAL TECHNIQUE

The optical absorption spectra of Rb_2MnCl_4 crystals were measured on a spectrometer with a resolution of 3 Å/mm. Magnetic fields with a strength up to 230 kOe were generated in a pulsed solenoid with a pulse duration of 20 ms. The spectra were recorded on photographic film.

1063-7834/03/4508-1500$24.00

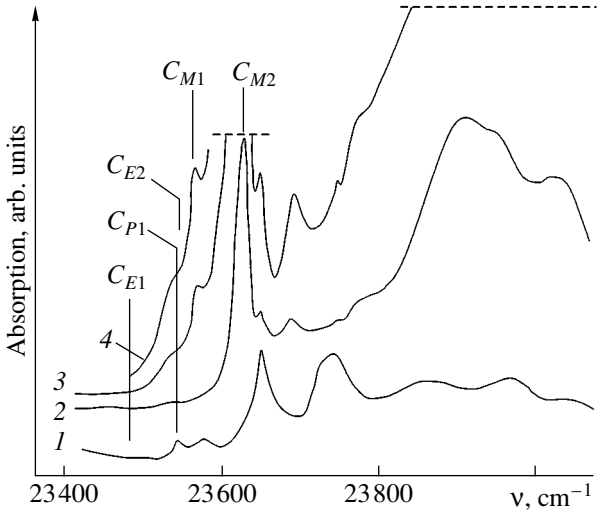

Fig. 1. Polarized spectra of Rb_2MnCl_4 crystals in the range of the transition ${}^6A_{1g} \longrightarrow {}^4A_{1g}, {}^4E_g({}^4G)$ at $T = 4.2$ K: (*1*) π polarization, $h = 2.2$ mm; (*2*) α polarization, $h = 0.14$ mm; (*3*) α polarization, $h = 0.5$ mm; and (*4*) σ polarization, $h = 1.51$ mm.

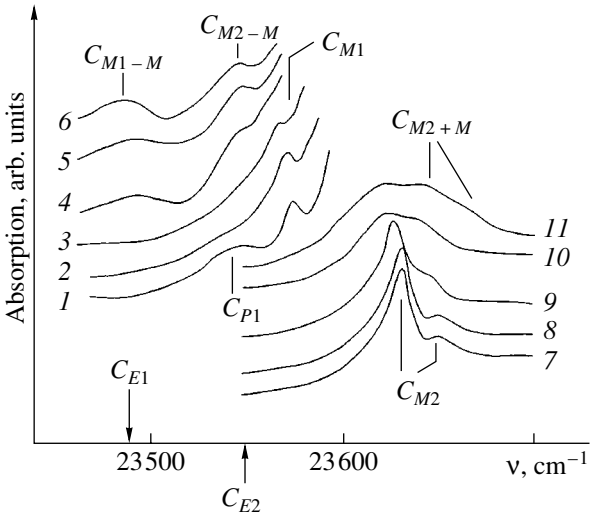

Fig. 2. Absorption spectra of Rb_2MnCl_4 crystals for the α polarization in magnetic fields *H*: (*1*, *7*) 0, (*2*, *8*) 46, (*3*) 70, (*4*, *9*) 135, (*5*, *10*) 160, and (*6*, *11*) 230 kOe. Sample thickness *h*: (*1*–*6*) 1.65 and (*7*–*11*) 0.08 mm. $T = 4.3$ K, $\mathbf{H} \parallel C_4$.

3. RESULTS AND DISCUSSION

The polarized absorption spectra of crystal samples with different thicknesses *h* at the temperature $T = 4.2$ K are shown in Fig. 1. According to the selection rules, the magnetodipole exciton bands in the optical spectra of the Rb_2MnCl_4 crystal should be observed for the polarizations α (the wave vector **k** is aligned parallel to the C_4 axis of the crystal, and the electric-field vector **E** is perpendicular to the C_4 axis) and π ($\mathbf{k} \perp C_4$, $\mathbf{E} \parallel C_4$), whereas the electrodipole single-magnon satellites of the exciton bands should manifest themselves for the polarizations α and σ ($\mathbf{k} \perp C_4$, $\mathbf{E} \perp C_4$). We failed to observe exciton bands in the spectra of crystal samples of the specified thickness. Vervoitte *et al.* [4] measured the spectrum of magnetic circular dichroism and revealed two dichroic magnetodipole bands (23489 and 23547 cm^{-1}). The locations of these bands are indicated in Fig. 1, and the bands themselves are designated as C_{E1} and C_{E2}, respectively, and are interpreted as exciton bands. In [4], the bands C_{P1} and C_{M1} were identified as photon and magnon satellites of the exciton band C_{E1}, respectively. The band C_{M1} is located at a distance of ~80 cm^{-1}, which corresponds to the magnon frequency at the boundary of the Brillouin zone.

We measured the absorption spectra of Rb_2MnCl_4 crystals in different magnetic fields and at temperatures ranging from 1.8 to 100 K. It turned out that the temperature dependences of the spectral characteristics do not provide useful information. As the temperature increases to the Néel point T_N, the half-width of the bands increases; consequently, it becomes impossible to determine the location of most of them to sufficient accuracy. The only isolated band, namely, C_{M2}, which can be clearly observed up to the temperature T_N and higher, does not undergo a noticeable shift at temperatures $T < T_N$. This is a typical manifestation of the two-dimensional magnetic structure of the crystal [5].

Figure 2 illustrates the evolution of the red edge of the α-polarized absorption spectra of thick and thin crystal samples in different magnetic fields at $T = 4.3$ K. In the case when the magnetic field exceeds the field of the spin-flop transition and the magnetic moments of the sublattices exhibit angularity, the spectrum undergoes a considerable transformation. It can be seen that an intense broad band, namely, C_{M2+M}, appears in the spectrum, increases in intensity, and overlaps with the C_{M2} band whose intensity decreases. As the magnetic field increases above 100 kOe, there appear two new bands, namely, C_{M1-M} and C_{M2-M}, at frequencies corresponding to pure exciton transitions and their intensities increase. Judging from the field dependences of the aforementioned bands, the C_{M2+M} band can be identified as an exciton–two-magnon band (a magnon satellite of the exciton–magnon band C_{M2}), whereas the C_{M1-M} and C_{M2-M} bands can be treated as hot satellites of the exciton–magnon bands. The integrated intensity of these bands should be proportional to $\sin^2 2\theta \sin^4\theta$, where $\cos\theta = H/2H_E$ and θ is half the angle between the sublattices. However, in the former case, the band is unusually broad. In the latter case, the intensities of the bands should be proportional to the magnon population [6]: $n = [\exp(\varepsilon_m/kT) - 1]^{-1}$, which is small at the temperature of the experiment; hence, these bands should not be observed. In order to explain the above facts, the specific features of the magnetic structure of the crystal must be taken into account.

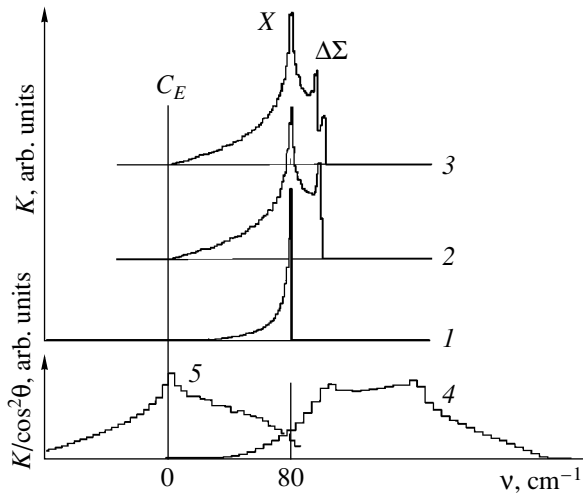

Fig. 3. Calculated band shapes: (*1*) the exciton–magnon band at $K_1 = 0$, $K_2 = 0$; (*2*) the exciton–magnon band at $K_1 = 0$, $K_2 = 2.5$; (*3*) the exciton–magnon band at $K_1 = 0.1$, $K_2 = 2.5$; (*4*) the cold magnon satellite of the exciton–magnon band at $K_1 = 0$, $K_2 = 2.5$; and (*5*) the hot magnon satellite of the exciton–magnon band at $K_1 = 0$, $K_2 = 2.5$.

The shapes of the absorption bands were calculated taking into account the results obtained in [6]. The absorption coefficients at the frequency ω were calculated for the exciton–magnon band from the relationship

$$K^{e+m}(\omega) \propto \sum_{\mu,\,\mathbf{k}} |\mathbf{P}(\mathbf{k})|^2 \Phi_\mu^{e+m}(\mathbf{k})\delta(\omega - E_\mu(\mathbf{k}) - \varepsilon_\mu(-\mathbf{k})),$$

for the cold magnon satellite of the exciton–magnon band from the expression

$$K^{e+m+m}(\omega) \propto \sum_{\mu,\,\mathbf{k}} |\mathbf{P}(\mathbf{k})|^2 \Phi_\mu^{e+m+m}(\mathbf{k})\delta$$
$$\times\left(\omega - E_\mu(\mathbf{k}) - \sum_{\mathbf{k}_1 - \mathbf{q} = -\mathbf{k}}\left(\varepsilon_\mu(\mathbf{k}_1) + \sum_{\mathbf{q}}\varepsilon_\mu(\mathbf{q})\right)\right),$$

and for the hot magnon satellite of the exciton–magnon band from the formula

$$K^{e+m-m}(\omega) \propto \sum_{\mu,\,\mathbf{k}} |\mathbf{P}(\mathbf{k})|^2 \Phi_\mu^{e+m-m}(\mathbf{k})\delta$$
$$\times\left(\omega - E_\mu(\mathbf{k}) - \sum_{\mathbf{k}_1 - \mathbf{q} = -\mathbf{k}}\left(\varepsilon_\mu(\mathbf{k}_1) - \sum_{\mathbf{q}}\varepsilon_\mu(\mathbf{q})\right)\right).$$

Here, $\mathbf{P}(\mathbf{k})$ is the dipole moment of the transition in the $\mathbf{k}$ space and $\Phi_\mu^{e+*}(\mathbf{k})$ are the functions dependent on the direction of the magnetic moments of the sublattices, the population of magnon states, and the structure of the crystal. The summation is carried out over all vectors $\mathbf{k}$ of the Brillouin zone and over the zones μ. The exciton energy $E_\mu(\mathbf{k})$ and magnon energy $\varepsilon_\mu(\mathbf{k})$ were calculated in the nearest neighbor approximation according to the expressions

$$E_\mu(\mathbf{k}) = \Delta\tilde{\varepsilon} + A\cos\theta\tilde{z}\tilde{M}\tilde{\gamma}(\mathbf{k}) - (-1)^\mu z|M|\gamma(\mathbf{k})\cos^2\theta,$$

$$\varepsilon_\mu(\mathbf{k})$$
$$= SI(0)\sqrt{1 - \gamma^2(\mathbf{k}) + 2\cos^2\theta\gamma(\mathbf{k})[\gamma(\mathbf{k}) - (-1)^\mu]},$$

$$\gamma(\mathbf{k}) = \cos\left(\frac{ak_x}{2}\right)\cos\left(\frac{ak_y}{2}\right),$$

$$\tilde{\gamma}(\mathbf{k}) = \frac{1}{2}(\cos ak_x + \cos ak_y),$$

where a is the lattice parameter. In contrast with the case considered in [6], we ignored the renormalization of the exciton energy due to the exciton–magnon interaction Δ and assumed that $|\Delta(\mathbf{k}, \mu)|^2 = \Delta\sin^2 2\theta$. The role of the exciton–magnon interaction, in our case, consists in resolving the magnon satellites of the exciton–magnon band. All the other designations correspond to those presented in [2]. In our calculations, we varied the parameters $K_1 = |M|\cos^2\theta$ and $K_2 = \tilde{M}$ determining the transfer of excitation inside and between the sublattices.

The calculated shapes of the exciton–magnon band and its cold single-magnon satellite having characteristic weakly pronounced peaks associated with the specific features of the density of states corresponds to the observed shape under the condition $K_2 = 2.5|J|$ (Fig. 3). Here, $|J|$ is the quantity characterizing the intralayer exchange between the nearest neighbors. The magnitude $|M|$ can be determined from the Davydov splitting of the exciton band. We failed to do this because no weak exciton band was observed for crystals of the specified thickness. For this reason, in our calculations, we chose small values of K_1 in units of $|J|$, which is specified by the range of the magnetic fields used. In this case, the shapes of the bands change insignificantly, whereas the maxima of the intensity should vary as $\sin^4\theta$ and $\sin^2 2\theta\sin^4\theta$ for the single-magnon and two-magnon satellites, respectively. Figure 3 displays the calculated shape of the two-magnon satellite for small values of K_1, which is described by a function $\sim K^{e+m+m}(\omega)/\cos^2\theta$, because when $H = 0$ and $\theta = \pi/2$ (and, correspondingly, $K_1 = 0$), we obtain $K^{e+m+m}(\omega) = 0$. An increase in the fraction of magnons with wave vectors at points of the general type, as compared to that at singular points in a 2D antiferromagnet, gives rise to a broad two-magnon band.

Unlike the cold magnon satellite of the exciton–magnon band, the hot magnon satellite of this band exhibits a sharp peak on the background of the wide dome at a frequency close to the frequency of the exci-

ton (Fig. 3) for $K_2 = 2.5$ and $K_1 = 0$. Consequently, the bands C_{M-M1} and C_{M-M2} are relatively narrow. They are characterized by a high intensity and a weak temperature dependence due to the two-dimensional magnetic structure. According to [6], we can write the relationship $\Phi_{\mu}^{e+m-m}(\mathbf{k}) \sim n_{\mu}(\mathbf{k})$. The decrease in the magnetization due to zero-point oscillations was calculated for a two-dimensional Heisenberg antiferromagnet in [7]. It was shown that this decrease at $T = 0$ reaches ~20% [7]. Therefore, at a low temperature, n takes on a value of no less than 0.2, which ensures a sufficient number of magnons for the participation in the hot absorption of light. The shape of the band was calculated under the assumption that magnons are uniformly distributed in the Brillouin zone.

Upon summing the band intensities with weights dependent on the sublattice angularity in the magnetic field, we obtain a spectrum similar to that observed in the experiment.

ACKNOWLEDGMENTS

This work was supported in part by the Russian Federal Program “Integration,” project no. 0017.

REFERENCES

1. V. V. Gorbach, M. A. Pakizh, and É. G. Petrov, Ukr. Fiz. Zh. **37**, 1670 (1992).
2. V. V. Eremenko, N. F. Kharchenko, Yu. G. Litvinenko, and V. M. Naumenko, *Magneto-Optics and Spectroscopy of Antiferromagnets* (Naukova Dumka, Kiev, 1989).
3. H. T. Witteveen, J. Solid State Chem. **11** (3), 245 (1974).
4. A. Vervoitte, J. C. Canit, B. Briat, and U. Cambli, Phys. Status Solidi B **124** (1), 87 (1984).
5. N. Kojima, T. Ban, and I. Tsujikawa, J. Phys. Soc. Jpn. **44**, 919 (1978).
6. V. V. Gorbach and É. G. Petrov, Fiz. Tverd. Tela (Leningrad) **32**, 1418 (1990) [Sov. Phys. Solid State **32**, 828 (1990)].
7. S. G. Ovchinnikov and O. G. Petrakovskiĭ, Fiz. Tverd. Tela (Leningrad) **29**, 1866 (1987) [Sov. Phys. Solid State **29**, 1073 (1987)].

Translated by O. Moskalev

Physics of the Solid State, Vol. 45, No. 8, 2003, pp. 1504–1512. Translated from Fizika Tverdogo Tela, Vol. 45, No. 8, 2003, pp. 1432–1439.

MAGNETISM AND FERROELECTRICITY

Spin Dynamics and Phase Transitions in Quasi-2D Antiferromagnets R_2CuO_4 (R = Pr, Nd, Sm, Eu, Gd)

E. I. Golovenchits and V. A. Sanina

Ioffe Physicotechnical Institute, Russian Academy of Sciences, Politekhnicheskaya ul. 26, St. Petersburg, 194021 Russia

e-mail: e.golovenchits@mail.ioffe.ru

Received January 14, 2003

Abstract—The spin and lattice dynamics of the R_2CuO_4 quasi-2D antiferromagnetic crystals (R = Pr, Nd, Sm, Eu, Gd) were studied in the millimeter-range electromagnetic wave band. Strong variations of the absorption coefficient were observed to occur at temperatures $T \approx T_0$. Absorption lines of electrical nature due to lattice dynamics were also revealed near the T_0 temperatures. The observed anomalies are assumed to originate from phase transitions at $T \approx T_0$, which entail changes in the structural and magnetic properties. © *2003 MAIK "Nauka/Interperiodica".*

1. INTRODUCTION

This paper reports on a study of the absorption spectra of electromagnetic waves in R_2CuO_4 quasi-2D antiferromagnets (R = Pr, Nd, Sm, Eu, Gd) in the frequency range 20–250 GHz and at temperatures from 5 to 350 K. The measurements were conducted on stoichiometric, dielectric single crystals.

R_2CuO_4 crystals with R = Pr, Nd, Sm, and Eu have T'-type tetragonal symmetry (space group $I4/mmm$ [1]) at all temperatures. La_2CuO_4 and Gd_2CuO_4 were observed to undergo, at 600–650 K, structural transitions from the high-temperature (tetragonal) to low-temperature (orthorhombic) phase [2, 3].

Figure 1 shows the structure of La_2CuO_4 and R_2CuO_4 with rare-earth (RE) ions for R = Pr, Nd, Sm, Eu, and Gd. The structures of all these crystals have a common feature: they are all quasi-2D. At the same time, La_2CuO_4 and R_2CuO_4 with RE ions differ in the nearest environment of the Cu^{2+} ions. In La_2CuO_4, these ions are surrounded by O^{2-} octahedra (coordination number $Z = 6$), while in R_2CuO_4 with RE ions, they are surrounded by oxygen ion squares ($Z = 4$) in CuO_2 sheets.

In terms of their magnetic properties, La_2CuO_4 and all R_2CuO_4 crystals with RE ions are quasi-2D Heisenberg antiferromagnets based on CuO_2 sheets with Cu^{2+} ions (spin $S = 1/2$). There is strong in-plane 2D Heisenberg exchange interaction (exchange constant $J_{IP} \sim$ 120–150 meV [4]). The Néel temperatures (T_N) for the quasi-2D antiferromagnetic order maintained by a weak out-of-plane exchange $J_{OP} \sim 10^{-5} J_{IP}$ are $T_N \sim 250$–300 K. The noncollinear antiferromagnetic structure, magnetic anisotropy, spin-wave excitation spectra, and the part played by the R^{3+}–Cu^{2+} and Cu^{2+}–Cu^{2+} pseudodipole interactions in the R_2CuO_4 tetragonal crystals with RE ions are considered in [5, 6].

The spin dynamics in R_2CuO_4 was studied earlier by using antiferromagnetic resonance (AFMR) [7, 8] in crystals with R = Pr, Nd, and Gd and by using inelastic neutron scattering [6, 9, 10] in compounds with R = Pr and Nd.

Magnetic resonance lines were observed in [7, 8] at low temperatures, $T < 15$–20 K. As the temperature was increased, the resonance lines measured by sweeping the external magnetic field were broadened and then practically disappeared. Inelastic neutron scattering

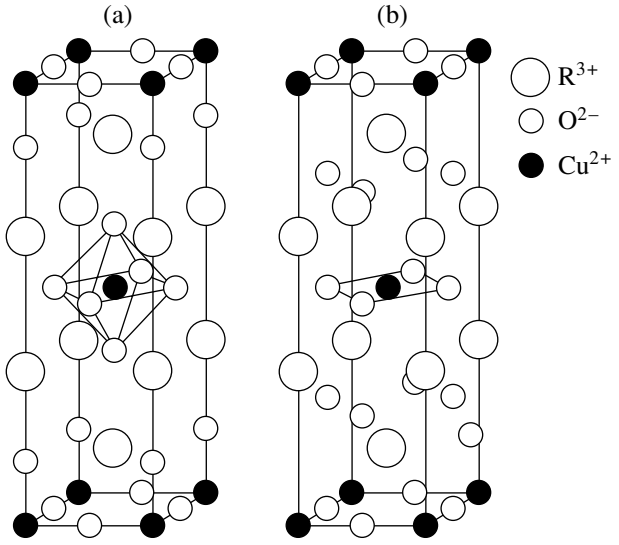

Fig. 1. Structure (a) of La_2CuO_4 crystals of T-type symmetry in the high-temperature phase and (b) of R_2CuO_4 crystals (R = Pr, Nd, Sm, Eu, Gd) of T'-type tetragonal symmetry.

studies revealed both in-plane (with a gap Δ_{IP}) and out-of-plane (Δ_{OP}) spin-wave excitations [6, 9, 10]. The values of the gap width Δ_{IP} obtained for Pr_2CuO_4 and Nd_2CuO_4 in inelastic neutron scattering measurements and the AFMR frequencies differed only slightly.

This study covered temperature and frequency dependences for the absorption spectra of R_2CuO_4 with RE ions (R = Pr, Nd, Sm, Eu, Gd) measured using the quasi-optical method, both with and without application of an external magnetic field. This permitted us to investigate the absorption lines and bands which did not depend (or depended only weakly) on magnetic field and could not be observed using conventional AFMR (by sweeping an external magnetic field at a fixed frequency). As a result, we observed, in addition to the magnetic resonance lines studied in [7, 8], absorption lines and bands that had not been detected previously. The presence of such bands is characteristic of all the R_2CuO_4 crystals investigated.

The position of the low-frequency absorption band edge in Pr_2CuO_4 and its temperature dependence are in accord with the corresponding data for the in-plane spin-wave excitation gap obtained by inelastic neutron scattering [10].

In R_2CuO_4 with R = Pr, Sm, and Eu, the above-mentioned absorption bands originating from excitation of in-plane spin waves became manifest, under heating of the crystal, in the form of a strong increase in absorption near the temperatures $T \approx T_0$ = 20, 80, and 150 K, respectively. It is near $T \approx T_0$ = 150 K that a phase transition in Eu_2CuO_4, in which both the structural and magnetic properties of the crystal changed simultaneously, was observed earlier by using various experimental methods [11–14]. The similarity between the temperature dependences of the measured absorption spectra in R_2CuO_4 with different RE ions suggests that all these crystals undergo similar phase transitions at temperatures $T \approx T_0$.

In all crystals with phase transitions occurring near $T \approx T_0$, one observed, near the same temperatures, not only absorption bands of spin nature but also absorption lines apparently due to lattice dynamics. These lines lie at frequencies $f > 20$ GHz, up to the edge of the in-plane spin-wave excitation band, and partially overlap the latter. Thus, in the crystals studied, the in-plane spin-wave and lattice excitations are mixed, at least, at temperatures close to T_0.

2. EXPERIMENTAL RESULTS

The absorption spectra of R_2CuO_4 single crystals (R = La, Pr, Nd, Sm, Eu, Gd) were measured over the frequency range 20–250 GHz at temperatures 5–300 K. The samples were $5 \times 4 \times 0.5$-mm plates with the larger face perpendicular to the c axis of the crystal. The single crystals were grown using the spontaneous crystallization method described in [15, 16]. The quasi-optical spectrometer employed used backward-wave lamps (BWL) as a generator and liquid helium–cooled InSb detectors as a receiver. The experimental technique is described in considerable detail in [17].

The larger face of a sample was oriented perpendicular to the direction of microwave power propagation. The propagated wave had a plane wavefront such that the ac magnetic (**h**) and electric (**e**) fields were in the sample plane. The sample could be rotated about the axis of the holder. The electric field e was parallel to the holder axis and remained in the plane of the larger face when the sample was turned. In contrast, the magnetic field **h** deflected from this plane through the corresponding angle with rotation of the sample. A dc magnetic field $\mathbf{H}_0$ of up to 1.6 T could be applied perpendicular to the direction of microwave power propagation.

We measured temperature dependences of the microwave power transmitted through the sample, $P(T)$, at fixed frequencies. The temperature dependences of the relative absorption coefficients $\Gamma = 1 - P(T)/P(T = 5\ \mathrm{K})$ at fixed frequencies, $\Gamma_f(T)$, were calculated. The $\Gamma_f(T)$ plots were used to calculate the frequency dependences of the relative absorption coefficient of a sample at fixed temperatures, $\Gamma_T(f)$. Note that, to quantify the absorption coefficient, one needs to know the phase of the propagated wave and the reflected power, which are difficult to obtain without ensuring the single-mode measurement regime. However, in order to determine the position of the absorption lines and bands only, one can restrict oneself to measurement of the $\Gamma_f(T)$ coefficient. It is also appropriate to note that, when measuring relative absorption coefficients, the nonuniformity of the frequency response of the generator (BWL) is inessential.

Three types of $\Gamma_f(T)$ dependences differing in behavior were observed in the crystals in the frequency range 20–250 GHz.

(1) Sharp and strong stepped variation of the absorption coefficients $\Gamma_f(T)$ within narrow temperature intervals near T_0 = 20, 80, and 150 K for R_2CuO_4 crystals with R = Pr, Sm, and Eu, respectively (Fig. 2). These jumps occurred within a broad frequency region $f >$ 100–120 GHz up to 250 GHz (the maximum frequency at which the measurements were conducted).

(2) Sharp, but weaker changes in the absorption coefficient $\Gamma_f(T)$ in R_2CuO_4 crystals with R = Pr, Nd, Sm, and Eu occurring near $T \approx T_0$ = 20, 6, 80, and 150 K, respectively (Fig. 3). Unlike absorption bands of the first type, these jumps in absorption were observed in a narrow frequency interval close to 30 GHz.

(3) Absorption lines, i.e., maxima in the $\Gamma_f(T)$ dependences (Fig. 4). These lines were observed in R_2CuO_4 crystals (R = Pr, Nd, Sm, Eu) in the vicinity of $T \approx T_0$ within a broad frequency range, from 20 GHz to the low-frequency edge of the broad absorption band of the first type. These lines are most clearly seen on the

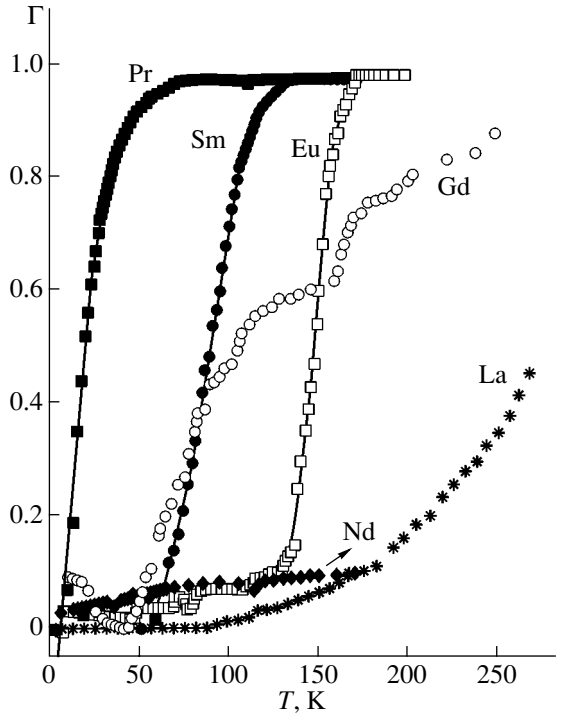

Fig. 2. Temperature dependence of the relative absorption coefficient measured at a frequency f = 169 GHz for La_2CuO_4, Pr_2CuO_4, Nd_2CuO_4, Sm_2CuO_4, Eu_2CuO_4, and Gd_2CuO_4. The curves were measured under a slow warm-up of the samples following their slow cooling. The solid lines for R_2CuO_4 (R = Pr, Sm, and Eu) are fits by Boltzmann equations.

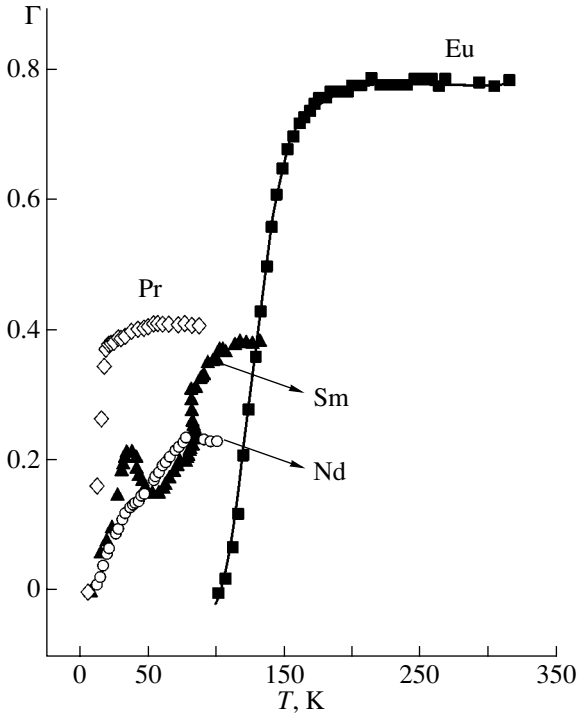

Fig. 3. Stepwise absorption near temperatures T_0 for the Pr_2CuO_4, Nd_2CuO_4, Sm_2CuO_4, and Eu_2CuO_4 crystals at frequencies 30.5, 29, 33.9, and 34 GHz, respectively.

wing of the broad absorption band in Eu_2CuO_4, where their intensity was the strongest (see [18, Fig. 2]).

At temperatures $T < T_0$, where the crystals studied were practically transparent for $f > 100$ GHz, strongly magnetic field-dependent absorption lines were observed (they are seen in Fig. 2 for Gd_2CuO_4 at $T \approx 10$ K and in Fig. 3 for Nd_2CuO_4 at $T \approx 30$ and 75 K and for Sm_2CuO_4 at $T \approx 30$ K). No comprehensive investigation of these lines was made here; they apparently originate from magnetic resonances.

Consider the specific features of the above three types of absorption spectra in more detail.

We first discuss the properties of the broad, strong absorption band at frequencies $f > 100$ GHz, which appears near $T \approx T_0$. As seen from Fig. 2, the variation of absorption for R_2CuO_4 crystals with R = Pr, Sm, and Eu has the shape of a smooth step, with the $\Gamma_f(T)$ coefficient changing by tens of times within a fairly narrow temperature interval near $T \approx T_0 = 20$, 80, and 150 K, to remain subsequently nearly constant with a further increase in temperature. This pattern persists up to a limiting frequency of 250 GHz. Note that the temperature dependence of the absorption coefficient $\Gamma_f(T)$ for La_2CuO_4, which is presented for comparison in Fig. 2, is different. Indeed, the absorption grows more smoothly in this case with temperature up to 400 K without reaching a constant level. No frequency dependence of absorption is observed within the operating range for this crystal. Note that the absorption for La_2CuO_4 at the maximum temperature (Fig. 2) is substantially smaller than that measured in R_2CuO_4 crystals (R = Pr, Sm, Eu) for $T > T_0$. It appears only natural that this absorption is related to the thermal release of carriers from traps. Generally speaking, absorption of this type should take place in all crystals of this class; however, this absorption is practically indistinguishable in R_2CuO_4 with R = Pr, Sm, and Eu when viewed superposed on strong absorption bands.

The absorption in these strong bands is primarily of magnetic nature. This was checked by polarization measurements. Rotation of samples about the crystal holder caused a sharp decrease in the relative absorption coefficient $\Gamma_f(T)$. When a sample is rotated in this way, the ac magnetic field leaves the CuO_2 layer plane, whereas the ac electric field maintains its orientation in these layers. The observed magnetic absorption band is most likely associated with spin-wave excitations in the CuO_2 sheets.

It was found that the best fit to the experimental points (with the smallest rms deviations) in Figs. 2 and 3 is reached when using a Boltzmann equation of the type $\Gamma = (\Gamma_1 - \Gamma_2)/\{1 + \exp[(T - T_0)/dT]\} + \Gamma_2$, which describes a stepwise variation of the parameter Γ within a temperature interval dT in the vicinity of T_0. Here, Γ_1

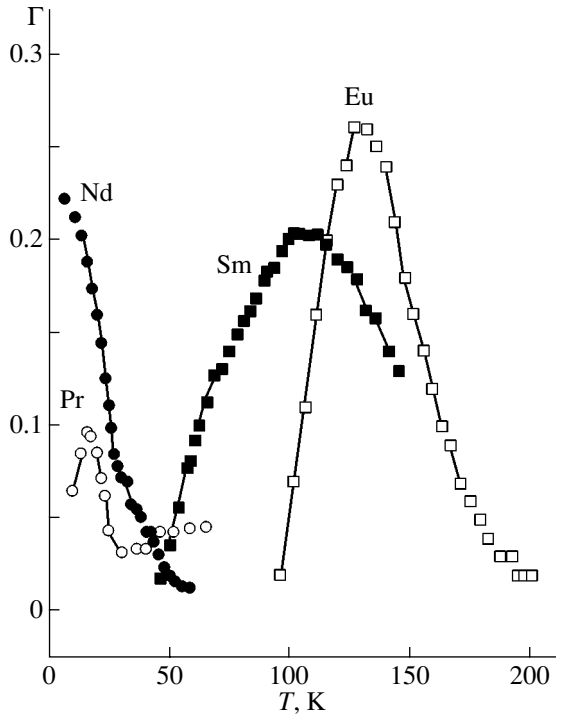

Fig. 4. Absorption lines near temperatures T_0 for Pr_2CuO_4, Nd_2CuO_4, Sm_2CuO_4, and Eu_2CuO_4 obtained at 55 GHz. Solid lines are drawn to guide the eye.

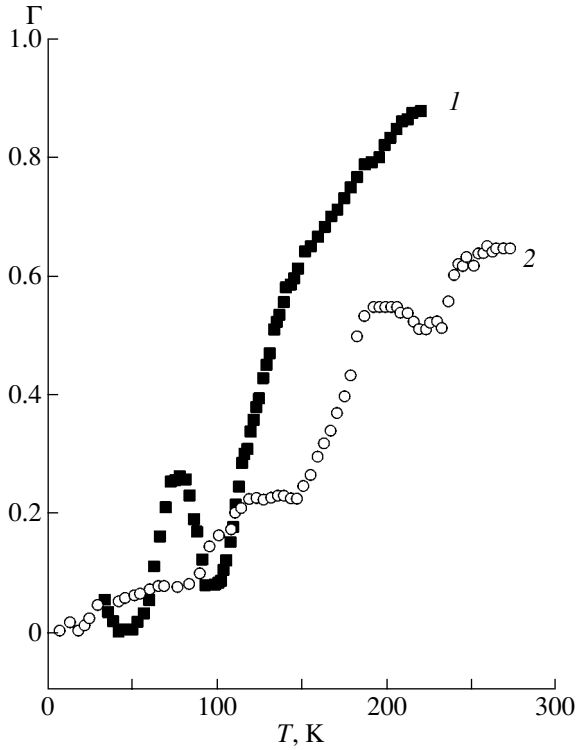

Fig. 5. Temperature dependence of the absorption coefficient of Gd_2CuO_4 measured under slow warm-up following (*1*) slow and (*2*) fast cooling.

is the absorption coefficient for $T = -\infty$, Γ_2 is that for $T = +\infty$, T_0 is the temperature at which $\Gamma = 0.5(\Gamma_1 + \Gamma_2)$, and dT is the width of the temperature interval within which Γ varies sharply in magnitude. Computer fitting yields the minimum-error values of all four parameters within the possible range of their variation. The values of T_0 and dT for the R_2CuO_4 crystals (R = Pr, Sm, Eu) are, respectively, 19.52 ± 2.13 K and 13.03 ± 0.79 K with a variance $\chi^2 = 0.00039$ characterizing the accuracy of approximation for Pr; 86.09 ± 0.24 K and 10.49 ± 0.21 K with $\chi^2 = 0.00023$ for Sm; and 115.82 ± 0.62 K and 10.78 ± 0.53 K with $\chi^2 = 0.00052$ for Eu. We readily see that, for the Eu_2CuO_4 and Sm_2CuO_4 crystals, the ratio $dT/T_0 \ll 1$, whereas for Pr_2CuO_4, we have $dT/T_0 \sim 0.7$. Thus, the values of dT for these crystals are similar and the temperatures T_0 depend on the RE ion species.

In Gd_2CuO_4, the increase in the absorption coefficient with temperature was more smooth than in R_2CuO_4 (R = Pr, Sm, Eu); in terms of the pattern of the temperature and frequency responses and the magnitude of the absorption coefficient, this crystal is closer to tetragonal R_2CuO_4 (R = Pr, Sm, Eu) than to the La_2CuO_4 case (Fig. 2). The absorption in Gd_2CuO_4 depended substantially on the sample prehistory, more specifically, on the cooling rate and the presence method of applying the external magnetic field. In non-equilibrium samples cooled at a high rate (>30 K/min) or after application of a magnetic field of 1.5 T near the Néel temperature, the increase in absorption with temperature occurred stepwise rather than smoothly. Figure 5 displays the pattern of $\Gamma(T)$ variation in the case of fast cooling. We readily see that the equilibrium sample (cooled at a rate less than 1 K/min in a zero external field) exhibits an absorption line of magnetic nature at a temperature of ~75 K and f = 169 GHz. This line broadened under quenching and was shifted by an external magnetic field.

No sharp variation of the coefficient $\Gamma_f(T)$, similar to that seen in R_2CuO_4 (R = Pr, Sm, Eu), was observed to occur in Nd_2CuO_4 at frequencies $f \leq 250$ GHz (Fig. 2).

Figure 6 presents the $\Gamma_f(T)$ relations obtained under slow heating and cooling of the samples. Eu_2CuO_4 is seen to display a strong temperature hysteresis. Pr_2CuO_4 and Sm_2CuO_4 crystals also reveal a hysteresis, but it is considerably weaker.

Consider now the absorption properties near 30 GHz. As already mentioned, this absorption appeared in R_2CuO_4 crystals with R = Pr, Nd, Sm, and Eu (Fig. 3) at temperatures $T \approx T_0$ = 20, 6, 80, and 150 K, respectively, while for $T > T_0$, the absorption remained practically independent of temperature up to 300–350 K. The value of $\Gamma_f(T)$ for $T > T_0$ in this case is

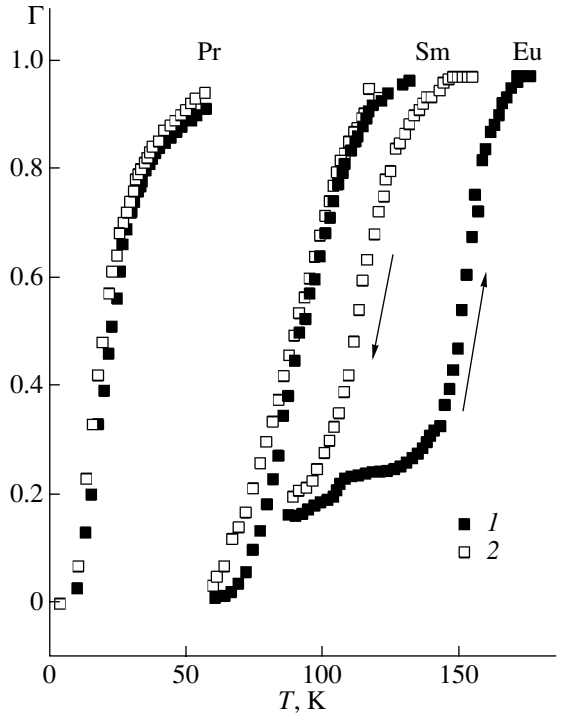

Fig. 6. Hysteresis in the temperature dependence of the absorption coefficient of Pr_2CuO_4, Sm_2CuO_4, and Eu_2CuO_4 obtained at 169 GHz under (*1*) slow heating and (*2*) slow cooling.

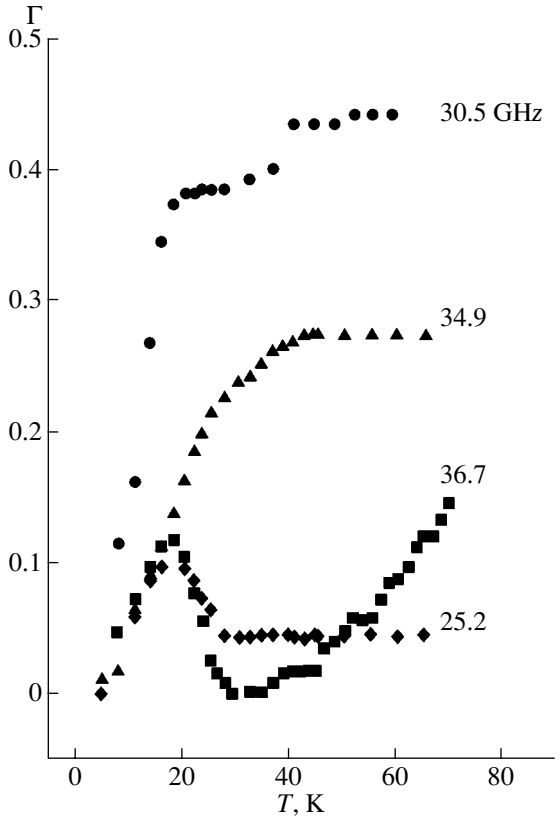

Fig. 7. Temperature dependence of the relative absorption coefficient of Pr_2CuO_4 at frequencies close to 30 GHz.

smaller than that for steps of the first type. Figure 7 exemplifies some $\Gamma_f(T)$ relations obtained at frequencies near 30 GHz on Pr_2CuO_4, which illustrate the nonmonotonic character of variation of $\Gamma_f(T)$ with $T > T_0$ and with frequency varied near 30 GHz. Similar dependences were observed in the vicinity of and above the temperatures $T \approx T_0$ = 6, 80, and 150 K in Nd_2CuO_4, Sm_2CuO_4, and Eu_2CuO_4, respectively.

Consider finally absorption lines of the third type. These lines were observed near the temperatures $T \approx T_0$ in R_2CuO_4 crystals (R = Nd, Pr, Sm, Eu) within a fairly broad frequency range above 20 GHz (Fig. 4). The upper frequency limit of this absorption is difficult to establish, because it overlaps the edge of the strong spin-involving absorption band of the first type. Polarization measurements showed these lines to be excited primarily by the ac electric field, because the relative absorption coefficient of the sample changed only slightly when the sample was rotated about the sample holder along which the ac electric field was directed. An external magnetic field had practically no effect on the position and intensity of the absorption lines.

Figure 8 displays the frequency dependences of the absorption coefficient $\Gamma_T(f)$ of R_2CuO_4 crystals (R = Pr, Sm, Eu) derived for a number of temperatures from the experimentally measured $\Gamma_f(T)$ relations (Figs. 2, 3, 7). One clearly sees a narrow absorption line near 30 GHz and a broad absorption band at higher frequencies. The position of the edge of this band (i.e., the gap for the corresponding spin excitations) can be characterized by the frequency f_{gap} that corresponds to one half of absorption at the saturation level for each fixed temperature. As the temperature increases, the absorption edge is seen to shift toward lower frequencies and its position no longer varies with temperature for $T > 90$ K (for Pr_2CuO_4). Figure 9 shows temperature dependences of the frequency gaps of the corresponding spin excitations measured for R_2CuO_4 crystals (R = Pr, Sm, Eu).

3. ANALYSIS OF THE EXPERIMENTAL DATA

The experimental data presented in the preceding section show that the absorption spectra of R_2CuO_4 tetragonal crystals with different RE ions share a number of common features.

For temperatures $T > T_0$, all crystals, except Nd_2CuO_4, exhibit, within a broad frequency range above 100 GHz, a strong absorption band, which is apparently due to excitation of in-plane spin waves. In the case of Pr_2CuO_4, the magnitude of the frequency gap for such excitations and its temperature response agree with those of the gap Δ_{IP} reported in [10] (Fig. 9).

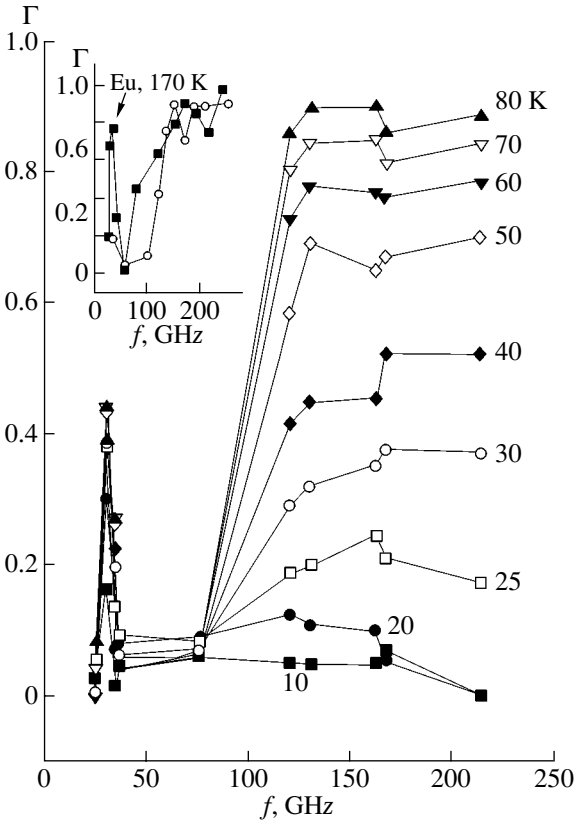

Fig. 8. Frequency dependence of the relative absorption coefficient of Pr_2CuO_4 obtained at fixed temperatures. Inset shows the same dependence measured for Sm_2CuO_4 and Eu_2CuO_4 at temperatures of 100 and 170 K, respectively.

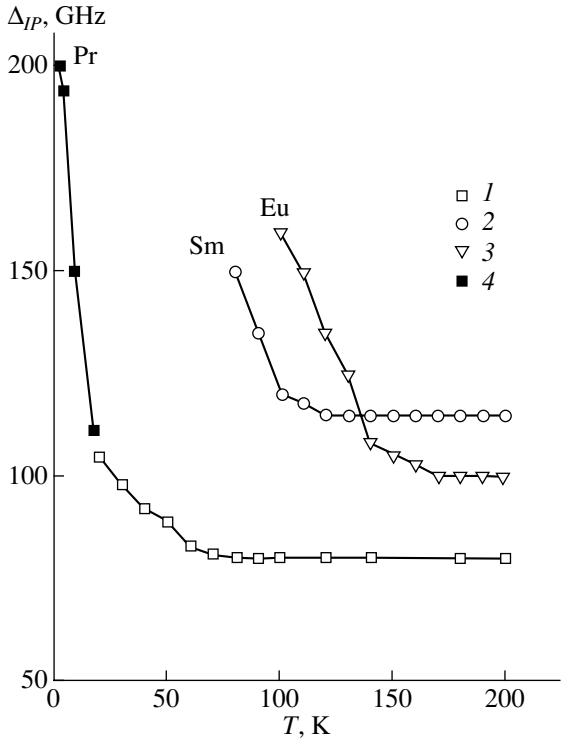

Fig. 9. Temperature behavior of the in-plane spin-wave excitation frequency gaps Δ_{IP} for the Pr_2CuO_4, Sm_2CuO_4, and Eu_2CuO_4 crystals. (*1–3*) This work and (*4*) inelastic neutron scattering data for Pr_2CuO_4 [10].

The similarity between the gaps for the observed strong magnetic absorption bands and between their temperature behaviors in R_2CuO_4 crystals (R = Pr, Sm, Eu) (Fig. 9) suggests that the bands in all these crystals are caused by in-plane spin-wave excitations in the CuO_2 sheets with gaps Δ_{IP}. The widths of the gaps are determined by the in-plane anisotropy, which is similar for crystals with R = Pr, Sm, and Eu and is primarily due to the Cu–Cu interaction in the layers. The RE ions (R = Pr, Sm, Eu) only weakly affect the in-plane anisotropy. Indeed, Pr_2CuO_4 and Eu_2CuO_4 have practically nonmagnetic ground-state RE ions and, in Sm_2CuO_4, the magnetic moments of the Sm^{3+} ions are aligned with the c axis of the crystal [19].

As follows from data on inelastic neutron scattering for Nd_2CuO_4 [9], the gap Δ_{IP} in this compound is nearly an order of magnitude larger than that in Pr_2CuO_4. Our operating frequencies are lower than the gap width Δ_{IP}, and it is apparently for this reason that we did not observe the corresponding band in Nd_2CuO_4. In Nd_2CuO_4, the magnetic moments of the Nd^{3+} ions, as well as those of the Cu^{2+} ions, are known to lie in the CuO_2 sheets and the Nd–Cu interaction is indeed capable of changing the in-plane anisotropy and shifting the gap.

As already mentioned, Eu_2CuO_4 was established [11] to undergo, near $T \approx T_0 = 150$ K, a phase transition, during which the structural and magnetic properties change (see also [12, 14, 15, 20]). Rhombic distortions, caused primarily by oxygen ion displacements, were found to form for $T \leq T_0$ in CuO_2 layers on a local scale of ~30 Å [11]. It appears natural to relate the change in the absorption coefficient and the temperature behavior of the gap Δ_{IP} in Eu_2CuO_4 near 150 K to the existence of this phase transition. A broad absorption band is observed within the operating frequency range in the high-temperature tetragonal phase, but this band does not arise in the low-temperature phase with local rhombic distortions. The existence of such distortions in the low-temperature phase gives rise to a stronger interlayer coupling and a larger in-plane magnetic anisotropy, which broadens the gap and results in the observed increased transmission of the crystal. The high-temperature tetragonal phase of Eu_2CuO_4 is also reported [12, 14] to exhibit dispersion of the dielectric susceptibility along the c axis, which is characteristic of the structural glassy state. This is possibly what

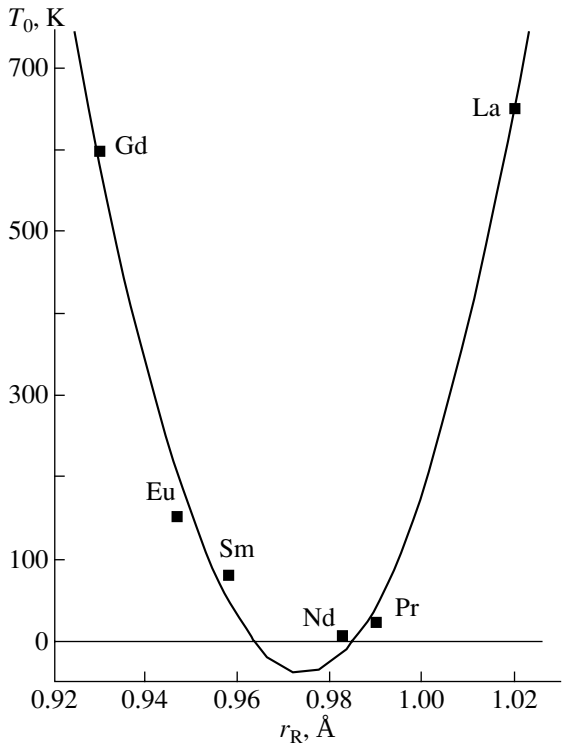

Fig. 10. Phase transition temperatures T_0 plotted vs. R-ion radius (r_R) for R_2CuO_4 crystals (R = La, Pr, Nd, Sm, Eu, Gd). The ionic radii were taken from [22].

accounts for the anomalously large width of the observed spin-wave absorption band.

In view of the similarities between the characteristics of the absorption bands observed in R_2CuO_4 crystals (R = Pr, Sm, Eu) near the T_0 temperatures, one may also expect the existence of similar phase transitions in R_2CuO_4 crystals (R = Pr, Sm) at temperatures $T_0 \approx 20$ and 80 K, respectively. The temperature hysteresis of the absorption coefficient in R_2CuO_4 (R = Sm, Eu) (see Fig. 6 and [18, Fig. 2]) is evidence of a first-order phase transition. In Pr_2CuO_4, this transition is diffuse ($dT/T_0 \sim 0.7$) and is apparently of the first order close to second order.

The gaps Δ_{IP} in Nd_2CuO_4 and Pr_2CuO_4 were found to be strongly temperature dependent for $T < 10$ K and $T < 20$ K, respectively [9, 10]. In the case of Nd_2CuO_4, this temperature behavior was related in [9, 10] to the strong dependence of the magnetization of Nd^{3+} ions on temperature and to the effect of the Nd^{3+}–Cu^{2+} interaction on the in-plane magnetic anisotropy. The temperature dependence of the gap Δ_{IP} in Pr_2CuO_4, where the Pr^{3+} ion is practically nonmagnetic, was explained as being due to spin–spin interaction in the two-dimensional CuO_2 sheets;, this interaction appears when the square magnetic anisotropy is taken into account [21].

If, however, one assumes the existence of phase transitions near the temperatures T_0, the temperature dependence of the frequency gap can also be accounted for by a change in the in-plane anisotropy originating from the structural distortions brought about in such a transition.

Let us discuss now the absorption lines of electric nature, which we assign to lattice dynamics near the phase transitions occurring in the R_2CuO_4 crystals (R = Pr, Nd, Sm, Eu) (Fig. 4). These lines are observed in a continuous frequency range extending from 20 GHz to the edge of the spin-involving absorption bands and can be associated with the dynamics of a set of coexisting relaxation centers, for which the condition $\omega\tau = 1$ is satisfied near the temperatures T_0. The lifetimes τ of these centers are distributed over the interval $0.8 \times 10^{-11} \geq \tau > 0.5 \times 10^{-12}$ s^{-1}, which indicates a limited size scale of the regions with structural correlations existing near the temperatures T_0. For Eu_2CuO_4, this is in agreement with the data obtained in structural studies [11]. The frequency overlap of the lattice absorption lines with absorption bands of spin nature observed to occur near the temperatures T_0 argues for the lattice and spin dynamics mixing near the T_0 temperatures.

Unlike crystals with R = Pr, Sm, and Eu, in Nd_2CuO_4, as already mentioned, no strong spin-wave absorption band was observed. Near 6 K, however, a line was detected which was similar to the lattice absorption lines found near the temperatures T_0 in R_2CuO_4 (R = Pr, Sm, Eu). Therefore, a similar phase transition also occurs apparently in Nd_2CuO_4 at $T_0 \approx 6$ K and, for the spin-wave absorption bands to be observed, the operating frequency has to be increased.

Thus, similar R_2CuO_4 crystals (R = Pr, Nd, Sm, Eu) differing in the R-ion species are assumed to undergo identical phase transitions at different temperatures T_0. In this case, it appears only natural to relate the differences in T_0 to the R-ion type.

We looked for correlations between the values of T_0 and magnetic moments, as well as with the ionic radii r_R of the R ions (using data obtained by Shannon [22]). The T_0 temperatures of the crystals studied correlate only weakly with the magnetic state of the corresponding R ions. Indeed, for the Eu^{3+} ion ($^7F_0$), which is nonmagnetic in the ground state, we have $T_0 \approx 150$ K. For the weakly magnetic Pr^{3+} ions (spin singlet in the ground state), $T_0 \approx 20$ K. For the magnetic ions Sm^{3+} and Nd^{3+} (Kramers doublets in the ground state), $T_0 \approx 80$ and 6 K, respectively. There is, however, a correlation between T_0 and the RE-ion radii (Fig. 10), which argues for the phase transitions near the temperatures T_0 being associated with a change in the structural state of the crystals. The nonmonotonic character of the $T_0(r_R)$ dependence, which is fitted best of all by a quadratic curve, suggests the existence of certain values of r_R that are optimal for the T' structure and make it stable down to the lowest temperatures. Decreasing or increasing r_R from these optimal values gives rise to an

instability in the T' structure, the extent of which depends on the size of the R ion. Note that the values of T_0 for the crystals with R = Nd, Pr, and Sm obtained by us and the temperatures of the structural phase transitions for crystals with R = La, Gd, and Eu determined earlier in independent experiments [2, 3, 11] fall reasonably well on the curve depicted in Fig. 10.

Gd_2CuO_4 was shown to contain coexisting macroscopic regions with rhombic and tetragonal symmetry (structural domains), which make the crystal structure close to the stability limit [3, 20, 23–25]. The pattern of the in-plane spin-wave excitation spectra observed by us in Gd_2CuO_4 is in agreement with the concept of existence of such structural domains at all temperatures below the Néel point. As the temperature is increased, the amount of the tetragonal phase increases either smoothly or jumpwise, depending on the actual method of preparation of the sample and on the sample state (Fig. 5).

Let us turn now to the narrow absorption lines near 30 GHz observed in R_2CuO_4 crystals (R = Pr, Nd, Sm, Eu, Gd) for $T > T_0$ (Figs. 3, 7, 8). These lines can be associated with the anomalies in the dynamic magnetic susceptibility revealed by us earlier in R_2CuO_4 (R = Pr, Eu, Gd) in the same frequency range [14, 26, 27]. We assumed the observed anomalies to originate from 2D homogeneous, well-defined spin-wave excitations in the CuO_2 sheets. The gap width (ω_{2D}) for these excitations was governed by the fairly strong uniaxial anisotropy along the c axis, which provided spin correlation on a scale smaller than the correlation length of 2D spin fluctuations [14, 26]. This interpretation of the nature of the narrow absorption lines close to 30 GHz is not at odds with the results reported here. The fact that the spin-wave excitations with ω_{2D} in R_2CuO_4 crystals with R = Pr, Nd, Sm, Eu, and Gd are observed at a similar frequency ~30 GHz implies the existence, in the CuO_2 sheets of all these crystals at temperatures $T > T_0$, of 2D spin fluctuations with large correlation lengths and of a uniaxial anisotropy of similar magnitude along the c axis.

4. CONCLUSION

Thus, similar absorption bands have been observed above 100 GHz in R_2CuO_4 crystals with R = Pr, Sm, and Eu for temperatures $T > T_0 \approx 20$, 80, and 150 K, respectively. R_2CuO_4 crystals with R = Pr, Nd, Sm, and Eu were found to have similar absorption bands in the vicinity of 30 GHz for $T > T_0 \approx 20$, 6, 80, and 150 K, respectively. These bands and lines originate, respectively, from quasi-2D in-plane spin-wave excitations and well-defined 2D spin-wave excitations governed by the uniaxial anisotropy along the c axis. These crystals also revealed absorption lines caused by lattice dynamics near temperatures T_0 in a continuous frequency range from 20 GHz to the in-plane spin-wave absorption edge. The observed features in the spin and lattice dynamics suggest the existence of phase transitions in these crystals near the T_0 temperatures; these transitions are associated with the changes in the structural and magnetic properties of the crystals. The temperatures T_0 depend on the actual RE-ion species, with the value of T_0 and the RE-ion radius being correlated.

The features observed in the spin-wave absorption bands and absorption lines indicate a lack of homogeneity in the quasi-2D spin and structural states for $T > T_0$ and the existence of spin–lattice correlations near temperatures T_0.

ACKNOWLEDGMENTS

This study was supported by the Russian Foundation for Basic Research (project no. 02-02-16140a and, in part, project no. 00-15-96757) and, in part, by the Basic Research Foundation of the Presidium of the RAS (project “Quantum Macrophysics”).

REFERENCES

1. H. Muller-Buschbaum and W. Wollschlager, Z. Anorg. Allg. Chem. **414**, 76 (1975).
2. L. A. Muradyan, R. A. Tamazyan, A. M. Kevorkov, *et al.*, Kristallografiya **35**, 861 (1990) [Sov. Phys. Crystallogr. **35**, 506 (1990)].
3. M. Braden, W. Paulus, A. Cousson, *et al.*, Europhys. Lett. **25**, 625 (1994).
4. S. Chakravarty, B. Halperin, and D. Nalson, Phys. Rev. B **39**, 2344 (1989).
5. R. Sachidanandam, T. Yildirim, A. B. Harris, *et al.*, Phys. Rev. B **56**, 260 (1997).
6. D. Petitgrand, S. V. Maleyev, P. Bourges, and A. S. Ivanov, Phys. Rev. B **59**, 1079 (1999).
7. V. V. Eremenko, S. A. Zvyagin, and V. V. Pishko, Pis’ma Zh. Éksp. Teor. Fiz. **52**, 955 (1990) [JETP Lett. **52**, 338 (1990)].
8. A. I. Smirnov, S. N. Barillo, and D. I. Zhigunov, Zh. Éksp. Teor. Fiz. **100**, 1690 (1991) [Sov. Phys. JETP **73**, 934 (1991)].
9. A. S. Ivanov, P. Bourges, D. Petitgrand, and J. Rossat-Mignod, Physica B (Amsterdam) **213–214**, 60 (1995).
10. A. S. Ivanov, P. Bourges, and D. Petitgrand, Physica B (Amsterdam) **259–261**, 879 (1999).
11. V. P. Plakhty, A. B. Stratilatov, and S. Beloglazov, Solid State Commun. **103** (12), 683 (1997).
12. A. V. Babinskiĭ, S. L. Ginzburg, E. I. Golovenchits, and V. A. Sanina, Pis’ma Zh. Éksp. Teor. Fiz. **57** (5), 289 (1993) [JETP Lett. **57**, 299 (1993)].
13. T. Chattopadhyay, J. W. Lynn, N. Rosov, *et al.*, Phys. Rev. B **49**, 9944 (1994).
14. E. I. Golovenchits, V. A. Sanina, and A. V. Babinskiĭ, Zh. Éksp. Teor. Fiz. **110**, 714 (1996) [JETP **83**, 386 (1996)].
15. A. V. Babinskiĭ, E. I. Golovenchits, N. V. Morozov, *et al.*, Fiz. Tverd. Tela (St. Petersburg) **34**, 60 (1992) [Sov. Phys. Solid State **34**, 31 (1992)].

16. A. A. Levin, Yu. I. Smolin, Yu. F. Shepelev, *et al.*, Fiz. Tverd. Tela (St. Petersburg) **42**, 147 (2000) [Phys. Solid State **42**, 153 (2000)].
17. E. I. Golovenchits and V. A. Sanina, Zh. Éksp. Teor. Fiz. **69**, 1301 (1975) [Sov. Phys. JETP **42**, 665 (1975)].
18. E. I. Golovnchits and V. A. Sanina, Pis'ma Zh. Éksp. Teor. Fiz. **74**, 22 (2001) [JETP Lett. **74**, 20 (2001)].
19. I. W. Sumarlin, S. Skanthakumar, J. W. Lynn, *et al.*, Phys. Rev. Lett. **68**, 2228 (1992).
20. E. I. Golovenchits and V. A. Sanina, Fiz. Tverd. Tela (St. Petersburg) **41**, 1437 (1999) [Phys. Solid State **41**, 1315 (1999)].
21. S. V. Maleyev, Phys. Rev. Lett. **85**, 3281 (2000).
22. R. D. Shannon, Acta Crystallogr. A **32**, 751 (1976).
23. M. Udagawa, Y. Nagaoka, N. Ogita, *et al.*, Phys. Rev. B **49**, 585 (1994).
24. Z. Fisk, P. G. Pagliuso, J. A. Sanjurjo, *et al.*, Physica B (Amsterdam) **305**, 48 (2001).
25. E. I. Golovenchits, V. A. Sanina, A. A. Levin, *et al.*, Fiz. Tverd. Tela (St. Petersburg) **44**, 2035 (2002) [Phys. Solid State **44**, 2130 (2002)].
26. E. I. Golovenchits, S. L. Ginzburg, V. A. Sanina, and A. V. Babinskiĭ, Zh. Éksp. Teor. Fiz. **107**, 1641 (1995) [JETP **80**, 915 (1995)].
27. E. I. Golovenchits and V. A. Sanina, Physica B (Amsterdam) **284–288**, 1369 (2000).

Translated by G. Skrebtsov

Physics of the Solid State, Vol. 45, No. 8, 2003, pp. 1513–1518. Translated from Fizika Tverdogo Tela, Vol. 45, No. 8, 2003, pp. 1440–1445.

MAGNETISM AND FERROELECTRICITY

Magnetic Properties of Electron-Irradiated Quasi-Layered Manganites $La_{2-2x}Sr_{1+2x}Mn_2O_7$ (x = 0.3, 0.35, 0.4)

T. I. Arbuzova, S. V. Naumov, and V. L. Arbuzov

Institute of Metal Physics, Ural Division, Russian Academy of Sciences, ul. S. Kovalevskoĭ 18, Yekaterinburg, 620219 Russia

Received September 6, 2002; in final form, January 16, 2003

Abstract—The magnetic properties of $La_{2-2x}Sr_{1+2x}Mn_2O_7$ polycrystals (x = 0.3–0.4) are studied over a broad temperature range 80–600 K. Quasi-two-dimensional manganites have a complex magnetic structure that undergoes several transitions from one type of magnetic ordering to another. A specific feature of these manganites is a hyperbolic dependence of inverse susceptibility in the transition region from the magnetically ordered to paramagnetic state for $T > 360$ K. This suggests the onset of ferrimagnetism. Electron irradiation to a fluence $\Phi = 1 \times 10^{18}$ electrons/cm^2 is shown to have no effect on the long-range magnetic order while favoring the formation of paramagnetic polarons and of an inhomogeneous paramagnetic state. © *2003 MAIK "Nauka/Interperiodica".*

1. INTRODUCTION

The current interest in perovskite-like manganite oxides of the Ruddlesden–Popper $A_{n+1}Mn_nO_{3n+1}$ series (n = 1, 2, …, ∞) stems from the colossal magnetoresistance effect [1, 2]. These compounds can be classified as magnetic semiconductors with strongly coupled magnetic and electronic subsystems. The most comprehensive study has been made of the physical properties of the $La_{1-x}A_xMnO_3$ three-dimensional (3D) manganites (n = ∞). $A_3Mn_2O_7$ (n = 2) has quasi-two-dimensional crystal structure. The MnO_2 magnetic bilayers are a large distance apart and are separated by insulating spacers. This can give rise to low-dimensional magnetism at not very low temperatures. To reveal the effect of structural dimensionality on the magnetic properties of the manganites, Moritomo *et al.* [3] studied the temperature dependences of magnetization in a field H = 100 Oe for $La_{0.6}Sr_{0.4}MnO_3$ (3D) and $La_{1.2}Sr_{1.8}Mn_2O_7$ (quasi-2D) single crystals with the same strontium content and showed them to be substantially different. $La_{0.6}Sr_{0.4}MnO_3$ has a high T_c = 361 K and exhibits a strong decrease in magnetization near T_c, which is characteristic of homogeneous ferromagnets. In $La_{1.2}Sr_{1.8}Mn_2O_7$, T_c = 90 K and the magnetization at T = 5 K is considerably lower. In the region $100 < T < 360$ K, the $M(T)$ dependence is slightly diffuse. Neutron diffraction studies made at low temperatures, $T < 10$ K, showed that $La_{2-2x}Sr_{1+2x}Mn_2O_7$ with x = 0.3 is a collinear antiferromagnet and that the compositions with x = 0.32–0.40 are collinear ferromagnets [2, 4]. The magnetic moments in the bilayer are ferromagnetically ordered, but the spin orientation depends on the doping level. There is currently no consensus on magnetic order in the intermediate temperature region $T_c < T < 360$ K. In [5, 6], $La_{1.4}Sr_{1.6}Mn_2O_7$ single crystals were reported to have 2D ferromagnetic correlations in the region $90 < T < 270$ K, while in [7], no 2D spin correlations were found. In [8], an inelastic neutron scattering study of $La_{1.2}Sr_{1.8}Mn_2O_7$ led to the conclusion that antiferromagnetic clusters with correlation length $\xi = 6.7 \pm 2.2$ Å coexist with ferromagnetic fluctuations with a correlation length $\xi = 9.3 \pm 1.3$ Å for $T > T_c$. Neutron diffraction measurements are not always capable of revealing noncollinear magnetic structures. Important information on the magnetic state can be derived from magnetic measurements, in particular, at high temperatures. The pattern of the temperature dependence of $\chi^{-1}(T)$, the sign of the Curie paramagnetic temperature θ, the relative magnitude of $T_c(T_N)$ and θ, and the magnitude of the effective magnetic moment μ_{eff} permit one to make conclusion regarding magnetic order, exchange interaction mechanisms, exchange parameters, and the valence state of magnetic ions. Data on magnetic measurements performed on quasi-layered manganites at high temperatures are practically lacking.

Investigation of the effect that the lattice and spin interactions exert on magnetic properties is important for proper understanding of the nature of the physical phenomena occurring in transition-metal oxides, including low-dimensional systems. Radiation-induced disorder in manganites can change the Mn–O bond lengths and Mn–O–Mn angles and shift the magnetic phase transition temperatures. $La_{1-x}A_xMnO_3$ exhibits a noticeable decrease in T_c only under high electron or ion irradiation doses [9, 10]. No study of the effect of radiation defects on the magnetic properties of quasi-two-dimensional manganites has been made. This communication reports on a study of the magnetic properties of original and electron-irradiated $La_{2-2x}Sr_{1+2x}Mn_2O_7$ manganites (x = 0.3–0.4) performed over a broad tem-

1063-7834/03/4508-1513$24.00

Table 1. Lattice parameters of $La_{2-2x}Sr_{1+2x}Mn_2O_7$ ($x = 0.3$–0.4)

Compound	a, Å (±0.002 Å)	c, Å (±0.002 Å)
$La_{1.4}Sr_{1.6}Mn_2O_7$	3.872	20.208
$La_{1.3}Sr_{1.7}Mn_2O_7$	3.874	20.120
$La_{1.2}Sr_{1.8}Mn_2O_7$	3.872	20.081

perature interval covering both the magnetically ordered and paramagnetic regions.

2. SAMPLES AND EXPERIMENTAL RESULTS

Polycrystalline samples of $La_{1.2}Sr_{1.8}Mn_2O_7$, $La_{1.3}Sr_{1.7}Mn_2O_7$, and $La_{1.4}Sr_{1.6}Mn_2O_7$ were synthesized using standard ceramic technology. The samples were prepared in two stages. First, a mixture of La_2O_3, $SrCO_3$, and Mn_3O_4 was calcined in air at 1400°C for 50 h. After thorough grinding and pelleting, the calcining was repeated. The samples thus prepared were single phase with *I*4/*mmm* tetragonal lattice symmetry. Table 1 lists the lattice parameters for $La_{2-2x}Sr_{1+2x}Mn_2O_7$ (x = 0.3, 0.35, 0.4). As the strontium concentration increases, the parameter a practically does not change, whereas the parameter c decreases noticeably, which implies a decrease in the magnetic-bilayer separation.

The temperature and field dependences of the magnetization and of the magnetic susceptibility were measured with a magnetic balance in the temperature region T = 80–600 K. The samples were irradiated by 5-MeV electrons to a fluence $\Phi = 1 \times 10^{18}$ electrons/cm^2 at T = 273 K in a helium-flow cryostat. After the electron irradiation and subsequent holding at room temperature for several days, no changes in the lattice parameters were observed.

Figure 1 displays temperature dependences of the specific magnetization $\sigma(T)$ of $La_{1.4}Sr_{1.6}Mn_2O_7$ measured in various dc magnetic fields. At H = 350 Oe, an increase in temperature near T = 100 K brings about a sharp decrease in magnetization down to σ = 3.0 G cm^3/g. In this temperature region, the metal–insulator transition occurs and the magnetoresistance reaches a maximum. The sharp drop in $\sigma(T)$ and the large value of the susceptibility imply the onset of a magnetic phase transition. In the region $120 < T < 360$ K, the magnetization of $La_{1.4}Sr_{1.6}Mn_2O_7$ falls off smoothly with increasing T. If magnetic order is completely destroyed, the field dependences of the magnetization $\sigma(H)$ should extrapolate linearly to zero. The presence of magnetization hysteresis loops at room temperature indicates, however, a persistence of ferromagnetic spin correlations [11]. Figure 2 presents the temperature dependence of inverse susceptibility, which shows that at high temperatures $La_{1.4}Sr_{1.6}Mn_2O_7$ resides in the paramagnetic state. Above T = 400 K, the susceptibility does not depend on magnetic field and follows the Curie–Weiss law $\chi = N\mu_{eff}/3k(T - \theta)$ with a positive Curie temperature θ and effective magnetic moment μ_{eff} close to the theoretical value. Qualitatively similar $\sigma(T)$ and $\chi^{-1}(T)$ dependences were obtained for $La_{1.3}Sr_{1.7}Mn_2O_7$.

$La_{1.2}Sr_{1.8}Mn_2O_7$ exhibits a somewhat different behavior of the magnetization $\sigma(T)$ above T = 100 K (Fig. 3). Near T = 165 K, the susceptibility $\chi = \sigma/H$ passes through a maximum, as does the $\chi(T)$ in the three-dimensional manganites $La_{1-x}Ca_xMnO_3$ for $0.6 \le x \le 0.9$ [12]. The maximum in χ is usually observed in antiferromagnets near the Néel temperature T_N and in

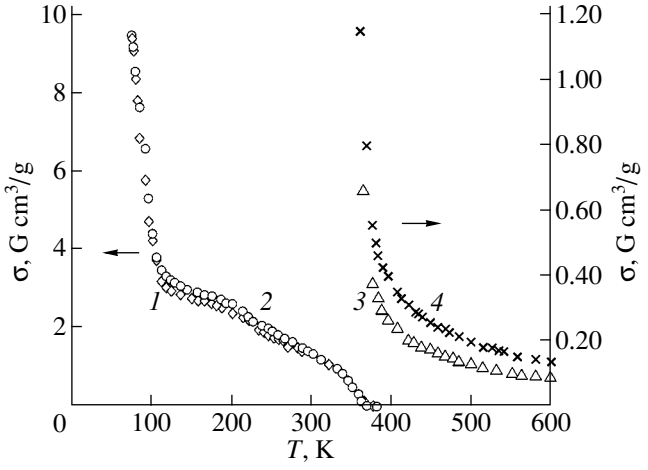

Fig. 1. Temperature dependences of the specific magnetization for (*1*, *3*) the original (Φ = 0) and (*2*, *4*) irradiated ($\Phi = 1 \times 10^{18}$ electrons/cm^2) $La_{1.4}Sr_{1.6}Mn_2O_7$ samples measured in magnetic field H equal to (*1*, *2*) 0.35 and (*3*, *4*) 2.65 kOe.

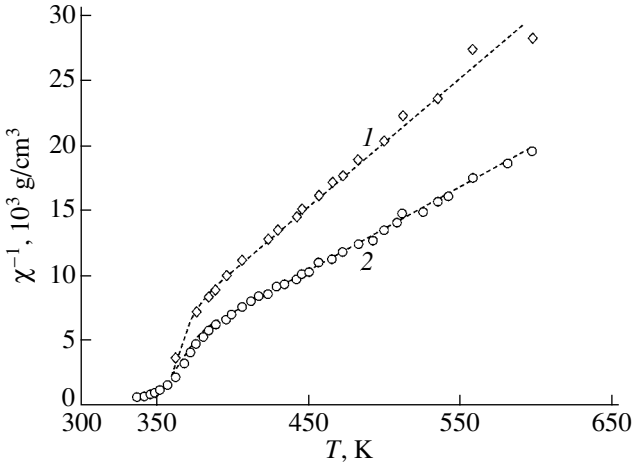

Fig. 2. Temperature dependences of the inverse susceptibility for $La_{1.4}Sr_{1.6}Mn_2O_7$ measured in a field H = 2.65 kOe. (*1*) Φ = 0 and (*2*) 1×10^{18} electrons/cm^2.

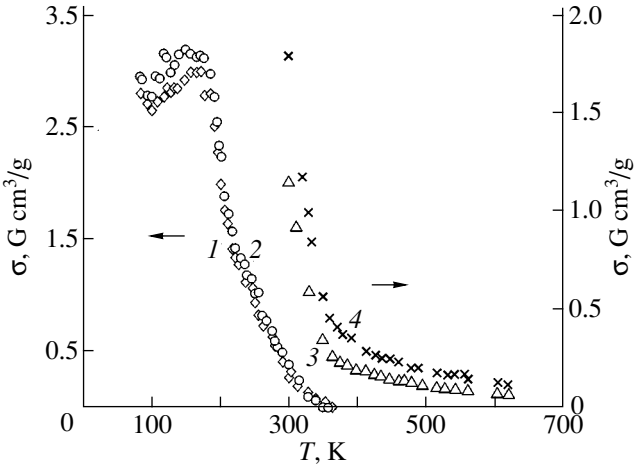

Fig. 3. Temperature dependences of specific magnetization for (*1*, *3*) the original (Φ = 0) and (*2*, *4*) irradiated (Φ = 1×10^{18} electrons/cm^2) samples of $La_{1.2}Sr_{1.8}Mn_2O_7$ measured in magnetic field *H* equal to (*1*, *2*) 0.35 and (*3*, *4*) 2.65 kOe.

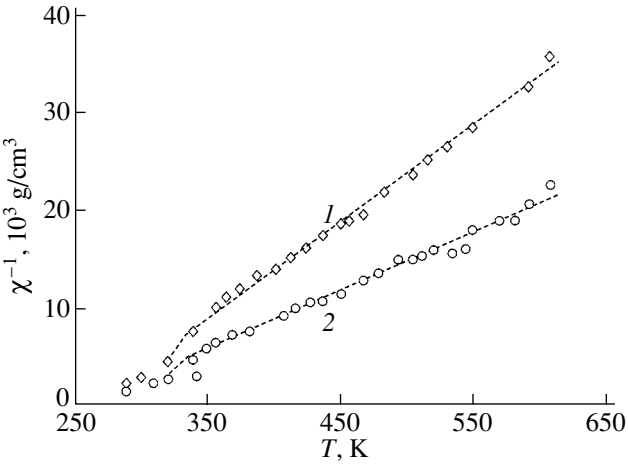

Fig. 4. Temperature dependences of the inverse susceptibility of $La_{1.2}Sr_{1.8}Mn_2O_7$ measured in a field *H* = 2.65 kOe. (*1*) Φ = 0 and (*2*) 1×10^{18} electrons/cm^2.

collinear ferrimagnets with two and more magnetic sublattices with $T_N > T_c$ [13]. Above T_N, such compounds become paramagnetic. In $La_{1.2}Sr_{1.8}Mn_2O_7$, the susceptibility depends on the magnetic field *H* above the temperature of the maximum in magnetization, which indicates preservation of the ferromagnetic component of the moment. At high temperatures, $T > 400$ K, $La_{1.2}Sr_{1.8}Mn_2O_7$, similar to $La_{1.3}Sr_{1.7}Mn_2O_7$ and $La_{1.4}Sr_{1.6}Mn_2O_7$, transfers to the paramagnetic state, but with an effective magnetic moment $\mu_{eff} = 6.71\mu_B$ that is higher than the theoretical value (Fig. 4, Table 2).

After the measurements, the samples were subjected to electron irradiation. To reveal the effect of radiation defects on the magnetic properties of quasi-two-dimensional manganites, the $\sigma(T)$ and $\chi^{-1}(T)$ dependences were obtained for the original and irradiated samples (Figs. 1–4). We readily see that after the electron irradiation the magnetic properties in the magnetic-order region $T < 360$ K practically did not change. Only $La_{1.2}Sr_{1.8}Mn_2O_7$ exhibits a slight increase in the ferromagnetic contribution for $T < 180$ K. The effect of electron irradiation is most clearly pronounced in the paramagnetic region. Although the values of the paramagnetic Curie temperature θ remained unchanged after irradiation, the effective magnetic moment increased substantially in all samples (Table 2). The observed values of μ_{eff} cannot be accounted for by the presence of Mn^{2+} ions with spin $S = 5/2$; rather, they indicate preservation of exchange coupling between magnetic ions in the high-temperature region.

3. DISCUSSION OF RESULTS

The $A_2Mn_2O_7$ perovskite-like manganites have a quasi-two-dimensional structure; namely, the MnO_2 manganite bilayers made up of MnO_6 octahedra are separated along the *c* axis by AO_2 insulating nonmagnetic spacers. The magnetic properties of the manganites are determined by the sum of contributions from several exchange interaction mechanisms, more specifically, superexchange interaction of manganese ions via oxygen ions, double exchange in the presence of man-

Table 2. Magnetic characteristics of $La_{2-2x}Sr_{1+2x}Mn_2O_7$ ($x = 0.3$–0.4)

Parameter	$La_{1.4}Sr_{1.6}Mn_2O_7$	$La_{1.3}Sr_{1.7}Mn_2O_7$	$La_{1.2}Sr_{1.8}Mn_2O_7$
$T_c^{(1)}$, K	100	112	≤90
$T_c^{(2)}$, K	354	350	315
θ, K	300	310	260
μ_{eff}, μ_B (theory)	6.53	6.46	6.39
μ_{eff}, μ_B (original sample)	6.54	6.51	6.71
μ_{eff}, μ_B (irradiated sample)	8.27	7.82	8.47
$\chi \times 10^{-2}$, cm^3/g ($T = 80$ K, $H = 350$ Oe)	4.0144	4.4678	2.6994

ganese ions in different valence states, and indirect exchange via free carriers. The last two mechanisms are qualitatively similar and account for the ferromagnetic coupling between the magnetic ions. The magnitude and sign of the Mn–O–Mn superexchange depend both on the lattice parameters and on the degree to which the 3*d*–2*p* wave functions overlap. Substitution of part of the La^{3+} by Sr^{2+} ions gives rise to the appearance of Mn^{4+} ions. It is known that the Mn^{3+}–O^{2-}–Mn^{3+} and Mn^{4+}–O^{2-}–Mn^{4+} superexchange interactions in perovskite-like compounds are antiferromagnetic and the Mn^{3+}–O^{2-}–Mn^{4+} interactions are ferromagnetic [14]. Our samples exhibit metallic conduction for $T < T_c^{(1)}$; therefore, in addition to superexchange, double exchange plays an important part in the onset of ferromagnetic order at low temperatures. Indirect exchange cannot set in for these compositions because of the low concentrations of free carriers. As the temperature increases up until $La_{2-2x}Sr_{1+2x}Mn_2O_7$ (x = 0.3, 0.35, 0.4) transfers to the semiconducting state, the role of superexchange strongly increases.

At high temperatures, the $La_{2-2x}Sr_{1+2x}Mn_2O_7$ quasi-2D manganites (x = 0.3–0.4) are paramagnets. As the temperature is lowered in the region 300–400 K, the $\chi^{-1}(T)$ curve assumes a hyperbolic, concave-down shape. The shape of the $\chi^{-1}(T)$ curve for ferromagnets and antiferromagnets near T_c and T_N, respectively, should be convex toward the temperature axis because of the persisting short-range order, as it is observed in the $La_{1-x}A_xMnO_3$ three-dimensional manganites. The hyperbolic $\chi^{-1}(T)$ dependence in the transition region from the paramagnetic state and the Curie temperature relation $0 < \theta < T_c$ imply ferrimagnetic spin ordering and the existence of more than one magnetic sublattice. Breakup into several magnetic sublattices and the onset of ferrimagnetism are possible in manganites, because the magnetic moments of the Mn^{3+} and Mn^{4+} ions and their concentrations are different [14]. The main feature of perovskite-type compounds is the weak interaction between ions residing on different sublattices. Noncollinear spin ordering of the Yaffet–Kittel type can set in within a certain temperature region. In $La_{2-2x}Sr_{1+2x}Mn_2O_7$, the lattice parameter c substantially exceeds the parameter a, which favors weakening of the superexchange coupling between the MnO_2 bilayers. For instance, the spin correlation length in the MnO_2 sheets of $La_{1.2}Sr_{1.8}Mn_2O_7$ above T_c = 112 K is twice that in the perpendicular direction [15]. Note that triangular magnetic ordering was experimentally established to exist in some manganites.

The orientation of the magnetic moments of the sublattices in noncollinear ferrimagnets depends not only on temperature but also on the external magnetic field. An increase in H changes the angles between the spin directions and the absolute values of the sublattice magnetic moments. The magnetization does not saturate even in strong H fields. The pattern of the temperature dependences of magnetization may be different in different fields. We observed such a behavior of magnetization in $La_{2-2x}Sr_{1+2x}Mn_2O_7$ (x = 0.3–0.4) at temperatures $80 < T < 360$ K. A change in the angles caused by a magnetic field in quasi-layered manganites is reported in a study [15], according to which, in $La_{1.2}Sr_{1.8}Mn_2O_7$, the angle between the magnetic moment and the b axis for $T = 125\ \text{K} > T_c = 112$ K varies with the field, to become 86.6° at H = 0, 74.1° at H = 1 T, and 53° at H = 2 T. At low temperatures, triangular ordering is less stable than collinear ordering. We believe that at low temperatures $La_{2-2x}Sr_{1+2x}Mn_2O_7$ is in the collinear ferromagnetic state due to the carrier-assisted exchange coupling and to the stability of collinear ordering. Near 100 K, where the compounds transfer to the semiconducting state, antiferromagnetic superexchange becomes comparable to the ferromagnetic interaction. The magnetic structure breaks down into sublattices, and noncollinear ferrimagnetism sets in in the intermediate temperature region. Direct transition of noncollinear ferrimagnetism to paramagnetism is impossible [13]. There should exist a region in which noncollinear spin ordering transforms to collinear and only after this does the compound transfer to the paramagnetic state.

The distinctive features of the quasi-2D manganites (compared to $AMnO_3$) are the smooth decrease in magnetization within a broad temperature region, the absence of magnetization saturation even in strong magnetic fields, and the hyperbolic shape of the temperature dependences of inverse susceptibility. These features are characteristic of an inhomogeneous state and noncollinear ferrimagnetic magnetic-moment ordering of the Yaffet–Kittel type [13, 14]. The existence of antiferromagnetic clusters side by side with ferromagnetic correlations [8, 16] likewise suggests a complex magnetic structure of $La_{2-2x}Sr_{1+2x}Mn_2O_7$ in the intermediate temperature region $100 < T < 360$ K. The magnetic characteristics of quasi-two-dimensional manganites are given in Table 2. We denoted the temperature of transition from the collinear ferromagnetic to inhomogeneous magnetically ordered state by $T_c^{(1)}$ and that from the inhomogeneous to the paramagnetic state, by $T_c^{(2)}$. Although they are lower than $T_c^{(2)}$, the positive values of the paramagnetic Curie temperature θ imply that the ferromagnetic and antiferromagnetic interactions are of the same order of magnitude. The lattice parameter c decreases with increasing Sr content. The decrease in bilayer separation brings about an enhancement of antiferromagnetic coupling between them. The decrease in the values of $T_c^{(1)}$, $T_c^{(2)}$, and θ in $La_{1.2}Sr_{1.8}Mn_2O_7$ may be considered as supportive evidence for the increase in the antiferromagnetic component of the total exchange interaction.

Radiation usually generates ion disorder. In contrast to ion and neutron irradiation, the electrons are light and produce point defects (vacancies and interstitials). At low irradiation doses, it is primarily oxygen ions that can be displaced from their sites. As shown by calculations, the threshold energy of oxygen displacement in HTSC compounds, which also have perovskite structure and are similar to the manganites in some of their properties, is five to six times lower than that for heavy elements and the number of displaced oxygen ions is two orders of magnitude larger [17]. It may be conjectured that we have a similar situation in manganites. We believe that the chemical composition of our samples did not change, because the irradiation was performed at a low temperature, and that the lattice parameters of the irradiated samples remained the same.

$La_{2-2x}Sr_{1+2x}Mn_2O_7$ has five identical Mn–O(1) short bonds (one apical and four equatorial) and one Mn–O(2) long bond involving the oxygen at the apex of the octahedron between the MnO_6 bilayers [18]. The most probable consequence of the irradiation is displacement of oxygen ions from this position. A displaced oxygen ion can localize only in the same sites O(2), because only these positions have vacancies [19]. Note that the parameter c and, hence, the bilayer separation in quasi-layered manganites are large; therefore, the possibility of a displaced oxygen ion being localized at interstices between the MnO_6 bilayers cannot be excluded. The observation that the length of the Mn–O apex bond in $La_{2-2x}Sr_{1+2x}Mn_2O_7$ undergoes a larger change than the equatorial bond length under hydrostatic pressure [20] can serve as indirect support of this conjecture. The fairly large dynamic structural distortions [16] may also produce favorable conditions for oxygen ion displacement. For instance, in $La_{2-2x}Sr_{1+2x}Mn_2O_7$, atomic displacements from regular-lattice sites in the region of $T = 360$ K are $u = 0.077$ Å, which is substantially larger than $u = 0.061$ Å for conventional thermal behavior. In our samples, irradiation to a dose $\Phi = 1 \times 10^{18}$ electrons/cm^2 did not change the values of T_c and θ or, hence, the averaged exchange parameters. Irradiation-induced displacements of oxygen from its positions may, however, produce oxygen-enriched regions in which the excess oxygen acts as an acceptor. The alignment of the carrier spin with the local-moment direction of the Mn ions closest to the ionized acceptor brings about a considerable gain in energy [21]. This situation gives rise to the formation of spin polarons with a susceptibility higher than that of the free spins. The free energy of the spin polarons is the lowest when compared with the homogeneous paramagnetic state [22]. Above T_c, the magnetic system placed in a magnetic field has "local" moments of two types, namely, paramagnetic spin polarons and free single Mn-ion moments. Because of the small size of the paramagnetic polarons and fluctuations in the orientation of their magnetic moments, the system as a whole resides in the paramagnetic state at high temperatures but with an enhanced magnetic moment.

The $La_{2-2x}Sr_{1+2x}Mn_2O_7$ quasi-layered manganites ($x = 0.3$–0.4) are three-dimensional magnets that undergo a number of order-order and order–disorder phase transitions. At low temperatures, $T < T_c^{(1)} \sim 100$ K, they undergo collinear ferromagnetic ordering. In the intermediate temperature region, $100 < T < 350$ K, the long-range order persists, but the magnetic system breaks up into sublattices; ferrimagnetic ordering sets in, which is indicated by the hyperbolic pattern of the temperature dependence of inverse susceptibility and the relation between the paramagnetic and ferromagnetic Curie temperatures. In $La_{1.2}Sr_{1.8}Mn_2O_7$, the temperature dependence of the susceptibility has a complex shape with a maximum near 165 K, which may be due to the $M(T)$ dependences for different sublattices following different behaviors. One should not overlook the possibility of the magnetic moments forming a triangular configuration. At high temperatures, $T > 400$ K, the quasi-layered manganites transfer to the homogeneous paramagnetic state. Low-dose electron irradiation does not affect long-range magnetic order. Radiation-induced disorder gives rise to the formation of paramagnetic polarons with an enhanced magnetic moment in the vicinity of point defects and manifests itself as an inhomogeneous paramagnetic state at high temperatures.

ACKNOWLEDGMENTS

This study was supported by the Russian Foundation for Basic Research (project no. 02-02-16429) and by the Ministry of Industry, Science, and Technologies of the Russian Federation (project no. 40.012.1.1.1153-14/02).

REFERENCES

1. E. Dagotto, T. Hotta, and A. Moreo, Phys. Rep. **344**, 1 (2001).
2. T. Kimura and Y. Tokura, Annu. Rev. Mater. Sci. **30**, 451 (2000).
3. Y. Moritomo, A. Asamitsu, H. Kuwahara, and Y. Tokura, Nature **380**, 141 (1996).
4. T. G. Perring, G. Aeppli, T. Kimura, *et al.*, Phys. Rev. B **58**, R14693 (1998).
5. Y. Tokura, T. Kimura, and T. Ishikawa, J. Korean Phys. Soc. **33**, 168 (1998).
6. R. Osborn, S. Rosenkranz, D. N. Argyrion, *et al.*, Phys. Rev. Lett. **81**, 3964 (1998).
7. R. H. Heffner, D. E. Mac Laughlin, G. J. Nieuwenhuys, *et al.*, Phys. Rev. Lett. **81**, 1706 (1998).
8. T. G. Perring, G. Aeppli, Y. Moritomo, and Y. Tokura, Phys. Rev. Lett. **78**, 3197 (1997).
9. B. I. Belevsev, V. B. Krasovitsky, and V. V. Bobkov, Eur. Phys. J. B **15**, 461 (2000).

10. C.-H. Chen, V. Talyanski, C. Kwon, *et al.*, Appl. Phys. Lett. **69** (20), 3089 (1996).
11. T. I. Arbuzova, I. B. Smolyak, S. V. Naumov, and A. A. Samokhvalov, Phys. Met. Metallogr., Suppl. 1 **91**, 5219 (2000).
12. T. I. Arbuzova, I. B. Smolyak, S. V. Naumov, *et al.*, Zh. Éksp. Teor. Fiz. **119**, 115 (2001) [JETP **92**, 100 (2001)].
13. J. Smit and H. P. J. Wijn, *Ferrites* (Wiley, New York, 1959; Inostrannaya Literatura, Moscow, 1962).
14. J. B. Goodenough, *Magnetism and the Chemical Bond* (Interscience, New York, 1963; Metallurgiya, Moscow, 1968).
15. S. Rosenkranz, R. Osborn, J. F. Mitchell, *et al.*, J. Appl. Phys. **83**, 7348 (1998).
16. R. P. Sharma, P. Fourmier, R. L. Greene, *et al.*, J. Appl. Phys. **83**, 7351 (1998).
17. V. V. Kirsanov, N. N. Musin, and E. I. Shamarina, Sverkhprovodimost: Fiz. Khim. Tekh. **7**, 427 (1994).
18. R. D. Sanchez, J. Rivas, C. Vazques-Vazques, *et al.*, Appl. Phys. Lett. **68**, 134 (1996).
19. J. F. Mitchell, D. N. Argyrion, J. D. Jorgensen, *et al.*, Phys. Rev. B **55**, 63 (1997).
20. T. Kimura, A. Asamitsu, Y. Tomioka, and Y. Tokuraet, Phys. Rev. Lett. **79**, 3720 (1997).
21. É. L. Nagaev, Usp. Fiz. Nauk **166** (8), 833 (1996) [Phys. Usp. **39**, 781 (1996)].
22. X. Vang and A. F. Freeman, J. Magn. Magn. Mater. **171**, 103 (1997).

Translated by G. Skrebtsov

Physics of the Solid State, Vol. 45, No. 8, 2003, pp. 1519–1522. Translated from Fizika Tverdogo Tela, Vol. 45, No. 8, 2003, pp. 1446–1449.

MAGNETISM AND FERROELECTRICITY

Inverse Magnetoresistance in (FeCoB)–(Al_2O_3) Magnetic Granular Composites

A. S. Andreenko*, V. A. Berezovets, A. B. Granovskiĭ*, I. V. Zolotukhin***, M. Inoue****, Yu. E. Kalinin*, A. V. Sitnikov***, O. V. Stogneĭ***, and T. Palevski*******

**Moscow State University, Vorob'evy gory, Moscow, 119899 Russia*

***Ioffe Physicotechnical Institute, Russian Academy of Sciences, Politekhnicheskaya ul. 26, St. Petersburg, 194021 Russia*

****Voronezh State Technical University, Moskovskiĭ pr. 14, Voronezh, 394026 Russia*

*****Toyohashi University of Technology, Toyohashi, 441-8580 Japan*

******International Laboratory of Strong Magnetic Fields and Low Temperatures, Wrocław, 53-421 Poland*

Received January 16, 2003

Abstract—The magnetoresistance, magnetization, and microstructure of granular composites with the general formula $(Fe_{40}Co_{40}B_{20})_x(Al_2O_3)_{100-x}$ were studied for contents of the amorphous metallic component both above and below the percolation threshold ($x \approx 43$). The low-temperature transverse magnetoresistance of the composites is negative at $x = 41$ and practically zero for $x = 49$. For metal contents below the percolation threshold ($x = 31$), a noticeable (7–8%) positive magnetoresistance, reached in magnetic fields of about 17 kOe, was observed. Possible mechanisms of the generation of inverse (positive) magnetoresistance are discussed. © *2003 MAIK "Nauka/Interperiodica".*

1. INTRODUCTION

The transverse magnetoresistance (MR) of crystalline and amorphous ferromagnets, magnetic multilayers, and granular films is, as a rule, negative; i.e., the resistivity ρ decreases as the sample is magnetized in a direction perpendicular to the current flow. For homogeneous ferromagnets, this property is a consequence of spin–orbit coupling, which brings about spontaneous anisotropy of the MR [1]. The giant MR revealed in metallic multilayers and granular metal–metal-type alloys (see, e.g., [2]) results from spin-dependent scattering and is also negative in all cases where the ferromagnetic layers or grains are from the same magnet. If the layers are from different ferromagnets, positive MR, which is termed inverse [3], may also be observed at certain values of the parameters of the spin-dependent scattering. One of the possible mechanisms of the inverse MR in metallic granular alloys, originating from the existence of two (*s* and *d*) current channels for each spin index, was proposed in [4].

A similar situation occurs in systems with tunnel contacts, such as sandwiched structures, multilayers, or metal–insulator granular alloys. Indeed, tunneling MR can be positive only in the case of inequivalent ferromagnets between which tunneling takes place; in addition, they must either possess spin polarizations of opposite signs or contain impurities of 3*d* elements near or on the surface of one of the layers [5]. Note also that scattering from domain walls, including nanosized ones [6], or crossing of a nanocontact by a spin-polarized electron [7] likewise gives rise to negative MR.

Positive transverse MR observed in Fe-based amorphous alloys has not found convincing interpretation [8]. Recently, Aronzon and Varfolomeev with coworkers [9, 10] detected positive MR in Fe–SiO_2 granular alloys with compositions close to the percolation threshold.

This communication reports on a study of the electrical resistivity, transverse MR, magnetization, and microstructure of the amorphous-ferromagnetic-metal–insulator composites $(Fe_{40}Co_{40}B_{20})_x(Al_2O_3)_{100-x}$. For compositions below the percolation threshold (the insulating phase) and magnetic fields below the saturation level, the MR is positive and can be called inverse by analogy with the inverse MR observed in metallic multilayers [3].

2. EXPERIMENTAL TECHNIQUE

Thin-film composites of the general formula $(Fe_{40}Co_{40}B_{20})_x(Al_2O_3)_{100-x}$ were prepared using ion-beam sputtering on a glass ceramic substrate. Using combined metal-alloy targets on whose surface aluminum oxide plates were fixed at different distances from one another permitted us to obtain, in one technological cycle, a series of samples of alloys with metal concentrations varying from 25 to 64 at. %. The method of sample preparation employed is described in considerable detail in [11]. This composition was chosen because of the spin polarization of the FeCo alloy being larger than that of Fe and Co; furthermore, by using Al_2O_3 as the insulator component in tunnel contact systems, a low tunneling barrier and a high tunneling MR

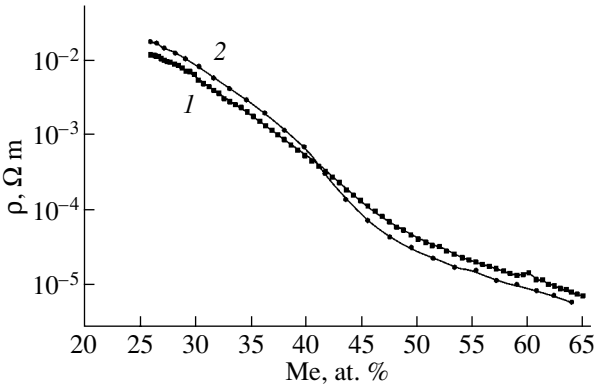

Fig. 1. Room-temperature electrical resistivity plotted vs. atomic fraction of the metal in the $(Co_{41}Fe_{39}B_{20})_x(Al_2O_3)_{100-x}$ composites deposited on fixed substrates (*1*) in the original state and (*2*) after annealing for 30 min at $T = 400$°C.

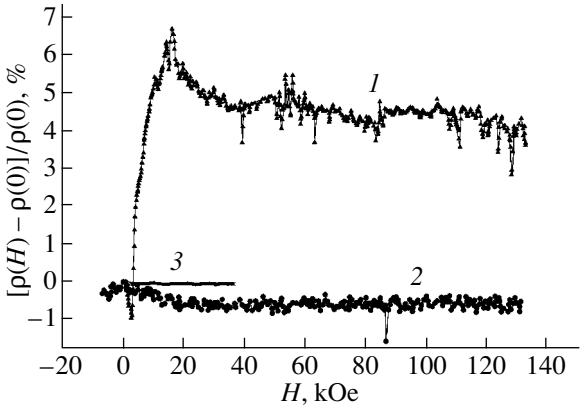

Fig. 2. Relative variation of electrical resistivity at $T = 4.2$ K plotted vs. perpendicular magnetic field for $(Co_{41}Fe_{39}B_{20})_x(Al_2O_3)_{100-x}$ in the original state for various values of x (at. %): (*1*) 31, (*2*) 41, and (*3*) 49.

can be obtained in this case [12]. The use of high-resistivity amorphous metals in place of crystalline ones was expected to favor electron injection into the insulator.

The thickness of the films thus prepared was about 10 μm. Electron microscopy studies of the structure of the samples showed them to consist of metal grains distributed randomly through the Al_2O_3 dielectric host. The grains were, on the average, 2–5 nm in size. Note that the metal grains produced in sputtering are not completely isolated from one another (even for high insulator concentrations) but instead form small conglomerates and chains in the film plane.

The transverse MR (with the magnetic field applied perpendicular to the film plane) was measured using the standard four-probe method at $T = 4.2$ K in fields of up to 140 kOe. The measurements were conducted with both dc and ac current at frequencies of 7 and 53.5 Hz.

The magnetization was measured at 4.2 K with a capacitance magnetometer in fields of up to 140 kOe. To permit comparison with the magnetoresistance data and to exclude the effect of the demagnetizing factor, the measurements were carried out in the same geometry; i.e., the field was applied perpendicular to the sample plane.

3. RESULTS AND DISCUSSION

Figure 1 presents composition dependences of the electrical resistivity ρ measured at room temperature (curve *1*). We readily see that, as the metal content is increased from 25 to 64 at. %, the conductivity of the system changes nonmonotonically by four orders of magnitude. The room-temperature resistivity of the granular alloy with $x = 64$ exceeds that of the $Fe_{40}Co_{40}B_{20}$ amorphous alloy by one and a half order of magnitude, which suggests the importance of the role played by the grain contacts. The strong increase in electrical resistivity with increasing content of the insulating phase is fairly obvious, because the metallic character of conduction transforms to nonmetallic. The metal–insulator transition follows a smooth course, and, as is well known, it is difficult to derive the percolation threshold from the concentration dependence of the resistivity alone. To determine the percolation threshold more accurately, the composites were heat-treated at 400°C. Heat treatment of the composites brings about an increase in the electrical resistivity of the alloys below the percolation threshold and its decrease beyond the threshold (curve *2* in Fig. 1). The crossing point of the concentration dependences of electrical resistivity of the original and heat-treated composites yields the percolation threshold, which was found to be $X \cong 42$ at. %.

Figure 2 displays magnetic field dependences of the resistivity for three alloys with $x = 31$, 41, and 49 measured at the temperature $T = 4.2$ K. In the metal-rich alloy with $x = 49$, i.e., above the percolation threshold, $x > x_c$, the resistivity is practically independent of magnetic field. In view of the metallic conduction in this compound (Fig. 1), this appears fairly obvious. For the composition close to the percolation threshold ($x = 41$) on the insulator side of the metal–insulator transition, the resistivity is seen to decrease by 0.7% in a field $H = 20$ kOe. The resistivity remains constant thereafter with increasing field. This negative MR is typical of systems with tunnel contacts. The reason for the somewhat smaller values of the tunneling MR than, for instance, in the Fe–SiO_2 [9] or CoFe–MgF_2 [12] systems is most likely that the grains in our composites near the percolation threshold are combined in clusters with the same magnetic moment orientation rather than being completely isolated by the insulating host matrix. Below the percolation threshold (the alloy with $x = 31$), a considerable increase in the electrical resistivity, up to 6–7%, is observed. This inverse MR occurs at fields close to saturation (Fig. 3), but as the field continues to increase

the resistivity decreases slightly. The inverse MR decreases rapidly with increasing temperature and practically does not exist at room temperature. Note also that resistivity measurements made on samples of this composition at a frequency of 53.5 Hz involve inductance, the imaginary part of the impedance; therefore, the dc and ac electrical resistivity dependences on magnetic field slightly differ.

Consider the possible mechanisms of inverse MR in the granular alloys studied. First, one should disregard mechanisms involving intragrain scattering, more specifically, the anisotropic MR, which is negative in transverse geometry; the Lorentz contribution, which is certain to be small for small free paths; and scattering from domain walls. This conclusion follows immediately from a comparison of the MR for the samples with x = 31 and 49. Second, the magnetic field suppresses the quantum interference effects, which may be significant at low temperatures near the percolation threshold [13], and, therefore, weak localization can give rise to negative MR. Furthermore, the effect observed is too large (7–8%) to be assigned to quantum interference processes. Third, we also have to exclude the part played by scattering from intergrain contacts, which likewise produces negative MR [7]. Finally, the effect of size quantization should also be neglected because of the inevitable dispersion of grains in size and their fairly large dimensions.

Tunneling MR can be positive if the magnetic moments of the grains responsible for the electrical resistivity are originally parallel in the film plane (in the insulating phase, the fraction of these grains is insignificant). Upon application of the field, the magnetic moments of these grains are first oriented antiparallel along the field direction (or, which is more likely, the magnetic moment of one of the grains becomes aligned with the field while that of the other retains its in-plane orientation) and then become parallel in the saturation field. This mechanism cannot be completely excluded, although in the initial stage of magnetization (Fig. 2) the resistivity decreases, which argues for the conventional mechanism of negative MR in weak fields, and no features were observed in the field dependences of magnetization measured up to 200 Oe.

Another possible explanation may involve field-induced magnetic blockage. Transport in the insulator phase occurs either by tunneling or by activated hopping over localized states. The activation energy may contain, besides the main Coulomb term (Coulomb blockage), an additional term associated with *sd* exchange of the conduction electron with the magnetic moment of the grain, which was first put forward in the classical study [14] and called magnetic blockage. The possibility of this mechanism of positive MR being operative in a system of superparamagnetic or single-domain grains was also pointed out in [15]. This additional term is fairly simple to estimate. The corresponding energy $E_M = kT_0$ is of the order of the conduction

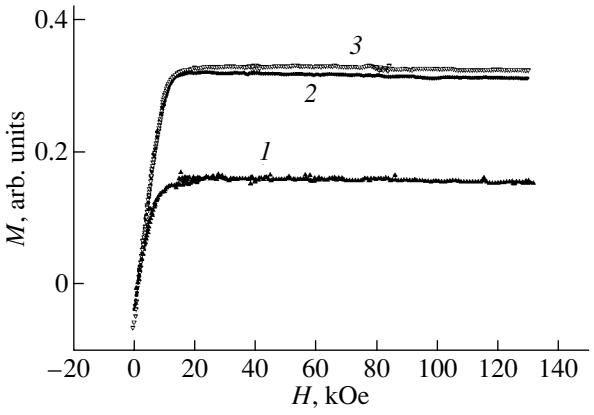

Fig. 3. Variation of the magnetization of $(Co_{41}Fe_{39}B_{20})_x(Al_2O_3)_{100-x}$ with perpendicular magnetic field at T = 4.2 K for various values of x (at. %): (*1*) 31, (*2*) 41, and (*3*) 49.

electron magnetization energy; i.e., T_0 is about 5–10 K, which coincides with the estimate made in [15]. This effect can be significant only at low temperatures comparable to T_0 and can disappear at high temperatures, exactly what was observed experimentally. Rather than ruling out completely the validity of this mechanism, one should point out two observations that disagree with this interpretation. First, in weak fields, the MR is negative, and, second, as shown by preliminary measurements, inverse MR is practically absent in the longitudinal geometry (with the magnetic field applied in the film plane along the direction of current flow).

A third possible explanation relates to magnetostriction. Assume for definiteness that the conduction is of activated nature (the actual form of the temperature dependence of ρ has no importance whatsoever for our subsequent estimates), $\rho = A\exp(E_a/kT)$, where the activation energy $E_a(s)$ depends on the tunneling gap s, i.e., on the grain separation. In the case where a field is applied perpendicular to the film surface and the magnetostriction constant λ_s is positive (which is characteristic of Fe-rich alloys), the grains stretch along the field, thereby causing an increase in their separation in the transverse direction, i.e., in the direction of the current flow. The activation energy increases to produce a positive MR:

$$\Delta\rho/\rho \approx \Delta s/s(E_a/kT) \approx \lambda(r/s)(E_a/kT), \qquad (1)$$

where r is the grain size in the direction of the field. As follows from this estimate, for the typical values of the parameters $\lambda \approx 10^{-5}$–10^{-4}, $r \approx 10$ nm, and $s \approx$ 1–10 nm, the MR becomes as high as 1–10% for a reasonable ratio of the activation energy to temperature, $E_a/kT \approx 10^2$–10^3, provided the temperature is of the order of liquid-helium temperature. This estimate is of a purely qualitative nature; a self-consistent theory should draw on the theory of three-dimensional percolation with electrons following optimal trajectories. This estimate

also shows that inverse MR (i) should vanish rapidly with increasing temperature, (ii) exists only in an insulating phase with a high activation energy, (iii) is practically zero in the longitudinal geometry in the case of positive magnetostriction, and (iv) is small for nanosized grains. The magnetostriction-induced change in grain dimensions and, hence, the inverse MR reach the maximum value at saturation magnetization. All these conclusions are in agreement with the experiment. Moreover, an increase in the effective tunneling gap should also become manifest in the imaginary part of the impedance, which, as the capacitive and inductive components of an electric circuit, is connected with the gap geometry.

4. CONCLUSION

Thus, low-temperature transverse MR of the composites $(Fe_{40}Co_{40}B_{20})_x(Al_2O_3)_{100-x}$ is practically zero for metal alloys beyond the percolation threshold and negative in its immediate vicinity; for metal contents less than the value corresponding to the percolation threshold, the MR in the insulating phase is inverse (positive). The inverse MR can be as large as 7–8% in magnetic fields of about 17 kOe, i.e., in fields corresponding to saturation. Analysis of the possible mechanisms of inverse MR permits the suggestion that the observed features in the MR behavior are of magnetostriction nature. Direct evidence for the proposed mechanism may come from comprehensive measurements of the field dependence of magnetostriction and longitudinal magnetoresistance. This study is planned for the near future.

ACKNOWLEDGMENTS

This study was supported in part by the Russian Foundation for Basic Research (project nos. 02-02-16102, 03-02-96436, 03-02-16127), the "Universities of Russia" program, and the Ministry of Education, Science, Sports, and Culture of Japan (grant no. 14-205045).

REFERENCES

1. A. V. Vedyaev, A. B. Granovskiĭ, and O. A. Kotel'nikova, *Kinetic Phenomena in Disordered Ferromagnetic Alloys* (Mosk. Gos. Univ., Moscow, 1992).
2. D. Dieny, S. Sankar, M. R. McCattney, *et al.*, J. Magn. Magn. Mater. **185**, 283 (1998).
3. C. Vouille, A. Barthelemy, F. Elokan Mpondo, *et al.*, Phys. Rev. B **60**, 6710 (1999).
4. A. Granovskiĭ, V. Kovalev, and J. P. Clerc, Vestn. Mosk. Univ., Ser. 3: Fiz., Astron., No. 2, 60 (2000).
5. D. Bagrets, A. Bagrets, A. Vedyayev, and B. Dieny, Phys. Rev. B **65**, 064430 (2002).
6. M. Viret, Y. Samson, P. Warin, *et al.*, Phys. Rev. Lett. **85**, 3962 (2000).
7. N. Garcia, M. Munoz, V. V. Osipov, *et al.*, J. Magn. Magn. Mater. **240**, 92 (2002).
8. M. Prudnikova, A. Granovsky, and V. Prudnikov, J. Magn. Magn. Mater. **166**, 201 (1997).
9. B. A. Aronzon, D. Yu. Kovalev, A. E. Varfolomeev, *et al.*, Fiz. Tverd. Tela (St. Petersburg) **41** (6), 944 (1999) [Phys. Solid State **41**, 857 (1999)].
10. A. E. Varfolomeev and M. V. Sedova, Fiz. Tverd. Tela (St. Petersburg) **45** (3), 500 (2003) [Phys. Solid State **45**, 529 (2003)].
11. Yu. E. Kalinin, A. T. Ponomarenko, A. V. Sitnikov, and O. V. Stogneĭ, Fiz. Khim. Obrab. Mater. **5**, 14 (2001).
12. N. Kobayashi, S. Onuma, T. Masumoto, and H. Fujimori, J. Appl. Phys. **90**, 4159 (2001).
13. C. Wan and P. Sheng, Phys. Rev. B **66**, 075309 (2002).
14. J. I. Gittleman, Y. Goldstein, and S. Borowsky, Phys. Rev. B **5**, 3609 (1972).
15. J. Inoue and S. Maekawa, Phys. Rev. B **53**, 11927 (1996).

Translated by G. Skrebtsov

Physics of the Solid State, Vol. 45, No. 8, 2003, pp. 1523–1529. Translated from Fizika Tverdogo Tela, Vol. 45, No. 8, 2003, pp. 1450–1455.

MAGNETISM AND FERROELECTRICITY

Displacive Magnetic Phase Transitions upon Spin Ordering in Magnets with Strong Single-Ion Anisotropy

V. M. Kalita* and V. M. Loktev**

** Institute of Physics, National Academy of Sciences of Ukraine, pr. Nauki 46, Kiev, 03028 Ukraine*

*** Institute of Theoretical Physics, National Academy of Sciences of Ukraine, Kiev, 03143 Ukraine*

e-mail: vloktev@bitp.kiev.ua

Received October 30, 2002; in final form, January 20, 2003

Abstract—This paper reports on the results of investigations into the magnetic ordering of magnets with integer spins of ions and sufficiently strong easy-plane single-ion anisotropy. It is demonstrated that magnetic ordering in the studied systems occurs through a displacive magnetic phase transition. The magnetic polarization of ionic states, which spontaneously arises at the phase transition point, acts as an order parameter in displacive magnetic phase transitions. The magnetically ordered state in the magnets under consideration is formed as a result of competition between the exchange interaction and single-ion anisotropy. © *2003 MAIK "Nauka/Interperiodica".*

1. INTRODUCTION

It is known that, in magnets with easy-plane anisotropy, the single-ion anisotropy, like the interionic anisotropy, has an orienting effect on the spins but, unlike the latter anisotropy, prevents magnetic ordering in the system [1]. As was shown in our recent work [2], the effect of single-ion anisotropy induced by a crystal field affecting the spins through the spin–orbit interaction is similar to disordering caused by the entropy. The role played by single-ion anisotropy becomes particularly important either in the case when the ground state of transition ions in a cubic field appears to be degenerate (nonfrozen orbital motion) or in rare-earth magnets. Systems with an integer spin frequently occur in states such that three closely spaced levels turn out to be the lowest lying levels [1]; consequently, these system can be described in the framework of a simple spin model with an effective single-site spin $S = 1$. Within this model, single-ion anisotropy has the simplest form represented by terms quadratic in the spin-projection operators. Note that, for rare-earth magnets, the anisotropy parameters can be very large and even comparable to the exchange interaction parameters. For this reason, the anisotropic interactions considered in earlier works [3, 4] were treated in an Ising form.

Despite the occurrence of an exchange interaction with sufficiently strong easy-plane single-ion anisotropy in spin systems with an integer spin S, the nonmagnetic state with a zero average ion magnetization [1, 5] can arise not from an equal population of all spin states but from a singlet (van Vleck) nature of the lowest state. However, even though such a singlet-type magnet has a zero initial magnetization, the application of an external magnetic field aligned with the hard axis can result in a phase transition from a paramagnetic state to a magnetically ordered state. This is a first-order phase transition in the case of Ising spin–spin interactions and strong single-ion anisotropy [1]. However, in the case when ions in the system undergo isotropic spin–spin interactions of the Heisenberg type, the magnetic field induces a second-order phase transition [2, 6–8]. Earlier [2], we demonstrated that, as the magnetic field reaches a critical value, each ion is polarized and the crystal as a whole becomes magnetized; i.e., the material undergoes a continuous transition. In [2], this transition was treated as a displacive magnetic phase transition. Note that, upon the above phase transitions in the magnetic systems under investigation, no displacement of the ions is revealed (magnetoelasticity is disregarded). The particular interest expressed by researchers in similar magnetic phase transitions stems from the fact that a large number of magnetic materials undergo phase transitions of this type [9].

The term "displacive magnetic phase transition" was introduced in [2] with the aim of emphasizing that the magnetic phase transition studied in that work cannot be considered an order–disorder phase transition. The fundamental difference between transitions of these types lies in the fact that all (magnetic and nonmagnetic) systems undergoing displacive phase transitions are formed by ions with a single-well potential, whereas systems with order–disorder phase transitions are composed of ions whose potential is characterized by at least two wells.

It should be noted that the magnetic structure formed in a system exhibits a magnetic order with a nonzero average magnetic moment of the ion [10]. According to modern concepts, the magnetic structure in the majority of magnets, as a rule, is formed upon an order–disorder phase transition [11]. This fact was orig-

1063-7834/03/4508-1523$24.00

inally established by Landau [12]. In the course of the phase transition, the spectrum of paramagnetic ions forming the lattice changes, the states with opposite spin projections at the phase transition point (and above) become equally probable, and the system as a whole transforms into a disordered state.

The fact that the transition from a singlet state to a ferromagnetic state was considered a displacive magnetic phase transition implied that this transition, being, in essence, an order–disorder transition, cannot be treated in terms of the concepts used in [10, 11]. Actually, the magnetic field–induced phase transition studied in [2] corresponds to the case when $T = 0$, whereas the magnetic structure and the magnetically ordered state in [10, 11] are formed upon spontaneous (rather than external field–induced) lowering of the symmetry due to the simultaneous appearance of magnetic moments of ions at the Curie point (and below it). As will be shown below, this transition in an isotropic ferromagnet is accompanied by a substantial transformation of the single-ion spin spectrum and belongs to order–disorder phase transitions. Therefore, in order to justify the applicability of the concept of displacive magnetic phase transitions to anisotropic magnets, it is necessary to analyze the possibility of arising spontaneous magnetization of paramagnetic ions with a decrease in the temperature under conditions where their spectrum retains its initial structure upon the transition and the average magnetization of the crystal is achieved as a result of the polarization of ionic states in a spontaneously induced exchange field. Recall that, upon order–disorder magnetic phase transitions, the spin projections of ions in the paramagnetic state are nonzero but the average magnetizations of the ion and the crystal as a whole are equal to zero due to the equal probabilities of atomic states.

The order–disorder magnetic phase transition from a paramagnetic state to a ferromagnetic (or antiferromagnetic) state occurs as a result of competition between the exchange interaction providing ordering and the entropy tending to maximum disordering of the system. At the same time, the displacive magnetic phase transition to a magnetically ordered state at the Curie point T_C is due to competition between interactions of two types, namely, exchange and anisotropic interactions.

Below, we will analyze the displacive magnetic phase transition. For this purpose, we will construct the theory of a ferromagnet with an isotropic exchange interaction between the nearest spins with $S = 1$ and easy-plane single-ion anisotropy. In this case, the polarization of ionic states plays the role of an order parameter.

It should be noted that, in earlier studies [1, 5, 7–9], magnetic phase transitions in similar ferromagnets, as a rule, were considered within the mean-field approximation in which the average magnetization served as the order parameter. However, this approach failed to reveal the differences between the displacive magnetic phase transition and the order–disorder magnetic phase transition.

2. HAMILTONIAN

The simplest Hamiltonian of the model ferromagnetic system under consideration can be written in the form

$$H = -\frac{J}{2}\sum_{\mathbf{n},\,\boldsymbol{\rho}} S_{\mathbf{n}} S_{\mathbf{n}+\boldsymbol{\rho}} + D\sum_{\mathbf{n}} (S_{\mathbf{n}}^{Y})^2, \qquad (1)$$

where $J > 0$ is the parameter of the exchange interaction between the nearest spins and $\mathbf{n}$ and $\mathbf{n} + \boldsymbol{\rho}$ are the vectors specifying their positions. The single-ion anisotropy constant is positive ($D > 0$), which corresponds to the easy-plane anisotropy. The Y axis is aligned along the hard axis.

In the magnetically ordered state without an external magnetic field, the vector of the average magnetic moment of each ion lies in the easy plane. Let us assume that the Z axis is aligned along the vector of the average magnetization and the X axis is perpendicular to the Z and Y axes. Then, within the mean-field approximation, the single-ion Hamiltonian can be represented in the following form:

$$H_0 = -h_{ex}S^Z + D(2 - (S^Z)^2 - (S^X)^2). \qquad (2)$$

Here, $h_{ex} = Jzs$ is the mean (exchange) field acting on the spin of the ion, s is the average thermodynamic spin of ion, $\mathbf{s} \parallel Z$, and z is the number of the nearest neighbors.

The spectrum of Hamiltonian (2) is well known [13]. The energy eigenvalues of this Hamiltonian have the form

$$\varepsilon_0 = \frac{1}{2}D - \sqrt{h_{ex}^2 + \frac{1}{4}D^2}, \quad \varepsilon_1 = D, \quad \varepsilon_2 = \frac{1}{2}D + \sqrt{h_{ex}^2 + \frac{1}{4}D^2}. \qquad (3)$$

The lowest energy ε_0 corresponds to the ground state, and the energies of the excited states are equal to ε_1 and ε_2. From relationships (3), it follows that the inequality $\varepsilon_2 > \varepsilon_1$ is always satisfied. The spin projections onto the Z axis in each state are given by the formulas

$$s_0 = \frac{h_{ex}}{\sqrt{h_{ex}^2 + D^2/4}}, \quad s_1 = 0, \quad s_2 = -s_0. \qquad (4)$$

It can be seen from formulas (4) that the spin projections depend on the mean field h_{ex} or the average spin $s = s(T)$ and, hence, on the temperature.

It is of interest to compare the evolution of the single-ion spectra for the exchange ferromagnet at $D = 0$ [expressions (3) and (4) admit the passage to the limit $D \longrightarrow 0$] and the evolution for the ferromagnet with the

easy-plane single-ion anisotropy at $D \longrightarrow 2Jz$. In the former case, at $T < T_C$, we have $h_{ex} \neq 0$, three levels are equidistantly arranged, and the spin projections are as follows: $s_0 = -s_2 = 1$ and $s_1 = 0$. When the temperature reaches a critical value ($T = T_C$), the exchange interaction field vanishes ($h_{ex} = 0$) and the ion has one triply degenerate level with zero energy. In the paramagnetic phase ($T > T_C$), the external field $\mathbf{h} \perp Y$ removes this degeneracy but the spin projections in each state are equal to those in the ferromagnetic phase, irrespective of the field h (even at $h \longrightarrow 0$). Therefore, at $D = 0$, the phase transition between the ferromagnetic state and the paramagnetic state is an order–disorder transition.

For an anisotropic ferromagnet, when the single-ion anisotropy constant D is not very small (in particular, when $D \longrightarrow 2Jz$), the spin projections already at $T = 0$ are substantially less than the limiting value $s_0(T = 0) = \sqrt{1 - D^2/4J^2z^2} \ll 1$; i.e., $|2Jz - D| \ll D$ [1, 2, 5, 7, 9, 13]. In this case, the inequality $h_{ex} \ll D$ is satisfied over the entire temperature range of existence of the ferromagnetic state (including temperatures $T \longrightarrow T_C$). The three-level spectrum of the ion has a quasi-two-level structure consisting of the ground level and two closely spaced excited levels. The excited levels have close energies [the splitting between the excited levels is determined by the ratio $(h_{ex}/D)^2 \ll 1$], and the energy separation between the ground and excited levels is $\sim D$. Undeniably, the spin projections at $T \neq 0$ are less than $s_0(T = 0)$. An increase in the temperature T results in a decrease in the spin projections. At the phase transition point and over the entire temperature range of the paramagnetic phase, the spin projections in all single-ion states (including the splitting) are equal to zero. In the paramagnetic state, the application of the external field leads to splitting of the doublet. If the field is aligned along the easy plane, the energy in the ground state decreases. At $\mathbf{h} \parallel Y$, the levels are split without changing the energy of the ground state. This is explained by the fact that the magnetic field aligned with the hard axis does not polarize the ground state of the ions, which remains unchanged. On the other hand, the field $\mathbf{h} \perp Y$ polarizes the ground state of the ion. Specifically, in the paramagnetic state, the stronger the field, the larger the projections of the spin induced by this field. At $h \longrightarrow 0$, these projections vanish.

According to the theory of magnetic phase transitions, it is this infinitely weak field that is responsible for the appearance and orientation of the average magnetic moment in the easy plane [14]. Hence, it is quite evident that, when the ground state of the ion in the paramagnetic phase is represented by a singlet whose population is always larger than the population of the levels of the higher lying doublet, the spontaneous magnetization can be absent only at $s_0 = 0$. Consequently, we can draw the inference that, in the anisotropic magnet under consideration, not the total average spin of the ion but the partial projection of the spin of the ion in the ground state (this projection becomes equal to zero at the phase transition point) should serve as the order parameter upon phase transition from the ferromagnetic state to the paramagnetic state. In the absence of the external field **h**, the spontaneous magnetization in this magnet is due to the collective spontaneous polarization of single-ion states, which is self-consistently induced by the exchange field. The theory accounting for these specific features can be constructed using the Gorsky–Bragg–Williams method [15].

3. THE FREE ENERGY AND EQUATIONS OF STATE

By definition, the free energy can be written in the form $F = E - TS_{en}$, where E is the internal energy and S_{en} is the entropy. Note that, in the mean-field approximation, S_{en} is the configurational entropy. The internal energy of system (1) per particle is defined by the relationship

$$E = -\frac{Jz}{2}s^2 + D(2 - Q_{ZZ} - Q_{XX}), \tag{5}$$

where Q_{ZZ} and Q_{XX} are the thermodynamic averages of the operators $(S^Z)^2$ and $(S^X)^2$, which are related to the spin quadrupole moments of the ions [13]. The expression for the entropy has the standard form

$$S_{en} = -\sum_{j = 0, 1, 2} p_j \ln p_j, \tag{6}$$

where p_j are the probabilities of the single-ion states (3), so that $\sum_{j = 0, 1, 2} p_j = 1$.

The eigenfunctions corresponding to the energy eigenvalues (3) of Hamiltonian (2) can be represented in the following form:

$$\begin{gathered}\psi_0 = \cos\phi|1\rangle + \sin\phi|-1\rangle, \quad \psi_1 = |0\rangle, \\ \psi_2 = -\sin\phi|1\rangle + \cos\phi|-1\rangle,\end{gathered} \tag{7}$$

where $|\pm 1\rangle$ and $|0\rangle$ are the eigenfunctions of the operator S^Z. Now, let us calculate the spin projections and the averages of the operators $(S^Z)^2$ and $(S^X)^2$. From relationships (7), it is easy to find that the spin projections in each particular state take the form $s_0 = -s_2 = \cos 2\phi$ and $s_1 = 0$. In this case, the partial averages of the operator $(S^Z)^2$ are constant and equal to 1, 0, and 1 and the averages of the operator $(S^X)^2$ are equal to $(1/2)(1 + \sin 2\phi)$, 1, and $(1/2)(1 - \sin 2\phi)$, respectively. Then, according to the definition, the thermodynamic averages s, Q_{ZZ}, and Q_{XX} can be written as

$$\begin{gathered}s \equiv s(T) = \cos 2\phi p_0 - \cos 2\phi p_2 \equiv \cos 2\phi \Delta p, \\ \Delta p > 0,\end{gathered} \tag{8}$$

$$Q_{ZZ} = p, \tag{9}$$

$$Q_{XX} = \frac{1}{2}(1+\sin 2\phi)p_0 + p_1 + \frac{1}{2}(1-\sin 2\phi)p_2 \equiv 1 - \frac{p}{2} + \frac{\Delta p}{2}\sin 2\phi. \quad (10)$$

Here, we introduced the variables $p_0 + p_2 = p$ and $p_0 - p_2 = \Delta p$. With the use of these variables, relationship (6) can be rewritten as

$$S_{en} = -\frac{p+\Delta p}{2}\ln\frac{p+\Delta p}{2} - \frac{p-\Delta p}{2}\ln\frac{p-\Delta p}{2} - (1-p)\ln(1-p). \quad (11)$$

The final expression for the free energy of the ferromagnet with $S = 1$ and the easy-plane single-ion anisotropy follows from relationships (5) and (11) with due regard for formulas (8)–(10); that is,

$$F = -\frac{1}{2}Jz(\Delta p)^2\cos^2 2\phi + D\left(1 - \frac{p}{2} - \frac{\Delta p}{2}\sin 2\phi\right) + T\left\{\frac{p+\Delta p}{2}\ln\frac{p+\Delta p}{2} + \frac{p-\Delta p}{2}\ln\frac{p-\Delta p}{2} + (1-p)\ln(1-p)\right\}. \quad (12)$$

The sought equilibrium state corresponds to the minimum of the free energy (12). In this case, ϕ, p, and Δp are the variational parameters. The minimization of the free energy with respect to these parameters gives the equations of state

$$2Jz(\Delta p)^2\cos 2\phi\sin 2\phi - D\Delta p\cos 2\phi = 0, \quad (13)$$

$$-Jz\Delta p\cos^2 2\phi - \frac{D}{2}\sin 2\phi + \frac{T}{2}\ln\frac{p+\Delta p}{p-\Delta p} = 0, \quad (14)$$

$$-D + T\ln\frac{p^2-(\Delta p)^2}{4(1-p)^2} = 0. \quad (15)$$

Note that the determination of the free energy by varying F with respect to the angle ϕ [see relationships (7)] is equivalent to its determination with the use of the self-consistent procedure [16], which is inappropriate in the given specific case (and at $T \neq 0$), because, as was noted above, the quantity $s(T)$ defined by relationship (8) is not an order parameter. For the ferromagnetic state, from expression (13), we have

$$\sin 2\phi = \frac{D}{2Jz\Delta p}. \quad (16)$$

It can be seen that the difference Δp substantially affects the quantity $s_0(T)$ [given by formula (4)]. Indeed, an increase in the temperature T results in a decrease in Δp; hence, the right-hand side of Eq. (16) can reach its limiting value $\sin 2\phi = 1$, which corresponds to $\cos 2\phi = 0$. On the other hand, the spin projection in the ground state can be represented by the expression

$$s_0(T) \equiv s_0 = \sqrt{1 - \frac{D^2}{4J^2z^2(\Delta p)^2}}. \quad (17)$$

From this expression, it follows that, with an increase in the temperature T, the partial spin projection corresponding to the ground state of the ion varies so that $s_0(T_C) = 0$. The temperature T_C at which the equality $s_0 = 0$ becomes valid is the temperature of the magnetic phase transition. As will be shown below, at this temperature, the magnetic susceptibility of the paramagnetic phase becomes infinite and the phase transition continuously proceeds as a second-order phase transition.

It is important that the phase transition is attended not by the splitting of the initially degenerate states and the magnetization but by the spontaneous polarization (owing to the exchange interaction) of the nondegenerate ionic states at the phase transition point. This results in a change in the spin projection of the ion in the ground state. In our opinion, it is this phase transition from the paramagnetic state to the ferromagnetic state that should be considered the displacive magnetic phase transition. The nondegenerate paramagnetic state of the singlet magnet is ordered and characterized by $\Delta p \neq 0$ and $s_0 = 0$.

The temperature T_C of the magnetic phase transition can be easily found from Eqs. (14) and (15) at $\sin 2\phi = 1$ [see relationship (16)]; that is,

$$T_C = \frac{D}{\ln\left(1 + \frac{D}{Jz}\right) - \ln\left(1 - \frac{D}{2Jz}\right)}. \quad (18)$$

At $D = 0$, from expression (18), we obtain $T_C = 2Jz/3$ for the system of spins with $S = 1$ [17]. At small ratios $D/Jz \ll 1$, the orientating effect of the anisotropy is dominant and, hence, from expression (18), we have

$$T_C = \frac{2}{3}Jz\left(1 + \frac{D}{4Jz}\right). \quad (19)$$

This implies an increase in the magnetic phase transition temperature T_C. On the other hand, with a substantial increase in the anisotropy at $D/2Jz \longrightarrow 1$, the temperature T_C [see expression (8)] decreases to zero [1].

The paramagnetic state with zero magnetization occurs in the range $T > T_C$. In this state, the condition $\Delta p \neq 0$ is always satisfied but the degree of ordering depends on the temperature; that is,

$$\Delta p(T) = \frac{1 - e^{-\frac{D}{T}}}{1 + 2e^{-\frac{D}{T}}}. \quad (20)$$

As follows from relationship (20), complete disordering ($\Delta p \longrightarrow 0$) in the paramagnetic state is achieved at temperatures corresponding to the inequality $D \ll T$. At $D \sim T$, the system in the paramagnetic state has a high degree of ordering due to a sufficiently large difference in the populations of the single-ion states. Therefore, at $T_C \sim D$, the phase transition to the ferromagnetic state proceeds as an order–disorder transition.

4. FREE ENERGY FOR THE CASE OF AN EXTREMELY WEAK EXCHANGE FIELD

The exchange field in an anisotropic magnet decreases as the phase transition point is approached (at $T \longrightarrow T_C$) and in the case when the anisotropy constant and the exchange interaction parameter become close in magnitude. Actually, at $D \le 2Jz$, the inequality $s_0 \ll 1$ holds at $T = 0$. Let us analyze this case. Within the approximation $h_{ex}/D \ll 1$, the energy eigenvalues given by expressions (3) can be rewritten in the form

$$\varepsilon_0 = -\frac{h_{ex}^2}{D}, \quad \varepsilon_1 = D, \quad \varepsilon_2 = D + \frac{h_{ex}^2}{D}. \tag{21}$$

Since we have $\varepsilon_{1,2} - \varepsilon_0 \approx D$ at $h_{ex}/D \ll 1$, it is assumed that $\varepsilon_1 \approx \varepsilon_2$. In turn, this implies that the influence of the exchange interaction on the populations of these levels can be ignored. Under this assumption, the level populations and the probabilities $p(T)$ and $\Delta p(T)$ over the entire temperature range (including the range $T < T_C$), according to expression (20), are determined only by the ratio D/T. As a result, the quantity s_0 remains the sole unknown (with an uncertain dependence on the temperature T) and, thus, appears to be the sole order parameter in the problem under consideration. By assuming that $s_0 \longrightarrow 0$ and retaining terms up to the fourth power in the series, we obtain

$$F = \frac{1}{4}[D\Delta p(T) - 2Jz(\Delta p(T))^2]s_0^2 + \frac{1}{16}D\Delta p(T)s_0^4. \tag{22}$$

It should be noted that, in the approximation used, the coefficient of s_0^2 in expression (22) becomes equal to zero at the temperature T_C specified by formula (18), which was derived from the exact solution.

Relationship (22) can be transformed into the following form:

$$F = \frac{1}{4}[D(T) - 2J(T)z]s_0^2 + \frac{1}{16}D(T)s_0^4. \tag{23}$$

Here, we introduced the designations $D(T) = D\Delta p(T)$ and $J(T) = J(\Delta p(T))^2$. It follows from expression (23) that the expansion of the free energy coincides with that of the ground-state energy for an easy-plane ferromagnet at $T = 0$ [2]. The temperature-dependent parameters $J(T)$ and $D(T)$ in expression (23) can be treated as effective parameters accounting for the level populations. Note that the exchange interaction parameter is quadratic in $\Delta p(T)$ and the single-ion anisotropy constant is proportional to $\Delta p(T)$. This behavior of the temperature dependences of the effective exchange interaction parameter and the effective single-ion anisotropy constant is clearly understood, because the exchange interaction is a two-particle interaction, whereas single-ion anisotropy has a one-particle nature.

Next, we use the approximate relationship (23) for the free energy in order to determine the temperature dependence of the static magnetic susceptibility χ of the paramagnetic phase under the condition $\mathbf{h} \perp Y$. At $h \longrightarrow 0$, the static magnetic susceptibility is defined by the expression $\chi = \partial s/\partial h_{h \to 0}$. The external field h is taken into account by the Zeeman term in Hamiltonian (1). As a result, the product hs should be subtracted from the internal energy (5). Correspondingly, the product $h\Delta p\cos 2\phi$ should be subtracted in relationships (12) and (23) for the free energy. Furthermore, the terms that describe the change in the free energy should also be included in the equations of state (13) and (14). As a result, the equation of state for the free energy (23) transforms into the equation

$$\frac{1}{2}[D(T) - 2J(T)z]s_0 + \frac{1}{4}D(T)s_0^3 - h\Delta p = 0. \tag{24}$$

According to formula (8), the expression for the static magnetic susceptibility χ should involve two terms; that is,

$$\chi = s_0\frac{\partial \Delta p}{\partial h}\bigg|_{h \to 0} + \Delta p\frac{\partial s_0}{\partial h}\bigg|_{h \to 0}. \tag{25}$$

The first term in expression (25) is associated with the change in the level population in response to the external field h at a constant temperature T, because the states with the spin projection aligned with the field are more energetically favorable as compared to the states with opposite or zero projections. It is this term that determines the static magnetic susceptibility at $h \longrightarrow 0$ in isotropic ferromagnets, for which the spin projections in the paramagnetic phase are as follows: $s_0 = S$, $s_1 = S - 1$, etc. Hence, in this case, the second term is absent in principle.

The second term in expression (25) accounts for the magnetic field–induced polarization of single-ion states. In the ferromagnet with the easy-plane single-ion anisotropy, this contribution is caused by the spin projection s_0 (at a given Δp). Note that, as was shown above, since $s_0 = 0$ in the paramagnetic phase, the contribution of the first term to the static magnetic susceptibility χ in this phase is zero. Therefore, the magnetization in the paramagnetic phase of the easy-plane ferromagnet arises from the polarization of the ionic states by the external magnetic field.

By differentiating relationship (24) with respect to h, we obtain the derivative $\partial s_0/\partial h$. The appropriate calculations with allowance made for the temperature dependence of Δp [relationship (20)] offer the following formula for the static magnetic susceptibility χ:

$$\chi = 2\frac{1-e^{-\frac{D}{T}}}{D-2Jz+2(D+Jz)e^{-\frac{D}{T}}}. \quad (26)$$

Despite the approximate expression (22) used for the free energy F, the denominator of formula (26) at the phase transition point $T = T_C$ [see relationship (18)] becomes equal to zero and the static magnetic susceptibility tends to infinity ($\chi \longrightarrow \infty$). It follows from formula (26) that, as the phase transition point T_C is approached, the temperature behavior of the static magnetic susceptibility deviates from the Curie–Weiss law. This deviation is explained by the retained ordering of the paramagnetic state [$\Delta p \neq 0$, see relationship (20)] and the temperature dependence of the derivative $\partial s_0(T)/\partial h$, which determines the polarization of ions under the effect of the external field **h**.

At high temperatures, when the inequality $D/T \ll 1$ is satisfied and the paramagnetic state is completely disordered [$\Delta p(T) \longrightarrow 0$], the temperature dependence of the static magnetic susceptibility is identical to that observed in the isotropic ferromagnet (whose paramagnetic state is always completely disordered) and can be described by the relationship

$$\chi = \frac{2}{3}\frac{1}{T-T_\theta}, \quad (27)$$

where $T_\theta = 2/3(Jz + D)$ is the paramagnetic Curie temperature. For any values of the single-ion anisotropy constant and the exchange interaction parameter, we have $T_\theta \neq T_C$ ($T_C < T_\theta$). In other words, the quasi-classical approximation according to which the thermodynamic averages of the spin operators squared can be replaced by the corresponding thermodynamic averages squared does not hold. At the same time, this approximation is valid for systems with order–disorder phase transitions.

Therefore, for a strongly anisotropic ferromagnet with the easy-plane single-ion anisotropy, the approximate expression (23) can be used for describing the phase transition to the ferromagnetic state, in which the exchange interaction and single-ion anisotropy depend on the temperature.

The free energy F can always be expanded in terms of s_0 (irrespective of the ratio D/Jz, provided that $D/2Jz < 1$) in the vicinity of the phase transition point at $T \longrightarrow T_C$. Note that, in the magnetically ordered state, a weak exchange field cannot considerably affect the level populations, which are determined only by the ratio D/T. Taking into account that this approximation holds true over a narrow temperature range ΔT in the vicinity of the point T_C, the temperature in the expansion of the free energy F can be represented in the form $T = T_C - \Delta T$. Then, the expression for the free energy F can be written in a form similar to the Landau thermodynamic potential; that is,

$$F = \frac{1}{2}\alpha\Delta T s_0^2 + \frac{1}{16}D\Delta p(T_C)s_0^4, \quad (28)$$

where

$$\alpha = \frac{1}{2}[4Jz\Delta p(T_C) - D]\partial\Delta p/\partial T_{T=T_C}.$$

Minimization of the free energy [relationship (28)] with respect to s_0 makes it possible to determine the dependence $s_0(T)$ in the ferromagnetic state in the vicinity of the phase transition point. At $T < T_C$, the temperature dependence of the spin projection is typical of the second-order phase transition; that is,

$$s_0(T) = 2\sqrt{\frac{|\alpha|}{D\Delta p(T_C)}\Delta T}. \quad (29)$$

According to relationship (8), the average thermodynamic spin in the ferromagnetic state can be represented as the product of two order parameters $s = s_0\Delta p$. In the paramagnetic state up to the phase transition point, the singlet is the ground state of the ion and $\Delta p(T > T_C) \neq 0$. Therefore, the average spin is equal to zero [$s(T) = 0$] if $s_0(T > T_C) = 0$. Although the average thermodynamic spin depends on s_0, it can be seen that the temperature dependence $s(T)$ in the vicinity of the phase transition exhibits a critical behavior; that is,

$$s(T) = 2\sqrt{\frac{|\alpha|\Delta p(T_C)}{D}\Delta T}. \quad (30)$$

This is consistent with the phenomenological theory of second-order phase transitions. According to this theory, the Landau potential can be represented as a functional in which the average spin (or the average magnetization) is the order parameter. However, the displacive magnetic phase transitions from a paramagnetic phase to a ferromagnetic phase and order–disorder phase transitions are identically described in terms of the theory that includes this order parameter [5] and allows only for the change in the symmetry. To put it differently, these phase transitions are indistinguishable in the framework of the phenomenological approach.

It should be noted that expression (23) was derived in the single-ion mean-field approximation and holds for $D/2Jz \ll 1$. As was shown above, in this case, we have $D/T_C \ll 1$ and $\Delta p(T_C) \longrightarrow 0$. Under these conditions, it is necessary to take into account fluctuations which are appreciably enhanced as the phase transition point is approached [15, 17]. The fluctuation fields bring about a considerable change in the spectrum of ionic states. As a result, this spectrum differs from the spectrum obtained within the single-ion approximation.

The fluctuations also affect the polarization of ionic states. Therefore, expression (23) is satisfied only when the ratio $D/2Jz$ is not small and the range $T - T_C$ (at least, in the magnetically ordered phase) covers the fluctuation range. This reasoning does not hold for the first case when $D \longrightarrow 2Jz$.

5. CONCLUSIONS

Thus, the above calculations demonstrated that, in a system of ions with spin $S = 1$ and easy-plane single-ion anisotropy, the phase transition to a ferromagnetic state is associated with the spontaneous formation of a nonzero spin projection of the magnetic ion in a nondegenerate state. The critical behavior of this polarization is governed by competition of the exchange interaction and single-ion anisotropy.

In these magnets, the appearance of the magnetic moment of ions and the transition to the ferromagnetic state cannot be assigned to the most commonly encountered order–disorder magnetic phase transitions. The results obtained give grounds to believe that, in the case under consideration, the phase transition from the paramagnetic state to the ferromagnetic state with a change in the temperature in the absence of an external magnetic field can be treated as a displacive magnetic phase transition.

ACKNOWLEDGMENTS

We would like to thank S.M. Ryabchenko, who called our attention to the analogy between magnetic ordering in magnetic materials with strong single-ion anisotropy and ordering in displacive ferroelectrics.

This work was supported in part by the National Academy of Sciences of Ukraine, project nos. 1.4.1VTs/95 and 0102U002332.

REFERENCES

1. A. K. Zvezdin, V. M. Matveev, A. A. Mukhin, and A. I. Popov, *Rare-Earth Ions in Magnetically Ordered Crystals* (Nauka, Moscow, 1985).
2. V. M. Kalita and V. M. Loktev, Fiz. Nizk. Temp. **28**, 1254 (2002) [Low Temp. Phys. **28**, 883 (2002)].
3. H. W. Capel, Physica (Amsterdam) **32**, 966 (1966); Physica (Amsterdam) **33**, 295 (1967).
4. M. Blume, V. J. Emery, and R. B. Griffiths, Phys. Rev. A **4**, 1071 (1971).
5. É. L. Nagaev, *Magnets with Complex Exchange Interactions* (Nauka, Moscow, 1988).
6. F. P. Onufrieva, Zh. Éksp. Teor. Fiz. **89**, 2270 (1985) [Sov. Phys. JETP **62**, 1311 (1985)].
7. Yu. N. Mitsaĭ, A. N. Maĭorova, and Yu. A. Fridman, Fiz. Tverd. Tela (St. Petersburg) **34**, 66 (1992) [Sov. Phys. Solid State **34**, 34 (1992)].
8. V. V. Val'kov and G. N. Matsuleva, Preprint No. 645F, IF SO AN SSSR (Inst. of Physics, Siberian Division, USSR Academy of Sciences, Novosibirsk, 1987).
9. M. F. Collins and O. A. Petrenko, Can. J. Phys. **75**, 605 (1997).
10. V. G. Bar'yakhtar and B. A. Ivanov, in *Solid-State Physics: An Encyclopedia*, Ed. by V. G. Bar'yakhtar (Naukova Dumka, Kiev, 1996), Vol. 1, p. 488.
11. V. A. L'vov, in *Solid-State Physics: An Encyclopedia*, Ed. by V. G. Bar'yakhtar (Naukova Dumka, Kiev, 1996), p. 496.
12. L. D. Landau, *Collected Works* (Nauka, Moscow, 1967), Vol. 1, p. 234.
13. V. M. Loktev and V. S. Ostrovskiĭ, Fiz. Nizk. Temp. **20**, 983 (1994) [Low Temp. Phys. **20**, 775 (1994)].
14. S. V. Tyablikov, *Methods in the Quantum Theory of Magnetism*, 3rd ed. (Plenum, New York, 1967; Nauka, Moscow, 1988).
15. R. H. Brout, *Phase Transitions* (Benjamin, New York, 1965; Mir, Moscow, 1967).
16. V. M. Kalita and V. M. Loktev, Fiz. Nizk. Temp. **28**, 667 (2002) [Low Temp. Phys. **28**, 475 (2002)].
17. J. S. Smart, *Effective Field Theories of Magnetism* (Saunders, London, 1966; Mir, Moscow, 1968).

Translated by O. Borovik-Romanova

Physics of the Solid State, Vol. 45, No. 8, 2003, pp. 1530–1536. Translated from Fizika Tverdogo Tela, Vol. 45, No. 8, 2003, pp. 1456–1462.

MAGNETISM AND FERROELECTRICITY

Magnetorefractive Effect in $(Co_{50}Fe_{50})_x(Al_2O_3)_{1-x}$ Granular Films

V. G. Kravets*, A. N. Pogorelyĭ, A. F. Kravets**, A. Ya. Vovk**, and Yu. I. Dzhezherya****

** Institute of Problems of Information Recording, National Academy of Sciences of Ukraine, Kiev, 03113 Ukraine*

*** Institute of Magnetism, National Academy of Sciences of Ukraine, Kiev, 03680 Ukraine*

e-mail: kravets@imag.kiev.ua

Received January 28, 2003

Abstract—The reflectivity spectra and the magnetorefractive effect (MRE) of $(Co_{50}Fe_{50})_x(Al_2O_3)_{1-x}$ metal–dielectric granular films ($0.07 < x < 0.52$) are analyzed in the IR spectral range $\lambda = 2.5$–25 μm. It is revealed that the specific features observed in the spectra at $\lambda \approx 8.5$ and 20 μm are associated with the excitation of phonon modes in the dielectric matrix. The magnetorefractive effect in the films is observed below the percolation threshold only in *p*-polarized light and above the percolation threshold for both the *p* and *s* polarizations. It is demonstrated that the optical properties of $(Co_{50}Fe_{50})_x(Al_2O_3)_{1-x}$ films in the IR spectral range, to a first approximation, can be interpreted in the framework of the effective-medium theory and the magnetorefractive effect can be explained in terms of the modified Hagen–Rubens relation. © *2003 MAIK "Nauka/Interperiodica".*

1. INTRODUCTION

The considerable interest expressed by researchers in metal–dielectric granular films composed of metallic ferromagnetic nanograins in a nonmagnetic dielectric matrix is associated with the tunneling magnetoresistance (TMR) effect observed in these materials, which makes them promising for practical use [1–10]. The tunneling magnetoresistance effect is caused by spin-dependent tunneling of polarized electrons through dielectric interlayers between magnetic grains. In 1999, Granovskiĭ *et al.* [11] theoretically predicted the magnetorefractive effect (MRE), which resides in the fact that the magnetic field affects the reflection and transmission spectra of films in the IR spectral range. More recently, this effect was experimentally found in metallic [12, 13] and metal–dielectric [14] granular films. The optical phenomena observed in metals in the IR spectral range are governed by intraband optical transitions and can be treated by analogy with electrical resistance [15]. Since the tunneling magnetoresistance and magnetorefractive effects have a similar nature, their joint treatment can provide valuable information on the electronic states in the conduction band in the vicinity of the Fermi level for two subsystems of conduction electrons whose spins are oriented along the magnetization [the upward spin ($\uparrow$)] and in the opposite direction [downward spin ($\downarrow$)]. Elucidation of the correlation between these effects can provide an answer to the question of the possible use of the magnetorefractive effect for contactless control of the magnetoresistance in magnetoresistive materials.

The magnetoresistive and magnetorefractive properties of metal–dielectric grain structures depend on the concentration of ferromagnetic grains and change radically above the percolation threshold when magnetic grains come in contact with each other. For the most part, these properties are governed by the ratio of the contributions from metallic and tunneling conductivities, the type of electron tunneling between grains, the potential barrier height, and localized states in the matrix. A large number of problems concerning the influence of the matrix and grain materials on the properties of granular films still remain unclear.

Metal–dielectric granular films with a giant tunneling magnetoresistance are usually prepared from an Al_2O_3-based matrix with high permittivity and thermal stability [3, 6, 9, 10, 14]. As a rule, such films are produced either by electron-beam coevaporation of a magnetic material and Al_2O_3 with simultaneous vapor deposition on a substrate under vacuum [9, 10, 16] or by magnetron sputtering of composite targets [3, 6, 14]. Since the surface energy of a metal is considerably higher than that of a dielectric material, upon their codeposition, the metal does not wet the oxide and form grains with a crystal structure. Films of these alloys below the percolation threshold have a granular structure in which nearly spherical metallic nanograins are randomly distributed over the dielectric matrix and form an abrupt interface with the matrix [10].

The purpose of this work was to reveal a correlation between the optical properties in the IR spectral range and the tunneling magnetoresistance of $(Co_{50}Fe_{50})_x(Al_2O_3)_{1-x}$ metal–dielectric granular films over a wide range of concentrations *x* of the magnetic component in an applied magnetic field and to analyze the influence of the Al_2O_3 dielectric matrix on the properties of the films.

1063-7834/03/4508-1530$24.00

2. SAMPLE PREPARATION AND EXPERIMENTAL TECHNIQUE

Metal–dielectric granular films of $(Co_{50}Fe_{50})_x(Al_2O_3)_{1-x}$ with a volume fraction of the metallic component in the range $0.07 < x < 0.52$ were prepared by electron-beam coevaporation of dielectric (Al_2O_3) and metallic (a $Co_{50}Fe_{50}$ equiatomic alloy) components from two independent stabilized sources and by mixed-vapor deposition of the components on cover glass substrates at a temperature of ~200°C under high vacuum (at a residual pressure of 10^4 Pa). The film thickness was approximately equal to 400 nm. The geometry of the mutual arrangement of the substrates and evaporation sources provided simultaneous preparation of films whose composition continuously varied in the aforementioned concentration range along the length of the substrate holder (450 mm). This procedure of preparing metal–dielectric films was described in detail in [16].

The evaporation rate and the volume content of each component in granular films were controlled using two quartz sensors. The film composition was determined by energy dispersive x-ray analysis. The film structure was investigated using x-ray diffraction and high-resolution transmission electron microscopy. The magnetoresistance of films was measured by the four-point probe method at room temperature in magnetic fields up to 50 kOe. The reflectivity spectra of $(Co_{50}Fe_{50})_x(Al_2O_3)_{1-x}$ granular films in the middle-IR wavelength range from 2.5 to 25 μm were recorded on a Nicolet 670 Fourier spectrometer with an MCT-B HgCdTe photodetector cooled by liquid nitrogen. The optical measurements in polarized light were performed using a KRS-5 grid polarizer. In the magnetorefractive experiments (the measurement of the dependence of the reflectivity spectra on the magnetic field), the mirrors of the Fourier spectrometer were mounted outside the spectrometer in order to focus IR radiation on a sample located in a gap of the external electromagnet. In this case, the angle of incidence of light on the sample was approximately equal to 65°.

3. RESULTS AND DISCUSSION

The x-ray diffraction patterns of $(Co_{50}Fe_{50})_x(Al_2O_3)_{1-x}$ granular films exhibit a broad peak at the Bragg angle corresponding to the (001) plane of the body-centered cubic $Co_{50}Fe_{50}$ crystal. This suggests that the $Co_{50}Fe_{50}$ metallic grains distributed in the Al_2O_3 dielectric matrix have a nanocrystalline structure. The data of high-resolution transmission electron microscopy confirm this inference and demonstrate that the mean size of ferromagnetic particles in granular films below the percolation threshold varies from 1 to 3 nm [10].

For $(Co_{50}Fe_{50})_x(Al_2O_3)_{1-x}$ granular films, the maximum tunneling magnetoresistance effect (~6%) is observed in the vicinity of the percolation threshold ($x_p \approx 0.17$ [9]) in a magnetic field of 10 kOe (Fig. 1).

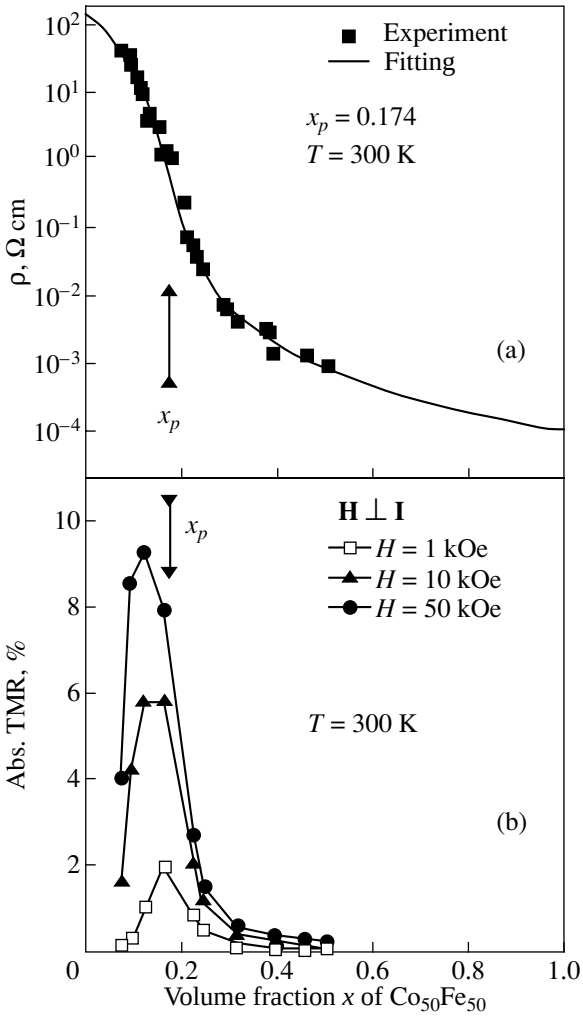

Fig. 1. Concentration dependences of (a) the resistivity and (b) the tunneling magnetoresistance for $(CoFe)_x(Al_2O_3)_{1-x}$ granular films at $T = 300$ K.

The current–voltage characteristics of the granular films are consistent with the Simmons theory of electron tunneling [17] and confirm the tunneling nature of the magnetoresistance. In the framework of this theory, the height of the tunneling barrier and its width for the film at $x = 0.15$ are estimated as $\phi \sim 2.15$ eV and $d_s \sim 2$ nm, respectively. The tunneling nature of the magnetoresistance is also supported by its measurements in the temperature range from 5 to 300 K [9, 10].

The reflectivity Fourier spectra $R(\lambda)$ of the $(Co_{50}Fe_{50})_x(Al_2O_3)_{1-x}$ granular films in the middle-IR range were recorded using both unpolarized and *p*- and *s*-polarized incident light. These spectra were normalized to the corresponding spectra of thick silver films. The IR reflectivity spectra of the $(Co_{50}Fe_{50})_x(Al_2O_3)_{1-x}$ granular films and Al_2O_3 and $Co_{50}Fe_{50}$ pure materials in unpolarized light are shown in Fig. 2. In the range of concentrations *x* corresponding to an appreciable tunneling magnetoresistance of the $(Co_{50}Fe_{50})_x(Al_2O_3)_{1-x}$

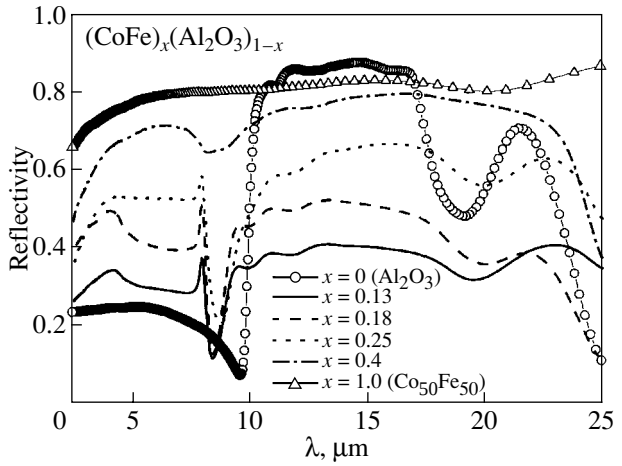

Fig. 2. IR reflectivity spectra of $(CoFe)_x(Al_2O_3)_{1-x}$ granular films in unpolarized light.

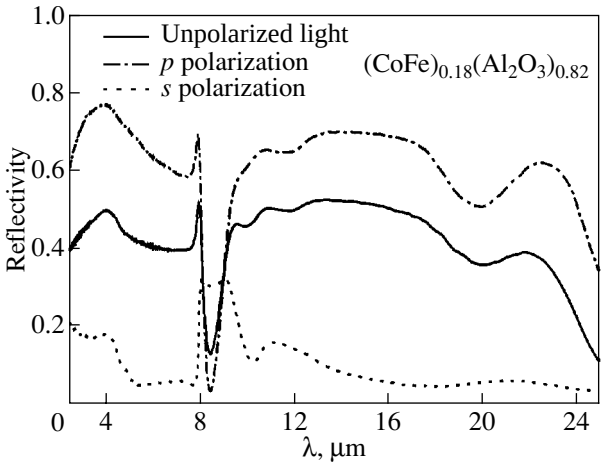

Fig. 3. IR reflectivity spectra of the $(CoFe)_{0.18}(Al_2O_3)_{0.82}$ granular film.

granular films ($0.07 < x < 0.3$), the IR reflectivity spectra exhibit characteristic features, namely, clear minima at $\lambda \sim 8.5$ and ~20 μm. With an increase in the concentration (at $x > 0.35$), the characteristic minima in the reflectivity spectra gradually disappears and the spectra $R(\lambda)$ become similar to the IR reflectivity spectra of pure $Co_{50}Fe_{50}$. The reflectivity spectra of the granular film at $x = 0.18$ (with the specific features typical of the spectra of films at $x < 0.3$) in unpolarized and *p*- and *s*-polarized light are depicted in Fig. 3. It should be noted that the spectra $R(\lambda)$ at $\lambda \sim 8.5$ μm exhibit minima for *p*-polarized light and maxima for *s*-polarized light (Fig. 3). These specific features observed in the spectra of granular films with a high Al_2O_3 content can be associated with the excitation of phonon modes in the dielectric matrix. The narrow minimum at $\lambda \sim 8.5$ μm can be attributed to the excitation of the longitudinal optical (LO) phonon mode in Al_2O_3, whereas the broader minimum at $\lambda \sim 20$ μm can be assigned to the excitation of the transverse optical (TO) phonon mode. Substantial broadening of the minimum corresponding to the transverse mode can be associated with the amorphous state of the system, which leads to a frequency distribution. According to the data available in the literature for crystalline Al_2O_3 [18, 19], the most intense peaks are located at 23.3 and ~14.7 μm for the transverse phonon modes and at 10.5 and 19.5 μm for the longitudinal phonon modes. The disordering in the amorphous Al_2O_3 matrix is responsible for the change in the distance between Al and O atoms on the short-range order scale and in the coordination environment of these atoms. In turn, these variations lead to a change in the positions of the spectral features corresponding to phonon vibrations in the granular films. The spectral features that are observed in the IR reflectivity spectra of the $(Co_{50}Fe_{50})_x(Al_2O_3)_{1-x}$ granular films and are associated with the TO and LO phonon modes can be identified with the use of *p*- and *s*-polarized light.

The optical properties of metal–dielectric granular films with tunneling magnetoresistance can be described in the effective-medium approximation. Within this approximation, the optical conductivity σ_e of $(Co_{50}Fe_{50})_x(Al_2O_3)_{1-x}$ granular films can be determined from the relationship [20, 21]

$$x\frac{\sigma_e - \sigma_m}{\sigma_m + 2\sigma_e} + (1-x)\frac{\sigma_e - \sigma_d}{\sigma_d + 2\sigma_e} = 0, \qquad (1)$$

where σ_e is the effective optical conductivity of the granular film and σ_d and σ_m are the optical conductivities of the Al_2O_3 dielectric matrix and $Co_{50}Fe_{50}$ metallic grains, respectively. The frequency dependence of the optical conductivity for the dielectric film in the IR range is defined by the following expression [20, 21]: $\sigma_d = i\varepsilon_0\varepsilon_d\omega$, where ω is the optical frequency, ε_0 is the permittivity of free space, and ε_d is the permittivity of Al_2O_3. The dielectric function of Al_2O_3 in the IR range can be derived on the basis of the phenomenological model of Lorentz oscillators [18, 22]

$$\varepsilon = \varepsilon_\infty \prod_j \frac{\Omega_{\mathrm{LO}j}^2 - \omega^2 + i\gamma_{\mathrm{LO}j}\omega}{\Omega_{\mathrm{TO}j}^2 - \omega^2 + i\gamma_{\mathrm{TO}j}\omega}, \qquad (2)$$

where ε_∞ is the high-frequency permittivity; $\Omega_{\mathrm{LO}j}$ and $\Omega_{\mathrm{TO}j}$ are the frequencies of the LO and TO *j*th phonons, respectively; ω is the frequency of exciting light; and $\gamma_{\mathrm{LO}j}$ and $\gamma_{\mathrm{TO}j}$ are the damping constants of the LO and TO *j*th phonons, respectively. In the framework of this model, we calculated the reflectivities of the $(Co_{50}Fe_{50})_x(Al_2O_3)_{1-x}$ granular films at different concentrations *x* (Fig. 4). The optical conductivity of $Co_{50}Fe_{50}$ ferromagnetic grains in the IR spectral range was represented as the sum of the contributions from the Drude conductivities of two spin subsystems: (i) electrons with spins aligned with the magnetization [upward spin (↑)] and (ii) electrons with spins oriented

in the opposite direction [downward spin (↓)] [11, 23]; that is,

$$\sigma(\omega) = \sigma_\uparrow(\omega) + \sigma_\downarrow(\omega) = \frac{\sigma_\uparrow(\omega = 0)}{1 + i\omega\tau_\uparrow} + \frac{\sigma_\downarrow(\omega = 0)}{1 + i\omega\tau_\downarrow}, \quad (3)$$

where $\sigma_{\uparrow(\downarrow)}(\omega = 0)$ and $\tau_{\uparrow(\downarrow)}$ are the static conductivities and the electron relaxation times for the two spin subsystems, respectively. The static conductivities were determined from the formula $\sigma_{\uparrow(\downarrow)}(\omega = 0) = n_{\uparrow(\downarrow)}e^2\tau_{\uparrow(\downarrow)}/m$, where $n_{\uparrow(\downarrow)}$ are the electron densities for the two electron subsystems and m is the electron mass. The electron densities $n_{\uparrow(\downarrow)}$ were evaluated within the free-electron gas model, according to which $n_{\uparrow(\downarrow)} = (k^F_{\uparrow(\downarrow)})^3/3\pi^2$, where the Fermi wave vectors $k^F_\uparrow \sim 7.5$ nm^{-1} and $k^F_\downarrow \sim 4.5$ nm^{-1} were taken from [23]. The optical conductivity of ferromagnetic grains was determined with the use of the spin asymmetry parameter $\alpha_p = \tau_\uparrow/\tau_\downarrow = 3.5$ ($\tau_\uparrow = 15$ fs) taken from [23].

After determining the effective optical conductivity σ_e of the $(Co_{50}Fe_{50})_x(Al_2O_3)_{1-x}$ granular films, the optical constants n and k were calculated from the expression [11, 23]

$$n - ik = \sqrt{\varepsilon_1 + i\varepsilon_2} = \sqrt{\varepsilon_r - \frac{i\sigma_e}{\varepsilon_0\omega}}. \quad (4)$$

Here, $\varepsilon_0 = 0.885 \times 10^{-11}$ F/m is the permittivity of free space, ε_r is the relative permittivity (which, to a first approximation, is equal to unity), and the dielectric functions ε_1 and ε_2 are related to the optical constants through the expressions $\varepsilon_1 = n^2 - k^2$ and $\varepsilon_2 = 2nk$.

The reflectivity of the $(Co_{50}Fe_{50})_x(Al_2O_3)_{1-x}$ granular films in the IR spectral range was calculated from the relationship obtained in the second-order approximation with respect to t/λ (where t is the film thickness and λ is the optical wavelength) [24], which holds for $t \ll \lambda$; that is,

$$R(\lambda) = \frac{(n_0 - n_s)^2 + (n_0 - n_s)p + q}{(n_0 + n_s)^2 + (n_0 + n_s)p + q}. \quad (5)$$

Here, n_0 is the refractive index of air, n_s is the refractive index of the substrate, and q and p are the functions dependent on the optical constants and the film thickness and can be represented in the form

$$q = [\varepsilon_1^2 + \varepsilon_2^2 - (n_0^2 + n_s^2)\varepsilon_1 + n_0^2 n_s^2]\eta^2,$$
$$p = 2\varepsilon_2\eta, \quad \eta = 2\pi t/\lambda. \quad (6)$$

The above model makes it possible to calculate the IR reflectivity spectra $R(\lambda)$ of the $(Co_{50}Fe_{50})_x(Al_2O_3)_{1-x}$ granular films. The experimental (Fig. 2) and theoretical (Fig. 4) spectra $R(\lambda)$ are in good agreement. The theoretical spectra $R(\lambda)$ were evaluated for unpolarized probe radiation, because light with a specific polarization excites only particular phonon modes.

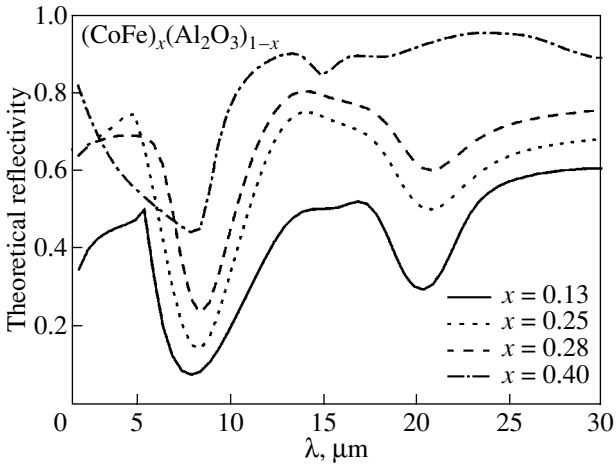

Fig. 4. Theoretical IR reflectivity spectra of $(CoFe)_x(Al_2O_3)_{1-x}$ granular films.

As follows from analyzing the experimental results, the reflectivity spectra of the $(Co_{50}Fe_{50})_x(Al_2O_3)_{1-x}$ granular films in *p*- and *s*-polarized light differ substantially (see, for example, Fig. 3). The reflectivity spectra of the films, especially at low concentrations x, depend strongly on the properties and parameters of the Al_2O_3 dielectric matrix. In the amorphous Al_2O_3 matrix, there arises a continuum of Al–O oscillators with the dipole moment aligned with the film plane. The contribution of these oscillators to the reflectivity spectra depends on the angle of incidence and the polarization of light [25]. At normal incidence ($\phi = 0°$), the light excites only the transverse phonon modes at 690 cm^{-1} (14.5 μm). The longitudinal phonon modes manifest themselves, to a greater extent, at 950 cm^{-1} (10.5 μm) and at the angle of incidence $\psi = 75°$ in *p*-polarized light. The spectral position of the maximum corresponding to the LO mode also considerably depends on the thickness and structure of the Al_2O_3 film [25].

By analogy with the tunneling magnetoresistance effect TMR = $\Delta\rho/\rho = [(\rho_{H=0} - \rho_H)/\rho_H] \times 100\%$, we determined the magnetorefractive effect MRE = $\Delta R/R = [(R_{H=0} - R_H)/R_H] \times 100\%$, where $\Delta\rho/\rho$ and $\Delta R/R$ are the relatives changes in the electrical resistivity and the reflectivity of the $(Co_{50}Fe_{50})_x(Al_2O_3)_{1-x}$ granular films upon application of an external magnetic field. It was found that the MRE curves substantially depend on the polarization of incident light and the concentration x of metallic grains. In particular, the MRE curves for the films with concentrations of ferromagnetic grains below the percolation threshold ($x < 0.17$) only in *p*-polarized light exhibit specific features (Fig. 5) which are not observed upon excitation with *s*-polarized light. The MRE spectral curves for the granular films at $0.1 < x < 0.17$ have maxima in the vicinity of 8.5 μm (see Fig. 5, curves at $x = 0.15$, 0.1) whose locations strictly

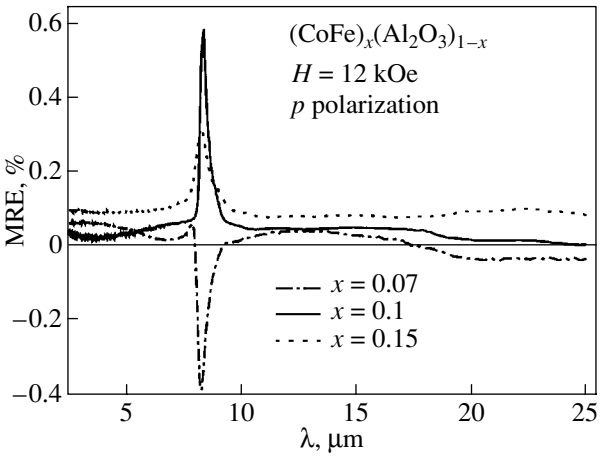

Fig. 5. MRE curves for $(CoFe)_x(Al_2O_3)_{1-x}$ granular films in p-polarized light. x = 0.07, 0.1, and 0.15.

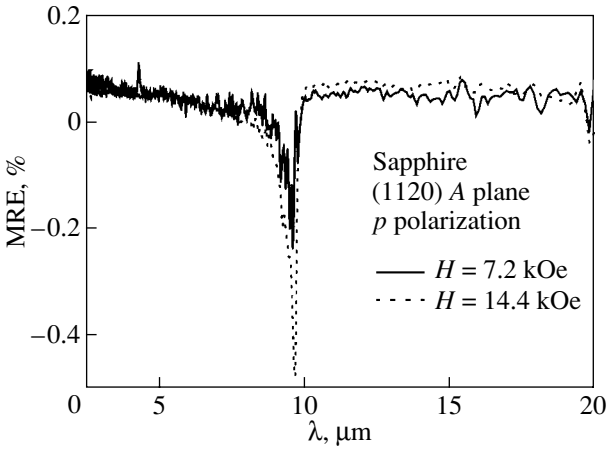

Fig. 6. MRE curves for Al_2O_3 in p-polarized IR light at different magnetic field strengths.

correlate with those of the minima in the spectra $R(\lambda)$ (Fig. 2). A decrease in the grain concentration ($x < 0.1$) leads to a change in the MRE curve, so that the MRE curve (Fig. 5, curve at $x = 0.07$), like the spectrum $R(\lambda)$, contains a deep minimum at a characteristic wavelength of 8.5 μm. At low concentrations of ferromagnetic grains, the reflectivity spectra $R(\lambda)$ of the $(Co_{50}Fe_{50})_x(Al_2O_3)_{1-x}$ granular films become similar to the spectrum of the Al_2O_3 matrix (Fig. 2). Our investigation into the influence of the magnetic field on the reflectivity spectrum of pure Al_2O_3 revealed that the magnetic field affects the reflectivity of the dielectric matrix. In this case, the MRE curve for pure Al_2O_3 is characterized by a deep minimum at $\lambda \approx 9$ μm (Fig. 6). It should be emphasized that the magnetorefractive effect in the IR range in the granular films and pure Al_2O_3 strongly depends on the wavelength λ of incident light and the magnetic field strength H.

The magnetorefractive effect observed in the Al_2O_3 dielectric matrix is associated with the manifestation of gyrotropic properties in the magnetic field [26]. This is accompanied by the appearance of the gyration vector and off-diagonal components in the permittivity tensor. In isotropic materials and crystals with cubic symmetry, the magneto-optical effects can be rather strong and the corresponding corrections to the refractive index are linearly proportional to the magnetic field strength [26]. The possibility of observing the magnetorefractive effect in dielectrics over the entire frequency range is limited by the sensitivity of the measuring instrument. However, at a frequency corresponding to the total transparency in the vicinity of the phonon mode ($\lambda \approx 9$ μm for Al_2O_3, Fig. 6), the magnetorefractive effect is relatively large in magnitude against the background of the weak reflection and can be measured with a rather high accuracy. We also observed a similar magnetorefractive effect in ionic crystals with cubic symmetry. The theory of this phenomenon will be considered in detail in a separate work. Here, we only note that this effect allows one to determine the gyration coefficient in dielectrics with a high accuracy.

The MRE curves for granular films at $0.17 < x < 0.4$ show specific features in s- and p-polarized exciting light (see, for example, the MRE curves for the granular film at $x = 0.25$ in Figs. 7, 8). For the films at $x > 0.4$, the magnetorefractive effect is observed only in s-polarized light and the reflectivity spectrum $R(\lambda)$ of the granular films becomes similar to the spectrum of pure $Co_{50}Fe_{50}$.

The magnetorefractive effect in the long-wavelength IR range can be explained in terms of the Hagen–Rubens relation. By ignoring the ferromagnetic properties of the material, the optical constants in the IR range can be determined from the expression $n \approx k \approx (1/2\varepsilon_0\omega\rho_0)^{1/2}$, where ρ_0 is the resistivity of the material at $\omega = 0$ and ε_0 is the permittivity of free space. In this case, the reflectivity R at the normal incidence of light can be written in the form [15]

$$R \cong 1 - [2\varepsilon_0\omega\rho_0]^{1/2}. \quad (7)$$

Relationship (7) is valid at $\omega\tau_\uparrow(\tau_\downarrow) \ll 1$ (for the majority of metals, this holds at $\lambda \geq 20$ μm). It can be seen from relationship (7) that the reflectivity $R(\lambda)$ directly depends on ρ_0 and is independent of the electron relaxation time $\tau_\uparrow(\tau_\downarrow)$.

The expression relating the reflectivity and the resistivity permits us to estimate the change ΔR in the reflectivity due to the change $\Delta\rho$ in the resistivity in the magnetic field [11, 13]:

$$\Delta R = -[2\varepsilon_0\omega\rho_0]^{1/2}\Delta\rho/\rho_0 = -[2\varepsilon_0\omega\rho_0]^{1/2}\mathrm{TMR}, \quad (8)$$

where TMR is the tunneling magnetoresistance of the $(Co_{50}Fe_{50})_x(Al_2O_3)_{1-x}$ granular films. However, the theoretical MRE curves obtained with the use of relationship (8) disagree with the experimental MRE curves in the range of wavelengths shorter than 15 μm. From the expression for $R(\lambda)$ in the Hagen–Rubens

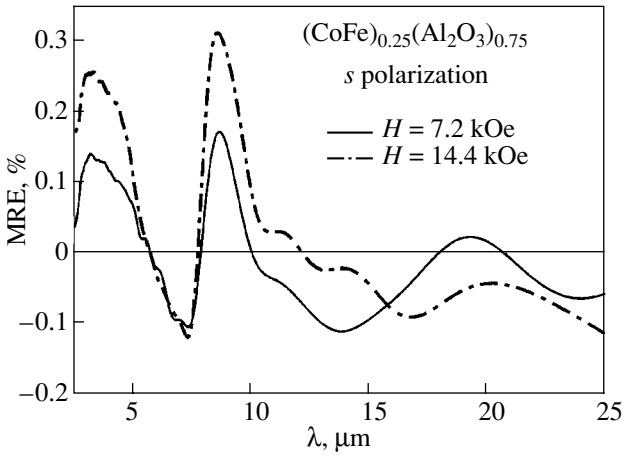

Fig. 7. MRE curves for the $(CoFe)_{0.25}(Al_2O_3)_{0.75}$ granular film in *s*-polarized light at different magnetic field strengths.

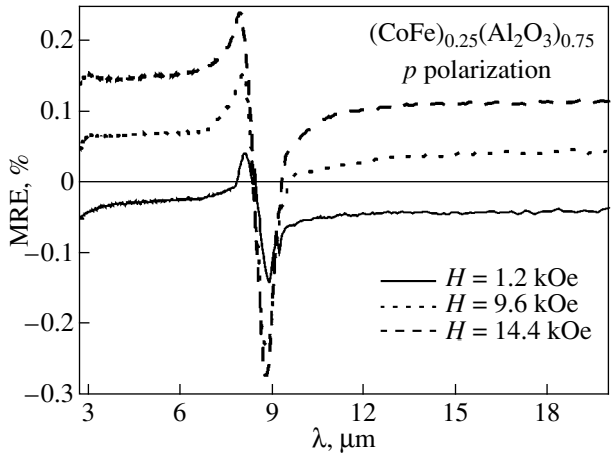

Fig. 8. MRE curves for the $(CoFe)_{0.25}(Al_2O_3)_{0.75}$ granular film in *p*-polarized light at different magnetic field strengths.

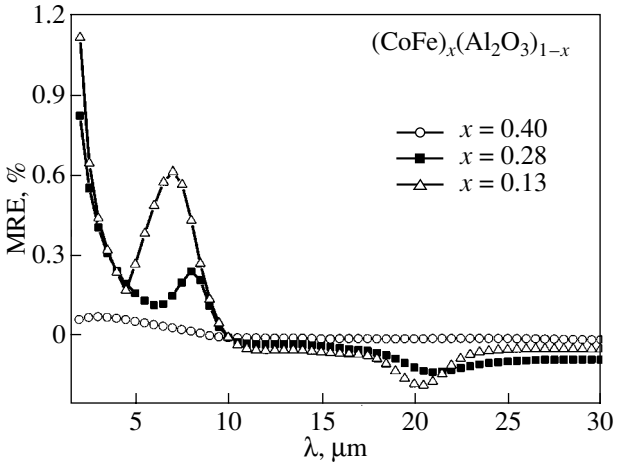

Fig. 9. Theoretical MRE curves for $(CoFe)_x(Al_2O_3)_{1-x}$ granular films.

approximation, it follows that $\Delta R \propto \lambda^{-1/2}$. Therefore, we can assume that the dependence of ΔR on the relaxation time of the spin subsystems can be taken into account in the form of a power series [13]:

$$\Delta R = -\alpha\lambda^{-1/2} + \beta\lambda^{-3/2} + 0(\lambda^{-5/2}). \quad (9)$$

This approximation includes only the first terms of the power series in λ. For calculations, the constant α was derived within the effective-medium approximation: $\alpha = [(1 - R)/2]$TMR. The values of the TMR were determined from the experimental data (Fig. 1). The parameter β was chosen from the best fitting to the experimental data and, as a rule, was of the order of 0.1α. The MRE spectral curves calculated for the $(Co_{50}Fe_{50})_x(Al_2O_3)_{1-x}$ granular films with the use of the described technique are depicted in Fig. 9. A comparison of the experimental and theoretical results demonstrates that the theoretical MRE curves exhibit all the main features observed in the experimental MRE curves (Figs. 5, 7, 8). Note that the MRE curves were calculated only for unpolarized light. According to the experimental data, the MRE curves for unpolarized and *p*-polarized incident light are similar to each other. The specific features in the experimental and theoretical MRE curves are most pronounced in the vicinity of wavelengths corresponding to excitation of the TO and LO phonon modes.

4. CONCLUSIONS

Thus, the results obtained in this work demonstrated that the $(Co_{50}Fe_{50})_x(Al_2O_3)_{1-x}$ granular films possess a considerable tunneling magnetoresistance near the percolation threshold ($x \approx 0.17$). It was found that the magnetorefractive effect in these films manifests itself in the range of wavelengths corresponding to the optical phonon modes. The MRE curves depend on the concentration of magnetic grains and the polarization of exciting light. In particular, the magnetorefractive effect is observed only in *p*-polarized light below the percolation threshold, in both *p*- and *s*-polarized light in the concentration range $0.17 < x < 0.4$, and only in *s*-polarized light at $x > 0.4$. It was demonstrated that the reflectivity spectra of the $(Co_{50}Fe_{50})_x(Al_2O_3)_{1-x}$ granular films in the IR spectral range, to a first approximation, can be described in the framework of the effective-medium theory and the magnetorefractive effect can be explained in terms of the modified Hagen–Rubens relation. The magnetorefractive effect revealed in Al_2O_3 in the wavelength range corresponding to the excitation of optical phonons is associated with the manifestation of gyrotropic properties of Al_2O_3 in the magnetic field. It was established that the Al_2O_3 matrix substantially affects the tunneling mechanism of conduction in $(Co_{50}Fe_{50})_x(Al_2O_3)_{1-x}$ granular films and their optical and magnetorefractive properties in the IR range.

REFERENCES

1. J. I. Gittleman, Y. Goldstein, and S. Bozovski, Phys. Rev. B **5** (9), 3609 (1972).
2. J. S. Helman and B. Abeles, Phys. Rev. Lett. **37** (21), 1429 (1976).
3. H. Fujimori, S. Mitani, and S. Ohnuma, Mater. Sci. Eng. B **31** (1–2), 219 (1995).
4. A. Milner, A. Gerber, B. Groisman, *et al.*, Phys. Rev. Lett. **76** (3), 475 (1996).
5. S. Honda, T. Okada, M. Nawate, and M. Tokumoto, Phys. Rev. B **56** (22), 14566 (1997).
6. S. Mitani, S. Takahashi, K. Takanaski, *et al.*, Phys. Rev. Lett. **81** (13), 2799 (1998).
7. B. A. Aronzon, A. E. Varfolomeev, D. Yu. Kovalev, *et al.*, Fiz. Tverd. Tela (St. Petersburg) **41** (6), 944 (1999) [Phys. Solid State **41**, 857 (1999)].
8. S. Sankar, A. E. Berkowitz, and D. J. Smith, Phys. Rev. B **62** (21), 14273 (2000).
9. A. Ya. Vovk, J. Q. Wang, A. M. Pogoriliy, *et al.*, J. Magn. Magn. Mater. **242–245** (P1), 476 (2002).
10. A. Ya. Vovk, J. Q. Wang, W. Zhou, *et al.*, J. Appl. Phys. **91** (12), 10017 (2002).
11. A. B. Granovskiĭ, M. V. Kuz'michev, and J. P. Clerc, Zh. Éksp. Teor. Fiz. **116** (5), 1762 (1999) [JETP **89**, 955 (1999)].
12. J. P. Camplin, S. M. Thompson, D. R. Loraine, *et al.*, J. Appl. Phys. **87** (9), 4846 (2000).
13. V. G. Kravets, D. Bozec, J. A. D. Matthew, *et al.*, Phys. Rev. B **65** (5), 054415 (2002).
14. I. V. Bykov, E. A. Gan'shina, A. B. Granovskiĭ, and V. S. Gushchin, Fiz. Tverd. Tela (St. Petersburg) **42** (3), 487 (2000) [Phys. Solid State **42**, 498 (2000)].
15. A. V. Sokolov, *Optical Properties of Metals* (Fizmatgiz, Moscow, 1961; Elsevier, New York, 1967).
16. G. A. Niklasson and C. G. Grandvist, J. Appl. Phys. **55** (9), 3382 (1984).
17. J. G. Simmons, J. Appl. Phys. **34** (6), 1793 (1963).
18. M. Schubert, T. E. Tiwald, and C. M. Herzinger, Phys. Rev. B **61** (12), 8187 (2000).
19. J. S. Ahn, K. H. Kim, T. W. Noh, *et al.*, Phys. Rev. B **52** (21), 15244 (1995).
20. D. J. Bergman and D. Stroud, Solid State Phys. **46** (4), 147 (1992).
21. F. Brouers, J. P. Clerc, G. Giraud, *et al.*, Phys. Rev. B **47** (2), 666 (1993).
22. M. Gadenne, V. Podolskiy, P. Gadenne, *et al.*, Europhys. Lett. **53** (3), 364 (2001).
23. J. van Driel, F. R. de Boer, R. Coehoorn, *et al.*, Phys. Rev. B **61** (22), 15321 (2000).
24. F. Abeles, *Optical Properties of Solids* (Elsevier, Amsterdam, 1972).
25. P. Brüesch, R. Kötz, H. Neff, and L. Pietronero, Phys. Rev. B **29** (8), 4691 (1984).
26. L. D. Landau and E. M. Lifshitz, *Course of Theoretical Physics*, Vol. 8: *Electrodynamics of Continuous Media*, 2nd ed. (Nauka, Moscow, 1982; Pergamon, New York, 1984).

Translated by O. Borovik-Romanova

Physics of the Solid State, Vol. 45, No. 8, 2003, pp. 1537–1542. Translated from Fizika Tverdogo Tela, Vol. 45, No. 8, 2003, pp. 1463–1468.

MAGNETISM AND FERROELECTRICITY

Polarization of Strontium–Barium Niobate Crystals in Pulsed Fields

T. R. Volk*, D. V. Isakov*, and L. I. Ivleva**

** Shubnikov Institute of Crystallography, Russian Academy of Sciences, Leninskiĭ pr. 59, Moscow, 119333 Russia*
e-mail: volk@ns.crys.ras.ru

*** Institute of General Physics, Russian Academy of Sciences, ul. Vavilova 38, Moscow, 117942 Russia*

Received November 11, 2002; in final form, December 29, 2002

Abstract—Polarization (ferroelectric switching) of SBN crystals in pulsed fields differs from the same process in model ferroelectrics. Polarization in most SBN crystals is characterized by slow kinetics, which can be approximated by a power-law dependence, with relaxation times of the order of seconds (in fields $\gg E_c$). The process smoothness results in the absence of a characteristic peak in the switching-current curve. Some crystals are characterized by fast (jumplike) polarization processes, whose characteristics (the kinetics and the field dependence of the switched charge) also differ from model ones. *© 2003 MAIK "Nauka/Interperiodica".*

1. INTRODUCTION

Ferroelectric crystals $Sr_xBa_{1-x}Nb_2O_6$ (SBN-x) are widely used in optical systems, in particular, as a holographic medium for optical memory and for optical-data processing in the dynamic-recording regime, as well as for optical radiation frequency conversion on the domain structure in the phase-quasi-matching regime. In this context, ferroelectric switching is of particular interest. This process underlies the effect of field fixing of holograms, which permits their nondestructive readout in ferroelectrics [1–4]. Polarization reversal under the influence of an internal (photorefractive) field [5–7] or under simultaneous exposure to photorefractive and external fields [8, 9] can be used for producing a regular domain structure (RDS). Ferroelectric switching, in principle, can make it possible to control the intensity and spectral composition of radiation converted in a crystal with domain structure [10–12].

Analysis of the numerous publications devoted to these optical effects suggests that switching processes in SBN differ from the classical scenario considered in well-known monographs. This conclusion is also confirmed by studies [13, 14] of the SBN polarization kinetics in quasi-static fields and by observations [15] of the SBN domain structure dynamics. Attempts made by authors to develop general methods of field control of the optical processes in SBN (e.g., a unified method for fixing holograms [3], RDS formation [8, 9], and field control of the converted radiation intensity [12]) have been ineffective, since the model mechanism was taken as a basis in solving these problems for lack of information on the specific features of polarization switching in these crystals. The data from direct studies on the pulsed switching of SBN crystals that are necessary for developing such methods are absent in the literature, except for our publication [16], where switching currents were measured for some SBN crystals in pulsed fields and some fundamental features were detected.

This paper is devoted to detailed study of pulsed polarization switching in a large number of SBN crystals, both pure and doped with various impurities.

2. CRYSTALS UNDER STUDY AND EXPERIMENTAL TECHNIQUE

The crystals were grown, using the modified Stepanov method, at the Scientific Center of Laser Materials and Technologies of the Institute of General Physics [17] and, using the Czochralski method, at the Physical Faculty of the Osnabrück University (Germany). The following compositions were studied in detail: SBN-0.75, SBN-0.61, SBN-0.61 doped with 1 wt % La_2O_3 (designated below as SBN-0.61:La), SBN-0.61 doped with 0.4 wt % CeO_2 (SBN-0.61:Ce), SBN-0.61 doped with a double ligature of 1 wt % La and 0.1 wt % CeO_2 (SBN-0.61:La:Ce), and SBN-0.61 doped with 0.5 wt % Nd (SBN-0.61:Nd).

These objects were chosen for the following reasons. Crystal SBN-0.75 is a composition in which the effect of field fixing of holograms during switching has been studied in detail [1–4]. Crystals SBN-0.61 with rare-earth (RE) impurities are convenient for study, since RE doping results in a significant decrease in T_c [16, 18] and a corresponding decrease in E_c. The effect of field switching of the two-beam-coupling gain factor Γ, associated with ferroelectric switching, was detected and studied in the SBN-0.61:Ce and SBN-0.61:La:Ce crystals [18, 19]. In crystals SBN-0.61:Nd, lasing with microdomain-induced frequency self-doubling was observed in [10, 11]. Thus, the contribution of switch-

Table 1. Ferroelectric properties of the SBN crystals under study

Crystal	T_c, °C	E_c, 10^3 V cm^{-1}	$\varepsilon_{33,\,max}$	ε_{33}(20°C)
SBN-0.75	50	~1	12000	7000
SBN-0.61	81	2–3	33000	800
SBN-0.61:0.4 wt % Ce	58	1–1.2	16000	2500
SBN-0.61:1 wt % La	~45		30000	7200
SBN-0.61:1 wt % La:0.1 wt % Ce	~45	~1	24000	7500
SBN-0.61:0.5 wt % Nd	61	2–2.5	23000	2700

Note: ε_{33} (20°C) and $\varepsilon_{33,\,max}$ are the permittivities under standard conditions and at T_c, respectively, measured in multidomain crystals at 1 kHz.

ing or a domain structure to nonlinear-optical processes was observed in all the objects under study.

The ferroelectric properties of the crystals under study are listed in Table 1. The values of E_c were obtained by measuring the *P–E* hysteresis loops in quasi-static fields [13, 14]. The coercive field cannot be unambiguously determined in SBN crystals [13, 14] due to their relaxor character [20]; therefore, the values of E_c given in Table 1 are rather conditional (averaged over the crystal volume).

Pulsed polarization was studied using the Merz technique (see, e.g., [21]). Rectangular pulses with a rise time no longer than 2.5×10^{-8} s and a duration t_p in the range 3×10^{-6} to 10 s were applied to the crystals. The load resistance was 1–10 Ω, while the crystal resistance was 10^{14} Ω, which allowed us to disregard leakage currents. The signal from the load resistor was recorded using a high-frequency ADC card integrated with a computer. The time dependence of the switching current $i(t)$ was displayed on a monitor in real-time mode. The best resolution of the signal, controlled by the discretization frequency of the ADC, was 2×10^{-8} s. The measurements were carried out in the single-pulse mode. The crystals were prepared as polar *z*-cut plates 1–2 mm thick with deposited electrodes (silver paste). The upper field limit was ≈ 10–12×10^3 V cm^{-1}, since a further field increase often caused mechanical destruction of the crystals probably due to the significant piezoelectric effect characteristic of them.

Several samples of each composition were studied. The measurements were carried out on multidomain (annealed in the paraelectric phase) and single-domain samples. The single-domain state was achieved through gradual cooling of the crystals from the paraelectric phase down to room temperature in an external field $(2$–$3) \times 10^3$ V cm^{-1}. The poling was monitored by measuring the pyroelectric coefficient using the static method.

3. RESULTS AND DISCUSSION

We recall the fundamental features of the pulsed switching [21], which were studied in model objects (TGS, $BaTiO_3$) in detail and are characteristic of all ferroelectrics in general. As a field pulse stronger than E_c is applied, the Merz circuit detects a switching current with a resolved peak corresponding to an enhanced, avalanche-like rise in the switched charge Q_s (or, what is the same, to an avalanche-like growth of domains). The charge Q_s approaches its saturated value $Q_s \approx P_s$ with a relaxation rate dependent on the applied field.

Two types of current responses accompanying the applied field pulses are observed in the SBN crystals. In most of the crystals, in contrast to model ferroelectrics, the switching current appears as a short decaying signal and is observed up to breakdown fields (Fig. 1). In appearance, this signal is similar to the response arising in model ferroelectrics at $E \ll E_c$; however, its fundamental difference is a pronounced nonexponential decay (see below). On the contrary, $i(t)$ in nonswitching model ferroelectrics falls off exponentially, which was confirmed in our reference measurements on TGS crystals in weak fields.

The "classical" switching current (with a peak), qualitatively similar to the signal in model ferroelectrics, arises in a much smaller number of SBN crystals. It should be emphasized that the two alternative types of current signals in SBN are not related to the composition or quality of the crystals. Signals of different types were observed in identical field regimes in various samples of the same composition cut out from the same crystalline boule even though the ferroelectric properties (the temperature and smearing of the phase transition, permittivity ε, etc.) of these samples were identical.

In some cases, the classical switching signal (with a peak) in the crystal under study was irreversibly transformed into a first-type signal after prolonged annealing in the paraelectric phase or poling. The characteristics of signals of the two types are independent of the pulse duration in the t_p range covered. The signals of both types exhibit oscillations (probably of piezoelectric character) with a frequency of approximately 200 kHz (Figs. 1b, 3a, 4a) which are suppressed by an RC filter.

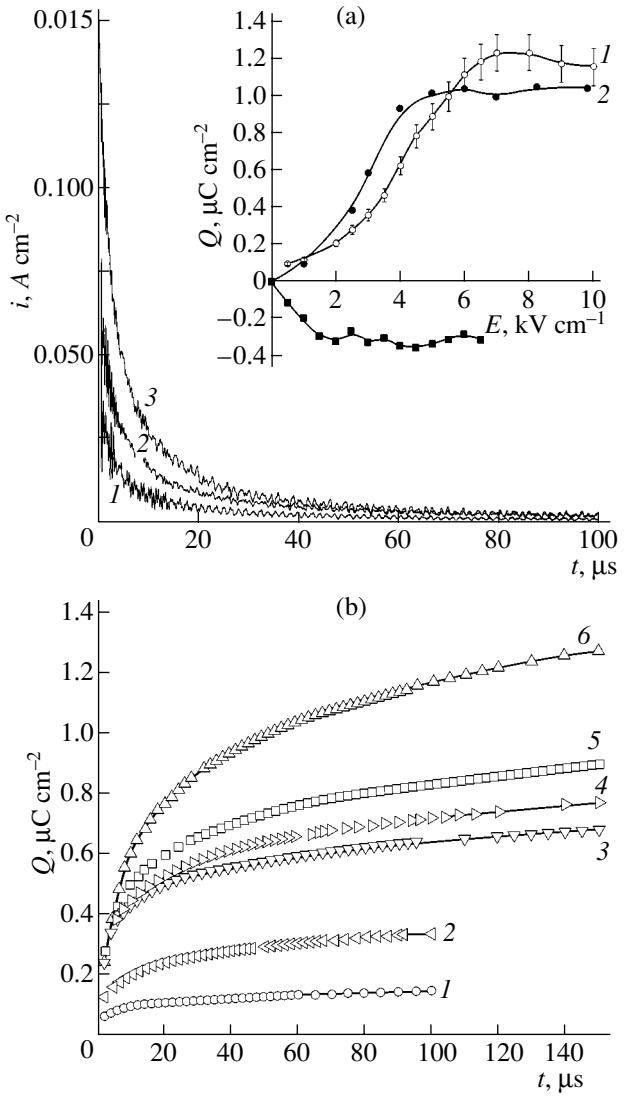

Fig. 1. Switching kinetics of the SBN-0.61:La:Ce crystal: (a) switching currents in fields of (*1*) 3.5, (*2*) 5, and (*3*) 9 kV cm^{-1} and (b) the charge kinetics in fields of (*1*) 1, (*2*) 2, (*3*) 3, (*4*) 4, 5 (*5*), and (*6*) 9 kV cm^{-1}. The inset in (a) shows the field dependence of the charge in (*1*) multi- and (*2*) single-domain states; (*3*) the field dependence of the charge in the single-domain crystal in fields coinciding in sign with the poling field.

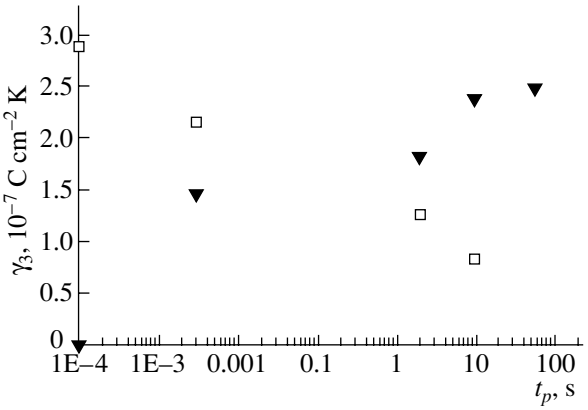

Fig. 2. Dependence of the pyroelectric coefficient on the duration of a 5-kV cm^{-1} single pulse in the multi- (triangles) and single-domain (squares) SBN-0.61:La:Ce crystal.

Let us consider the two types of currents observed in SBN as pulsed voltages are applied. First, we discuss the most commonly encountered (fast-falling) signal $i(t)$; it is exemplified by an arbitrarily chosen sample of the SBN-0.61:Ce:La crystal (Fig. 1). Figure 1a shows the $i(t)$ curves for various values of E in the initially multidomain crystal; these curves almost coincide (except in sign) for fields of both polarities. The shape of the $i(t)$ curves does not change up to $E = 12 \times 10^3$ V cm$^{-1} \gg E_c \approx 1 \times 10^3$ V cm^{-1}. In the single-domain crystal, the characteristics of $i(t)$ in a field opposite to the poling field are almost identical to the $i(t)$ characteristics in the multidomain crystal. The inset to Fig. 1a shows the field dependences of the charge $Q_s(E)$ for multi- and single-domain states (curves *1*, *2*, respectively) obtained by integrating the $i(t)$ curves; for comparison, curve *3* illustrates $Q_s(E)$ obtained in the single-domain crystal in fields coinciding in sign with the poling field, i.e., in the absence of switching. The saturated values of Q_e are approximately 1.5×10^{-6} and 1.1×10^{-6} C cm^{-2} in multi- and single-domain crystals, respectively, which are significantly lower than $P_s \approx (8–9) \times 10^{-6}$ C cm^{-2} (the rather low value of P_s in the crystal of this composition is explained by the low value of T_c and significant smearing of the phase transition [13, 14]).

At first glance, the Q_e smallness indicates the absence of switching, as is the case in model ferroelectrics in weak fields. However, measurements of the dependence of the pyroelectric coefficients on field pulses in SBN indicate that, in actual fact, the polarization significantly changes as a pulse is applied. We explain this effect with reference to the crystal whose switching currents are shown in Fig. 1a. The influence of single pulses of $E = 5 \times 10^3$ V cm^{-1} (of fixed polarity) of various durations on the pyroelectric coefficient γ was measured. The coefficient γ was measured before and after application of a pulse. Before each pulse application, the crystal was restored to its initial (multi- or single-domain) state.

The dependences of γ on t_p are shown in Fig. 2 for multidomain (triangles) and single-domain (squares) initial states. In the multidomain crystal, $\gamma = 0$; application of a field pulse to the crystal caused a significant pyroelectric effect increasing with t_p. After application of a pulse with $t_p \geq 10$ s, the value of γ is saturated and is approximately 0.8γ of the single-domain crystal. Thus, the crystal is significantly polarized as a result of applying a single field pulse of 5×10^3 V cm^{-1} with $t_p \geq 10$ s; a rough estimation yields $Q_s \approx 0.8P_s \approx (5–6) \times 10^{-6}$ C cm^{-2}. Application of the same field pulses (5×10^3 V cm^{-1}) to

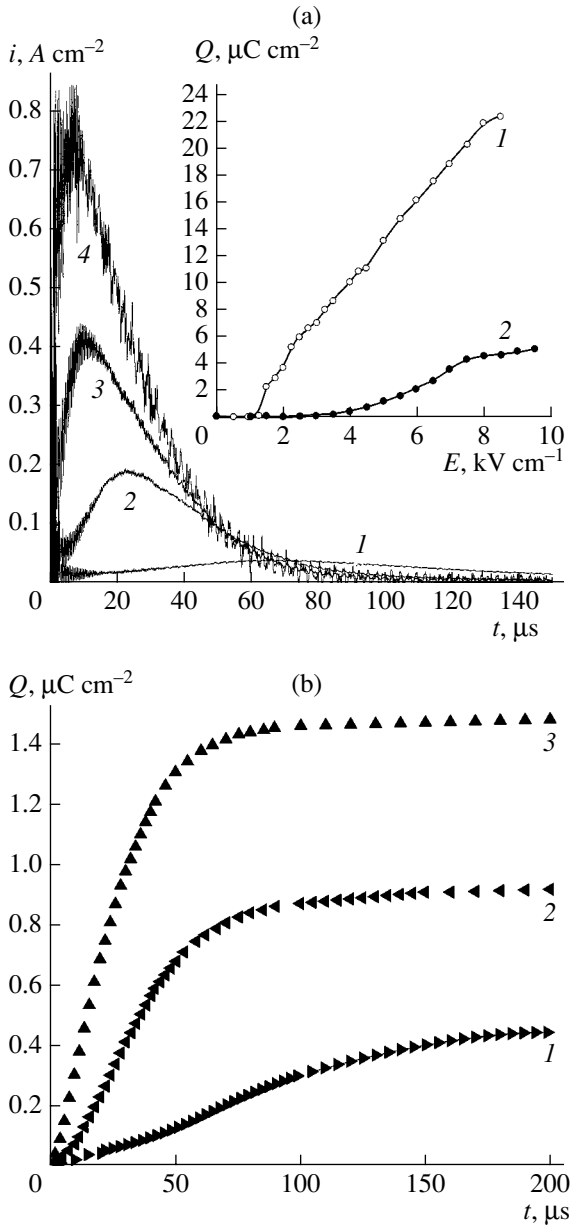

Fig. 3. Switching kinetics of the SBN-0.61:Nd crystal: (a) switching currents in fields of (*1*) 2.5, (*2*) 3.75, (*3*) 5.6, and (*4*) 8.5 kV cm^{-1} and (b) the charge kinetics in fields of (*1*) 1, (*2*) 2, and (*3*) 3 kV cm^{-1}. The inset in (a) shows the field dependence of the charge in (*1*) multi- and (*2*) single-domain states.

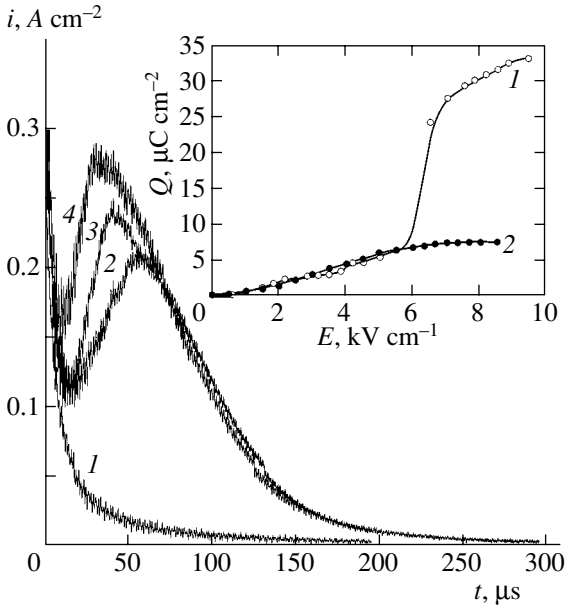

Fig. 4. Switching currents in the SBN-0.75 crystal in fields of (*1*) 6, (*2*) 6.5, (*3*) 7.4, and (*4*) 8.5 kV cm^{-1}. The inset shows the field dependence of the charge in (*1*) multi- and (*2*) single-domain states.

the single-domain crystal causes a significant decrease in γ, i.e., depolarization (Fig. 2). At $t_p \approx 10$ s, we have $\gamma \approx 0$; i.e., the crystal is in a multidomain state. At t_p equal to a few tens of seconds, the pyroelectric current changes sign; i.e., sign reversal (switching) of the total crystal polarization takes place. When the same pulse $E = 5 \times 10^3$ V cm^{-1} of duration t_p in this interval is applied to the multidomain crystal, the switching current is described by curve *2* in Fig. 1a; integration of this curve yields a very low value $Q_s \approx 0.9 \times 10^{-6}$ C cm$^{-2} \ll P_s$. Thus, although the pyroelectric current measurements make evident a significant change in polarization as single pulses are applied, measurements of switching currents do not detect this change.

This switching-current behavior can be understood by analyzing the switched-charge $Q_s(t)$ kinetics, which differs fundamentally from the charge kinetics in the model crystals. The $Q_s(t)$ curves (Fig. 1b) calculated from $i(t)$ for various fields can be closely approximated by the power-law dependence

$$Q(t) = Q_e\left[1 - \frac{1}{(1 + t/a)^n}\right], \qquad (1)$$

where Q_e (saturated value of Q_s), a, and n are adjustable parameters (Table 2). This dependence is identical to the expression describing the polarization kinetics in SBN, in particular, of the same composition SBN-0.61:Ce:La, in quasi-static fields [13, 14]. Let us carry out some estimations. The results of least square approximation to the experimental $Q_s(t)$ curves for several field values are listed in Table 2. For example, the approximation for $E = 5 \times 10^3$ V cm^{-1} in the multidomain crystal (curve *5* in Fig. 1b) yields $Q_e \approx 3.6 \times 10^{-6}$ C cm^{-2}. This value is in satisfactory agreement with the above rough estimate (from pyroelectric measurements): $Q_s \approx (5–6) \times 10^{-6}$ C cm^{-2} for this crystal in the case of application of a pulse $E = 5 \times 10^3$ V cm^{-1} with $t_p \geq 10$ s.

Thus, most of the SBN crystals (we will refer to them as the first group) are characterized by gradual slow polarization variations described by Eq. (1). These variations occur over very long times (a few seconds) even in fields that exceed E_c tenfold; therefore, the major factor controlling the polarized (switched) volume is the pulse duration (Fig. 2) rather than the field strength (Table 2). This conclusion on the SBN polarization processes, made in this study for a time interval of 10^{-4} to 10 s, qualitatively agrees with the results of the study of polarization kinetics in these crystals in the range $\approx$10–10^4 s [13, 14]. The "nonclassical" shape of the switching-current curve is explained by the absence of the fast (avalanche-like) polarization stage characteristic of the model ferroelectrics in strong fields.

Now, we discuss the other type of switching currents, which is less often observed in SBN and is qualitatively similar to the switching current in the model ferroelectrics. Representative examples are shown in Fig. 3 (sample SBN-0.61:Nd) and Fig. 4 (sample SBN-0.75). Figures 3a and 4 display the $i(t)$ curves for multidomain crystals. In the case of SBN-0.61:Nd, the characteristic peak in the $i(t)$ curve is observed at $E \geq E_c$ (Table 1); in SBN-0.75, the peak occurs at $E = 6 \times 10^3$ V cm$^{-1} \gg E_c \approx 10^3$ V cm^{-1} (in weaker fields, the signal falls off rapidly, as discussed above).

The insets to Figs. 3a and 4 show $Q_s(E)$ obtained by integrating the $i(t)$ curves for initially multi- and single-domain states (curves *1*, *2*, respectively, in the insets in both figures). The steep rise of the $Q_s(E)$ curve for the SBN-0.75 crystal at $E > 6 \times 10^3$ V cm^{-1} (inset to Fig. 4) corresponds to the change in the current response shape. The switched charge in the multidomain crystals gradually increases with increasing field up to $E \gg E_c$, and saturation is reached in some cases (inset to Fig. 4). It is interesting to note that the tendency to saturation in SBN-0.75 is observed at $Q_s \sim 30 \times 10^{-6}$ C cm^{-2}, which is close to the spontaneous-polarization estimate $P_s \sim 33 \times 10^{-6}$ C cm^{-2} made for this composition on the basis of the Abrahams structural criterion [22].

In the single-domain crystals, the $Q_s(E)$ dependence in rather weak fields flattens (curves *2* in the insets to Figs. 3a and 4); however, the saturated value is significantly (sometimes, an order of magnitude) lower than the value obtained for the same crystal in the multidomain state. Such dependences, namely, the gradual increase in $Q_s(E)$ in multidomain crystals and low saturated value of Q_e in single-domain crystals, are typical of all the SBN samples in which the classical switching current is observed. Figure 3b shows the $Q_s(t)$ kinetics calculated from $i(t)$. As follows from Figs. 3 and 4, notwithstanding the classical shape of the switching currents, the $Q_s(E)$ and $Q_s(t)$ dependences in these SBN crystals differ fundamentally from the corresponding dependences in the model crystals, where both quantities in single- and multidomain states asymptotically approach P_s. In SBN, the values of Q_e in multi- and single-domain states differ sharply. In the multidomain crystal, for each field $E > E_c$ there is a certain limiting value $Q_e < P_s$ that increases with E.

Table 2. Relaxation parameters of the SBN:La:Ce crystal

E, kV cm^{-1}	Q_e, 10^{-6} C cm^{-2}	a, μs	n
4	3.0	0.52	0.05
5	3.6	0.65	0.05
9	4.2	1.7	0.07

The fields at which $Q_s(E)$ tends to saturation (Fig. 4) significantly exceed the values of E_c measured from quasi-static hysteresis loops. The switching scenario in crystals of this group differs from the above-described slow polarization process in crystals of the first group. In this case, for some reason, the volume involved in switching is polarized (switched) in jumps; the controlling factor in this case is the field strength rather than the pulse duration (as is the case in the crystals of the first group). As a result of poling (due to prolonged exposure to an external field), the volume polarized in jumps decreases abruptly. However, in the crystals of the first group, such "freezing" effects are not observed, since the polarization changes caused by a given field pulse are very similar in multi- and single-domain states (see insets to Figs. 1a, 2). We note that, notwithstanding the classical shape of the switching currents in the second group of SBN crystals, the dependence of Q_e on E in the multidomain state and the smallness of $Q_e \ll P_s$ in the single-domain state do not allow consideration of the switching process in terms of the switching rate $v_s = 1/t_s$. Here, by definition [21], the switching time t_s corresponds to the switching-current decreasing to 10% of its value at a constant switched charge $Q_s \longrightarrow P_s$.

The features of the polarization kinetics of SBN crystals in pulsed fields, in particular, very long times, may be qualitatively explained by a nonuniformly distributed internal field [13, 14] (or, what is the same, pinning centers [23]) existing in the relaxor ferroelectric [20]. In terms of the classical switching model, this means the existence of a wide spectrum of switching activation fields, which, as is known, characterize the rate and time t_s of switching [21]. As a result, the polarization process (switching current) is described by a set of relaxation times and proceeds smoothly.

The faster switching kinetics observed in some SBN crystals is explained by the fact that the energy distribution of pinning centers (and, therefore, the spectrum of relaxation times) becomes rather narrow due to random causes and the given volume is polarized in jumps. However, as was already mentioned, external influences, bringing about, e.g., the formation of the single-domain state, often cause a change in the polarization kinetics type: the kinetics becomes slow, probably due to changes in the internal-field distribution. The conclu-

sion that the polarization processes in SBN crystals are slow is confirmed by the domain dynamics observation [15], according to which the sideway motion of domain walls (characteristic of the model ferroelectrics) is hindered in SBN, frontal domain growth prevails, and the formation of the single-domain state proceeds extremely slowly.

Based on the data obtained, certain practical conclusions may be drawn. For example, the technique of RDS formation used for $LiNbO_3$ (ultrashort field pulses with high strength [24]) is not applicable for most SBN crystals. Causes for the nonreproducible effect of field fixing of holograms in SBN may be suggested: this effect is rarely observed in pulsed fields [1, 2], probably because it occurs only in crystals of the second group, where jumplike ferroelectric switching of different portions of the crystal takes place (this is what is precisely necessary for hologram fixing).

4. CONCLUSIONS

Thus, SBN crystal polarization and ferroelectric switching in pulsed fields differ from the same processes in model ferroelectrics. In most SBN crystals, these processes are characterized by very slow kinetics, with relaxation times reaching a few seconds in fields significantly exceeding (up to ten times) the coercive fields estimated from quasi-static *P–E* loops. Due to the absence of the enhanced (avalanche-like) increase in polarization characteristic of the model ferroelectrics at $E > E_c$, the switching currents do not exhibit peaks. The jumplike polarization observed in some SBN crystals also differs from the model process: the switched charge Q_s increases with field in the entire field region $E \gg E_c$ and becomes much larger in multidomain than in single-domain crystals. The features observed may be qualitatively explained by a nonuniform distribution of the internal field in the relaxor ferroelectric volume.

ACKNOWLEDGMENTS

The authors thank V.V. Gladkiĭ for helpful discussions.

This study was supported by the Russian Foundation for Basic Research (project no. 00-02-16624) and INTAS (grant no. 01-0173).

REFERENCES

1. F. Micheron and G. Bismuth, Appl. Phys. Lett. **23**, 71 (1973).
2. Y. Qiao, S. Orlov, D. Psaltis, and R. R. Neurgaonkar, Opt. Lett. **18** (12), 1004 (1993).
3. J. Ma, T. Y. Chang, J. H. Hong, and R. R. Neurgaonkar, Phys. Rev. Lett. **78** (15), 2960 (1997).
4. M. Hisaka, H. Ishitobi, and S. Kawata, J. Opt. Soc. Am. B **17** (3), 422 (2000).
5. F. Kahmann, R. Pankrath, and R. A. Rupp, Opt. Commun. **107**, 6 (1994).
6. A. S. Kewitsch, M. Segev, A. Yariv, *et al.*, Appl. Phys. Lett. **64** (23), 3068 (1994).
7. A. S. Kewitsch, M. Segev, A. Yariv, *et al.*, Phys. Rev. Lett. **73** (8), 1174 (1994).
8. M. Horowitz, A. Bekker, and B. Fischer, Appl. Phys. Lett. **62** (21), 2619 (1993).
9. A. Bekker and B. Fischer, Appl. Phys. Lett. **64** (14), 1756 (1994).
10. A. A. Kaminskiĭ, J. Garcia-Sole, S. N. Bagaev, *et al.*, Kvantovaya Élektron. (Moscow) **25**, 1059 (1998).
11. J. Romero, D. Jaque, J. Garcia-Sole, and A. A. Kaminskii, Appl. Phys. Lett. **78** (14), 1961 (2002).
12. Y. Y. Zhu, J. S. Fu, R. F. Xiao, and G. K. L. Wong, Appl. Phys. Lett. **70** (14), 1793 (1997).
13. V. V. Gladkiĭ, V. A. Kirikov, S. V. Nekhlyudov, *et al.*, Pis'ma Zh. Éksp. Teor. Fiz. **71**, 38 (2000) [JETP Lett. **71**, 24 (2000)].
14. V. V. Gladkiĭ, V. A. Kirikov, T. R. Volk, and L. I. Ivleva, Zh. Éksp. Teor. Fiz. **120** (3), 678 (2001) [JETP **93**, 596 (2001)].
15. N. R. Ivanov, T. R. Volk, L. I. Ivleva, *et al.*, Kristallografiya **47** (6), 1065 (2002) [Crystallogr. Rep. **47**, 1023 (2002)].
16. T. R. Volk, V. Yu. Salobutin, L. I. Ivleva, *et al.*, Fiz. Tverd. Tela (St. Petersburg) **42**, 2066 (2000) [Phys. Solid State **42**, 2129 (2000)].
17. L. I. Ivleva, N. V. Bogodaev, N. M. Polozkov, and V. V. Osiko, Opt. Mater. **4**, 168 (1995).
18. T. Volk, Th. Woike, U. Doerfler, *et al.*, Ferroelectrics **203**, 457 (1997).
19. T. Volk, L. Ivleva, P. Lykov, *et al.*, Appl. Phys. Lett. **79** (6), 854 (2001).
20. L. E. Cross, Ferroelectrics **76**, 241 (1987).
21. M. E. Lines and A. M. Glass, *Principles and Applications of Ferroelectrics and Related Materials* (Oxford Univ. Press, Oxford, 1977; Mir, Moscow, 1981).
22. S. C. Abrahams, S. K. Kurtz, and P. B. Jamieson, Phys. Rev. **172**, 555 (1968).
23. T. Granzov, U. Doerfler, Th. Woike, *et al.*, Phys. Rev. B **63**, 174101 (2001).
24. R. L. Byer, J. Nonlinear Opt. Phys. Mater. **6**, 549 (1997).

Translated by A. Kazantsev

Physics of the Solid State, Vol. 45, No. 8, 2003, pp. 1543–1548. Translated from Fizika Tverdogo Tela, Vol. 45, No. 8, 2003, pp. 1469–1474.

LATTICE DYNAMICS AND PHASE TRANSITIONS

Mean-Square Displacements of Metal and Boron Atoms in Crystal Lattices of Rare-Earth Hexaborides

V. V. Novikov

Bryansk State Pedagogical Institute, Bezhitskaya ul. 14, Bryansk, 241036 Russia

e-mail: vvnovikov@mail.ru

Received January 8, 2003

Abstract—The intensities of the I_{410} and I_{411} reflections of nine rare-earth hexaborides MB_6 (M = La, Ce, Pr, Nd, Sm, Eu, Gd, Tb, Dy) are experimentally studied in the temperature range 4.2–300 K. The mean-square displacements of metal and boron atoms are calculated from the temperature dependences of the intensities $I_{410}(T)$ and $I_{411}(T)$. The characteristic temperatures of the metal (θ_M) and boron (θ_B) sublattices of rare-earth hexaborides are determined in the Debye approximation. It is found that the characteristic temperatures decrease with an increase in the atomic number of the metal. © *2003 MAIK "Nauka/Interperiodica".*

1. INTRODUCTION

It is known that rare-earth hexaborides crystallize in a CsCl-type structure in which a cube consisting of heavy metal atoms is centered as an octahedron composed of six rigidly bound lighter atoms of boron. This group of B_6 atoms can be considered a structural unit, namely, a pseudoatom $B^* \equiv B_6$ [1]. It is worth noting that the distances between boron atoms belonging to the adjacent cells are shorter than those inside the B_6 group [2, 3]. The specific features observed in the crystal structure of rare-earth hexaborides are responsible to a large extent for the unusual temperature dependences of their crystal chemical properties: heat capacity [4, 5], thermal expansion [6, 7], elastic constants [8], etc.

Paderno and Shitsevalova [9] demonstrated that the characteristic temperatures θ_{MB_6} calculated from the experimental temperature dependences of the thermodynamic characteristics of rare-earth hexaborides differ significantly. In this respect, it is of interest to determine separately the characteristic temperatures of the metal and boron sublattices of hexaborides from analyzing the available experimental data.

This paper reports on the results of systematic experimental investigations into the temperature variations in the mean-square displacements of metal and boron atoms in the crystal lattices of rare-earth hexaborides with the use of experimental data on the intensities of x-ray reflections.

2. EXPERIMENTAL TECHNIQUE

X-ray diffraction experiments were performed with hexaboride powder samples used earlier in studies of the temperature dependences of the heat capacity and thermal expansion [6, 7]. The intensities of the (410) and (411) reflections were measured on a DRON-3.0 x-ray diffractometer (CoK_α radiation) equipped with a helium cryostat. The sample temperature was determined with a Cu/Cu–0.1 wt % Fe thermocouple, which was calibrated against the germanium and platinum standard resistance thermometers at the All-Russia Research Institute of Physicotechnical and Radio Engineering Measurements. During the experiment, the temperature was automatically maintained constant to within ±0.2 K.

3. EXPERIMENTAL RESULTS

The experimental intensities of the (410) and (411) reflections of rare-earth hexaborides studied in the temperature range 4.2–300 K are presented in Fig. 1. It can be seen from Fig. 1 that the intensities of the scattered x-ray beam are scarcely affected by the magnetic ordering typical of the majority of hexaborides at temperatures below 30 K, which is most likely due to a considerable dispersion of the experimental points. For the DyB_6 hexaboride, the intensities of experimental reflections were measured at temperatures above T = 22 K. At lower temperatures, the reflections of the second phase, which are not observed at higher temperatures, are superposed on the (410) and (411) reflections in the x-ray diffraction patterns.

As is clearly seen from Fig. 1, the intensity $I(T)$ varies only slightly in the low-temperature range (4.2–50 K) and decreases monotonically as the temperature increases. A considerable dispersion of the experimental points (3–5%) can be associated with the properties of the studied sample.

4. DISCUSSION

The intensity of an x-ray reflection I_{hkl} depends on the Bragg angle θ, atomic scattering factor f, structural

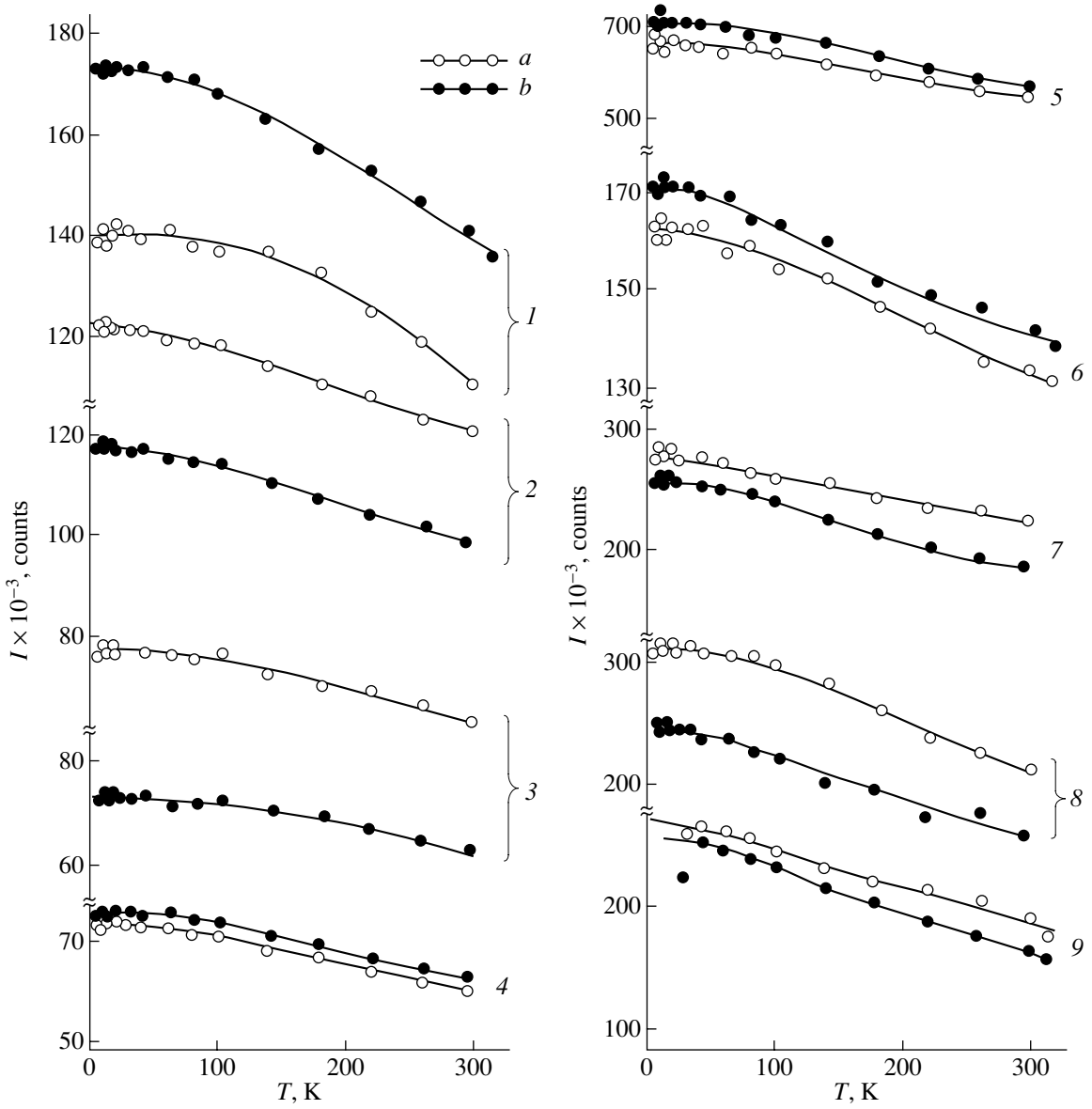

Fig. 1. Intensities of (*a*) I_{411} and (*b*) I_{410} reflections of rare-earth hexaborides in the temperature range 4.2–300 K: (*1*) LaB_6, (*2*) CeB_6, (*3*) PrB_6, (*4*) NdB_6, (*5*) SmB_6, (*6*) EuB_6, (*7*) GdB_6, (*8*) TbB_6, and (*9*) DyB_6.

factor F_{hkl}, multiplicity factor P_{hkl}, polarizability, extinction coefficient, etc. [10, 11]:

$$I_{hkl} = A\frac{1+\cos^2 2\theta}{\sin^2\theta\cos\theta}|F_{hkl}|^2 P_{hkl}. \quad (1)$$

In the temperature range 0–300 K, the scattering angle varies insignificantly, whereas the multiplicity factor remains constant at specified indices *h*, *k*, *l*. Consequently, the intensity ratio of a reflection at a given temperature and absolute zero temperature is equal to the ratio of the squares of the structural factors under the same conditions; that is,

$$\frac{I_{hkl}(T)}{I_{hkl}(0)} = \frac{|F_{hkl}(T)|^2}{|F_{hkl}(0)|^2}. \quad (2)$$

The structural factor is determined by the atomic scattering factors f_i and the atomic coordinates (x_i, y_i, z_i) of the unit cell:

$$F_{hkl} = \sum f_i e^{2\pi i(hx_i + ky_i + lz_i)}.$$

As a result, we can write the expression

$$|F_{hkl}|^2 = \sum f_i \cos 2\pi(hx_i + ky_i + lz_i)^2 + \sum f_i \sin 2\pi(hx_i + ky_i + lz_i)^2. \quad (3)$$

Here, f_i is the atomic scattering factor for the ith atom of the unit cell at absolute zero temperature [12] and x_i, y_i, and z_i are the coordinates of the ith atom (expressed in terms of a lattice constant). The rare-earth hexaborides under investigation have a CaB_6-type structure with the following coordinates of the metal and boron atoms: M (0, 0, 0) and B (1/2, 0.207, 1/2; 0.207, 1/2, 1/2; 1/2, 0.793, 1/2; 0.793, 1/2, 1/2; 1/2, 1/2, 0.793; 1/2, 1/2, 0.207). For the (410) and (411) reflections studied in this work, we obtain the following relationships for the squares of the magnitudes of the structural factors at absolute zero:

$$\begin{aligned} |F_{410}|^2 &= (f'_M - 2.408 f'_B)^2, \\ |F_{411}|^2 &= (f'_M - 0.216 f''_B)^2. \end{aligned} \quad (4)$$

Here, single and double primes indicate the atomic scattering factors of the metal and boron atoms for the (410) and (411) reflections, respectively.

The temperature dependence of the structural factor is characterized by the factor e^{-C_i}, where $C_M = 8\pi^2 s^2 \overline{U_M^2}$ and $C_B = 8\pi^2 s^2 \overline{U_B^2}$. Here, **s** is the scattering vector with magnitude $\sin\theta/\lambda$ and $\overline{U_M^2}$ and $\overline{U_B^2}$ are the mean-square dynamic displacements of the metal and boron atoms from their equilibrium positions.

As a consequence, from relationships (2) and (4), we can derive the following expressions:

$$\begin{aligned} \frac{I_{410}(T)}{I_{410}(0)} &= \frac{|F_{410}(T)|^2}{|F_{410}(0)|^2} = \frac{(f'_M e^{-C_M} - 2.41 f'_B e^{-C_B})^2}{(f''_M - 2.41 f''_B)^2}, \\ \frac{I_{411}(T)}{I_{411}(0)} &= \frac{|F_{411}(T)|^2}{|F_{411}(0)|^2} = \frac{(f''_M e^{-C_M} - 0.126 f''_B e^{-C_B})^2}{(f''_M - 0.126 f''_B)^2}, \end{aligned} \quad (5)$$

$$\begin{aligned} C'_M &= 8\pi^2 \overline{U_M^2}(s')^2, \quad C''_M = 8\pi^2 \overline{U_M^2}(s'')^2, \\ C'_B &= 8\pi^2 \overline{U_B^2}(s')^2, \quad C''_B = 8\pi^2 \overline{U_B^2}(s'')^2. \end{aligned} \quad (6)$$

For the LaB_6 hexaboride, we obtain $\sin\theta_{410} = 0.882$ and $\sin\theta_{411} = 0.916$. Hence, the magnitudes of the scattering vectors are determined to be $s' = 0.497$ Å^{-1} and $s'' = 0.511$ Å^{-1}; i.e., s' and s'' are close in magnitude and differ from the mean value $s = (s' + s'')/2 = 0.504$ Å^{-1} by no more than 1.5%. This value is less than the dispersion of the experimental intensities. For this reason, in our calculations, the values of s' and s'' were taken to be identical and equal to the mean value s.

The mean-square dynamic displacements $\overline{U_M^2}$ for rare-earth metal atoms and $\overline{U_B^2}$ for boron atoms in the crystal lattices of the hexaborides were calculated from relationships (5) and (6). The results of these calculations for $\overline{U_{RE}^2}$ at the temperature $T = 300$ K are in close agreement with the data reported in [13–20]. However, the disagreement between the results obtained in this work and data available in the literature on $\overline{U_B^2}$ becomes noticeable with an increase in the atomic number of the metal.

The temperature dependence of the mean-square dynamic displacement $\overline{U^2}(T)$ for the lanthanum and boron sublattices can be represented as the sum of the zero-point and temperature-dependent mean-square atomic displacements:

$$\overline{U_D^2} = \overline{U_T^2} + \overline{U_{00}^2} = (\Phi(x)/x + 0.25)3h^2/4\pi^2 mk\theta. \quad (7)$$

Here, $\overline{U_{00}^2}$ is the mean square of the amplitude of zero-point atomic vibrations, $\overline{U_T^2}$ stands for the temperature-dependent part of the mean-square displacements, θ is the Debye characteristic temperature, $x = \frac{\theta}{T}$, $\Phi(x)$ is the Debye function, m is the atomic weight, h is the Planck constant, and k is the Boltzmann constant. The parenthetic term 0.25 accounts for the contribution of the zero-point vibrations.

The temperature dependence $\overline{U_{La}^2}(T)$ is satisfactorily approximated by the Debye curve for $\theta_{La} = 250$ K (Fig. 2a).

The imperfection of the metal and boron sublattices in rare-earth hexaborides makes a temperature-independent contribution to the mean-square atomic displacements. It is believed that this is particularly true in regard to the sublattice of boron atoms [13]. In order to determine the temperature-dependent part of the mean-square displacements of boron atoms $\overline{U_B^2}(T)$ for lanthanum hexaboride, the value of 0.8×10^{-23} m^2, which involves both the contribution of zero-point vibrations $\overline{U_{00}^2}$ and the contribution of vacancies and other defects $\overline{U_d^2}$, was subtracted from the experimental values of $\overline{U_B^2}$. The subtracted value was determined at the intersection point of the ordinate axis and the curve (dashed line in Fig. 2b) that interpolates the experimental values of $\overline{U_B^2}$.

From analyzing the temperature-dependent part of the mean-square displacements of boron atoms $\overline{U_B^2}(T)$ [relationship (7) without the parenthetic term 0.25], the Debye characteristic temperature of the boron sublattice in lanthanum hexaboride was chosen as $\theta_B = 760$ K.

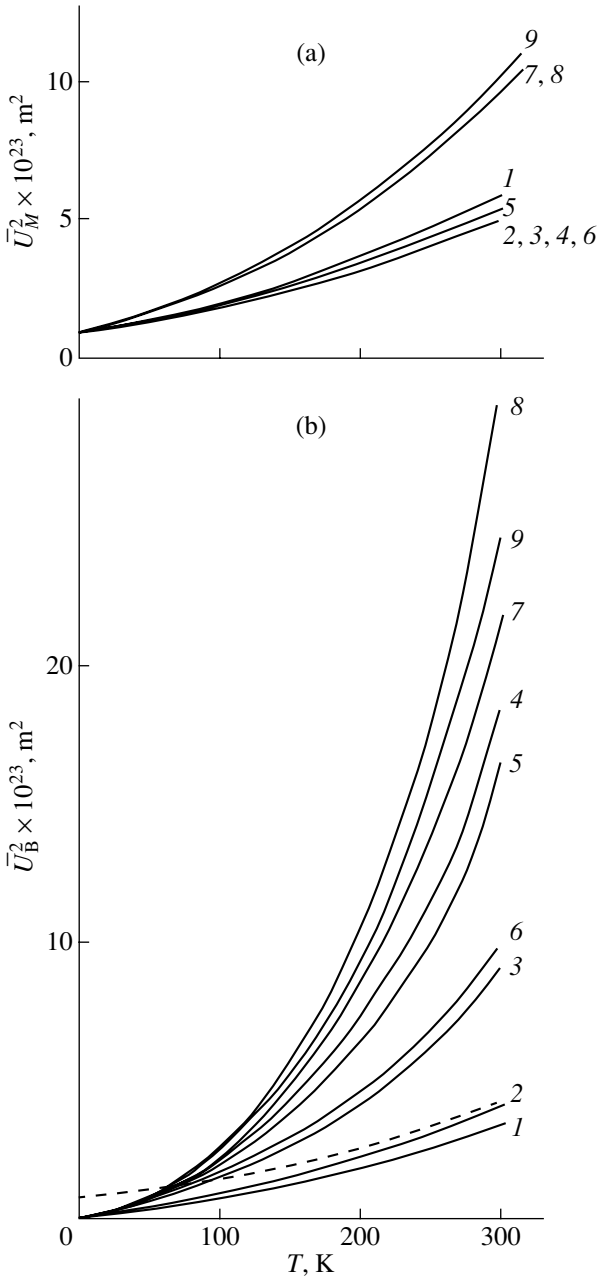

Fig. 2. (a) Mean-square displacements of rare-earth metal atoms $\overline{U_M^2}$ and (b) temperature-dependent part of the mean-square displacements of boron atoms $\overline{U_B^2}$ in the crystal lattices of hexaborides. The dashed line represents the experimental curve $\overline{U_B^2}(T)$ for LaB_6. Numerals near the curves correspond to those in Fig. 1.

Figure 3 depicts the dependence $\overline{U_i^2}(T)$ for the metal and boron sublattices of lanthanum hexaboride LaB_6 in the temperature range 300–900 K. These curves were calculated from the Debye temperatures θ_{La} and θ_B (see above). For comparison, Fig. 3 presents

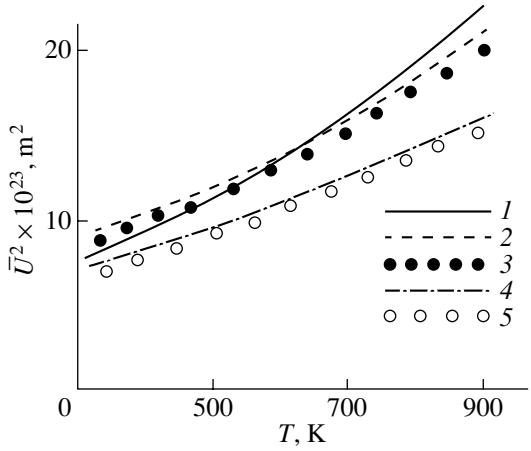

Fig. 3. Mean-square displacements of lanthanum and boron atoms in LaB_6 at high temperatures: (*1*) calculated dependence $\overline{U_{La}^2}(T)$ in the Einstein approximation at θ_E = 150 K, (*2*) experimental dependence $\overline{U_B^2}(T)$ according to the data taken from [21], (*3*) calculated dependence $\overline{U_{La}^2}(T)$ in the Debye approximation at θ_{La} = 250 K, (*4*) experimental dependence $\overline{U_B^2}(T)$ [21], and (*5*) calculated dependence $\overline{U_B^2}(T)$ in the Debye approximation at θ_B = 760 K.

the experimental data taken from [21]. It can be seen that the temperature dependences of the mean-square atomic displacements of lanthanum $\overline{U_{La}^2}(T)$ (curve *3*) and boron $\overline{U_B^2}(T)$ (curve *5*), which were calculated in the Debye approximation, are in close agreement with the experimental data. The curve $\overline{U_{La}^2}(T)$ calculated for the lanthanum sublattice in the Einstein approximation at the characteristic temperature θ_E = 150 K (according to the data obtained in [13]) lies above the experimental dependence.

By analogy with the treatment performed for LaB_6, we analyzed the mean-square dynamic displacements $\overline{U_M^2}$ for rare-earth metal atoms and $\overline{U_B^2}$ for boron atoms in the sublattices of cerium, praseodymium, and neodymium hexaborides in the temperature range 4.2–300 K (Fig. 2) and obtained the following characteristic temperatures: θ_{Ce} = 250 K and θ_B = 780 K for CeB_6, θ_{Pr} = 250 K and θ_B = 570 K for PrB_6, and θ_{Nd} = 250 K and θ_B = 550 K for NdB_6.

For the LaB_6, CeB_6, PrB_6, and NdB_6 hexaborides, the Debye temperatures of the metal sublattices coincide to within the error of estimation. Blomberg *et al.* [15] determined the Einstein temperatures of the metal sublattices in NdB_6 and SmB_6 as follows: θ_{Nd} = 120 K

and θ_{Sm} = 120 K. According to the results obtained by Trunov *et al.* [22], the Einstein temperature of the lanthanum sublattice in LaB_6 proved to be θ_{La} = 150 K, which substantially exceeds the above value.

In the hexaboride series under consideration (LaB_6, CeB_6, PrB_6, and NdB_6), there exists a tendency toward a decrease in the Debye temperature of the boron sublattice with an increase in the atomic number of the metal. This result is consistent with the inferences made by Chernyshov *et al.* [19].

Since samarium ions in SmB_6 have a mixed valence and europium ions in EuB_6 reside in a bivalent state, the bonding of atoms in the crystal lattices of these hexaborides can change in character as compared to that of trivalent metals.

An analysis of the temperature dependences of the intensities $I_{hkl}(T)$ for metal sublattices of samarium and europium leads to characteristic temperatures close to those obtained for trivalent hexaborides: θ_{Sm} = 220 K and θ_{Eu} = 220 K.

The tendency to a decrease in the Debye characteristic temperature of the boron sublattice with an increase in the atomic number of the metal does not hold for europium hexaboride: θ_B = 420 K for SmB_6 and θ_B = 500 K for EuB_6.

The temperature dependences of the intensities $I_{410}(T)$ and $I_{411}(T)$ for gadolinium, terbium, and dysprosium hexaborides are qualitatively similar to those for the rare-earth hexaborides considered above. At the same time, the mean-square displacements of atoms in the metal and boron sublattices differ in both temperature behavior and magnitude. Consequently, the characteristic temperature of the metal sublattice decreases with an increase in the atomic number of the metal as follows: θ_{Gd} = 170 K and θ_B = 325 K for GdB_6, θ_{Tb} = 165 K and θ_B = 410 K for TbB_6, and θ_{Dy} = 165 K and θ_B = 380 K for DyB_6.

An examination of the intensities of x-ray reflections for DyB_6 revealed that, at temperatures below T = 22 K, the x-ray diffraction patterns contain reflections of the second phase. This suggests that, at these temperatures, dysprosium hexaboride undergoes a structural phase transition and magnetic ordering [23, 24]. Moreover, the transformations occurring in hexaborides manifest themselves both in a double peak observed in the temperature dependence of the heat capacity $C_p(T)$ [5, 25, 26] and in pronounced anomalies found in the temperature dependence of the thermal expansion coefficient $\alpha(T)$ in the range of negative values [5, 7]. Since terbium hexaboride is characterized by similar anomalies in the temperature dependences $C_p(T)$ and $\alpha(T)$, it can be assumed that this compound also undergoes transformations of nonmagnetic nature at low temperatures.

It should be noted that the large dispersion of the experimental intensities of x-ray reflections, especially at the lowest temperatures (4.2–20 K), introduces an appreciable uncertainty into the intensity $I_{hkl}(0)$, which is obtained by extrapolating the averaged dependence $I_{hkl}(T)$ to absolute zero and enters into the relationships (5) used to calculate the mean-square displacements of atoms in the metal and boron sublattices. According to our estimates, the error introduced into the determination of the characteristic temperatures for the metal and boron sublattices due to the dispersion of the experimental intensities can reach 10–20 K for the metal sublattice and 20–30 K for the boron sublattice.

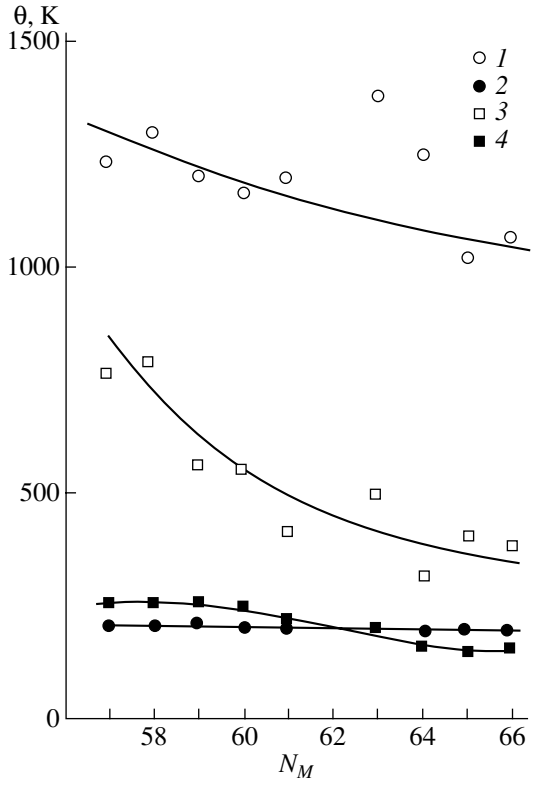

Fig. 4. Characteristic temperatures (*1*, *2*) θ_B of the boron sublattice and (*3*, *4*) θ_M of the metal sublattice in rare-earth hexaborides as functions of the atomic number of the rare-earth element according to (*1*, *3*) calorimetric and (*2*, *4*) x-ray diffraction measurements.

Figure 4 illustrates variations in the characteristic temperatures of boron (θ_B) and metal (θ_M) sublattices of rare-earth hexaborides with a change in the atomic number of the rare-earth metal according to the results of calorimetric [5] and x-ray diffraction measurements. As can be seen from Fig. 4, the characteristic temperatures θ_M determined for the metal sublattices from the calorimetric and x-ray diffraction data differ by a relatively small value.

At the same time, the characteristic temperatures θ_B obtained for the boron sublattice from the results of calorimetric and x-ray diffraction measurements differ significantly (by a factor of 1.5–2.5). The observed difference indicates that, in these cases, the Debye charac-

teristic temperatures correspond to vibrations of different structural elements of the crystal lattice of hexaborides. The high Debye temperatures θ_B, which were determined from the calorimetric data [5], are most likely associated with vibrations of individual boron atoms in a B_6 octahedron, whereas the lower Debye temperatures θ_B, which were obtained from the x-ray diffraction data, should be attributed to vibrations of the B* pseudoatom sublattice.

5. CONCLUSIONS

The main results obtained in the experimental x-ray diffraction investigation of the mean-square displacements of metal and boron atoms in the crystal lattices of rare-earth hexaborides can be summarized as follows.

(1) The mean-square displacements $\overline{U_M^2}$ for metal atoms and $\overline{U_B^2}$ for boron atoms were experimentally determined in the temperature range 4.2–320 K. Experimental values of the mean-square atomic displacements for GdB_6, TbB_6, and DyB_6 were obtained for the first time.

(2) The Debye characteristic temperatures θ_M for the metal sublattice and θ_B for the boron sublattice of rare-earth hexaborides were calculated in the Debye approximation from the temperature dependences of the mean-square displacements $\overline{U_M^2}(T)$ and $\overline{U_B^2}(T)$. It was found that the characteristicθ_M temperatures θ_M and θ_B decrease with an increase in the atomic number of the metal.

(3) Unlike the Debye temperatures θ_B, which were determined from the calorimetric data and correspond to vibrations of boron atoms in a B_6 octahedron, the considerably lower temperatures θ_B, which were obtained from the x-ray diffraction data, characterize vibrations of the octahedra as a whole.

ACKNOWLEDGMENTS

I would like to thank N.N. Sirota for expressing considerable interest in this study and participating in discussions of the results and A.A. Sidorov for his assistance in performing the measurements.

REFERENCES

1. W. B. Pearson, *Crystal Chemistry and Physics of Metals and Alloys* (Wiley, New York, 1972; Mir, Moscow, 1998), Part 1.
2. K. E. Spear, in *Phase Diagrams, Materials Science, and Technology*, Vol. 4: *The Use of Phase Diagrams in Technical Materials*, Ed. by A. M. Alper (Academic, New York, 1976).
3. M. M. Korsukova, V. N. Gurin, T. Lundstrom, and L. E. Tergenius, J. Less-Common Met. **117**, 73 (1986).
4. E. F. Westrum, *Les Elements des Terres Rares* (Centre Nat. Sci., Paris, 1970), p. 443.
5. V. V. Novikov, Fiz. Tverd. Tela (St. Petersburg) **43**, 289 (2001) [Phys. Solid State **43**, 300 (2001)].
6. P. A. Alekseev, E. S. Konovalova, V. N. Lazukov, *et al.*, Fiz. Tverd. Tela (Leningrad) **30** (7), 2024 (1988) [Sov. Phys. Solid State **30**, 1167 (1988)].
7. N. N. Sirota, V. V. Novikov, and A. V. Novikov, Fiz. Tverd. Tela (St. Petersburg) **42** (11), 2033 (2000) [Phys. Solid State **42** (11), 2093 (2000)].
8. S. Nakamura, T. Goto, S. Kunii, *et al.*, J. Phys. Soc. Jpn. **67** (2), 623 (1994).
9. Yu. B. Paderno and N. Yu. Shitsevalova, Preprint (Inst. of Materials Science Problems, National Academy of Sciences of Ukraine, Kiev, 1990), p. 1.
10. N. N. Sirota and V. D. Yanovich, *Chemical Bonding in Semiconductors and Solids* (Nauka i Tekhnika, Minsk, 1965), p. 211.
11. A. I. Kitaigorodsky, *X-ray Diffraction Analysis* (Gostekhizdat, Moscow, 1950).
12. D. M. Kheĭker, *X-ray Diffractometry of Single Crystals* (Mashinostroenie, Leningrad, 1973).
13. M. M. Korsukova, T. Lundstrom, V. N. Gurin, and L. E. Tergenius, Z. Kristallogr. **168**, 299 (1984).
14. M. M. Korsukova, T. Lundstrom, L. E. Tergenius, and V. N. Gurin, Solid State Commun. **63** (3), 187 (1987).
15. M. K. Blomberg, M. J. Nerisalo, M. M. Korsukova, and V. N. Gurin, J. Less-Common Met. **146**, 309 (1989).
16. V. A. Trunov, A. L. Malyshev, D. Yu. Chernyshov, *et al.*, J. Appl. Cryst. **24**, 888 (1991).
17. V. A. Trunov, A. L. Malyshev, D. Yu. Chernyshov, *et al.*, Condens. Matter **5**, 2479 (1993).
18. M. Korsukova, JJAP Ser., No. 10, 15 (1994).
19. D. Yu. Chernyshov, M. M. Korsukova, A. L. Malyshev, *et al.*, Fiz. Tverd. Tela (St. Petersburg) **36** (4), 1078 (1994) [Phys. Solid State **36**, 585 (1994)].
20. M. K. Blomberg, M. J. Merisalo, M. M. Korsukova, and V. N. Gurin, J. Alloys Compd. **217**, 123 (1994).
21. Ya. I. Dutchak, Ya. I. Fedyshin, Yu. B. Paderno, and D. I. Vadets, Izv. Vyssh. Uchebn. Zaved., Fiz., No. 1, 154 (1973).
22. V. A. Trunov, A. L. Malyshev, D. Yu. Chernyshov, *et al.*, Fiz. Tverd. Tela (St. Petersburg) **36** (9), 2687 (1994) [Phys. Solid State **36**, 1465 (1994)].
23. K. Takahashi, H. Nojiri, K. Ohoyama, *et al.*, J. Magn. Magn. Mater. **118–122**, 177 (1998).
24. K. Takahashi, H. Nojiri, K. Ohoyama, *et al.*, Physica B (Amsterdam) **241–243**, 696 (1998).
25. N. N. Sirota and V. V. Novikov, J. Mater. Process. Manuf. Sci. **7**, 111 (1998).
26. N. N. Sirota, V. V. Novikov, and V. A. Vinokurov, Zh. Fiz. Khim. **74** (10), 1924 (2000).

Translated by O. Borovik-Romanova

Physics of the Solid State, Vol. 45, No. 8, 2003, pp. 1549–1556. Translated from Fizika Tverdogo Tela, Vol. 45, No. 8, 2003, pp. 1475–1481.

LATTICE DYNAMICS AND PHASE TRANSITIONS

Interrelation of Structural Features and Vibrational Dynamics of Atoms in the Crystal Lattice of Lithium Orthogermanate in the Superionic State

V. I. Voronin*, A. P. Stepanov*, I. F. Berger*, L. Z. Akhtyamova*, A. L. Buzlukov*, G. Sh. Shekhtman, and E. I. Burmakin****

** Institute of Metal Physics, Ural Division, Russian Academy of Sciences, ul. S. Kovalevskoĭ 18, Yekaterinburg, 620219 Russia*
e-mail: Voronin@imp.uran.ru

*** Institute of High-Temperature Electrochemistry, Ural Division, Russian Academy of Sciences, ul. S. Kovalevskoĭ 20, Yekaterinburg, 620219 Russia*

Received January 22, 2003

Abstract—The crystal structure and vibrational dynamics of lithium atoms in $Li_{3.75}Ge_{0.75}V_{0.25}O_4$ and $Li_{3.70}Ge_{0.85}W_{0.15}O_4$ solid electrolytes in the superionic state are investigated using neutron diffraction and nuclear magnetic resonance (NMR) spectroscopy. It is found that, in the crystal lattice, lithium ions occupy four nonequivalent positions in the tetrahedral and octahedral oxygen ion environment with vacancies in the octahedra. These findings are in good agreement with the NMR data on the dynamic inhomogeneity of lithium cations in the lattice. It is shown that the origin of the superionic state in the studied compounds is associated primarily with the geometric factor, i.e., with an increase in the size of cavities in the oxygen polyhedra surrounding lithium cations. *© 2003 MAIK "Nauka/Interperiodica".*

1. INTRODUCTION

Solid solutions based on lithium orthogermanate in Li_4GeO_4–$Li_3A^VO_4$ (A = P or V) and Li_4GeO_4–$Li_2B^{VI}O_4$ (B = S, Cr, Se, Mo, or W) systems are very promising solid electrolytes with lithium cationic conductivity [1]. The electrical conductivity of these compounds reaches 10^{-4} S cm^{-1} at room temperature and exceeds 1 S cm^{-1} at 870 K in the superionic state. The $Li_{3.75}Ge_{0.75}V_{0.25}O_4$ and $Li_{3.70}Ge_{0.85}W_{0.15}O_4$ compounds are typical representatives of this class of materials. The former compound exhibits maximum conductivity at high temperatures, whereas the conductivity of the latter compound is maximum at low temperatures. Unfortunately, the nature of the superionic state and the dynamics of its formation are still poorly understood. This can be explained by the lack of detailed information on the thermal behavior, phase transitions, and stability of solid electrolytes at high temperatures. In this respect, the main objective of the present work was to elucidate the mechanisms and criteria of the formation of the superionic state. For this purpose, we used high-temperature neutron diffraction and NMR spectroscopy, which made it possible to investigate fine structure characteristics that are "averaged" over the volume, on the one hand, and exhibit local (on the scale of interatomic distances) sensitivity to the nearest environment, on the other.

2. EXPERIMENTAL TECHNIQUE

Samples of $Li_{3.75}Ge_{0.75}V_{0.25}O_4$ and $Li_{3.70}Ge_{0.85}W_{0.15}O_4$ solid electrolytes were synthesized according to a standard procedure described in detail in [2, 3]. The neutron diffraction investigations of the crystal structure were performed at temperatures of 298 and ~850 K with the use of a D7a neutron diffractometer installed at the horizontal channel of an IVV-2M reactor (Zarechnyĭ, Russia). The measurements were carried out in the angle range 9°–111° with a step of 0.1°; the angular resolution of the diffractometer at the wavelength λ = 1.515 Å was $\Delta d/d$ = 0.3% [4]. At high temperatures, the samples were placed in sealed silica tubes in order to prevent their contact with air. The structural parameters (coordinates, site occupancies, unit cell parameters, etc.) were refined by the Rietveld full-profile method [5] with the Fullprof program package [6].

The nuclear magnetic resonance (NMR) investigations of the solid electrolytes were carried out on a modified Bruker SXP4-100 pulsed spectrometer in the temperature range 290–800 K. The spin–lattice relaxation times for ^{7}Li nuclei were measured during the course of nuclear magnetization recovery after saturation of the NMR line. The frequency was 27.3 MHz.

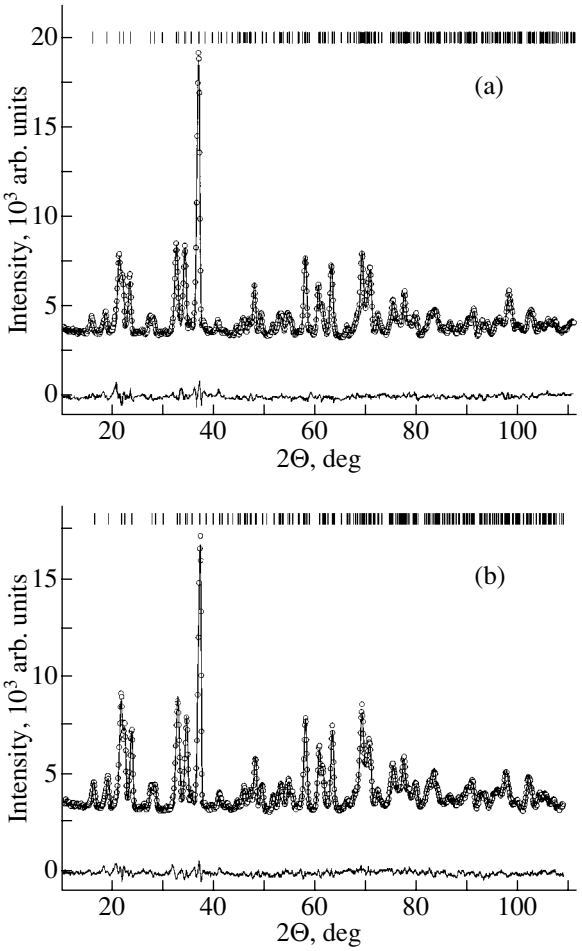

Fig. 1. Neutron diffraction patterns of (a) $Li_{3.75}Ge_{0.75}V_{0.25}O_4$ and (b) $Li_{3.70}Ge_{0.85}W_{0.15}O_4$ compounds at room temperature. Circles represent experimental data. The upper solid lines are the calculated neutron diffraction curves. The lower solid lines show the difference between the experimental and calculated data. Tic marks indicate the angular positions of reflections.

3. RESULTS

3.1. Crystal Structure

Figure 1 shows the neutron diffraction patterns of the $Li_{3.75}Ge_{0.75}V_{0.25}O_4$ (Fig. 1a) and $Li_{3.70}Ge_{0.85}W_{0.15}O_4$ (Fig. 1b) compounds at room temperature. As can be seen from this figure, the experimental neutron diffraction patterns of both samples are similar to each other. All reflections in these diffraction patterns are indexed in the orthorhombic space group *Pnma*. This is in good agreement with the x-ray diffraction data obtained by Burmakin *et al.* [7], according to which the crystal structure of these compounds is similar to the structure of the so-called γ phases (derivatives of the γ modification of Li_3PO_4). This structure was described earlier by Zemann [8]. More recent neutron diffraction investigations [9, 10] demonstrated that, in the isostructural compound $Li_{3.5}Ge_{0.5}V_{0.5}O_4$, excess lithium ions occupy octahedral interstitial position. The proposed model of the crystal lattice served as the starting model for analyzing our experimental neutron diffraction patterns of the $Li_{3.75}Ge_{0.75}V_{0.25}O_4$ and $Li_{3.70}Ge_{0.85}W_{0.15}O_4$ compounds. The refinement procedure was as follows. At the first stage of the refinement, the occupancies of germanium (vanadium) and oxygen positions were fixed, whereas lithium ions were distributed with an equal probability over the possible positions. At this stage, we varied the scale factor, the occupancies of the crystallographic positions of lithium atoms, and all the atomic coordinates. It turned out that, in general, this model adequately describes the experimental data. However, the *R* factors characterizing the discrepancy (or agreement) between the experimental and calculated data were relatively large (15–20%). For this reason, the refinement at the second stage included the occupancies of germanium (vanadium) positions, the shape and width of reflections, and thermal parameters in the isotropic approximation. The thermal parameters for germanium atoms were taken equal to those for vanadium atoms. Moreover, the thermal parameters for all lithium atoms were assumed to be identical. It was found that the total occupancy of lithium sites and the amount of lithium used in the synthesis coincide to within the limits of experimental error. Taking into account this circumstance, the total amount of lithium in the lattice was fixed in further refinement. At the next stage, we additionally varied the thermal parameters of lithium atoms under the assumption that their values for tetrahedral positions are equal to each other and that the thermal parameter of lithium ions in octahedral positions are also identical. As a result, the convergence was considerably improved but the thermal parameters of lithium ions in the tetrahedral positions appeared to be relatively large ($B \approx 8$–10 Å^{-2}). Such large values of the thermal parameters suggest uncorrelated statistical displacements of the lithium cations inside the tetrahedra. By analogy with the model proposed in [9, 10], we can assume that, in the above tetrahedra, the 4*c* and 8*d* positions of lithium are split into two positions each. Under this assumption, the refinement offers more exact values of the thermal parameters. At the last stage of the refinement, we varied individual thermal parameters of the geranium and oxygen atoms in the anisotropic approximation. The calculated neutron diffraction patterns of the $Li_{3.75}Ge_{0.75}V_{0.25}O_4$ and $Li_{3.70}Ge_{0.85}W_{0.15}O_4$ compounds are depicted by the upper solid lines in Figs. 1a and 1b, respectively. Judging from the difference curves (lower solid lines in Figs. 1a and 1b), the experimental and calculated data are in close agreement. A similar procedure was also used to refine the structural parameters obtained at a high temperature; however, at the last stage, we revealed two facts indicating removal of the degeneracy at the tetrahedral lithium positions. First, the calculated Debye–Waller factors proved to be very small for tetrahedral lithium positions ($B \approx 1$–2 Å^2). Second, the occupancies of the split positions leveled off and the *x* coordinates of the atoms

became identical. Removal of the degeneracy did not deteriorate the convergence of the calculated and experimental data, and the thermal parameters of lithium atoms in these positions became close to those for the other atoms. The refined structural parameters are listed in Table 1.

3.2. NMR Data

The NMR spectra of the $Li_{3.75}Ge_{0.75}V_{0.25}O_4$ compound at three temperatures are shown in Fig. 2. The ^{7}Li NMR spectrum at T = 295 K contains only one broadened line (Fig. 2a). As the temperature increases to ~480 K, this line becomes narrower and satellite lines appear in the ^{7}Li NMR spectrum (Fig. 2b). With a further increase in the temperature, the intensities of the satellites decrease and they virtually disappear at T ~ 600 K (Fig. 2c). The ^{7}Li NMR spectrum at T = 625 K closely resembles the spectrum obtained at room temperature, except that, in the former case, the sole line is very narrow. The evolution of the NMR spectra of the $Li_{3.70}Ge_{0.85}W_{0.15}O_4$ compound with variations in the temperature is similar to that of the $Li_{3.75}Ge_{0.75}V_{0.25}O_4$ compound. However, the NMR spectra of the former compound slightly differ from those of the latter compound. For example, the NMR spectrum of the $Li_{3.70}Ge_{0.85}W_{0.15}O_4$ compound at room temperature also contains only one line, but its half-width (~4.6 kHz) is somewhat larger than that for the $Li_{3.75}Ge_{0.75}V_{0.25}O_4$ compound (~4 kHz). The heating of the $Li_{3.70}Ge_{0.85}W_{0.15}O_4$ compound also leads to the appearance of satellites in the NMR spectrum. However, they are more smeared than the satellites for the $Li_{3.75}Ge_{0.75}V_{0.25}O_4$ compound, even though the central intense line at these temperatures is narrower by a factor of more than two. As the temperature increases above 600 K, the satellites in the spectrum of the $Li_{3.70}Ge_{0.85}W_{0.15}O_4$ compound disappear, the central line becomes narrow, and its width is equal to the line width in the spectrum of the $Li_{3.75}Ge_{0.75}V_{0.25}O_4$ compound at the same temperature (Fig. 2c).

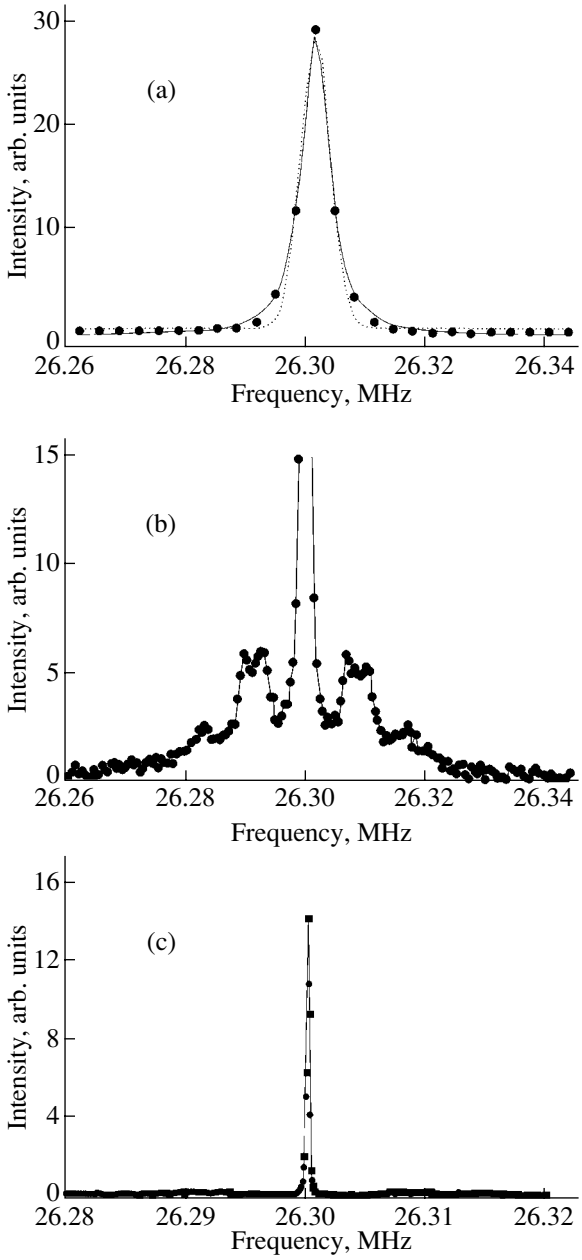

Fig. 2. Experimental NMR spectra of the $Li_{3.75}Ge_{0.75}V_{0.25}O_4$ compound at temperatures of (a) 295 (the solid and dotted lines represent the Lorentzian and Gaussian shapes, respectively), (b) 484, and (c) 625 K.

4. DISCUSSION

The crystal lattice of the $Li_{3.75}Ge_{0.75}V_{0.25}O_4$ and $Li_{3.70}Ge_{0.85}W_{0.15}O_4$ compounds is shown in Fig. 3. As was described in [8], the structure represents a rigid atomic framework consisting of oxygen tetrahedra centered at germanium (partially replaced by vanadium or tungsten) and lithium ions. In the figure, the tetrahedra are depicted in the form of solid polyhedra [darker for tetrahedra centered at germanium (vanadium or tungsten) ions and lighter for tetrahedra centered at lithium ions]. The adjacent tetrahedra are rotated through an angle of 180° with respect to each other and form a zigzag chain along the **a** axis (the vertical axis in the figure). The tetrahedra are slightly distorted and are tilted in different directions with respect to the **a** axis. From the structural parameters (Table 1), we calculated the cation–anion distances in the tetrahedra. The mean bond lengths [Ge(V)–O, ≈ 1.743 Å; Ge(W)–O, ≈ 1.771 Å] calculated from the experimental data for these compounds at room temperature are close to the theoretical values (Ge^{4+}–O, 1.785 Å; V^{5+}–O, 1.685 Å; W^{6+}–O, 1.73 Å) for the coordination number equal to four (tetrahedron) [11–14]. The lattice contains two types of tetrahedra centered at lithium ions. The mean lithium–oxygen distances in these tetrahedra are equal to 2.03 and 1.99 Å

Table 1. Experimental lattice parameters of $Li_{3.75}Ge_{0.75}V_{0.25}O_4$ and $Li_{3.70}Ge_{0.85}W_{0.15}O_4$ compounds at different temperatures

Position	Parameters	$Li_{3.75}Ge_{0.75}V_{0.25}O_4$		$Li_{3.70}Ge_{0.85}W_{0.15}O_4$	
		T = 25°C	T = 575°C	T = 25°C	T = 600°C
	a, Å	10.896(1)	11.043(3)	10.938(1)	11.052(1)
	b, Å	6.2516(8)	6.368(2)	6.274(1)	6.345(1)
	c, Å	5.1571(6)	5.223(1)	5.1609(6)	5.244(1)
	V, Å^3	351.35(7)	367.3(3)	354.18(7)	367.71(7)
Li(1)-(4c)	x	0.075(2)	0.114(7)	0.092(3)	0.110(8)
	z	0.644(5)	0.664(9)	0.668(7)	0.667(9)
	B, Å^2	1.49(3)	4.3(3)	0.59(8)	4.2(4)
	Site occupancy	0.75(5)	1.0	0.61(3)	1.0
Li(1a)-(4c)	x	0.114(6)		0.084(6)	
	z	0.765(8)		0.868(8)	
	B, Å^2	1.49(3)		0.59(8)	
	Site occupancy	0.25(5)		0.39(3)	
Li(2)-(8d)	x	0.169(2)	0.162(6)	0.168(2)	0.167(4)
	y	−0.011(3)	−0.069(9)	−0.024(3)	−0.031(6)
	z	0.313(3)	0.362(9)	0.325(4)	0.327(6)
	B, Å^2	1.78(9)	4.9(4)	1.13(9)	4.11(9)
	Site occupancy	1.37(4)	2.0	1.40(4)	2.0
Li(2a)-(8d)	x	0.143(4)		0.168(4)	
	y	0.027(6)		0.052(7)	
	z	0.109(8)		0.116(8)	
	B, Å^2	1.78(9)		1.13(9)	
	Site occupancy	0.63(4)		0.60(4)	
Li(4)-(8d)	x	0.327(6)	0.175(8)	0.285(9)	0.190(9)
	z	0.015(6)	0.094(9)	0.038(6)	−0.022(7)
	B, Å^2	3.5(8)	4.6(9)	0.67(9)	3.7(9)
	Site occupancy	0.26(1)	0.33(5)	0.16(2)	0.36(2)
Li(3a)-(4c)	x	0.031(6)	0.046(7)	0.039(4)	0.041(6)
	y	0.518(7)	0.496(7)	0.440(7)	0.485(9)
	z	0.389(7)	0.441(9)	0.384(7)	0.421(8)
	B, Å^2	3.5(8)	4.6(9)	0.67(9)	3.7(9)
	Site occupancy	0.49(1)	0.42(5)	0.54(2)	0.34(2)
Ge/V-(4c)	x	0.4152(7)	0.4164(8)	0.4157(5)	0.4156(5)
	z	0.339(1)	0.346(2)	0.345(1)	0.345(1)
	β_{11}	0.0022(6)	0.0061(21)	0.0032(9)	0.0082(19)
	β_{22}	0.0188(24)	0.0439(96)	0.0210(21)	0.0520(41)
	β_{33}	0.0196(29)	0.0336(89)	0.0072(17)	0.0272(57)
	Site occupancy	0.75/0.25	0.75/0.25	0.85/0.15	0.85/0.15
O(1)-(8d)	x	0.3363(5)	0.3332(9)	0.3353(5)	0.3352(6)
	y	0.0217(7)	0.033(1)	0.0215(8)	0.0226(11)
	z	0.2242(8)	0.233(1)	0.2217(8)	0.232(1)
	β_{11}	0.0025(4)	0.0055(13)	0.006(4)	0.007(4)
	β_{22}	0.0159(17)	0.0359(55)	0.0130(19)	0.0330(39)
	β_{33}	0.0099(15)	0.0200(83)	0.0177(21)	0.0277(31)
	Site occupancy	2.0	2.0	2.0	2.0
O(2)-(4c)	x	0.4134(6)	0.415(1)	0.4138(6)	0.4136(7)
	z	0.676(1)	0.666(1)	0.670(1)	0.671(1)
	β_{11}	0.0029(7)	0.0146(29)	0.0035(7)	0.0145(27)
	β_{22}	0.0107(25)	0.0134(65)	0.0176(29)	0.0196(49)
	β_{33}	0.0066(20)	0.0066(20)	0.0016(20)	0.0046(28)
	Site occupancy	1.0	1.0	1.0	1.0
O(3)-(4c)	x	0.0606(8)	0.060(2)	0.0623(7)	0.0601(7)
	z	0.280(1)	0.251(4)	0.259(1)	0.257(1)
	β_{11}	0.0039(8)	0.0056(20)	0.0019(8)	0.0069(18)
	β_{22}	0.0177(26)	0.0289(62)	0.0189(36)	0.0389(41)
	β_{33}	0.0150(33)	0.0615(99)	0.0414(55)	0.0514(65)
	Site occupancy	1.0	1.0	1.0	1.0

Note: a, b, and c are the unit cell parameters; V is the unit cell volume; x, y, and z are the fractional atomic coordinates; B is the isotropic thermal parameter; and β_{11}, β_{22}, and β_{33} are the anisotropic thermal parameters. Atoms at the 4c and 8d positions have the (x, 1/4, z) and (x, y, z) coordinates, respectively.

in the $Li_{3.75}Ge_{0.75}V_{0.25}O_4$ compound and 2.01 and 1.99 Å in the $Li_{3.70}Ge_{0.85}W_{0.15}O_4$ compound. The characteristic Li–O distance in the fourfold coordination varies from 1.99 to 2.04 Å, which agrees well with the experimental data. The coincidence between the theoretical and experimental interatomic distances allows us to make an inference regarding strong cation–oxygen bonding in the tetrahedra, which confirms the formation of a rigid framework in the structure of the studied compounds. On this basis, the formulas of the compounds can be rewritten as $Li_{4-zx}Ge_{1-x}M_xO_4$, where z is the difference between the oxidation states of the element M (in our case, V or W) and germanium. The formulas can also be represented as $Li_{1-zx}[Li_3Ge_{1-x}M_xO_4]$, where the formula in the square brackets corresponds to a rigid framework composed of tetrahedra in a crystal structure of the γ-Li_3PO_4 type. In this structure, the oxygen tetrahedra shared by vertices are closely packed, but, at the same time, sufficiently large octahedral holes are formed between them. Consequently, the Li_{1-zx} ions that are surplus for the structure of the γ-Li_3PO_4 modification occupy these octahedra (Fig. 3), which share faces with each other and with tetrahedra. Two important facts should be noted. First, in the $Li_{3.75}Ge_{0.75}V_{0.25}O_4$ and $Li_{3.70}Ge_{0.85}W_{0.15}O_4$ compounds, the volume of the octahedral holes is relatively large and lithium ions are weakly bound in them. Indeed, the mean experimental Li–O interatomic distances in the octahedral holes are equal to 2.29 and 2.32 Å, respectively. These distances exceed the theoretical Li–O distance (2.135 Å) for the sixfold coordination by more than 0.15 Å. Second, the positions under consideration are only partially occupied (~60%). These facts permit us to draw the inference that, at room temperature, the conduction in the $Li_{3.75}Ge_{0.75}V_{0.25}O_4$ and $Li_{3.70}Ge_{0.85}W_{0.15}O_4$ compounds is predominantly provided by weakly bound lithium ions in octahedra. It can be seen from Fig. 3 that, in the structure, the planes of lithium atoms in octahedra of two types alternate along the **a** axis. Most likely, the conduction occurs along these planes, even though it is quite possible that lithium ions can execute hoppings between the planes. The conductivity of the $Li_{3.75}Ge_{0.75}V_{0.25}O_4$ and $Li_{3.70}Ge_{0.85}W_{0.15}O_4$ compounds at room temperature is not very high, because the size of the cavities between oxygen ions, which separate two adjacent octahedra, is slightly less than the radius of lithium ions; hence, lithium ions should overcome the potential barrier between them. The potential barrier height for the $Li_{3.70}Ge_{0.85}W_{0.15}O_4$ compound is somewhat lower, since the size of tungsten ions is larger than that of vanadium ions. This results in an increase in the unit cell volume and, correspondingly, in the size of cavities that provide hopping of lithium ions. That is why the lithium cationic conductivity of the $Li_{3.70}Ge_{0.85}W_{0.15}O_4$ compound at room temperature is higher than that of the $Li_{3.75}Ge_{0.75}V_{0.25}O_4$ compound [2, 3]. It seems likely that lithium ions rigidly bound in tetrahedra are not involved in the conduction at room temperature.

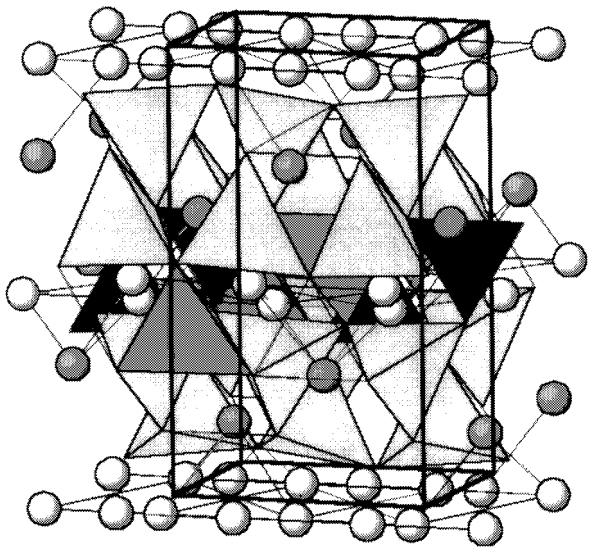

Fig. 3. Crystal lattice of the $Li_{3.75}Ge_{0.75}V_{0.25}O_4$ and $Li_{3.70}Ge_{0.85}W_{0.15}O_4$ compounds. Oxygen atoms occupy vertices of the tetrahedra. Dark oxygen tetrahedra are centered at germanium (vanadium or tungsten) atoms. Dark gray and light gray oxygen tetrahedra are centered at lithium ions in the Li(1) and Li(2) positions, respectively. Spheres are lithium ions in the octahedral positions Li(3) and Li(4).

As the temperature increases, the $Li_{3.75}Ge_{0.75}V_{0.25}O_4$ and $Li_{3.70}Ge_{0.85}W_{0.15}O_4$ compounds transform into the superionic state characterized by high conductivity. Let us consider the changes in the crystal structure upon transition to the superionic state. As can be seen from the data presented in Table 1, this transition is accompanied by a considerable increase in the unit cell volume, a redistribution of lithium ions over octahedra, and an increase in the amplitudes of thermal atomic vibrations. As was noted above, the degeneracy of lithium positions in tetrahedra is removed. Moreover, their vibrational amplitudes increase. The above changes lead to an increase in the interatomic distances in the lattice. In turn, this implies that an increase in the temperature is attended by an increase in the size of cavities between octahedra and tetrahedra. According to the calculations from the obtained structural parameters, the radius of cavities at a temperature of ≈850 K increases to ≈0.67–0.69 Å. This radius is larger than the typical lithium radii in tetrahedra (≈ 0.59 Å) and octahedra (≈0.64 Å). Furthermore, this radius can increase owing to thermal atomic vibrations whose mean amplitude exceeds 0.2 Å at the given temperature. Therefore, it can be stated that, in the superionic state, lithium ions rather easily migrate over the lattice and lithium ions of tetrahedra are also involved in the migration. It is reasonable that the aforementioned changes result in a substantial decrease in the height of the potential barrier (separating the occupied lithium site from an empty

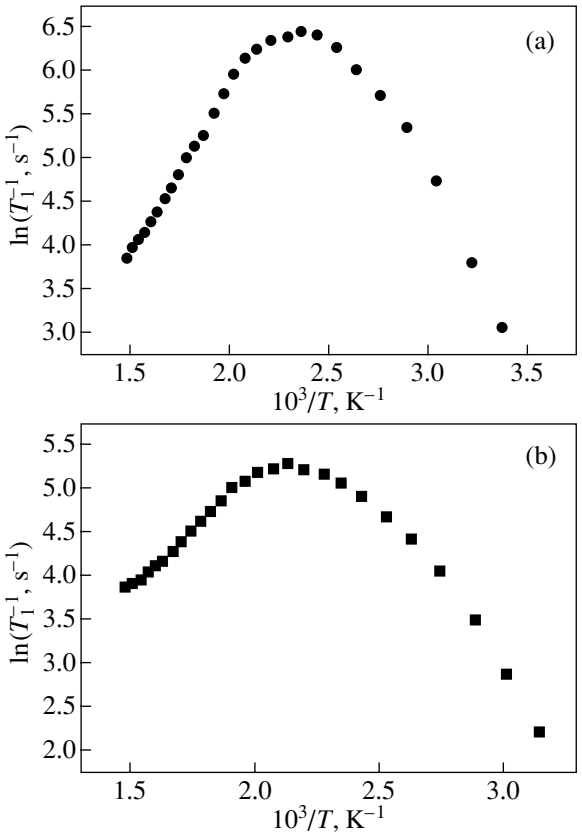

Fig. 4. Temperature dependences of the relaxation times for ^{7}Li nuclei in (a) $Li_{3.75}Ge_{0.75}V_{0.25}O_4$ and (b) $Li_{3.70}Ge_{0.85}W_{0.15}O_4$ compounds.

site) and, hence, in a decrease in the activation energy. This is in good agreement with the available data on the conductivity of the studied compounds [2, 3]. The temperature dependences of the conductivity for these solid solutions in the Arrhenius coordinates are characterized by high-temperature and low-temperature portions. Note that the activation energy for conduction at high temperatures is less than that at low temperatures. Moreover, the structural data allow understanding of the difference between the conductivities of the $Li_{3.75}Ge_{0.75}V_{0.25}O_4$ and $Li_{3.70}Ge_{0.85}W_{0.15}O_4$ compounds in the superionic state. The conductivity is determined by the mobility of charge carriers, on the one hand, and by their concentration, on the other. At low temperatures, the conductivity of the given compounds is governed primarily by the lithium cation mobility associated with the geometric factor. An increase in the temperature leads to a change in the contributions to the conductivity. In this case, the contribution of the carrier concentration increases and the conductivities of both compounds become equal to each other at a certain temperature. With a further increase in the temperature, the conductivity is predominantly determined by the carrier concentration, which is higher in the $Li_{3.75}Ge_{0.75}V_{0.25}O_4$ compound.

The above inferences were supported by the high-temperature NMR data for the studied compounds. The NMR spectra of both compounds at room temperature consist of a broad line (as an example, Fig. 2a shows the NMR spectrum of the $Li_{3.75}Ge_{0.75}V_{0.25}O_4$ compound). The shape of this line is intermediate between Gaussian and Lorentzian (although it is closer to a Lorentzian shape). This line shape suggests that, even at room temperature, lithium ions execute hoppings between the nearest empty sites in the lattice. This inference is confirmed by the results obtained by Burmakin and Lakhtin [15], who studied Li_4GeO_4–Li_2WO_4 solid solutions containing 10 and 20 mol % Li_2WO_4 by stationary NMR spectroscopy. Therefore, the $Li_{3.75}Ge_{0.75}V_{0.25}O_4$ and $Li_{3.70}Ge_{0.85}W_{0.15}O_4$ compounds possess lithium cationic conductivity at room temperature.

As was already mentioned, upon heating of the $Li_{3.75}Ge_{0.75}V_{0.25}O_4$ and $Li_{3.70}Ge_{0.85}W_{0.15}O_4$ compounds above room temperature, the lines in the spectra rapidly become increasingly narrow. An increase in the temperature to ≈480 K leads to the appearance of a narrow central line and satellites in the ^{7}Li NMR spectra (Fig. 2b). Since the satellites in the NMR spectrum of the $Li_{3.75}Ge_{0.75}V_{0.25}O_4$ compound are clearly defined as compared to those in the spectrum of the $Li_{3.70}Ge_{0.85}W_{0.15}O_4$ compound, the spectrum of the former compound is depicted in Fig. 2b. The satellites indicate a dynamic inhomogeneity of lithium cations, i.e., the coexistence of several nonequivalent lithium positions in the lattice. Judging from the number of satellites, the lithium ions can occupy four nonequivalent positions in the lattice, which is in complete agreement with the neutron diffraction data. The satellites are associated with the quadrupole interaction of ^{7}Li nuclei (with spin $I = 3/2$) in four nonequivalent positions. The quadrupole interaction constants are equal to 11, 17, 26, and 30 kHz. An increase in the temperature above 560 K results in a further narrowing of the central lines for both samples, a decrease in the intensity of the satellites, and their smearing (Fig. 2c). This behavior can be explained by the participation of all lithium ions in the diffusion motion. In neutron diffraction experiments, this manifests itself in a substantial increase in the amplitudes of atomic vibrations.

Analysis of the NMR data makes it possible to evaluate the activation energy for migration of lithium atoms and its temperature dependence. The recovery of ^{7}Li nuclear magnetization after saturation at temperatures below 500 K can be described by two exponential functions corresponding to strongly and weakly bound lithium ions in the lattice. By separating the rapidly relaxing component of the ^{7}Li nuclear magnetization, we calculated the temperature dependences of the spin–lattice relaxation time (Figs. 4a, 4b). These dependences exhibit a behavior typical of the translational diffusion of ions. At the maxima, the following relationship should be satisfied: $\omega\tau \approx 1$, where $\omega = 2\pi \times 27 \times 10^6$ rad s^{-1} and

Table 2. Activation energies E for migration of Li^+ cations according to the NMR data and the results of measurements of the electrical conductivity σ [2, 3] in the low-temperature (LT) and high-temperature (HT) ranges of the dependence of $\ln(1/T_1)$ on $1/T$

Compound	E, eV			
	from NMR data		from experimental data on the electrical conductivity σ	
	LT	HT	LT	HT
$Li_{3.75}Ge_{0.75}V_{0.25}O_4$	0.420 ± 0.014	0.311 ± 0.007	0.540 ± 0.010	0.340 ± 0.010
$Li_{3.70}Ge_{0.85}W_{0.15}O_4$	0.401 ± 0.007	0.182 ± 0.009	0.415 ± 0.010	0.235 ± 0.010

$1/\tau$ is the frequency of lithium ion hoppings (s^{-1}). Let us assume that the second moment M_2 of the resonance line at low temperatures is determined by the quadrupole interaction of the quadrupole moment of the ^7Li nucleus with an electric-field gradient at the nucleus in the lattice and that the narrowing of the resonance line and the change in the relaxation time T_1 are governed by the translational diffusion associated with the hoppings of lithium ions over equilibrium positions at the frequency $1/\tau$. In this case, according to [16], the spin–lattice relaxation rate can be determined by the expression

$$1/T_1 \sim M_2\tau/(1 + \omega^2\tau^2). \quad (1)$$

The hopping frequency is associated with the thermal excitations and can be represented by the Arrhenius relationship

$$\tau = \tau_0 \exp[E/kT]. \quad (2)$$

From these formulas, we can estimate the activation energy E for migration of lithium atoms. The results obtained are presented in Table 2. For comparison, the activation energies calculated from the data on the electrical conductivity [2, 3] are also given in this table. It can be seen that the activation energies determined from the high-temperature and low-temperature linear portions of the dependences of the relaxation rate on the reciprocal of the temperature differ significantly. The activation energy for ion migration at low temperatures exceeds the activation energy at high temperatures (Table 2), which is consistent with the inference drawn from the structural data. This circumstance and the smeared maxima of the above dependences indicate that the activation energy for migration is characterized by a distribution due to the nonequivalence of lithium positions in the structure.

The activation energies calculated from the temperature dependences of the electrical conductivity are higher than those determined from the NMR data. This ratio is rather frequently observed [17] and, as a rule, is explained by the fact that all ion hoppings (including local hoppings which do not contribute to the conductivity) can be revealed by the NMR method, whereas the activation energy determined from the electrical conductivity is associated with the translational motion of particles over large distances.

5. CONCLUSIONS

Thus, the $Li_{3.75}Ge_{0.75}V_{0.25}O_4$ and $Li_{3.70}Ge_{0.85}W_{0.15}O_4$ compounds were studied using neutron diffraction and nuclear magnetic resonance spectroscopy. The main results can be summarized as follows:

(1) In the crystal lattice, lithium cations occupy four nonequivalent positions and form either strong bonds in the tetrahedra or weak bonds in the octahedra.

(2) The electrical conduction of the studied compounds at room temperature is provided by weakly bound lithium cations at octahedral partially occupied sites.

(3) The electrical conductivity is determined by geometric factors, specifically by the size of cavities between the octahedra.

(4) The cavity size and, consequently, the electrical conductivity in the $Li_{3.70}Ge_{0.85}W_{0.15}O_4$ compound exceed the corresponding quantities in the $Li_{3.75}Ge_{0.75}V_{0.25}O_4$ compound.

(5) The geometric factor is responsible for the formation of the superionic state.

(6) In the superionic state, all the lithium cations located in octahedra and tetrahedra are involved in charge transfer. This is explained by the thermal expansion of the lattice and, hence, by the increase in the cavity size, which, in the superionic state, becomes larger than the radius of lithium cations.

(7) In the superionic state, the electrical conductivity is governed primarily by the charge carrier concentration. The carrier concentration in the $Li_{3.75}Ge_{0.75}V_{0.25}O_4$ compound is higher than that in the $Li_{3.70}Ge_{0.85}W_{0.15}O_4$ compound.

ACKNOWLEDGMENTS

This work was supported by the Russian Foundation for Basic Research (project no. 02-02-16406) and the State Scientific and Technical Program “Topical Directions in the Physics of Condensed Matter” (State Contract no. 40.012.1.1.11.50).

REFERENCES

1. E. I. Burmakin, *Solid Electrolytes with Alkali Cationic Conductivity* (Nauka, Moscow, 1992).
2. E. I. Burmakin, V. N. Alikin, and G. K. Stepanov, Neorg. Mater. **20**, 296 (1984).
3. E. I. Burmakin and V. N. Alikin, Élektrokhimiya **23**, 1124 (1987).
4. B. N. Goshchitskii and A. Z. Menshikov, Neutron News **7**, 12 (1996).
5. H. M. Rietveld, J. Appl. Crystallogr. **2**, 65 (1969).
6. J. Rodriges-Carvajal, Physica B (Amsterdam) **192**, 155 (1993).
7. E. I. Burmakin, G. K. Stepanov, and S. V. Zhidovinova, Élektrokhimiya **18**, 649 (1982).
8. J. Zemann, Acta Crystallogr. **13**, 863 (1960).
9. I. Abrahams and P. G. Bruce, Acta Crystallogr. B **47**, 696 (1991).
10. P. G. Bruce, I. Abrahams, and A. R. West, Solid State Ionics **40/41**, 293 (1990).
11. R. D. Shannon and C. T. Prewitt, Acta Crystallogr. B **25**, 925 (1969).
12. I. D. Brown and R. D. Shannon, Acta Crystallogr. A **29**, 266 (1973).
13. I. D. Brown and D. Aldermatt, Acta Crystallogr. B **41**, 244 (1985).
14. R. D. Shannon, Acta Crystallogr. A **32**, 751 (1976).
15. E. I. Burmakin and A. A. Lakhtin, Neorg. Mater. **27**, 837 (1991).
16. A. Abragam, *The Principles of Nuclear Magnetism* (Clarendon, Oxford, 1961; Inostrannaya Literatura, Moscow, 1963).
17. V. A. Vopilov, V. M. Buznik, and E. I. Burmakin, *Nuclear Magnetic Relaxation and Dynamics of Spin Systems* (Inst. Fiz. Akad. Nauk SSSR, Krasnoyarsk, 1983).

Translated by O. Borovik-Romanova

Physics of the Solid State, Vol. 45, No. 8, 2003, pp. 1557–1565. Translated from Fizika Tverdogo Tela, Vol. 45, No. 8, 2003, pp. 1482–1490.

LATTICE DYNAMICS AND PHASE TRANSITIONS

Inhomogeneous Microscopic Shear Strains in a Complex Crystal Lattice Subjected to Large Macroscopic Strains (Exact Solutions)

É. L. Aéro

Institute of Problems of Machine Science, Russian Academy of Sciences,
Vasil'evskiĭ ostrov, Bol'shoĭ pr. 61, St. Petersburg, 199178 Russia
e-mail: aero@microm.ipme.ru

Received January 17, 2003

Abstract—Nonlinear theory of microscopic and macroscopic strains is developed for the case of large inhomogeneous relative displacements of two sublattices making up a complex crystal lattice; in this case, in addition to an acoustic mode, a pseudooptical, strongly nonlinear mode is excited. The equation of relative motion of the sublattices can be solved exactly for the specific case of a centrosymmetric crystal. The corresponding equilibrium equation is the sine-Helmholtz equation and has a doubly periodic solution. This solution describes fragmentation of the lattice, more specifically, the appearance of a domain superstructure with large periods, whose building blocks contain oppositely sensed rotons separated by topological defects that are opposite in sign. Purely elastic microscopic strains are followed by elastoplastic ones. Both types of strain arise as a result of bifurcation, which causes a change from the initially homogeneous strain field to an inhomogeneous one. The domain sizes take on optimal values when the external homogeneous macroscopic strains reach a certain threshold magnitude. © *2003 MAIK "Nauka/Interperiodica".*

1. INTRODUCTION

Considerable recent attention has been focused on the problem of structural and phase transformations occurring in the presence of stress and strain fields. Earlier attempts to solve this problem within the complex-lattice model by introducing internal degrees of freedom have shown that the linear theory can predict new effects. However, this approach is inefficient, because small changes in the internal structure are merely a direct consequence of variations in the macroscopic geometry of the crystal lattice and give rise only to renormalization of the material constants; that is, the complex-structure model reduces, in essence, to the simple-structure model [1, 2]. The main new effects revealed are as follows: the appearance of new optical vibrational modes, spatial and time dispersion of elastic properties, and the related effects in statics. No radical structural changes have been revealed within the linear theory.

In this paper, we deal with strongly nonlinear optical vibrations and show that radical changes in the crystal structure (local topology) can occur. Among these changes are polymorphic transformations, bifurcations, the formation of defects, bond switching, and changes in short-range and long-range order.

For the sake of simplicity, we consider the case of two sublattices. In terms of the linear theory of crystal lattices [3, 4], we can write two equations of motion (for acoustic and optical modes, respectively):

$$\rho\ddot{U}_i = c_{ikj}u_{k,j} + \lambda_{ikjm}U_{k,jm} + O_1, \quad (1)$$

$$\mu\ddot{u}_i = -c_{kij}U_{k,j} - \hat{c}_{kij}u_{k,j} - p_{ik}u_k + k_{ikjm}u_{k,jm} + O_2. \quad (2)$$

Here, a dot indicates differentiation with respect to time and a comma among tensor indices indicates differentiation with respect to the corresponding spatial coordinates. A repeated subscript in a term implies that the term is summed over the values of the repeated index. In Eqs. (1) and (2), U_i is the displacement vector of the center of mass of a unit cell (the motif of the complex lattice) and u_i is the (reduced) relative displacement vector of the two atoms in each unit cell. The latter displacement is measured in units of the Bravais lattice (sublattice) period; therefore, if $|u_i| = 1$, the relative sublattice displacement is equal to one period. The quantity ρ is the atomic mass density and μ is the reduced mass density of two atoms in a unit cell. The terms O_1 and O_2 include higher derivatives with respect to the space coordinates; these terms are neglected in the long-wavelength approximation.

The elastic-constant tensors have the following symmetry properties: $p_{ij} = p_{ji}$ and $\hat{c}_{ikj} = -\hat{c}_{kij}$. The fourth-rank tensors k_{ikjm} and λ_{ikjm} are symmetric under permutations of indices in pairs (without permutation of the pairs) only in the case of pair (central) interactions. We note that, in the continuum elasticity theory, these tensors are also symmetric under a permutation of pairs of indices. The symmetry under permutations of indices in pairs is absent in the case of many-particle (noncentral) interactions.

First, we consider Eqs. (1) and (2). The first terms in the right-hand sides (with coefficients c_{kij} and $\hat{c}_{kij}$) are cross terms, which are responsible for local interaction among different modes and are nonzero only in the case

1063-7834/03/4508-1557$24.00

of noncentrosymmetric crystals (because the corresponding tensors are of odd rank). Higher order cross terms are included in the terms O_1 and O_2.

If we neglect the term O_1 with higher derivatives, Eq. (1) for acoustic modes reduces to a macroscopic equation for vibrations of a dispersionless elastic continuum. In general, higher order derivatives with respect to spatial coordinates allow for long-range forces and the gradients of macroscopic displacements $U_{i,k}$ characterize changes in the size and shape of the entire body (its external geometry).

In Eq. (2), the third term in the right-hand side does not involve a derivative and describes the interaction between neighboring atoms in a unit cell, i.e., the interaction between the sublattices. The displacement vector u_i in this term represents a change in the short-range order in the lattice, i.e., a change in the internal geometry (structure) of the medium.

2. BASIC RELATIONS

In order to describe large changes in the internal structure in terms of the internal degrees of freedom u_i, we generalize Eq. (2) in the following way. If the relative sublattice displacements u_i are large, the linear term should be replaced by a nonlinear odd vector function $P_i(u_j) = -P_i(-u_j)$. Since the complex lattice possesses translation symmetry, this function must be periodic and its period must be equal to the period b of the Bravais lattice along the direction of the corresponding displacement.

Thus, Eqs. (1) and (2) are replaced by the equations

$$\rho\ddot{U}_i = c_{ikj}u_{k,j} + \lambda_{ikjm}U_{k,jm} + O_1, \tag{3}$$

$$\mu\ddot{u}_i = -c_{kij}U_{k,j} - \hat{c}_{kij}u_{k,j} - P_i(u_j) + k_{ikjm}u_{k,jm} + O_2. \tag{4}$$

Here, the terms O_1 and O_2 have the same meaning as in the linear equations. Since the displacement u_j is measured in units of the Bravais lattice period (along the corresponding direction), the periods of the nonlinear function are integers. In particular, if $P_i \longrightarrow \sin(2\pi u)$, then, in the case of $u = |u_j| = 1$, the sublattices occupy a new, but crystallographically equivalent (nearest) position; therefore, the displacement u is defined to within an integer. For such displacements, the atomic bonds are switched and the nearest neighbors of each atom are changed; i.e., a change in the internal structure occurs. These effects will not take place if the displacements are not very large, $u < 1/2$. In this paper, we consider significantly nonlinear effects ($u \geq 1/2$).

A periodic vector function can be written as $P_i \equiv \partial d/\partial u_i$, where $d(u_j)$ is a periodic scalar function (invariant under symmetry transformations of the coordinates). In the case under study, this function is the energy of the rigidly translated sublattices relative to each other. An expression for this energy is given in the next section.

In this paper, we restrict our consideration to the simplest case of a centrosymmetric crystal, for which

$$\begin{aligned} c_{ikj} = \hat{c}_{kij} = 0, \quad u_i = (0, u, 0), \\ u = u(x, y), \quad P_i(u_j) \longrightarrow p\sin(2\pi u). \end{aligned} \tag{5}$$

It is clear that, in this case, we consider only low-frequency vibrations of the crystal and neglect high-frequency vibrations: the displacements (directed along the y axis) are time-independent. Further, for crystals with symmetry higher than monoclinic and triclinic, we have

$$k_{ikjm}u_{k,jm} \longrightarrow k_1\frac{\partial^2 u}{\partial x^2} + k_2\frac{\partial^2 u}{\partial y^2}. \tag{6}$$

This differential operator does not involve mixed derivatives, which is due to the high symmetry of the crystal lattice under study and to the fact that the vector u_i is assumed to have only one component.

Thus, we will consider the following two independent equations in the long-wavelength approximation:

$$\rho\ddot{U}_i = \lambda_{ikjm}U_{k,jm}, \tag{7}$$

$$0 = -p\sin(2\pi u) + k_1\frac{\partial^2 u}{\partial x^2} + k_2\frac{\partial^2 u}{\partial y^2}. \tag{8}$$

These equations do not contain cross terms; therefore, there is no local interaction between different deformation modes in the long-wavelength approximation (in centrosymmetric crystals). Theoretically, such interaction will arise if we include higher derivatives (nonlocal terms O_1, O_2), thereby allowing for finite characteristic length scales.

The inclusion of higher derivatives makes solution of these equations very complicated. For this reason, we develop a phenomenological theory in which the interaction between different modes arises as a result of spatial averaging on a mesoscopic scale (see Section 6).

3. MICROSCOPIC STRAINS ASSOCIATED WITH A RELATIVE DISPLACEMENT OF THE SUBLATTICES

First, we consider Eq. (8). This equation can be derived by minimizing the energy functional

$$2E = \int_{-H}^{H}\int_{-2B}^{2B}\left[k_1\left(\frac{\partial u}{\partial x}\right)^2 + k_2\left(\frac{\partial u}{\partial y}\right)^2 + 2p(1-\cos 2\pi u)\right]dxdy. \tag{9}$$

The limits of integration will be discussed later. The parameters k_1 and k_2 will be referred to as the shear and extension microscopic moduli, respectively. It should be noted that the dimensions of these moduli are different from those of the respective macroscopic moduli,

because atomic displacements are measured in units of the lattice period b. The (positive) parameter p is the amplitude of the periodic interaction potential between chains (sublattices) and, on the other hand, the maximum interaction force between the sublattices. The dimensions of this parameter are identical to those of the volume energy density.

The energy functional in Eq. (9) can be used to describe cubic, hexagonal, rhombohedral, tetragonal, and orthorhombic crystals in the case where the displacement vector has only one nonzero component, $u_i \longrightarrow (0, u_y, 0)$. Since the microscopic moduli k_1 and k_2 are not equal, the model at hand includes anisotropy.

The third, periodic term in Eq. (9) is the interaction energy d of the rigidly displaced atomic chains (sublattices) in the long-wavelength approximation, while the first two terms are the energies associated with elastic shear and tensional strains of the sublattices, respectively. Therefore, the model allows for inhomogeneous microscopic strains. Since the cosine is a periodic function, the energy functional in Eq. (9) is invariant under a relative displacement of the sublattices by an integral number of the lattice period ($u = n$). Therefore, solutions to Eq. (8) are determined to within an additive integer n.

4. LATTICE FRAGMENTATION

Equation (8) has no uniform solutions other than trivial ones (zero or integer solutions, corresponding to the case where the sublattices are displaced to crystallographically equivalent positions). Among nonuniform solutions, doubly periodic solutions are of special interest, because they are characterized by a finite scale of inhomogeneities.

The nonlinear equation (8), known as the sine-Helmholtz equation, has two length scales characterizing the coherence of the sublattice match:

$$l_1 = \sqrt{\frac{k_1}{p}}, \quad l_2 = \sqrt{\frac{k_2}{p}}. \tag{10}$$

These lengths determine the mesoscopic length scales on which the sublattices remain coherent (or, more precisely, congruent); i.e., they can be made to coincide with each other by rigidly displacing them, in spite of the presence of microscopic inhomogeneities. These length scales characterize the microscopic strain field, unlike the macroscopic one, which has no characteristic length. Formally, if $l_1 \longrightarrow 0$, we arrive at the Frenkel–Kontorova one-dimensional model, i.e., to an atomic chain located on a rigid periodic substrate.

In analyzing a solution to Eq. (8), we associate the excitation of the pseudooptical mode with possible fragmentation of the lattice, i.e., with microscopic rotations in individual blocks (half-domains). These rotations reduce, on the average, to pure shear strains if the average rotation angle is zero (Fig. 1). Clearly, the corresponding particular solution must be doubly periodic.

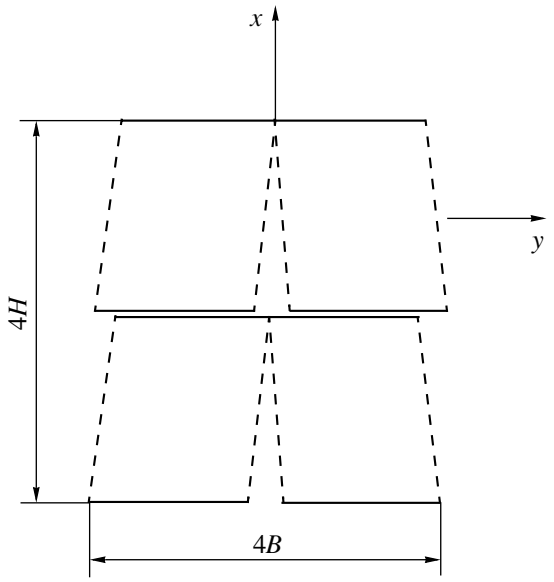

Fig. 1. Two pairs of domains separated by horizontal slip planes. Dashed lines indicate somewhat arbitrary boundaries.

Let us consider the case of critical atomic displacements, which is formally defined by the following conditions imposed on the atomic displacements at parallel equidistant slip lines x = const (which are interfaces between plane-parallel horizontal layers of thickness $2H$) and at the transverse boundaries y = const of building blocks: the relative atomic displacements at the interfaces of layers are equal (in magnitude) to the lattice period. In the interior of a layer, these displacements are smaller, $u \leq 1$. The displacements vary periodically and reverse sign in going from one half-domain ($2B$ wide) to the next; therefore, we have

$$\begin{aligned} u(H, y) &= -1, \quad u(0, y) = 0, \\ u(-H, y) &= +1, \quad (0 < y < 2B), \\ u(H, y) &= +1, \quad u(0, y) = 0, \\ u(-H, y) &= -1 \quad (-2B < y < 0). \end{aligned} \tag{11}$$

These conditions are repeated periodically along the x axis with period $2H$ and along the y axis with period $4B$.

In the interior of a layer, we have $u < 1$. In the regions where $u < 1/2$ (the interatomic potential barriers are not overcome), purely elastic microscopic strains arise; the elastic energy of domains is accumulated in these regions and then dissipated in the regions of plastic strains. On the whole, elastoplastic microscopic strains develop, which leads to the establishment of optimal strains in the lattice subjected initially to large homogeneous macroscopic deformations. The latter deformations will be discussed in Section 6.

We look for a solution to Eq. (8), subjected to these boundary conditions, by using the Lamb method of separation of variables [5, 6] and finally arrive at the expression

$$\tan(\pi u/2) = \pm\frac{\mathrm{tn}(xK_1/H)}{A\,\mathrm{sn}(yK_2/B)},$$
$$A^{-2} = a^2 = \frac{\sqrt{1-\nu_1^2}}{\nu_2}. \quad (12)$$

Here, the quantity a is considered formally as the amplitude of microscopic strains. The plus and minus signs in Eq. (12) correspond to two equivalent directions of atomic displacements; $2H$ and $4B$ are the periods of the elliptic tangent (tn) and elliptic sine (sn), respectively, in the right-hand side of Eq. (12). The quantities K_1 and K_2 are complete elliptic integrals of the first kind, and quantities ν_1 and ν_2 are the moduli of these elliptic integrals [7]. The values of these moduli lie in the range from zero to unity.

Thus, the elliptic integrals K_1 and K_2 determine the spatial frequencies (gradients) of microscopic strains; the quantities $1/H$ and $1/B$ determine the average frequencies. The spatial frequencies of the elliptic functions become very large when the values of the moduli approach unity. Using the relations $\mathrm{tn}0 = 0$ and $\mathrm{tn}K \longrightarrow \infty$ [7], it is easy to verify that solution (12) meets the boundary conditions (11). Clearly, the solution is periodic along the y and x axes with periods $4B$ and $2H$, respectively.

Thus, we found a doubly periodic solution which describes a doubly periodic superstructure arising in the deformed lattice. The initial translation symmetry of the lattice with period b is replaced, in the strained lattice, by the translation symmetry on larger scales, B and H.

In fact, we found the solution in all space. The formally introduced boundaries are internal, rather than external, interfaces arising in the field of large macroscopic stresses or strains.

As for the transverse domain boundaries, they contain vertical rows of Frenkel–Kontorova solitons (misfit dislocations) at $y = (2r + 1)B$ with $r = 0, \pm1, \pm2, \ldots$, where the left-hand side of Eq. (12) tends to infinity. Indeed, let us consider the vicinity of the origin of coordinates where the elliptic tangent and elliptic sine can be replaced by their linear approximations. In this case, Eq. (12) takes the form

$$\tan(\pi u/2) \approx \pm\frac{xk_1}{yk_2} = \pm\frac{k_1}{k_2}\tan\phi. \quad (13)$$

Here, ϕ is the polar angle in the local reference frame. Thus, the field of microscopic strains in the vicinity of the origin is a many-valued function whose value depends on the number of complete circles made around the origin. From Eq. (13), we obtain $\pi u/2 = \pm\arctan(k_1\phi/k_2)$, i.e., a topological defect of the field u with a positive (negative) charge. If the charge is equal to unity (at a certain value of the ratio between the microscopic moduli), we have an edge dislocation. If the charge is equal to a fractional number, we have a partial dislocation. In the case of $k_1 = k_2$, the charge is equal to ±4.

Such charged defects arise at each point that corresponds to a zero of the elliptic tangent ($x = 0, \pm2H, \pm4H, \ldots$) and, simultaneously, to a zero of the elliptic sine ($0, 2B, 4B, \ldots$). The signs of the charges alternate along horizontal layers but remain the same along vertical lines.

The defects are associated with fragmentation of the lattice, i.e., with slip in opposite directions (on finite sections of length $2B$) by the amount $|u| = 1$. Fragments are rotons (solid vortices), more exactly, pairs of vortices of opposite sign which alternate along the horizontal axis in accordance with the boundary conditions. Vortices of like sign are located along the vertical axis. Therefore, the crystal exhibits a texture having a herring-bone pattern (Fig. 1). At the sites of this superlattice, the field u undergoes discontinuities, which are Frenkel–Kontorova misfit solitons.

Thus, the theory presented here predicts the formation of defects in an initially perfect lattice and fragmentation of the lattice. The theory involves elliptic functions which become discontinuous in the limit as $\nu_1, \nu_2 \longrightarrow 1$. Although this limit is unattainable in practice, the spatial changes are sharp enough to be treated as discontinuities on a macroscopic scale.

5. LOCAL STABILITY OF MICROSCOPIC STRAINS

The periods of the superstructure cannot take on arbitrary values; they depend on the properties of the lattice and gradients of the microscopic strains, as well as on the macroscopic strains, which can be treated as an external field. The restrictions imposed on the periods follow from the dispersion relations, which can be derived by substituting Eq. (12) into Eq. (8). After straightforward algebra, we obtain

$$\left(\frac{k_1q_1^2}{A^2} + k_2q_2^2\right)S - 2p = 0,$$
$$S = (A^2 - 1)\left(1 - \frac{\nu_2^2}{A^2}\right), \quad (14)$$

$$k_1q_1^2 = A^2k_2q_2^2, \quad q_1 = \frac{K_1}{H}, \quad q_2 = \frac{K_2}{B}, \quad p \geq 0. \quad (15)$$

These equations relate the spatial frequencies q_1 and q_2 (gradients of microscopic strains) to the properties of the lattice, domain sizes, and the amplitude $a = 1/A$,

thereby determining the region of existence of the solution.

Since the parameter p is positive, it follows from Eq. (14) that $A > 1$, which is a criterion for elastoplastic shear strains.

Further restrictions can be found by eliminating the moduli ν_1 and ν_2 between Eqs. (14) and (15). Since the parameter A is a function of these moduli, according to Eq. (12), we express, e.g., ν_1 in terms of A and ν_2. At a fixed value of A, Eqs. (14) and (15) become relations between the variables B and H and the parameter ν_2. Eliminating this parameter between these equations, we obtain a relation between B and H at a given value of A.

The relation between A, B, and H can be represented by a family of curves plotted in the H–B plane for different values of A. In this case, each curve has a vertical ($B = B_t$) and a horizontal asymptote ($H = H_t$), so that

$$H < H_t < \infty, \quad B \longrightarrow B_t (B < \infty). \tag{16}$$

The values of these limits are

$$H_t = l_1(1 - A^{-2})K_{11}, \quad 2B_t = \pi l_2 \sqrt{A^2 - 1}. \tag{17}$$

Here, K_{11} is $K_1(\nu_1)$ for $\nu_1 = \sqrt{1 - A^{-4}}$. Clearly, the parameters H and B cannot take on arbitrary values. Restrictions on these parameters follow from Eqs. (16) and (17).

Let us discuss the stability of elastoplastic microscopic strains. Equation (8) determines the local minimum of energy functional (9) for fixed values of the limits of integration. Therefore, solution (12) is locally stable. However, in order to investigate the stability of the superstructure as a whole (against variations in parameters B, H), we should consider the extrema of the function $E(B, H)/8BH$, which is done in the next section for the case where the lattice is subject to macroscopic strains.

The case of purely elastic microscopic strains $u \leq 1/2$ was considered in [6]. In this case, we have $A < 1$ and the corresponding field $u_+(x, y)$ is shifted by 1/2; i.e.,

$$2u_+(x, y) = 2u(x, y) \mp 1. \tag{18}$$

The function $u(x, y)$ is the same as in Eq. (12). Due to this shift, boundary conditions (11) change in such a way that the amount of slip at the horizontal domain boundaries becomes twice as small and equal to one-half the interatomic distance; that is, atoms are located at the tops of the corresponding interatomic potential barriers. A more detailed analysis is made in [6].

By definition, the elastic solution is locally stable. However, the corresponding domain structure as a whole can be stable (as in the case of elastoplastic strains) only in the presence of external fields (see next section).

6. GLOBAL STABILITY IN AN EXTERNAL FIELD

The superstructure should be additionally optimized with respect to the parameters B and H, because, in the approximation used, the acoustic mode (macroscopic strains) is locally independent of the pseudooptical mode. In Eqs. (7) and (8), cross terms arise only if nonlocal terms O_1 and O_2 (containing higher derivatives) are included. Therefore, the interaction between these modes is "accumulated" in space and can be included through averaging over a spatial region. The averaged microscopic and macroscopic strains can be related to each other by using the condition of global stability of the superstructure or by minimizing the total energy at the cost of a decrease in the energy of homogeneous elastic strains through the formation of defects and lattice fragmentation.

In principle, this approach can be refined using a perturbation procedure; more specifically, we can retain cross terms (depending on the microscopic strains) in Eq. (7) for macroscopic strains and substitute solution (12) into these terms. In this case, the macroscopic strain field will contain additional terms, some of which will be singular because solution (12) is singular, as shown in Section 4. The refined macroscopic strain field will become inhomogeneous due to defects. We will focus on this subject in future investigations.

In analyzing the energy balance in the framework of the mesoscopic theory, it suffices to average the fields over domains. In this case, however, we must take into account that after averaging, a pair of half-domains with rotons of opposite sign becomes a domain without a vortex; therefore, the macroscopic strain field in the crystal in this case is a vortexless, purely shearing strain field. The interaction between different modes at the mesoscopic level can be included phenomenologically by neglecting the details of the macroscopic-field pattern within domains. Therefore, the only parameters of the superstructure are the domain sizes, which take on their optimal, equilibrium values. Below, we describe a phenomenological method for solving this problem.

Let us analyze the effect of macroscopic pure shearing strains ($\mathrm{curl} U = 0$) on the microscopic elastic and elastoplastic strains under the assumption that the macroscopic field is independent of the microscopic strains and can be found by solving Eq. (7). In this approximation, the macroscopic strains are treated as constants, which is consistent with the assumption that the superstructure is spatially uniform. In this case, there is no need to analyze Eq. (7).

Let us consider the total energy with inclusion of macroscopic strains and of interaction between modes (on the mesoscopic level). The averaged (over the volume of a domain) dimensionless total energy density is the sum of the macroscopic energy, a cross term (responsible for the interaction between modes), and the microscopic energy:

$$2\check{D} = \eta_1 \varepsilon_1^2 + \eta_1 \varepsilon_2^2 + 2\eta_2 \varepsilon_1 \varepsilon_2 - 2L + 2D, \tag{19}$$

$$D = \frac{E}{8pBH}, \quad \eta_1 = \frac{\lambda_1}{p}, \quad \eta_2 = \frac{\lambda_2}{p}, \quad \varepsilon_1 = \frac{\partial U_x}{\partial x}, \quad \varepsilon_2 = \frac{\partial U_y}{\partial y}; \tag{20}$$

the first three terms in Eq. (19) are the macroscopic-strain energy written for rhombohedral, tetragonal, hexagonal, or cubic crystals and D is the microscopic dimensionless energy density given by Eq. (9). It is important that, in the mesoscopic theory, the total energy can be calculated and analyzed as a function of the domain sizes and material parameters (correlation lengths) l_1 and l_2 alone.

The cross term L in the total energy can be written as a linear function of the average microscopic strains, because the macroscopic strains are homogeneous and do not include defects in the approximation used here.

However, it should be noted that the averaged (over a domain) microscopic strain is zero, whereas the microscopic strain averaged over a half-domain is nonzero and changes sign in going from one half-domain to the next along the y axis; this result is valid for both the cases $A < 1$ and $A > 1$. In other words, two adjacent half-domains are twins that differ in the sense of rotation (Fig. 1). This microscopic structure is consistent with the vortexless character of the macroscopic strain field assumed above.

Since the sum of the average microscopic strains (rotations) in the whole domain is zero, this quantity cannot be used as a thermodynamic variable, as is the case with the ferroelectric and the ferromagnet. In the phenomenological theory, an appropriate thermodynamic average is the difference of microscopic strains of two half-domains; this quantity is defined to within the sign.

Thus, as the thermodynamic variable, we take the average value of the microscopic gradient, which is characterized by the quantity $1/H$, or, in the dimensionless form, by l_1/H. In this case, the cross term in Eq. (19) for the total energy can be written as

$$L = \chi_1\frac{\varepsilon_1}{\check{H}} + \chi_2\frac{\varepsilon_2}{\check{B}}, \quad \check{H} = \frac{H}{l_1}, \quad \check{B} = \frac{B}{l_2}, \quad \chi_1 > 0, \quad \chi_2 > 0. \tag{21}$$

Here, χ_1 and χ_2 are striction coefficients and are assumed to be positive and $\check{H}$ and $\check{B}$ are dimensionless parameters of the superstructure.

The components of the strain tensor can have any sign. However, a stable superstructure will arise if the term involving L in Eq. (19) is negative. Therefore, we should assume that $\varepsilon_1, \varepsilon_2 > 0$. (There is an analogy with bifurcation that occurs in the case of compression, rather than tension, of a thin rod.) In this case, the interaction between microscopic and macroscopic strains decreases the height of the potential barrier and a minimum in the total energy arises, bringing about the formation of a stable superstructure. Due to the cross term L in Eq. (19), microscopic rotations of opposite sense (Fig. 1) cause the total energy to decrease and to possess a minimum at certain values of the dimensions H and B of the building blocks of a superstructure.

In order to minimize the total energy, we need to calculate the integral in Eq. (9) for the energy of microscopic strains and find the total energy density $\check{D}$ as a function of two variables $\check{H}$ and $\check{B}$ and of two given parameters ε_1 and ε_2.

Let us find the condition of an extremum of the total energy. First, we calculate the partial derivatives of the total energy. Substituting Eq. (21) for L into Eq. (19), we obtain

$$\frac{\partial\check{D}}{\partial(1/\check{H})} = -\chi_1\varepsilon_1 + \acute{D}_H, \quad \frac{\partial\check{D}}{\partial(1/\check{B})} = -\chi_2\varepsilon_2 + \acute{D}_B. \tag{22}$$

Here, the partial derivatives are defined as

$$\acute{D}_H = \frac{\partial D}{\partial(1/\check{H})} \quad (B = \text{const}), \qquad \acute{D}_B = \frac{\partial D}{\partial(1/\check{B})} \quad (H = \text{const}). \tag{23}$$

Equating the derivatives of the total energy in Eq. (22) to zero, we find the necessary conditions for an extremum of this energy:

$$0 = -\chi_1\varepsilon_1 + \acute{D}_H, \quad 0 = -\chi_2\varepsilon_2 + \acute{D}_B. \tag{24}$$

These relations can also be interpreted as conditions under which microscopic strains can occur only in the presence of macroscopic strains without other influences. It should be noted that, in principle, the external control parameters ε_1 and ε_2 can be varied independently of each other. However, their influences on the microstructure must be compatible. Formally, Eqs. (24) are two nonlinear equations for two unknown dimensions of an equilibrium domain.

The stability of the superstructure depends on the behavior of the total energy density (19). In the coordinates $\check{H}$ and $\check{B}$, this energy density is represented by a saddle-shaped surface that exhibits minima with varying $\check{H}$ and maxima with varying $\check{B}$. Each curve with a maximum terminates in certain finite points (one on the left and one on the right of the maximum) at which the energy density is minimum.

The corresponding analytical expression is fairly cumbersome, and we present only plots of derivatives (22); Figs. 2 and 3 show the $\acute{D}_H(1/\check{H})$ and $\acute{D}_B(1/\check{B})$ dependences for fixed values of $\check{B}$ and $\check{H}$, respectively.

The dashed lines in these figures indicate the boundary of the region of purely elastic domains. In Fig. 2,

this region lies on the left of the boundary, and in Fig. 3, on the right. This boundary does not refer to microscopic elastoplastic strains; therefore, there are regions of mixed states (in Fig. 2, this region is on the left of the boundary in question). In these regions, each curve is double: for each value of the parameter $\check{B}$ = const, we plotted two curves, the lower of which (terminating in the boundary) corresponds to purely elastic domains. In Fig. 3, the region of mixed states lies on the right of the boundary in question and the splitting of the curves is small.

It is notable that each curve in Figs. 2 and 3 starts and terminates at a point. Therefore, the dimensions of domains $\check{B}$ and $\check{H}$ cannot be arbitrarily large or arbitrary small. We note that some terminal points lie beyond the limits of Fig. 2.

It is seen that the curves in Fig. 2 are convex downward and, therefore, the second derivative of the total energy density with respect to $1/\check{H}$ is positive, while the curves in Fig. 3 are convex upward and, therefore, the second derivative with respect to $1/\check{B}$ is negative. Thus, we have

$$D_{HH} > 0, \quad D_{HH} = \frac{\partial^2 D}{\partial(1/\check{H})^2},$$
$$D_{BB} < 0, \quad D_{BB} = \frac{\partial^2 D}{\partial(1/\check{B})^2}. \tag{25}$$

These results allow us to estimate the derivatives of the total energy in Eqs. (22) and make a conclusion as to the character of its extrema. It follows from Eqs. (22) that these derivatives differ from the derivatives $\acute{D}_H$ and $\acute{D}_B$ (shown in Figs. 2, 3) in that they have constants proportional to the macroscopic strains ε_1 and ε_2. If these strain tensor components are both zero together, the function $\check{D}(\check{B}, \check{H})$ has no extrema, because its derivatives do not vanish (the curves in Figs. 2, 3 lie above the abscissa axes). The same conclusion can be drawn when both stress components are negative, because the additive constants in Eqs. (22) for the derivatives are positive in this case.

It is clear that a superstructure can arise only in the case where the macroscopic-strain components are positive. In this case, the curves of the total energy are obtained from the $\acute{D}_H(\check{H}, \check{B})$ and $\acute{D}_B(\check{H}, \check{B})$ curves by shifting them downward by amounts proportional to the corresponding components of the macroscopic stress tensor. Therefore, conditions for the formation of stable domains arise. An analysis shows that these conditions are related to the positions of the initial and terminal points of the curves in Fig. 3. Without going into detail, we illustrate the results in Fig. 4.

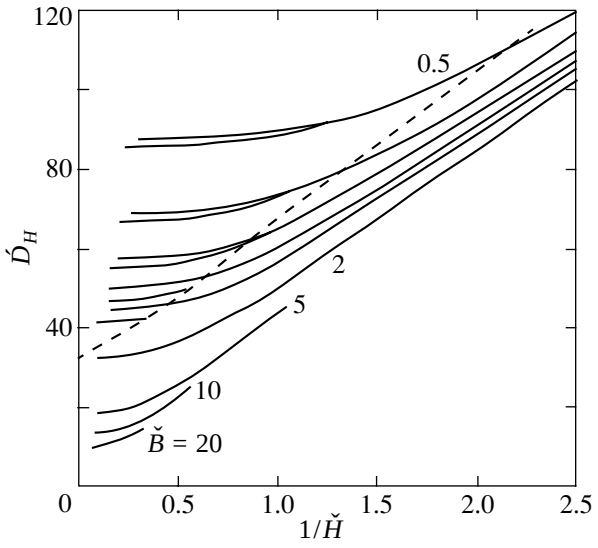

Fig. 2. Derivative (with respect to $1/\check{H}$) of the energy density of microscopic strains as a function of $1/\check{H}$ for $\check{B}$ = 20, 10, 5, 2, and 0.5. The dashed line separates the regions of elastic (on the left) and elastoplastic strains.

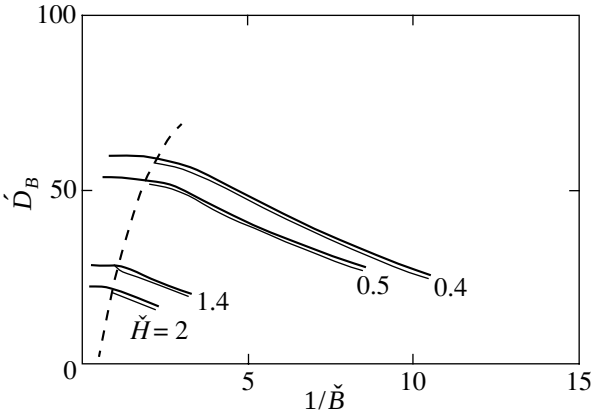

Fig. 3. Derivative (with respect to $1/\check{B}$) of the energy density of microscopic strains as a function of $1/\check{B}$ for $\check{H}$ = 2, 1.4, 0.5, and 0.4. The dashed line separates the regions of elastic (on the right) and elastoplastic strains.

First, we discuss the compatibility of conditions (24) for the domain formation. The corresponding dependences are presented in Fig. 4 in the coordinates $(1/\check{H}, 1/\check{B})$. The thin dashed curves, which fall off as one goes to the right, correspond to different fixed values of $\acute{D}_H \sim \varepsilon_1$ (these values decrease as the origin of coordinates is approached). The thick dashed lines (which are straight on the scale of Fig. 4) correspond to different fixed values of $\acute{D}_B \sim \varepsilon_2$, which also decrease as the origin is approached. The intersection points of

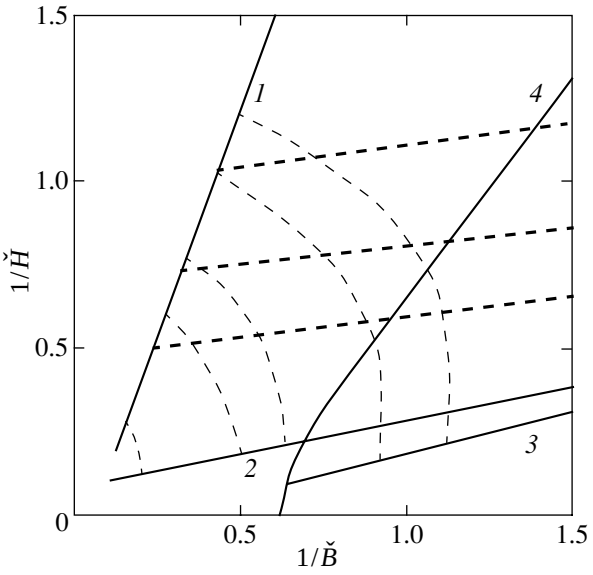

Fig. 4. Regions of existence of equilibrium domains for given macroscopic strains. Solid lines correspond to stable (*1*, *2*) elastoplastic and (*3*, *4*) purely elastic domains. Dashed lines correspond to domains unstable with respect to variations in their length and stable against variations in their thickness.

these two families of lines give solutions to the nonlinear set of equations (24); the coordinates of the intersection points determine the dimensions of equilibrium domains, which are, however, unstable to variations in $\check{B}$.

Line *1* (which is nearly straight on the scale of Fig. 4) corresponds to the initial points ($\check{B} = \check{B}_0$) of the curves in Fig. 3, i.e., to stable elastoplastic domains that are long in the horizontal direction. Straight line *2* corresponds to the lowest (terminal) points of these curves ($\check{B} = \check{B}_{00}$), i.e., to stable elastoplastic domains that are long in the vertical direction. Straight line *3* corresponds to purely elastic stable short domains, and curve *4*, to the same domains but with a larger length, $\check{B} = \check{B}_c$.

The point of intersection of straight line *1* with thin dashed curves gives both dimensions ($\check{B}_0$, $\check{H}_0$) of stable elastoplastic domains extended in the horizontal direction. The corresponding value of $\acute{D}_B \sim \varepsilon_2$ is equal to the ordinate $\acute{D}_B$ of the initial point $\check{B}_0$ in the curve $\check{H}_0$ = const in Fig. 3.

Stable elastoplastic domains that are extended in the vertical direction correspond to the intersection points of thin dashed curves with straight line *2*. The abscissas of these intersection points give the dimension $\check{B}_{00}$. The ordinate of the terminal point of the corresponding curve in Fig. 3 gives the quantity $\acute{D}_B \sim \varepsilon_2$ and, therefore, the value of the second component of the macroscopic strain tensor.

Clearly, all states of elastoplastic domains lie within the bifurcation fork; the limiting branches of the fork correspond to stable states (with the lowest total energy), while the intermediate states are characterized by a saddle-shaped energy surface. The states belonging to the different limiting branches are separated by a potential barrier. One branch (straight line *1* in Fig. 4) corresponds to domains with sharp vertical boundaries (narrow domain wall), while the stable domains belonging to the other branch have sharp horizontal boundaries (slip lines) and diffuse vertical boundaries.

Thus, stable elastoplastic domains are anisotropic; they are elongated in the horizontal ($\check{B} \longrightarrow \check{B}_0$) or vertical direction ($\check{B} \longrightarrow \check{B}_{00}$). The latter domains arise earlier (i.e., at smaller values of ε_2) than the former domains.

For purely elastic domains, we also have a bifurcation fork. One branch of the fork (corresponding to short domains) is straight line *3* in Fig. 4, while the other branch (longer domains) is curve *4* (the boundary of the region of existence of elastic domains). The states belonging to different branches are separated by a potential barrier. Short domains (belonging to the first branch) have sharp horizontal and diffuse vertical boundaries. Longer domains corresponding to the other branch (limited, however, by the condition $\check{B} < \pi/2$), on the contrary, have diffuse horizontal boundaries.

Thus, we arrive at the following important results. At certain values of the two components of the macroscopic strain tensor, ε_1 and ε_2, only two types of stable domains (elastic and elastoplastic) can form. As the macroscopic strains increase, the dimensions of these domains decrease; the domains correspond to two pairs of diverging (with decreasing domain size) branches of stable domains differing in anisotropy. Each of these branches is characterized by a certain ratio between the components of the macroscopic strain tensor or by a certain path along which the body should be strained. Otherwise, domains with different anisotropy do not separate and mixed structures of these domains arise because of the bifurcation mentioned above.

Let us discuss the strain threshold for the formation of a superstructure. For this purpose, we write Eq. (24) for the smallest average macroscopic strains ε_{1b} and ε_{2b} (which may be nonzero) corresponding to the stability limit (as indicated by the subscript).

The possible existence of the threshold follows from the fact that the derivatives $\acute{D}_H$ and $\acute{D}_B$ tend to nonzero limits as the average microscopic strains $1/\check{H}$ and $1/\check{B}$ approach zero (Figs. 2, 3). These limits determine the

strain thresholds $\acute{D}_{Hb}$ and $\acute{D}_{Bb}$. Analytically, these thresholds can be found, in principle, using Eq. (9), as the zero-order terms in the expansions of $\acute{D}_H$ and $\acute{D}_B$ in powers of $1/\check{H}$ and $1/\check{B}$. Extrapolation of straight lines *1* and *2* in Fig. 4 gives threshold values $\acute{D}_H \approx 8$ and $\acute{D}_B \approx 0$. From Eqs. (24), one can determine the threshold values of macroscopic strains ε_{1b} and ε_{2b}. Below the corresponding bifurcation points, a superstructure does not form and the body is strained as an elastic continuum, whose energy is determined by the first three terms in Eq. (19).

The interaction between different modes allowed for in this section makes additional contributions to the macroscopic stresses rather than to the strains. The corresponding expressions can be obtained by differentiating the total energy in Eq. (19) with respect to strains ε, in which case the contributions from microscopic strains will be due to the linear term L.

7. CONCLUSIONS

Thus, the model of nonlinear sublattice interaction allows one to adequately describe elastic and anelastic changes in the short-range and long-range order, i.e., structural transformations caused by an external strain field.

An important feature of this model is the allowance for the strong nonlinearity of the processes under study. It has been shown that the crystal structure undergoes bifurcation; the crystal properties are radically changed and new properties arise. We first discovered such nontrivial effects as the formation of defects in an initially perfect lattice, fragmentation of the lattice, the loss of stability of homogeneous strains whose strength exceeds a certain threshold value, the appearance of slip bands and twinning, distortions of the long-range and short-range order, and bond switching. Our model is also capable of describing anelastic diffusionless microscopic strains occurring in martensitic transformations. In other words, the model explicitly allows for local topological changes in the crystal.

Microscopic strains can be considered as incoherent displacements of the sublattices and their gradients (averaged over a domain), as a parameter characterizing the breakdown of the translational symmetry of the complex crystal lattice. In a strained state, the sublattices become incommensurate and large-scale superstructure arises. In principle, the microscopic strain field can sharply change in space (discontinuously, on a macroscopic scale) in the region of defect clusters, slip planes, and bond switching.

ACKNOWLEDGMENTS

This study was supported in part by the Russian Foundation for Basic Research (project no. 01-01-00307) and the Ministry of Industry, Science, and Technology of the Russian Federation (project no. 40.010.1-1.1195).

REFERENCES

1. I. A. Kunin, *Theory of Elastic Media with Microstructure* (Nauka, Moscow, 1975).
2. M. R. Korotkina, in *Elasticity and Inelasticity* (Mosk. Gos. Univ., Moscow, 1975), No. 4, p. 225.
3. M. Born and K. Huang, *Dynamical Theory of Crystal Lattices* (Clarendon, Oxford, 1954; Inostrannaya Literatura, Moscow, 1958).
4. A. M. Kosevich, *Theory of Crystal Lattice* (Vishcha Shkola, Kharkov, 1988).
5. G. L. Lamb, Jr., *Elements of Soliton Theory* (Wiley, New York, 1980; Mir, Moscow, 1983).
6. É. L. Aéro, Fiz. Tverd. Tela (St. Petersburg) **42**, 1113 (2000) [Phys. Solid State **42**, 1147 (2000)].
7. E. Jahnke, F. Emde, and F. Lösch, *Tables of Higher Functions*, 6th ed. (Teubner, Stuttgart, 1960; McGraw-Hill, New York, 1960; Nauka, Moscow, 1977).

Translated by Yu. Epifanov

Physics of the Solid State, Vol. 45, No. 8, 2003, pp. 1566–1571. Translated from Fizika Tverdogo Tela, Vol. 45, No. 8, 2003, pp. 1491–1496.

LATTICE DYNAMICS AND PHASE TRANSITIONS

Heterogeneous Nucleation of Martensite on Precipitates and the Martensitic-Transformation Kinetics in Shape Memory Alloys

G. A. Malygin

Ioffe Physicotechnical Institute, Russian Academy of Sciences, Politekhnicheskaya ul. 26, St. Petersburg, 194021 Russia
e-mail: malygin.ga@mail.ioffe.ru

Received December 27, 2002

Abstract—The formation of martensite in an elastic stress field near a disk-shaped coherent precipitate is discussed in terms of the theory of diffuse martensitic transformations. The heterogeneous martensite nucleation on precipitates is found to increase the characteristic martensitic-transformation temperature, which increases linearly with the volume density of precipitates. The theoretical results are illustrated quantitatively using the example of the $B2 \longrightarrow R$ phase transition in titanium nickelide alloys. © *2003 MAIK "Nauka/Interperiodica".*

1. INTRODUCTION

It has been established experimentally that particles of a new phase in shape memory alloys affect the parameters of the martensitic transformation and the strain-induced effects associated with this transformation [1–4]. Electron-microscopic studies of crystals of equiatomic titanium nickelide alloys have shown that martensite nuclei arise near coherent precipitates of the Ti_3Ni_4 phase [4–7]. The formation of these nuclei is associated with the presence of elastic stress fields near coherent precipitates and with stress relaxation caused by a local martensitic transformation. This martensitic transformation–assisted relaxation of internal stresses near precipitates is believed to be the cause of the so-called bidirectional shape memory effect observed in TiNi crystals [1, 4].

In [8], the formation of martensite nuclei in elastic fields of screw and edge dislocations and of their planar clusters was considered in the framework of the theory of diffuse martensitic transformations (DMTs) [9, 10]. The influence of two-dimensional networks of edge dislocations on the kinetics and parameters of the martensitic transformations in shape memory alloys was also analyzed in [8].

In this paper, we discuss the formation of martensitic nuclei near disk-shaped precipitates in terms of the DMT theory. For example, the Ti_3Ni_4 precipitates mentioned above have the shape of a lens [4]; they form in a TiNi alloy during annealing in the temperature range 500–900 K [1–4]. Such precipitates arise if the Ni atomic concentration in the alloy is no less than 50.5 at. %. The Ti_3Ni_4 particles have a rhombohedral crystal lattice and, when arising in the initial bcc lattice of the $B2$ phase, they undergo a dilatation along the direction normal to the plane of the disk-shaped precipitate [4]. The precipitates are coherently joined with the matrix if their radii do not exceed 0.5 μm [2, 5].

This paper is organized as follows. In Section 2, we calculate the elastic stresses near the precipitates mentioned above. In Section 3, using the DMT theory, the mechanism of heterogeneous nucleation of martensite near an isolated precipitate is considered on the example of the $B2 \longrightarrow R$ phase transformation in titanium nickelide. The influence of the volume density of precipitates on the parameters of the martensitic transformation is discussed in Section 4.

2. STRESS FIELD NEAR A DISK-SHAPED PRECIPITATE

In order to calculate the stress field near a disk-shaped precipitate, we use the results of calculations performed by Eshelby [11] for the elastic strains near an ellipsoidal inclusion in a matrix. We approximate the disk-shaped precipitate by an ellipsoid of revolution of radius r_0 and height $2h_0 < 2r_0$:

$$\frac{r^2}{r_0^2} + \frac{z^2}{h_0^2} = 1. \tag{1}$$

The harmonic potential Φ for this ellipsoid, according to [11], has the form

$$\Phi(r, z) = \pi r_0^2 h_0 \int_\lambda^\infty \frac{W(r, z, l)}{\Delta(r, z, l)} dl,$$
$$W = 1 - \frac{r^2}{r_0^2 + l} - \frac{z^2}{h_0^2 + l}, \tag{2}$$
$$\Delta = (r_0^2 + l)(h_0^2 + l)^{1/2},$$

1063-7834/03/4508-1566$24.00

where $\lambda = \lambda(r, z)$ is the largest root of the equation $W(l) = 0$ and l is the variable of integration.

Introducing dimensionless coordinates $\bar{r} = r/r_0$ and $\bar{z} = z/h_0$ and parameter $\beta = h_0/r_0$ and performing integration in Eq. (2), we obtain

$$\Phi = \frac{\pi r_0 h_0}{(1-\beta^2)^{1/2}}\bar{\Phi}. \tag{3}$$

Here,

$$\begin{aligned}\bar{\Phi}(\bar{r},\bar{z}) &= \left(2-\frac{\bar{r}^2-2\beta^2\bar{z}^2}{1-\beta^2}\right)\arcsin\left(\frac{1-\beta^2}{\bar{\lambda}+1}\right)^{1/2}\\ &+\left(\frac{\bar{\lambda}+\beta^2}{1-\beta^2}\right)^{1/2}\frac{\bar{r}^2}{\bar{\lambda}+1}-\frac{2\beta^2\bar{z}^2}{(1-\beta^2)^{1/2}(\bar{\lambda}+\beta^2)^{1/2}},\\ \bar{\lambda}(\bar{r},\bar{z}) &= \frac{1}{2}[(\bar{r}^2-1)+\beta^2(\bar{z}^2-1)]\\ &+\left\{\frac{1}{4}[(\bar{r}^2-1)+\beta^2(\bar{z}^2-1)]^2+\beta^2[\bar{r}^2+\bar{z}^2-1]\right\}^{1/2}.\end{aligned} \tag{4}$$

Using potential (3), one can determine the displacement field near the inclusion if the strain of the precipitate in the free state is known. In our case, this strain (dilatation) is the relative difference in the spacing between the (111) planes of the $B2$ matrix and the Ti_3Ni_4 inclusion $\delta_{(111)} = (d_{B2} - d_R)/d_{B2} \approx 3 \times 10^{-2}$ [4]. This dilatation is purely axial, $\delta_{(111)} = \delta_z$. Therefore, according to [11], the radial u_r and axial u_z displacements are

$$\begin{aligned}u_r &= \frac{\delta_z h_0}{8(1-\nu)(1-\beta^2)^{1/2}}\left(\frac{1}{1-\beta^2}\frac{\partial H}{\partial\bar{z}}-2\nu\frac{\partial\bar{\Phi}}{\partial\bar{r}}\right),\\ u_z &= \frac{\delta_z h_0}{8(1-\nu)(1-\beta^2)^{1/2}}\\ &\times\left(-\frac{\beta}{1-\beta^2}\frac{\partial H}{\partial\bar{r}}-2\frac{1-\nu}{\beta}\frac{\partial\bar{\Phi}}{\partial\bar{z}}\right),\end{aligned} \tag{5}$$

where $H(\bar{r}, \bar{z}) = \bar{z}(\partial\bar{\Phi}/\partial\bar{r}) - \bar{r}(\partial\bar{\Phi}/\partial\bar{z})$ and ν is the Poisson ratio. Dilatations δ_x and δ_y, parallel to the plane of the disk, are half as large as δ_z [12]. Due to the shape of the precipitate chosen, these dilatations make insignificant contributions to displacements (5) and can be neglected. For displacements (5), the nonzero components of the elastic strain tensor in the cylindrical system of coordinates (r, θ, z) are [13]

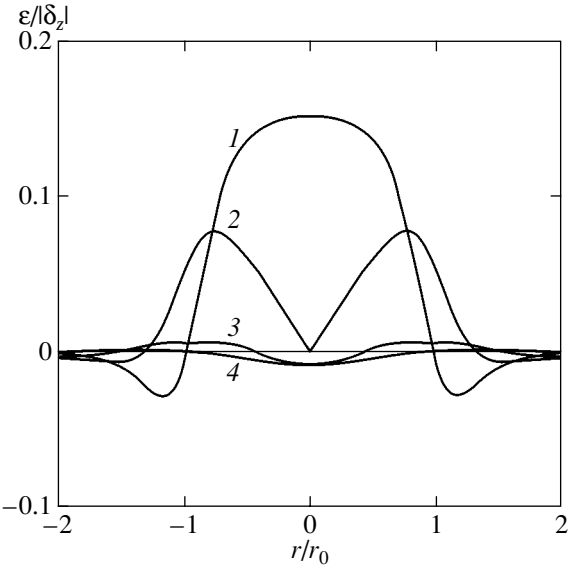

Fig. 1. Dependence of the different components of the elastic strain tensor on radius at the distance $z = 2h_0$ from the precipitate: (*1*) ε_{zz}, (*2*) ε_{rz}, (*3*) $\varepsilon_{\theta\theta}$, and (*4*) ε_{rr}.

$$\begin{aligned}\varepsilon_{rr} &= \frac{\partial u_r}{\partial r} = \beta\frac{\partial\bar{u}_r}{\partial\bar{r}},\quad \varepsilon_{\theta\theta} = \frac{u_r}{r} = \beta\frac{\bar{u}_r}{\bar{r}},\\ \varepsilon_{zz} &= \frac{\partial u_z}{\partial z} = \frac{\partial\bar{u}_z}{\partial\bar{z}},\\ \varepsilon_{rz} &= \frac{1}{2}\left(\frac{\partial u_r}{\partial z}+\frac{\partial u_z}{\partial r}\right) = \frac{1}{2}\left(\frac{\partial\bar{u}_r}{\partial\bar{z}}+\beta\frac{\partial\bar{u}_z}{\partial\bar{r}}\right).\end{aligned} \tag{6}$$

Here, $\bar{u}_r = u_r/h_0$ and $\bar{u}_z = u_z/h_0$ are dimensionless displacements. If the matrix is elastically isotropic, the normal and shear components of the stress field induced by the precipitate are given by

$$\begin{aligned}\sigma_r &= \frac{E}{(1-2\nu)(1+\nu)}[(1-\nu)\varepsilon_{rr}+\nu(\varepsilon_{\theta\theta}+\varepsilon_{zz})],\\ \sigma_\theta &= \frac{E}{(1-2\nu)(1+\nu)}[(1-\nu)\varepsilon_{\theta\theta}+\nu(\varepsilon_{rr}+\varepsilon_{zz})],\\ \sigma_z &= \frac{E}{(1-2\nu)(1+\nu)}[(1-\nu)\varepsilon_{zz}+\nu(\varepsilon_{\theta\theta}+\varepsilon_{rr})],\\ \sigma_{rz} &= \frac{E}{1+\nu}\varepsilon_{rz},\end{aligned} \tag{7}$$

where E is Young's modulus.

Displacements (5) and the corresponding strains (6) can be calculated by differentiating potential (3) with respect to the coordinates r and z. The formulas thus obtained are cumbersome and are not presented here. As an illustration, Fig. 1 shows the numerically calculated strains (6) at the distance $z = 2h_0$ from the precip-

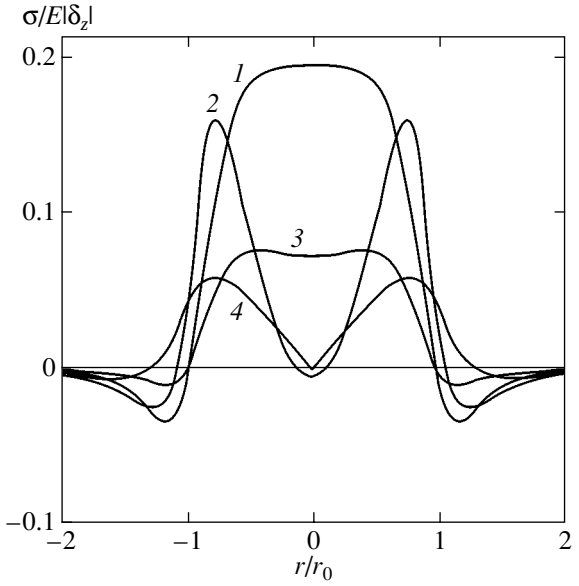

Fig. 2. Dependence of the different components of the elastic stress tensor on radius at the distance $z = 2h_0$ from the precipitate: (*1*) σ_z, (*2*) σ_{rz}, (*3*) σ_r, and (*4*) σ_θ.

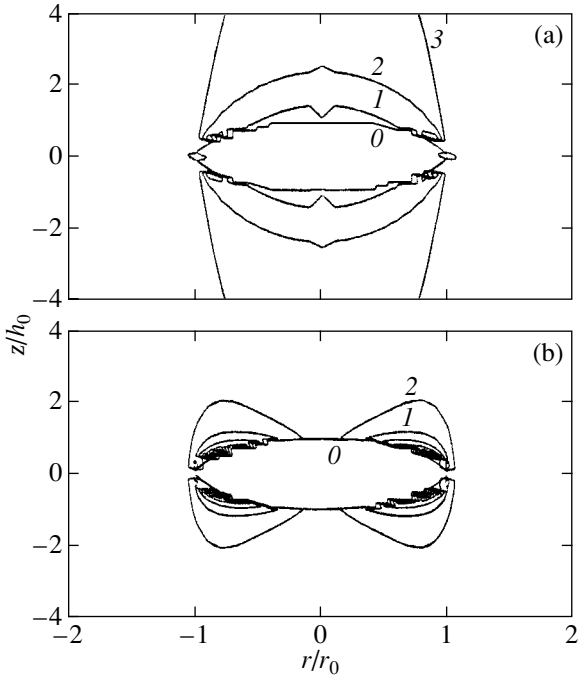

Fig. 3. Level lines of (a) axial σ_z and (b) shear σ_{rz} stresses near the precipitate. The values of σ are (*1*) 0.18, (*2*) 0.18, and (*3*) $0.04E|\delta_z|$; the values of σ_{rz} are (*1*) 0.13 and (*2*) $0.06E|\delta_z|$; and curve *0* is the boundary of the precipitate.

itate for the values of the parameters $h_0/r_0 = \beta = 0.2$, $\nu = 0.3$, and $\delta_z = -|\delta_z|$. As one would expect, the tensile axial strain ε_{zz} is dominant. It follows from Eq. (6) that the other components of the strain field become progressively smaller than ε_{zz} with decreasing parameter β, i.e., with increasing oblateness of the lens-shaped inclusion.

The components of the stress field (7) corresponding to these strains are shown in Fig. 2. It can be seen that above (and below) the central part of the precipitate the axial stress component σ_z is dominant (curve *1*), whereas near the edge of the precipitate the shear component σ_{rz} is dominant (curve *2*). Figure 3 presents the distribution of these stresses near the precipitate in the *rz* plane. Calculations show that, for $E = 40$ GPa and $|\delta_z| = 3 \times 10^{-2}$, the stresses near coherent Ti_3Ni_4 particles can be as large as 150–200 MPa.

In concluding this section, we note that the strain and stress fields inside the precipitate can also be found using potential (2). In this case, we should put $\lambda = 0$ in Eqs. (2) and (3) [11]. Calculations based on Eqs. (5)–(7) show that the elastic stresses and strains inside the precipitate are homogeneous and depend strongly on the parameter $\beta = h_0/r_0$. In this paper, the stresses inside the precipitate are of no interest to us and we set them equal to zero in what follows.

3. THE FORMATION OF MARTENSITE NEAR A COHERENT INCLUSION

According to the DMT theory, the (relative) volume density of the uniformly oriented martensite φ_M in the alloy under stress σ at temperature T is given by [9, 10]

$$\varphi_M(T, \sigma) = \left[1 + \exp\left(\frac{\Delta U}{kT}\right)\right]^{-1},$$
$$\Delta U = \omega \Delta u, \quad \Delta u = q\frac{T - T_{c0}}{T_{c0}} - m_{ijkl}\xi_{ik}\sigma_{jl}. \tag{8}$$

Here, ΔU is the change in the internal energy of the crystal associated with the transformation of an elementary volume ω of the austenite phase into martensite, Δu is the change in the internal energy per unit volume of the crystal due to this transformation, q is the specific heat of the phase transformation, T_{c0} is the critical (characteristic) temperature of the transformation in the absence of stress σ_{jl}, ξ_{ik} is the strain of the crystal lattice associated with its structural rearrangement, and m_{ijkl} is the orientational factor characterizing the matching of the reference frames of stresses σ_{jl} and lattice strains. It follows from Eq. (8) that the amount of martensite in the crystal depends on the value and sign of the energy Δu. The crystal is dominated by austenite if $\Delta u > 0$ and by martensite if $\Delta u < 0$. The condition $\Delta u = 0$, under which the amounts of martensite and austenite in the crystal are equal, defines the characteristic temperature of the transformation:

$$T_c = T_{c0} + T_{c0}\frac{m_{ijkl}\xi_{ik}\sigma_{jl}}{q}. \tag{9}$$

According to Eq. (9), the application of external stress to the crystal causes the critical temperature of the

transformation to change. Obviously, the presence of precipitates, which produce long-range elastic fields, will also affect the characteristic temperature.

Taking into account the orientational relations between the lattices of phase $B2$ and martensite R in the case of Ti_3Ni_4 particles and the $B2 \longrightarrow R$ phase transition considered above, we obtain $m_{ijkl}\xi_{ik}\sigma_{jl} \approx \xi_z\sigma_z$. The contributions to the energy change due to the martensitic transformation from the other components of the stress field can be neglected because of the smallness of these components in comparison with σ_z (Fig. 2). Substituting the change in energy into Eq. (8), we obtain the spatial distribution of the volume density of martensite near the precipitate at different temperatures:

$$\varphi_M(r, z, t) = \left\{1 + \exp\left[B\left(\frac{T - T_{c0}}{T_{c0}} - \frac{\xi_z\sigma_z(r, z)}{q}\right)\right]\right\}^{-1}. \quad (10)$$

Here, $B = \omega q/kT \approx \omega q/kT_{c0}$ is a parameter determining the spread in the transformation temperature $\Delta T_M = 4T_{c0}/B$ [9, 10]. In the case of the $B2 \longrightarrow R$ phase transition, for $\Delta T_R \approx 20$ K and $T_{c0} \approx 300$ K [1], we have $B = 60$. Setting $q_R = 30$ MJ m^{-3} [14], we find the elementary volume for R-martensite transformation to be $\omega \approx 5$ nm^3. It should be noted that the $B2 \longrightarrow R$ phase transition proceeds initially as a second-order transition, but then, as the temperature is lowered further, this transformation becomes a diffuse first-order phase transition with a temperature hysteresis of approximately 5–10 K [1, 14]. Although the DMT theory is capable of describing transformations intermediate between first and second order [15], we will assume the formation of the R martensite to be a pure first-order phase transition in our calculations.

To calculate the spatial distribution of martensite in the elastic field of the coherent precipitate numerically, we conveniently represent Eq. (10) in the dimensionless form

$$\varphi_M(\bar{r}, \bar{z}, t) = \{1 + \exp[B(t - 1 - a|S_z(\bar{r}, \bar{z})|)]\}^{-1},$$
$$S_z(\bar{r}, \bar{z}) = \frac{1}{(1 - 2\nu)(1 + \nu)}\left[\frac{1 - \nu}{|\delta_z|}\varepsilon_{zz}(\bar{r}, \bar{z}) + \frac{\nu}{|\delta_z|}[\varepsilon_{rr}(\bar{r}, \bar{z}) + \varepsilon_{\theta\theta}(\bar{r}, \bar{z})]\right], \quad (11)$$
$$S_z = \frac{\sigma_z}{E|\delta_z|}, \quad a = |\xi_z||\delta_z|\left(\frac{E}{q}\right), \quad t = T/T_{c0}.$$

Figure 4a shows the radial distribution of the R martensite calculated from Eq. (11) for $\xi_z = 1 \times 10^{-2}$ and $a_R = 0.4$ at distance $z = 2h_0$ from the precipitate for two values of temperature $T > T_{c0}$. It can be seen that, at both temperatures, the martensite concentration near the precipitate is significantly higher than that far from it. The distribution of the R martensite in the rz plane near the precipitate at a temperature of $1.05T_{c0}$ is presented in Fig. 4b. The increase in the volume density of martensite at a point in the crystal with decreasing temperature is illustrated in Fig. 5 in the absence (curve *1*) and in the presence (curve *2*) of the precipitate coherently joined with the matrix.

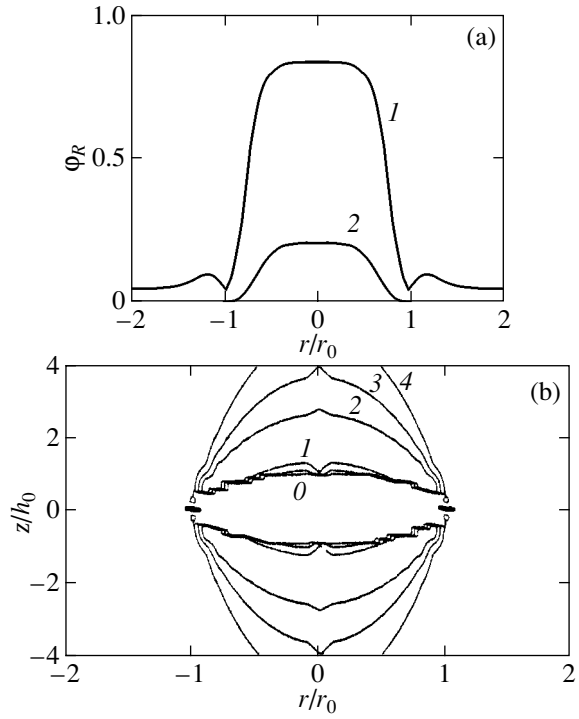

Fig. 4. (a) Dependence of the volume density of the R martensite on radius at the distance $z = 2h_0$ from the precipitate at different temperatures: (*1*) $1.05T_{c0}$ and (*2*) $1.1T_{c0}$. (b) Level lines of φ_R in the rz plane near the precipitate at a temperature of $1.05T_{c0}$; the values of φ_R are (*1*, *2*) 0.76, (*3*) 0.52, and (*4*) 0.29.

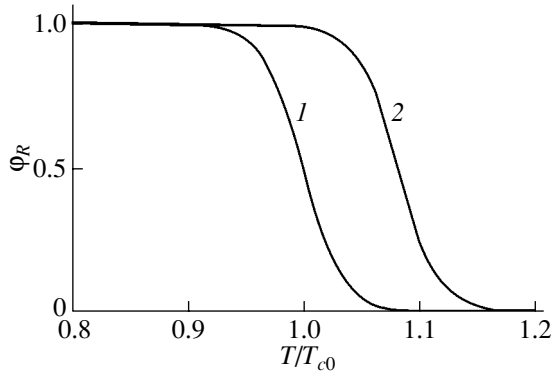

Fig. 5. Temperature dependence of the volume density of the R martensite at the point $r = 0$, $z = 2h_0$ (*1*) in the absence and (*2*) in the presence of the coherent precipitate.

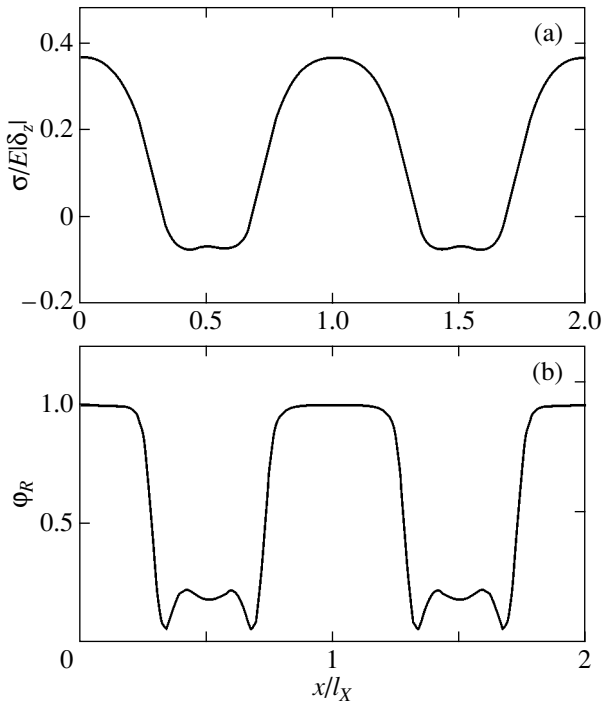

Fig. 6. Distributions of (a) internal stresses and (b) volume density of the *R* martensite in a crystal containing precipitates with a volume density of 9% at a temperature of $1.05T_{c0}$.

Electron-microscopic studies [4–6] show that the uniformly oriented *R* martensite near particles of Ti_3Ni_4 consists of lamellae one to several tens of nanometers thick and 10 to 200 nm long. The DMT theory does not describe the morphology of martensite but rather allows one to determine its volume density at a given point in the crystal. In the case of martensite lamellae, we have $\varphi_M = \Lambda_M/\Lambda$, where Λ_M is the thickness of martensite lamellae and Λ is the distance between them. In the initial stage, where the *R*-phase formation proceeds as a second-order phase transition, rhombohedral crystal nuclei arise, rather than lamellae, in the vicinity of precipitates [5].

4. THE INFLUENCE OF THE VOLUME DENSITY OF PRECIPITATES ON THE PARAMETERS OF THE MARTENSITIC TRANSFORMATION

According to electron-microscopic studies [6], *R*-martensite lamellae form not only near Ti_3Ni_4 particles but also between them, where the stress fields produced by individual precipitates overlap. The strength of the resultant stress field depends on the volume density and mutual orientation of precipitates.

In TiNi crystals annealed in the absence of an externally applied stress, there are four energetically equivalent, different orientations of Ti_3Ni_4 particles, in accordance with the number of habit planes of the (111) type for these particles [12]. Since the distribution of stresses near these particles is anisotropic, the resultant stress will be maximum if only one orientation of particles dominates in the disperse structure. This is the case, for example, in a TiNi alloy annealed in the presence of unidirectional stresses of either sign applied to the alloy [4, 12]. An anisotropic distribution in orientation of Ti_3Ni_4 particles is the cause of the bidirectional shape memory effect observed in TiNi alloys [1, 4]. We consider this case in what follows.

We assume that, in a TiNi alloy annealed in the presence of unidirectional stresses applied to the alloy, disperse particles are oriented along the same direction and form a spatial structure. For simplicity, we assume this structure to be regular, for example, close to tetragonal with the lattice parameters $l_X = l_Y$ and $l_Z < l_X$. The Ti_3Ni_4 particles are located at the sites of the tetragonal superlattice, so that the volume density of the particles is $f = V_0/V$, where $V_0 = (4/3)\pi r_0^2 h_0$ is the volume of a precipitate of the type indicated above and $V = l_X l_Y l_Z$ is the volume of the unit cell of the tetragonal superstructure. The *z* axes of the precipitates are directed along the *Z* axis of this structure.

The internal stress field produced by the regular superstructure can be written as a triple sum over the sites of its lattice. Using the notation introduced in Eq. (11) and the fact that $\bar{r}(\bar{x}, \bar{y}) = (\bar{x}^2 + \bar{y}^2)^{1/2}$, we obtain

$$S(\bar{x}, \bar{y}, \bar{z}) = \sum_{0}^{N}\sum_{0}^{N}\sum_{0}^{N} S_z(\bar{x} + m\dot{l}_X, \bar{y} + n\dot{l}_Y, \bar{z} + k\dot{l}_Z), \quad (12)$$

where $S = \sigma/E|\delta_z|$; σ is the total stress produced by the precipitates located at the sites of the superlattice; and $\dot{l}_X = l_X/r_0$, $\dot{l}_Y = l_Y/r_0$, and $\dot{l}_Z = l_Z/r_0$ are the dimensionless lattice parameters of the tetragonal superstructure.

Figure 6a shows the distribution of internal stresses in the disperse structure calculated from Eq. (12) with the parameters $l_X = l_Y = 3r_0$ and $l_Z = r_0$. The volume density of precipitates in this case is $f = 4\pi h_0/27r_0 \approx 9 \times 10^{-2}$. The curve in Fig. 6a is the dependence of the dimensionless stress $S(x, y, z)$ on the coordinate *x* within two unit cells of the tetragonal superlattice at distances $y = 0$ and $z = 2h_0$ from precipitates. It can be seen that, due to summation of the stresses produced by neighboring precipitates, the stress in the region between them is nearly twice as large as the stress produced by an individual precipitate (curve *1* in Fig. 2). The amount of martensite also increases in the regions of enhanced stresses. Figure 6b shows the dependence of the volume density of the *R* martensite on the coordinate *x* calculated for a temperature of $1.05T_{c0}$ from the expression

$$\varphi_R(x, y, z, t) = \{1 + \exp[B(t - 1 - a|S(x, y, z)|)]\}^{-1}. \quad (13)$$

It is seen that, in the regions where the interference of stresses produced by neighboring precipitates is constructive, the alloy transforms completely into martensite at the temperature indicated, whereas near an isolated precipitate a certain volume fraction of the austenite at this temperature has not yet undergone the transformation (curve *1* in Fig. 4a).

To investigate the influence of the volume density of precipitates f on the parameters of the martensitic transformation, we need to perform spatial averaging of the internal stresses (12) for different values of f. For this purpose, it will suffice to average the stress field over one tetragonal unit cell. The volume density of martensite (13) can also be averaged over a unit cell of the superlattice. However, these computations are very time consuming. Therefore, in order to estimate the average stress field, we use the results obtained by Eshelby [11, 12], according to which the averaged internal strain field in a crystal is proportional to the volume density of dilatation (or shear-strain) centers. Therefore, in our case, $\langle \varepsilon_z \rangle = \delta_z f$ and, according to Eqs. (9) and (11), the characteristic temperature of the martensitic transformation is a linear function of the volume density of precipitates:

$$T_c(f) = T_{c0}(1 + \alpha f), \quad \alpha = \frac{|\xi_z||\delta_z|}{1-2\nu}\left(\frac{1-\nu}{1+\nu}\right)\left(\frac{E}{q}\right). \quad (14)$$

For the values of the parameters of the $B2 \longrightarrow R$ phase transition indicated above, we obtain $\alpha \approx 0.5$. In the approximation of the average internal stress field, the volume density of martensite in a crystal with a volume density of precipitates f should vary with temperature according to the law

$$\varphi_M(T, f) = \left[1 + \exp\left(B\frac{T - T_c(f)}{T_{c0}}\right)\right]^{-1}. \quad (15)$$

5. CONCLUSION

Thus, the results of this study show that the DMT theory allows one to quantitatively analyze the mechanism of heterogeneous nucleation of martensite near an individual precipitate and investigate the influence of the volume density of precipitates on the parameters of the martensitic transformation. The results obtained here will be used to develop a quantitative theory of the bidirectional shape memory effect.

REFERENCES

1. N. Nishida and T. Honma, Scr. Metall. **18** (11), 1293 (1984).
2. J. Zhang, W. Cai, X. Ren, *et al.*, Mater. Trans., JIM **40** (12), 1367 (1999).
3. J. Kh. Allafi, X. Ren, and G. Eggeler, Acta Mater. **50** (4), 793 (2002).
4. T. Honma, in *Shape Memory Alloy-86*, Ed. by Ch. Youyi, T. Y. Hsu, and T. Ko (China Academic, Guilin, 1986), p. 83.
5. V. I. Zeldovich, G. A. Sobyanina, and V. G. Pushin, Scr. Mater. **37** (1), 79 (1997).
6. V. I. Zel'dovich, I. V. Khomskaya, N. Yu. Frolova, and G. A. Sbitneva, in *Proceedings of XXXVIII Seminar on Shape Memory Alloys and Other Perspective Materials* (St. Petersburg, 2001), Part 1, p. 63.
7. V. G. Pushin, V. V. Kondrat'ev, and V. N. Khachin, *Pretransition Phenomena and Martensitic Transformations* (Ural. Otd. Ross. Akad. Nauk, Yekaterinburg, 1998).
8. G. A. Malygin, Fiz. Tverd. Tela (St. Petersburg) **45** (2), 327 (2003) [Phys. Solid State **45**, 345 (2003)].
9. G. A. Malygin, Fiz. Tverd. Tela (St. Petersburg) **36** (5), 1489 (1994) [Phys. Solid State **36**, 815 (1994)].
10. G. A. Malygin, Usp. Fiz. Nauk **171** (2), 187 (2001) [Phys. Usp. **44**, 173 (2001)].
11. J. D. Eshelby, Solid State Phys. **3**, 79 (1956).
12. D. Y. Li and L. Q. Chen, Acta Mater. **45** (2), 471 (1997).
13. L. D. Landau and E. M. Lifshitz, *Course of Theoretical Physics*, Vol. 7: *Theory of Elasticity*, 5th ed. (Pergamon, New York, 1986; Fizmatlit, Moscow, 2001).
14. R. X. Wang, Y. Zohar, and M. Wong, J. Micromech. Microeng. **11** (6), 686 (2001).
15. G. A. Malygin, Fiz. Tverd. Tela (St. Petersburg) **43** (10), 1911 (2001) [Phys. Solid State **43**, 1989 (2001)].

Translated by Yu. Epifanov

Physics of the Solid State, Vol. 45, No. 8, 2003, pp. 1572–1578. Translated from Fizika Tverdogo Tela, Vol. 45, No. 8, 2003, pp. 1497–1502.

LATTICE DYNAMICS AND PHASE TRANSITIONS

Investigation of the Reconstructive Phase Transition between Metastable (α) and Stable (β) Modifications of the NH_4LiSO_4 Crystal

S. V. Mel'nikova, A. V. Kartashev, V. A. Grankina, and I. N. Flerov

Kirensky Institute of Physics, Siberian Division, Russian Academy of Sciences, Akademgorodok, Krasnoyarsk, 660036 Russia
e-mail: msv@iph.krasn.ru

Received January 8, 2003

Abstract—Crystals of ammonium lithium sulfate NH_4LiSO_4 in α and β modifications are studied, and conditions of their nucleation and growth are determined. The α modification of NH_4LiSO_4 and α ⟶ β phase transitions are investigated using polarized light microscopy, x-ray diffraction, and differential scanning calorimetry in the temperature range 80–530 K. It is found that, depending on the conditions of growth and storage, there exist two temperature ranges ($T_{\alpha\to\beta} \approx$ 340–350 and ≈440–450 K) in which the crystals can undergo an α ⟶ β reconstructive phase transition. The enthalpy of this transformation depends on the symmetry of the final phase. In the former case (340–350 K), the reconstructive phase transition leads to rapid destruction of the sample. In the latter case (440–450 K), the crystal structure undergoes a slow transformation (recrystallization) without noticeable distortions. The results obtained indicate that no structural phase transition occurs in the α modification of NH_4LiSO_4 at 250 K. © *2003 MAIK "Nauka/Interperiodica".*

1. INTRODUCTION

Ammonium lithium sulfate NH_4LiSO_4 (NLS) has been extensively studied over many years. It is established that, during cooling, this compound undergoes the following sequence of symmetry changes:

$$Pmcn(c = c_0)(G_0) \rightleftharpoons P2_1cn(c = c_0)(G_1)$$

$$\rightleftharpoons P2_1/c11(c = 2c_0)(G_2)$$

$$\rightleftharpoons C1c1(c = 2c_0)(G_3)$$

at T_i = 460, 284, and 27 K, respectively [1–3]. The phase is ferroelectric with considerable spontaneous polarization at room temperature and ferroelastic below ~284 K. On the other hand, there have appeared works in which new phase transitions in NH_4LiSO_4 were revealed or previously determined symmetry groups of the known phases were subjected to question [4]. Certainly, polymorphism of the NH_4LiSO_4 compound is also responsible to a large extent for the discrepancy in the experimental results obtained by different authors.

The above sequence of transitions is observed for NH_4LiSO_4 crystals in the β modification (β-NLS). These crystals have a tridymite-like pseudohexagonal structure consisting of SO_4 and LiO_4 tetrahedra joined together by their vertices and forming six-membered rings perpendicular to the *c* axis. In the structure, free vertices of one half of these tetrahedra are directed upward and the tetrahedra themselves are bound to the upper layer of the tetrahedra, whereas the vertices of the other half of the tetrahedra are oriented downward and the tetrahedra themselves are bound to the lower layer. The ammonium groups occupy cavities formed between the layers. The unit cell parameters of the β modification at room temperature are as follows: a = 5.280 Å, b = 9.140 Å, and c = 8.786 Å. A comprehensive review of the experimental data available in the literature for NH_4LiSO_4 crystals in the β modification was given by Polomska [5].

The α modification of the NH_4LiSO_4 compound (α-NLS) has been known for more than one hundred years. According to Pietraszko and Lukaszewicz [6] and Tomaszewski [7], the structure of the α modification is also composed of SO_4 and LiO_4 tetrahedra. However, in the α modification, unlike the β modification, the SO_4 and LiO_4 tetrahedra located in a layer perpendicular to the [001] direction can be joined not only by their vertices but also by their edges. The adjacent layers are bound to nitrogen atoms of the ammonium groups through hydrogen bonds and form a layered structure with the orthorhombic space group $Pbc2_1$ and the lattice parameters a = 4.991 Å, b = 10.196 Å, and c = 17.010 Å. It should be noted that, as a rule, samples of the α modification can involve several polytypes that differ in the lattice parameter c: $c_1 = c$, $c_2 = 2c$, and $c_3 = 3c$ [7].

The NH_4LiSO_4 compound in the α modification has an unstable structure and transforms into the β modification upon heating. According to the differential thermal analysis (DTA) performed by Polomska *et al.* [8], the as-grown crystals undergo a reversible phase transition at a temperature of approximately 250 K and an

irreversible ($\alpha \longrightarrow \beta$) phase transition at temperatures close to 350 K. These authors revealed a steplike anomaly in the DTA curves at 350 K and assigned this feature to the coexistence of different polytypes in the sample. Moreover, they investigated variations in the frequencies of librational and translational vibrations of SO_4^{2-}, NH_4^+, and Li^+ ions upon the $\alpha \longrightarrow \beta$ phase transition with the use of far-infrared spectroscopy [8].

The main objectives of the present work were as follows: (i) to elucidate the influence of the growth conditions of NH_4LiSO_4 crystals on the formation of the α and β modifications, (ii) to investigate the reversible phase transition to the α modification at 250 K, (iii) to examine the kinetics of the $\alpha \longrightarrow \beta$ reconstructive phase transition, and (iv) to analyze the thermodynamic parameters of the phase transitions in NH_4LiSO_4 crystals.

2. SAMPLE PREPARATION AND EXPERIMENTAL TECHNIQUE

In order to solve the problems formulated above, we used the techniques of measuring the heat capacity and birefringence and also observations in polarized light. The α and β phases in the studied samples were identified from the x-ray powder diffraction patterns recorded on a DRON-2 diffractometer. For optical investigations, the single-crystal samples were oriented with a URS-1 x-ray instrument.

Observations in polarized light and measurements of the birefringence of the crystals grown were performed in the range from ~80 K to temperatures corresponding to the decomposition of the studied compound (~530 K). The birefringence was measured on the (001) cleavage surfaces ($c = 17.01$ Å). The measurements were performed on a Berec compensator with an accuracy of $\cong 10^{-5}$ and a Senarmont compensator with a sensitivity of no less than 10^{-7}. The former compensator made it possible to investigate thin samples and to determine the birefringence magnitude. It should be noted that the temperature behavior of the birefringence of β-NLS crystals in the ranges of the ferroelectric and ferroelastic phase transitions is sufficiently well understood [9–11].

The thermodynamic properties were examined on a DSM-2M differential scanning microcalorimeter. The measurements were carried out in the temperatures range 150–370 K with a low-temperature unit and in the range 340–550 K with a high-temperature unit. The calorimetric experiments were conducted using, for the most part, single-crystal and, with rare exception, powder samples. In the case when the compound was studied in the form of a single crystal, close thermal contact between the sample and the cell was ensured by a KPT-8 organosilicon paste. The sample weight was approximately equal to 0.1–0.2 g. In order to determine the confidence intervals of the thermodynamic parameters under investigation, the measurements were performed with several samples for each crystallization. The weight of the samples was checked prior to and after heating in each experiment. In all the main experiments, the samples were heated or cooled at a rate of 8 K/min.

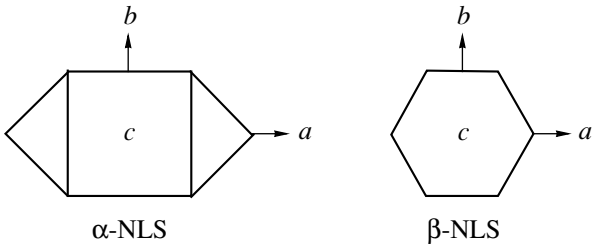

Fig. 1. Crystal habit of NH_4LiSO_4 in α and β modifications.

With the aim of determining the formation conditions for NH_4LiSO_4 single crystals in the α and β modifications, we performed five crystallizations from a solution under different conditions at temperatures of 281, 283, 293, and 303 K. Crystallizations at temperatures of 281 and 293 K proceeded through spontaneous growth without stirring of the solution (crystallizations *1, 2*). All other crystallizations (crystallizations *3–5*) occurred through slow growth with stirring of the solution at temperatures of 283, 293, and 303 K.

3. RESULTS AND DISCUSSION

The crystals grown in the α and β modifications can easily be distinguished by their habit. Single crystals of NH_4LiSO_4 in the α modification have the shape of rectangular plates with perfect cleavage planes (001). In the course of their growth, platelike crystals transform into hexahedra with an angle of 90° (Fig. 1). Single crystals in the β modification have the shape of hexagonal prisms. It is worth noting that crystallization at a temperature of 281 or 283 K results in the formation of the α modification alone, crystallization at 293 K leads to the formation of crystals in both modifications with an equal probability, and crystallization at 303 K brings about the formation of crystals only in the β modification. An analysis of the results obtained in our investigations demonstrated that, in [8], the scheme of the crystallographic axes of the unit cell in the α modification of the NH_4LiSO_4 crystal is invalid. The correct orientation of the crystallographic axes with respect to the growth faces is given in Fig. 1.

As was shown in numerous experiments, single crystals of NH_4LiSO_4 in the α modification slightly differ from one another. In the case when an as-grown crystal obtained through crystallization *1* or *2* (spontaneous growth without stirring of the solution) is held in a dry air atmosphere at room temperature, its transparency rapidly (either totally or partially) disappears. The x-ray powder diffraction pattern taken from the opaque

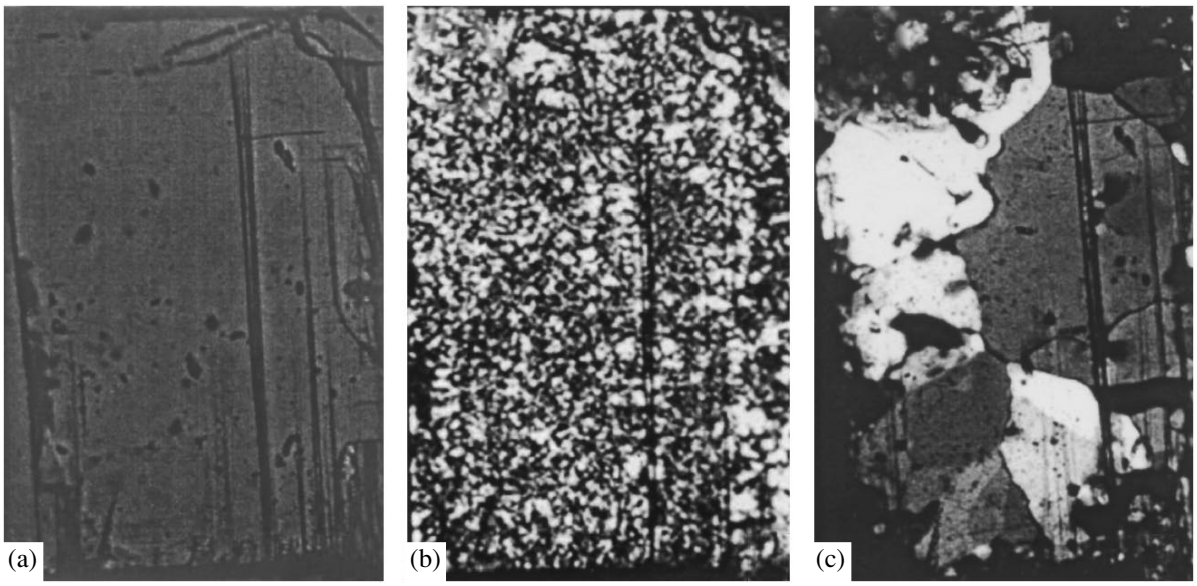

Fig. 2. Micrographs of the (001) cleavage surfaces of α-NLS crystals in polarized light: (a) T = 293 K, clear-cut extinctions; (b) T = 446 K, extinctions are absent; and (c) T = 446 K (exposure, 35 min), well-defined regions of the β phase.

part of the sample corresponds to the β-NLS structure. The transparent part of the sample remains in the α modification. Therefore, the α ⟶ β phase transition can occur at room temperature. When the samples prepared under the same conditions are kept in a hermetically closed vessel for a certain amount of time (two or three months), the process described above is not observed. This process is also not revealed in samples produced by crystallizations *3* and *4*, i.e., in the crystals grown, as might appear at first sight, under "ideal" conditions: very slow growth (within two months) with careful stirring of the solution. Consequently, all crystals grown in the α modification can be divided into two groups, namely, the group *A* (as-grown crystals that are prepared through the spontaneous crystallization without stirring of the solution and can undergo an α ⟶ β monotropic transition in a dry air atmosphere) and the group *B* (crystals grown either under ideal conditions or through any one of the above crystallizations and then held in a hermetically closed vessel during a sufficiently long period of time). Subsequently, the latter crystals keep quite well in a dry atmosphere. As will be shown below, the results of optical and calorimetric experiments performed with crystals of these groups differ significantly.

Upon gradual heating, samples of the *A* group undergo rapid destruction in the temperature range 330–350 K and become totally or partially opaque, as is the case with samples prepared through crystallization *1* or *2* and then held in a dry atmosphere at room temperature.

Crystals of the *B* group upon heating remain transparent and exhibit clear-cut extinctions at temperatures from 100 K to the range 440–450 K, in which there occurs an α ⟶ β phase transformation. As follows from numerous experiments, the α ⟶ β phase transition in the temperature range 440–450 K proceeds very slowly and, under isothermal conditions, does not necessarily lead to destruction of the sample. Figure 2 displays the micrographs obtained for the (001) cleavage surfaces of α-NLS crystals with the use of a polarizing microscope upon heating. It can be seen from Fig. 2a that, at room temperature, the sample is transparent and exhibits clear extinctions. Upon heating of the sample, extinctions become less pronounced at a temperature of 440 K and disappear at 446 K. As a result, the sample turns a speckled gray, which gives the impression that it is optically isotropic. This color is provided by small regions (with a size of the order of several microns) that exhibit extinctions upon rotation of the plate through different angles (Fig. 2b). After isothermal holding for 30 min, part of these regions rapidly grow (Fig. 2c) and transform into transparent regions of β-NLS with clear-cut extinctions. The regions thus formed are relatively large in size and frequently occupy the whole volume of the sample. Judging from the geometry of the optical indicatrices, the crystallographic directions in these regions are random and their orientation is in no way related to the initial crystallographic directions of the α phase. The formation of the β phase can proceed both at a constant temperature and during heating or cooling of the sample but, in all cases, only after the crystal experiences a pseudoisotropic state. However, the regions of the β phase formed upon heating or cooling are considerably larger in size.

The temperature dependences of the birefringence $\Delta n_c = (n_a - n_b)$ for NH_4LiSO_4 crystals in different modifications are shown in Fig. 3. Curve *1* is depicted for comparison and represents the temperature dependence

of the birefringence $\Delta n_c(T)$ for β-NLS crystals with an anomalous behavior in the range of two phase transitions [11]. Experimental data on the birefringence $\Delta n_c(T)$ for the two samples of α-NLS are shown by curves *2*. As can be seen from Fig. 3, the birefringences for different modifications of NH_4LiSO_4 in the [001] direction have opposite signs: $n_a > n_b$ for β-NLS [12] and $n_a < n_b$ for α-NLS. The temperature dependence of the birefringence for α-NLS exhibits linear behavior in the range 250–440 K. At temperatures below 250 K, the straight line smoothly becomes curved without a specific feature that could be assigned to a phase transition. This shape is typical of birefringence "tails" associated with pretransition phenomena (e.g., for $CsLiSO_4$ [13]). We believe that, in this case, the phase transition can occur at temperatures below 100 K. However, the temperature dependence of the birefringence $\Delta n_c(T)$ can deviate from linearity, for example, due to the freezing of a small amount of interlayer water, which, in turn, brings about macroscopic deformation of the sample. Most likely, this is the reason why the temperature dependences of the birefringence for the two samples slightly differ at temperatures below 250 K (Fig. 3). As the temperature increases to higher than 440 K, the birefringence magnitude rapidly decreases to zero and the crystal becomes optically pseudoisotropic, as described above. Note that the birefringence of the studied samples goes to zero at different temperatures. The experiments demonstrated that this point for different samples lies in the temperature range 440–450 K.

The thermodynamic parameters (T_1 = 460 ± 2 K, T_2 = 289 ± 2 K, ΔH_1 = 1170 ± 200 J/mol, ΔH_2 = 280 ± 50 J/mol) for the phase transitions observed in β-NLS crystals grown at a temperature above 300 K were obtained in our previous study [11]. In the present work, these values will be used as reference data in order to determine the state of the studied samples. In the subsequent discussion, we will focus only on the phase transitions occurring in crystals and, hence, will analyze graphic data only on the anomalous heat capacity.

Figure 4 shows the temperature dependences of the excess heat capacity measured in two experiments for as-grown samples of α-NLS (group *A*) crystallized at T = 281 K. The solid line represents the results obtained upon the first heating. As is clearly seen, the excess heat capacity has no anomalies at temperatures of 250 and 289 K, which correspond to the reversible phase transitions in α-NLS [8] and β-NLS ($G_1 \longrightarrow G_2$) [11], respectively. At the same time, the excess heat capacity exhibits an anomaly with a maximum at a temperature of 341 ± 2 K. This is in reasonable agreement with the previously determined temperature of the phase transition between the α and β modifications of NH_4LiSO_4 [8]. The change in the enthalpy associated with this anomaly is estimated as $\Delta H_{\alpha \to \beta}$ = 2400 ± 300 J/mol.

The excess heat capacity measured during the second heating (dashed line in Fig. 4) is characterized by

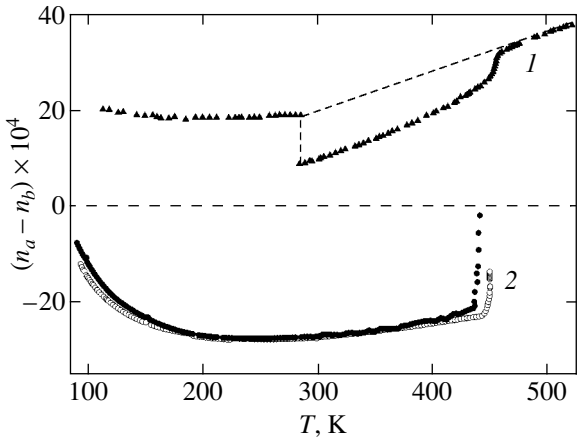

Fig. 3. Temperature dependences of the birefringence $\Delta n_c = (n_a - n_b)$ for NH_4LiSO_4 crystals in the (*1*) β and (*2*) α modifications.

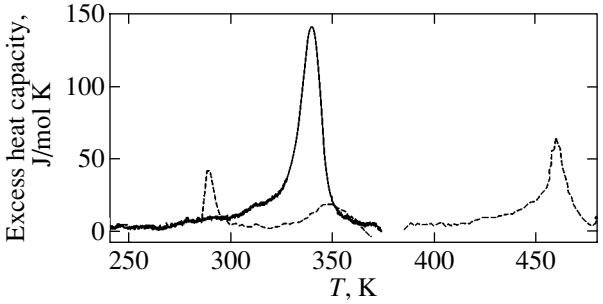

Fig. 4. Temperature dependences of the excess heat capacity for as-grown crystals of α-NLS (group *A*) upon the first heating (solid line) and the second heating (dashed line).

two anomalies at temperatures T_1 = 460 ± 2 K and T_2 = 290 ± 2 K, which correspond to the successive phase transitions $G_0 \longrightarrow G_1 \longrightarrow G_2$ in β-NLS. The enthalpy changes upon these transitions are as follows: ΔH_1 = 900 ± 200 J/mol and ΔH_2 = 280 ± 60 J/mol. These results are also in good agreement with the parameters obtained in our recent work [11] for the NH_4LiSO_4 crystal in the β modification. Therefore, the studied sample of α-NLS undergoes a monotropic phase transition at a temperature $T_{\alpha \to \beta}$ = 341 ± 2 K.

The temperature dependence of the excess heat capacity for a single crystal of α-NLS (group *B*) upon the first heating after prolonged holding at room temperature in a hermetically closed vessel is depicted by the solid line in Fig. 5. It can be clearly seen that, as in the preceding case, the excess heat capacity does not exhibit anomalies at temperatures of ~250 and ~289 K. However, we also did not reveal the anomaly attributed to the $\alpha \longrightarrow \beta$ phase transition at a temperature close to 341 K, which was observed for the as-grown sample of α-NLS upon the first heating. With a further increase in the temperature, there appears an anomaly in the

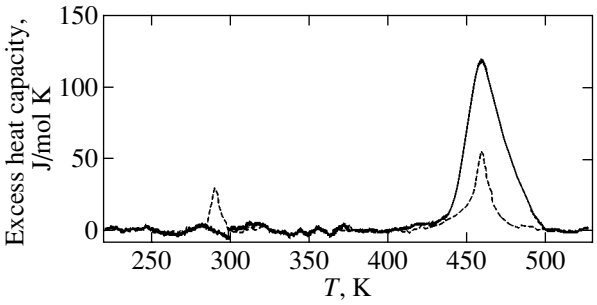

Fig. 5. Temperature dependences of the excess heat capacity for single crystals of α-NLS (group *B*) upon the first heating (solid line) and the second heating (dashed line).

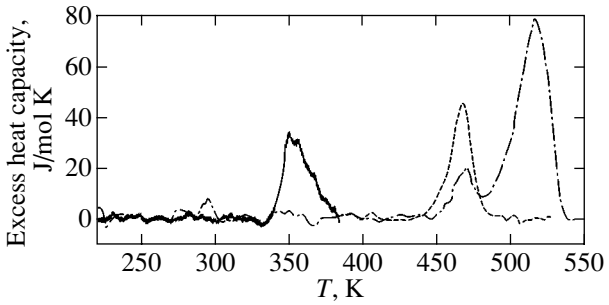

Fig. 6. Temperature dependences of the excess heat capacity for as-grown crystals of α-NLS (crystallization *3*) upon the first heating to 380 K (solid line), the second heating (dot-dashed line), and the third heating after cooling to ~370 K (dashed line).

excess heat capacity with a maximum at a temperature of 460 ± 2 K, which coincides with the temperature of the $G_0 \longrightarrow G_1$ phase transition in β-NLS [11]. It could be assumed that, in the course of ageing, the sample undergoes a monotropic phase transformation at room temperature, as in the situation described above. However, the change in the enthalpy associated with the observed anomaly in the heat capacity was found to be ΔH = 3600 ± 500 J/mol; this value substantially exceeds the enthalpy change characteristic of the $G_0 \longrightarrow G_1$ phase transition in β-NLS [11]. Such a large change in the enthalpy agrees satisfactorily with the sum of the enthalpies of the α ⟶ β monotropic phase transition ($\Delta H_{\alpha \to \beta} \approx 2400$ J/mol) and the $G_0 \longrightarrow G_1$ enantiotropic phase transition in β-NLS ($\Delta H_1 \approx 1000$ J/mol). Upon repeated heating, the sample is characterized by two anomalies in the excess heat capacity (dashed line in Fig. 5) with thermodynamic parameters (T_1 = 459 ± 2 K, T_2 = 290 ± 2 K, ΔH_1 = 920 ± 200 J/mol, ΔH_2 = 220 ± 50 J/mol) typical of phase transitions in β-NLS single crystals.

Analysis of the results obtained in the calorimetric investigations of as-grown samples prepared through slow growth under isothermal conditions with careful stirring of the solution (crystallizations *3*, *4*) demonstrated that the structure of bulk samples can contain crystal blocks of both groups *A* and *B* simultaneously. The experimental temperature dependences of the excess heat capacity for these samples are displayed in Fig. 6. The behavior of the excess heat capacity during the first heating to 380 K is illustrated by the solid line. As can be seen, no anomalies in the heat capacity are observed at temperatures of 250 and 289 K. However, as is the case with the sample prepared through crystallization at 281 K, there appears a small anomaly at a temperature of 347 ± 2 K due to the phase transition to the ferroelectric phase β-NLS. The enthalpy change (≈720 J/mol) proves to be considerably less than the predicted value and amounts to approximately 1/3 of the total enthalpy change $\Delta H_{\alpha \to \beta}$. Upon the second heating (dot-dashed line in Fig. 6), as could be expected, the excess heat capacity has an anomaly at a temperature of 293 ± 2 K, which is attributed to the $G_1 \longrightarrow G_2$ phase transition in β-NLS. It is worth noting that, in this case, the enthalpy change (≈100 J/mol) also amounts to approximately 1/3 of the total value ΔH_2. In the high-temperature range, the excess heat capacity measured during the second heating exhibits two more peaks, at temperatures of 465 ± 2 and 515 ± 2 K. The first temperature corresponds to the $G_0 \longrightarrow G_1$ phase transition in β-NLS, and the enthalpy change is also approximately equal to 1/3 of the total value ΔH_1. Integration with respect to the area under the peak in the heat capacity at T = 515 K gives an enthalpy change of ≈2200 J/mol, which amounts to approximately 2/3 of the sum $\Delta H_{\alpha \to \beta} + \Delta H_1$. Upon the third heating (dashed line in Fig. 6) after cooling to ≈370 K, the excess heat capacity is characterized by only one anomaly with thermodynamic parameters (T_1 = 465 ± 2 K, ΔH_1 = 860 ± 150 J/mol) typical of the $G_0 \longrightarrow G_1$ phase transition in β-NLS. The observed change in the enthalpy indicates that, after the second heating, the sample completely transforms into the β-NLS modification. Therefore, it can be concluded that the studied sample initially consisted of two parts with different temperatures of the α ⟶ β phase transition. The shift in the maxima of the heat capacity anomalies toward the high-temperature range above 450 K due to the α ⟶ β phase transition can be explained in terms of the kinetics of the process. According to observations made under a microscope, the time required to accomplish this phase transition is considerably longer than the time it takes for the studied sample to be heated in the course of a differential scanning microcalorimetric experiment at rates of 2–8 K/min.

An examination of the other samples prepared through crystallization *3* revealed that the percentage ratio between crystal parts with different temperatures of the α ⟶ β phase transition changes from case to case. For example, we obtained a sample in which only 5% of the entire volume was occupied by the crystal

undergoing a monotropic phase transition in the temperature range 340–350 K (group *A*).

Moreover, we made an attempt to establish a correlation between the existence of polytypes in the structure of α-NLS crystals [7] and the phase transition temperatures or the shape of the heat capacity anomaly discussed in [8]. It turned out that the x-ray diffraction patterns of the (001) single-crystal plates contain a large number of reflections. In addition to the (0 0 *h*) reflections (*h* is an even index), which are characteristic of all polytypes, the x-ray diffraction patterns exhibit reflections corresponding to the lattice parameters $c_2 \approx 34$ Å or $c_3 \approx 51$ Å. The intensities of the latter reflections also change from sample to sample. Hence, we believe that polytypes actually exist in the structure of α-NLS crystals; however, their influence on the experimental results was not revealed.

It seems likely that the origin of the α ⟶ β phase transition at room temperature can be explained in terms of the structural features inherent in the α modification. The crystal structure of α-NLS is composed of widely spaced tetrahedral layers with ammonium ions between them [6, 7]. Consequently, the solvent can be adsorbed in interlayer cavities during the crystal growth. The adsorption of the solvent most probably occurs in the course of a rapid growth, even without stirring of the solution, when the salt concentration decreases in the vicinity of the growing facet of the crystal. If the as-grown crystal is placed in a dry atmosphere, the water involved evaporates, thus initiating the α ⟶ β phase transformation of the structure. This process proceeds more vigorously in the region of intensive vaporization. Under the conditions where the crystal grows slowly or when the sample is held in a closed vessel, there occurs diffusional relaxation of impurities along the layers toward the crystal edges.

In order to verify the above assumption, we examined the behavior of a saturated solution under a microscope in the temperature range 200–350 K. It was found that the studied solution solidifies at a temperature of 250 K and undergoes melting at 256 K. The most intensive evaporation of the water from a saturated solution during heating is observed at temperatures above 330 K. For the same purpose, we performed a calorimetric investigation of the sample in the α modification prepared through the crystallization at a high rate (3–4 days). As can be seen from Fig. 7, the excess heat capacity of α-NLS crystals exhibits an anomaly with the maximum at a temperature of 255 ± 2 K (upon heating), which is in reasonable agreement with the results obtained in [8]. This anomaly was reproduced only in the case when the sample was not preliminarily heated to a temperature above 340–350 K, for which the mass loss of the sample reached approximately 2%.

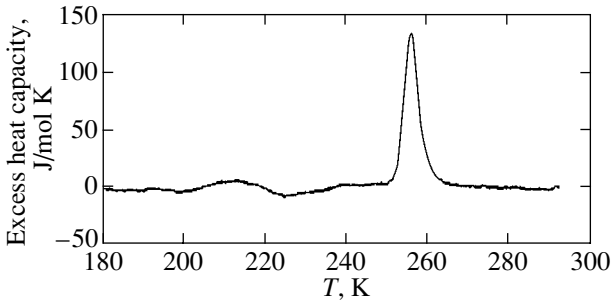

Fig. 7. Temperature dependence of the excess heat capacity for α-NLS prepared through crystallization at a high rate (3–4 days).

4. CONCLUSIONS

Thus, the experimental investigations of the birefringence and heat capacity demonstrated that no structural phase transition occurs in α-NLS crystals at a temperature of 250 K. The anomaly observed in the heat capacity in this range of temperatures was attributed to the incorporation of a large amount of water into the studied sample.

It was established that, depending on the conditions of growth and storage of NH_4LiSO_4 crystals, the temperature of the α ⟶ β monotropic phase transition can vary from room temperature to the boiling point of the salt solution (crystals of the *A* group). This transition is accompanied by complete destruction of the sample. Under the conditions where the crystals slowly grow with stirring or when the samples are held in a moist air atmosphere over a sufficiently long period of time (crystals of the *B* group), the α ⟶ β phase transition occurs in the temperature range 440–450 K. The crystal structure of these samples undergoes a slow transformation (recrystallization) without noticeable distortions. It was assumed that, in the temperature range 340–350 K, the reconstructive phase transition is initiated by the evaporation of a small amount of the water incorporated into the interlayer cavities (crystals of the *A* group). With time, the water molecules diffuse toward the crystal edges (crystals of the *B* group). The enthalpies of this transformation, which can proceed at different temperatures, also differ significantly. This can be explained by the fact that the NH_4LiSO_4 compound undergoes a phase transition to the G_1 ferroelectric phase of the β modification at $T = 340$–350 K and a phase transition to the G_0 paraelectric phase at $T \geq 460$ K. The investigations performed did not reveal a unique correspondence between the existence of polytypes in the structure of the α modification and the phase transition temperature $T_{\alpha \to \beta}$.

ACKNOWLEDGMENTS

This work was supported by the Russian Foundation for Basic Research, project no. 00-15-96790.

REFERENCES

1. A. I. Kruglik, M. A. Simonov, and K. S. Aleksandrov, Kristallografiya **23**, 494 (1978) [Sov. Phys. Crystallogr. **23**, 274 (1978)].
2. K. Itoh, H. Ishikura, and E. Nakamura, Acta Crystallogr. B **37**, 664 (1981).
3. A. Dollase, Acta Crystallogr. B **25**, 2298 (1969).
4. X. Solans, J. Mata, M. T. Calvet, and M. Font-Bardia, J. Phys.: Condens. Matter **11**, 8995 (1999).
5. M. Polomska, Phase Transit. **74**, 409 (2001).
6. A. Pietraszko and K. Lukaszewicz, Pol. J. Chem. **66**, 2057 (1992).
7. P. E. Tomaszewski, Solid State Commun. **81** (4), 333 (1992).
8. M. Polomska, B. Hilczer, and J. Baran, J. Mol. Struct. **325**, 105 (1994).
9. V. N. Anisimova and N. R. Ivanov, Kristallografiya **31** (5), 1018 (1986) [Sov. Phys. Crystallogr. **31**, 605 (1986)].
10. N. R. Ivanov and L. F. Kirpichnikova, Izv. Akad. Nauk SSSR, Ser. Fiz. **51** (12), 2216 (1987).
11. S. V. Mel'nikova, A. V. Grankina, and A. V. Kartashev, Fiz. Tverd. Tela (St. Petersburg) **44** (2), 365 (2002) [Phys. Solid State **44**, 379 (2002)].
12. A. T. Anistratov and S. V. Mel'nikova, Izv. Akad. Nauk SSSR, Ser. Fiz. **39** (4), 808 (1975).
13. S. V. Melnikova, A. D. Vasiliev, V. A. Grankina, *et al.*, Ferroelectrics **170**, 139 (1995).

Translated by O. Borovik-Romanova

Physics of the Solid State, Vol. 45, No. 8, 2003, pp. 1579–1585. Translated from Fizika Tverdogo Tela, Vol. 45, No. 8, 2003, pp. 1503–1509.

LOW-DIMENSIONAL SYSTEMS AND SURFACE PHYSICS

Acoustic, Optical, and Interface Phonons in BeTe/ZnSe Superlattices

I. I. Reshina, S. V. Ivanov, V. A. Kosobukin, S. V. Sorokin, and A. A. Toropov

Ioffe Physicotechnical Institute, Russian Academy of Sciences, Politekhnicheskaya ul. 26, St. Petersburg, 194021 Russia

e-mail: reshina@dnm.ioffe.rssi.ru

Received December 23, 2002

Abstract—Raman scattering in a number of BeTe/ZnSe type-II superlattices which share no common cations or anions in the interfaces was studied. Folded acoustic phonons; LO phonons of the first, second, and third order in the ZnSe layers; and Kliewer–Fuchs-type electrostatic interface phonons were observed when excited in resonance with the direct exciton transition in the ZnSe layers. Nonresonant excitation produced LO phonons in the ZnSe and BeTe layers and a high-frequency mechanical interface mode, assigned tentatively to a local vibration of the interface Be–Se bond. © *2003 MAIK "Nauka/Interperiodica".*

1. INTRODUCTION

AB/CD-type semiconductor superlattices (SLs) with zinc blende structure have recently been attracting considerable interest. The specific features of such SLs originate from the absence of common cation or anion atoms at their interfaces. Chemical bonds on both sides of the interface in a structure with a zinc blende lattice and a single heterointerface lie in mutually perpendicular planes, $(1\bar{1}0)$ and (110), which may result in optical anisotropy in the interface plane. The optical properties for light polarizations $\mathbf{e} \parallel [1\bar{1}0]$ and $\mathbf{e} \parallel [110]$ are different. In symmetric quantum wells with a common anion in the wells and barriers, this optical anisotropy has opposite signs at the direct and inverted interfaces and, therefore, is not manifested (canceled), provided both interfaces are equivalent. In *AB/CD*-type structures, however, the direct and inverted interfaces can differ chemically, thus producing strong optical anisotropy (up to 80–90%). A theoretical analysis of related problems can be found in [1, 2].

The BeTe/ZnSe structure belongs to the new *AB/CD*-type of superlattices. Its band structure has been established to be type II and to have very large band offsets [3]. The minimum of the conduction band is in the ZnSe layers, and the maximum of the valence band is in the BeTe layers. The electron and hole wave functions overlap only near the interfaces, and, therefore, the latter play a very essential role. The two interfaces (direct and inverted) are, in general, chemically different and contain specific bonds of the BeSe and ZnTe type which do not exist in the inner SL layers. The optical anisotropy of such SLs with inequivalent interfaces manifests itself in a very large linear polarization of indirect exciton luminescence [4–6].

The absence of common atoms at the interfaces also affects the phonon spectra. Calculations performed for the InAs/GaSb superlattice in terms of a linear chain model [7] have shown that the existence of specific GaAs- and InSb-type bonds at the interfaces gives rise to the formation of two additional specific phonon modes (transverse and longitudinal) which are localized at the interfaces. One of these modes, originating from the GaAs bond (at the so-called "light interface"), is very strongly localized and has the highest frequency in the spectrum. The other mode, caused by the InSb bond at the "heavy interface", lies between the acoustic and optical regions of the SL phonon spectrum and is localized more weakly. Similar modes were observed experimentally in the InAs/GaSb [8, 9] and CdSe/ZnTe [10, 11] SLs by using Raman spectroscopy. These local modes are sensitive to the nature and quality of an interface, and it was suggested that they could be employed for interface characterization.

To the best of our knowledge, Raman scattering from phonons in BeTe/ZnSe superlattices was studied only in [12], where folded acoustic and LO phonons of the BeTe and ZnSe layers were observed. It thus appears of interest to further the investigation of Raman scattering in BeTe/ZnSe superlattices under resonant and nonresonant excitation and to attempt to observe the interface phonons.

2. SAMPLE PREPARATION AND EXPERIMENTAL TECHNIQUES

We studied two sets of BeTe/ZnSe SLs grown through molecular-beam epitaxy (MBE). The SLs were grown on (001)-oriented GaAs semi-insulating substrates. An epitaxial GaAs buffer was grown to improve the surface quality. The growth was conducted at a substrate temperature of 300°C. In the first set, intended primarily for polarized-luminescence measurements, a 20-period BeTe(1.8 nm)/ZnSe(5 nm) superlattice was

Table 1. Superlattice parameters

Sample no.	Number of periods	$d = d_1 + d_2$, nm	d_1, nm (ZnSe)	d_2, nm (BeTe)	Interface type (determined by growth)
1522	20	6.76	4.97	1.79	ZnTe
1794	10	9.5	6.0	3.5	ZnTe
1795	10	8.0	3.76	4.24	ZnTe
1797	10	3.3	≈0.8	2.5	ZnTe
1798	10	3.3	≈0.8	2.5	ZnTe and BeSe
1799	10	3.3	≈0.8	2.5	BeSe

grown between comparatively thick $Be_{0.03}Zn_{0.97}Se$ cladding layers. The growth was performed in such a way as to make all interfaces primarily ZnTe type. With this purpose in mind, the BeTe–ZnSe interface (ZnSe epitaxy on BeTe), for example, was obtained by growing a 0.5 ZnTe monolayer on the BeTe surface, which terminated in Te atoms. After this, the Te source was shuttered and the surface was exposed to Zn flux for one second. The BeTe epitaxy on ZnSe was carried out with the shutters operating in the opposite sequence. The thicknesses of the ZnSe and BeTe layers were determined from x-ray measurements. The SL 1522 belongs to this type. The second SL set was prepared without $Be_{0.03}Zn_{0.97}Se$ layers. The substrate was not rotated during the course of growth. This resulted in a gradient in the Te/Be flux ratio and in the layer thicknesses along a certain direction in the sample plane. These SLs consisted of ten periods only; their central thicknesses derived from x-ray measurements and calibrated growth rates are listed in Table 1. Note that the layers in our samples are very thin; therefore, their properties should be very sensitive to the interfaces. In structures with ultrathin ZnSe films (2–3 monolayers) sandwiched between 2.5-nm thick BeTe layers, the concentration of interface bonds is comparable to that of the regular ZnSe bonds. As follows from x-ray studies, one cannot avoid the formation of BeSe bonds even when trying to grow only ZnTe-type interfaces [13]. As we see later on, this conclusion is supported by Raman studies.

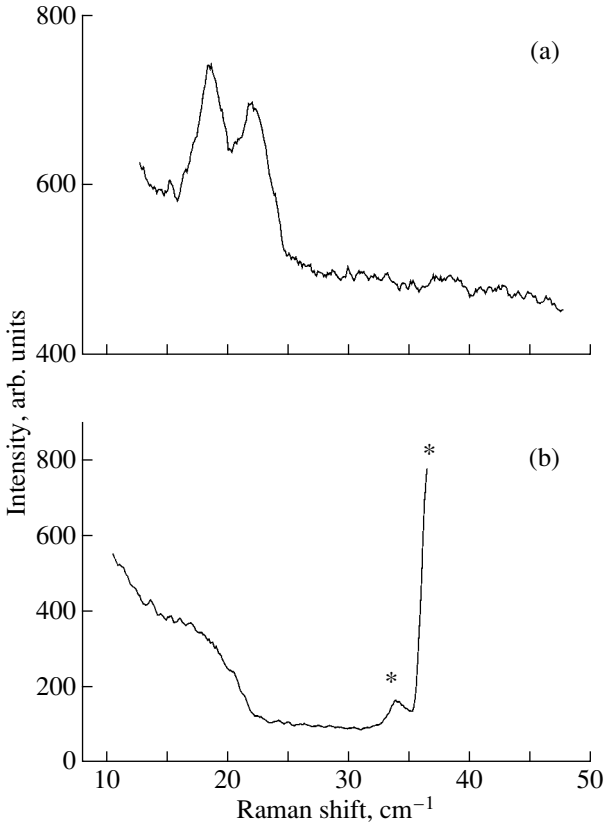

Fig. 1. (a) Raman scattering spectrum from folded acoustic phonons in SL 1522 obtained in the Stokes region; E_{ex} = 2.807 eV (resonance with the ZnSe exciton), T = 300 K. (b) Raman spectrum obtained under nonresonant excitation; E_{ex} = 2.54 eV (note scattering from the GaAs substrate; the star identifies the laser plasma line).

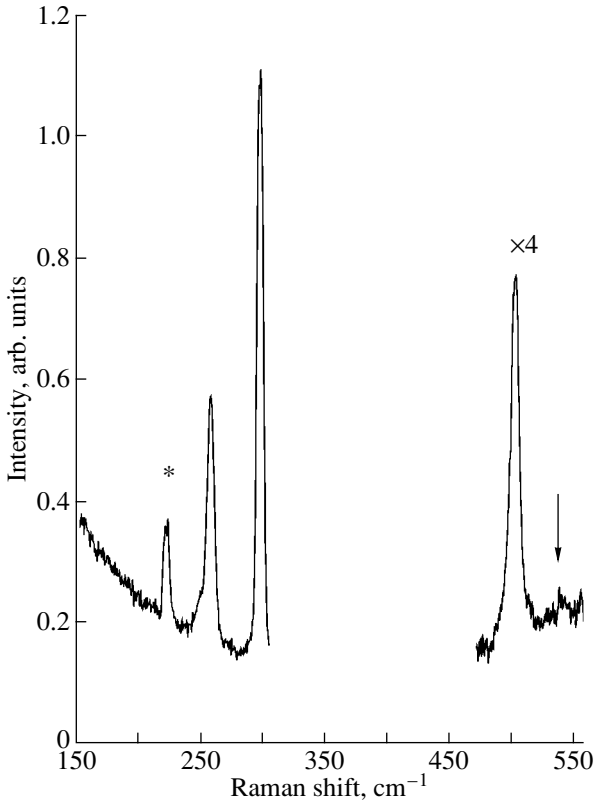

Fig. 2. Raman spectrum of SL 1522 obtained under nonresonant excitation in the optical phonon region; E_{ex} = 2.54 eV, T = 100 K. Note the scattering lines from the layers of the ZnSe (250 cm^{-1}), BeTe (497 cm^{-1}), and GaAs substrates (291 cm^{-1}). The very weak line at 534.6 cm^{-1} indicated by an arrow is tentatively assigned to interface Be–Se bonds. The star identifies the laser plasma line.

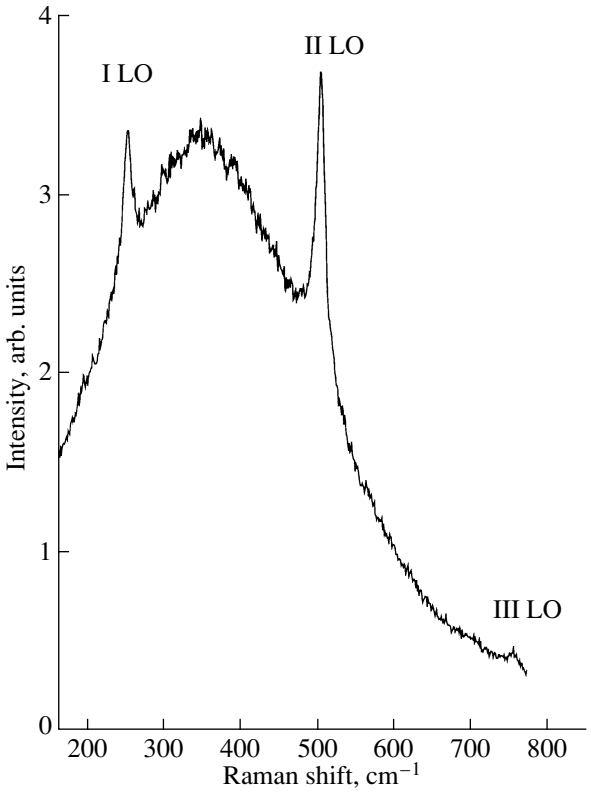

Fig. 3. Raman spectrum of SL 1522 obtained under excitation in resonance with the direct ZnSe exciton. E_{ex} = 2.807 eV, T = 300 K. Raman scattering from first-, second-, and third-order ZnSe LO phonons is seen against the background of the luminescence band from the claddings.

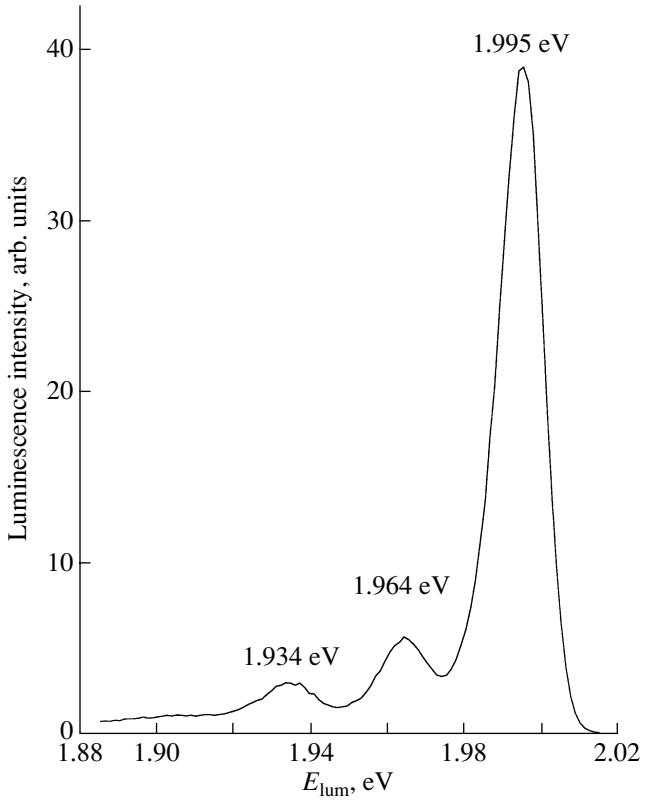

Fig. 4. Luminescence band of SL 1795 and two bands of its phonon replicas due to the ZnSe and BeTe LO phonons. T = 30 K, E_{ex} = 2.54 eV.

Raman scattering measurements were conducted in the 90° geometry at temperatures of 100 and 300 K on a double-monochromator U-1000 spectrometer (Jobin–Yvon) with a linear dispersion of 0.24 nm/cm. The spectra were excited by the 488-nm Ar^+ laser line or the 441.6-nm line of an He–Cd laser. The luminescence was measured at 30 K under excitation by the 488-nm line of an Ar^+ laser.

3. EXPERIMENTAL RESULTS, CALCULATIONS, AND DISCUSSION

Figure 1a presents a Raman spectrum of the SL 1522 obtained in the acoustic-phonon region under excitation by the 441.6-nm (2.807 eV) He–Cd laser line. At room temperature, this excitation energy is in resonance with the direct excitonic transition in the ZnSe layer. Even when measured at a low pump intensity (less than 2 mW), the spectrum in the Stokes and anti-Stokes regions exhibited a characteristic doublet peak corresponding to a first-order folded acoustic phonon. We used the frequency ν = 20.3 cm^{-1}, corresponding to the center of the doublet peak, and the sound velocity for ZnSe, $v = 4.07 \times 10^5$ cm/s, to derive the SL period $d = \nu/cv$ = 66.8 Å, which is in good agreement with the x-ray data listed in Table 1. The presence of a folded-phonon doublet peak in the spectrum argues for a high homogeneity in the period and in the layer thickness, as well as a satisfactory interface quality. No folded-phonon peaks were observed under nonresonant excitation (Fig. 1b). They are probably masked by some steplike structure in the spectrum, which is related apparently to scattering from the substrate or the GaAs buffer layer.

Figure 2 displays a Raman spectrum of the SL in the optical phonon region obtained under nonresonant pumping. The peak at 250 cm^{-1} is due to the LO phonon from the SL ZnSe layers and the $Be_{0.03}Zn_{0.97}Se$ cladding. The strong peak at 291 cm^{-1} corresponds to the LO phonon of the substrate and the GaAs buffer. The 497.0-cm^{-1} peak originates from the BeTe-layer LO phonon. A very weak peak is observed at 534.6 cm^{-1}. We assign this peak tentatively to interface BeSe bonds. The existence of such bonds (i.e., the inequivalence of the interfaces) is argued for by the very substantial (~50%) linear luminescence polarization of the indirect transition in this BeTe/ZnSe superlattice.

Figure 3 shows a Raman spectrum obtained under excitation in resonance with the direct exciton transi-

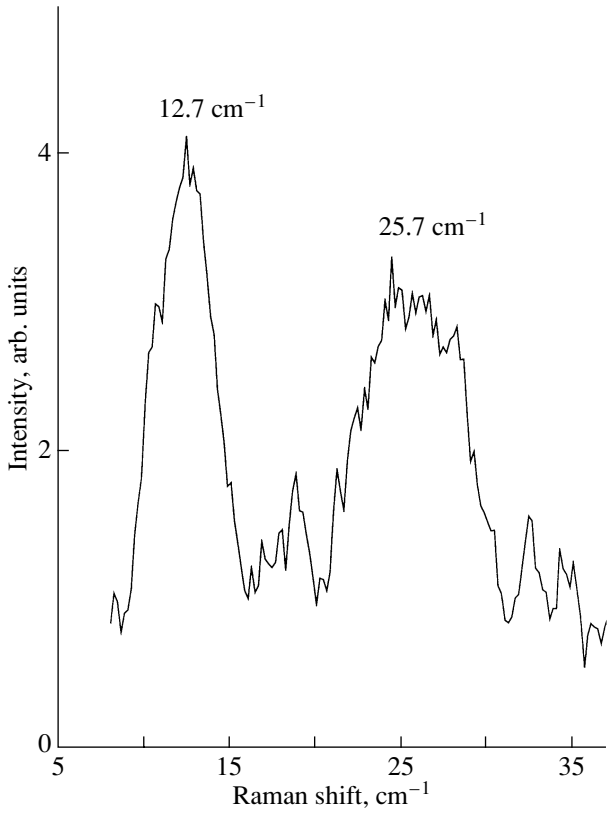

Fig. 5. Raman spectrum of SL 1794 from folded acoustic phonons of the first and second order obtained under resonance excitation (E_{ex} = 2.807 eV). T = 300 K. No doublet structure of the bands is observed.

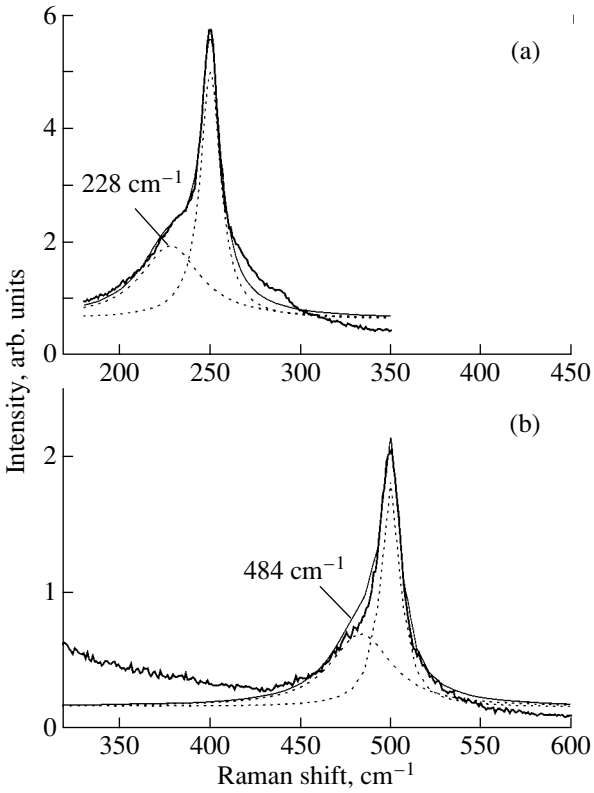

Fig. 6. Raman spectrum of SL 1794 from the ZnSe LO phonon of (a) the first and (b) second order obtained under excitation in resonance with the ZnSe exciton. E_{ex} = 2.807 eV, T = 300 K. Dashed lines illustrate unfolding of the observed peaks into two Gaussians. The low-frequency profiles correspond to (a) ZnSe-like and (b) BeTe-like electrostatic interface modes of the SL.

tion in ZnSe. One clearly sees strong first-, second-, and third-order LO phonons from the ZnSe layers superposed on the luminescence band produced in the BeZnSe cladding. Unfortunately, the ZnSe 2LO-phonon frequency in the BeTe/ZnSe superlattice coincides with the BeTe LO phonon frequency, with the result that the peaks corresponding to BeTe and to the BeSe interface mode excited in resonance with the direct ZnSe exciton are not seen. Excitation in resonance with the BeTe band gap is impossible because the gap width is in excess of 4 eV.

Let us turn now to a discussion of the results obtained with SLs without the cladding layers. As an illustration, consider the luminescence spectrum of SL 1795 measured at 30 K. We clearly see the indirect exciton transition line, as well as two replicas corresponding to the ZnSe and BeTe LO phonons. The linear polarization is ~10%. Excitation in resonance with the ZnSe direct exciton was achieved on SL 1794. Figures 5 and 6 display the corresponding Raman spectra in the acoustic- and optical-phonon regions, respectively. We believe that the peaks in Fig. 5 are due to unresolved first- and second-order folded phonons. The SL period, as derived from their frequencies, lies within the interval of the period values 84–105 Å determined from x-ray measurements for the sample from which the small piece used in the measurements was cleaved out. The fact that the peaks do not resolve in doublets implies a certain inhomogeneity of the sample, as well as a possible additional broadening associated with the small number of periods. As in the case of SL 1522 (see above), no folded phonons were observed under nonresonant excitation.

The optical-phonon region (Fig. 6) revealed strong ZnSe LO and 2LO phonon peaks. An unresolved structure is seen on the low-frequency side of these peaks. Each of the peaks was unfolded into two Gaussians, as shown in Fig. 6 by dashed lines. The low-frequency peaks lie at 228 and 484 cm^{-1}. We identify them with Kliewer–Fuchs-type electrostatic interface modes, which are related to the difference between the dielectric functions $\varepsilon_1(\omega)$ and $\varepsilon_2(\omega)$ of the two adjacent media. The intensity of the interface modes of this type is enhanced under resonance excitation. Neglecting

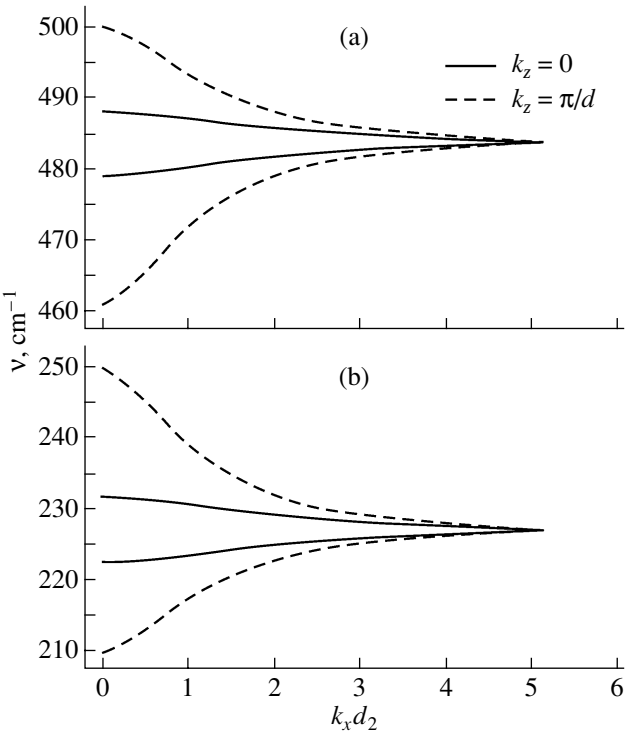

Fig. 7. Calculated electrostatic interface phonon miniband frequencies for SL 1794 plotted vs. $k_x d_2$ (d_2 is the BeTe layer thickness). $k_z = 0$ and π/d.

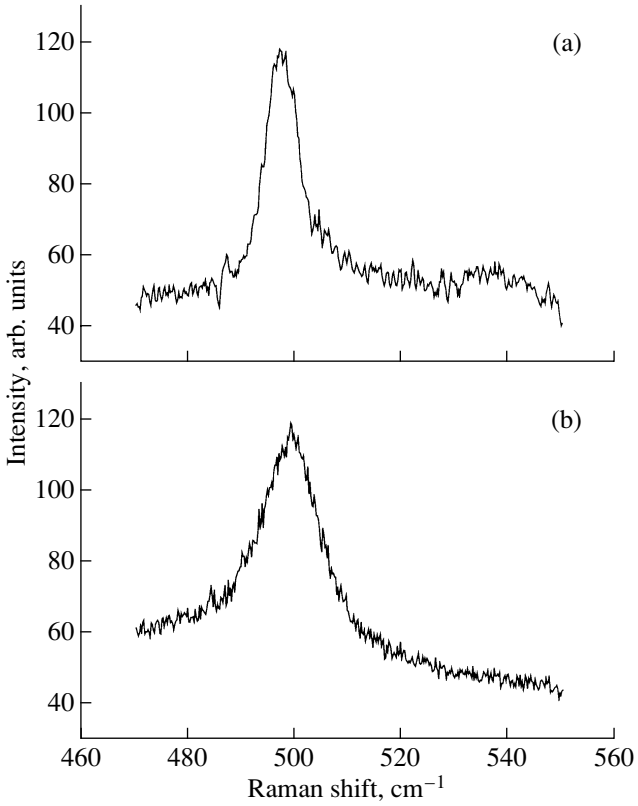

Fig. 8. Raman spectrum of SL 1794 in the region of 500 cm^{-1}. (a) E_{ex} = 2.54 eV and (b) E_{ex} = 2.807 eV (resonance with the ZnSe exciton). Spectrum (a) shows the BeTe LO phonon line and the local interface mode of Be–Se bond. Spectrum (b) shows only the broader line due to the ZnSe 2LO phonon.

retardation, their frequencies $\omega(k_x)$ can be derived from the dispersion relation [14]

$$\cos(k_z d) = [(\eta^2 + 1)/2\eta]\sinh(k_x d_1)\sinh(k_x d_2) + \cosh(k_x d_1)\cosh(k_x d_2), \quad (1)$$

where $d = d_1 + d_2$ and $\eta = \varepsilon_1(\omega)/\varepsilon_2(\omega)$. Here, $\varepsilon_1(\omega)$ and $\varepsilon_2(\omega)$ are the dielectric functions of ZnSe and BeTe, respectively, with $\varepsilon_i = \varepsilon_i^{\infty}(\omega^2 - \omega_{LOi}^2)/(\omega^2 - \omega_{TOi}^2)$, where ω_{LOi} and ω_{TOi} are the frequencies of the longitudinal and transverse optical phonons for the ith layer. Figure 7 plots the phonon frequencies calculated using Eq. (1) vs. $k_x d_2$ for the values $k_z = 0$ and π/d corresponding to the phonon miniband edges for the given value of k_x. The minibands of allowed frequencies are separated by a gap. The experimental values of the interface mode frequencies agree with the calculations for large values of k_x. Thus, scattering from interface modes occurs without wave vector conservation, which is possible with the participation of impurities and surface roughness [15].

Figure 8 compares two Raman spectra in the region of the BeTe LO phonon. The spectrum in Fig. 8a, which was obtained under nonresonant excitation, contains the BeTe LO phonon line and a higher-frequency mode, which we assign to the interface Be–Se bond. The spectrum in Fig. 8b, obtained under excitation in resonance with the ZnSe exciton, exhibits only the broader line of the ZnSe 2LO phonon. Thus, the line associated with the BeSe mode does not apparently undergo noticeable enhancement under excitation in resonance with the direct ZnSe exciton (in contrast to the electrostatic interface modes discussed above). This may indicate that the direct exciton is strongly localized within the ZnSe layer and only weakly overlaps the mechanical interface mode extending only over a few atomic layers.

Figure 9 displays Raman spectra of three SLs, 1797, 1798, and 1799, with BeTe layers equal in thickness (about 2.5 nm) and with very thin (2–3 monolayers) ZnSe layers. Attempts were made to grow only ZnTe-type interfaces in the SL 1797, alternate ZnTe-

Table 2. Longitudinal optical phonon frequencies and force constants of chemical bonds

Compound	ν_{LO}, cm^{-1}	κ, 10^5 dyn/cm
BeTe	500	0.621
ZnSe	250	0.66
BeSe	575	0.789
ZnTe	209	0.552

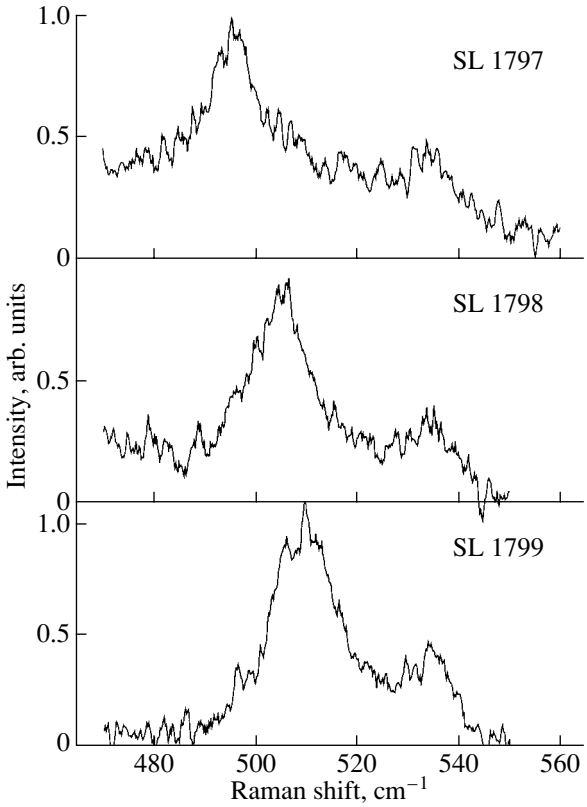

Fig. 9. Raman spectra in the region of 500 cm^{-1} obtained for three SLs with the shortest periods (SL 1797, 1798, 1799) grown in different conditions. The presence of a high-frequency line in the spectra indicates the existence of interface Be–Se bonds in all three samples. The relative intensity of this line (compared to the BeTe LO phonon line) is higher in short-period SLs.

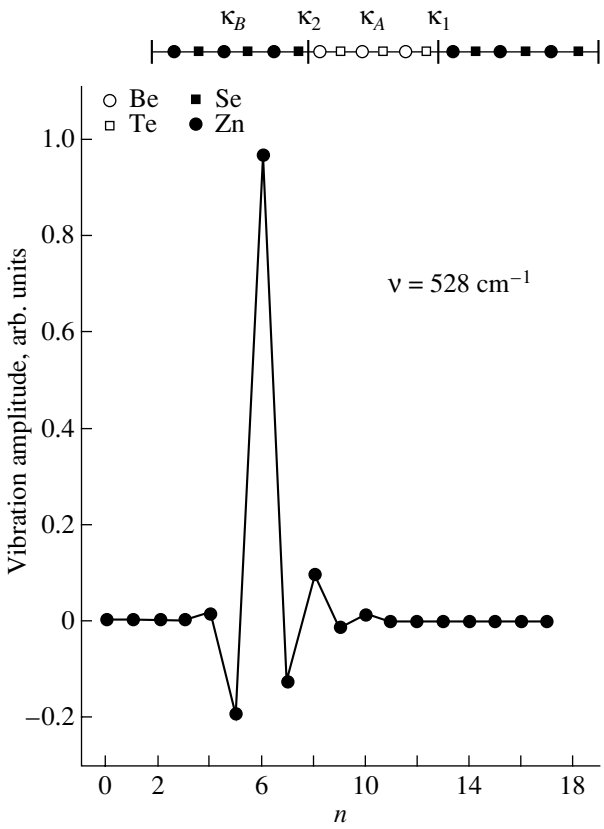

Fig. 10. Amplitude of atomic vibrations at the Be–Se interface for the 528-cm^{-1} mode. The calculation was carried out in terms of the linear–chain model for a structure of the type shown in the inset.

and BeSe-type interfaces in the SL 1798, and only BeSe-type interfaces in the SL 1799. However, the relative BeSe line intensity is seen to be only slightly higher in SL 1799. This signals the presence of interfaces of both types in all three SLs, irrespective of the growth conditions, which correlates with the x-ray measurements. It should be stressed, however, that the relative intensity of the BeSe line in these short-period samples is higher than in samples with a large period (for instance, in sample 1522), which finds natural explanation in the larger volume fraction of interfaces in the short-period samples. The fact that the BeTe LO phonon line in SLs 1798 and 1799 is broader and shifted toward higher frequencies may indicate poorer sample quality and the existence of additional stresses.

We carried out calculations of the Be–Se bond vibration frequency in terms of the linear-chain model for a structure of the type shown in the inset to Fig. 10. Only the nearest neighbor interactions were included. The linear-chain model yields the following equation of vibrational motion in the [001] direction for the nth atom with a displacement $u_n = e^{-i\omega t}U_n$:

$$-m_n\omega^2 U_n = \kappa_{n-1,n}(U_{n-1} - U_n) - \kappa_{n,n+1}(U_n - U_{n+1}), \quad (2)$$

where n is the atomic index ($1 \le n \le N$), m_n is its mass, and the effective force constants κ were chosen so that the linear chain model [16] reproduces the LO phonon frequencies for the bulk BeTe, ZnSe, BeSe, and ZnTe materials. These force constants are listed in Table 2.

Solving coupled equations (2) yields the frequency eigenvalues and the corresponding eigenvectors of normal vibrations. The results obtained show that the number of eigenfrequencies increases and their values change with increasing number of atoms. The maximum frequency 528 cm^{-1} (which exceeds the BeTe LO phonon frequency) does not, however, depend on N, and the corresponding eigenvector, as is evident from Fig. 10, has a noticeable magnitude only in the immediate vicinity of the BeSe light interface. The amplitude is the largest for the Be atom near the interface (the

sixth atom in the structure depicted in Fig. 10). Thus, we assign the frequency of 528 cm^{-1} to a local interface Be–Se bond mode. There is no such frequency in a structure that does not have Be–Se-type bonds. In view of the rough character of the calculations, the calculated Be–Se bond frequency may be considered to agree well with the experiment (534 cm^{-1}).

ACKNOWLEDGMENTS

The authors are indebted to A. Waag from the University of Ulm for cooperating in the MBE growth of the samples.

This study was supported by the Russian Foundation for Basic Research (project no. 00-02-16997); the Ministry of Industry, Science, and Technologies of the Russian Federation (project no. 95 and the program "Physics of Solid-State Nanostructures"); and the Russian–Ukrainian research program "Nanophysics and Nanoelectronics."

REFERENCES

1. O. Krebs and P. Voisin, Phys. Rev. Lett. **77** (9), 1829 (1996).
2. E. L. Ivchenko, A. A. Toropov, and P. Voisin, Fiz. Tverd. Tela (St. Petersburg) **40** (10), 1925 (1998) [Phys. Solid State **40**, 1748 (1998)].
3. A. Waag, F. Fischer, H. J. Lugauer, *et al.*, J. Appl. Phys. **80** (2), 792 (1996).
4. D. R. Yakovlev, E. L. Ivchenko, V. P. Kochereshko, *et al.*, Phys. Rev. B **61** (4), R2421 (2000).
5. A. A. Maksimov, S. V. Zaitsev, P. S. Dorozhkin, *et al.*, Phys. Status Solidi B **229** (1), 35 (2002).
6. D. R. Yakovlev, A. V. Platonov, E. L. Ivchenko, *et al.*, Phys. Rev. Lett. **88** (25), 257401 (2002).
7. A. Fasolino, E. Molinari, and J. C. Maan, Phys. Rev. B **33** (12), 8889 (1986).
8. B. V. Shanabrook, B. R. Bennett, and R. J. Wagner, Phys. Rev. B **48** (23), 17172 (1993).
9. S. G. Lyapin, P. C. Klipstein, N. J. Mason, and P. J. Walker, Phys. Rev. Lett. **74** (16), 3285 (1995).
10. R. Sugie, H. Ohta, H. Harima, and S. J. Nakashima, J. Appl. Phys. **80** (10), 5946 (1996).
11. Y. Jin, G. G. Siu, M. J. Stokes, and S. L. Zhang, Phys. Rev. B **57** (3), 1637 (1998).
12. V. Wagner, J. Geurts, T. Gerhard, *et al.*, Appl. Surf. Sci. **123/124**, 580 (1998).
13. V. Bousquet, M. Laügt, P. Vennéguès, *et al.*, J. Cryst. Growth **201/202**, 498 (1999).
14. E. P. Pokatilov and S. I. Beril, Phys. Status Solidi B **110**, K75 (1982); Phys. Status Solidi B **118**, 567 (1983).
15. A. K. Sood, J. Menéndez, M. Cardona, and K. Ploog, Phys. Rev. Lett. **54** (19), 2115 (1985).
16. C. Colvard, T. A. Gant, M. V. Klein, *et al.*, Phys. Rev. B **31** (4), 2080 (1985).

Translated by G. Skrebtsov

Physics of the Solid State, Vol. 45, No. 8, 2003, pp. 1586–1595. Translated from Fizika Tverdogo Tela, Vol. 45, No. 8, 2003, pp. 1510–1518.

LOW-DIMENSIONAL SYSTEMS AND SURFACE PHYSICS

Radiospectroscopic and Dielectric Spectra of Nanomaterials

M. D. Glinchuk and A. N. Morozovskaya

Frantsevich Institute of Materials Science Problems, National Academy of Sciences of Ukraine, ul. Krzhizhanovskogo 3, Kiev, 03680 Ukraine

e-mail: glin@materials.kiev.ua

Received December 27, 2002

Abstract—The shape of lines in the radiospectroscopic (NMR and EPR) and dielectric spectra of materials formed by nanoparticles (hereafter, nanomaterials) is analyzed theoretically. The theory is developed in the framework of the core and shell model according to which a nanoparticle consists of two regions whose properties are affected and unaffected by the surface, respectively. The changes in the resonance frequency, the relaxation time, and the static permittivity due to the surface tension are taken into account, and the Gaussian and Lorentzian shapes of homogeneously broadened lines are considered. The inhomogeneous broadening of the spectral lines is examined for several types of nanoparticle size distributions. It is demonstrated that the splitting of the initial lines in the spectra of bulk systems into pairs of lines with a decrease in the particle size is a specific feature of the spectra of nanoparticles. The intensities and half-widths of the lines are investigated as functions of the parameters of the size distribution of nanoparticles. The results of theoretical calculations are compared with recent experimental data on the ^{17}O and ^{25}Mg NMR spectra of nanocrystalline MgO. The theoretical dependences of the intensity, the resonance frequency, and the half-width of the spectral lines are in good agreement with the experimental data. The proposed theory offers a satisfactory explanation of the behavior of the static permittivity in $BaTiO_3$ ceramic materials with nanometer-sized grains. © *2003 MAIK "Nauka/Interperiodica".*

1. INTRODUCTION

Investigations into the properties of nanomaterials—nanoparticle powders, ceramics with grain sizes of the order of nanometers (nanoceramics), and nanocomposites in which nanoparticles of one material are incorporated into the matrix of another material—have attracted the attention of researchers for a number of reasons. In particular, the unusual physical properties and pronounced surface effects [1–3] make these materials very promising for different technical applications (see [4] and references therein).

The influence of size effects on the properties of nanoparticles is better understood than that of films prepared from different materials (see [5] and references therein). The existence of the critical size of ferroelectric particles, below which ferroelectricity is not observed in the particles, has been established by numerous investigations, including x-ray diffraction, transmission electron microscopy, dielectric measurements, and radiospectroscopy [6–8].

The considerable scatter in the critical sizes of nanoparticles can be explained by the different conditions of their preparation [9] and depends on their environment, which is different in powder, ceramic, and composite systems. For example, the critical size of nanoparticles in a $BaTiO_3$ ceramic material appears to be approximately ten times larger than that in powder samples [7]. Moreover, dielectric measurements have been performed in external electric fields. Consequently, dielectric investigations of nanoparticles provide information on the response of a particle–matrix system as a whole rather than on particles themselves. It is evident that radiospectroscopic methods do not have this disadvantage.

Information on the size distribution of particles is particularly important for analyzing spectral lines, because the spread in sizes leads to an inhomogeneous broadening and a shift of the lines [10, 11].

As is known, nanoparticles are characterized by size effects, such as surface tension, a substantial contribution from the correlation energy to the total energy of a particle, and others. In particular, Wenhui Ma *et al.* [12] demonstrated that the observed dependence of the frequency of phonon modes on the particle radius for nanocrystalline $PbTiO_3$ is associated with the internal stresses caused by the surface tension. It is also known that the surface tension is determined not only by the particle size but also by the surface energy (see, for example, [13]), which should be included in the free energy of the system [14].

In the present work, we analyzed the dielectric and radiospectroscopic spectra of a system composed of noninteracting particles, each treated in terms of a core and shell model. The internal stresses (induced by the surface tension) and the size distribution of particles were taken into account. The results of theoretical calculations were compared with the available experimental data.

1063-7834/03/4508-1586$24.00

2. MODEL

It is known that finite systems are characterized by inhomogeneous physical properties. In ferroelectric systems considered within phenomenological theories, this inhomogeneity can be included through the addition of the correlation energy to the free energy of the system. In turn, the correlation energy is determined by the appropriate invariant combination of spatial derivatives of the order parameter (see, for example, [5]).

The local properties of solids can be investigated using a relatively small number of methods, including NMR and EPR spectroscopy [11, 15]. Dielectric methods provide a means for measuring the response of a system as a whole. This response involves the contributions of all inhomogeneities, which corresponds to the spatial averaging of local properties. In a certain sense, this averaging is equivalent to averaging over the particle sizes. In spectra of similar systems, such averaging leads to an inhomogeneous broadening of the spectral lines [10]. For ferroelectric relaxors, the broadening is observed in the NMR spectra [16] and manifests itself as hole burning in the dielectric spectra [17].

In order to perform averaging over the particle sizes, it is necessary to elucidate the dependence of the physical properties of the material, in particular, the half-width and the position of the spectral line at the maximum, on the size (shape) of the system. In what follows, we will assume that the surface tension and the related internal stress substantially contribute to the particle properties.

As is known, internal stresses induced by surface tension in a spherical particle of radius r coincide with a uniform compressive strain under pressure $p = 2k/r$, where k is the surface tension coefficient [13]. It should be noted that, although the last quantity is always larger than zero, the influence of the pressure can lead to both a decrease and an increase in the natural frequencies of vibrations, the relaxation times, etc. Specifically, an increase in the surface tension results in a decrease in the frequency of the soft mode in nanocrystalline $PbTiO_3$ [12].

Another important size effect is associated with the aforementioned inhomogeneous physical properties of particles. This factor will be accounted for within a simple model according to which a particle consists of a core (the particle region $[0, r - \Delta r]$) and a shell (the particle region $[r - \Delta r, r]$). The properties of the former region are similar to those of the bulk system, whereas the properties of the latter region are affected by the surface and can differ from the properties of the former region. It is assumed that the shell thickness Δr does not depend on the particle size. Within this model, the spectra should contain pairs of lines, such that the lines in each pair are attributed to the core and the shell. The purpose of the present work is to determine the relative intensities of these lines and the conditions of their resolution.

3. NUCLEAR MAGNETIC RESONANCE SPECTRA

The shape of homogeneously broadened NMR or EPR lines is governed by the main mechanisms of broadening and can be described by Gaussian or Lorentzian functions [11, 15]. The total intensity of the line of one particle can be written in the form $I(\omega, R) = I_c(\omega, R) + I_s(\omega, R)$, where subscripts c and s indicate the contributions of the core and the shell, respectively. In this case, the line intensity takes the form

$$I_1(\omega, r) = \sum_{n = c, s} \frac{A_{1n}(r)}{\sqrt{2\pi}\Delta_{1n}} \exp\left(-\frac{(\omega - \omega_{1n}(r))^2}{2\Delta_{1n}^2}\right), \quad (1a)$$

$$I_2(\omega, r) = \sum_{n = c, s} \frac{A_{2n}(r)}{\pi} \frac{\Delta_{2n}}{(\omega - \omega_{2n}(r))^2 + \Delta_{2n}^2}. \quad (1b)$$

Here, formulas (1a) and (1b) refer to the Gaussian and Lorentzian shapes of individual lines, respectively. The quantities $\omega_{in}(r)$ and Δ_{in} (where $i = 1, 2$; $n = c, s$) are the resonance frequencies and the half-widths of lines, respectively. The half-width at half-maximum of a line is equal to Δ_{2n} for the Lorentzian line shape [relationship (1b)] and $\sqrt{2\ln(2)}\Delta_{1n} \approx 1.177\Delta_{1n}$ for the Gaussian line shape [expression (1a)]. The coefficients A_{in} (where $i = 1, 2$; $n = c, s$) depend on the intensity normalization. Apparently, the sum of the integrated intensities for each type of line shape is independent of the particle size. Then, the relative coefficients can be found from the condition of normalizing the total intensity to the volume of the system ($\int_{-\infty}^{\infty} I_{1,2}(\omega)d\omega = 1$); that is,

$$\begin{aligned} A_{1c}(r) &= A_{2c}(r) \equiv A_c(r) = \left(1 - \frac{\Delta r}{r}\right)^3, \\ A_{1s}(r) &= A_{2s}(r) \equiv A_s(r) = 1 - \left(1 - \frac{\Delta r}{r}\right)^3. \end{aligned} \quad (2a)$$

In formulas (1), it is assumed that the surface tension affects only the resonance frequencies

$$\omega_{in}(r) = \omega_{0n} - k_n/r, \quad (2b)$$

where the quantities k_c and k_s are proportional to the surface tension coefficient. The proportionality coefficients can be positive and negative and accounts for the effect of the external pressure on the frequencies of natural vibrations through the spin–phonon interaction. On the other hand, the dependence of the half-width on the pressure due to the spin–phonon and spin–spin interactions cannot be ruled out.

In order to analyze the properties of a set of particles, it is necessary to specify their size distribution

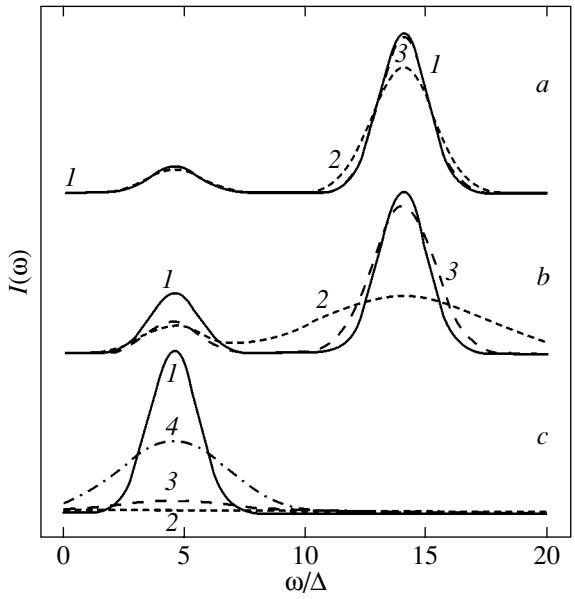

Fig. 1. NMR spectra calculated for the homogeneously broadened Gaussian line shape at the parameters ω_{0c}/Δ_c = 15, ω_{0s}/Δ_s = 5, $k_c/r_0\Delta_c$ = 1, and $k_s/r_0\Delta_s$ = 0.5. $\Delta r/r_0$ = (*a*) 0.05, (*b*) 0.1, and (*c*) 1. Spectrum *1* is calculated for the size distribution function (*3a*). The other spectra are calculated using the size distribution function (*3c*) at d/r_0 = (*2*) 0.8, (*3*) 0.5, and (*4*) 0.01.

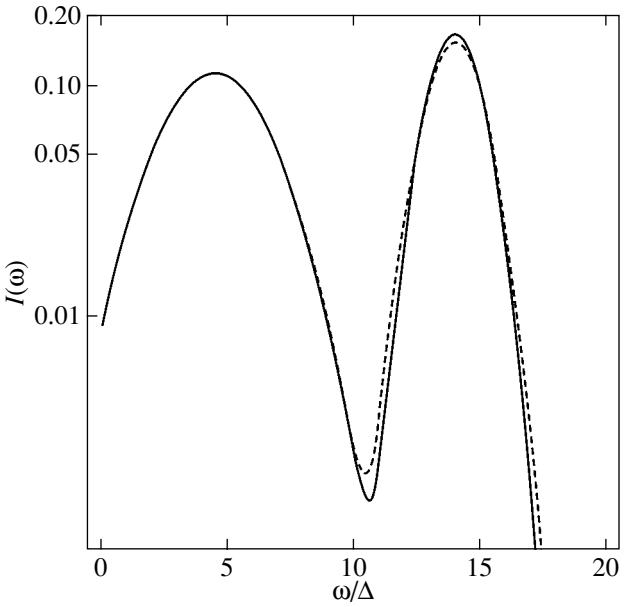

Fig. 2. NMR spectra calculated from relationships (4), (3c), and (1a) (solid line) and from approximate formulas (5) and (6) (dashed line) at $\Delta r/r_0$ = 0.25 and d/r_0 = 4. The other parameters are the same as in Fig. 1.

function. We consider the following three simple distribution functions:

$$f(r) = \frac{\delta(r - r_0)}{4\pi r_0^2}, \tag{3a}$$

where $\delta(x)$ is the Dirac delta function;

$$f(r) = \frac{3}{8\pi(3r_0^2 d + d^3)}\Theta(d - |r - r_0|), \tag{3b}$$

where $\Theta(x)$ is the Heaviside theta function and $r_0 > d$; and

$$f(r) = \frac{1}{4\pi^{3/2} r_0^2 d}\exp\left(-\frac{(r - r_0)^2}{2d^2}\right). \tag{3c}$$

Here, r_0 is the modal (mean) particle radius and d is the half-width of the distribution function. Note that, in function (3c), the normalization coefficient is written up to the principal term at $r_0 \gg d$, whereas corrections of the order of $\exp(-r_0^2/2d^2)$ are omitted under the assumption $r_0 > d$.

Now, the spectral line can be represented as the convolution of the distribution function (3) with intensity (1): that is,

$$I_{1,2}(\omega) = \int_0^\infty 4\pi r^2 dr f(r) I_{1,2}(\omega, r). \tag{4}$$

The simplest case of this convolution with the distribution function (3a) corresponds to the spectrum of a system formed by particles of radius r_0. It is clear that convolution (4) with the distribution function (3a) is reduced only to the replacing radius r by r_0. Hereafter, when examining spectra that are dependent on the particle radius, we will use the averaging with the distribution function (3a). The spectrum shape strongly depends on the ratio $\Delta r/r_0$. Evidently, in the two limiting cases $\Delta r/r_0 \longrightarrow 0$ and $\Delta r/r_0 \longrightarrow 1$, the spectrum involves only one line associated either with the core or with the shell, respectively.

In the intermediate case $\Delta r/r_0 < 1$, the lines can be resolved when the difference between the resonance frequencies is larger than the sum of the half-widths $|\omega_c(r_0) - \omega_s(r_0)| > \Delta_c + \Delta_s$. The spectrum shapes for the above three cases are shown by solid lines in Fig. 1. In what follows, we will assume that an increase in the surface tension leads to a decrease in the resonance frequencies; i.e., the coefficients k_c and k_s are positive in sign.

Integral (4) for distribution functions (3b) and (3c) was calculated numerically. The results of the averaging of line (1a) with the use of distribution functions (3b)

and (3c) are represented by the dashed and dotted lines in Fig. 1, respectively. It can be seen from this figure that the spread in the nanoparticle sizes leads to broadening of the line and a shift in the maximum.

Approximate analytical calculations of $I_1(\omega)$ with the distribution function (3c) can be performed using the Laplace method [18] when the inequality $r_0/d > k_{c,s}/(r_0\Delta_{c,s})$ is satisfied. As a result, we obtain

$$\tilde{I}_1(\omega) = \frac{A_c(r_0)}{\sqrt{2\pi}\tilde{\Delta}_{1c}}\exp\left(-\frac{(\omega-\omega_{0c}+k_c/r_0)^2}{2\tilde{\Delta}_{1c}^2}\right) + \frac{A_s(r_0)}{\sqrt{2\pi}\tilde{\Delta}_{1s}}\exp\left(-\frac{(\omega-\omega_{0s}+k_s/r_0)^2}{2\tilde{\Delta}_{1s}^2}\right), \quad (5)$$

where

$$\tilde{\Delta}_{1c,s} = \Delta_{1c,s}\sqrt{1+\left(\frac{k_{c,s}d}{r_0^2\Delta_{1c,s}}\right)} \quad (6)$$

are the renormalized widths of the Gaussian lines. As follows from relationship (5), the inhomogeneously broadened line is the sum of two Gaussian lines with the parameters renormalized by the surface tension and the size distribution. Note that the renormalized widths (6) increase with a decrease in the modal particle size r_0. Consequently, the lines are more smeared for particles with smaller sizes.

It should be emphasized that, although expressions (5) and (6) are approximate, the difference between the data obtained with expression (5) and the exact, numerically calculated results does not exceed, on the average, 10–20% (see the dashed and solid curves in Fig. 2). A comparison with the available experimental data, which will be given below, confirms the validity of expressions (5) and (6) over a wide range of particle sizes.

The calculations of $I_2(\omega)$ for the homogeneously broadened line with a Lorentzian shape offer results qualitatively similar to those derived by averaging the homogeneously broadened line with a Gaussian shape. The main qualitative difference is in the larger shift in the maximum of the Lorentzian line (cf. Figs. 3a, 3b).

4. DIELECTRIC SPECTRA

In the framework of the core and shell model, the permittivities of the core and the shell of the particle are denoted by ε_c and ε_s, respectively. To a first approximation, the permittivity of the particle is equal to the permittivity averaged over the particle volume [19]; that is,

$$\varepsilon(r) = \varepsilon_c(r)A_c(r) + \varepsilon_s(r)A_s(r). \quad (7)$$

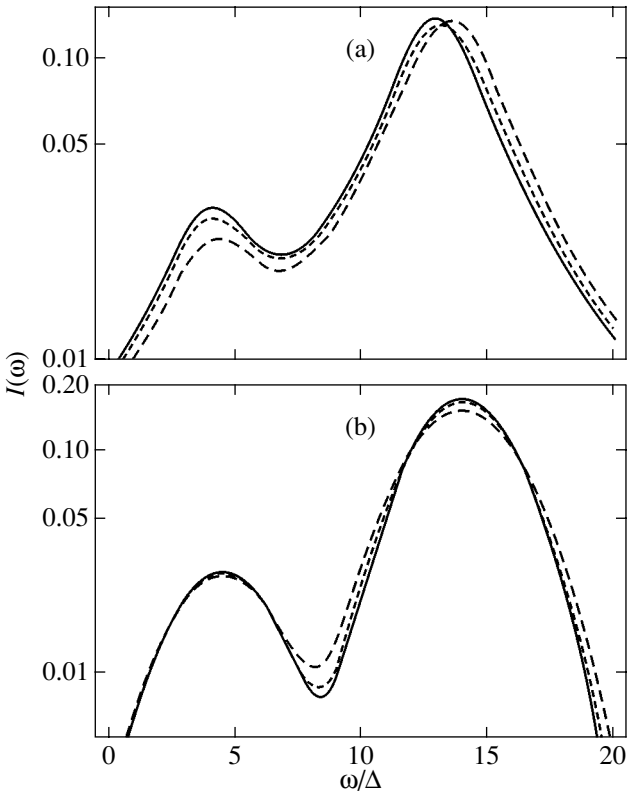

Fig. 3. NMR spectra calculated for (a) Lorentzian and (b) Gaussian line shapes at $\Delta r/r_0 = 0.05$ (the other parameters are the same as in Fig. 1). Inhomogeneously broadened spectra are calculated using the distribution functions (3a) (solid lines) and (3b) at $d/r_0 = 0.1$ (dashed lines) and 0.95 (dotted lines).

Apparently, in the same approximation, the mean permittivity of the system of particles has the form

$$\varepsilon = \int_0^\infty 4\pi r^2 dr\varepsilon(r)f(r). \quad (8)$$

We now derive the expression for the dynamic permittivity of the bulk system. The time dependence of the polarization P of a similar system in an ac external field can be described by the Landau–Khalatnikov equation with due regard for the kinetic energy [20]:

$$\mu\frac{d^2P}{dt^2} + \eta\frac{dP}{dt} + \alpha P + \beta P^3 = E\exp(-i\omega t), \quad (9)$$

where ω is the frequency of the external electric field, $\alpha = \alpha_T(T - T_c)$ and β are the coefficients of expansion of the Landau–Ginzburg–Devonshire free energy, T_c is the phase transition temperature, μ is the mass coefficient, and η is the vibration damping coefficient [20]. It is easy to show that the linear dielectric susceptibility $\chi = (dP/dE)|_{E=0}$ obeys the equation

$$(-\mu\omega^2 - i\eta\omega + \alpha + 3\beta P_s^2)\chi = 1, \quad (10)$$

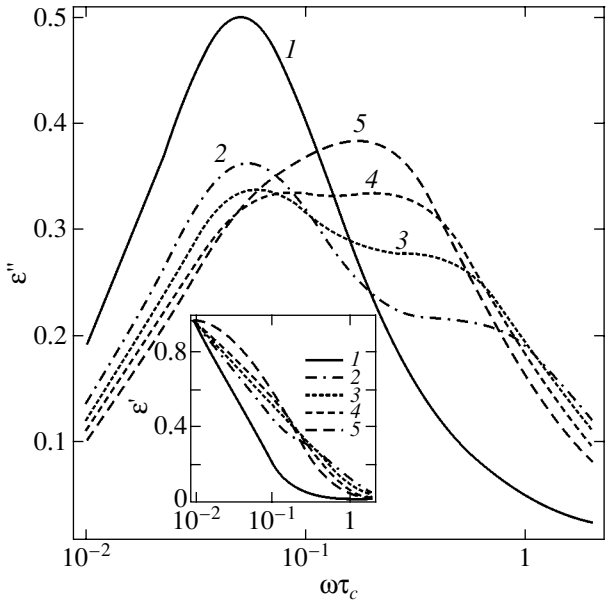

Fig. 4. Frequency dependences of the dynamic permittivity (16) at $\beta_c/r_0 = 0.95$ and the ratios $\beta_s/\beta_c =$ (*1*) 0, (*2*) 0.26, (*3*) 0.53, (*4*) 0.68, and (*5*) 0.79. Solid lines represent the results of calculations at $\Delta r/r_0 = 0$, and all the other lines correspond to $\Delta r/r_0 = 0.5$. The dependences of the imaginary part of the permittivity are depicted in the main part of the figure, and the inset shows the dependences of the real part of the permittivity.

where P_s is the static spontaneous polarization, which satisfies the equation $\alpha P_s + \beta P_s^3 = 0$. From Eq. (10) and the expression relating the permittivity and the susceptibility $\varepsilon(\omega) = \varepsilon_\infty + 4\pi\chi(\omega)$, we obtain the relationship

$$\varepsilon(\omega) = \varepsilon_\infty + \frac{\Delta\varepsilon_0}{1 - (\omega/\omega_0)^2 - i\omega\tau}. \quad (11)$$

Here, we introduced the designations

$$\omega_0 = \frac{1}{\sqrt{\chi_0\mu}}, \quad \tau = \chi_0\eta, \quad \Delta\varepsilon_0 = 4\pi\chi_0, \quad (12a)$$

where the static susceptibility χ_0 is defined by the expression

$$\chi_0 = \begin{cases} 1/\alpha, & \alpha > 0 \\ -1/(2\alpha), & \alpha < 0. \end{cases} \quad (12b)$$

It is obvious that relationship (11) describes the response of a system of the damped oscillator type with a frequency ω_0 of natural oscillations and a relaxation time τ. It can be seen from relationships (12) that, at the phase transition point, i.e., at $\alpha \longrightarrow 0$ ($\chi_0 \longrightarrow \infty$), the frequency ω_0 becomes equal to zero (soft mode) and the relaxation time τ tends to infinity (critical damping).

The hydrostatic pressure applied to the system shifts the phase transition point [20] and, hence, affects the coefficient α in formulas (9)–(12), which can be written in the following form:

$$\alpha(r) = \alpha_0 - Qp, \quad p = 2k/r, \quad (13)$$

where Q is a linear combination of electrostriction constants and α_0 is the coefficient α for the bulk system. In relationship (13), the sign minus is chosen because the hydrostatic pressure decreases the frequency of the soft mode in ferroelectric perovskites of the barium titanate type [12]. Substitution of formulas (13) into relationships (11) and (12) gives the expression

$$\varepsilon_{c,s}(\omega, r) - \varepsilon_\infty = \frac{\Delta\varepsilon_{0\infty}}{1 - \beta_{c,s}/r - (\omega/\omega_{0\infty})^2 - i\omega\tau_\infty}. \quad (14)$$

Here, all the quantities with subscript ∞ are obtained from the corresponding quantities without this subscript by replacing α by α_0 in relationships (12) and the following designation is introduced:

$$\beta_{c,s} = 2k_{c,s}Q/\alpha_0. \quad (15)$$

From expressions (7) and (14), we can easily obtain the total permittivity of the particle:

$$\varepsilon(\omega, r) - \varepsilon_\infty = \Delta\varepsilon_{0\infty}\left(\frac{A_c(r)}{1 - \beta_c/r - (\omega/\omega_{0\infty})^2 - i\omega\tau_\infty} + \frac{A_s(r)}{1 - \beta_s/r - (\omega/\omega_{0\infty})^2 - i\omega\tau_\infty}\right). \quad (16)$$

Making allowance for expression (2), relationship (16) describes the dynamic dielectric response of one particle or a system formed by noninteracting particles of radius r. In the latter case, the size distribution function is represented by formula (3a). It is clear that the spectrum shape depends on the relation between $\omega_{0\infty}$ and τ_∞, the parameters $\beta_{c,s}$, and the ratio of the shell thickness to the core radius. Hereafter, we will use the following dimensionless variables:

$$\tilde{\omega} = \omega\tau_\infty, \quad \rho = 1/\omega_{0\infty}\tau_\infty. \quad (17)$$

Figure 4 shows the dependences $\varepsilon(\omega, r)$ on $\tilde{\omega}$ at $\rho = 0$, i.e., for the purely relaxational response of the system. As can be seen from this figure, the imaginary part of the permittivity exhibits two maxima at the parameters $\Delta r/r = 0.5$ and $\beta_s/\beta_c < 0.7$. Two separate lines begin to merge together with an increase in the latter ratio. For example, at $\beta_s/\beta_c \approx 0.8$, there is only one asymmetric smeared line (Fig. 4, curve *5*). It is obvious that the spectrum of the bulk system (Fig. 4, curve *1*) considerably differs from the spectrum of the particles.

The dielectric spectrum turns out to be more complex for size distribution functions with a finite width, for example, in the case of the size distribution functions (3b) and (3c). For the size distribution function (3b),

the dielectric spectrum can be obtained in the analytical form

$$\frac{\varepsilon(\tilde{\omega}, r_0) - \varepsilon_\infty}{\Delta\varepsilon_{0\infty}} = \bar{\varepsilon}_c + \bar{\varepsilon}_s, \tag{18a}$$

where we used the following designations:

$$\bar{\varepsilon}_c = \frac{3r_0^3\xi_c(\tilde{\omega})}{\beta_c(3r_0^2 + d^2)}\left(1 + \frac{d^2}{3r_0^2} + (\xi_c(\tilde{\omega}) + 1)\left(\xi_c(\tilde{\omega}) - 3\frac{\Delta r}{r_0}\right)\right.$$
$$\left. + 3\left(\frac{\Delta r}{r_0}\right)^2 + \frac{r_0}{2d}\left(\xi_c(\tilde{\omega}) - \frac{\Delta r}{r_0}\right)^3 \times \ln\left(\frac{r_0(1 - \xi_c(\tilde{\omega})) + d}{r_0(1 - \xi_c(\tilde{\omega})) - d}\right)\right), \tag{18b}$$

$$\bar{\varepsilon}_s = \frac{9\Delta r r_0^2\xi_s(\tilde{\omega})}{\beta_s(3r_0^2 + d^2)}\left(1 + \xi_s(\tilde{\omega}) - \frac{\Delta r}{r_0} + \left(\xi_s^2(\tilde{\omega}) - \xi_s(\tilde{\omega})\frac{\Delta r}{r_0}\right.\right.$$
$$\left.\left. + \left(\frac{\Delta r}{r_0}\right)^2\right)\frac{r_0}{2d}\ln\left(\frac{r_0(1 - \xi_s(\tilde{\omega})) + d}{r_0(1 - \xi_s(\tilde{\omega})) - d}\right)\right), \tag{18c}$$

$$\xi_{c,s}(\tilde{\omega}) = \frac{\beta_{c,s}/r_0}{1 - \beta_{c,s}/r_0 - (\rho\tilde{\omega})^2 - i\tilde{\omega}}, \tag{18d}$$
$$\Delta r < r_0 - d, \quad \beta_{c,s} < r_0 - d.$$

At $d \ll r_0$, relationships (18) transform into expression (16) with the replacement of r by r_0.

The imaginary parts of permittivity (18) at $\rho = 0$ (the Debye relaxation response) for different ratios $\Delta r/r_0$ and small ratios d/r_0 are shown in Fig. 5. As can be seen from Fig. 5, the shape of the spectrum consisting of two lines (curves *b*, *c*, *d*) is sensitive to changes in the above ratios. An increase in the ratio d/r_0 results in the transformation of the spectrum into one broad line, whereas the spectrum corresponding to the response of the core (curve *e*) is virtually insensitive to a change in this ratio.

A special investigation demonstrated that, at large ratios $d/r_0 > 0.3$, the shape of the line corresponding to the shell substantially depends on this ratio. In particular, at $d/r_0 = 0.95$, the spectrum is somewhat broadened and the frequency of the maximum is shifted.

Numerical calculations of the dielectric spectrum averaged with the size distribution function (3c) at $\rho = 0$ offer results similar to the analytically obtained data presented in Fig. 5.

It is not evident that the theoretically predicted features can be observed experimentally, even though the spectral broadening is a characteristic feature of nanomaterials. It is not improbable that closer examination of the spectra could reveal specific features (such as separate lines corresponding to the core and the shell) that are not resolved due to the size distribution of particles.

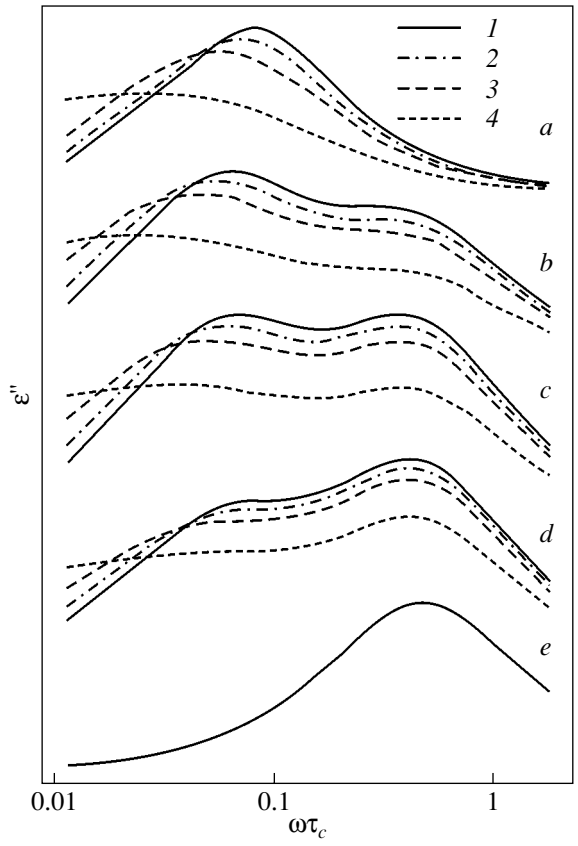

Fig. 5. Frequency dependences of the imaginary part of the dynamic permittivity (18) at $\Delta r/r_0$ = (*a*) 0.05, (*b*) 0.5, (*c*) 0.55, (*d*) 0.6, and (*e*) 0.95. d/r_0 = (*1*) 0, (*2*) 0.03, (*3*) 0.04, and (*4*) 0.049. $\beta_c/r_0 = \beta_s/r_0 = 0.95$.

5. DISCUSSION AND COMPARISON WITH EXPERIMENTAL DATA

The core–shell model according to which the core possesses properties similar to those of the bulk system and the properties of the shell are affected by the surface implies a simplified approach to a complex problem, whose solution should take into account a gradual variation in the physical properties of the system. It was shown that, in finite systems with an electric-polarization gradient, the ferroelectric phase transition temperature depends on the system size and becomes zero for particles at the critical radius r_c under certain boundary conditions [2, 5]. It is believed that, in systems formed by particles, the size-induced phase transition manifests itself as specific features in the physical properties in the vicinity of the critical radius.

However, the positions of maxima for powder and ceramic samples differ appreciably (the critical size of powder particles is approximately ten times smaller than the critical size of grains in barium titanate ceramic material [7]). The assumption that this effect can be associated with the scatter in the particle sizes was not confirmed, because the broadening of the size

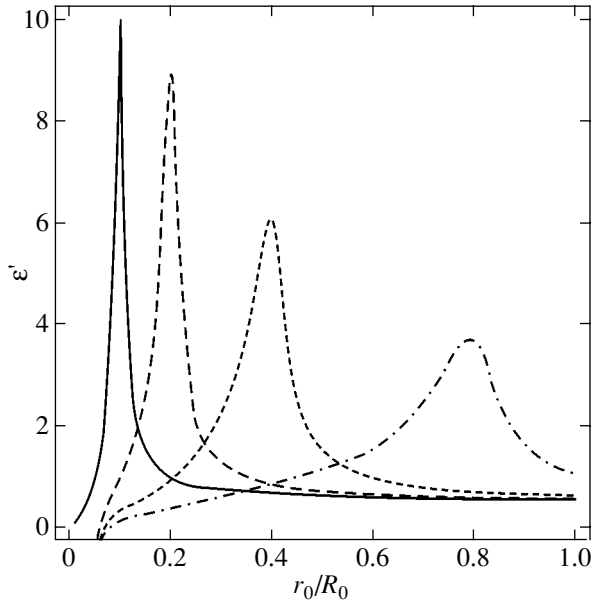

Fig. 6. Dependences of the static permittivity (19) on the radius at $\beta_c/R_0 = 0.1$, $\delta = 0.1$, $\Delta r/R_0 = 0.1$, and the ratios $\beta_s/\beta_c = 1$ (solid line), 2 (dashed line), 4 (dotted line), and 8 (dot-dashed line). Here, R_0 is the maximum particle radius.

distribution of particles leads to a shift in the maximum toward the small-size range [21].

Let us consider this problem in terms of the core–shell model. The static permittivity can be obtained from formula (16) at $\omega = 0$. It can be seen that the permittivity diverges at the radii $r_{1d} = \beta_c$ and $r_{2d} = \beta_s$. Taking into account that the permittivity in real systems is finite, the static permittivity can be written in the following form:

$$\frac{\varepsilon(r) - \varepsilon_\infty}{\Delta\varepsilon_{0\infty}} = \frac{A_c(r)}{\sqrt{(1-\beta_c/r)^2(1+\Theta(1-\beta_c/r))^2 + \delta^2}} + \frac{A_s(r)}{\sqrt{(1-\beta_s/r)^2(1+\Theta(1-\beta_s/r))^2 + \delta^2}}. \quad (19)$$

Here, the parameter δ determining the permittivity maximum and the Heaviside theta function $\Theta(x)$ are introduced in order to demonstrate that the permittivities in the paraelectric and ferroelectric phases (with the same temperature deviation from the phase transition point) differ by a factor of two (for second-order phase transitions).

As follows from relationship (19), the position of the maximum considerably depends on the parameter Δr and the ratio β_s/β_c. Figure 6 shows the dependences of the static permittivity on the radius at $\Delta r = \beta_c$ and different parameters $\beta_s \geq \beta_c$ (the dependence at β_s/β_c is depicted by the solid line). It can be seen from this figure that an increase in the ratio β_s/β_c results in a shift in the maximum to larger radii and an increase in the maximum width. The averaging of the static permittivity (19) with the size distribution function (3b) leads to additional broadening of the maximum and its shift toward

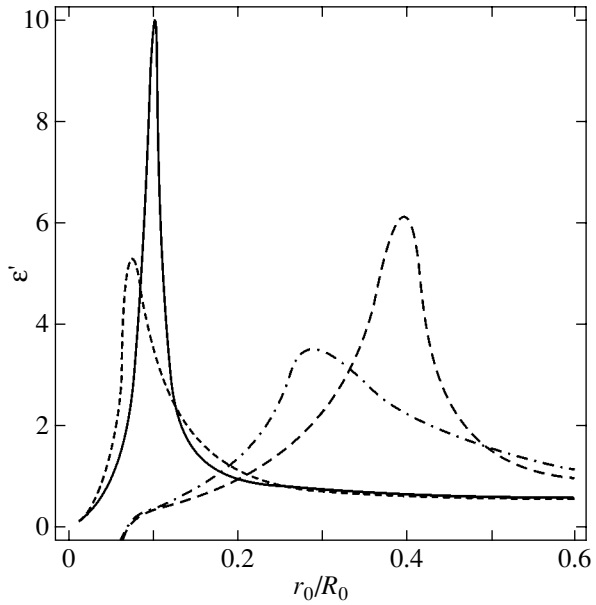

Fig. 7. Dependences of the static permittivity (19) averaged with the particle distribution function (3b) on the radius at $\beta_c/R_0 = 0.1$, $\delta = 0.1$, $\Delta r/R_0 = 0.1$, and different values of β_s/β_c and d/r_0: 1 and 0 (solid line), 4 and 0 (dashed line), 1 and 0.5 (dotted line), and 4 and 0.5 (dot-dashed line).

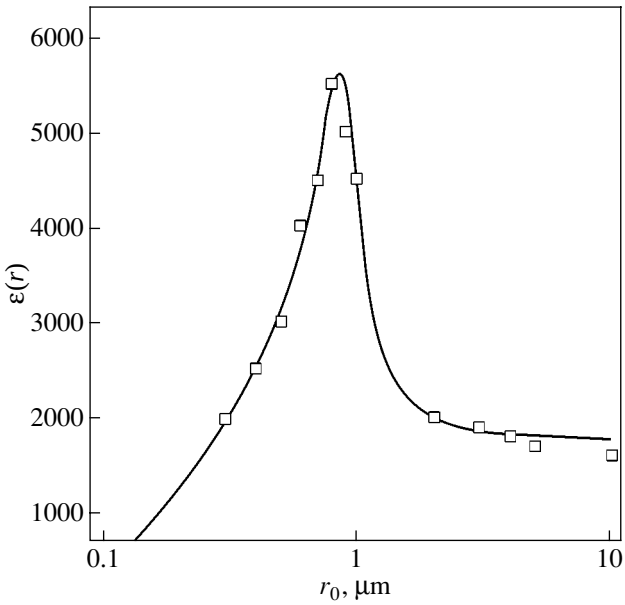

Fig. 8. Dependence of the static permittivity on the mean size of $BaTiO_3$ ceramic grains. Squares represent the experimental data taken from [14]. The solid line is the theoretical dependence (19) calculated at $\Delta r/r_0 = 0.1$, $\Delta\varepsilon_{0\infty} = 3500$, $\delta = 0.25$, $\beta_c = 0.1$ μm, and $\beta_s = 0.9$ μm.

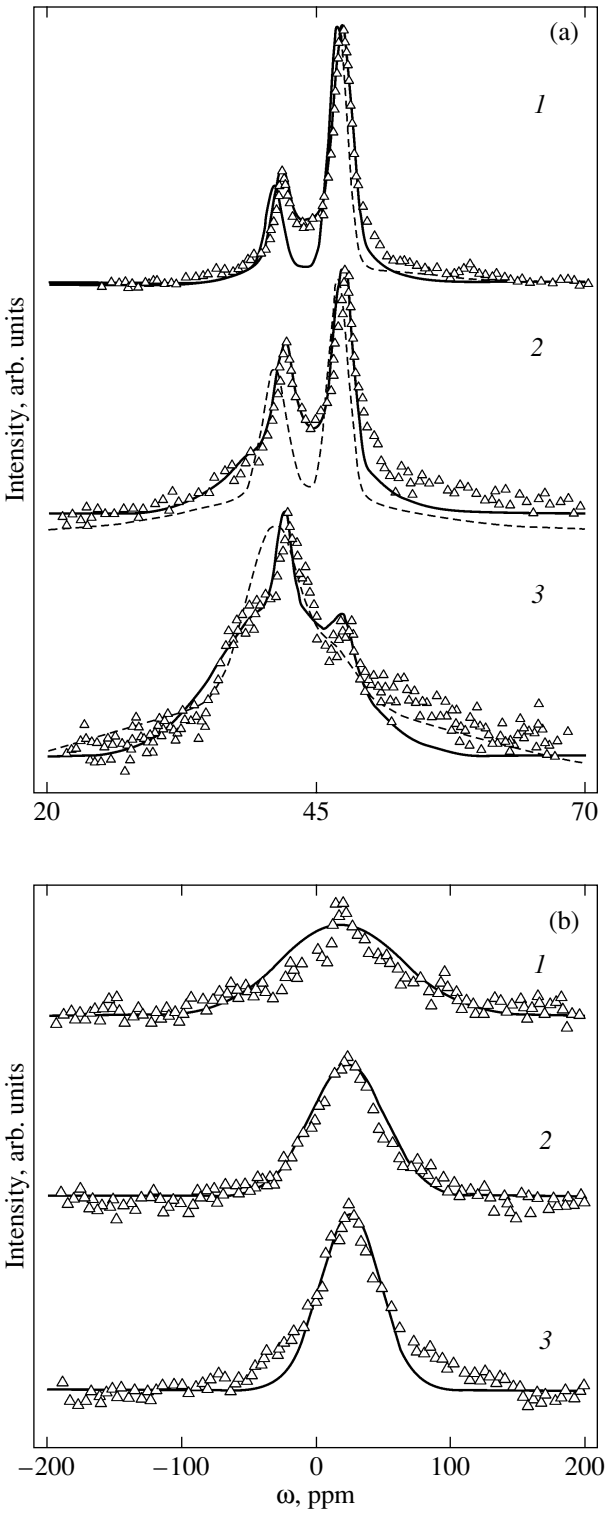

Fig. 9. (a) ^{17}O NMR and (b) ^{25}Mg NMR spectra of nanocrystalline MgO for different particles sizes: (a) (*1*) 4.5, (*2*) 2.5, and (*3*) 1.8 nm and (b) (*1*) 3, (*2*) 4.5, and (*3*) 5 nm. Solid lines correspond to the results of calculations from formulas (5) and (6). Triangles represent the experimental data taken from [22]. The fitting parameters are listed in Tables 1 and 2. Dashed lines indicate the decomposition of the NMR spectra according to [22].

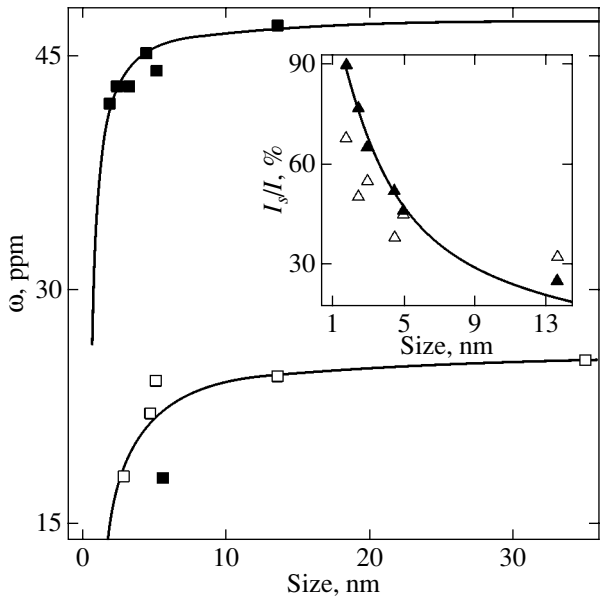

Fig. 10. Experimental dependences of the resonance frequency of ^{17}O NMR (closed squares) and ^{25}Mg NMR (open squares) spectra on the particle size [22]. Solid lines represent the theoretical dependences obtained from formula (2b) at $\omega_0 = 47.5$ ppm and $k = 5.25$ ppm nm for ^{17}O and $\omega_0 = 26$ ppm and $k = 10$ ppm nm for ^{25}Mg. The inset shows the dependence of the ratio of the integrated intensity I_s of the line associated with the shell to the total intensity I on the particle size. The solid line indicates the theoretical dependence $I_s/I = 1 - (1 - \Delta r/r_0)^3$ at $\Delta r = 0.48$ nm. Closed triangles are the fitting parameters used in this work, and open triangles are the experimental ^{17}O NMR data taken from [22].

the small-radius range (Fig. 7), which agrees with the results obtained in [21]. Consequently, the experimentally observed shift of the permittivity maximum for ceramic materials [7] can be associated with the fact that the inequality $\beta_s > \beta_c$ holds for the ceramic materials, whereas the opposite inequality is satisfied for the powders. Actually, this difference can be explained by the presence of the second phase in the systems under consideration. For example, the second phase in the ceramic materials can be contained in interlayers between grains. The experimental data taken from [14] for $BaTiO_3$ ceramic materials are compared with the theoretical dependence (19) in Fig. 8. It can be seen from Fig. 8 that the proposed core–shell model adequately describes the experimental static permittivity. This suggests that the surface tension, which was ignored in [2, 5], can affect the critical size determined in these works on the basis of the thermodynamic phenomenological theory.

The proposed model can also be applied to describe the experimental data obtained by Chadwick *et al.* [22]. In this work, the ^{17}O and ^{25}Mg NMR spectra were studied for nanocrystalline MgO with crystallite sizes from 1.8 to 35 nm (according to the estimates made from the

Table 1. Particle sizes, ^{17}O NMR data, and fitting results taken from [22] and the results of our fitting and theoretical calculations at $\omega_{c1} = 47.5$ ppm, $\omega_{c2} = 42$ ppm, $\omega_s = 47.5 - 5.25/r_0$ ppm ($\nu_0 = 40.18$ MHz), and $I_s/I = 1 - (1 - 0.4823/r_0)^3$

Size $2r_0$ (nm)	1.8	2.5	3	4.5	5	13.5	35
ω_{c1} (ppm) ± 0.5	47	47	47	47	47	47	47
I_{c1}/I (%) ± 2	5	30	21	47	52	68	100
I_{c1}/I (%) our fitting	4	23	26	37	48	75	
Δ_{c1} (Hz) ± 2	174	88	88	81	96	23	15
Δ_{c1} (Hz) our fitting	85	83	85	81	96	23	
ω_{c2} (ppm) ± 0.5	41	41	42	41	42		
Δ_{c2} (Hz) ± 2	235	105	120	76	58		
Δ_{c2} (Hz) our fitting	65	75	110	70	58		
I_{c2}/I (%) ± 2	27	20	24	15	3		
I_{c2}/I (%) our fitting	6	10	9	11	6		
ω_s (ppm) ± 2	42	43	43	45	44	47	
ω_s (ppm) theory	41.7	43.3	44	45.2	45.4	46.7	47.2
I_s/I (%) ± 2	68	50	55	38	45	32	
I_s/I (%) our fitting	90	77	65	52	46	25	
I_s/I (%) theory	90	76.8	68.8	51.2	47.4	19.9	8.0
Δ_s (Hz) ± 50	1300	840	650	920	460	170	
Δ_s (Hz) our fitting	550	500	150	350	250	170	

x-ray powder diffraction data). It was demonstrated that the spectral lines have a Gaussian shape due to the chemical shift. An interesting evolution of the ^{17}O NMR spectra was observed with a decrease in the particle size. Specifically, the NMR spectra of particles with the largest sizes (13.5, 35 nm) involve only one line, whose position is identical to that found for the bulk system. As the crystallite size decreases (5.0, 4.5, 3.0, 2.5, 1.8 nm), the line is broadened and splits into two lines (see the experimental spectra [22] shown in Fig. 9 for particles with mean sizes of 4.5, 2.5, and 1.8 nm). In [22], these spectra were represented as the sum of at least three Gaussian lines (Table 1). The frequencies corresponding to the maxima of two lines are virtually independent of the particle size, whereas the frequency of the third line shifts toward the low-frequency range with a decrease in the particle size. On this basis, we draw the inference that the first two lines ($c1$, $c2$) are associated with the core and the third line (s) is attributed to the shell. For particles with the smallest size (1.8 nm), the integrated intensity of the s line is substantially higher than the intensities of the $c1$ and $c2$ lines. The observed behavior of the spectra is in qualitative agreement with the predictions of the developed theory. A comparison of the experimental and theoretical integrated intensities makes it possible to determine the thickness of the shell $\Delta r \approx 0.48$ nm in MgO particles.

Table 2. Particle sizes and ^{25}Mg NMR data taken from [22] and the results of our theoretical calculations at $\omega_s = 26 - 10/r_0$ ppm ($\nu_0 = 18.3$ MHz)

Size $2r_0$ (nm)	ω (ppm) ± 0.5	ω (ppm) theory	Δ (Hz) ± 50
35	25.3	25.4	450
13.5	24.2	24.5	610
5	24.1	22	965
4.5	22.3	21.6	1200
3	18.0	19.3	1935
2.5	Not recorded		
1.8	Not measured		

Unlike the ^{17}O NMR spectra, the ^{25}Mg NMR spectra do not exhibit any well-defined splitting of the lines. A decrease in the particle size results only in a shift in the maximum and in line broadening (Table 2). The possible splitting can be unresolved because of the appreciable broadening of individual lines.

The dependences of the frequencies of the ^{17}O and ^{25}Mg NMR signals assigned to the shell on the particle size are plotted in Fig. 10. The inset in Fig. 10 shows the dependence of the ratio between the integrated intensity of the s line and the total integrated intensity of the ^{17}O NMR spectrum on the particle size. It can be seen from Fig. 10 that the theoretical and experimental dependences are in good agreement.

To the best of our knowledge, experimental data on the dependence of the dielectric spectra on the particle size are not available for nanomaterials. In our opinion, it is of interest to compare the specific features predicted by our theory with those experimentally

observed, for example, in hole-burning experiments [17]. This can provide valuable information on the inhomogeneously broadened dielectric spectra of systems formed by nanoparticles.

In the future, it would be expedient both to improve the existing theory and to perform a detailed experimental investigation into the influence of surface phenomena on the properties of nanoparticles.

REFERENCES

1. K. Ishikawa, T. Nomura, N. Okada, and K. Tokada, Jpn. J. Appl. Phys., Part 1 **35**, 5196 (1996).
2. J. Rychetsky and O. Hudak, J. Phys.: Condens. Matter **9**, 4955 (1997).
3. B. Jiang and L. A. Bursill, Phys. Rev. B **60**, 9978 (1999).
4. M. P. McNeal, Sei-Jou Jang, and R. E. Newnham, J. Appl. Phys. **83**, 3298 (1998).
5. W. L. Zhong, Y. G. Wang, P. L. Zhang, and B. D. Qu, Phys. Rev. B **50**, 698 (1994).
6. Xiaoping Li and Wei-Heng Shih, J. Am. Ceram. Soc. **80**, 2844 (1997).
7. J. C. Niepce, Electroceramics **4** (5–7), 29 (1994).
8. R. Bottcher, C. Klimm, H. C. Semmelhack, *et al.*, Phys. Status Solidi B **215**, R3 (1999).
9. A. V. Ragulya, Nanostruct. Mater. **10** (3), 349 (1998).
10. V. M. Stoneham, Rev. Mod. Phys. **41**, 82 (1969).
11. M. D. Glinchuk, V. G. Grachev, S. B. Roĭtsin, and L. A. Sislin, *Electrical Effects in Radiospectroscopy* (Nauka, Moscow, 1981).
12. Wenhui Ma, Mingsheng Zhang, and Zuhong Lu, Phys. Status Solidi A **166**, 811 (1998).
13. L. D. Landau and E. M. Lifshitz, *Statistical Physics*, 2nd ed. (Nauka, Moscow, 1964; Pergamon, Oxford, 1980).
14. P. Perriat, J. C. Niepce, and G. Gaboche, J. Therm. Anal. **41**, 635 (1994).
15. A. Abragam, *The Principles of Nuclear Magnetism* (Clarendon, Oxford, 1961; Inostrannaya Literatura, Moscow, 1963).
16. M. D. Glinchuk, V. V. Laguta, I. P. Bykov, *et al.*, J. Appl. Phys. **81**, 3561 (1997).
17. O. Kircher, B. Schiener, and R. Bohmer, Phys. Rev. Lett. **81**, 4520 (1998).
18. A. G. Sveshnikov and A. N. Tikhonov, *The Theory of Functions of a Complex Variable* (Nauka, Moscow, 1970).
19. L. D. Landau and E. M. Lifshitz, *Course of Theoretical Physics*, Vol. 8: *Electrodynamics of Continuous Media*, 1st ed. (Fizmatgiz, Moscow, 1959; Pergamon, Oxford, 1960).
20. M. E. Lines and A. M. Glass, *Principles and Application of Ferroelectric and Related Materials* (Clarendon, Oxford, 1977; Mir, Moscow, 1981).
21. C. L. Wang and S. R. P. Smith, J. Phys.: Condens. Matter **7**, 7163 (1995).
22. A. V. Chadwick, I. J. F. Poplett, D. T. S. Maitland, and M. E. Smith, Chem. Mater. **10** (3), 864 (1998).

Translated by O. Borovik-Romanova

Physics of the Solid State, Vol. 45, No. 8, 2003, pp. 1596–1599. Translated from Fizika Tverdogo Tela, Vol. 45, No. 8, 2003, pp. 1519–1522.

LOW-DIMENSIONAL SYSTEMS AND SURFACE PHYSICS

Photoelectron Si 2*p* Spectra of Ultrathin $CoSi_2$ Layers Formed on Si(100)2 × 1

M. V. Gomoyunova, I. I. Pronin, N. R. Gall', S. L. Molodtsov, and D. V. Vyalykh

Ioffe Physicotechnical Institute, Russian Academy of Sciences, Politekhnicheskaya ul. 26, St. Petersburg, 194021 Russia

e-mail: Marina.Gomoyunova@mail.ioffe.ru

Received December 27, 2002

Abstract—Solid-phase formation of ultrathin $CoSi_2$ layers on Si(100)2 × 1 was studied using high-resolution (~140 meV) photoelectron spectroscopy with synchrotron radiation ($h\nu$ = 130 eV). The evolution of Si 2*p* spectra was recorded both under deposition of cobalt on the surface of samples maintained at room temperature and in the course of their subsequent annealing. It was shown that Co adsorption on Si(100)2 × 1 is accompanied by a loss of reconstruction of the original silicon surface while not bringing about the formation of a stable $CoSi_2$-like phase. As the amount of deposited cobalt continues to increase (up to six monolayers), a discontinuous film of the Co–Si solid solution begins to grow on the silicon surface coated by chemisorbed cobalt. The solid-phase reaction of $CoSi_2$ formation starts at a temperature close to 250°C and ends after the samples have been annealed to ~350°C. © *2003 MAIK "Nauka/Interperiodica".*

1. INTRODUCTION

Photoelectron core-level spectra measured with a high energy resolution provide a wealth of information on the electronic states of atoms in a solid and their structural surroundings. Therefore, photoelectron spectroscopy is widely used to study electronic and atomic surface structure, as well as the various atomic processes occurring in the near-surface region of a solid. Application of this method to investigation of the initial stages in the growth of cobalt disilicide on the silicon surface, whose films enjoy wide use in modern solid-state electronics, appears promising. Although formation of the Co/Si(100) interface has been studied already for about two decades, the main stages in the solid-phase reaction of $CoSi_2$ formation in this system still remain unclear and the relevant publications are in many respects contradictory. It is maintained, for instance, that after two cobalt monolayers (MLs) have been deposited on a room-temperature Si(100)2 × 1 surface, one observes layer-by-layer metal film growth on it [1]. At the same time, in practically the same conditions (deposition of 2.6 ML Co), cobalt atoms were found to enter into a strong chemical reaction with the substrate, accompanied by $CoSi_2$ formation [2].

Photoelectron core-level spectroscopy has been used to study the initial stages in the silicide formation in the Co/Si(100) system only in a few works [3–5], and the energy resolution achieved was about 350 meV, in which case the silicon doublet $2p_{1/2}$, $2p_{3/2}$ usually employed to derive information on the energy shifts of the silicon core levels could not be reliably resolved. This communication reports on an experiment carried out at a higher resolution, which permitted us to obtain new information on the mechanism of the process under consideration.

2. EXPERIMENTAL

The study was carried out on the Russian–German synchrotron channel BESSYII in an ultrahigh-vacuum photoelectron spectrometer with a full energy resolution (monochromator plus analyzer) of ~140 meV. The measurements were performed at a photon energy $h\nu$ = 130 eV, which corresponds to the highest surface sensitivity in excitation of the Si 2*p* core levels. The instrument detected photoelectrons emitted in a cone oriented along the surface normal.

The samples used were cut from KÉF-1 single-crystal silicon plates. The misalignment of their surface relative to the (100) face was less than 0.1°. Prior to being loaded into the photoelectron spectrometer chamber, the samples were subjected to chemical treatment following the technique of Shiraki [6], after which they were heated for a short time in ultrahigh vacuum to a temperature of 1200°C. The crystal cooling rate did not exceed 50°C/min, which yielded a Si(100)2 × 1 reconstructed surface free of carbon and oxygen contamination. Cobalt was deposited on a room-temperature substrate from a thoroughly outgassed source in which a wire of very pure cobalt was heated by electron bombardment. The rate of cobalt deposition was ~1 ML/min [1 ML = 6.8×10^{14} atoms/cm^2, which corresponds to the silicon atom concentration on the (100) face]. The Si 2*p* spectra were measured at room temperature in a vacuum of 1.2×10^{-8} Pa.

1063-7834/03/4508-1596$24.00

3. RESULTS OF THE MEASUREMENTS AND DISCUSSION

3.1. Cobalt Deposition on Si(100)2 × 1

We followed the evolution of the Si 2*p* spectrum in both stages of the cobalt disilicide solid-phase epitaxy, namely, when Co was evaporated on a silicon substrate at room temperature and in the course of the solid-phase reaction during the subsequent annealing of the samples. Figure 1 illustrates the data obtained in the first stage as Si 2*p* spectra measured for a clean Si(100)2 × 1 surface and after deposition of three increasing cobalt doses on this surface. As seen from the curves, the deposition of cobalt modifies the substrate spectrum noticeably as the coverage increases. The humped curve with a step on the right-hand side is replaced by a broader maximum with a nearly flat top. Note the decrease in the total intensity of the silicon 2*p* electron emission.

The measured spectra were decomposed by computer fitting into components differing in the core electron binding energy. This energy is reckoned from the energy of the pure-silicon bulk mode by assuming the negative shifts to be due to core electrons whose binding energies are lower than those of the bulk atom electrons. To describe all modes of the spectrum, Voigt functions were used [7], which are usually employed in similar spectroscopic problems. These functions are actually convolutions of the Lorentz functions, which include the core hole lifetime, with Gaussians describing the phonon broadening of the lines and the energy resolution of the instrument. The spectra were unfolded by properly varying the widths of the lines and their energy positions and intensities. The best-fit values of the halfwidths of the Lorentzians were found to be 70 meV, and those of the Gaussians, 300 meV. The 2*p* doublet splitting was fixed at 608 meV, and the intensity ratio of the doublet components $2p_{3/2}$ and $2p_{1/2}$ was assumed equal to two.

Figure 1a shows the results obtained for clean-surface samples. The spectrum of the Si(100)2 × 1 reconstructed surface is fairly complex and, according to recent data [8], consists of a bulk mode and five surface components. Evaporation of adsorbate atoms on the silicon surface should primarily affect the uppermost substrate atomic layer consisting of asymmetric dimers with which the surface spectral modes S_u and S_d are associated. Therefore, to make the spectral changes caused by the cobalt adsorption more revealing, the decomposition presented in Fig. 1a shows the above S_u and S_d modes, as well as the component B_1, which is the sum of all other modes of the spectrum (the bulk mode and those associated with the Si atoms in the first and second layers under the dimers). In addition, for the sake of convenience, only the curves for the $3p_{3/2}$ component of the Si 2*p* doublet are shown.

Unfolding of the Si 2*p* spectra obtained after deposition of increasing cobalt doses on the substrate is

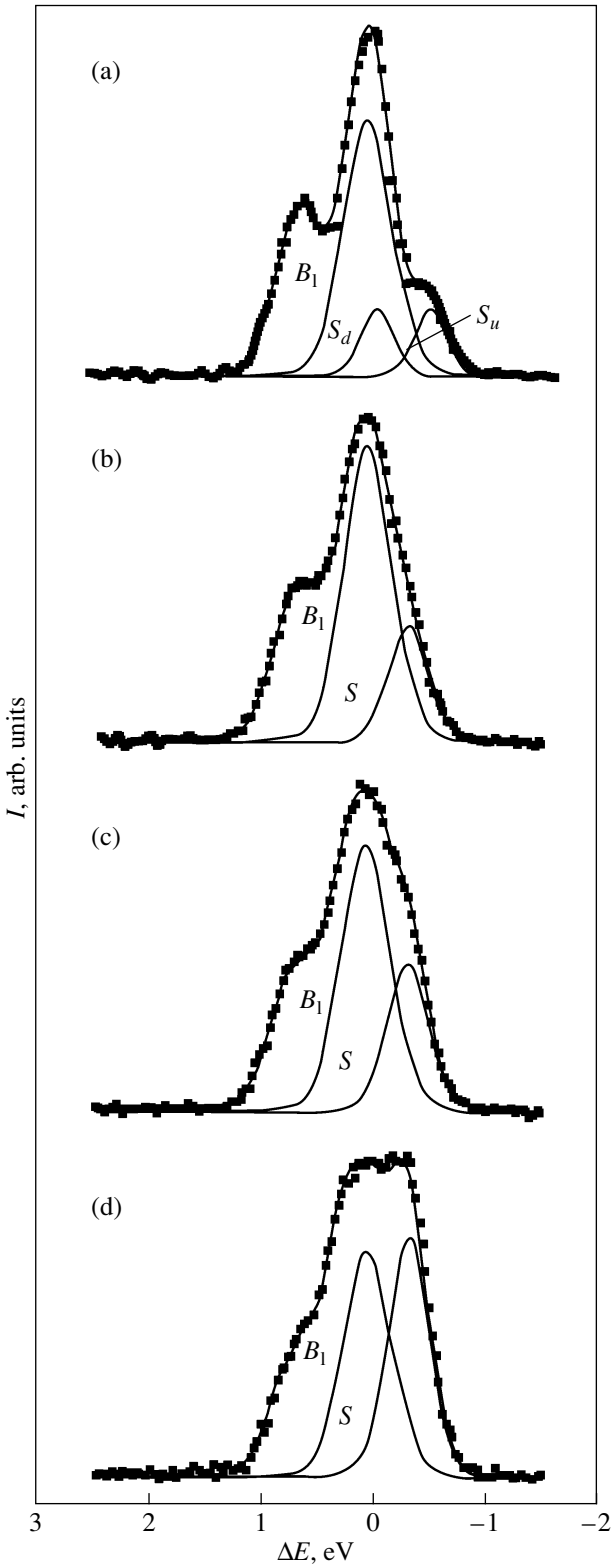

Fig. 1. 2*p* photoelectron spectra of the Si(100)2 × 1 surface, measured at $h\nu$ = 130 eV, and their decomposition into constituents. (a) Clean surface. Evaporated Co doses: (b) 1.2, (c) 2.5, and (d) 6 ML. Spectral modes: B_1 is the bulk mode combined with part of the surface modes, S_u and S_d are the modes of the upper and the lower asymmetric-dimer atom, and S is the Co–Si solid-solution mode.

illustrated in Figs. 1b–1d. These spectra do not contain the S_u and S_d modes, but a new mode *S* associated with the presence of the adsorbate on the sample emerges. The absence of the asymmetric dimer components in the spectrum implies that cobalt adsorption is accompanied by atomic rearrangement of the silicon surface, with the original surface losing its restructuring. As for adsorption sites, recent theoretical calculations of the Co binding energy with the Si(100)2×1 surface [9] suggest that the sites with the largest number of interatomic bonds are energetically preferable for the Co atoms. In view of this, we believe that cobalt atoms are localized in the uppermost layer of the nonreconstructed Si(100) surface between the four Si atoms to form seven interatomic bonds with the substrate. This conclusion is argued for by the results of an extended x-ray absorption fine structure (EXAFS) study [10]. The fact that the (2×1)-type diffraction pattern is retained in the submonolayer coverage region suggests that chemisorbed Co atoms become aligned in rows similar to those of the dimers on the Si(100)2×1 surface. We describe a more comprehensive study of the cobalt adsorption stage on Si(100)2×1 in [11].

As seen from Fig. 1, as the deposited cobalt dose increases, the relative intensity of the B_1 mode decreases and that of the new mode, *S*, increases. The position of the latter mode, –300 meV, practically does not change with increasing Co dose and falls into the shift range for Si atoms in the Co–Si solid solution obtained in [3, 4, 12] for the case of Co deposited on room-temperature silicon. We also identify this mode with the Si atoms in the Co–Si solution. The negative sign of the shift should possibly be assigned to enhancement of the extratomic relaxation initiated by the cobalt valence 3*d* electrons present in the Co–Si solid solution.

The similarity between the intensities of the bulk component of pure silicon and the component of the silicon present in the Si–Co solid solution under deposition of 6 ML Co, where the layer of the Co–Si solid solution formed can be expected to screen the silicon crystal to a considerable extent, might, at first glance, appear strange. Note that an anomalously high intensity of the pure-silicon mode, even in excess of the Co–Si solid solution component intensity, was also observed in [4] in the case of five cobalt monolayers deposited on Si(100)2×1 at room temperature. We believe the reason for this consists in the fact that the Co–Si solid solution layer growing on the Si(100) substrate with a chemisorbed submonolayer (0.5 ML) Co coating has pinholes rather than being continuous. In view, however, of the intensity ratio of the above modes and of the Si concentration in the solid solution, which cannot be high, we come to the conclusion that the area of these pinholes must not be large.

3.2. Annealing Samples with Deposited Cobalt Films

Let us turn now to the results of our study of the second stage in solid-phase epitaxy, in which the samples on whose surface the 6 ML Co had been deposited were subjected to annealing. The annealing was effected at progressively increased temperatures by heating the crystal for short times (~2 min) in the ramping mode. The spectra were measured at room temperature in the intervals between the annealings. Changes in the spectra, indicating the onset of the solid-phase reaction of Co with Si, were revealed only after annealing the samples to ~250°C, and the changes were enhanced as the temperature was raised even further. Figure 2 presents Si 2*p* spectra recorded in this series after annealing the crystal at increasing temperatures. The dynamics of the variation of the spectra is reminiscent of their evolution observed under cobalt deposition but occurs in reverse order. The broad, nearly flat-topped maximum transforms gradually into a double-humped one, and a step appears on its right-hand slope, making it similar to the clean-substrate spectrum.

These curves, like the spectra obtained in the first stage of the process, were unfolded into their constituents; the results of this decomposition are shown in Fig. 2. As is evident from the figure, the changes in the Si 2*p* spectrum caused by the sample annealing at ~280°C are due, first, to a decrease in the amplitudes of both constituents of the spectrum (primarily of the *S* mode of the Co–Si solid solution) and, second, to the emergence of a new mode *D* in the region of positive shifts $\Delta E = 300$ meV.

Similar values of positive shifts of Si 2*p* electrons have been reported for cobalt disilicide with a stable CaF_2 structure [4, 5, 12]. $CoSi_2$ with a CsCl-type metastable structure revealed [13, 14] a positive shift of about 300–350 meV relative to the stable phase. In this connection, we assign the new component *D*, observed under annealing, to the bulk mode of the cobalt disilicide with CaF_2 structure usually produced in the course of a solid-phase reaction. Note that the positive sign of the shift of this mode is accounted for by the Si atoms having a small excess positive charge (compared to pure Si), whose presence in the stable CaF_2 structure of the cobalt disilicide was established in [15].

Increasing the annealing temperature to 350°C causes a further rise in the cobalt disilicide peak *D*, which becomes dominant in the spectrum, and to a strong decrease in amplitude of the pure-silicon mode B_1. The component *S* with a negative shift becomes very small and slightly changes its position, thus suggesting a change of its origin. If we reckon the energy position of this component from that of the bulk $CoSi_2$ mode, the energy turns out to be about –600 meV, which is in good agreement with the value for the surface mode S_D obtained for a $CoSi_2$(100) single crystal in [16]. This agreement indicates disappearance of the solid-solution phase and, hence, completion of the

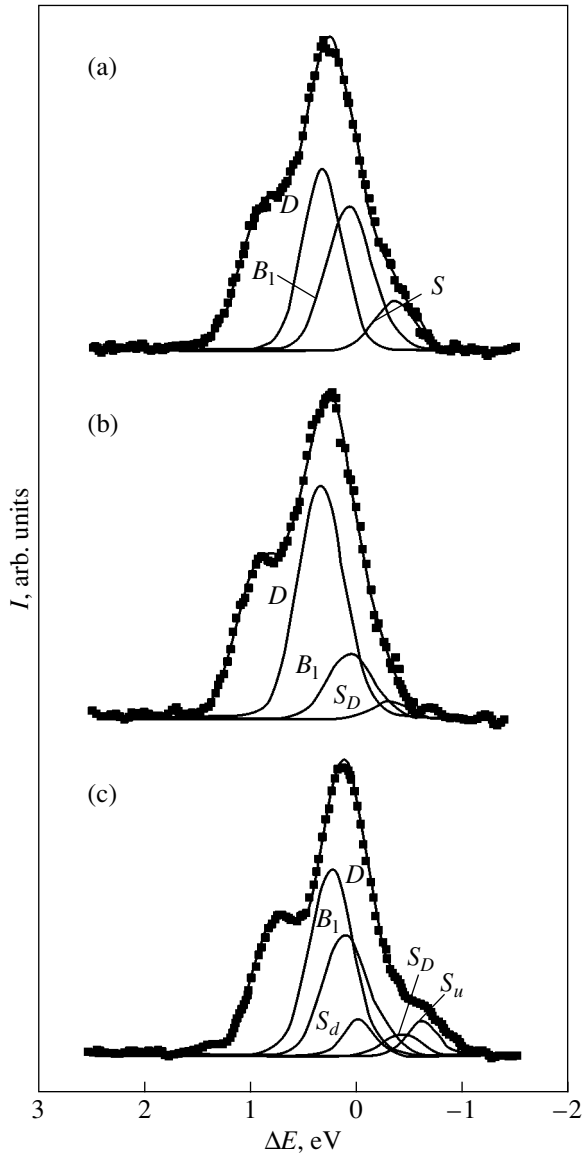

Fig. 2. 2*p* photoelectron spectra of a Si(100) crystal coated by a cobalt film, measured after annealing, and their decomposition into constituents. Anneal temperatures: (a) 280, (b) 350, and (c) 600°C. Spectral modes: B_1 is the bulk mode of pure Si combined with part of the surface modes, S_u and S_d are the modes of the upper and the lower asymmetric-dimer atom, *S* is the Co–Si solid-solution mode, and *D* and S_D are the bulk and surface modes of $CoSi_2$.

solid-phase reaction and the formation of a $CoSi_2(100)$ epitaxial film.

Annealing a sample to 600°C modifies the spectrum differently; indeed, the cobalt disilicide components *D* and S_D decrease in amplitude, the substrate component B_1 grows, and the surface modes of the substrate S_u and S_d appear, which indicates the appearance of pinholes in the Si(100)2×1 reconstructed surface.

4. CONCLUSION

Thus, the application of core-level photoelectron spectroscopy with an energy resolution higher than that previously reached permitted us to detect, in the first stage of solid-phase cobalt disilicide formation, a phase of chemisorbed cobalt and pinholes in a growing Co–Si solid-solution film and, in the second stage of the process, to establish the temperature intervals of the reaction and to observe the initial stage of pinhole formation in samples annealed to a temperature of about 600°C.

ACKNOWLEDGMENTS

This study was supported by the Russian Foundation for Basic Research (project no. 01-02-17288); the Ministry of Industry, Science, and Technologies (State contract 40.012.1.1.1152); and the Russian–German laboratory at BESSY II.

REFERENCES

1. W. S. Cho, J. Y. Kim, N. G. Park, *et al.*, Surf. Sci. **453**, L309 (2000).
2. U. Starke, W. Weiss, G. K. Heinz, *et al.*, Surf. Sci. **352**, 89 (1996).
3. J. M. Gallego, R. Miranda, S. Molodtsov, *et al.*, Surf. Sci. **239**, 203 (1990).
4. G. Rangelov, P. Augustin, J. Stober, and Th. Fauster, Phys. Rev. B **49** (11), 7535 (1994).
5. G. Rangelov and Th. Fauster, Surf. Sci. **365**, 403 (1996).
6. A. Ishizaka and Y. Shiraki, J. Electrochim. Soc. **133**, 666 (1986).
7. E. Landemark, C. J. Karlsson, Y.-C. Chao, and R. I. G. Uhrberg, Phys. Rev. Lett. **69** (10), 1588 (1992).
8. T.-W. Pi, C.-P. Ouyang, J.-F. Wen, *et al.*, Surf. Sci. **514**, 327 (2002).
9. A. P. Horsfield, S. D. Kenny, and H. Fujitani, Phys. Rev. B **64**, 245332 (2001).
10. H. L. Meyrheim, U. Döbler, and A. Puschmann, Phys. Rev. B **44** (11), 5738 (1991).
11. M. V. Gomoyunova, I. I. Pronin, N. R. Gall', *et al.*, Pis'ma Zh. Tekh. Fiz. **29** (12) (2003) (in press).
12. F. Boscherini, J. J. Joyce, M. W. Ruckman, and J. H. Weaver, Phys. Rev. B **35** (9), 4216 (1987).
13. C. Pirri, S. Hong, M. H. Tuilier, *et al.*, Phys. Rev. B **53** (3), 1368 (1996).
14. K.-J. Kim, T.-H. Kang, K.-W. Kim, *et al.*, Appl. Surf. Sci. **161**, 268 (2000).
15. W. R. L. Lambrecht, N. E. Christensen, and P. Blöchl, Phys. Rev. B **36** (5), 2493 (1987).
16. R. Leckey, J. D. Riley, R. L. Johnson, *et al.*, J. Vac. Sci. Technol. A **6** (1), 63 (1988).

Translated by G. Skrebtsov

Physics of the Solid State, Vol. 45, No. 8, 2003, pp. 1600–1605. Translated from Fizika Tverdogo Tela, Vol. 45, No. 8, 2003, pp. 1523–1527.

LOW-DIMENSIONAL SYSTEMS AND SURFACE PHYSICS

Charge Ordering Induced by Intrinsic Defects in Sn/Ge(111) Submonolayers with a Coverage Close to 1/3

V. N. Men'shov and V. V. Tugushev

Russian Research Centre Kurchatov Institute, pl. Akademika Kurchatova 1, Moscow, 123182 Russia

e-mail: vvtugushev@mail.ru

Received August 19, 2002; in final form, December 15, 2002

Abstract—A thermodynamic model is suggested for a (3×3)-type structure formation with a charge density wave (CDW) arising against the background of a $(\sqrt{3} \times \sqrt{3})R30°$-type structure in a Group IV metal (Sn, Pb) submonolayer adsorbed with a coverage of ≈1/3 at the (Ge, Si) semiconductor (111) surface. Calculations are carried out by using a self-consistent theory for static fluctuations of the order parameter amplitude. It is shown that the low-symmetry (3×3) phase can nucleate at point defects of the submonolayer as charge-ordered areas of finite radius. The spatial configuration of the CDW and its temperature dependence are calculated. The results obtained are compared with the experimental data for the Sn/Ge(111) system. © *2003 MAIK "Nauka/Interperiodica".*

1. INTRODUCTION

Currently, the phenomenon of the $(\sqrt{3} \times \sqrt{3}) \longrightarrow (3 \times 3)$ reconstruction in metal submonolayers (Pb, Sn) adsorbed at the (111) surface of diamond-like semiconductors (Ge, Si) with a coverage close to 1/3 (see [1, 2] and references therein) is being actively discussed [3, 4]. As the temperature T decreases, such an isovalent system undergoes a structural phase transition from the $(\sqrt{3} \times \sqrt{3})R30°$ phase with a single metal atom in the surface unit cell to the (3×3) phase, where the unit cell contains three metal atoms. Two of these atoms are positively charged and displaced downward, and one atom is negatively charged and displaced upward. At $T = 0$, the (3×3) surface structure allows description in terms of a triangular-lattice model with a charge density wave (CDW) [1]; the possible mechanisms of CDW formation involving electron correlations in a narrow surface region were studied in [1, 5]. According to this model, due to the electron–electron and (or) electron–phonon coupling, the ground state with the $(\sqrt{3} \times \sqrt{3})$ structure is unstable with respect to the transition to the (3×3) structure, with the corresponding charge redistribution and change in the electron spectrum. This instability can be enhanced due to both the nesting (congruence) at a portion of the Fermi surface and a Van Hove singularity in the electron density of states near the Fermi level. Both these factors, favorable for surface electrons ordering with CDW formation, were qualitatively analyzed in [5] within the simplest triangular-lattice model in the tight-binding approximation. The main conclusion made in [5] is that the influence of the nesting on the CDW formation depends heavily on the approximation used and manifests itself when the surface band is almost half-filled, which takes place in actual systems. This situation obviously takes place in structures with neutral adsorbate layers, where there is no significant charge redistribution between the surface and bulk of the semiconductor and where there is no surface doping due to defects. We note that numerical calculations [1, 6] of the surface electron spectrum for the systems under consideration show the absence of nesting in the case of the half-filled surface band.

The influence of a Van Hove singularity on the CDW formation with the (3×3) structure is almost independent of the approximation used and seems to be more significant. This singularity probably causes the static response function $\chi^0(\mathbf{q})$ of the $(\sqrt{3} \times \sqrt{3})R30°$ lattice to have a pronounced peak at $\mathbf{q} \approx \mathbf{P}$, where $\mathbf{P}$ is the vector of the (3×3) reciprocal lattice coinciding with the vector ΓK in the Brillouin zone of the $(\sqrt{3} \times \sqrt{3})R30°$ lattice. This feature of the function $\chi^0(\mathbf{q})$ becomes stronger when the Fermi level is shifted slightly upward in energy with respect to the position corresponding to the half-filled band [7]; therefore, the influence of doping on charge ordering, strictly speaking, should not be neglected.

We recall that possible CDW formation in the ground state of the correlated electron system is qualitatively determined by the instability criterion

$$1 - V(\mathbf{q})\chi^0(\mathbf{q}) \le 0, \qquad (1)$$

where $V(\mathbf{q})$ is the effective electron–electron interaction potential, depending, in general, on the wave vector $\mathbf{q}$, and $\chi^0(\mathbf{q})$ is the response function of noninteracting electrons at zero temperature. The product

$V(\mathbf{q})\chi^0(\mathbf{q})$ peaks at the wave vector $\mathbf{q}_{max}$ corresponding to an "optimum" (lowest in energy) CDW spatial structure. If the potential $V(\mathbf{q})$ is independent of $\mathbf{q}$, the vector $\mathbf{q}_{max}$ strictly corresponds to the peak of the function $\chi^0(\mathbf{q})$. However, as was first indicated in [1], the potential $V(\mathbf{q})$ becomes heavily dependent on $\mathbf{q}$ with a maximum at the wave vector $\mathbf{P} = (4\pi/3a)\mathbf{e}$ (where $\mathbf{e}$ is the unit vector in the ΓK direction in the Brillouin zone of the $(\sqrt{3} \times \sqrt{3})R30°$ surface lattice with period a) when the Coulomb interaction between electrons at the nearest neighbor sites of the triangular lattice is taken into account. At the same time, the peak of the function $\chi^0(\mathbf{q})$ does not meet the necessary condition for satisfying criterion (1) at $\mathbf{q} = \mathbf{P}$. Taking into account this circumstance, the conditions of the onset of charge ordering on a triangular lattice were determined and the ground state of the system with a commensurate CDW with wave vector $\mathbf{P}$ was found in [5] within a microscopic approach.

We will extend the model considered in [1, 5] to finite temperatures, assuming that the existence of a peak of the potential $V(\mathbf{q})$ at $\mathbf{q} = \mathbf{P}$ is the principal cause of the CDW formation with the (3×3) structure, while the feature in the $\chi^0(\mathbf{q})$ dependence is of secondary importance. However, defects existing in the system can significantly change criterion (1). In actual practice, doping always takes place in the adsorbed submonolayer due to irremovable intrinsic defects (e.g., germanium atoms, substituting for tin, or tin vacancies in the structure Sn/Ge(111) [7, 8]). As the temperature decreases, such defects can become formation centers of local regions of the new (3×3) phase inside the initial $(\sqrt{3} \times \sqrt{3})$ phase. This study is aimed at constructing a thermodynamic model of the phase transition with the formation of a planar CDW in the presence of point defects.

2. SELF-CONSISTENT CHARGE FLUCTUATIONS

In the model suggested, the charge instability condition, depending on the temperature and band filling, is dictated only by the parametric dependence of the susceptibility $\chi^0(\mathbf{q})$ on T and μ, where μ is the Fermi energy shift with respect to the half-filling. According to formula (1), the temperature T_c^0 of the second-order phase transition from the $(\sqrt{3} \times \sqrt{3})$ (at $T > T_c^0$) to the low-symmetry (3×3) phase (at $T < T_c^0$) in the mean-field approximation is found from the condition

$$1 - V(\mathbf{P})\chi^0(\mathbf{P}, T_c^0) = 0, \qquad (2)$$

where $\chi^0(\mathbf{P}, T)$ is the response function of free electrons at the wave vector $\mathbf{P}$ at temperature T. In two-dimensional systems, thermodynamic fluctuations of the order parameter play an important role, significantly decreasing the actual transition temperature T_c in comparison with the mean-field temperature T_c^0 ($T_c \ll T_c^0$) [9] and changing the phase transition from the second to the first order [10]. Hence, the quantity T_c^0 should be considered only as a certain formal characteristic temperature that probably even exceeds the deposition or melting temperature of the adsorbed submonolayer in actual Sn/Ge(111)-type structures.

For qualitative estimations from Eq. (2), we use a simple model for the surface electron density of states $\rho(\varepsilon)$, assuming that the major contribution to the temperature dependence of $\chi^0(\mathbf{P}, T)$ is made by a rectangular peak of $\rho(\varepsilon)$ near the Fermi level. We assume the absence of nesting in the electron spectrum $\varepsilon(\mathbf{k})$, in which case the difference $|\varepsilon(\mathbf{k}) - \varepsilon(\mathbf{k} + \mathbf{P})|$ is of the order of the band halfwidth W at all values of $\mathbf{k}$ near the Fermi surface. Since the inequality $T \ll W$ ($W \approx 0.1$–0.3 eV, $T \leq 300$ K) is met in the temperature range under study, we can use the expansion

$$\chi^0(\mathbf{P}, T) \approx \chi^0(\mathbf{P}) - \Theta T^2, \qquad (3)$$

where $\Theta \sim \bar{\rho} W^{-2}$, with $\bar{\rho}$ being the average density of states at the Fermi surface. Substituting Eq. (3) into Eq. (2), we obtain an upper estimate for the critical temperature:

$$T_c^0 \sim \sqrt{\frac{|\alpha|}{\bar{\rho}}} W.$$

The characteristic temperature T_c^0 is small in comparison with the energy W, provided the inequality $\frac{|\alpha|}{\bar{\rho}} = \frac{\chi^0(\mathbf{P}) - V^{-1}(\mathbf{P})}{\bar{\rho}} \ll 1$ is valid; nevertheless, this temperature significantly exceeds the actual transition temperature T_c [9, 10]. In the temperature range between T_c^0 and T_c, there are significant thermodynamic fluctuations and short-range order. In this range, we have a mixed state of two phases, $(\sqrt{3} \times \sqrt{3})$ and (3×3), and the CDW induced by intrinsic defects of the submonolayer has a very complex, spatially inhomogeneous structure. In this case, the upper temperature limit is defined most likely by the temperature of metal submonolayer deposition onto the semiconductor surface, rather than by the temperature T_c^0, which therefore has no certain physical meaning.

To describe the formation of a (3×3) CDW structure near an isolated defect on the $(\sqrt{3} \times \sqrt{3})$ lattice above the actual transition temperature T_c, we use the well-known and very pictorial concept of a "local phase transition" with a macroscopic, but finite, correlation

length of charge fluctuations [11], based on the Landau expansion of the free-energy functional $F[\Delta]$, where $\Delta(\mathbf{r})$ is the order parameter characterizing the envelope $\delta n(\mathbf{r})$ of the charge density for wave vectors close to $\mathbf{P} = \frac{4\pi}{3a}\mathbf{e}$. The charge density distribution $n(\mathbf{r})$ and its envelope are given by

$$n(\mathbf{r}) = \delta n(\mathbf{r})\cos(\mathbf{P}\mathbf{r}),$$
$$\delta n(\mathbf{r}) = \sum_{\mathbf{q}} \frac{\Delta_{\mathbf{q}}}{V(\mathbf{P}+\mathbf{q})}\exp(i\mathbf{q}\mathbf{r}). \quad (4)$$

In the absence of defects and provided the condition $\frac{\Delta}{W} \ll 1$ is met, the functional $F[\Delta]$ can be written as

$$F_0[\Delta] = \int f(\mathbf{r})d\mathbf{r}, \quad (5)$$

$$f(\mathbf{r}) = \alpha\Delta^2(\mathbf{r}) + \beta\Delta^4(\mathbf{r}) + \gamma\left(\frac{\partial\Delta(\mathbf{r})}{\partial\mathbf{r}}\right)^2 + \nu\left(\frac{\partial^2\Delta(\mathbf{r})}{\partial\mathbf{r}^2}\right)^2. \quad (6)$$

Integration in formula (5) is carried out over the entire (x, y) plane; the coefficients α, β, γ, and ν in the expansion in Eq. (6) are almost independent of temperature; $\alpha = -|\alpha| = V(\mathbf{P})^{-1} - \chi^0(\mathbf{P})$ is a negative quantity, while β, γ, and ν are positive ($\beta \sim W^{-2}\bar{\rho}$, $\gamma \sim \bar{\rho}\xi_0^2$, $\nu \sim \bar{\rho}\xi_0^4$, $\xi_0 = v_F/W$, with v_F being the velocity at the Fermi surface). We assume that $|\alpha| \ll \bar{\rho}$; thus, in the mean-field approximation at $T = 0$, functional (5) is minimum at $\Delta_0 = \sqrt{|\alpha|/2\beta} \ll W$. At finite values of T, the thermodynamics described by Eqs. (5) by (6) is controlled by charge fluctuations, which we consider in the Gaussian approximation, as is done, e.g., in the theory of renormalized (self-consistent) spin fluctuations [12]. Separating the mean-field $\varphi(\mathbf{r})$ and fluctuation $\eta(\mathbf{r})$ components of the order parameter, $\Delta(\mathbf{r}) = \varphi(\mathbf{r}) + \eta(\mathbf{r})$, and averaging the functional given by Eqs. (5) and (6) over the random variable $\eta(\mathbf{r})$, we redefine the effective free energy $F_0[\varphi]$ as

$$F_0[\varphi] = \int f(\mathbf{r})d\mathbf{r}, \quad (7)$$

$$f(\mathbf{r}) = \tilde{\alpha}\varphi^2(\mathbf{r}) + \beta\varphi^4(\mathbf{r}) + \gamma\left(\frac{\partial\varphi(\mathbf{r})}{\partial\mathbf{r}}\right)^2 + \nu\left(\frac{\partial^2\varphi(\mathbf{r})}{\partial\mathbf{r}^2}\right)^2, \quad (8)$$

$$\tilde{\alpha} = \alpha + 6\beta\langle\eta^2\rangle, \quad (9)$$

where $\langle\eta^2\rangle$ is the mean-square fluctuation of the order parameter, which depends in the strict sense, on φ and should be calculated in a self-consistent way.

When $\varphi = 0$, the fluctuation $\langle\eta^2\rangle$ in the main logarithmic approximation is given by

$$\langle\eta^2\rangle = \frac{\pi T}{2\gamma}\ln[(lq_c)^2 + 1], \quad (10)$$

where $l = \sqrt{\gamma/\tilde{\alpha}}$ is the correlation length and q_c is the cutoff quasimomentum; above the transition temperature T_c, where $\varphi = 0$, we have $\tilde{\alpha} > 0$. If $(lq_c)^2 \gg 1$ and $T < T^*$, the $\tilde{\alpha}(T)$ dependence has the form $\tilde{\alpha}(T) \approx \gamma q_c^2\exp(-T^*/T)$, where $T^* = \frac{|\alpha|\gamma}{3\pi\beta}$ is the crossover temperature. We note that $T^* \ll T_c^0$ at $|\alpha| \ll \tilde{\rho}$, since $T^* \sim (|\alpha|/\bar{\rho})W$ and $T_c^0 \sim \sqrt{|\alpha|/\bar{\rho}}W$. As the temperature decreases, the system exhibits a first-order phase transition at the point $T_c < T^*$ to a state with $\varphi \neq 0$, where $\langle\eta^2\rangle$ is strongly renormalized [10]. Estimate (10) is obviously invalid below the point T_c. The regime of $(lq_c)^2 \ll 1$ becomes possible at the temperature $T > T^*$; in this case, we have $\tilde{\alpha}(T) \approx \sqrt{3\beta\pi T}q_c$. In the phenomenological theory of static charge fluctuations, the cutoff momentum q_c is introduced as an external parameter determined in the microscopic approach by inelastic scattering of electrons by plasmons or phonons and (in order of magnitude) is proportional to T/v_F above the transition temperature T_c. This means that the temperature dependence of the correlation length changes an from exponential, $l^{-1}(T) \sim T\exp\left(-\frac{T^*}{2T}\right)$, to a power-law form, $l^{-1}(T) \sim T^{3/4}$, when T increases passing through the crossover region near T^*.

The figure shows the results of a numerical analysis of the set of equations (9) and (10) in the linear (in T) approximation for the cutoff momentum $q_c = sT/v_F$, where s is a coefficient independent of T; the dimensionless parameter $k = \frac{s^2\gamma^2T^*}{3\pi\beta v_F^2}$ is much smaller than unity in the model suggested. It is evident that at $T > T^*$ the $l^{-1}(T)$ dependence can be roughly approximated in a wide temperature range by a linear function $l^{-1}(T) \sim T$, whose slope is defined by the parameter k, and the relation $l^{-1}(T) \sim T^{3/4}$ becomes valid only at $T \gg T^*$.

3. CHARGE DENSITY WAVE FORMATION NEAR AN ISOLATED POINT DEFECT

Now, we discuss the isolated-point-defect model for CDW formation based on the concept of the local phase

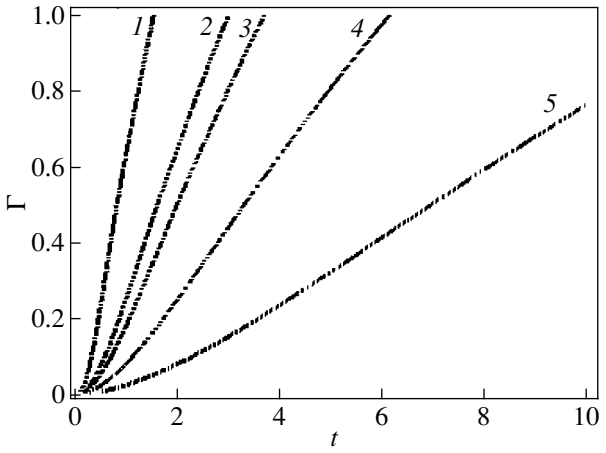

Temperature dependence of the inverse correlation length of charge fluctuations ($t = \frac{T}{T^*}$, $\Gamma = \frac{1}{l}\sqrt{\gamma/|\alpha|}$) at various values of the parameter k: (*1*) 1, (*2*) 0.1, (*3*) 0.05, (*4*) 0.01, and (*5*) 0.001.

transition. Considering the functional $F_0[\varphi]$ in Eq. (7) as an effective free energy of an undoped system above the phase transition point ($\tilde{\alpha} > 0$), we introduce a term $\delta F[\varphi]$ representing a perturbation near a defect and having the simplest form of a "point source." Then, the total energy takes on the form

$$F[\varphi] = F_0[\varphi] + \delta F[\varphi], \quad (11)$$

$$\delta F[\varphi] = \int \lambda(\mathbf{r})\varphi(\mathbf{r})d\mathbf{r}. \quad (12)$$

Physically, the term $\delta F[\varphi]$ in Eqs. (11) and (12) is the energy of charge redistribution around the defect calculated to the first order in the perturbing potential $\lambda(\mathbf{r})$. In the local approximation, when the effective radius of the isolated defect is small in comparison with the correlation length, we have $\lambda(\mathbf{r}) = \lambda\delta(\mathbf{r})$, with $\lambda \sim U_0/W$, where U_0 is the matrix element of the perturbing potential at the wave vector $\mathbf{P}$; this matrix element is positive or negative depending on the defect charge sign (e.g., a substitutional atom or vacancy). In approximation (11), we disregarded the coefficient $\tilde{\alpha}$ of renormalization due to the defect potential, assuming that $(\varphi^2/\eta^2) \ll 1$, which seems quite reasonable in the case of a low defect concentration above the transition temperature.

Minimization of free energy (11) with respect to the order parameter $\varphi(\mathbf{r})$ yields the self-consistency equation

$$\left[\nu\frac{\partial^4}{\partial\mathbf{r}^4} - \gamma\frac{\partial^2}{\partial\mathbf{r}^2} + \tilde{\alpha} + 2\beta\varphi^2(\mathbf{r})\right]\varphi(\mathbf{r}) = -\frac{\lambda}{2}\delta(\mathbf{r}), \quad (13)$$

where the term with the fourth derivative is purposely retained, due to which it is possible to eliminate the singularity of the function $\varphi(\mathbf{r})$ at $\mathbf{r} \longrightarrow 0$ in the point-defect model. If we omit the nonlinear term $\sim\varphi^3$ in Eq. (13), which is correct at least far from the defect at $r \gg l$, then the solution to Eq. (13) can be written as

$$\varphi(\mathbf{r}) = -\frac{\lambda}{4\pi\nu(p_+^2 - p_-^2)}[K_0(p_-r) - K_0(p_+r)], \quad (14)$$

$$p_\pm^2 = \frac{\gamma \pm \sqrt{\gamma^2 - 4\nu\tilde{\alpha}}}{2\nu}, \quad (15)$$

where $K_0(z)$ is the modified Bessel function of order zero [13]. The CDW amplitude near the defect is given by

$$\varphi(0) = -\frac{\lambda\ln\left(\frac{p_+}{p_-}\right)}{4\pi\nu(p_+^2 - p_-^2)}, \quad (16)$$

or, in the limit $\frac{\tilde{\alpha}\nu}{\gamma^2} \ll 1$ characteristic of the problem under study,

$$\varphi(0) \approx -\frac{\lambda}{8\pi\gamma}\ln\frac{\gamma^2}{\tilde{\alpha}\nu}. \quad (17)$$

If the condition $\frac{U_0}{W} \ll \frac{\sqrt{\tilde{\alpha}/\bar{\rho}}}{\ln(\bar{\rho}/\tilde{\alpha})}$ is satisfied, the nonlinear term $\sim\varphi^3$ in Eq. (13) is insignificant at any distance $\mathbf{r}$ from the defect. The asymptotic form of the function $\varphi(\mathbf{r})$ at $p_\pm r \gg 1$ is

$$\varphi(\mathbf{r}) \approx -\frac{\lambda}{8\sqrt{\pi(\gamma^2 - 4\tilde{\alpha}\nu)}} \times\left[\frac{\exp(-p_-r)}{\sqrt{p_-r}} - \frac{\exp(-p_+r)}{\sqrt{p_+r}}\right]. \quad (18)$$

In the limit $\frac{\tilde{\alpha}\nu}{\gamma^2} \ll 1$, at $r \gg l$, Eq. (18) takes on the form

$$\varphi(\mathbf{r}) \approx -\frac{\lambda}{4\sqrt{2\pi}\gamma}\frac{\exp(-r/l)}{\sqrt{r/l}}, \quad (19)$$

therefore, the CDW envelope behavior at large distances is independent of the coefficient ν and the characteristic localization length of the order parameter coincides with the renormalized correlation length $l(T)$ of charge fluctuations.

The isolated point defect model for a surface remains correct only with the constraint $n_d l^2 \ll 1$, where n_d is the defect concentration. As the temperature decreases, the charge rearrangement region induced by defects grows proportionally to $l(T)^2$ and, on reaching

the characteristic temperature $\tilde{T}$, where $n_d \sim l^{-2}(\tilde{T})$, almost the entire surface is reconstructed. Most likely, the mixed phase above the temperature $\tilde{T}$ can be represented as a superposition of weakly overlapped local (3×3) CDW regions randomly distributed in the plane against the background of the $(\sqrt{3} \times \sqrt{3})$ structure and can be described by the generalized order parameter $\Phi(\mathbf{r}) \cong \sum_n \varphi_n(\mathbf{r} - \mathbf{R}_n)$, where $\mathbf{R}_n$ is the nth-defect position vector. The coordinate dependence of the envelope function $\varphi_n(\mathbf{r} - \mathbf{R}_n)$ is described by formulas (14)–(19), and its sign is defined by the matrix element of the nth-defect potential $\lambda_n = \lambda\cos(\mathbf{PR}_n)$ and can be both positive and negative. Thus, after averaging over the defect coordinates at the surface at $T > \tilde{T}$, we have $\langle\Phi(\mathbf{r})\rangle = 0$, but $\langle\Phi(\mathbf{r})^2\rangle \neq 0$. In the mixed state above the temperature $\tilde{T}$, the fraction of the (3×3) phase induced by defects in the $(\sqrt{3} \times \sqrt{3})$ phase reduces continuously with increasing T. The quantity $\tilde{T}$ may be considered a characteristic temperature of the smeared order-disorder phase transition from the mixed state with CDW islands to a state with a homogeneous CDW structure, which persists down to very low temperatures.

Now, let us discuss some experimental data on the Sn/Ge(111) system. Scanning tunneling microscopy experiments [8, 13, 14] show that the metal monolayer of this system always contains intrinsic defects: Ge atoms substituting for 3–4% of Sn atoms and Sn vacancies. These defects induce a (3×3) CDWs phase surrounded by the $(\sqrt{3} \times \sqrt{3})R30°$ phase; therefore, the state with a mixed structure is formed already at room temperature. The evolution of this structure from the island phase to an almost homogeneous (3×3) phase below 120 K [15] confirms the pattern of the phase transition induced by defects. A photoemission study [7] of the mixed phase revealed an energy gap near the Brillouin zone edge of the (3×3) lattice in the temperature range from 300 to 80 K, which counts in favor of the existence of the (3×3) CDW phase. According to [8], the temperature dependence of the inverse characteristic radius of a local CDW induced by a defect is close to linear, one $l^{-1}(T) \sim T$, at high values of T, which agrees qualitatively with the results we obtained (see Section 3). Using the empirical data from [8], we can also estimate the temperature $T^* \approx 70$ K as the boundary between the regions of the strong (at $T > T^*$) and the weak $l^{-1}(T)$ dependence (at $T < T^*$). Unfortunately, it is impossible to immediately extend the approach under consideration to the low-temperature region $T < T^*$, where the correlation length $l(T)$ exceeds the average distance between defects ($n_d l^2 \gg 1$) and the isolated-defect approximation becomes invalid. Strictly speaking, one can only make assumptions on the comparability of our theoretical estimate $l^{-1} \sim T\exp\left(-\frac{T^*}{2T}\right)$ to the experimental dependence obtained in [8] at $T < 70$ K.

4. CONCLUSIONS

The phenomenon of submonolayer reconstruction with CDW formation induced by defects is observed not only in the Sn/Ge(111) structure. For example, a weak local modulation of the charge density near defects was detected using reflective high-energy electron diffraction from a tin submonolayer coating (1/3 monolayer) on Si(111) at $T = 120$ K [16]. Another interesting example is one-dimensional metal chains on the In/Si(111)-(4×1) surface. Scanning tunnel microscopy of this surface at room temperature explicitly shows the existence of a new (4×2) structure of these chains, localized at sodium adatoms, whose electron spectrum is characterized by a dielectric gap inherent in systems with CDWs [17]. The theoretical scheme suggested in this paper seems to allow one to describe (at least in a qualitative manner) the thermodynamics of the phase transition with CDW formation in the presence of defects in such systems.

ACKNOWLEDGMENTS

This study was supported by the Ministry if Industry, Science, and Technologies of the Russian Federation (program "Nanoelectronics").

REFERENCES

1. G. Santoro, S. Scandolo, and E. Tosatti, Phys. Rev. B **59** (3), 1891 (1999).
2. S. Sokolowski, K. Binder, and A. Patrykiejew, Surf. Sci. Rep. **37** (6–8), 207 (2000).
3. L. Peterson, A. Ismail, and E. W. Plummer, Phys. Rev. Lett. **88** (18), 189701 (2002).
4. T. E. Kidd, T. Miller, M. Y. Chou, and T.-C. Chiang, Phys. Rev. Lett. **88** (18), 189702 (2002).
5. M. Avin'on, V. N. Men'shov, and V. V. Tugushev, Fiz. Tverd. Tela (St. Petersburg) **43** (3), 543 (2001) [Phys. Solid State **43**, 563 (2001)].
6. J. Ortega, R. Perez, and F. Flores, J. Phys. C **12** (1), L21 (2000).
7. T. E. Kidd, T. Miller, M. Y. Chou, and T.-C. Chiang, Phys. Rev. Lett. **85** (17), 3684 (2000).
8. A. V. Melechko, J. Braun, H. H. Weitering, and E. W. Plummer, Phys. Rev. B **61** (3), 2235 (2000).
9. M. Barber, Phys. Rep. **59** (6), 375 (1980); J. M. Kosterlitz and K. J. Thouless, Prog. Low Temp. Phys. **7B** (2), 371 (1978).
10. E. A. Zhukovskiĭ and V. V. Tugushev, Pis'ma Zh. Éksp. Teor. Fiz. **60** (4), 267 (1994) [JETP Lett. **60**, 280 (1994)].

11. A. P. Levanyuk, V. V. Osipov, A. S. Sigov, and A. A. Sobyanin, Zh. Éksp. Teor. Fiz. **76** (1), 345 (1979) [Sov. Phys. JETP **49**, 176 (1979)].
12. K. Murata and S. Doniach, Phys. Rev. Lett. **29** (2), 285 (1972); G. G. Lonzarich and L. Taillefer, J. Phys. C **18** (22), 4339 (1985).
13. J. Carpinelly, H. H. Weitering, M. Bartowiak, *et al.*, Phys. Rev. Lett. **79** (15), 2859 (1997).
14. A. V. Melechko, J. Braun, H. H. Weitering, and E. W. Plummer, Phys. Rev. Lett. **83** (5), 999 (1999).
15. T. Kidd, T. Miller, and T.-C. Chiang, Phys. Rev. Lett. **83** (14), 2789 (1999).
16. H. Morikawa, I. Matsuda, and S. Hasegava, Phys. Rev. B **65** (20), 201308 (2002).
17. S. S. Lee, J. R. Ahn, N. D. Kim, *et al.*, Phys. Rev. Lett. **88** (19), 196401 (2002).

Translated by A. Kazantsev

Physics of the Solid State, Vol. 45, No. 8, 2003, pp. 1606–1612. Translated from Fizika Tverdogo Tela, Vol. 45, No. 8, 2003, pp. 1528–1534.

POLYMERS AND LIQUID CRYSTALS

Thermal Expansion of the Skeleton of Chain Molecules in Polymer Crystals

V. I. Vettegren*, A. I. Slutsker*, V. L. Gilyarov*, V. B. Kulik*, and L. S. Titenkov**

** Ioffe Physicotechnical Institute, Russian Academy of Sciences, Politekhnicheskaya ul. 26, St. Petersburg, 194021 Russia*
e-mail: Victor.Vettegren@mail.ioffe.ru

*** Moscow State Textile University, Malaya Kaluzhskaya ul. 1, Moscow, 119991 Russia*

Received December 20, 2002

Abstract—The expansion of the carbon skeleton of molecules in crystallites and the longitudinal contraction of the crystallite lattice in poly(ethylene) (PE) and poly(caproamide) (PCA) with an increase in the temperature are measured using IR and Raman spectroscopy and x-ray diffraction. The thermal expansion of the carbon skeleton due to transverse vibrations is theoretically calculated within the atomic chain model. The theoretical and experimental data on the thermal expansion of the carbon skeleton are in good agreement. © *2003 MAIK "Nauka/Interperiodica".*

1. INTRODUCTION

Polymer crystals are built up of regularly arranged straight segments of chain molecules. The longitudinal (along the molecular axes) rigidity of covalent bonds in molecular skeletons is substantially higher than the flexural rigidity of molecules and the rigidity of van der Waals or hydrogen bonds between molecules. These factors are responsible for the specific features observed in the elasticity and internal dynamics of polymer crystals: (i) strong anisotropy of the elastic properties of polymer crystals (the moduli of longitudinal elasticity are approximately two orders of magnitude larger than those of transverse elasticity) and (ii) the high longitudinal rigidity of molecules and, consequently, the high characteristic temperature of longitudinal vibrations (~1500 K) [1]. As a result, thermal longitudinal vibrations are virtually not excited at temperatures up to the melting point of polymer crystals (400–500 K).

The characteristic temperatures of transverse vibrations are considerably lower (100–300 K) [1]; hence, these vibrations are excited at 300 K. Therefore, the transverse vibrations dominate in polymer crystals.

The domination of transverse vibrations determines the following features in the thermal expansion of polymer crystals.

(1) In the transverse direction, the lattice undergoes a conventional "solid-state" (positive) expansion through the vibrational–anharmonic mechanism due to transverse vibrations of molecules involved in anharmonic intermolecular interactions [1, 2].

(2) In the longitudinal direction, the lattice is subject to a negative thermal expansion (contraction) associated with the membrane mechanism of thermal deformation [1–3].

The theory of negative longitudinal expansion in polymer crystals has been developed in a number of works and offered reasonable agreement between the calculated and experimental data [4, 5]. In these works, it was assumed that, in the course of transverse vibrations, the molecules remain nonstretchable in the longitudinal direction owing to a high longitudinal rigidity [1, 4, 5]. This inference is consistent with the concept that transverse vibrations are attended by a decrease in the axial length of the molecule (the projection of the molecular skeleton contour onto the molecular axis) due to a tilting of nonstretchable chemical bonds in the molecular skeleton (and, hence, by a decrease in their projection onto the molecular axis).

However, we should emphasize the following circumstance. The inference regarding the bond nonstretchability in the course of transverse vibrations holds true only under the assumption that the end points of the bending molecular segment execute a free longitudinal displacement. This assumption seems to be unrealistic, casts some doubt on the conclusion that the interatomic bonds are nonstretchable, and stimulates elucidation of the question as to how the transverse vibrations of the molecule under consideration affect the molecular skeleton in polymer crystals.

In earlier works [6–8], the longitudinal thermal contraction of polymer crystals was measured from the thermally induced angular displacement of the meridional reflections in x-ray diffraction experiments. However, these measurements do not provide a clear understanding of the behavior of the contour length of the molecular skeleton.

In recent years, thermal phenomena in polymer crystals have been investigated using IR and Raman spectroscopy [9–12]. It has been found that the shifts in the frequency of vibrations of the molecular skeleton

under temperature variations correspond to an increase in the thermal expansion of the molecular skeleton upon heating. This gives a more realistic idea of the nature of the phenomena under investigation: transverse vibrations of molecules in polymer crystals bring about two effects, namely, a decrease in the axial length and a simultaneous increase in the contour length.

As far as we know, theoretical treatment of the expansion of a molecular skeleton due to transverse vibrations has never been performed before.

In this work, we undertook a combined experimental investigation into the thermal behavior of polymer crystals with the use of IR and Raman spectroscopy and x-ray diffraction and carried out a theoretical analysis of the deformation of the molecular skeleton in the course of transverse vibrations.

2. EXPERIMENTAL TECHNIQUE

The uniaxially oriented crystallizing polymers poly(ethylene) (PE) and poly(caproamide) (PCA) were chosen as the objects of our investigation. The crystallite (longitudinal and transverse) sizes in these polymers were approximately equal to 10–20 nm.

The shifts of the band at 1130 cm^{-1} in the spectra of PE and the band at 930 cm^{-1} in the spectra of PCA (the frequencies of the bands are given at 298 K) were determined using Raman and IR spectroscopy, respectively. These regularity bands correspond to vibrations of the carbon skeleton of molecules in the form of *trans–trans* regular sequences [13, 14]. The IR spectra were recorded on DS-403G and Specord 75IR spectrophotometers. The Raman spectra were measured on a Ramalog-5 spectrophotometer. The spectral measurements were performed in the temperature range from 90 to 500 K. The bandwidth of the spectral slit was equal to 1 cm^{-1} and did not exceed ~0.25 of the halfwidth of the bands at 90 K. For this reason, the distortion of the band shape due to the bandwidth of the spectral slit was no more than 10%. With the aim of minimizing dynamic distortions, the scanning velocity did not exceed 1 $(cm\ min)^{-1}$. The spectra were processed with inclusion of the distortions caused both by radiation of the sample and the cell at high temperatures [15] and by the overlap of band wings.

The angular displacements of the meridional (i.e., along the axes of chain molecules in the crystals) reflections (002) for PE and (0140) for PCA were measured using x-ray diffraction in the temperature range from 5 to 450 K. The measurements were performed on DRON-1 and DRON-3 x-ray diffractometers with the use of filtered CuK_α radiation ($\lambda = 0.154$ nm) and MoK_α radiation ($\lambda = 0.071$ nm). The instrumental angular collimation width was 2′.

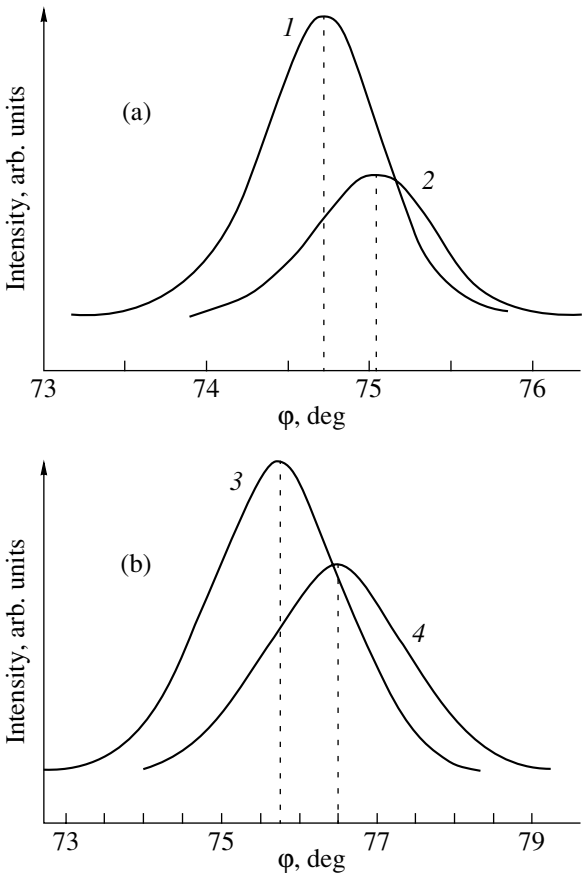

Fig. 1. Meridional x-ray reflections (CuK_α radiation): (a) (002) for PE at (*1*) 5 and (*2*) 347 K and (b) (0140) for PCA at (*3*) 5 and (*4*) 413 K.

3. X-RAY DIFFRACTION DATA

The shifts of the meridional reflections with an increase in the temperature from 5 to 450 K were measured using reflections of two orders for the purpose of obtaining more reliable data.

Figure 1 shows the angular contour of the meridional reflections for PE and PCA at two temperatures. It can be seen that an increase in the temperature results in a shift of the reflections toward the large-angle range. According to the Bragg equation, this direction of the shift implies a contraction of the PE and PCA crystal lattices in the longitudinal direction (along the molecular axis).

The temperature dependences of the longitudinal thermal contraction $\varepsilon_\parallel$ of the PE and PCA crystal lattices were determined from the temperature dependences of the angular position of the meridional reflections. The strain was calculated from the expression derived by differentiating the Bragg equation, that is,

$$\varepsilon(T) = \frac{\Delta d(T)}{d} = -\frac{\Delta\varphi_m(T)}{2\tan\dfrac{\varphi_m}{2}},$$

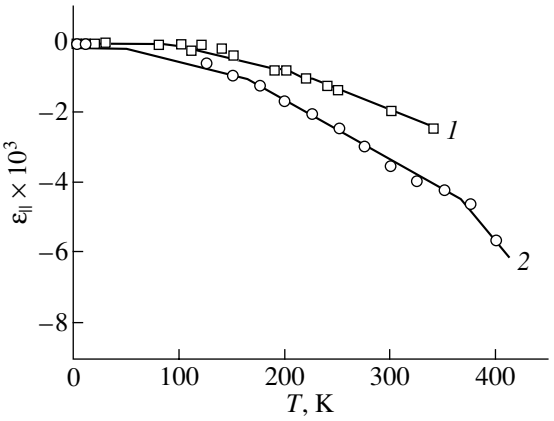

Fig. 2. Temperature dependences of the thermal component of the longitudinal contraction of the (*1*) PE and (*2*) PCA lattices.

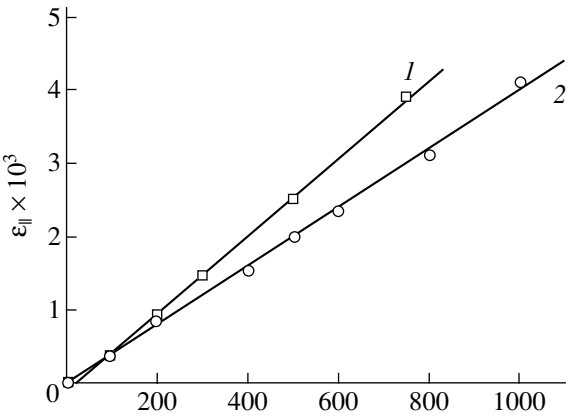

Fig. 3. Dependences of the longitudinal expansion of the (*1*) PE and (*2*) PCA lattices on the tensile stress at 110 K.

where d and $\Delta d(T)$ are the interplanar distance and its change with an increase in the temperature, respectively; and φ_m and $\Delta\varphi_m(T)$ are the angular position of the reflection and its change with an increase in the temperature, respectively. The value of $\Delta\varphi_m(T)$ is reckoned from φ_m at $T = 0$. This allows us to determine directly only the thermal component of the expansion.

The dependences $\varepsilon_{\|}(T) = \Delta d_{\|}(T)/d_{\|}$ for PE and PCA are depicted in Fig. 2. These dependences are similar to each other and exhibit a nonlinear behavior: the longitudinal contraction more steeply increases with an increase in the temperature. The nonlinearity is associated with the sequential quantum defreezing initially of torsional and then bending transverse vibrations responsible for the longitudinal contraction of the crystal lattice [12].

The thermal longitudinal contraction of the polymer crystal lattice due to transverse vibrations implies that the projection of the macromolecular skeleton contour onto the molecular axis (i.e., the axial length of the macromolecule) decreases as the temperature increases. As was noted above, information on the effect of the temperature on the contour length of the molecular skeleton cannot be obtained from the x-ray diffraction data.

On the other hand, the change in the contour length of the molecular skeleton under the force (rather than thermal) action on the lattice can be determined by x-ray diffraction. An increase in the longitudinal tensile stress (especially at low temperatures when the transverse vibrations are not excited) necessarily leads to expansion of the carbon skeleton of molecules in the lattice. The longitudinal tensile stress results in angular displacements of the meridional reflections but (unlike the thermally induced displacements of reflections) toward the small-angle range [16]. The experimental dependences of the longitudinal expansion of the PE and PCA lattices on the tensile stress at a low temperature (110 K) are plotted in Fig. 3. The longitudinal elastic moduli $E_{\|} = (\Delta\varepsilon_{\|}/\Delta\sigma)^{-1} \approx 200$–$250$ GPa calculated from the slopes of the linear dependences $\varepsilon_{\|}(\sigma)$ are close to the theoretical values of the longitudinal elastic moduli of polymer molecules with a carbon-chain skeleton [16]. This confirms the inference regarding the expansion of the molecular skeletons under tensile stress.

The dependences $\varepsilon_{\|}(\sigma)$ measured for PE and PCA will be used in the analysis of the spectroscopic data.

4. IR AND RAMAN SPECTROSCOPIC DATA

As an illustration, Fig. 4 shows the band at 1130 cm^{-1} in the Raman spectra of PE at temperatures of 90 and 350 K and the band at 930 cm^{-1} in the IR spectra of PCA at temperatures of 90 and 450 K. It can be seen from Fig. 4 that an increase in the temperature leads to a shift in the maxima of the bands toward the low-frequency range. The temperature dependences of the shift in the frequency $\Delta\nu(T)$ for PE and PCA are depicted in Fig. 5.

A question now arises as to the origin of the observed temperature shift in the frequencies. In order to elucidate this question, we measured the spectra of the same polymers but under tensile stresses rather than under temperature variations. The evolution of the Raman spectra of PE is illustrated in Fig. 6. It can be seen from Fig. 6 that, in this case, too, the band is shifted toward the low-frequency range. As was noted above, the tensile stress results in expansion of the molecular skeleton. Therefore, the shift in the maxima of the bands toward the low-frequency range with an increase in the temperature is caused by the expansion of the molecular skeleton. The dependence of the longitudinal expansion of the molecular skeleton on the tensile stress (Fig. 3) and data analogous to that presented in Fig. 6 can be used to "calibrate" the frequency shifts, i.e., to construct the depen-

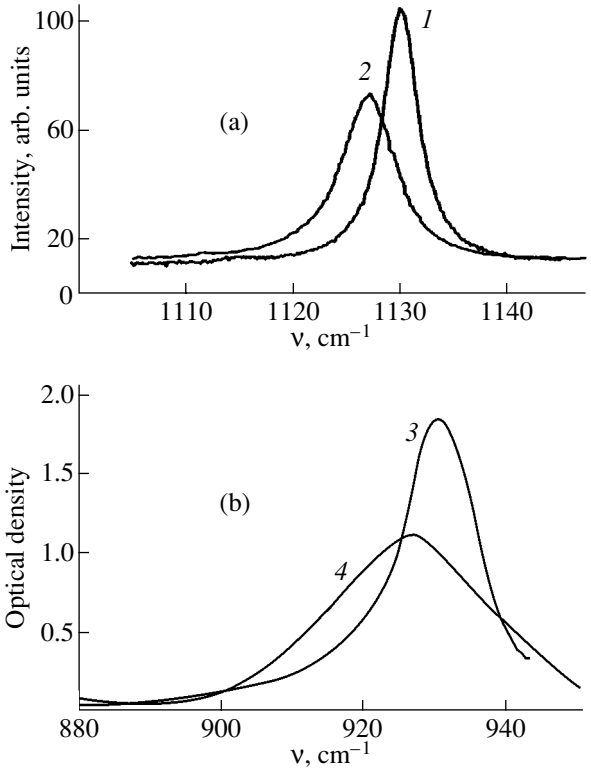

Fig. 4. (a) Band at 1130 cm^{-1} in the Raman spectra of PE at (*1*) 90 and (*2*) 350 K and (b) band at 930 cm^{-1} in the IR spectra of PCA at (*3*) 90 and (*4*) 450 K.

dence of the frequency shift $\Delta\nu$ on the expansion ε_C of the molecular skeleton. The calibration curves thus obtained are plotted in Fig. 7.

As a result, we obtained the frequency shifts $\Delta\nu = 1470\varepsilon_C$ for the band at 1130 cm^{-1} in the Raman spectrum of PE and $\Delta\nu = 925\varepsilon_C$ for the band at 930 cm^{-1} in the IR spectrum of PCA.

The shift in the frequency of the C–C stretching vibrations under uniaxial tensile stresses was investigated experimentally and theoretically in [17–28]. It was demonstrated that the relative frequency shift is proportional to the expansion of the molecular skeleton and the Grüneisen parameter is the proportionality coefficient. The curves $\Delta\nu(\varepsilon_C)$ obtained in the present work agree with the results reported in [17–28].

The calibration curves $\Delta\nu(\varepsilon_C)$ (Fig. 7) can be used to transform the dependences shown in Fig. 5 into temperature dependences of the longitudinal expansion $\varepsilon_C(T)$. These dependences are depicted in Fig. 8.

As can be seen, the temperature dependences of the longitudinal expansion of the molecular skeleton exhibit a nonlinear behavior: the slope of the curves $\varepsilon_C(T)$ increases with an increase in the temperature. Since the expansion of the molecular skeleton (like the contraction of the crystal lattice) is associated with the transverse vibrations, the nonlinearity of the dependence $\varepsilon_C(T)$ is caused by the sequential quantum defreezing of the transverse vibrations, as is the case with the nonlinearity of the dependence $\varepsilon_{\|}(T)$.

Note that the values of ε_C and $\varepsilon_{\|}$ are comparable in magnitude (Figs. 2, 8).

Thus, there are grounds to believe that, with an increase in the temperature, the transverse vibrations of molecules in polymer crystals bring about both longitudinal contraction of the lattice and expansion of the molecular skeleton.

In closing the experimental section, it should be noted that an increase in the temperature and the tensile stress lead to angular displacements of the x-ray diffraction reflections in opposite directions. At the same time, similar changes in the temperature and the tensile stress result in frequency shifts of the bands in the Raman and IR spectra in one direction (toward the low-frequency range). This is associated with the difference in the thermal behavior of the lattice and its constituent chain molecules.

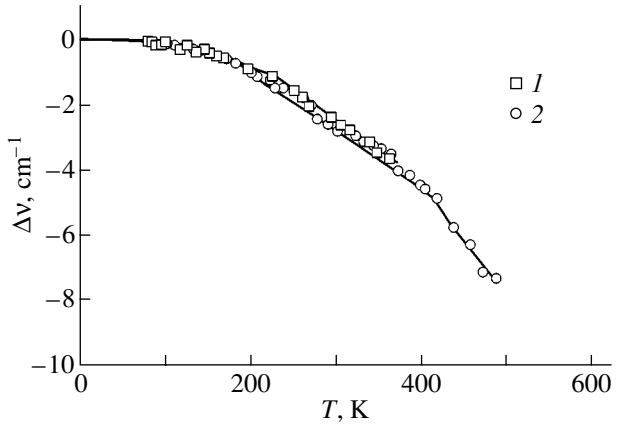

Fig. 5. Temperature dependences of the shift in the frequency of stretching vibrations of (*1*) PE and (*2*) PCA molecules.

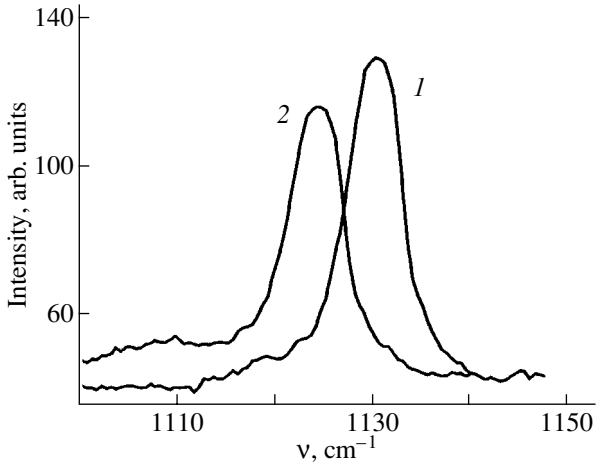

Fig. 6. Band at 1130 cm^{-1} in the Raman spectra of PE: (*1*) unloaded sample and (*2*) the same sample at a tensile stress of 1 GPa. T = 300 K.

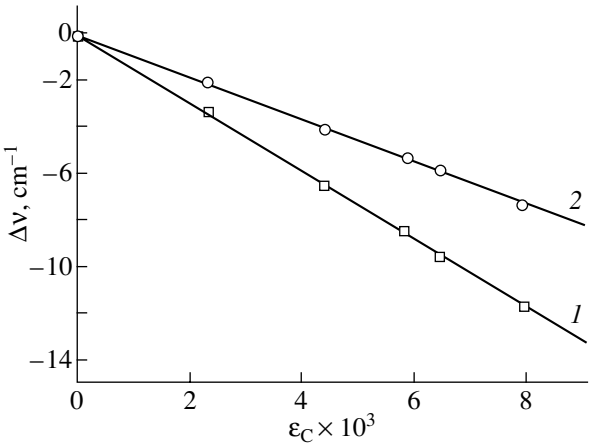

Fig. 7. Dependences of the shift in the frequency of C–C stretching vibrations on the expansion of the carbon skeleton of (*1*) PE and (*2*) PCA molecules under a load.

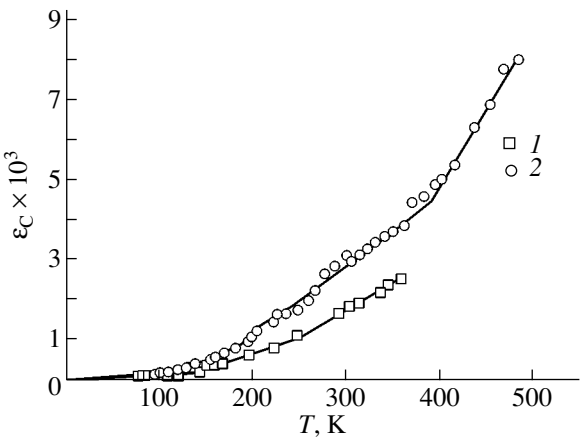

Fig. 8. Temperature dependences of the expansion of the carbon skeleton of (*1*) PE and (*2*) PCA molecules.

5. CALCULATION OF THE AVERAGE CONTOUR LENGTH OF AN ATOMIC CHAIN EXECUTING THERMAL VIBRATIONS

The average contour length will be calculated within a straight chain model with allowance made for the longitudinal rigidity of interatomic bonds and the flexural rigidity of the chain. Calculations in the framework of this model were previously carried out in [4, 29, 30]. However, in those works, attention was focused on the determination of the axial length of a chain executing transverse vibrations (i.e., the negative longitudinal expansion of polymer crystals) and the contour length was not analyzed. Below, we will calculate just the contour length.

The average contour length is calculated as the sum of the lengths of individual bond in a molecule. We introduce the following designations: a is the initial bond length and $r_{n,n-1}$ is the length of the nth bond in the vibrating chain. Then, the elongation of the bond can be written in the form $\Delta a_n = r_{n,n-1} - a$. The average elongation per unit length of the bond and, hence, the entire contour length of the chain can be represented as

$$\varepsilon_C = \frac{1}{a}\langle \Delta a_n \rangle.$$

Our problem here is to determine the average elongation $\langle \Delta a_n \rangle$.

The average value of any dynamic quantity q in the classical temperature range can be calculated from the general formula

$$\langle q \rangle = \frac{\int q e^{-\beta H} d\Gamma}{\int e^{-\beta H} d\Gamma}. \quad (1)$$

Here, H is the Hamiltonian of the system, $\beta = 1/kT$, q is the averaged quantity (in our case, the elongation Δa_n of the nth bond), and $d\Gamma$ is the elementary phase volume.

The Hamiltonian of the system under consideration has the form

$$H = \sum_n \left[\frac{1}{2}K_s \Delta a_n^2 + \frac{1}{2}K_b \Delta \varphi_n^2\right], \quad (2)$$

where K_s is the elastic constant of bonds in the chain, K_b is the elastic constant of the bond angle, and $\Delta\varphi_n$ is the change in the bond angle. In our model, allowance is made only for the interaction of nearest neighbor atoms.

It is assumed that, in this case, the z axis is aligned parallel to the chain axis and the x axis is perpendicular to the chain axis. The bond strain can be determined to the third order in atomic displacements from the formula

$$\Delta a_n = r_{n,n-1} - a \approx z_{n,n-1} + \frac{x_{n,n-1}^2}{2a} - \frac{z_{n,n-1}x_{n,n-1}^2}{2a}, \quad (3)$$

where $z_{n,n-1}$ and $x_{n,n-1}$ are the relative displacements of nearest neighbor atoms along the z and x axes, respectively. The change in the bond angle can be written as

$$\Delta\varphi_n = \arcsin\left(\frac{x_{n,n+1}}{r_{n,n+1}}\right) - \arcsin\left(\frac{x_{n,n-1}}{r_{n,n-1}}\right). \quad (4)$$

The difference between our model and the models considered in earlier works [4, 29, 30] lies in the subsequent treatment of the quantity $\Delta\varphi_n$. In particular, Chen *et al.* [4] included only terms up to the second order in the expansion of the quantity $\Delta\varphi_n$ and assumed that the bonds are nonstretchable (i.e., $\Delta r_{n,n-1} = \Delta r_{n,n+1} = a$).

In this work, we do not make such assumptions. Relationship (4) is expanded into a series to the third order in atomic displacements. As a result, we determine the bond strains induced by the transverse vibrations of atoms in the chain.

Since expansions (3) and (4) contain terms of the third order in atomic displacements, Hamiltonian (2) can be represented as the sum of two components: the harmonic component Q involving the quadratic terms and the anharmonic component A including the higher order terms. As usual, we assume that the anharmonic component is sufficiently small in magnitude. Hence, from expression (1), we obtain the average elongation $\langle \Delta a_n \rangle$ in the form

$$\langle \Delta a_n \rangle \approx \frac{\int \Delta a_n e^{-\beta Q}(1-\beta A)d\Gamma}{\int e^{-\beta Q}(1-\beta A)d\Gamma} = \langle \Delta a_n \rangle_0 + \beta \langle \Delta a_n \rangle_0 \langle A \rangle_0 - \beta \langle \Delta a_n A \rangle_0. \quad (5)$$

Here, $\langle \ldots \rangle_0$ indicates averaging with the use of the harmonic Hamiltonian Q.

Further analysis requires knowledge of the Hamiltonian A in an explicit form. The anharmonic Hamiltonian A can be written as the sum of two components:

$$A = A_r + A_\varphi,$$

where A_r is the component related to the potential of the bond elasticity and A_φ is the component governed by the potential of the strain caused by the change in the bond angle.

The component related to the bond strain can be calculated to the third order in atomic displacements by the expression

$$A_r = \frac{K_s}{2}\sum_n \left[\frac{z_{n,n-1}x^2_{n,n-1}}{a}\right]. \quad (6)$$

The component associated with the chain bending is determined to the third order in atomic displacements from the formula

$$A_\varphi = \frac{K_b}{2}\sum_k \left[-\frac{2x^2_{k,k-1}z_{k,k-1}}{a} - \frac{2x^2_{k,k+1}z_{k,k+1}}{a} + \frac{2z_{k,k+1}x_{k,k+1}x_{k,k-1}}{a} + \frac{2z_{k,k-1}x_{k,k+1}x_{k,k-1}}{a}\right]. \quad (7)$$

Next, we can calculate the average values of the terms in relationship (5).

As follows from expression (3), the first term $\langle \Delta a_n \rangle_0$ has the form

$$\langle \Delta a_n \rangle_0 \approx \frac{\langle x^2_{n,n-1} \rangle}{2a}. \quad (8)$$

Expression (8) contains the contribution only from the second term in formula (3), because the first and third terms are odd functions and, hence, do not make a contribution.

The second term in relationship (5) does not involve terms linear in temperature, because it is equal to the product of the quantity given by expression (8) (linear in temperature) and the sum of the averages of the anharmonic Hamiltonian components (6) and (7) containing only terms that are quadratic in temperature. As a result, the second term in relationship (5) is of the second order in temperature and, hence, is small.

The third term in relationship (5) can be represented as $\beta\langle \Delta a_n A \rangle_0 = \beta\langle \Delta a_n A_r \rangle_0 + \langle \Delta a_n A_\varphi \rangle_0$. The term $\beta\langle \Delta a_n A_r \rangle_0 = \beta\langle z_{n,n-1}A_r \rangle_0 \approx \langle \Delta a \rangle_0$ was calculated to the first order in temperature in [4]. It can be seen that, making allowance for its sign in relationship (5), this term cancels the first term [defined by expression (8)] in relationship (5). Consequently, the term $\langle \Delta a_n A_\varphi \rangle_0$ makes the dominant contribution.

Taking into account relationship (7), the contribution linear in temperature to the average bond strain has the form

$$\langle \Delta a_k A_\varphi \rangle_0 \approx \left\langle z_{k,k-1}\frac{K_b}{2} \times \sum_k \left[-\frac{2x^2_{k,k-1}z_{k,k-1}}{a} - \frac{2x^2_{k,k+1}z_{k,k+1}}{a} + \frac{2z_{k,k+1}x_{k,k+1}x_{k,k-1}}{a} + \frac{2z_{k,k-1}x_{k,k+1}x_{k,k-1}}{a}\right]\right\rangle_0. \quad (9)$$

The contribution to the bond strain is made by only the first two terms in expression (9), because the last two terms are odd functions of the displacements. In our calculations, we invoked the results obtained by Chen *et al.* [4]. Expression (9) coincides in form with the relationship obtained for $\langle \Delta z_{n,n-1} \rangle$ in [4] with an accuracy up to factors. After reducing to the normal modes and calculating the longitudinal and transverse integrals, the quantity defined by expression (9) turns out to be proportional to the temperature squared.

As a result, relationship (5) with due regard for the factor β takes the form

$$\langle \Delta a_n \rangle \approx \frac{2kT}{aK_s}\frac{K_b}{K_e}. \quad (10)$$

The effective force constant K_e introduced in [4] accounts for the contribution of the spatial dispersion of bending vibrations and the intermolecular interaction of atomic chains. Chen *et al.* [4] proved that $K_e \approx K_b$. Consequently, for the bond strain, we have

$$\varepsilon_C = \frac{\langle \Delta a_n \rangle}{a} \approx \frac{2kT}{K_s}.$$

Thus, the results of the above analysis can be summarized as follows: (1) It was established that the transverse vibrations lead to the elongation of bonds in the chain and, hence, to an increase in the average contour length of the skeleton of the chain (polymer) molecule. (2) The approximate relationship for the average elongation of bonds in the chain as a function of the temperature was derived.

6. COMPARISON OF THEORETICAL AND EXPERIMENTAL DATA

Let us estimate the thermal expansion of the chain with the use of relationship (10) at $T = 300$ K, $K_s = 400$ N/m (this value is taken from [31]), and $a \approx 1.3 \times 10^{-10}$ m (the axial length of the C–C bond). As a result, we obtain $\langle \varepsilon_C \rangle \approx 1.5 \times 10^{-3}$. The measured thermal expansion of the carbon skeleton of molecules at $T = 300$ K (Fig. 8) is approximately equal to 1.7×10^{-3} for PE and 2.7×10^{-3} for PCA. As can be seen, the calculated value of $\langle \varepsilon_C \rangle$ is in reasonable agreement with the experimental data on the thermal expansion of molecular carbon skeletons.

Thus, the measured expansion of the skeleton of the chain molecules in the crystal due to transverse vibrations is confirmed by the results of calculations.

It should be emphasized that our calculations were carried out for the atomic chain rather than for one vibrating bond, which permitted us to take into account the interaction of atoms along the chain. In turn, this made it possible to elucidate the origin of the bond elongation, i.e., the emergence of longitudinal tensile forces induced by the transverse vibrations. Upon transverse displacement of any atom, the nearest and next-to-nearest neighbor atoms along the chain offer resistance to longitudinal shear, which gives rise to a tensile force and, as a consequence, expansion (elongation) of the bond. To put it differently, longitudinal displacements of atoms are not free when their neighbors are displaced in the transverse direction. This mechanism of expansion of the skeleton of the chain molecule can be referred to as the "quasi-string" mechanism (by analogy with a string with fixed ends that must necessarily extend upon transverse displacement of its central segment).

ACKNOWLEDGMENTS

This work was supported by the Russian Foundation for Basic Research, project no. 00-03-33064a.

REFERENCES

1. Yu. K. Godovskiĭ, *Thermal Physics of Polymers* (Khimiya, Moscow, 1982).
2. A. I. Slutsker, L. A. Laĭus, I. V. Gofman, *et al.*, Fiz. Tverd. Tela (St. Petersburg) **43** (7), 1327 (2001) [Phys. Solid State **43**, 1382 (2001)].
3. I. M. Lifshitz, Zh. Éksp. Teor. Fiz. **22** (4), 475 (1952).
4. F. C. Chen, C. L. Choy, and K. Young, J. Polym. Sci., Polym. Phys. Ed. **18**, 2313 (1980).
5. F. C. Chen, C. L. Choy, S. P. Wang, and K. Young, J. Polym. Sci., Polym. Phys. Ed. **19**, 971 (1980).
6. J. H. Wakelin, A. Sutherland, and L. R. Beck, Polym. Sci. **42** (1), 278 (1960).
7. J. Kobajashi and A. Keller, Polymer **11** (1), 114 (1970).
8. G. Dadobaev and A. I. Slutsker, Fiz. Tverd. Tela (Leningrad) **23** (8), 1936 (1981) [Sov. Phys. Solid State **23**, 1131 (1981)].
9. S. V. Bronnikov, V. I. Vettegren, and S. Ya. Frenkel, Polym. Eng. Sci. **32**, 1204 (1992).
10. V. I. Vettegren, L. S. Titenkov, and S. V. Bronnikov, J. Therm. Anal. **38**, 1031 (1992).
11. V. I. Vettegren, V. B. Kulik, L. S. Titenkov, and N. L. Zaalishvili, Vysokomol. Soedin., Ser. A **44** (6), 933 (2002).
12. A. I. Slutsker, V. I. Vettegren, V. L. Gilyarov, *et al.*, Fiz. Tverd. Tela (St. Petersburg) **44** (10), 1847 (2002) [Phys. Solid State **44**, 1936 (2002)].
13. P. C. Painter, M. Coleman, and J. L. Koenig, *The Theory of Vibrational Spectroscopy and Its Application to the Polymeric Materials* (Wiley, New York, 1986).
14. J. Dechant, R. Danz, W. Kimmer, and R. Schmolke, *Ultrarotspectroscopische Untersuchungen an Polymeren* (Akademie, Berlin, 1972).
15. V. I. Vettegren, L. S. Titenkov, and R. R. Abdul'manov, Zh. Prikl. Spektrosk. **41** (2), 251 (1984).
16. I. Sakurada, T. Ito, and K. Nakamae, J. Polym. Sci., Part C: Polym. Lett. **15**, 75 (1966).
17. V. I. Vettegren and K. Yu. Fridlyand, Opt. Spektrosk. **38**, 521 (1975) [Opt. Spectrosc. **38**, 294 (1975)].
18. V. E. Korsukov, V. I. Vettegren, and I. N. Novak, Mekh. Polim., No. 1, 167 (1970).
19. V. E. Korsukov and V. I. Vettegren, Probl. Prochn., No. 2, 51 (1970).
20. V. I. Vettegren and I. I. Novak, J. Polym. Sci., Polym. Phys. Ed. **11** (10), 2135 (1973).
21. R. P. Wool and R. S. Bretzlaff, J. Polym. Sci., Part B: Polym. Phys. **24**, 1039 (1986).
22. D. T. Grubb and Z.-F. Li, Polymer **33**, 2587 (1992).
23. R. J. Meier and H. Vansweefelt, Polymer **36**, 3825 (1995).
24. K. Tashiro, G. Wu, and M. Kobayashi, Polymer **29**, 1768 (1988).
25. L. Berger, Doctoral Scientific and Technical Thesis No. 1704 (EPFL, Lausanne, 1997).
26. A. I. Gubanov and V. A. Kosobukin, Mekh. Polim., No. 1, 33 (1975).
27. V. A. Kosobukin, Mekh. Polim., No. 1, 3 (1972).
28. V. A. Kosobukin, Mekh. Polim., No. 4, 579 (1971).
29. W. H. Stockmayer and C. E. Hecht, J. Chem. Phys. **21**, 1954 (1953).
30. A. I. Slutsker, V. L. Gilyarov, G. Dadobaev, *et al.*, Fiz. Tverd. Tela (St. Petersburg) **44** (5), 923 (2002) [Phys. Solid State **44**, 964 (2002)].
31. K. Bann, Trans. Faraday Soc. **35**, 482 (1939).

Translated by O. Borovik-Romanova